



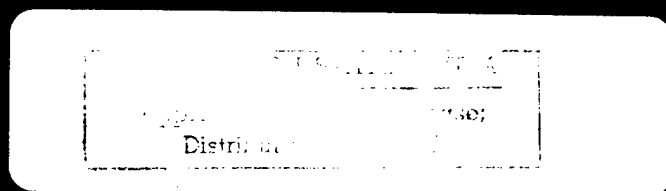
MATERIALS
RESEARCH
SOCIETY
SYMPOSIUM PROCEEDINGS

Volume 478

Thermoelectric Materials—New Directions and Approaches

EDITORS

**Terry M. Tritt
Mercouri G. Kanatzidis
Hylan B. Lyon, Jr.
Gerald D. Mahan**



**Thermoelectric Materials—
New Directions and Approaches**

DTIC QUALITY INSPECTED 5

19980721 090

**MATERIALS RESEARCH SOCIETY
SYMPOSIUM PROCEEDINGS VOLUME 478**

Thermoelectric Materials— New Directions and Approaches

Symposium held March 31–April 3, 1997, San Francisco, California, U.S.A.

EDITORS:

Terry M. Tritt
*Clemson University
Clemson, South Carolina, U.S.A.*

Mercouri G. Kanatzidis
*Michigan State University
East Lansing, Michigan, U.S.A.*

Hylan B. Lyon, Jr.
*Marlow Industries
Dallas, Texas, U.S.A.*

Gerald D. Mahan
*University of Tennessee
Knoxville, Tennessee, U.S.A.*

DISTRIBUTION STATEMENT A

**Approved for public release;
Distribution Unlimited**



PITTSBURGH, PENNSYLVANIA

This work was supported in part by the Army Research Office under Grant Number ARO: DAAG55-97-1-1025. The views, opinions, and/or findings contained in this report are those of the author(s) and should not be construed as an official Department of the Army position, policy, or decision, unless so designated by other documentation.

This work was supported in part by the Office of Naval Research under Grant Number ONR: N00014-97-1-0164. The United States Government has a royalty-free license throughout the world in all copyrightable material contained herein.

Single article reprints from this publication are available through University Microfilms Inc., 300 North Zeeb Road, Ann Arbor, Michigan 48106

CODEN: MRSPDH

Copyright 1997 by Materials Research Society.
All rights reserved.

This book has been registered with Copyright Clearance Center, Inc. For further information, please contact the Copyright Clearance Center, Salem, Massachusetts.

Published by:

Materials Research Society
506 Keystone Drive
Warrendale,, Pennsylvania 15086
Telephone (412) 779-3003
Fax (412) 779-8313
Website: <http://www.mrs.org/>

Library of Congress Cataloging in Publication Data

Thermoelectric materials—new directions and approaches : symposium held March 31–April 3, 1997, San Francisco, California, U.S.A. / editors, Terry M. Tritt, Mercouri G. Kanatzidis, Hylan B. Lyon, Jr., Gerald D. Mahan p. cm—(Materials Research Society symposium proceedings ; v. 478)
Includes bibliographical references and index.
ISBN 1-55899-382-7

I. Thermoelectric materials—Congresses. I. Tritt, Terry M.

II. Kanatzidis, Mercouri G. III. Lyon, Jr., Hylan B. IV. Mahan, Gerald D.

V. Series: Materials Research Society symposium proceedings ; v. 478.

TK2950.T49 1997

97-22698

620.1'1296—dc21

CIP

Manufactured in the United States of America

CONTENTS

Preface	ix
Acknowledgments	xi
Material Research Society Symposium Proceedings	xii
The Thermoelectric Process	3
<i>C.B. Vining</i>	
Selection and Evaluation of Materials for Thermoelectric Applications II	15
<i>Jeff W. Sharp</i>	
Measurement and Characterization Techniques for Thermoelectric Materials	25
<i>Terry M. Tritt</i>	
Experimental Transport Phenomena and Optimization Strategies for Thermoelectrics	37
<i>A.C. Ehrlich and D.J. Gillespie</i>	
*Design Concepts for Improved Thermoelectric Materials	47
<i>Glen A. Slack</i>	
*Prospects for High Thermoelectric Figures of Merit in 2D Systems	55
<i>M.S. Dresselhaus, X. Sun, S.B. Cronin, T. Koga, G. Dresselhaus, and K.L. Wang</i>	
Thermoelectric Power of Bi and Bi_{1-x}Sb_x Alloy Thin Films and Superlattices Grown by MBE	67
<i>Sunglae Cho, Antonio DiVenere, George K. Wong, John B. Ketterson, Jerry R. Meyer, and Craig A. Hoffman</i>	
*Enhancement in Figure of Merit With Superlattice Structures for Thin-Film Thermoelectric Devices	73
<i>R. Venkatasubramanian and T. Colpitts</i>	
Thermal Conductivity and Heat Transfer in Superlattices	85
<i>G. Chen, M. Neagu, and T. Borca-Tasciuc</i>	
*Studies of Bulk Materials for Thermoelectric Cooling	91
<i>Jeff W. Sharp, George S. Nolas, and Edward H. Volckmann</i>	
Thermal Conductivity of Zn_{4-x}Cd_xSb₃ Solid Solutions	103
<i>T. Caillat, A. Borshchevsky, and J-P. Fleurial</i>	

*Invited Paper

A New Class of Materials With Promising Thermoelectric Properties: $MNiSn$ ($M = Ti, Zr, Hf$)	109
<i>H. Hohl, A.P. Ramirez, W. Kaefer, K. Fess, Ch. Thurner, Ch. Kloc, and E. Bucher</i>	
Development of Bi-Sb-Te Ternary Alloy With Compositionally Graded Structure	115
<i>A. Yamamoto and T. Ohta</i>	
Thermoelectric Properties of p-Type $(Bi_{1-x}Sb_x)_2Te_3$ Fabricated by Mechanical Alloying Process	121
<i>Boo Yang Jung, Jae Shik Choi, Tae Sung Oh, and Dow-Bin Hyun</i>	
Microstructural and Thermoelectric Properties of p-Type Te-Doped $Bi_{0.5}Sb_{1.5}Te_3$ and n-Type SbI₃-Doped $Bi_2Te_{2.85}Se_{0.15}$ Compounds	127
<i>J. Seo, K. Park, C. Lee, and J. Kim</i>	
The Enhancement of Thermoelectric Power and Scattering of Carriers in $Bi_{2-x}Sn_xTe_3$ Single Crystals	133
<i>V.A. Kulbachinskii, H. Negishi, M. Sasaki, Y. Giman, and M. Inoue</i>	
Microstructure, Mechanical Properties, and Thermoelectric Properties of Hot-Extruded p-Type Te-Doped $Bi_{0.5}Sb_{1.5}Te_3$ Compounds	139
<i>K. Park, J. Seo, and C. Lee</i>	
Thermoelectric Properties of ZnSb Films Grown by MOCVD	145
<i>R. Venkatasubramanian, E. Watko, and T. Colpitts</i>	
Thermoelectric Properties of n-Type $Bi_2(Te_{1-x}Se_x)_3$ Fabricated by Mechanical Alloying and Hot Pressing	151
<i>Hee-Jeong Kim, Jae-Shik Choi, Tae-Sung Oh, and Dow-Bin Hyun</i>	
*Thermoelectric Properties of $M_2Mo_6Se_6$ ($M = Ti, In$)	157
<i>D.T. Verebelyi, J.E. Payne, G.X. Tessema, and E. Mangistu</i>	
Thermoelectric Transport in Superlattices	161
<i>T.L. Relnecke and D.A. Broido</i>	
Quantum Confinement Effects on the Thermoelectric Figure of Merit in $Si/Si_{1-x}Ge_x$ System	169
<i>X. Sun, M.S. Dresselhaus, K.L. Wang, and M.O. Tanner</i>	
*Low Thermal Conductivity Skutterudites	175
<i>J-P. Fleurial, T. Caillat, and A. Borshchevsky</i>	
*Computational Studies of Novel Thermoelectric Materials	187
<i>D.J. Singh, I.I. Mazin, S.G. Kim, and L. Nordstrom</i>	

*Invited Paper

*Filled Skutterudite Antimonides: Validation of the Electron-Crystal Phonon-Glass Approach to New Thermoelectric Materials	199
<i>D. Mandrus, B.C. Sales, V. Keppens, B.C. Chakoumakos, P. Dai, L.A. Boatner, R.K. Williams, J.R. Thompson, T.W. Darling, A. Migliori, M.B. Maple, D.A. Gajewski, and E.J. Freeman</i>	
Synthesis of New Thermoelectrics Using Modulated Elemental Reactants	211
<i>Marc D. Hornbostel, Heike Sellinshcgg, and David C. Johnson</i>	
Properties of CoSb₃ Films Grown by Pulsed Laser Deposition	217
<i>Hans-Martin Christen, David G. Mandrus, David P. Norton, Lynn A. Boatner, and Brian C. Sales</i>	
*Rare-Earth Thermoelectrics	223
<i>G.D. Mahan</i>	
Optimization of Materials for Thermomagnetic Cooling	231
<i>A. Migliori, T.W. Darling, F. Freibert, S.A. Trugman, E. Moshopoulou, and J.L. Sarrao</i>	
Thermoelectric Behavior of Conducting Polymers: On the Possibility of "Off-Diagonal" Thermoelectricity	243
<i>N. Mateeva, H. Niculescu, J. Schlenoff, and L. Testardi</i>	
Electrical Transport Properties of the Pentatelluride Materials HfTe₅ and ZrTe₅	249
<i>T.M. Tritt, M.L. Wilson, R.L. Littleton, Jr., C. Feger, J. Kolis, A. Johnson, D.T. Verebelyi, S.J. Hwu, M. Fakhruddin, and F. Levy</i>	
*Thermopower, Electrical, and Hall Conductivity of Undoped and Doped Iron Disilicide Single Crystals	255
<i>A. Heinrich, G. Behr, H. Griessmann, S. Teichert, and H. Lange</i>	
Fabrication of p-β-Fe_{1-x}Mn_xSi₂/n-Si Heterostructure Diode and Their Electrical and Optical Properties	267
<i>T. Takada, H. Katsumata, Y. Makita, N. Kobayashi, M. Hasegawa, and S. Uekusa</i>	
Structural and Optical Properties of β-FeSi₂/Si(100) Prepared by Laser Ablation Method	273
<i>H. Kakemoto, Y. Makita, A. Obara, Y. Tsai, S. Sakuragi, S. Ando, and T. Tsukamoto</i>	
Thermoelectric Cooling Container for Medical Applications	279
<i>A.A. Aivazov, Y.I. Shtern, B.G. Budaguan, K.B. Makhachev, and M. Pastor</i>	

*Invited Paper

*Overview of Industry Interest in New Thermoelectric Materials	285
<i>H.B. Lyon, Jr.</i>	
*Advanced Thermoelectric Materials and Systems for Automotive Applications in the Next Millennium	297
<i>Donald T. Morelli</i>	
*Thermoelectric Applications as Related to Biomedical Engineering for NASA Johnson Space Center	309
<i>C.D. Kramer</i>	
Transport Properties of Partially-Filled $\text{Ce}_y\text{Co}_4\text{Sb}_{12}$	315
<i>C. Uher, B. Chen, S. Hu, D.T. Morelli, and G.P. Meisner</i>	
Measurement of the Thermoelectric Properties of Quasicrystalline AlPdRe and AlCuFe Alloys	321
<i>M.L. Wilson, S. LeGault, R.M. Stroud, and T.M. Tritt</i>	
Electrical Properties and Figures of Merit for New Chalcogenide-Based Thermoelectric Materials	327
<i>Jon L. Schindler, Tim P. Hogan, Paul W. Brazis, Carl R. Kannewurf, Duck-Young Chung, and Mercouri G. Kanatzidis</i>	
*Searching for New Thermoelectrics in Chemically and Structurally Complex Bismuth Chalcogenides	333
<i>Duck Young Chung, Tim Hogan, Jon Schindler, Lykourgos Iordanidis, Paul Brazis, Carl R. Kannewurf, Baoxing Chen, Ctirad Uher, and Mercouri G. Kanatzidis</i>	
Author Index	345
Subject Index	347

*Invited Paper

PREFACE

Thermoelectric materials are utilized in a wide variety of applications related to solid-state refrigeration or small-scale power generation. Thermoelectric cooling is an "environmentally friendly" method of small-scale cooling in specific applications such as cooling computer chips and laser diodes. Thermoelectric materials are used in a wide range of applications from beverage coolers to power generation for deep-space probes such as the Voyager missions. Over the past thirty years, alloys based on the Bi-Te systems $(\text{Bi}_{1-x}\text{Sb}_x)_2(\text{Te}_{1-x}\text{Se}_x)_3$ and $\text{Si}_{1-x}\text{Ge}_x$ systems have been extensively studied and optimized for their use as thermoelectric materials to perform a variety of solid-state thermoelectric refrigeration and power generation tasks. Despite this extensive investigation of the traditional thermoelectric materials, there is still a substantial need and room for improvement, and thus, entirely new classes of compounds will have to be investigated.

Over the past two-to-three years, research in the field of thermoelectric materials has been undergoing a rapid rebirth. The enhanced interest in better thermoelectric materials has been driven by the need for much higher performance and new temperature regimes for thermoelectric devices in many applications. The essence of a good thermoelectric is given by the determination of the material's dimensionless figure of merit, $ZT = (\alpha^2\sigma/\lambda)T$, where α is the Seebeck coefficient, σ the electrical conductivity and λ the total thermal conductivity. The best thermoelectric materials have a value of $ZT \approx 1$. This $ZT \approx 1$ has been an upper limit for more than 30 years, yet no theoretical or thermodynamic reason exists for why it can not be larger. The focus of the symposium is embodied in the title, "Thermoelectric Materials: New Directions and Approaches." Many of the researchers in the field believe that future advances in thermoelectric applications will come through research in new materials. We have many new methods of materials synthesis and much more rapid characterization of these materials than were available 20-to-30 years ago. We have tried to focus the symposium on new directions and new materials such as skutterudites, quantum well and superlattice structures, new metal chalcogenides, rare earth systems, and quasicrystals. Other new materials are also presented in these proceedings.

Many new researchers and new ideas are appearing in this field and this gives us cause for anticipation about the future of the field. It is the hope of the organizers of this symposium that these proceedings will provide a benchmark for where we are in the field as well as where we are going. These proceedings should also provide the background for new people in the field and will hopefully inspire even more directions and approaches for research than are presented here.

Terry M. Tritt
Mercouri G. Kanatzidis
Hylan B. Lyon, Jr.
Gerald D. Mahan

June 1997

ACKNOWLEDGMENTS

The organizers of Symposium Q, "Thermoelectric Materials: New Directions and Approaches," would like to acknowledge a number of people who made this symposium and proceedings possible. First, we would like to acknowledge Dr. John Pazik, of the Office of Naval Research, who has been a champion of the rebirth in this field and who helped in organizing this symposium in the early stages. Next, we would like to acknowledge the financial support of the Office of Naval Research, The Army Research Office, DARPA and the Naval Research Laboratory. We would like to also acknowledge the MRS staff who were essential in the success of our symposium. One of us (TMT) would like to acknowledge the secretarial support of Ms. Jennifer Wilson in assisting in all phases of putting the symposium and proceedings together. There are too many other people who had a part in the success of this symposium than we can mention, but their contributions are also very much appreciated.

MATERIALS RESEARCH SOCIETY SYMPOSIUM PROCEEDINGS

- Volume 438— Materials Modification and Synthesis by Ion Beam Processing, D.E. Alexander, N.W. Cheung, B. Park, W. Skorupa, 1997, ISBN: 1-55899-342-8
- Volume 439— Microstructure Evolution During Irradiation, I.M. Robertson, G.S. Was, L.W. Hobbs, T. Diaz de la Rubia, 1997, ISBN: 1-55899-343-6
- Volume 440— Structure and Evolution of Surfaces, R.C. Cammarata, E.H. Chason, T.L. Einstein, E.D. Williams, 1997, ISBN: 1-55899-344-4
- Volume 441— Thin Films—Structure and Morphology, S.C. Moss, D. Ila, R.C. Cammarata, E.H. Chason, T.L. Einstein, E.D. Williams, 1997, ISBN: 1-55899-345-2
- Volume 442— Defects in Electronic Materials II, J. Michel, T. Kennedy, K. Wada, K. Thonke, 1997, ISBN: 1-55899-346-0
- Volume 443— Low-Dielectric Constant Materials II, K. Uram, H. Treichel, A. Lagendijk, 1997, ISBN: 1-55899-347-9
- Volume 444— Materials for Mechanical and Optical Microsystems, M.L. Reed, M. Elwenspoek, S. Johansson, E. Obermeier, H. Fujita, Y. Uenishi, 1997, ISBN: 1-55899-348-7
- Volume 445— Electronic Packaging Materials Science IX, S.K. Groothuis, P.S. Ho, K. Ishida, T. Wu, 1997, ISBN: 1-55899-349-5
- Volume 446— Amorphous and Crystalline Insulating Thin Films—1996, W.L. Warren, R.A.B. Devine, M. Matsumura, S. Cristoloveanu, Y. Homma, J. Kanicki, 1997, ISBN: 1-55899-350-9
- Volume 447— Environmental, Safety, and Health Issues in IC Production, R. Reif, M. Heyns, A. Bowling, A. Tonti, 1997, ISBN: 1-55899-351-7
- Volume 448— Control of Semiconductor Surfaces and Interfaces, S.M. Prokes, O.J. Glembocki, S.K. Brierley, J.M. Gibson, J.M. Woodall, 1997, ISBN: 1-55899-352-5
- Volume 449— III-V Nitrides, F.A. Ponce, T.D. Moustakas, I. Akasaki, B.A. Monemar, 1997, ISBN: 1-55899-353-3
- Volume 450— Infrared Applications of Semiconductors—Materials, Processing and Devices, M.O. Manasreh, T.H. Myers, F.H. Julien, 1997, ISBN: 1-55899-354-1
- Volume 451— Electrochemical Synthesis and Modification of Materials, S.G. Corcoran, T.P. Moffat, P.C. Searson, P.C. Andricacos, J-L. Deplancke, 1997, ISBN: 1-55899-355-X
- Volume 452— Advances in Microcrystalline and Nanocrystalline Semiconductors—1996, R.W. Collins, P.M. Fauchet, I. Shimizu, J-C. Vial, T. Shimada, A.P. Alivisatos, 1997, ISBN: 1-55899-356-8
- Volume 453— Solid-State Chemistry of Inorganic Materials, P.K. Davies, A.J. Jacobson, C.C. Torardi, T.A. Vanderah, 1997, ISBN: 1-55899-357-6
- Volume 454— Advanced Catalytic Materials—1996, M.J. Ledoux, P.W. Lednor, D.A. Nagaki, L.T. Thompson, 1997, ISBN: 1-55899-358-4
- Volume 455— Structure and Dynamics of Glasses and Glass Formers, C.A. Angell, K.L. Ngai, J. Kieffer, T. Egami, G.U. Nienhaus, 1997, ISBN: 1-55899-359-2
- Volume 457— Nanophase and Nanocomposite Materials II, S. Komarneni, J.C. Parker, H.J. Wollenberger, 1997, ISBN: 1-55899-361-4
- Volume 458— Interfacial Engineering for Optimized Properties, C.L. Briant, C.B. Carter, E.L. Hall, 1997, ISBN: 1-55899-362-2
- Volume 459— Materials for Smart Systems II, E.P. George, R. Gotthardt, K. Otsuka, S. Trolier-McKinstry, M. Wun-Fogle, 1997, ISBN: 1-55899-363-0

MATERIALS RESEARCH SOCIETY SYMPOSIUM PROCEEDINGS

- Volume 460— High-Temperature Ordered Intermetallic Alloys VII, C.C. Koch, C.T. Liu, N.S. Stoloff, A. Wanner, 1997, ISBN: 1-55899-364-9
- Volume 461— Morphological Control in Multiphase Polymer Mixtures, R.M. Briber, C.C. Han, D.G. Peiffer, 1997, ISBN: 1-55899-365-7
- Volume 462— Materials Issues in Art and Archaeology V, P.B. Vandiver, J.R. Druzik, J.F. Merkel, J. Stewart, 1997, ISBN: 1-55899-366-5
- Volume 463— Statistical Mechanics in Physics and Biology, D. Wirtz, T.C. Halsey, 1997, ISBN: 1-55899-367-3
- Volume 464— Dynamics in Small Confining Systems III, J.M. Drake, J. Klafter, R. Kopelman, 1997, ISBN: 1-55899-368-1
- Volume 465— Scientific Basis for Nuclear Waste Management XX, W.J. Gray, I.R. Triay, 1997, ISBN: 1-55899-369-X
- Volume 466— Atomic Resolution Microscopy of Surfaces and Interfaces, D.J. Smith, R.J. Hamers, 1997, ISBN: 1-55899-370-3
- Volume 467— Amorphous and Microcrystalline Silicon Technology—1997, E.A. Schiff, M. Hack, S. Wagner, R. Schropp, I. Shimizu, 1997, ISBN: 1-55899-371-1
- Volume 468— Gallium Nitride and Related Materials II, C.R. Abernathy, H. Amano, J.C. Zolper, 1997, ISBN: 1-55899-372-X
- Volume 469— Defects and Diffusion in Silicon Processing, S. Coffa, T. Diaz de la Rubia, P.A. Stolk, C.S. Rafferty, 1997, ISBN: 1-55899-373-8
- Volume 470— Rapid Thermal and Integrated Processing VI, T.J. Riley, J.C. Gelpey, F. Roozeboom, S. Saito, 1997, ISBN: 1-55899-374-6
- Volume 471— Flat Panel Display Materials III, R. Fuls, G. Parsons, D. Slobodin, T. Yuzuriha, 1997, ISBN: 1-55899-375-4
- Volume 472— Polycrystalline Thin Films—Structure, Texture, Properties and Applications III, J. Im, S. Yaliso, B. Adams, Y. Zhu, F.R. Chen, 1997, ISBN: 1-55899-376-2
- Volume 473— Materials Reliability in Microelectronics VII, J.J. Clement, J.E. Sanchez, Jr. K.S. Krisch, Z. Suo, R.R. Keller, 1997, ISBN: 1-55899-377-0
- Volume 474— Epitaxial Oxide Thin Films III, D.G. Schlom, C.B. Eom, M.E. Hawley, C.M. Foster, J.S. Speck, 1997, ISBN: 1-55899-378-9
- Volume 475— Magnetic Ultrathin Films, Multilayers and Surfaces—1997, D.D. Chambliss, J.G. Tobin, D. Kubinski, K. Barmak, W.J.M. de Jonge, T. Katayama, A. Schuhl, P. Dederichs, 1997, ISBN: 1-55899-379-7
- Volume 476— Low-Dielectric Constant Materials III, C. Case, P. Kohl, T. Kikkawa, W.W. Lee, 1997, ISBN: 1-55899-380-0
- Volume 477— Science and Technology of Semiconductor Surface Preparation, G.S. Higashi, M. Hirose, S. Raghavan, S. Verhaverbeke, 1997, ISBN: 1-55899-381-9
- Volume 478— Thermoelectric Materials—New Directions and Approaches, T.M. Tritt, M.G. Kanatzidis, H.B. Lyon, Jr., G.D. Mahan, 1997, ISBN: 1-55899-382-7
- Volume 479— Materials for Optical Limiting II, P. Hood, R. Pachter, K. Lewis, J.W. Perry, D. Hagan, R. Sutherland, 1997, ISBN: 1-55899-383-5
- Volume 480— Specimen Preparation for Transmission Electron Microscopy of Materials IV, R.M. Anderson, S.D. Walck, 1997, ISBN: 1-55899-384-3

**Thermoelectric Materials—
New Directions and Approaches**

THE THERMOELECTRIC PROCESS

C. B. Vining
ZT Service, Inc., 2203 Johns Circle, Auburn, AL 36830 USA, vining@zts.com

ABSTRACT

The efficiency of thermoelectric technology today is limited by the properties of available thermoelectric materials and a wide variety of new approaches to developing better materials have recently been suggested. The key goal is to find a material with a large ZT , the dimensionless thermoelectric figure of merit. However, if an analogy is drawn between thermoelectric technology and gas-cycle engines then selecting different materials for the thermoelements is analogous to selecting a different working gas for the mechanical engine. And an attempt to improve ZT is analogous to an attempt to improve certain thermodynamic properties of the working-gas. An alternative approach is to focus on the thermoelectric process itself (rather than on ZT), which is analogous to considering alternate cycles such as Stirling vs. Brayton vs. Rankine etc., rather than 'merely' considering alternative 'gases'. Focusing on the process is a radically different approach compared to previous studies focusing on ZT . Aspects of the thermoelectric process and alternative approaches to efficient thermoelectric conversion are discussed.

INTRODUCTION

Modern thermoelectric energy conversion devices achieve only a small fraction of Carnot efficiency. The fundamental problem is that the transport properties of available materials are insufficient. In spite of significant effort, neither the experimental nor the theoretical situation has changed substantially in several decades [1].

Experimentally, there are several rather different thermoelectric materials available which achieve about the same efficiency over different temperature ranges (approximate peak efficiency temperatures shown in parenthesis): BiSb alloys (100 K), Bi₂Te₃-based alloys (300-400 K), PbTe-based alloys (600 K-700 K), and SiGe alloys (1100-1200 K). The best thermoelectric materials each achieve peak efficiency values up to about 17% of Carnot efficiency. Moreover, it is not simply the case that more efficient materials are known but are impractical for some reason. There simply aren't any known materials with significantly better thermoelectric properties.

Theoretically, however, there is no known upper limit to the efficiency of thermoelectric conversion beyond the usual Carnot limit. A natural question is, then: why do the best known thermoelectric materials exhibit about the same, relatively low efficiency?

Rather than focusing on the properties of individual thermoelectric materials, this paper attempts to illuminate the question by examining the nature of the thermoelectric conversion process itself. It is shown that an analogy can be drawn between the thermoelectric conversion process and a type of thermodynamic process involving exchange of particles which, it turns out, exhibits many features usually associated with thermoelectric processes.

The following sections outline the essential phenomenology of thermoelectricity and using a parallel formalism a particular open thermodynamic process. Based on this analogy, the 'thermoelectric cycle' can be described. A more familiar example, based on a conventional pressure-volume-temperature (P - V - T) is also described in a similar way. Some typical

experimental results and resulting efficiencies are briefly discussed and finally, some conclusions are presented.

THERMOELECTRICITY

Thermoelectricity may be characterized by the simultaneous effects of both electrical and thermal currents. Using the conventional definitions for the transport coefficients, thermoelectric behavior is well approximated by

$$\begin{aligned}\vec{i} &= \sigma_T (\vec{E} - \alpha \vec{\nabla} T) \\ \vec{q} &= T \vec{s} \\ &= \alpha T \vec{i} - \lambda_E \vec{\nabla} T\end{aligned}\tag{1}$$

or

$$\begin{pmatrix} \vec{i} \\ \vec{s} \end{pmatrix} = L \begin{pmatrix} \vec{E} \\ -\vec{\nabla} T \end{pmatrix}\tag{2}$$

with the transport matrix L given by

$$L = \begin{pmatrix} \sigma_T & \sigma_T \alpha \\ \sigma_T \alpha & \lambda_E / T \end{pmatrix}\tag{3}$$

Here i is the electric current density, E is the electric field, q is the heat current density, s is the entropy current, ∇T is the temperature gradient, σ_T is the electrical conductivity and α is the Seebeck coefficient. λ_E is the thermal conductivity measured under the condition of zero electric field. The symmetry of Eq. (3) (i.e. that the off diagonal elements of the coefficient matrix are identical) is due to one of the Onsager reciprocal relations [2].

Because measurement of thermal conductivity under the condition $E=0$ presents experimental difficulties, the ordinary thermal conductivity (λ_i) is measured under the condition $i=0$. Similarly, the electrical conductivity may be measured in more than one way. The ordinary electrical conductivity (σ_T) is measured with zero temperature gradient. In principle, however, the electrical conductivity could also be measured under adiabatic conditions, that is with $q=0$. The adiabatic electrical conductivity (designated σ_q) is smaller than the isothermal electrical conductivity. Using the definitions and Eq. (3), the relationships between the thermal and electrical coefficients may be succinctly summarized by

$$\begin{aligned}\gamma_{Ei} &\equiv \frac{\lambda_E}{\lambda_i} \\ &= \frac{\sigma_T}{\sigma_q} \\ &= 1 + \frac{\sigma_T \alpha^2 T}{\lambda_i} \\ &\equiv 1 + ZT\end{aligned}\tag{4}$$

where ZT is the dimensionless thermoelectric figure of merit. The symbol γ is introduced here because of the similarity (which will be illustrated below) with the ratio of the constant pressure to constant volume specific heat.

THERMODYNAMICS OF AN OPEN, ONE COMPONENT SYSTEM

The thermodynamics of an open, one component system can be described using a notation similar in form to the notation used above for thermoelectricity. Consider a substance consisting of N particles characterized by a chemical potential μ and temperature T , each of which is allowed to vary. In particular, consider the thermodynamics of adding a particle to the system. The changes in N , heat and entropy are given by

$$\begin{aligned} dN &= \left. \frac{\partial N}{\partial \mu} \right|_T d\mu + \left. \frac{\partial N}{\partial T} \right|_\mu dT \\ dQ &= TdS \\ &= -\mu dN + dU \\ &= \left(\left. \frac{\partial U}{\partial N} \right|_T - \mu \right) dN + \left. \frac{\partial U}{\partial T} \right|_N dT \end{aligned} \quad (5)$$

which is conveniently summarized in matrix form as

$$\begin{pmatrix} dN \\ dS \end{pmatrix} = C \begin{pmatrix} d\mu \\ dT \end{pmatrix} \quad (6)$$

with the capacity matrix, C , given by

$$C = \begin{pmatrix} \left. \frac{\partial N}{\partial \mu} \right|_T & \left. \frac{\partial N}{\partial T} \right|_\mu \\ \frac{1}{T} \left. \frac{\partial N}{\partial \mu} \right|_T \left(\left. \frac{\partial U}{\partial N} \right|_T - \mu \right) & \frac{1}{T} \left[\left. \frac{\partial U}{\partial T} \right|_N + \left. \frac{\partial N}{\partial T} \right|_\mu \left(\left. \frac{\partial U}{\partial N} \right|_T - \mu \right) \right] \end{pmatrix} \quad (7)$$

The symmetry of C is a consequence of the second law of thermodynamics and the off-diagonal elements are exactly equal

$$\begin{aligned} C_{12} &= \left. \frac{\partial N}{\partial T} \right|_\mu \\ &= C_{21} \\ &= \frac{1}{T} \left. \frac{\partial N}{\partial \mu} \right|_T \left(\left. \frac{\partial U}{\partial N} \right|_T - \mu \right) \end{aligned} \quad (8)$$

C_{22} may be identified as the entropy capacity at constant μ (C_{μ}) and using Eqs. 7 and 8

$$\begin{aligned}
C_\mu &\equiv \frac{1}{T} \left. \frac{\partial U}{\partial T} \right|_\mu \equiv C_{22} \\
&= \frac{1}{T} \left[\left. \frac{\partial U}{\partial T} \right|_N + \left. \frac{\partial N}{\partial T} \right|_\mu \left(\left. \frac{\partial U}{\partial N} \right|_T - \mu \right) \right] \\
&= \frac{1}{T} \left. \frac{\partial U}{\partial T} \right|_N \left[1 + \frac{\left. \frac{\partial N}{\partial \mu} \right|_T \left(\left. \frac{\partial U}{\partial N} \right|_T - \mu \right)^2}{\left. \frac{\partial U}{\partial T} \right|_N} \right]
\end{aligned} \tag{9}$$

The prefactor of Eq. 9 is just the entropy capacity at constant N (C_N), and a γ can now be defined for this system as well

$$\begin{aligned}
\gamma_{\mu N} &= \frac{C_\mu}{C_N} \\
&= 1 + \frac{\left. \frac{\partial N}{\partial \mu} \right|_T \left(\left. \frac{\partial U}{\partial N} \right|_T - \mu \right)^2}{\left. \frac{\partial U}{\partial T} \right|_N}
\end{aligned} \tag{10}$$

At this point the structure of the capacity matrix C may not appear particularly similar to the structure of the transport coefficient matrix L , but the primary difference is that the coefficients of C are simply less familiar.

CONVERSION EFFICIENCY

Define the thermoelectric efficiency as

$$\epsilon_{Et} \equiv \frac{-\vec{E} \cdot \vec{i}}{\vec{s} \cdot (-\vec{\nabla} T)} \tag{11}$$

Using Eq. (1) to eliminate E and q , and optimizing with respect to i , the maximum efficiency can be derived for a fixed ∇T :

$$\epsilon_{Et}^{\max} = \frac{\sqrt{\gamma_{Et}} - 1}{\sqrt{\gamma_{Et}} + 1} \tag{12}$$

This is the usual expression for the efficiency of a thermoelectric generator, which approaches unity as γ_{Et} (or ZT) diverges.

The analogous efficiency expression for the μ - N system is

$$\epsilon_{\mu N} \equiv \frac{-d\mu dN}{dSdT} \tag{13}$$

$d\mu dN$ is simply the infinitesimal chemical (or electrochemical, if the particles are charged) work performed by a cyclical process of two constant chemical potential processes $d\mu$ apart and two constant particle number processes dN apart. This work is illustrated schematically in Fig. 1.

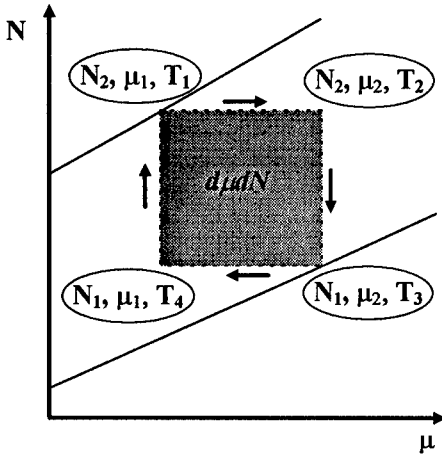


Fig. 1: Schematic representation of $d\mu dN$ work. The lines indicate the N - μ equation of state at T_1 and T_3 .

$dSdT$ represents the infinitesimal work performed by a cyclical process consisting of two isothermal steps dT apart and two adiabatic steps dS apart in entropy. The efficiency defined in Eq. (0) is, therefore, the ratio of the actual work performed in this type of process to the work performed by a Carnot cycle operating between two temperatures represented by dT .

The maximum efficiency for this type of process is derived in precise analogy to the thermoelectric expression above: use Eq. 7 to eliminate $d\mu$ and dS , and optimize with respect to dN

$$\varepsilon_{\mu N}^{\max} = \frac{\sqrt{\gamma_{\mu N}} - 1}{\sqrt{\gamma_{\mu N}} + 1} \quad (14).$$

The similarity in form between the expression for the efficiency of this μ - N system and the thermoelectric system carries over to the magnitude of the efficiency also, which may

be illustrated by the following discussion.

As a specific example, consider a non-degenerate electron gas with the usual equation of state

$$N = 2.5 \times 10^{19} \left(\frac{T}{300} \right)^{1.5} e^{\mu/kT} \text{ cm}^{-3} \quad (15)$$

and internal energy

$$U = \frac{3}{2} NkT \quad (16)$$

from which we can calculate the capacity matrix

$$C = \frac{N}{kT} \begin{pmatrix} 1 & k \left[\frac{3}{2} - \frac{\mu}{kT} \right] \\ k \left[\frac{3}{2} - \frac{\mu}{kT} \right] & k^2 \left\{ \frac{3}{2} + \left[\frac{3}{2} - \frac{\mu}{kT} \right]^2 \right\} \end{pmatrix} \quad (17)$$

and the ratio of the entropy capacities

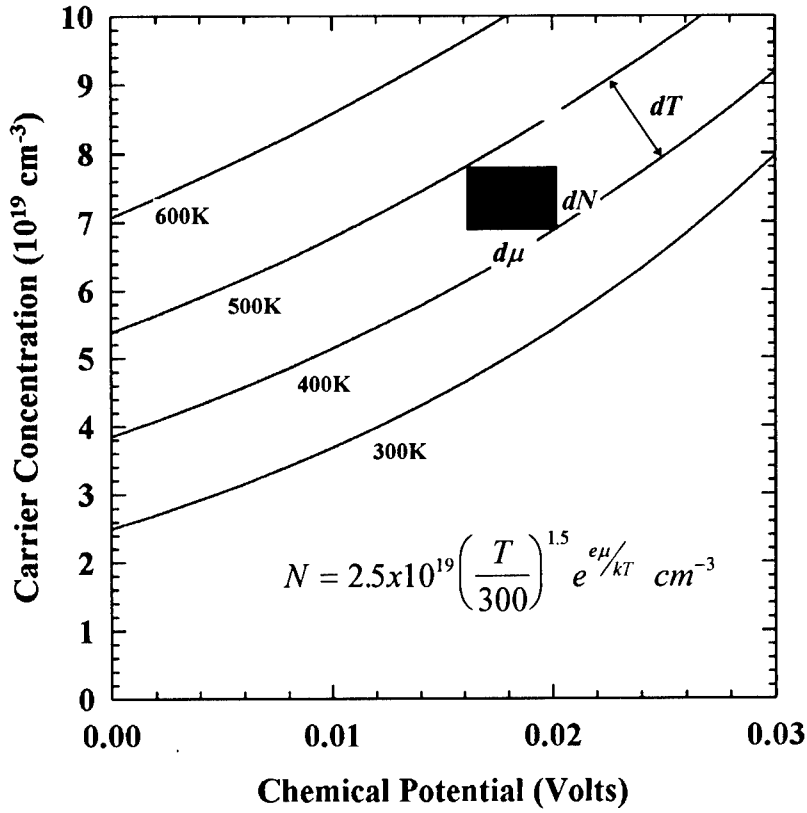


Fig. 2: Equation of state for a non-degenerate electron gas illustrating $d\mu dN$ work.

$$\gamma_{\mu N} = 1 + \frac{\left(\frac{3}{2} - \frac{\mu}{kT}\right)^2}{\frac{3}{2}} \quad (18).$$

If we further assume an energy independent mean free path and we neglect heat transport due to phonons, we can calculate the transport matrix

$$L = \sigma_T \begin{pmatrix} 1 & \frac{k}{e} \left[2 - \frac{\mu}{kT} \right] \\ \frac{k}{e} \left[2 - \frac{\mu}{kT} \right] & \left(\frac{k}{e} \right)^2 \left\{ 2 + \left[2 - \frac{\mu}{kT} \right]^2 \right\} \end{pmatrix} \quad (19)$$

and the ratio of the thermal conductivities

$$\gamma_{Et} = 1 + ZT = 1 + \frac{\left(2 - \frac{\mu}{kT}\right)^2}{2} \quad (20)$$

which is the usual result for ZT under these conditions.

In this case the transport matrix is very similar to the capacity matrix, differing primarily by the introduction of a characteristic relaxation time (which enters into the isothermal electrical conductivity, σ_T) and a minor modification of the numerical coefficients (i.e. where “3/2” enters several coefficients in C , “2” enters in L). Properly accounting for genuine transport effects (primarily the energy dependence of the relaxation time) and heat loss mechanisms (primarily phonon transport) greatly complicate this comparison, but it may be of interest to note that the order of magnitude of thermoelectric effects can be understood as originating from these fundamental thermodynamic considerations.

THE ‘THERMOELECTRIC CYCLE’

This section describes the thermodynamic cycle by analogy to the μ - N system described above. While this system is obviously not identical to the thermoelectric process, it nevertheless appears to capture many of the features essential to understanding thermoelectric phenomena and deserves some attention for that reason.

Fig. 2 illustrates the equation of state and $d\mu dN$ -type work discussed above for a non-degenerate electron gas. Since the process is far removed from a Carnot-cycle (composed of two isotherms and two adiabats), the efficiency is low. Nevertheless, at very low carrier concentrations (i.e. large, negative values of μ), $\gamma_{\mu N}$ diverges and the efficiency approaches unity, as indicated by of Eqs. 18 and 14.

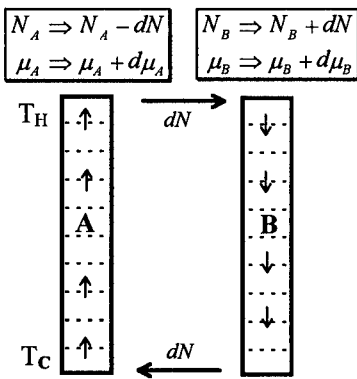


Fig. 3: The ‘thermoelectric cycle’ may be described as a succession of $d\mu dN$ processes, passing an infinitesimal charge (dN) around a closed circuit of dissimilar materials.

Fig. 3 illustrates how a conventional thermocouple may be thought of as a succession of infinitesimal $d\mu dN$ processes in which an infinitesimal charge dN circulates around the closed circuit. The work performed and efficiency of this process is surprisingly well described by entirely neglecting the true transport nature of the process and instead examining only the purely thermodynamic considerations described here, particularly if the effect of phonon transport is neglected.

THERMODYNAMICS OF A P - V SYSTEM

As a final example we consider a P - V system, which may be more familiar than the N - μ system above and where experimental data indicate at least one method for achieving high efficiencies. Using the ordinary thermodynamic definitions, state changes in a P - V system may be represented in an entirely similar way by

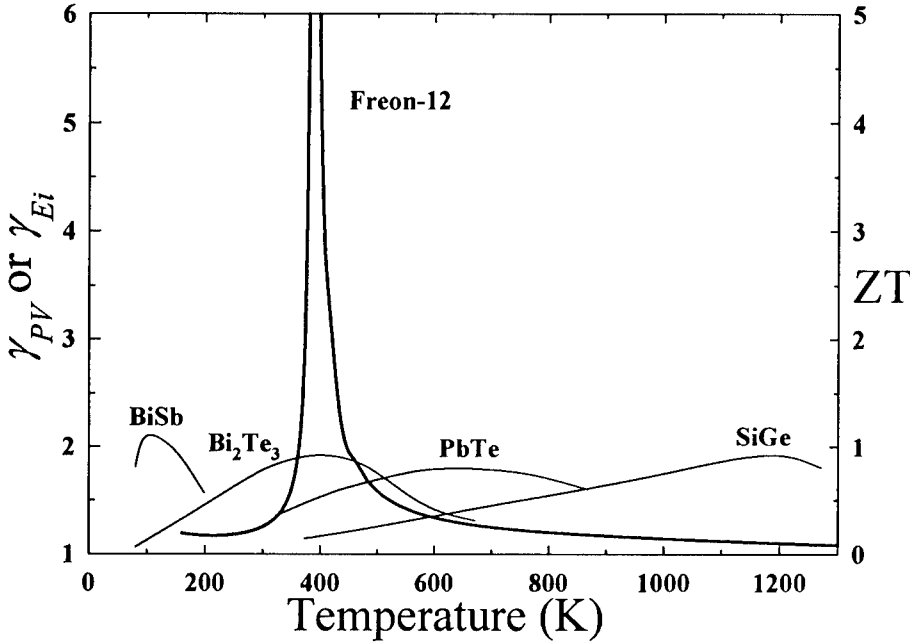


Fig. 4: Specific heat ratios, γ_{PV} for a PV system (Freon 12) and thermal conductivity ratios, $\gamma_{Ei}=1+ZT$, for selected n-type semiconductor alloys as a function of temperature.

$$\begin{pmatrix} dV \\ dS \end{pmatrix} = \begin{pmatrix} V\kappa_T & V\beta \\ V\beta & C_P/T \end{pmatrix} \begin{pmatrix} -dP \\ dT \end{pmatrix} \quad (21)$$

Here dV , dP , dS and dT have their usual thermodynamic meaning. κ_T is the isothermal compressibility, β is the volume coefficient of thermal expansion and C_P is the constant pressure specific heat. As above, the symmetry Eq. (21) (i.e. that the off diagonal elements of the coefficient matrix are identical) is a result of the well known Maxwell relations.

It is convenient to also define the constant volume specific heat (C_V) measured with $dV=0$ and the adiabatic compressibility (κ_S) measured with $dS=0$. The relationships between the heat capacities and compressibilities may be simply summarized by

$$\begin{aligned} \gamma_{PV} &\equiv \frac{C_P}{C_V} \\ &= \frac{\kappa_T}{\kappa_S} \\ &= 1 + \frac{V\beta^2 T}{\kappa_T C_V} \end{aligned} \quad (22),$$

where now γ_{PV} has the conventional thermodynamic meaning.

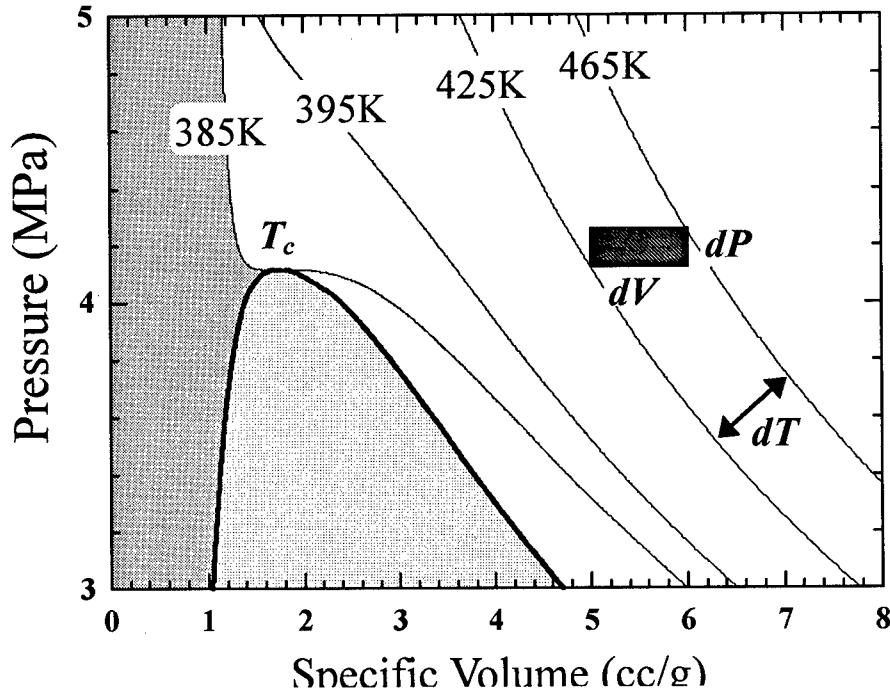


Fig. 5: PV diagram for Freon-12 (CCl_2F_2). The two phase region is light gray and the liquid is the darker gray region to the left. Isotherms are indicated by light lines and a typical $dPdV$ element is indicated by the rectangle.

TYPICAL EXPERIMENTAL RESULTS FOR THERMOELECTRICS

The thermoelectric figure of merit, ZT , has been measured for many materials and Fig. 4 shows representative results for three of the best n-type semiconductor alloys known. Even for the best known materials ZT does not yet significantly exceed unity, which is to say that γ_{Ei} does not significantly exceed 2.

TYPICAL RESULTS FOR GASES

For an ideal classical gas the equipartition theorem yields,

$$\gamma_{PV} = 1 + \frac{2}{f} \quad (23)$$

where f is the number of degrees of freedom associated with a single gas molecule. Since $f \geq 3$, $\gamma_{PV} < 1.67$ for ideal gases. At low pressures, for example, monatomic gases such as Argon exhibit $\gamma_{PV} \cong 1.67$.

Condensable gases, however, can exhibit values for γ_{PV} much greater than 2. As a typical example, the experimental properties of Freon 12 (calculated from fits given in [3]) have been used to illustrate the key features in Fig. 5.

Note that $\frac{\partial P}{\partial T} = 0$ at the critical temperature, T_c . Thus κ_T , C_P , and γ_{PV} all diverge at T_c . γ_{PV} of Freon 12 gas has been calculated from fits of the experimental results [3] for: $T < T_c$ along the boundary between the gas phase and the two phase region and for $T > T_c$ at the critical density (0.556 g/cm³). The results are shown in Fig. 4 for comparison purposes.

Freon 12 has been chosen for illustrative purposes only and a great many other condensable gases exhibit qualitatively similar behavior: γ_{PV} is large for conditions near the critical point and approaches a value between 1 and 1.67 for conditions far from the critical point. The large values observed for γ_{PV} near the critical point are in sharp contrast to the universally small values of γ_{EI} (less than about 2) reported for thermoelectric materials.

CONVERSION EFFICIENCY FOR THE ANALAGOUS P - V SYSTEM

The analogous efficiency expression for the P - V system is

$$\epsilon_{PV} \equiv \frac{dP dV}{dS dT} \quad (24)$$

Interpretation is particularly simple for the PV system. $dP dV$ is simply the infinitesimal mechanical work performed by a cyclical process of two constant pressure steps dP apart and two constant volume steps dV apart. This work is illustrated by the small rectangle in Fig. 4.

Again, the maximum efficiency for this type of process is derived in precise analogy to the thermoelectric expression above (use Eq. 21 to eliminate dP and dS , and optimize with respect to dV):

$$\epsilon_{PV}^{\max} = \frac{\sqrt{\gamma_{PV}} - 1}{\sqrt{\gamma_{PV}} + 1} \quad (25)$$

While γ_{PV} becomes very large for PV conditions near the critical point, under most conditions γ_{PV} is actually quite small. For example Freon 12, at 300 K and 0.1 MPa (1 atm.), has $\gamma_{PV} = 1.14$ and ϵ_{PV} of only 0.033 (i.e. 3.3% of Carnot efficiency).

It is important to point out that the familiar condensable gas conversions systems (such as Freon-based refrigerators and steam engines) are not based on the $dP dV$ -type process described by Eq. (25), but on a much more efficient vaporization/condensation cycle. High values of γ_{PV} are not important to the efficiency of such devices.

For at least a limited range of PVT conditions near a critical point, very high γ_{PV} have been observed and it might be interesting to look for thermoelectric materials with analogous critical points where high γ_{EI} and ZT values might well be expected.

CONCLUSION

Several key features of thermoelectricity may be understood by analogy to the thermodynamics of an open system (referred to here as a μ - N system) which may exchange

particles and heat with it's surroundings. In particular the relative magnitudes of the transport coefficients and the order of magnitude of the energy conversion efficiency largely originate in the thermodynamics of exchanging particles, at least for simple systems where scattering rates depend only weakly on energy and phonon transport can be neglected.

The analysis presented here suggests at least three distinct methods to achieve higher thermoelectric efficiency: 1) examine systems near an appropriate electronic phase transition where large γ_{Ei} (and ZT) values can be expected, in analogy to the large γ_{pV} exhibited near (for example) the gas-liquid critical conditions, 2) emphasize systems with strong interactions among the carriers where the transport matrix L may become dominated by purely transport effects (like scattering) and 3) seek to modify the 'thermoelectric cycle' to utilize more favorable thermodynamic processes.

The first two suggestions seek to improve the properties of the 'working fluid', while the final suggestion focuses attention on improving the 'engine' itself, a radically new approach to thermoelectric energy conversion.

ACKNOWLEDGMENTS

The author would like to thank Dr. C. Swenson for pointing out the divergence of Cp/Cv for a gas in equilibrium with its liquid. Helpful discussions with Mr. B. Cook, Mr. J. Harringa, Mr. S. Han and Mr. K. Pixius are also gratefully acknowledged..

REFERENCES

1. C. Wood, Rep. Prog. Phys., **51**(4), 459 (1988).
2. L. Onsager, Phys. Rev. **37**, 405 (1931); **38**, 2265 (1931).
3. R. C. Downing , *Flouorocarbon Refrigerants Handbook* (Prentice-Hall, Englewood Cliffs, NJ, 1988), 317-395.

SELECTION AND EVALUATION OF MATERIALS FOR THERMOELECTRIC APPLICATIONS II

Jeff W. Sharp

Marlow Industries, Inc., 10451 Vista Park Rd., Dallas, TX 75238-1645

ABSTRACT

In good thermoelectrics phonons have short mean free paths, and charge carriers have long ones. The other requirements are a multivalley band structure and a band gap greater than 0.1 eV for the 200 to 300 K temperature range. We discuss the use of solid state physics and chemistry concepts, along with atomic and crystal structure data, to select the new materials most likely to meet these criteria.

BACKGROUND AND FUNDAMENTALS

At the conceptual level, good thermoelectrics were defined in 1909-11 as materials in which $Z = S^2\sigma/\lambda$ is large, with S , σ and λ being the Seebeck coefficient, electrical conductivity, and thermal conductivity respectively [1]. At the material level, the work in thermoelectrics prior to 1960 demonstrated that the best thermoelectric materials would be semiconductors formed of heavy elements. According to these principles, Bi_2Te_3 - Sb_2Te_3 - Bi_2Se_3 , Bi-Sb , PbTe-PbSe and Si-Ge were found as the best systems for exploiting the Peltier (refrigeration) and Seebeck (power generation) effects.

A large atomic mass contributes to low lattice thermal conductivity. Since the ZT is inversely proportional to the total thermal conductivity, it is obvious that a low lattice contribution is required. It is, in fact, only the lattice portion that distinguishes different candidates in transport models based on simplified bands [2]: optimized ZT 's depend on the type of carrier scattering and the unitless parameter

$$\beta \propto T^{\frac{5}{2}} \frac{U}{\lambda_{\text{Lattice}}} \quad (1)$$

U is the weighted mobility for the electrons or holes which have mobility μ , mass m^* (free electron mass units), and which populate N_v equivalent valleys of the band structure:

$$U = N_v \mu (m^*)^{3/2} \quad (2)$$

If U and λ_{Lattice} are expressed in $\text{m}^2 \text{V}^{-1} \text{s}^{-1}$ and $\text{W m}^{-1} \text{K}^{-1}$ respectively, then

$$\beta \approx 9 \frac{U}{\lambda_{\text{Lattice}}} \left(\frac{T}{300 \text{ K}} \right)^{5/2} \quad (3)$$

The materials used in today's thermoelectric coolers have $\beta \approx 0.35$.

We want high carrier mobility but, since μ decreases as m^* increases, it is not obvious whether the effective mass should be large. A considerable range of effective mass magnitudes is found in good thermoelectrics. Definitely, though, we want a long relaxation time for the carriers, and a large number of valleys in the band structure. It is also known that the semiconductor's band gap should be greater than $6 k_B T$ [2], or perhaps $10 k_B T$ [3].

Figure 1 shows lines of constant ZT in the U - λ_{Lattice} plane. We can conclude that an advanced thermoelectric is very likely to have $\lambda_{\text{Lattice}} < 3 \text{ W m}^{-1} \text{ K}^{-1}$ and $U > 0.02 \text{ m}^2 \text{ V}^{-1} \text{ s}^{-1}$. The highest U values known are around $0.2 \text{ m}^2 \text{ V}^{-1} \text{ s}^{-1}$, and the lowest λ_{Lattice} values known for crystalline solids are around $0.4 \text{ W m}^{-1} \text{ K}^{-1}$. Both limits must be approached in the same material to obtain $ZT = 3$, which will allow thermoelectrics to compete with 1/3 horsepower compressors.

The explicit temperature dependence of β , $T^{2.5}$, implies a very strong dependence of ZT on T . However, it is often the case that $m \sim T^{-1.5}$ and $\lambda_{\text{Lattice}} \sim T^{-0.5}$ in good thermoelectrics. Assuming these dependencies, $\beta \sim T^{1.5}$. Because ZT varies sublinearly with β for optimally doped samples (see below), a typical T dependence of ZT for a given compound is $ZT \sim T$, until intrinsic conduction becomes influential. We might expect, then, that $ZT = 1$ at 100 K is as great a challenge as $ZT = 3$ at 300 K, or $ZT = 6$ at 600 K. On the other hand, lower temperatures allow smaller band gaps, and less thermal stability is required, so the search for cooling materials is less constrained than the search for power generation materials.

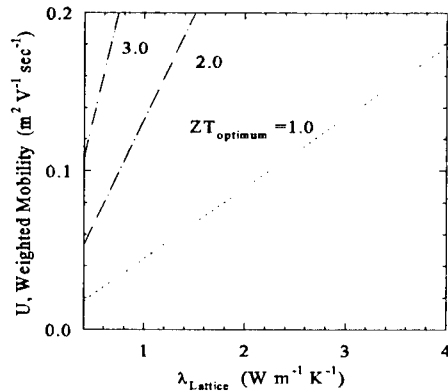


Figure 1. Lines of constant ZT showing the region of materials parameters space that can lead to $ZT > 1$. The lines are for an extrinsic, optimally doped semiconductor at 300 K, with carriers scattered by acoustic phonons.

FURTHER CONSIDERATIONS

In order to move forward in the search for high ZT, further guidelines for materials selection have been developed to find high U and low λ_{Lattice} semiconductors. These guidelines can be separated into those concerned with electronic transport, and those concerned with thermal transport.

Thermal

The λ_{Lattice} 's of the semiconductors InSb and SnTe differ by one order of magnitude, even though they have virtually the same average mass. This drastic difference is attributed to the differing atomic environments in the two materials: tetrahedral in InSb, and octahedral in SnTe [4]. We do not know of an analysis of connecting bonding polyhedra and lattice conductivity. One can speculate that the longer bonds associated with higher coordinations are characterized by smaller force constants (meaning a lower Debye temperature), and greater anharmonicities.

Unit cell complexity also bears on the magnitude of λ_{Lattice} . All other factors being equal, a more complex cell is expected to propagate heat less efficiently. This is principally due to the decrease of the acoustic phonon Debye temperature as the primitive cell grows in size [5]. When the Debye temperature is small, a greater fraction of the thermal excitations are ones which may undergo Umklapp scattering.

A unique approach to finding a material with low λ_{Lattice} is to look for structures with large empty cages into which one can introduce "fillers." The idea is to create low frequency, highly anharmonic vibrational modes in order to scatter acoustic phonons, hopefully achieving a λ_{Lattice} close to the theoretical minimum, λ_{min} . Slack introduced this concept to thermoelectrics [6], and proposed that it be attempted with the skutterudite structure, which has two cages per unit cell. The striking decrease of λ_{Lattice} in filled skutterudites [7, 8] gives credibility to the approach, and could lead to similar successes. In the ideal case the filler will be a neutral atom or molecule whose motion is random with respect to that of its neighbors. Although the more general strategy described here is not directly related to the λ_{min} approach, it has provided a basis for finding new materials whose structures contain cages.

Electronic

Quantum wells of thermoelectric materials can have much improved power factors ($S^2\sigma$), relative to the bulk values. The reason is predominantly that the effective density of states is increased by confinement in the direction of composition modulation. If the mobilities in the two longitudinal directions do not change much, the conductivity is higher for a given position of the fermi level. For bulk materials selection, the lesson to be learned is that an anisotropic effective mass tensor is advantageous if transport is arranged in the direction of lowest effective mass. Significantly anisotropic effective masses are found, for example, in naturally layered materials.

It is also held that thermoelectrics are likely to have a low degree of ionicity, so that the atomic cores carry little net charge. An oscillating ion will scatter electrons more than a similarly vibrating atom that is nearly neutral. There are some interesting issues associated with this criterion. First, since thermoelectrics will contain large atoms the covalent contribution to the

band gap, which is (qualitatively) inversely proportional to the square of bond length, will be small. If the ionic contribution is also small, then the total gap will be small. Second, the measure of ionicity that is used in practice is the electronegativity, but the definition of an electronegativity scale based on atomic properties is an ongoing area of research [9-12]. Finally, if there is little density of the carrier wavefunctions in the vicinity of an ion, the impact of that ion on the carrier mobility will be lessened. Such might be the case when charge is contributed to a covalent network by alkali metal or alkali earth constituents of a Zintl phase.

Unusual electronic properties are the reason that rare earth semiconductors are receiving renewed attention as possible thermoelectrics. The large effective masses of f bands can yield high power factors, even in metals. According to theory, a similar effect in a semiconductor with low λ_{attice} might yield very high values of ZT [13]. Our own experimental testing of this theory is beginning with compounds that do have a low λ_{attice} .

APPLYING THE CRITERIA

If it is accepted that most of the unexplored potential of new bulk materials lies in ternaries and quaternaries [14], then it must also be accepted that there will be little direct experimental foundation for selecting materials. This is because the number of synthesized and tested ternary semiconductors is too small a fraction of the totality of ternary semiconductors to indicate a direction for research. In our view, the selection process must rely on our understanding, both empirical and conceptual, of binary semiconductors.

In the selection process we are employing, the first step is to limit the constituents. This is done by focusing on the heaviest (non-halogen) anions: Ge, Sn, Sb, Te, Pb and Bi. (Silicon, arsenic and selenium are also of some interest, but mainly to the extent that they share chemical tendencies with germanium, antimony and tellurium respectively.) These anions are of the greatest value to thermoelectrics not only because they are heavy, but also because their bonds often show only weak s orbital influence, as evidenced by smaller bond angles and longer bond lengths than in tetrahedral arrangements. Further, the large size of these anions makes them the most polarizable, which means their compounds may have large dielectric constants to screen impurity scattering. These virtues are all less true of Ge than of the other five preferred anions; Ge is included mainly to address the need for high melting point compounds for power generation applications. It is also the case that Sn and Pb form relatively few (binary) semiconductors; including Ge greatly increases the number of compounds to consider that have a Group IV anion.

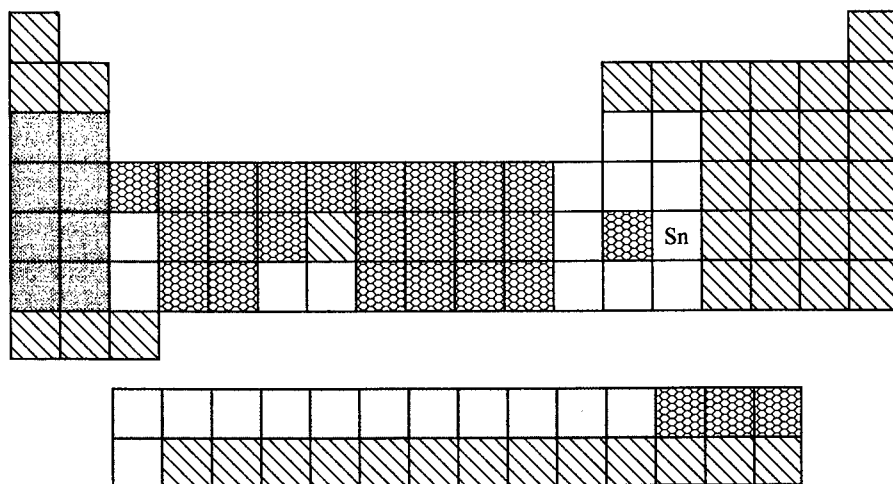
We have sifted through the binary compounds known for our six anions and 56 selected cations. A large majority are metals or ionic semiconductors (average bond electronegativity difference > 0.5 , [15]). Yet, a few distinct binary compounds (counting isostructural, isovalent systems as one compound) that have the semblance of good thermoelectrics (covalent, high average mass, high atomic coordinations, anisotropic crystal structure) apparently have not been investigated. All of these compounds are polyanionic, i.e., they contain anion-anion bonds. In turn, many of the polyanionic compounds are Zintl phases, in which the cation is an alkali metal or alkali earth element. One example, BaSb_3 , is discussed in another paper in these proceedings.

In addition to uncovering a few binary compounds that are good thermoelectric candidates, our survey of the known binaries gives us a basis for exploring unknown compounds, primarily ternaries for now. For instance, K makes semiconductors with both Sn and Sb, and Sn often acquires a bonding environment similar to that of Sb in its elemental form (distorted octahedral).

For these reasons, we conjectured that KSnSb would be a semiconductor with a crystal structure similar to that of Sb , but with K introduced in the van der Waals gaps. This conjecture is correct: KSnSb , first reported in 1987, has the expected structure [16], and is a narrow band gap semiconductor according to theory (local density approximation with augmented spherical wave method) [17].

Maps of semiconductivity in binary systems may be useful as a basis for exploring ternary compounds in a more general fashion. The map for Sn is given in the **Figure 2**. For combination with Sn , columns V through VIII of the main group were ignored, along with elements that are radioactive, or too light to be suitable cations. Elements that form no compounds or only metals with Sn are blank or dotted respectively. Dark gray areas represent elements for which binary semiconductors with Sn as the anion are known. Light gray areas represent those elements for which such compounds are believed to exist, with the basis for the belief being the generalized 8-N rule.

FIG. 2. Binary map of semiconductivity for Sn as the anion. Key to map: slanted lines--ignored, blank--no compounds, honeycomb--metals only, light gray--presumed semiconductors (see text), dark gray elements--known semiconductors.



Mooser and Pearson formulated the generalized 8-N rule in 1956 [18]. The 8-N rule states that an atom of an element of the N th main group ($N = 4$ to 8, the non-metals) will participate in 8-N covalent bonds. The generalized version extends this idea to compounds by relating the valences of the cation(s) and anion(s), and their self coordination numbers, to predict whether a compound is a semiconductor/semimetal or a metal. In indexing approximately 1200 binary compounds, we have used the generalized 8-N rule, when necessary and applicable, to distinguish between metals and semiconductors.

In most cases, application of the generalized 8-N rule is straightforward, and so it is widely used

by structural chemists [19, 20]. However, if the valence of the cation is ambiguous (a transition element), or if there is no clear division between bonded and non-bonded neighbors, then the confidence level drops. One must then deal with issues such as the relation between transition element environment and valence [21], and/or the relation between charge state and radius. Comparisons with known semiconductors are helpful. For instance, in BaSb, 1/3 of the Sb has 3 Sb neighbors and the remainder has 2 Sb neighbors. Then the compound is non-metallic if both Ba valence electrons are used for bonds with Sb, but the structure data show that each Ba atom has a single Ba neighbor at $\sim 4.30 \text{ \AA}$, virtually the same as in metallic Ba. Since semiconductors are known in isostructural compounds (BaP, type) [22] with similar cation-cation distances, we infer that these do not count as bonds in the general valence formulation. The explanation is that Ba carries a positive charge, and its actual radius is reduced.

EVALUATION

Once a phase of interest has been isolated and the transport properties of an extrinsic sample have been measured, there are methods to evaluate its *optimized* ZT. One scenario is as follows:

1. Derive the scattering parameter, r , from the temperature dependence of the carrier mobility: $\mu \propto T^{-1}$ if lattice scattering is indicated; $\mu \propto T^r$ if point defect scattering is indicated. As a rule, μ will decrease as T increases in the former case, and increase as T increases in the latter case [23].
2. With S (absolute value) in units of $k_B/e = 87 \text{ } \mu\text{V/K}$, calculate an initial value for β from:

$$\beta^{-1} = e^{(S+r+5/2)} \left[\frac{S^2}{ZT} - (r+5/2) \right] \quad (4)$$

It is then possible to divide the approximate β by the following correction factors, f , to obtain better accuracy:

$$\begin{aligned} r=-1/2: \quad f &= 1 + \frac{0.0123}{S} + \frac{0.123}{S^2}; \quad 0.7 < S < 1.6 \\ r=1/2: \quad f &= 1 - \frac{0.497}{S} + \frac{2.749}{S^2} - \frac{0.627}{S^3}; \quad 0.9 < S < 4.0 \\ r=3/2: \quad f &= 1 - \frac{1.237}{S} + \frac{6.931}{S^2} + \frac{2.213}{S^3}; \quad 1.1 < S < 5.0 \end{aligned} \quad (5)$$

These are (non-physical) fits to published correction factors derived from computations [23]. For the specified ranges of S (absolute values), **Eq. 5** is accurate to within a few percent. For S greater than the upper limit of these ranges, the correction factors are very close to unity, and can be ignored. In the limit $\beta \rightarrow \infty$, ZT is dependent only on the non-degenerate Lorenz number, $L = r + 5/2$, and the Seebeck coefficient: $ZT = S^2/L$.

3. Extract the lattice thermal conductivity: $\lambda_{\text{lattice}} = \lambda_{\text{Total}} - L(k_B/e)^2 \sigma T$. To find L , either samples with different but similar carrier concentrations can be used, or L can be estimated from r and S . L varies monotonically between $r + 5/2$ (non-degenerate) and $\pi^2/3$ (degenerate), and lies about halfway between these two limits for $S \approx 2(r + 2)/3$ (k_B/e).

4. Project the amount by which λ_{lattice} might be reduced, and calculate β accordingly. When alloying is used to reduce λ_{lattice} , a semi-empirical formula to find the alloy lattice conductivity from the average value of the pure elements/compounds is

$$\lambda_{\text{alloy}} = \frac{\sqrt{\lambda_{\text{avg}}}}{c} \arctan(c\sqrt{\lambda_{\text{avg}}}) \quad (6)$$

$$c = \left(\left[\frac{\delta m}{m} \right]^2 + A \left[\frac{\delta d}{d} \right]^2 \right) g(1-g)$$

Equation 6 is adapted from formal theory [24]. The thermal conductivity units being used are $\text{W m}^{-1} \text{K}^{-1}$. A factor of $\omega_D^{-1/2}$, where ω_D is the Debye frequency, should accompany each $\lambda_{\text{avg}}^{1/2}$, but the point is to make an estimate based on readily available input. The form in which c is parameterized accounts for both mass fluctuation and strain scattering. m and d are the average mass and bond length for the formula unit, and δm and δd are the mass and radii differences between the two alloyed constituents, which are present with fractions g and $1-g$. We find that a value of $A=300$ for the adjustable parameter usually gives agreement within 30% of experimental results for a broad range of compounds. Using initial data, a better value of A can be calculated for a given structure.

If the reduction of λ_{lattice} is to occur by void-filling, then the goal is to reach λ_{min} , which can be calculated for any structure [5]. Then λ_{min} , or some multiple of it, can be used as the projected λ_{lattice} . In the case of filled skutterudites, λ_{lattice} has reached as low as $3\lambda_{\text{min}} = 1 \text{ W m}^{-1} \text{K}^{-1}$ at room temperature [8].

5. ZT can be interpolated from **Table I**:

Table I. Values of β that correspond to benchmark ZT's for two common scattering parameters.

	ZT=0.5	ZT=1.0	ZT=1.5	ZT=2.0	ZT=2.5	ZT=3.0
$r = -1/2$	0.16	0.40	0.76	1.19	1.71	2.42
$r = 3/2$	0.014	0.05	0.12	0.22	0.36	0.55

Some of the first samples of a new material might be intrinsic. In this case, the above procedure is invalid, but other useful information can be obtained. One signature of an intrinsic sample is a Seebeck coefficient that declines with temperature. If measurements are done at low enough temperature, a Seebeck peak will be found, and the band gap can be estimated: $E_g \approx 2eS_{\text{peak}}T_{\text{peak}}$, where e is the electron charge. Details of this procedure and refinements to this basic result will be published elsewhere [25]. It is helpful to know the band gap because, as mentioned earlier, thermoelectric materials are efficient only if $E_g > 6 k_B T_{\text{operation}}$.

PROSPECTS

To a first approximation, binary semiconductors are fully explored and ternary semiconductors are unexplored. The compositions that have been tested as thermoelectrics, then, lie on the perimeters of triangles; the interiors of the triangles await evaluation. If one considers quaternary formulas, then the triangles are merely faces of trigonal pyramids. The thermoelectrics community probably cannot afford, however, to take the position that binary compounds are as insignificant physically as they are topologically.

Study of the binaries has taught us what characteristics a good thermoelectric is likely to have, and this description is not likely to change. Therefore, a prudent approach to ternary exploration may be to ask what one hopes to gain by adding a third, and perhaps fourth, element. In thermoelectrics, is more different, or just more of the same? Given that atomic environments and unit cell complexity are important characteristics, the answer is that more *is* different. For instance, octahedrally coordinated Fe and tetrahedrally coordinated Cd are divalent cations suitable for forming potential thermoelectrics with Sb. Using both together may allow one to construct qualitatively different crystal structures in which Sb could have different bonding environments than it does when combining with these cations separately. Intuitively, we expect also that larger primitive cells will result as the number of different coordination configurations increases.

To make the argument somewhat quantitative, we refer to the classification of “intermetallic” compounds according to their atomic environments. Daams et al. [26] list 128 valid cubic structure types, the great majority of which are binary or ternary. Of approximately twenty binary cubic prototypes that have an adequate anion content to be semiconductors, only five have three or more atomic environments. For ternaries, the corresponding fraction is twenty of twenty-six. The atomic environments are most often regular polyhedra, which are connected in various ways to form one, two or three dimensional networks. One would expect to form a greater variety of structures with three or more building blocks than with two. This flexibility may be essential in the attempt to design materials that have novel structures with, according to the above sketch, highly anisotropic anion networks, highly coordinated cations, and large primitive cells.

We can see no reason that this approach cannot uncover a material with $ZT > 1$. To achieve $ZT = 3$, however, may require a truly exceptional material. This is good reason to pursue approaches such as quantum confinement, “rattling fillers” and, perhaps, f band conduction. With $ZT > 3$ as a “stretch goal”, it should be borne in mind that any increase in ZT that can be translated into improved device efficiency will create a more than proportional growth in the use of thermoelectrics.

ACKNOWLEDGEMENTS

We extend our thanks to NASA/DARPA for their support (contract NAS9-19358).

REFERENCES

1. E. Altenkirch, *Phys. Zs.* **10** (1909), 560; **12**, p. 920 (1911).
2. R.P. Chasmar and R. Stratton, *J. Electron. Control* **7**, p. 52 (1959).
3. G.D. Mahan, *J. Appl. Phys.* **65**, p. 1578 (1989).
4. D.P. Spitzer, *J. Phys. Chem. Sol.* **31**, p. 19 (1970).
5. G.A. Slack, *Sol. St. Phys.* **34**, p. 1 (1979).
6. G.A. Slack and V.G. Tsoukala, *J. Appl. Phys.* **76**, p. 1665 (1994).
7. D.T. Morelli and G.P. Meisner, *J. Appl. Phys.* **77**, p.3777 (1995).
8. G.S. Nolas, G.A. Slack, D.T. Morelli, T.M. Tritt and E.C. Ehrlich, *J. Appl. Phys.* **79**, p. 4002 (1996).
9. R.E. Watson and L.H. Bennett, *Phys. Rev. B* **18**, p. 6439 (1978); *J. Phys. Chem. Sol.* **39**, p. 1235 (1978).
10. A.I. Martynov and S.S. Batsanov, *Russ. J. Of Inorg. Chem.* **25**, p. 1737 (1980).
11. T.K. Ghanty and S.K. Ghosh, *J. Phys. Chem.* **100**, p. 17429 (1996).
12. D. Bergmann and J. Hinze, *Angew. Chem. Int. Ed. Engl.* **35**, p. 150 (1996).
13. G.D. Mahan and J.O. Sofo, *Proc. Natl. Acad. Sci. USA* **93**, p. 7436 (1996).
14. G.D. Mahan, B.C. Sales and J.W. Sharp, *Physics Today* **50**, #3, p. 42 (1997).
15. Source of electronegativity data: Lange's Handbook of Chemistry, 14th Ed., edited by John A. Dean (McGraw-Hill, New York, 1992), p. 4.12.
16. K.-H. Lii and R.C. Haushalter, *J. Sol. St. Chem.* **67**, p. 374 (1987).
17. P.C. Schmidt, D. Stahl, B. Eisenmann, R. Kniep, V. Eyert and J. Kubler, *J. Sol. St. Chem.* **97**, p. 93 (1992).
18. E. Mooser and W.B. Pearson, *Phys. Rev.* **101**, p. 1608 (1956); *J. Electronics* **1**, p. 629 (1956).

-
19. J.D. Corbett, *Chem. Rev.* **85**, p. 383 (1985); H.-G.von Schnerring and Wolfgang Hönle, *ibid.*, **88**, p. 243 (1988).
20. B. Eisenmann, *Angew. Chem. Int. Ed. Engl.* **32**, p. 1693 (1993).
21. U. Müller, *Inorganic Structural Chemistry*, (John Wiley & Sons, NY, 1991), ch. 8.
22. W. Bauhofer, E. Gmelin, M. Mollendorf, R. Nesper and H.G. von Schnerring, *J. Phys. C: Sol. St. Phys.* **18**, p. 3017 (1985).
23. H.J. Goldsmid, *Electronic Refrigeration*, (Plenum Press, New York, 1986), pp 58-62.
24. J. Callaway and H.C. von Baeyer, *Phys. Rev.* **120**, p. 1149 (1960); B. Abeles, *ibid.*, **131**, p. 1906 (1963).
25. H.J. Goldsmid and J.W. Sharp, in preparation.
26. J.L.C. Daams, J.H.N. van Vucht, *J. Alloys Comp.* **182**, p. 1 (1992).

MEASUREMENT AND CHARACTERIZATION TECHNIQUES FOR THERMOELECTRIC MATERIALS

TERRY M. TRITT
DEPARTMENT OF PHYSICS AND ASTRONOMY
CLEMSON UNIVERSITY, CLEMSON, SC

Abstract:

Characterization of thermoelectric materials can pose many problems. A temperature difference can be established across these materials as an electrical current is passed due to the Peltier effect. The thermopower of these materials is quite large and thus large thermal voltages can contribute to many of the measurements necessary to investigate these materials. This paper will discuss the characterization techniques necessary to investigate these materials and provide an overview of some of the potential systematic errors which can arise. It will also discuss some of the corrections one needs to consider. This should provide an introduction to the characterization and measurement of thermoelectric materials and provide references for a more in depth discussion of the concepts. It should also serve as an indication of the care that must be taken while working with thermoelectric materials.

Introduction:

Approximately 30 years ago there was a lot of research activity in the field of thermoelectric materials. Materials such as alloys based on the Bi_2Te_3 systems and $\text{Si}_{1-x}\text{Ge}_x$ systems were investigated as thermoelectric (TE) materials. These materials were extensively studied and optimized for their use in TE applications (solid state refrigeration and power generation) ^{1,2} and remain state of the art materials for their specific temperature use. The research on TE materials eventually began a steady decline, and essentially vanished, especially at the university level, about 20 years ago. Consequently, there exists somewhat of a void in the training of students and future researchers in the field of TE materials.

Recently there has been renewed interest in the field of thermoelectrics driven by certain applications which need materials that exhibit higher performance than existing materials.³⁻⁹ Many new researchers have come into this field often with new ideas and new concepts for materials. Multidisciplinary training in solid-state physics, solid state chemistry, materials science and engineering as well as extensive characterization of both the electrical and thermal transport of materials is necessary for successful research in thermoelectrics. One of the difficulties in investigating TE materials lies in obtaining reliable and accurate measurements of their thermal and electrical properties. Tremendous efforts were expended in the late 50's and 60's in relation to the measurement and characterization of TE materials. These efforts were made by a generation of scientists who for the most part are no longer active, and this expertise would be lost to us unless we are aware of the great strides they made during their time.

The purpose of this paper is a reminder of these efforts and to introduce new researchers to the difficulties of the measurements which lie ahead for them. It should also provide a number of references which might prove quite useful. This paper will discuss the techniques employed to characterize TE materials and provide an overview of some of the systematic errors in these techniques which can be "potential pitfalls" to the researcher being able to achieve reliable and accurate measurements. Statistical errors will not be discussed in this paper, since

understanding statistical errors is necessary for analyzing typical experimental data and reference will be made to a couple of excellent texts for analyzing statistical errors.¹⁰⁻¹¹

Thermoelectric materials

Thermoelectric energy conversion utilizes the Peltier heat generated when an electric current is passed through a TE material to provide a temperature gradient with heat being absorbed on the cold side and rejected at the heat sink, thus providing a refrigeration capability. Conversely, an imposed ΔT will result in a voltage or current, i.e. small scale power generation.¹² This aspect is widely utilized in deep space applications. A radioactive material acts as the heat source in these RTG's (radioactive TE generators) and thus provides a long-lived energy supply. The advantages of TE solid state energy conversion are compactness, quietness (no moving parts) and localized heating or cooling. Applications include cooling of CCD's, infrared detectors, low noise amplifiers, computer chips and biological specimens.

The essence of defining a good TE material lies primarily in determining the material's dimensionless figure of merit, $ZT = \alpha^2 \sigma T / \lambda$, where α is the Seebeck coefficient, σ the electrical conductivity, λ the total thermal conductivity ($\lambda = \lambda_L + \lambda_E$; the lattice and electronic contributions respectively) and T is the absolute temperature in K. The Seebeck coefficient, or thermopower, is related to the Peltier effect by $\Pi = \alpha T = Q_p / I$, where Π is the Peltier coefficient, Q_p is the rate of heating or cooling and I is the electrical current.¹³ The efficiency (η) and coefficient of performance (COP) of a device are directly related to the figure of merit of the material. Both η and COP are proportional to $(1 + ZT)^{1/2}$. There are a number of excellent references which discuss the materials aspects, the measurement aspects and thoroughly discuss the field of thermoelectric materials.^{1,2,14-16} These also contain many of the early references which can prove to be invaluable to the new researcher in this field.

Semiconductors have long been the material of choice for TE applications. The most promising materials typically have carrier concentrations of approximately 10^{19} carriers/cm³. The power factor, $\alpha^2 \sigma$, is typically optimized through doping to give the largest Z . High mobility carriers are most desirable, thus yielding the highest electrical conductivity for a specific carrier concentration. In addition, to improve the figure of merit of these materials, attempts are made to lower the lattice thermal conductivity without decreasing the power factor proportionally and thus further increasing the figure of merit.

The measurements necessary to characterize a TE material are listed in Table I below and each will be discussed later in this paper. These terms are defined as follows: μ is the carrier mobility, n is the carrier concentration, L_0 is the sample distance between the measuring leads, A is the cross sectional area, R_H is the Hall coefficient and e is the charge of the carrier, $-e$ (electrons) or $+e$ (holes). Of course, there are many other factors that go into the full understanding of the thermal and electrical transport in a material but the properties previously mentioned will be given as a fundamental starting point.

Estimation of errors in Determination of ZT :

Let us consider the importance of accurate measurements of specific properties such as α , σ and λ_T , by performing a calculation of ZT using what we define as the real numbers and numbers from measurements with errors. For the real ZT , take: $\alpha = 275 \mu V/K$, $\sigma = 10^{+3} (\Omega\text{-cm})^{-1}$, $\lambda_T = 2 \text{ watts / m-K}$ and $T = 300K$. These numbers would give $ZT = 1.13$. If we

were to perform the measurements with some systematic errors in our system we can see how this would affect this calculation. We will take the thermopower or Seebeck coefficient to be $\approx 10\%$ low ($\alpha' = 250 \mu\text{V/K}$), the error could possibly come from a ΔT that is measured to be 10% higher than the real ΔT across the sample. This could be due to poor thermal anchoring of the thermocouples to the sample or inaccurate calibrations of the thermocouples. We take the conductivity ($\sigma' = 1.05 \times 10^{+3} (\Omega\text{-cm})^{-1}$) to be 5% too high. This could result from inaccurate determination of the sample dimensions ($3\text{-}4\%$) (recall $\rho = 1/\sigma = RA/L_0$) or determination of the sample current through the sample ($\approx 1\text{-}2\%$). Let the thermal conductivity ($\lambda_T' = 2.2 \text{ watts/m-K}$) be 10% too high. This could result from inaccurate determination of the sample dimensions, errors in ΔT or errors in determining the power through the sample. We will assume that there will be no error in determining the sample temperature ($T' = 300\text{K}$). Given these systematic errors in our measurement, which are not unreasonable unless one is very careful, we would obtain a $(ZT)' = 0.89$ which has an error of 21% from the real ZT value. It should be obvious then, that accurate determination of these properties is very important.

TABLE I: Properties of Interest for Thermoelectric Materials:

Sample Property	Relationship	Note
Seebeck coefficient:	$\alpha = -\Delta V / \Delta T$	{ $Q_P = \alpha IT$ }
Electrical Conductivity:	$\sigma = ne\mu$	{ $Q_I = I^2 R$ }
Thermal Conductivity:	$\lambda = Q_K L_0 / A \Delta T$	{ $Q_K = \lambda A \Delta T / L_0$ }
Hall Voltage	$V_H = R_H BI/w$	{ w : sample thickness}
Hall Coefficient	$R_H = 1/ne$	{yields n and carrier sign}
Carrier Mobility	$\mu_H = \sigma R_H$	{want high μ for fixed n }
Carrier Concentration	$n = 1/R_H e$	{ $n \approx 10^{17}\text{-}10^{19} \text{cm}^{-3}$ }

Measurement Criteria:

One important point to remember is to be sure of your measurements or conversely to know the level of the systematic errors in your measurements. One way to do this is to develop **standards** (materials with known and established thermoelectric properties) to check your apparatus and measurement techniques. An idea being discussed among the thermoelectrics research community is to develop laboratory standard materials to be shared between researchers and to develop "round robin" or "blind measurements" to assure the accuracy of results that are being reported. Recently an error in measurement resulted in a very large ZT ($ZT \approx 2$) being reported and this report was subsequently withdrawn. This report caused quite a "stir" within this research field. The error turned out to be very subtle; decomposition of the sample at the surface which resulted in an erroneous resistivity measurement.

Another criteria is to make all the reported measurements (α , σ , λ , n and R_H) on one sample and not report the best measurements on samples from a batch. Also, making the measurements as close to the same time and temperature is important. This will eliminate sample deterioration with time or strong temperature dependence of the material's properties. Electrical and thermal transport properties can have a very strong dependence on crystallographic direction, sometimes by orders of magnitude. Thus, measurements all in the

same crystallographic direction, (or even "pressed pellet" polycrystalline direction) is very important. Measurements on more than one sample, if possible, and averaging the results is needed. This will help to average the sample to sample differences, and possibly minimize discrepancies between various groups.

Resistivity (or electrical conductivity)

In principle, resistivity is the easiest of the three measurements to make. Today materials come in many different forms, from bulk materials (a few mm for each dimension) to either thick ($\approx 1 - 5 \mu\text{m}$) or thin films ($\approx 100 - 1000 \text{ \AA}$). Oxide layers can form on the surfaces and since many of the materials are semiconductors, contacts (p-n junctions) can be a real problem. Determination of sample dimensions is important since ($\rho = RA / L_0$) and typical resistances of samples of these TE materials is only a few m Ω . Also, recall when a current is passed through a TE material a ΔT is generated which in turn results in a thermal voltage, $V_{TE} = \alpha \Delta T$, which adds to the IR voltage, V_S , of the sample. The measurement must be made relatively fast ($\approx 2-3$ secs) which means ac or fast dc switching. The current must be reversed and the thermal voltage subtracted to measure the IR voltage (i.e. $V_S = 0.5[V(I^+) - V(I^-)]$) and thus the sample resistance. Accurate measurement of the current through the sample is also important. A high precision resistor ($\approx 0.01 - 0.1\%$) in series with the sample will help determine the sample current; don't just trust the setting on your current source. Also a four probe method for measurement of the sample resistance is essential, that is the current is injected into the sample in one pair of leads and the sample voltage is measured on a completely separate set of leads. This will eliminate the effect of the contact resistance (that is in series with the sample) on the voltage measurement. Also, to insure uniform current flow through the sample at the point of the voltage measurement, the lead should be positioned at a distance from the end of the sample (the position of the current lead) such that ; ($L - L_0 \geq 2w$), where L is the total length of the sample, L_0 is the distance between the voltage probes and w is the thickness of the sample. Error in position of the voltage probes, L_0 , can be somewhat minimized by an array of voltage probes along the length of the sample and averaging the calculated resistivity values.

Contacts and contact effects:

Excellent electrical contacts to these TE materials is essential. Large contact resistances which result in Joule heating at the contacts ($I^2(R_{C1} + R_{C2})$) can make these TE measurements extremely difficult and Joule heating can totally cancel the desirable Peltier heat flow. A temperature difference, ΔT , can arise in the sample from just a difference in contact resistance of each current contact, $\Delta T \approx P \approx I^2 (R_{C1} - R_{C2})$. For the Bi_2Te_3 class of materials contacts were a major concern. Contact materials such as Cu or Au would easily diffuse into the sample between the Te-Te planes and thus eliminate the desirable thermoelectric properties of these materials. It was necessary to first plate the end of the sample to inhibit diffusion (at the current contact) and then apply the solder or contact material. Oxide layers or sample decomposition at the surface may lead to erroneous measurements and must be eliminated. Each new material will have their own electrical contact issues to be solved and it is necessary to remember the importance of the electrical contacts. Many contact techniques exist and a few are listed: solder (many different types and temperatures), arc welding - capacitor discharge (localized point, robust sample to avoid damage), metal-sputtering or evaporation (Au, Ag or Cu etc.), ion-implantation or diffused contacts, Ag-paints (e.g. Dupont 4929™ Ag paint or SPI™ Ag coating for SEM), metal-plating or metal epoxies, and also needle pressure probes (e.g. "Pogo™ contacts").

Resistivity of Thin Discs or Thin Films.

Specific techniques are known for the measurement of the resistivity of thin discs or films or samples of arbitrary shape. The four point probe technique for the measurement of a thin rectangular sample is given in Figure 1¹⁷. The needle point probes are co-linear and evenly spaced along the sample. The important dimensions are given by the sample dimension parallel to the contact line (**a**); the sample dimension perpendicular to the contact line (**b**); spacing between the contact probes (**s**) and the thickness of the sample (**w**). The relationship between the resistivity, ρ , and the sheet resistivity, ρ_s , is given by $\rho = \rho_s w$. The resistivity for this configuration is given by:

$$\rho = \{(V w) / I\} \{C_1(a/d) C_2(w/s)\} \quad (1)$$

The terms in equation 1 are $C_1(a/d)$, a correction factor for the planar dimensions, eg. for an infinite sheet ($C_1(a/d) = \pi / \ln 2$) and $C_2(w/s)$, a correction factor for the ratio of thickness to the contact spacing (eg. $C_2(w/s) = 0.9995$ for $w/s = 0.4$ and $C_2(w/s) = 0.9214$ for $w/s = 1$). Values for these correction factors are taken from reference 17 and are given in Tables I and II. If $C_1(a/d) = \pi / \ln 2$ then the thickness dependence is given by:

$$\rho = \{(V w) / I\} \{(\pi / \ln 2) C_2(w/s)\} \quad (2)$$

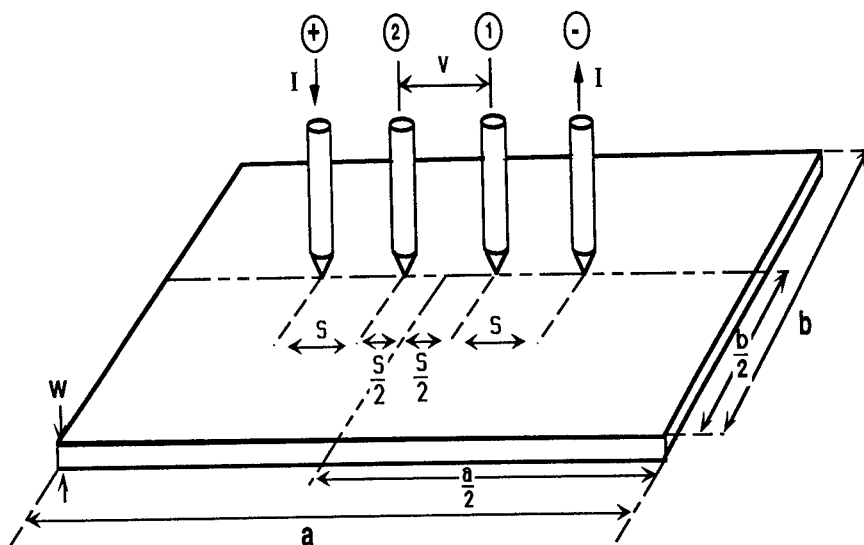


Figure 1.) Diagram of a four point probe configuration for the measurement of resistivity of a thin disc. The sample dimensions are length, **a**, width, **b**, thickness, **w**, and spacing between the contact probes, **s**. (after reference 17)

TABLE II: Correction Factor for Planar Dimensions, $C_1(a/d)$:

d/s	circle diam d/s	a/d = 1	a/d = 2	a/d = 3	a/d ≥ 4
1.0				0.9988	0.9994
1.3				1.2467	1.2248
1.5			1.4788	1.4893	1.4893
1.8			1.7196	1.7238	1.7238
2.0			1.9454	1.9475	1.9475
2.5			2.3532	2.3541	2.3541
3.0	2.2662	2.4575	2.7000	2.7005	2.7005
4.0	2.9289	3.1137	3.2246	3.2248	3.2248
5.0	3.3625	3.5098	3.5749	3.5750	3.5750
7.5	3.9273	4.0095	4.0361	4.0362	4.0362
10.0	4.1716	4.2209	4.2357	4.2357	4.2357
15.0	4.3646	4.3882	4.3947	4.3947	4.3947
20.0	4.4364	4.4516	4.4553	4.4553	4.4553
40.0	4.5076	4.5120	4.5129	4.5129	4.5129
∞	4.5324	4.5324	4.5324	4.5325	4.5324

TABLE III: Correction Factor for Ratio of Thickness/Contact Spacing, $C_2(w/s)$:

w/s	$C_2(w/s)$
0.4000	0.9995
0.5000	0.9974
0.5555	0.9948
0.6250	0.9898
0.7143	0.9798
0.8333	0.9600
1.0000	0.9214
1.1111	0.8907
1.2500	0.8490
1.4286	0.7938
1.6666	0.7225
2.0000	0.6336

A technique for measuring samples of arbitrary shape was developed by van der Pauw in the late 50's.¹⁸⁻¹⁹ Many others have elaborated on this technique with additional corrections in latter years and these references are given.²⁰⁻²² The resistivity is given by:

$$\rho = F\{(\pi w) / \ln 2\} \{ R_{AB,CD} + R_{BC,DA} \} / 2 \quad (3)$$

where $F = \text{Fnc}(R_{AB,CD} / R_{BC,DA})$ and $R_{AB,CD}$ and $R_{BC,DA}$ are the resistances measured in the different contact configurations (I^+ , I^-) and (V^+ , V^-) rotated by 90 degrees with respect to each other. The function $F \approx 1$ for $(R_{AB,CD} / R_{BC,DA}) \leq 1.5$. The van der Pauw technique assumes the contacts are placed on the extreme edges of the sample. A correction also exists for

the placement of the contacts onto the sample.²¹ If d is the distance from the edge of the sample to the contact point and D is diameter of the sample then the error in the resistivity is given by:

$$\Delta \rho / \rho = - \ln \{ 1 + (d/D)^2 / (1-d/D)^2 \} / 2(\ln 2) \quad (4)$$

If d is less than $0.1D$ then the error in $\Delta \rho / \rho$ is less than 1%. Care must be taken for oxide layers on the samples or surface decomposition of the sample. These needle probes are usually able to "break through ordinary oxide layers. Also, another technique which is utilized to determine the resistivity tensor of single crystal samples is known as the Montgomery technique.²³ It utilizes a series of probe configurations on each face of the sample and then various current and voltage combinations.

Seebeck Coefficient.

The Seebeck coefficient or thermopower, α , is an intrinsic property of a material related to the material's electronic structure. It is a bulk property measurement much like the resistivity. The thermopower will yield information about the sign of the charge carrier and is essentially the entropy per carrier divided by the charge of the carrier.²⁴⁻²⁶ The temperature dependence of the thermopower can be quite complicated and difficult to interpret. Many other contributions, such as phonon drag for example, can be involved in combination with the simple diffusion thermopower (linear in T) which is typical of metals. The thermopower is not geometry specific and is given by a measurement of the ratio of the sample voltage (electric field) to the temperature difference (temperature gradient) along the sample;

$$\alpha_{ab} = \Delta V / \Delta T = (V_H - V_L) / (T_H - T_L) \quad (5)$$

where $\alpha_{ab} = \alpha_b - \alpha_a$ is the measured value of the thermopower which includes both the sample contribution, α_a , as well as the lead contribution α_b . The lead contribution, typically Au, Cu or Chromel, must be known and subtracted from each data point at each temperature. Thermopower appears to be a relatively easy measurement and is probably the easiest of the three that go into ZT except some care must be taken. It is very easy to get the sign of the thermopower wrong and so a word of caution is appropriate. Another source of error is the determination of the temperatures, T_H and T_L at the voltage probes, V_H and V_L , respectively. One way to do this is to arc-weld the thermocouples to the sample and use one leg of each thermocouple as the sample voltage lead itself. This means essentially using a new thermocouple for each sample. It may be desirable to use a permanently mounted thermocouple and thermally anchor the sample and the thermocouple through a common medium using varnish or some other contacting adhesive. This has advantages but is more likely to cause a thermal anchoring problem resulting in a wrong ΔT reading. Thermal anchoring errors are discussed quite thoroughly in an article by Kopp and Slack.²⁷ One should definitely test out this technique by measuring known standards and comparing values. The sample is its own best thermometer or thermocouple. One can compare changes in the thermocouple voltage to that of the sample voltage as the ΔT is varied using an oscilloscope to measure the time differences in their response to ΔT , as another check. A poor thermal contact between the thermocouple and the sample will also typically be pressure dependent. As the gas or air is pumped out the thermal link between the sample and the thermocouple becomes worse and the thermopower will change a few percent, due to an erroneous ΔT measurement. Another source of error is in the calibration and subtraction of the lead contribution. At lower temperatures the lead wires can be calibrated against a high T_C superconductor (with transition temperatures, T_C

as large as $T_C \approx 130\text{K}$). Since the thermopower of a superconductor below T_C is zero the lead contribution is the only contribution to the measured value.

The simplest technique of measuring the thermopower is the small ΔT method. This involves sweeping the ΔT around a set temperature and measuring the voltage of the sample. The slope is α_{ab} . This technique is somewhat slow and cumbersome as a function of T . Many times one can slowly vary the temperature and take only 2-3 pts. One must be sure that ΔV is linear in ΔT and goes through $\Delta V = 0$ at $\Delta T = 0$. This is similar to how one typically takes resistance measurements; assume Ohm's law. This technique may be checked periodically at fixed temperatures, perform ΔV vs. ΔT sweeps, calculate the slope and compare to the other data. High resistance contacts can exhibit ac pickup resulting in a rectified dc offset voltage which can also lead to errors. Again, reliable calibrations, and measuring standards can eliminate many erroneous measurements.

Thermal Conductivity.

Thermal conductivity measurements are by far the most difficult to make with relatively high accuracy. There are many excellent texts and techniques available which discuss in detail many of the corrections and potential errors one must consider and I refer the reader to a few of these.^{16, 28-31} Many other excellent references exist. The thermal conductivity, λ_T , of good TE materials is very low, typically $\lambda_T \leq 2$ watts / m-K. This makes the measurement more difficult since the heat will flow through other paths of higher thermal conductivity and result in an error in determination of the power input into the sample. Thus, calculating the heat loss corrections and proper thermal shielding techniques to minimize these corrections is critical for these TE materials. The thermal conductivity for a typical "steady state" method is given by:

$$\lambda_T = Q_T L_0 / A \Delta T \quad (6)$$

where Q_T is the heating power through the sample, L_0 is the length between the thermocouple leads. Errors due to radiation loss or gain between the surroundings and the sample, convection and conduction through any lead wires can be substantial. The radiation loss is given by:

$$Q = \epsilon \sigma_{S-B} A (T_0^4 - T_S^4) \quad (7)$$

where T_0 (T_S) is the temperature of the sample and the surroundings, respectively and σ_{S-B} is the Stephan-Boltzman constant ($\sigma_{S-B} = 5.7 \times 10^{-8} \text{ W/m}^2\text{-K}^4$) and ϵ ($0 < \epsilon < 1$) is the emissivity. Proper thermal shielding and thermal anchoring are essential for reliable and accurate measurements. Heat losses can also be due to convection or circulating gas flow around the sample. The best way to minimize these convection losses is to operate the measurement with the sample in a moderate vacuum (10^{-4} - 10^{-5} torr). This will also reduce the heat loss due to conduction through the gaseous medium. The other substantial heat loss mechanism is due to conduction. This can be due to loss from the thermocouple or other leads attached to sample for temperature measurement. Long lead lengths of small diameter (small A) attached to the sample with sufficient thermal anchoring, so essentially no ΔT arises between the sample and shield is important for minimizing this effect. One must accurately determine the power through the sample by considering the various loss mechanisms. Thermal resistance of leads, heaters etc. as well as interface anchoring between the sample, the heater and the heat

sink is also important. Again, measuring known standards and thoroughly calibrating the apparatus is essential.

Many techniques other than the standard steady state method are valid. In the comparative technique a known standard is put in series between the heater and the sample. This technique is best when the thermal conductivity of the standard is comparable to that of the sample. This technique ultimately depends on the accuracy to which the thermal conductivity of standard is known. Also, the same type of errors and corrections must be considered as for the steady state technique. The power through the standard (1) is equal to the power through the sample (2) and given the thermal conductivity of the standard λ_1 , the thermal conductivity of the sample λ_2 is given by:

$$\lambda_2 = \lambda_1 \{A_1 \Delta T_1 L_2 / A_2 \Delta T_2 L_1\} \quad (8)$$

Another technique that is becoming popular for TE materials, as well as for many non-conducting low thermal conductivity systems, is the "3- ω technique."^{32,33} This method uses a metal film, typically Au or Pt, deposited on sample for an I^2R heater and using the temperature dependence of the metal $\{R(T) = \text{Fnc}(T)\}$ as a thermometer. An ac current is supplied to the sample, $I \approx \exp(i\omega t)$, which results in a 2ω heating of the strip ($P = I^2R \approx \Delta T$). The resistance of the metal film resistor will vary as $\Delta T \approx \exp(i2\omega t)$ and the voltage on the strip will vary as the 3ω component, $\Delta V = I\Delta R \approx \exp(i3\omega t)$. The thermal conductivity, λ , is related to the temperature difference; ΔT and $\log(\omega)$. This technique has many advantages. The temperature dependence of the thermal conductivity can be acquired much more readily than the steady state technique, with essentially no radiation errors, which allows more accuracy at higher temperatures (1000K). It is user friendly and inexpensive. A non-conducting layer must be applied to a conducting sample before depositing the metal strip, it measures the perpendicular thermal conductivity and requires some level of microlithography to be available. The 3ω technique may be the best "pseudo - contact" method available. Other techniques which will not be discussed include "laser flash" diffusivity and thermal diffusivity (D) methods, $D = \lambda / C_V$, where C_V is the specific heat of the sample.

Hall Coefficient, Carrier Concentration and Mobility.

The power factor of a TE material is typically optimized around some carrier concentration, n , where $n \approx 10^{17} - 10^{19} \text{ cm}^{-3}$. Thus, it is necessary to measure the carrier concentration by measuring the Hall Effect ($V_H = BIb / neA = R_H BI / w$) and the Hall coefficient, $R_H = 1/ne$. The Hall voltage, V_H , is due to the Lorentz force ($F = qE = qV/b$) acting on a charged particle moving with a velocity, v , in a magnetic field B , where b is the width of the sample and w , the thickness. The parameters; I , B and V_H are all perpendicular to each other. For a rectangular sample, B is the magnetic field (B_z), I is the current (I_x) and V_H is measured in the y direction. The Hall effect and Hall measurements in metals and semiconductors are discussed in many texts and references.³⁴⁻³⁸ The conductivity is related to the carrier mobility, $\mu = R_H \sigma$, ($\sigma = ne\mu = 1/\rho$) and for a fixed n , μ must be large for a good TE ($\mu \approx 1000 \text{ cm}^2/\text{V-s}$ for Bi_2Te_3 and skutterudites). For a semiconductor of one carrier type: $R_H = 3\pi / 8ne$. In general, $R_H = r / ne$, where $1 \leq r \leq 2$ and r is known as the Hall factor which depends on magnetic field, temperature and the scattering mechanism. Measurements of V_H , $R_H = 1/ne$ and μ are important for fully characterizing and understanding a TE material. There are again errors that must be considered. Misalignment of the leads (IR voltage) or magnetic field can lead to errors unless corrected and terms must be canceled that are not proportional to BI . There are also other corrections such as

the TE voltages since ΔT 's will lead to voltage differences. Care should be taken to eliminate any ΔT 's. There are also other magneto-thermoelectric effects which must be considered and corrected for such as: Nernst effect, Ettinghausen effect and the Ridgi-Leduc effect. These will not be discussed here due to space constraints but these are discussed in detail elsewhere.³⁴⁻³⁸ The Hall voltage is given by:

$$V_H \approx \{V(I^+, B^+) + V(I^-, B^-) - V(I^-, B^+) - V(I^+, B^-)\} / 4 \quad (9)$$

thus cancelling out all the terms discussed above except the Ettinghausen effect, which should only be a small correction to the Hall voltage (except of course where $R_H \approx 0$). An ac Hall measurement may prove the most applicable with fewest corrections for these TE materials.

Z-Meters or ("Harman Technique").

Another technique which is widely used for characterizing TE materials is the so called "Harman Technique" or Z-meter.^{12, 16, 39-43} Consider the voltage as a function of time for a TE material under various conditions. If there is no ΔT and $I = 0$, then $V_S = 0$, where V_S is the sample voltage. Apply a current, I , and the voltage will increase by IR_S , where R_S is the sample resistance. When a current is applied to a TE material a ΔT arises from the Peltier effect ($Q_P = \alpha IT$) and a, V_{TE} , will add to the IR_S voltage. Under steady state or adiabatic conditions the heat pumped by the Peltier effect will be equal to heat carried by the thermal conduction;

$$(\alpha IT) = (\lambda A \Delta T / L) \quad (10)$$

One can derive a relationship between ZT and the adiabatic voltage ($V_A = V_{IR} + V_{TE}$) and the IR sample voltage, V_{IR} ^{12, 16}

$$ZT = (V_A / V_{IR}) - 1 = (\alpha^2 T / \rho \lambda) \quad (11)$$

This relationship is a reasonable approximation to ZT but assumes ideal conditions unless a number of corrections are accounted for such as contacts, radiation effects and losses for example. The first criteria is that the sample needs to possess a $ZT \geq 0.2$. Also, contact effects, sample heating from the contacts and the sample resistance should be very small and ΔT effects from contact resistance differences should be negligible. The thermal conductivity can be estimated from the Harman technique in two ways, Measure, R and α and then measure ZT from equation 11 and the thermal conductivity can then be determined. Another way is to use equation 10 in the form below:

$$I = \lambda(A / \alpha TL) \Delta T \quad (12)$$

Then at a constant temperature, $I = \lambda(A / \alpha TL) \Delta T = \lambda C_0 \Delta T$, where C_0 is a constant at a given T . Thus, the linear part of the slope of an I - ΔT plot will yield the thermal conductivity. The ZT determined from the Harman method is essentially an "effective ZT", one which yields the operating figure of merit of the device. This technique requires essentially no contact effects, (recall $I^2(R_{C1} - R_{C2}) = \Delta P_C \approx \Delta T$ across the sample from $I^2 R$ heating). Information from this technique should be compared to the measurements of the individual parameters that go into ZT. It should not be a substitute for knowing the individual parameters.

Summary:

It should be obvious from the many issues we have discussed, that it is no easy task to come up with highly reliable and accurate measurements of the parameters that go into ZT. Many potential errors and corrections for these TE materials must be taken into consideration. Thus, reports of materials that are only a few percent different from previous materials are not so convincing and of course are really not that much of an advancement. Many new researchers are coming into this field and should be aware that many excellent techniques for measuring their properties were developed in the late 50's and 60's. Careful investigation of the literature can provide valuable information and insight into the measurement of TE materials. The errors that can be made are sometimes very subtle and if we are to achieve much higher ZT materials, $ZT \approx 2-3$, then we will have to be able to validate these numbers. Measuring standards, careful and accurate calibrations, and potential sharing of samples through "round robin" measurements are very important to eliminate erroneous information from being reported. The information contained in this paper will be informative to some of you, especially people new to the field, while it may serve only as an elementary reminder to established experts in the field.

References.

- 1.) H. J. Goldsmid, Electronic Refrigeration, (Pion Limited Publishing, London, (1986)
- 2.) CRC Handbook of Thermoelectrics, edited by D. M. Rowe, CRC Press, Boca Raton (1995)
- 3.) L. D. Hicks and M. S. Dresselhaus, Phys. Rev. B, **47**, 12727 (1993)
- 4.) J. P. Fleuriet, T. Calliet and A. Borshchevsky, Proc. of the XIII International Conference on Thermoelectrics, AIP, p 40-44 (1995)
- 5.) B. C. Sales, D. Mandrus and R. K. Williams, Science, **272**, 1325 (1996)
- 6.) D. T. Morelli et. al., Phys. Rev. B, **51**, 9622 (1995)
- 7.) Glen A. Slack and V. G. Toukala, Jour. Appl. Phys. **76**, 1635 (1994)
- 8.) G. Nolas, G. Slack, D. T. Morelli, T. M. Tritt and A. C. Ehrlich, Jour. Appl. Phys., **79**, 4002 (1996)
- 9.) T. M. Tritt et. al., Jour. Appl. Phys., **79**, 8412 (1996)
- 10.) H. D. Young, Statistical Treatment of Experimental Data, McGraw Hill, New York, (1962)
- 11.) An Introduction to Error Analysis: The Study of Uncertainties in Physical Measurements John R. Taylor, University Science Books, Mil Valley CA (1982)
- 12.) Terry M. Tritt, Science, **272**, 1276 (1996)
- 13.) All the "Q-terms" discussed in this paper will relate to rate of heat transfer or power related to that phenomena.
- 14.) C. W. Wood, Rep. Prog. Phys. **51**, 459-539 (1988)
- 15.) D. M. Rowe and C. M. Bhandari, Modern Thermoelectrics, Reston Publishing Co. Reston VA, 1983
- 16.) Thermoelectricity, edited by P. H. Egli, John Wiley and Sons, New York (1960)
- 17.) F. M. Smits, Bell System Technical Journal, p 711, May 1958
- 18.) L. J. van der Pauw, Philips Research Reports, **13**, 1, 1958
- 19.) L. J. van der Pauw, Philips Research Reports, **16**, 187, 1961
- 20.) J. D. Wasscher, Philips Research Reports, **16**, 301, 1961
- 21.) D. W. Koon et. al., Rev. Sci. Instrum., **60**, 275, 1989
- 22.) D. W. Koon et. al., Rev. Sci. Instrum., **60**, 271, 1989

- 23.) H. C. Montgomery, Jour. Appl. Phys., **42**, 2971 (1971)
- 24.) P. M. Chaikin, An Introduction to Thermopower, Organic Superconductivity, editors: V. Z. Kresin and W. A. Little, Plenum Press, New York 1990
- 25.) Thermoelectric Power of Metals, F. Blatt, P. Schroeder, C. Foiles and D. Greig, Plenum Press, New York (1976)
- 26.) Thermoelectricity: An Introduction to Principles: D. K. C. MacDonald, John Wiley and Sons, New York (1962)
- 27.) J. Kopp and G. A. Slack, Cryogenics, p 22 (Feb. 1971)
- 28.) Solid State Physics, G. A. Slack, (Academic, New York) 1979
- 29.) Thermal Conductivity Vol I and Vol II, edited by R. P. Tye, (Academic Press, New York) 1969
- 30.) Thermal Conduction in Solids, R. Berman (Clarendon Press, Oxford) 1976
- 31.) Methods of Experimental Physics: Solid State Physics, Vol 6, editor: L. Marton, (Academic Press, New York) 1959
- 32.) David Cahill, Rev. Sci. Instrum., **61**, 802 (1990)
- 33.) David Cahill et. al., J. Vac. Sci. Technol. A, **7**, 1260 (1989)
- 34.) Solid State and Semiconductor Physics, J. P. McKelvey, (Harper and Row, New York) 1966
- 35.) Semiconductor Measurements and Instrumentation, W. R. Runyan, (McGraw Hill, New York) 1975
- 36.) The Hall Effect and Related Phenomena, E. H. Putley, (Butterworths, London) 1960
- 37.) The Hall Effect in Metals and Alloys, C. Hurd, (Plenum Press, New York) 1972
- 38.) A. C. Ehrlich, The Hall Effect, The Electrical Engineering Handbook, Editor, Richard C. Dorf, CRC Press, Boca Raton, 1993, p1106
- 39.) T. C. Harman, Jour. Appl. Phys., **30**, 1373 1959
- 40.) T. C. Harman, J. H. Cahn and M. J. Logan, Jour. Appl. Phys., **30**, 135, 1959
- 41.) A. W. Penn, J. Sci. Instrum., **41**, 626, 1964.
- 42.) A. E. Bowley et. al., J. Sci. Instrum., **38**, 433, 1961.
- 43.) R. Buist., Proc. of the XI International Conference on Thermoelectrics, AIP, (1992)

EXPERIMENTAL TRANSPORT PHENOMENA AND OPTIMIZATION STRATEGIES FOR THERMOELECTRICS

A. C. Ehrlich and D. J. Gillespie
Code 6341, U. S. Naval Research Laboratory, Washington, DC 20375

ABSTRACT

When a new and promising thermoelectric material is discovered, an effort is undertaken to improve its "figure of merit". If the effort is to be more efficient than one of trial and error with perhaps some "rule of thumb guidance" then it is important to be able to make the connection between experimental data and the underlying material characteristics, electronic and phononic, that influence the figure of merit. Transport and fermiology experimental data can be used to evaluate these material characteristics and thus establish trends as a function of some controllable parameter, such as composition. In this paper some of the generic-materials characteristics, generally believed to be required for a high figure of merit, will be discussed in terms of the experimental approach to their evaluation and optimization. Transport and fermiology experiments will be emphasized and both will be outlined in what they can reveal and what can be obscured by the simplifying assumptions generally used in their interpretation.

INTRODUCTION

Starting in the 1950's and for approximately ten years thereafter a very substantial effort in this country was directed towards developing improved thermoelectric materials for cooling and power generation applications. Significant progress was made and a set of criteria regarding desirable characteristics of the electronic and lattice structure was established. The preferred materials would be semiconductors/semimetals; the energy gap between the conduction and valence band would be large enough to avoid the generation of minority carriers at the temperature of operation but not very much larger; high element mass materials would be preferred; etc. [1]. The intent of all these criteria was to help find a usable material with the highest possible efficiency; i.e., one that would generate the most cooling, for example, for a given quantity of input energy. A measure of this is the so called thermoelectric figure of merit, Z , or the dimensionless figure of merit, ZT , where T is the absolute temperature. Z is given by [2]

$$Z = S^2\sigma/\kappa \quad (1)$$

where S is the Seebeck coefficient (or thermoelectric power), σ is the electrical conductivity and κ is the thermal conductivity. Although somewhat more progress has occurred at higher

temperatures, the highest room temperature value of ZT achieved has remained approximately unity.

The search for higher ZT's has involved, in large measure, electronic transport experiments with their interpretation as a window on the electronic structure and simple theoretical modeling of the thermoelectric consequences of changes in this structure. In this manuscript we will emphasize a few of the often overlooked complications associated with electron scattering effects that can influence the interpretation of data as well as the precautions to take in treating an electron gas that is neither purely classical nor purely quantum. Then, a particular kind of scattering center will be used in a model calculation to illustrate how scattering effects can be used to enhance the thermoelectric power. Finally, some of the pitfalls in interpreting various transport coefficients that impact a search for thermoelectric materials will be mentioned.

THEORETICAL CONSIDERATIONS

Fundamental Equations

The three transport coefficients that constitute Z in equation (1) can be given, in the spherical band approximation, by combinations of a class of integrals, M_n , and are [3]

$$\sigma = e^2 M_1 \quad (2)$$

$$S = [M_2 - \eta M_1] / e M_1 T \quad (3)$$

$$\kappa_e = [M_1 M_3 - M_2^2] / M_1 T \quad (4)$$

where,
$$M_n = \frac{-4}{3m^*} \int N(E) \tau(E) E^n \frac{\partial f_0}{\partial E} dE \quad (5)$$

and $\eta(T)$ is the fermi energy measured from the edge of the band, e is the electronic charge, m^* is the carrier effective mass (electron or hole), $N(E)$ is the density of states, E is the carrier energy, also measured from the edge of the band, $\tau(E)$ is the carrier scattering time, f_0 is the fermi function and κ_e is the electronic contribution to the thermal conductivity. The total thermal conductivity, κ , includes a lattice or phonon contribution, κ_p , so that

$$\kappa = \kappa_e + \kappa_p \quad (6)$$

Three kinds of scattering mechanisms will be considered; acoustic phonons, ionized impurities and neutral impurities. The first two are the most commonly considered in

thermoelectricity and the third serves as a kind of standard by virtue of its simplicity. The energy dependencies of these are generally taken as $\tau \propto E^{-1/2}$ (acoustic phonons), $\tau \propto E^{3/2}$ (ionized impurities) and $\tau = \text{constant}$ (neutral impurities) [4].

The reasons that Z cannot easily be made very large is not immediately obvious. From equations 2-5 it seems clear that any of the components of Z can be made larger or smaller by manipulating the composition and structure of materials. The reason Z cannot be so easily increased is that all the components of Z depend on the same material parameters, so they cannot be individually varied, and nature has conspired, so far, to make difficult the obtaining of values of ZT much in excess of unity.

A second complication is that κ has two components, as seen in equation (6). Often in the most promising semimetallic materials κ_p is comparable to or greater than κ_e . Thus even if a material with a very favorable electronic structure is found, it must often be compromised by alloying, for example, in order to reduce κ_p . In part because of this complication and even more important because thermal conductivity is by far the most difficult transport parameter in Z to measure, materials are usually screened by determining their so called power factor, $P = S^2\sigma$. Thus $Z = P/\kappa$ and an approach to maximizing Z has often been to maximize P and then try to minimize κ by minimizing κ_p while altering the electronic structure as little as possible.

There is a well known characteristic curve of P as a function of conduction electron density which has a maxima at about 10^{19} electrons/cm³ [5]. Equations (2) and (3) predict this but show that where the peak occurs depends on the energy dependence of τ . Figure 1 shows the result of a numerical evaluation of equations (2) and (3) using a room temperature value of kT (k is the Boltzmann constant) with the $\tau = \text{constant}$ curve peak occurring at electron concentrations above that for $\tau \propto E^{-1/2}$. In fact the $\tau \propto E^{3/2}$ curve will not manifest a peak at all. (In an actual experimental situation, of course, a purely $E^{3/2}$ dependence of τ on the electron energy at room temperature would never occur. There would always be phonons.) Thus modifying a material to minimize κ_p can affect your power factor not only by changing

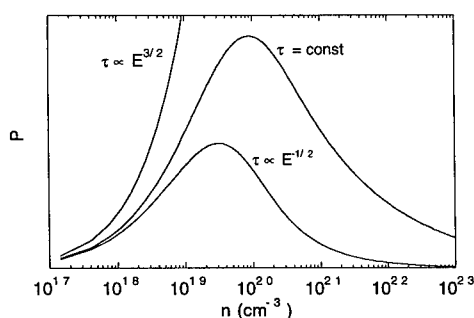


Fig. 1 The power factor, $S^2\sigma$, as a function of the electron concentration in arbitrary units for three different energy dependences of the electron scattering time, τ .

the electronic structure or the average mobility of the electrons (the average of τ over energy) but simply changing the dominant form of the scattering. This is particularly true below room temperature since above room temperature the scattering is phonon dominated.

Because many of the early and best references on thermoelectric materials were written before computational facilities were conveniently accessible, material optimization strategies were

based on calculations that could be carried out analytically. To this end the appropriate expressions were developed using equations (2)-(5) with classical (Maxwell-Boltzman) statistics for the electron gas, i.e., it was assumed that $kT \gg \eta$. In fact the best materials, for a given temperature range, typically operate where $kT \sim \eta$ [6], which we will call the intermediate temperature range. It is therefore of some interest to examine traditional strategies and approximations in light of more accurate numerical calculations easily obtainable with desktop computers.

Equation (1) has sometimes been rewritten

$$ZT = S^2 \sigma T / \kappa = S^2 \sigma T / (\kappa_e + \kappa_p) = S^2 / \{(\kappa_e + \kappa_p) / \sigma T\} = S^2 / \{L + \kappa_p / \sigma T\} \quad (7)$$

where L is the Wiedermann-Franz ratio, $\kappa_e / \sigma T$, and is typically taken as a constant for the purpose of either planning new experiments or interpreting already existing experimental data. In fact L is a different "constant" depending on whether one is dealing with a Fermi-Dirac (quantum) or Maxwell-Boltzmann (classical) gas and if dealing with a classical gas, depends on the parameter q where $\tau \propto E^q$. Specifically, $L = Ak^2/e^2$ where A is $\pi^2/3$ for a quantum gas and is $[(5/2)+q]$ for a classical electron gas [7]. Furthermore, data taken as a function of temperature in the intermediate range, where the carriers are becoming increasingly classical with increasing temperature, will obviously reflect a temperature dependence of $L(T)$. This is shown in Fig. 2 for the three scattering mechanisms considered in this manuscript and for two zero-temperature fermi energies, η_0 . From the metallic value at $T=0$, L falls by almost 40% at high temperatures for $q=0$ (25% for $q=-1/2$) whereas it rises by more than 20% for $q=3/2$. Furthermore, for the fermi energies ~ 50 meV found in typical thermoelectric materials, the transitions take place over several hundred degrees and should be taken into account in the interpretation and analysis of transport data. Finally it should be noted that the variation of L

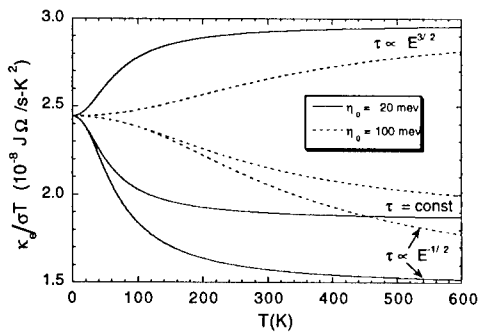


Fig.2 The Wiedermann-Franz ratio, $\kappa_e/\sigma T$, is shown as a function of temperature for two values of η_0 and three different energy dependences of the electron scattering time, τ .

seen in Fig. 2 is due to the change with temperature of η/kT both because of an increasing T and because of a falling of η with temperature.

It should also be noted that in a real material there will be variations of L as a function of temperature that arise because of a change with temperature of the dominant form of scattering. For example, at low temperatures the dopants in a donor doped

semiconductor would not be ionized

and could constitute neutral impurity scattering centers driving L below the $T=0$ value, L_0 . As the temperature is raised the dopants ionize, become the dominant scattering center and push L above L_0 . Finally at still higher temperatures, phonons dominate the scattering processes and return L to values below L_0 .

Effect of Energy Dependence of Scattering on S .

The importance of σ and κ notwithstanding, the magnitude of S is primary. As is apparent from equations (3) and (5) S is given by a fraction of two integrals of the form

$$S = \frac{\int G(E)\tau(E)(E - \eta)dE}{eT \int G(E)\tau(E)dE} \quad (8)$$

Thus since $G(E)$ and $\tau(E)$ each retain the same signs throughout the range of integration, S is proportional to a difference of negative and positive contributions of the numerator's integrand from electron energies below and above η respectively. For a single band of electrons, say, maximizing S involves minimizing one of those two contributions, preferably that below the fermi energy (it is typically the smaller contribution). Having η at or below the band edge, of course, completely eliminates any contribution from E 's below η . In fact, the more the weighting factor $(E - \eta)$ can be augmented, say by having a sharp positive variation of $\tau(E)$ with E , the larger will be S . These trends are seen in Fig. 3 where we have calculated S as a function of temperature for three functional forms of τ for a semimetal with a zero-temperature fermi energies of 20 and 100 mev. The positive variation of τ with E provides the largest value of S for both energies as would be expected. This approach is simply a variation on the well known theme of searching for a material which has a lot of structure in its band characteristics

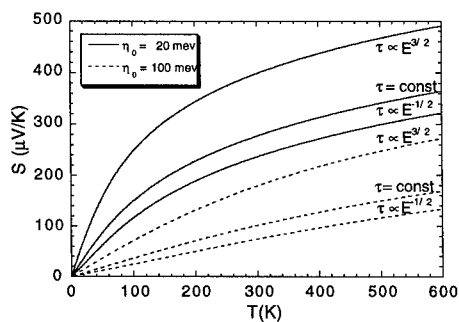


Fig.3 The Seebeck coefficient, S , is shown as a function of temperature for two values of η_0 and three different energy dependences of the electron scattering time, τ .

[8]. In fact it is structure in the integrand of the numerator of equation (7) that is required, i.e., for electrons, a rapid increase in the integrand with energy, E , which, in principle, can be obtained by the selection of the scattering centers as well as the electronic structure.

Another example of how a relaxation mechanism with a particular energy dependence can effect S is the potential electron scattering properties

of the virtual bound state [9]. When an impurity atom is imbedded in a matrix it sometimes retains some character of its free atom atomic energy levels. Although these levels hybridize with the matrix band states and spread out over some energy range, for d-states and much more so for f-states, the spreading is narrow compared to the band width. Locally in space around the impurity there is an enhanced density of states with an energy dependence that has a Lorentzian shape. Since the electron scattering rate, $1/\tau$, is proportional to the density of states we shall assume a $1/\tau(E)$ that varies with energy as a Lorentzian. That is $1/\tau = b/[(E-E_0)^2+b^2]$ as shown in the inset of Fig. 4a, $\tau(E)$ itself is obviously a parabola centered at E_0 with a minimum magnitude of b . For illustrative purposes we take one example with a zero-temperature fermi energy, η_0 , of 20 meV and one with 100 meV. In both cases we use Lorentzians with line widths (full width at half maximum) of 2 meV that do not change their energy width or energy position with temperature. In both cases also we carry out the calculation for two cases. In one, the Lorentzians are centered 20 meV above and in the second 20 meV below the zero-temperature fermi surface. The results of these calculations are shown in Figs. 4a and 4b with, in addition, the calculation for a constant (energy independent) τ for comparison.

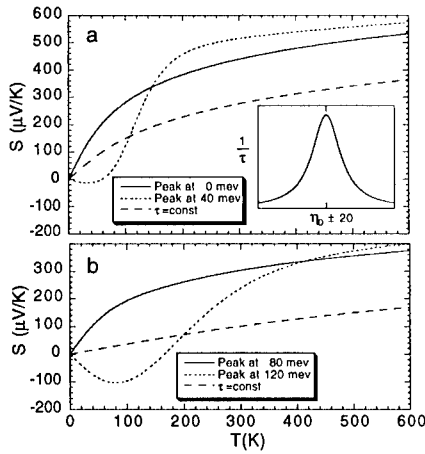


Fig.4 The Seebeck coefficient is shown as function of temperature for two values of the zero-temperature fermi energy, η_0 , and three different energy dependences of the electron scattering time. The energy dependences of τ are $1/\tau$ equal to a Lorentzian with a full width at 1/2 the maximum of 2 meV and a peak centered 20 meV below η_0 , $1/\tau$ equal to the same Lorentzian but centered 20 meV above η_0 , and a τ which is energy independent. The Lorentzian function is shown in the inset in Fig. 4a. Fig.4a shows the Seebeck coefficient for a free electron band with a 20 meV fermi energy and Fig.4b shows the coefficient for a band with a 100 meV fermi energy.

The curves in Figs. 4 have a number of interesting features. Firstly, if the Lorentzian is centered above the fermi energy, starting at $T=0$, the S vs. T curves decrease initially before displaying the usual upward trend. Secondly, the curve associated with the Lorentzian centered above the fermi energy starts below that associated with the Lorentzian below the zero-temperature fermi energy but at some temperature the curves cross and the latter is predicted to have a larger thermoelectric power than the former. The temperature at which this occurs depends on the zero-temperature fermi energy. Finally, above some temperature, both Lorentzian scattering functions give rise to larger thermoelectric powers than does an energy independent scattering mechanism.

The first of these features can be qualitatively understood in the following way. When $\eta \gg kT$, the contribution to S of the electrons above η exceed those below η for the most common energy dependencies of $\tau(E)$ that have been considered. If, however, $1/\tau(E)$ is a Lorentzian centered above η at $T=0$ then clearly the electrons with $E > \eta$ suffer much greater scattering and, for some combinations of parametric values, the electrons with $E < \eta$ will dominate the numerator of equation (8). This gives rise to the negative going values of S vs. T near $T=0$. As the temperature rises toward $\eta \sim kT$, the energy distribution of the electron gas is broadened and increasingly large contributions to S are made by electrons with energies far from η including electrons whose energies fall above the center point of the Lorentzian. These are further weighted to higher energies in the integrand of the numerator of equation (8) by the factor $(E-\eta)$. Significant contributions to the numerator of equation (8) continue for many kT above η . Below η , contributions are much smaller because $G(E)$ is smaller and they cease at the band edge. This asymmetry becomes increasingly important with rising temperature and spreading electron energy spectrum until finally S turns upward and even crosses the $S=0$ axis.

The second feature, the crossing of the two S vs. T curves representing the two Lorentzian scattering rates might at first seem surprising. The Lorentzian at higher energies, after all, is always the more effective scattering function for the most energetic electrons. These electrons make the positive and the largest contribution to S by way of the numerator of equation (8). Since scattering reduces the numerator of equation (8) one might not expect the crossing we find. The explanation is that the numerator is reduced less than the denominator when the Lorentzian is placed at 20 meV above the zero-temperature Fermi energy because of the somewhat subtle interplay between the energy dependence of $\partial f_0 / \partial E$ and the $E-\eta$ weighting factor.

The fact that both Lorentzians give rise to a larger S than does an energy independent τ at all but the lowest temperatures is simple to understand. The rapidly increasing τ 's with E , which is associated with the Lorentzians, can lead to a domination of S by the highest energy electrons. This will happen above some temperature where the energy spread of the electrons yields enough of these higher energy electrons.

Sorting Out the Electronic Structure

For semiconductors and semimetals the Hall effect and Fermiology techniques have been the most powerful tools to investigate the aspects of electronic structure that impact the transport properties. At temperatures of 4K and lower, the electron gas in thermoelectric materials is reliably degenerate ($kT \ll$ the Fermi energy). If the high magnetic field regime can be attained ($\omega_c \tau \gg 1$ where ω_c is the cyclotron frequency) then such measurements as the high field Hall effect and de Haas-Shubnikov effect can be made and often, but not always, be reliably interpreted. If they can, then these two measurements together can provide Fermi

surface sizes, shapes effective masses and sometimes even the fermi energy [10-12]. For the simplest fermi surface geometries this can sometimes be done even without the Hall effect data. In addition one can often obtain at least some information regarding the electron scattering [10-12]. Unfortunately, as the temperature is raised to levels of interest for applications of thermoelectric materials many of these parameters can change. Furthermore, fermiology experiments cannot be carried out at these temperatures (where $\omega_c\tau \ll 1$) and Hall effect measurements, though they can be made and are worth doing, are much more problematic in their interpretation.

Among the difficulties in interpreting the Hall effect is that the high field limit cannot be achieved. In the high field limit the Hall effect depends only on the difference in the number of holes and electrons, Δn , $R_H = 1/(\Delta ne)$. In contrast, for example, for a classical single band electron gas in the low field limit and with n electrons

$$R_H = \frac{\langle \tau^2 \rangle}{ne \langle \tau \rangle^2} \quad (9)$$

where $\langle \tau \rangle = \frac{4}{3\pi^2} \int \tau(E) x^{3/2} e^{-x} dx$, $x = E/kT$. The brackets $\langle \rangle$ indicate an average over occupied states. For the three basic scattering cases considered in this paper [13],

$$\begin{array}{ll} \langle \tau^2 \rangle / \langle \tau \rangle^2 = 1 & \tau \text{ is constant} \\ \langle \tau^2 \rangle / \langle \tau \rangle^2 = 3\pi/8 = 1.18 & \tau(E) \sim E^{-1/2} \\ \langle \tau^2 \rangle / \langle \tau \rangle^2 = 315\pi/512 = 1.93 & \tau(E) \sim E^{3/2} \end{array} \quad (10)$$

If $1/\tau(E)$ is a Lorentzian, the situation is more complicated and $\langle \tau^2 \rangle / \langle \tau \rangle^2$ depends on its width and position relative to the fermi energy. If the electron gas is not strictly classical, but rather intermediate, then the situation is even more complicated. One can, never the less, devise useful strategies. For example for a thermoelectric material one has presumably arranged to have either holes or electrons but not both. A low temperature high field Hall effect measurement could give you their number and since this has a good chance of not being a function of temperature, this and a higher temperature Hall effect measurement could be used to help extract the energy dependence of τ from equation (10) or its intermediate electron gas equivalent. But the answer obtained will not be unique so all other available information will be important including theory, systematics of the experimental results, and perhaps other measurements such as the magnetoresistance. There is, however, no fixed strategy for all situations.

CONCLUSION

The figure of merit of thermoelectric materials is most strongly influenced by S . We have emphasized that the scattering characteristics of the electrical carriers can be as important as the underlying electronic structure in determining S and they may be much simpler to manipulate than the overall electronic structure. This is particularly true at lower temperatures where the phonon scattering is less important. It has been further emphasized that in planning a research program or in understanding the data as it accumulates in the program it is important to explicitly take into consideration the classical, quantum or intermediate nature of the electron gas.

REFERENCES

1. D.M. Rowe and C.M. Bhandari, Modern Thermoelectrics, (Reston Publishing Company, Inc., Reston, Virginia 1983) pp. 35-48.
2. Ibid, p 23.
3. F.J. Blatt, Physics of Electronic Conduction in Solids, (McGraw-Hill, Inc. New York 1968) pp. 183, 203, 209.
4. Ibid, pp. 179, 255.
5. C.M. Bhandari and D.M. Rowe, in CRC Handbook of Thermoelectrics, edited by D. M. Rowe (CRC Press, Inc. Boca Raton 1995), p. 44.
6. H.J. Goldsmith, Applications of Thermoelectricity, (John Wiley and Sons, Inc. New York, 1960) p.32.
7. F.J. Blatt, Physics of Electronic Conduction in Solids, (McGraw Hill, Inc. New York 1968) pp. 127-128.
8. G.D. Mahan and J.O. Sofo, Proc. Natl. Acad. Sci. **93**, 7436 (1996).
9. J. Friedel, in Metallic Solid Solutions, edited by J. Friedel and A. Guinier (Benjamin, New York 1963) Paper XIX-1
10. A.C. Ehrlich and D.J. Gillespie in Proceedings of the Fifteenth International Conference on Thermoelectrics, edited by T. Caillat, A. Borshchevsky and J.-P. Fleurial, Pasadena, CA, 1996, pp. 397-401.
11. G.N. Kamm, D.J. Gillespie, A. C. Ehrlich and T.J. Wieting, Phys. Rev. B, **31**, 7617 (1985).
12. G.N. Kamm, D.J. Gillespie A.C. Ehrlich and D.L. Peebles, Phys. Rev. B, **35**, 1223 (1987).
13. F.J. Blatt, Physics of Electronic Conduction in Solids, (McGraw-Hill, Inc. New York 1968) p. 288.

DESIGN CONCEPTS FOR IMPROVED THERMOELECTRIC MATERIALS

GLEN A. SLACK

Department of Physics, Applied Physics and Astronomy, Rensselaer Polytechnic Institute, Troy,
NY 12180-3590

ABSTRACT

Some new guidelines are given that should be useful in the search for thermoelectric materials that are better than those currently available. In particular, clathrate and crypto-clathrate compounds with filler atoms in their cages offer the ability to substantially lower the lattice thermal conductivity.

INTRODUCTION

The present discussion is addressed to the problem of finding better bulk thermoelectric materials than those in present use. Some of the ideas here have been presented previously in the "CRC Handbook of Thermoelectrics" [1]. From 1956 up to the present the major design concepts for thermoelectrics were those used by Ioffe [2]. These were to select binary semiconducting compounds composed of heavy elements from the lower part of the periodic table, and then to reduce their lattice thermal conductivity by forming mixed crystals [3]. This approach yielded the thermoelectrics based on Bi, PbTe, and Bi_2Te_3 . Since then the concept of the minimum lattice thermal conductivity [4] has shown that there is a lower limit, K_{\min} , to the lattice thermal conductivity, K_G , of any semiconductor (or metal), and that mixed crystal formation does not produce [4] enough phonon scattering to lower K_G to K_{\min} . This can be clearly seen in the PbTe-PbSe system [1].

THEORY

Caged Atoms

The new concept [1], which avoids this limitation, is that some crystals can be constructed that possess "rattling" atoms entrapped in cages or voids that are already present in the crystal structure. One of the first systems to employ this method of reducing K_G was Li-doped KCl [5]. Here the small, light-mass Li atom has eight possible equilibrium positions in a K vacancy. Because of the small mass of Li compared to K, and lithium's limited solid solubility, the thermal conductivity reduction is only appreciable below 20K. A much larger drop in K_G was found for

yttrium atoms encaged in boron [6] in the compound $B_{68}Y$. The Y atoms are much more massive than the boron, their concentration is higher than for Li in KCl, and now $K_G = K_{min}$. Another "rattling" system that exhibits minimum thermal conductivity [7] is xenon hydrate, $46H_2O[8Xe]$. Again there are heavy mass encaged atoms at high concentration.

A second method of reducing K_G , noted by Slack [1] is to build atoms into the structure that have weak bonding and low coordination number. Such is the case [1] for As in Tl_3AsSe_3 where the coordination number is 3, and the As "wobbles" back and forth between two positions 0.50Å apart. A second example is Cu_2O where the coordination number of the Cu is 2. The lattice thermal conductivity of Cu_2O is low, almost temperature independent [8], and much lower than that [9] of ZnO. The number of crystal structures that incorporate these "wobbling" atoms appears to be very small, particularly among semiconducting compounds. One other candidate [10] is $PbAgAsS_3$ with 3-coordinated Ag atoms. A number of compounds of monovalent Ag and Au have 2-coordinated atoms, for example [11] Ag_3AuTe_2 . Their thermal conductivities are not known, but may well be quite small.

It appears reasonable to conclude that the crytals with "rattling" atoms in oversize cages will be easier to construct and will have lower K_G values than those with "wobbling" atoms.

Limits on ZT

The dimensionless figure of merit, ZT, for a material at temperature T with a Seebeck coefficient, S, and an electrical conductivity, σ , is given by

$$ZT = \frac{S^2 \sigma T}{K_E + K_G} \quad (1)$$

In Eq. (1) the electronic and lattice thermal conductivities are K_E and K_G respectfully. For semiconductors of use in thermoelectric devices, one generally finds $1000 \geq S \geq 30$ microvolt/K. If $K_G = 0$ and $S = 1000$ microvolt/K, then

$$ZT = S/(L_o)^{1/2} = 41 \quad (2)$$

However, the lowest real limit on K_{min} would be for a heavy-atom crystal with a Debye temperature of about 100K. This lowest value is about 1 milliwatt/cmK at room temperature. If we pick a realistic [1] upper limit on the weighted mobility, U, where

$$U = \mu(m^*/m_o)^{3/2} \quad (3)$$

to be $U=1800\text{cm}^2/\text{Vsec}$ at room temperature and combine this with this lower limit on K_G , we can obtain

$$ZT \sim 5 \quad (4)$$

for an optimally doped material with $S \sim 440$ microvolt/K and with $10^{18}/\text{cm}^3$ carriers. This assumes normal parabolic bands in the semiconductor.

If one could tailor the electron density of the states so that it exhibits a delta-function singularity, then according to Mahan and Sofo [12], one might obtain

$$ZT \sim 14 \quad (5)$$

This requires a very fancy control of the electrical properties, but would produce [12] a "Best Thermoelectric".

We conclude that ZT values greater than unity at room temperature are theoretically possible, but require low K_G values and good electrical properties.

"PGEC"

The concept of a "phonon glass and an electron crystal" or PGEC was introduced by Slack [1] as the limiting material for a good thermoelectric. In order to select good "electron crystals", we note that Mahan [13] has shown that the energy gap of a good thermoelectric is related to its absolute operating temperature, T , by:

$$E_G \sim 10KT \quad (6)$$

For operating temperatures below 1200K, this means E_G values less than 1eV. There is a useful correlation between E_G values and the electronegativity differences, $|\Delta X|$, in compound semiconductors given by Slack [1]. All of the useful materials, so far, have $|\Delta X| < 1.0$. See Fig. 10 of Ref. 1. There is also a systematic correlation between U and $|\Delta X|$, see Fig. 11 of Ref. 1. The good thermoelectrics with $U > 100\text{cm}^2/\text{Vsec}$ all have $|\Delta X| < 0.5$. Thus it appears that if we are choosing an "electron crystal," it should have $|\Delta X| \leq 0.5$. If we want materials better than Bi_2Te_3 , we should pick $|\Delta X| \leq 0.2$.

Another criterion for good thermoelectrics is that they should have highly polarizable atoms so that ionized impurity scattering of the charge carriers is minimized. This is especially important for thermoelectrics where high doping levels are common. This means choosing compounds or mixed crystals of the elements Sn, Sb, Bi, or Te. For binary semiconducting

compounds this restriction limits [1] one to compounds of Mo, Re, Ru, Os, Co, Rh, Ir, or Pt with the elements Sb or Te.

Clathrate Crystals

The approach to finding good thermoelectric materials now is to select those heavy-element compound semiconductors of Sb or Te with low $|\Delta X|$ that have voids in their structures. These voids are then populated partially or completely with atoms that can "rattle" about in the voids in order to reduce K_G toward K_{min} . The "phonon glass" is achieved when K_G equals K_{min} . A list of such candidates with their void diameters and the coordination number of the voids is given in Table 1. The largest voids are those in $IrSb_3$ at 4.08Å. This just about matches the elemental diameter of krypton at 4.02Å, it is noticeably larger than the diameter of La at 3.74Å. Thus La atoms or the other, smaller, rare earth atoms can "rattle" when trapped in these voids. The effects of rare earth atoms on K_G have been measured by Nolas et al [14], and the La incorporation drops the room temperature thermal conductivity, K_G , a factor of 11. The decrease in K_G at lower temperatures is even larger. In addition the smaller and heavier rare earth atoms produce [14] an even larger decrease in K_G .

The conclusion to be drawn is that the "rattle in a cage" method of reducing K_G actually works. What other crystals might be found to which this type of phonon scattering can be applied?

Table 1: Void Diameters in True Clathrates

Host	Diameter, Å	Coord. No.	K_{min} , milliwatt/cmK
Ge	2.44	4	5.0
Ir_3Te_8	2.46	6	~4.0
Re_3Te_5	2.66	4	~4.0
Mo_6Te_8	3.44	8	~4.0
$CoSb_3$	3.78	12	3.1
$RhSb_3$	4.04	12	3.1
$IrSb_3$	4.08	12	3.1
Grey Sn	2.81	4	2.5

Crypto-Clathrate Crystals

In the true clathrates the voids in the structure are present in the host crystal even when no guest atoms are present. In crypto-clathrates (or hidden-clathrates) the voids only arise in the presence of the guest atoms. Thus the guest atoms actually change the crystal structure of the host. The well known crypto-clathrates are ice, silicon, germanium, and tin. The ice clathrates have been known since 1810. The Si, Ge, and Sn clathrates were discovered in 1965 by Kasper et al [15]. A recent paper by Adams et al [16] gives many references to work in this area. The two common types [15] of Si, Ge, and Sn clathrate structures (I and II) are the same as those found for H₂O. The structures are three-dimensional, cubic networks of tetrahedrally bonded Ge atoms with 12-sided, 14-sided, and 16-sided voids inside. The electrons move about on the network bonds; the weakly-bonded guest atoms "rattle" about inside the voids. The diameters of the voids are given in Table 2. These voids are considerably larger than those in IrSb₃. Thus the atomic "rattling" should be greater, and the K_G reduction should be larger. Note in Table 2 that almost any of the atoms in the periodic table could be accommodated in the larger voids. No thermal conductivity values have been reported to date on any of these clathrates.

Table 2: Void Diameters in Crypto-Clathrates

Host	Structure Type	Small Diameter, Å	Large Diameter, Å
Si	I	4.11	4.59
Ge	I	4.35	4.67
Sn	I	4.85	5.29
Si	II	4.11	5.35
Ge	II	4.35	5.61
Sn	II	4.85	(6.43)*

*unknown structure

Guest Atom Diameters, Å			
Na	3.70	He	3.00
Cs	5.24	Xe	4.38

A large number of Si, Ge, and Sn clathrates have been made since 1965. Table 3 lists 20 different Ge clathrates that have been made so far by various authors. The host atoms are often Ge atoms mixed with some other atoms that go easily into the tetrahedral framework. The guest atoms in the voids are both larger and heavier, and both electropositive and electronegative guests have been trapped. Very little work has been done on the electronic properties of these materials, but they all appear to be semiconductors if the number of electrons per host atom is just 4.0. For example there are 8 voids and 46 host atoms in the unit cell of the Type I crystal structure. If each void contains a K^{1+} ion, these will donate 8 electrons to the host. These electrons can be taken up by 4 zinc atoms in order to maintain 4 electrons per host atom. The resulting compound would be: $K_8Zn_4Ge_{42}$. This should be an intrinsic semiconductor.

The Seebeck coefficients and electrical conductivities of some samples have been measured by Cros et al [17], while Chu et al [18] have measured σ versus T. Some band structure calculations have been carried out by Saito and Oshiyama [19] which predict good semiconductor behavior for these clathrate structures.

Table 3: Germanium Clathrates, $Ge_{46}X$
Type I ($a_0 \sim 10.8\text{\AA}$)

Host	Guest	Year	Host	Guest	Year
Ge	K	1968	Ga-Ge	Ba	1986
Ge	Rb	1970	Cd-Ge	Ba	1995
Al-Ge	Na	1977	In-Ge	K	1975
Al-Ge	K	1977	In-Ge	Ba	1995
Al-Ge	Ba	1986	Ga-Ge-Sb	I	1976
Zn-Ge	Ba	1995	Ge-As	Br	1972
Ga-Ge	Na	1977	Ge-As	I	1972
Ga-Ge	K	1975	Ge-Sb	Br	1972
Ga-Ge	Sr	1986	Ge-Sb	I	1972

Type II ($a_0 \sim 15.4\text{\AA}$)

$Ge_{136}Na_8$	1970
$Ge_{136}Cs_8$	1970

CONCLUSIONS

New and better thermoelectric materials can, in all probability, be found. Some of the rules for these new materials are:

1. Look for semiconducting compounds with $E_G \approx 0.50\text{eV}$ of Ge, Sn, Sb, or Te with small $|\Delta X|$ values and heavy atoms.
2. Find binary or ternary systems where the electrons travel about on a three-dimensional network and heavy-mass atoms "rattle" about in voids in the structure.
3. Attempt to reduce the lattice thermal conductivity to values close to K_{\min} . Then ZT values approaching 3 near room temperature should be possible.

REFERENCES

1. G.A. Slack, "New Materials and Performance Limits for Thermoelectric Cooling" in CRC Handbook of Thermoelectrics, edited by D.M. Rowe, CRC Press, Boca Raton, 1995, pp. 407-440.
2. A.V. Ioffe and A.F. Ioffe, *Sov. Phys.-Solid State* **2**, p. 719 (1960).
3. A. Eucken and G. Kuhn, *Zeit. Phys. Chem.* **134**, p. 193 (1928).
4. G.A. Slack, *Solid State Physics* **34**, p. 1 (1979).
5. J.P. Harrison, P.P. Peressini, and R.O. Pohl, *Phys. Rev.* **171**, p. 1037 (1968).
6. D.G. Cahill, H.E. Fischer, S.K. Watson, R.O. Pohl, and G.A. Slack, *Phys. Rev.* **B40**, p. 3254 (1989).
7. Y.P. Handa and J.G. Cook, *J. Phys. Chem.* **91**, p. 6327 (1987).
8. W. Vogt, *Ann. d. Physik* **7**, p. 183 (1930).
9. G.A. Slack, *Phys. Rev.* **B6**, p. 3791 (1972).
10. B.J. Wuensch and W. Nowacki, *Zeit. f. Kristallog.* **125**, p. 459 (1967).
11. A.J. Frueh, *Am. Mineralogist* **44**, p. 693 (1959).
12. G.D. Mahan and J.O. Sofo, *Proc. Natl. Acad. Sci.* **93**, p. 7436 (1996).
13. G.D. Mahan, *J. Appl. Phys.* **65**, p. 1578 (1989).
14. G.S. Nolas, G.A. Slack, D.T. Morelli, T.M. Tritt, and A.C. Ehrlich, *J. Appl. Phys.* **79**, p. 4002 (1996).

-
15. J.S. Kasper, P. Hagenmuller, M. Pouchard, and C. Cros, *Science* **150**, p. 1713 (1965).
 16. G.B. Adams, M. O'Keefe, A.A. Demkov, O.F. Stankey, and Y.M. Huang, *Phys. Rev.* **B49**, p. 8048 (1994).
 17. C. Cros, M. Pouchard, and P. Hagenmuller, *J. Solid State Chem.* **2**, p. 570 (1970).
 18. T.L. Chu, S.S. Chu, and R.L. Ray, *J. Appl. Phys.* **53**, p. 7102 (1982).
 19. S. Saito and A. Oshiyama, *Phys. Rev.* **B51**, p. 2628 (1995).

PROSPECTS FOR HIGH THERMOELECTRIC FIGURES OF MERIT IN 2D SYSTEMS

M. S. Dresselhaus^{*#}, X. Sun^{*}, S. B. Cronin^{*}, T. Koga[†], G. Dresselhaus[†], K. L. Wang^{**}

^{*}Department of Physics, Massachusetts Institute of Technology, Cambridge, MA 02139

[#]Department of Electrical Engineering and Computer Science, Massachusetts Institute of Technology, Cambridge, MA 02139

[†]Francis Bitter Magnet Lab., Massachusetts Institute of Technology, Cambridge, MA 02139

^{**}Department of Electrical Engineering, University of California, Los Angeles, CA 90024

[‡]Division of Engineering and Applied Sciences, Harvard University, Cambridge, MA 02138

ABSTRACT

Enhanced ZT has been predicted theoretically and observed experimentally in 2D quantum wells, with good agreement between theory and experiment. Advantages of low dimensional systems for thermoelectric applications are described and prospects for further enhancement of ZT are discussed.

INTRODUCTION

The usefulness of thermoelectric materials for refrigeration or power generation applications is typically expressed by the dimensionless quantity ZT where T is the temperature (in degrees Kelvin) and Z is the thermoelectric figure of merit

$$Z = \frac{S^2 \sigma}{\kappa}, \quad (1)$$

where S is the thermoelectric power or Seebeck coefficient, σ is the electrical conductivity and κ is the thermal conductivity. Clearly high ZT requires high S , high σ , and low κ . Since an increase in S normally implies a decrease in σ because of carrier density considerations, and since an increase in σ implies an increase in the electronic contribution to κ as given by the Wiedemann-Franz law, it is very difficult to increase Z in typical thermoelectric materials. The best commercial 3D thermoelectric material is in the $\text{Bi}_{2(1-x)}\text{Sb}_{2x}\text{Te}_{3(1-y)}\text{Se}_{3y}$ family with room temperature $ZT \approx 1$ for $\text{Bi}_{0.5}\text{Sb}_{1.5}\text{Te}_3$ [1]. It is generally considered that only incremental improvements in the ZT of this system are possible. For this reason, efforts are being expended in the identification of new families of materials with a high density of states at the Fermi level [2-4] and with cage-like structures partially occupied by constituent rattling atoms [5, 6]. This approach appears to be promising, and values of $ZT \simeq 1.4$ have been achieved in $\text{CeFe}_4\text{Sb}_{12}$ at $T = 900 \text{ K}$ [7].

Reduced dimensionality [as occurs in quantum wells (2D) or quantum wires (1D)] offers another strategy for enhancing ZT [8, 9], because of (1) enhancement of the density of states near E_F leading to an enhancement of the Seebeck coefficient, (2) increased carrier mobilities at a given carrier concentration due to quantum confinement, modulation doping and δ -doping phenomena, (3) opportunities to take advantage of the anisotropic Fermi surfaces in multivalley semiconductors, (4) increased boundary scattering of phonons at the barrier-well interfaces, while effectively preserving carrier mobilities by exploiting the different length

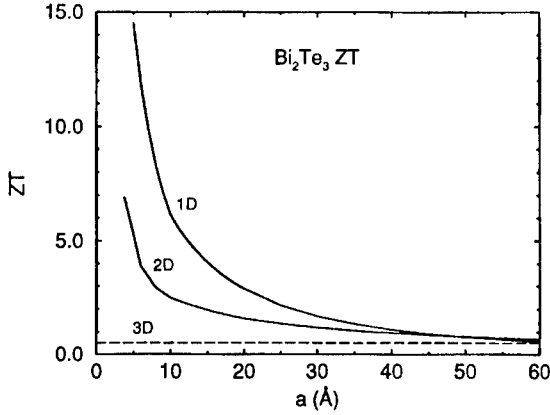


Figure 1: Dependence of ZT on the width of the quantum well (wire) for a Bi_2Te_3 -like material for transport in the highest mobility a_0 direction in the $a_0 - b_0$ plane, where a_0 and b_0 denote lattice constants [8, 10, 14].

scales for phonon and electron scattering, and (5) the different temperature dependences of the transport properties and intrinsic carrier excitation in low dimensional systems relative to 3D systems. The dependence of the S , σ , κ , on quantum well thickness is, of course, the principal method for enhancing ZT , both through quantum confinement effects and reduced thermal conductivity [8, 10–13].

Calculations based on the simplest possible model for a quantum confined two-dimensional (2D) electron gas [8], and described in the next section, indicate that it should be possible to obtain significant enhancement in ZT for a Bi_2Te_3 -like material when prepared as a 2D quantum well, and even greater enhancement in ZT when prepared as a 1D quantum wire [10, 14], as shown in Fig. 1. The results of Fig. 1 suggest that a good thermoelectric material in 3D might be expected to exhibit even higher ZT values in reduced dimensions. Furthermore, as discussed below, some materials which are not favorable for high ZT in 3D may exhibit high ZT in 2D [15]. However, the confinement lengths required for enhanced ZT are quite small for a Bi_2Te_3 -like material (see Fig. 1). Thus, it may not be possible to realize such an enhancement experimentally for both materials science issues (pertaining to interface integrity) and physics-related issues (pertaining to quantum confinement and applicability of band theory). Since the solutions of the Schrödinger equation for a particle in a box $E_n = \hbar^2 \pi^2 n^2 / (2m^* a^2)$ scale with quantum well width a , similar enhancements of ZT would be expected to occur at larger quantum well widths for materials with light effective mass components in the direction of quantum confinement.

In this paper we discuss very simple theoretical models that show enhancement of ZT in 2D quantum wells, experimental proof-of-principle of the enhanced ZT in PbTe quantum wells, advantages of quantum well structures for achieving enhanced ZT more generally, strategies for using temperature dependent phenomena to increase ZT in quantum wells, and finally the advantages of bismuth as a low dimensional thermoelectric material.

THEORETICAL MODELING

In the simplest model for thermoelectricity in 2D quantum well structures, it is assumed that the electrons in the valence and conduction bands are in simple parabolic energy bands and that the electrons occupy only the lowest ($n=1$) sub-band of the quantum well. The electronic dispersion relations are then given by

$$\mathcal{E}(k_x, k_y) = \frac{\hbar^2 k_x^2}{2m_x} + \frac{\hbar^2 k_y^2}{2m_y} + \frac{\hbar^2 \pi^2}{2m_z a^2}, \quad (2)$$

where a is the width of the quantum well, and m_x , m_y , and m_z are the effective mass tensor components of the constant energy surfaces. It is further assumed that the current flows in the x direction and that quantum confinement is in the z direction. Solution of Boltzmann's equation for S , σ , and κ_e (the electronic contribution to the thermal conductivity) then yields [8] the following expression for the dimensionless figure of merit in 2D

$$Z_{2D}T = \frac{\left(\frac{2F_1}{F_0} - \zeta^*\right)^2 F_0}{\frac{1}{B_{2D}} + 3F_2 - \frac{4F_1^2}{F_0}}, \quad (3)$$

where the Fermi-Dirac function F_i is given by

$$F_i = F_i(\zeta^*) = \int_0^\infty \frac{\xi^i d\xi}{e^{(\xi - \zeta^*)} + 1}, \quad (4)$$

and $\zeta^* = \zeta/k_B T$ is the reduced chemical potential relative to the edge of the first sub-band. The expression for B_{2D} in Eq. (3) is sensitive to the materials properties of the quantum well, and B_{2D} is given by

$$B_{2D} = \frac{1}{2\pi a} \left(\frac{2k_B T}{\hbar^2} \right) \frac{k_B^2 T (m_x m_y)^{1/2} \mu_x}{e \kappa_{ph}}, \quad (5)$$

where μ_x is the carrier mobility for current flow in the x direction and κ_{ph} is the phonon contribution to the thermal conductivity. The results for Z_{2D} in a quantum well are to be contrasted to the corresponding 3D results [8, 14]:

$$Z_{3D}T = \frac{\frac{3}{2} \left(\frac{5F_{3/2}}{3F_{1/2}} - \zeta^* \right)^2 F_{1/2}}{\frac{1}{B_{3D}} + \frac{7}{2} F_{5/2} - \frac{25F_{3/2}^2}{6F_{1/2}}}, \quad (6)$$

where B_{3D} in Eq. (6) is given by

$$B_{3D} = \frac{1}{3\pi^2} \left(\frac{2k_B T}{\hbar^2} \right)^{3/2} \frac{k_B^2 T (m_x m_y m_z)^{1/2} \mu_x}{e \kappa_{ph}}. \quad (7)$$

In the simple 2D model [Eqs. (3) and (5)], the phonon contribution to the thermal conductivity κ_{ph} is conservatively approximated using 3D experimental data for κ_{ph} for the phonon mean free path $\ell > a$, and using $\ell = a$ for quantum well widths less than a .

The expressions for Z_{3D} and Z_{2D} both depend on the electrochemical potential ζ , and therefore on the carrier concentration, which can be controlled experimentally to achieve the

maximum ZT for each thermoelectric material at the desired temperature of operation, and at the desired quantum well thickness (with large a yielding the 3D limit). The quantities B_{3D} and B_{2D} are particularly sensitive to the electronic structure and to the sample quality of each thermoelectric material, and it is readily seen that a high carrier mobility in the direction of current flow is desirable, as is a high density of states. Equations (3) and (5) indicate that by going to small quantum well widths a , enhanced Z_{2D} should be possible. In the next section, we review the observation of enhanced Z_{2D} in n -type PbTe quantum wells.

EXPERIMENTAL PROOF-OF-PRINCIPLE

PbTe was chosen as the materials system for demonstrating proof-of-principle of enhanced ZT in quantum wells because of its desirable thermoelectric and materials science properties. Regarding its thermoelectric properties, PbTe has a reasonably high room temperature ZT in bulk form ($ZT \simeq 0.4$), reflecting the high carrier mobility, multiple anisotropic carrier pockets, and low thermal conductivity that can be achieved under isoelectronic alloying. In addition, calculations indicate that carrier confinement and enhanced ZT could be achieved for quantum well widths < 40 Å [16]. It was also known that high mobility quantum well superlattices could be prepared with PbTe as the quantum well material and $\text{Pb}_{1-x}\text{Eu}_x\text{Te}$ as the barrier material [17,18], with well controlled and stable interfaces, using epitaxial growth techniques such as molecular beam epitaxy. Good lattice matching and similar thermal expansion coefficients across the interfaces permitted the preparation of PbTe/PbEuTe superlattices with ~ 40 superlattice periods [19]. Experiments by Harman [20] indicated that Bi could be introduced into the $\text{Pb}_{0.927}\text{Eu}_{0.073}\text{Te}$ barrier region, yielding quantum wells with $> 10^{19}$ electrons/cm³ within the quantum well, with only a small reduction in the measured Hall mobility (from 1600 cm²/Vs in 3D films to 1400 cm²/Vs in a 2D quantum well superlattice sample for $x = 0.073$, where $\mu = 45$ cm²/Vs in a thick film having the same composition as the barrier region) [20]. Calculations by Hicks [14] corroborated that quantum confinement could be achieved for $x = 0.073$, where the band offsets for the conduction and valence bands were calculated to be 171 meV and 140 meV, respectively, for a band gap of 630 meV in the barrier regions and 319 meV in the quantum wells at 300 K [17].

Experimental results for the quantity S^2n on a number of n -type PbTe quantum wells for a variety of quantum well widths from 17 Å to 55 Å are given as points in Fig. 2(a) as a function of quantum well width (thickness), and in Fig. 2(b) as a function of doping levels (as determined from Hall effect measurements). Using the value for the carrier mobility $\mu = 1400$ cm²/Vs, an estimate of the power factor $S^2\sigma$ can be obtained. The solid curves in Figs. 2(a) and (b) are obtained with no adjustable parameters using the envelope function approximation to calculate the bound states and using literature values for the band parameters and other physical properties of PbTe [17]. Enhancement in the power factor in the 2D PbTe quantum wells by a factor of 3–4 over 3D bulk values has been obtained in n -type PbTe. The experimental data in Fig. 2 clearly shows that a greater enhancement in ZT is achieved with decreasing quantum well widths, at least for quantum wells down to 20 Å. The bound states in the quantum wells that were used to calculate the curves in Fig. 2 were all obtained by applying the general theoretical model described in the previous section to the specific material PbTe, using literature values for the parameters for the 2D electronic band structure for PbTe quantum wells [16]. Proof-of-principle for enhanced ZT in 2D quantum wells is provided by the good fit of the experimental points to the calculated curves in Fig. 2. Further corroboration is provided by the good agreement between the

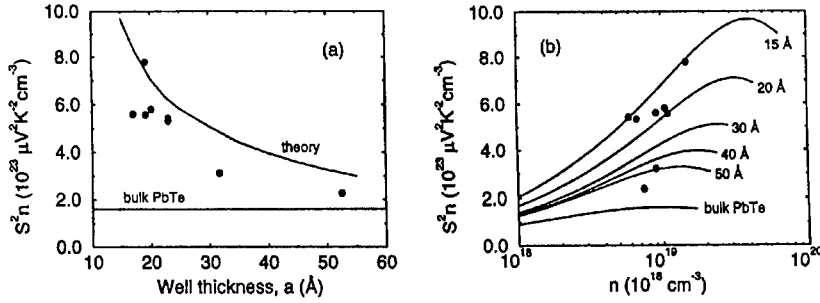


Figure 2: (a) S^2n results for n -type (Bi-doped) PbTe/Pb_{0.927}Eu_{0.073}Te MQWs (full circles) as a function of quantum well thickness a at 300 K. For comparison, the best experimental bulk PbTe value for S^2n is also shown. Calculated results for optimum doping are shown as a solid line. (b) S^2n results for the same PbTe/Pb_{0.927}Eu_{0.073}Te MQW sample (full circles) as a function of carrier density n at 300 K. Calculated results for different indicated well thicknesses are shown as solid curves [16].

infrared transmission measurements and the calculated bound state energies [16]. From the solid curves in Fig. 2(b), the optimum carrier concentration as a function of quantum well thickness can be inferred. The results show that higher doping concentrations are needed with decreasing quantum well width a . Because of the solubility limit that was encountered experimentally for the Bi dopant in the barrier material Pb_{1-x}Eu_xTe ($x = 0.073$), it is believed that further increases in S^2n might be possible at higher electron carrier concentrations, once the materials science problem regarding dopant solubility can be solved. As discussed below, the best room temperature values that were obtained for the n -type PbTe quantum wells is a power factor of $130 \mu W/cmK^2$ and a thermoelectric figure of merit of $Z_{2D}T = 1.2$.

ADVANTAGES OF QUANTUM WELLS FOR ACHIEVING HIGH ZT

Having demonstrated enhancement of ZT in quantum wells of a specific material, we would now like to review the advantages of 2D quantum wells over bulk materials from a more general vantage point, in the hope of identifying other materials systems that might be even more favorable than PbTe for low dimensional thermoelectric applications. Calculations carried out on other materials suggest that Si/Si_{1-x}Ge_x, Bi_{1-x}Sb_x, Bi_{2(1-x)}Sb_{2x}Te_{3(1-y)}Se_{3y}, and p -type PbTe are all favorable quantum well materials for enhanced 2D thermoelectric performance. Our theoretical model suggests that if a material is a good thermoelectric in 3D, it should be even better in 2D and 1D.

Quantum confinement associated with a quantum well system is expected to give rise to an increase in the magnitude of the Seebeck coefficient $|S|$ for the same carrier density, with the increased $|S|$ arising from an increase in the density of electron states at the Fermi level for the 2D electron gas. Experimental evidence (Fig. 3) for the enhancement of $|S|$ for n -type PbTe quantum wells shows a significant enhancement in $|S|$ for quantum wells of

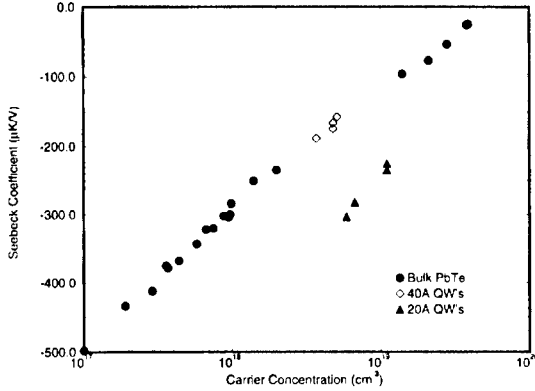


Figure 3: Dependence of the room temperature Seebeck coefficient S on carrier concentration in n -type PbTe for bulk samples (full circles) and quantum wells with widths of 40 Å (open squares) and 20 Å (full triangles) [20]. For n -type semiconductors, S is negative so that S decreases in magnitude for increasing carrier concentration n .

20 Å well widths, while the larger 40 Å n -type PbTe quantum wells show about the same $|S|$ as bulk samples of the same carrier concentrations (see also Fig. 2).

The theoretical analysis given above shows that increased carrier mobility leads to higher ZT values in all cases (3D, 2D and 1D). Experimentally, enhancement in the carrier mobility relative to bulk values can be achieved using the attributes of low dimensional systems, including quantum confinement, modulation doping and δ -doping techniques. In this way the dopants can be introduced into the barrier regions, far from the quantum wells where the carriers are located, thereby greatly reducing the carrier scattering by the impurity dopant ions that are responsible for the carrier generation. This advantage of 2D systems should be of particular importance at low temperature where electron-phonon scattering is less important and impurity scattering tends to dominate, thereby increasing the possibility for preparing a viable low temperature thermoelectric material.

A third advantage of the 2D aspects of quantum wells is the exploitation of the anisotropy of the constant energy surfaces of typical multivalleyed semiconductors. For 3D systems, the k -space anisotropic effects of the various ellipsoidal carrier pockets tend to cancel when summing over the contributions from all the ellipsoids to the transport properties of a multivalleyed cubic semiconductor such as PbTe or Si. However, the symmetry-lowering introduced by the quantum well superlattice periodicity allows the possibility of better exploiting the anisotropy of the individual ellipsoidal carrier pockets. This is illustrated in Fig. 4 where the power factor $S^2\sigma$ for bulk n -type PbTe is plotted vs T , in comparison to $S^2\sigma$ for 2D quantum wells. In this figure we consider two hypothetical extreme cases (shown as thin lines) to illustrate anisotropy effects in 2D quantum well systems. In the first case, all four carrier pockets of PbTe are aligned in such a way that the longitudinal axes of the four pockets are all perpendicular to the quantum well layers. This configuration gives the lowest $S^2\sigma$ value because there is no mass anisotropy in the 2D layers. In the second case, the longitudinal axes for all four ellipsoidal carrier pockets are taken to be in the plane of

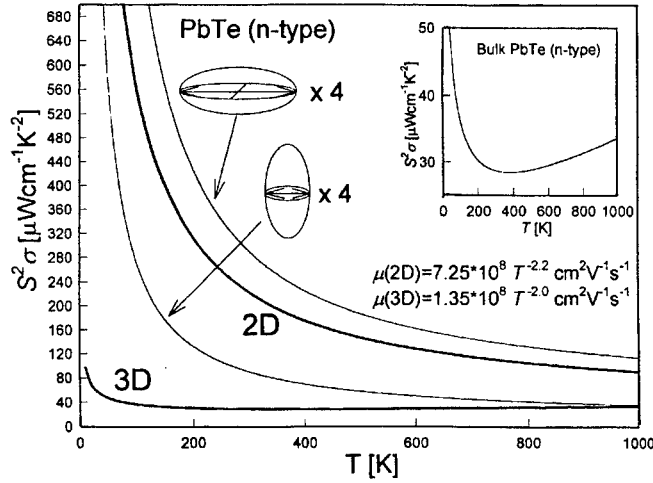


Figure 4: Plot of the power factor $S^2\sigma$ vs T for bulk 3D n -type PbTe, and the corresponding results for 2D quantum wells, showing the effect of the Fermi surface anisotropy on the power factor for 2D quantum well systems (see text). The inset shows $S^2\sigma$ vs T for 3D PbTe on a magnified scale.

the quantum well, thereby maximizing the contribution of the factor $(m_l/m_t)^{1/2}$ to B_{2D} in Eq. (5). A more realistic picture is obtained in the thick curve labeled 2D in Fig. 4, where the contributions from the four carrier pockets (which are equivalent in 3D but not in 2D) are projected in the (111) direction to give one circular pocket and three elliptical constant energy surfaces in 2D. The measured temperature dependences of the carrier mobility in 2D and 3D are used, as indicated. It is clear from this figure that the thermoelectric properties of (111) PbTe multiple quantum wells are dominated by the three elliptical carrier pockets which have the higher density of states masses. From these arguments we conclude that semiconductors with favorable low dimensional thermoelectric properties should have (1) a large number of equivalent carrier pockets, (2) highly anisotropic constant energy surfaces, (3) high carrier mobilities, and (4) the superlattice growth direction selected to maximize the effect of the anisotropic Fermi surface.

A number of experimental and theoretical studies have been carried out to show that the quantum well/barrier interfaces can significantly increase the phonon-phonon scattering without increasing the electron scattering very much because of the different length scales that are involved in these scattering processes. Because of the increased phonon scattering at the quantum well interfaces, it is likely that the $Z_{2D}T$ values given in this paper represent conservative estimates.

Isoelectronic alloying, which is commonly used in 3D thermoelectric systems, can also be used effectively in quantum well superlattices, both in the quantum well regions and in the barrier regions. In addition, δ -doping with carbon or with SiC ($E_g = 2.9$ eV) within the $\text{Si}_{1-x}\text{Ge}_x$ barrier region of a $\text{Si}/\text{Si}_{1-x}\text{Ge}_x$ superlattice could be used to effectively increase the band gap within the barrier region, so that smaller barrier widths would be needed for

quantum confinement [21]. The δ -doping approach thus leads to reduced κ for the superlattice thermoelectric material due to both a reduction in the barrier widths and increased phonon scattering at the SiC interfaces within the barrier region.

In addition to the advantages of 2D quantum well thermoelectrics mentioned in this section, there are a variety of temperature-dependent effects where quantum wells offer additional advantages, as discussed in the next section.

TEMPERATURE DEPENDENCE

Since all of the transport properties (e.g., S , σ , κ) have different temperature dependences in 2D and 3D, differences in the temperature dependence of ZT are expected. For typical thermoelectric materials, ZT tends to increase with increasing temperature in the extrinsic carrier density range, but once temperatures are reached where thermal carrier generation becomes significant, the approximate cancellation between the thermally excited electron and hole carrier contributions to the Seebeck coefficient S leads to a reduction in ZT as a function of temperature. Thus $(ZT)_{\max}$ occurs at higher temperatures for wider gap (E_g) semiconductors, since intrinsic carrier excitation begins to occur at higher T as E_g increases. Bulk materials exhibiting an increase in E_g with increasing T (such as PbTe) will tend to push $(ZT)_{\max}$ to higher temperatures, thereby increasing the maximum value of ZT that can be reached. On the other hand, materials (such as Si), where E_g decreases with increasing T , the opposite effect is expected.

In addition to the temperature-dependent effects described above which apply to both 3D and 2D systems, the presence of bound states in 2D quantum wells increases the effective band gap to significantly higher energies, thereby significantly increasing the temperature where $(ZT)_{\max}$ occurs, and at the same time increasing the magnitude reached by $(ZT)_{\max}$. Thus, the physics of quantum wells favors high temperature thermoelectric applications relative to that of the bulk material. However, thermal diffusion across the quantum well-barrier interfaces will become important with increasing T and this effect will limit the temperature range where quantum wells can be used for practical thermoelectric applications.

Quantum well thermoelectrics are also of particular interest for low temperature applications, where there are presently no thermoelectrics with high ZT values, though there could be a real need for such materials for the cooling of high T_c superconducting devices. The reduction in carrier-impurity scattering associated with modulation doping and δ -doping could be of particular importance at low temperature for 2D thermoelectrics, for which the carrier concentrations necessary to achieve the optimum doping condition tend to be very high. Since the interface scattering cross-section for phonons would be expected to be temperature independent, this scattering mechanism could be especially important at low temperature where the phonon density is not so high.

Figure 5 shows a model calculation for the temperature dependence of $Z_{2D}T$ that was made on our best n -type PbTe quantum well sample using temperature-dependent band parameters found in the literature [22] and room temperature measurements made on this sample [16]. The empirical temperature dependence of the electrical conductivity $\sigma = 2.2 \times 10^8 T^{-2} \Omega^{-1} \text{cm}^{-1}$ was used in the calculation. The bulk lattice thermal conductivity κ_{ph} was estimated from literature data and the electronic thermal conductivity κ_e was estimated from σ using the Wiedemann-Franz law. The results thus obtained indicate that $Z_{2D}T \sim 2$ just above 400 K, with further increases in $Z_{2D}T$ expected at higher temperatures. It should be noted that non-parabolic effects, which are not taken into account in our present model,

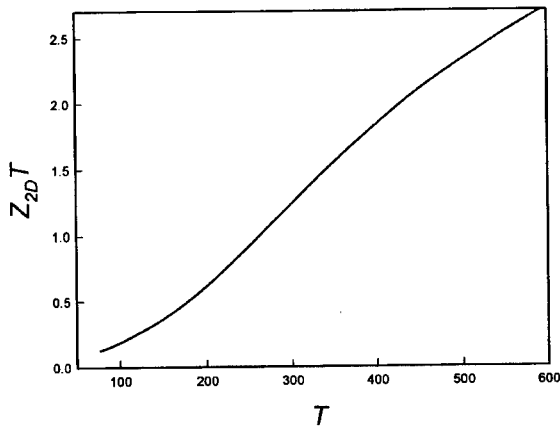


Figure 5: Theoretical estimation of $Z_{2D}T$ as a function of T for our best n -type PbTe quantum well sample. The calculation is based on a two band model which includes temperature dependent longitudinal and oblique bound states [16].

tend to give further enhancement for S at elevated temperatures. We therefore feel that the theoretical estimation for $Z_{2D}T$ in Fig. 5 is conservative.

BISMUTH AS A LOW DIMENSIONAL THERMOELECTRIC

Bismuth is a very attractive material for low dimensional thermoelectricity because of the large anisotropy of the three ellipsoidal constant energy surfaces for electrons at the L point in the rhombohedral Brillouin zone ($m_x^* = 0.00651m_0$, $m_y^* = 1.362m_0$, $m_z^* = 0.00993m_0$), and the high mobility of the carriers ($\mu = 3.5 \times 10^4$ cm²/Vs for light mass electrons in the binary direction with a carrier density 2×10^{18} /cm³ at 300 K) [23–25]. As the quantum well width decreases, the lowest bound state in the conduction band rises above the highest bound state in the valence band, inducing a semimetal-semiconductor transition. If the 2D bismuth system is then doped to the optimum doping level, a large enhancement in $Z_{2D}T$ is predicted (see Fig. 6) with decreasing quantum well width [15]. Of particular interest is the observation that the $Z_{2D}T$ enhancement is large for quite large quantum well widths. For example, Fig. 6 predicts a $Z_{2D}T \sim 4$ at room temperature for a 50 Å Bi quantum well. Such quantum well widths should be achievable experimentally, if one could only identify a suitable barrier material.

Bismuth can be alloyed isoelectronically with antimony to yield a high mobility and highly desirable thermoelectric properties. From what is known about the bismuth-antimony phase diagram (Fig. 7), it should be possible to prepare both n -type and p -type $\text{Bi}_{1-x}\text{Sb}_x$ quantum wells for x in the range $0.09 < x < 0.17$. In this narrow composition range, the lowest conduction band and the highest valence band are both at the L point in the Brillouin zone, and both bands have very similar highly anisotropic constant energy surfaces giving rise to high mobility carriers.

Bismuth and $\text{Bi}_{1-x}\text{Sb}_x$ are highly desirable low dimensional thermoelectric because of

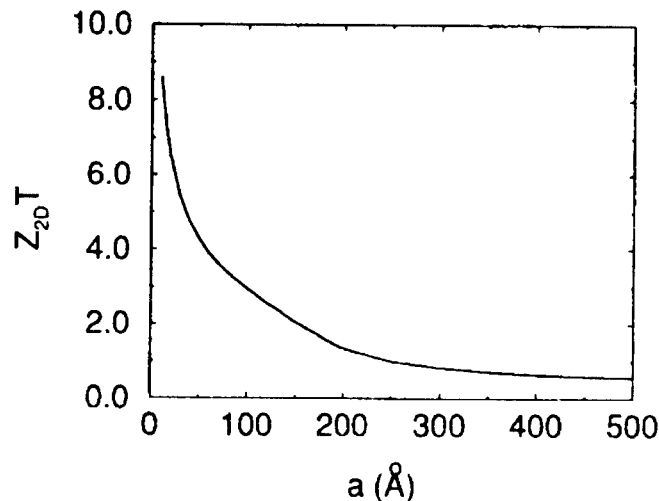


Figure 6: Dependence of $Z_{2D}T$ on quantum well width for a Bi well in the highest mobility (binary) direction [15].

their large Fermi surface anisotropy, high mobility carriers, very long electron mean free paths, heavy mass ions to effectively scatter phonons and yield low phonon mean free paths, and opportunities to achieve $Z_{2D}T$ enhancement for both n -type and p -type doping. Bi and $\text{Bi}_{1-x}\text{Sb}_x$, however, have a serious deficiency for 2D quantum well applications because of the unavailability until the present time of a suitable barrier material.

CONCLUSIONS

At present, $Z_{2D}T \sim 1.2$ has been achieved in n -type PbTe quantum wells at room temperature, and values of $Z_{2D}T > 2$ are expected at higher temperatures. It is likely that high $Z_{2D}T$ values will soon be demonstrated in other quantum well systems. Quantum well systems offer advantages both for low temperature and high temperature thermoelectric performance. However, the utilization of quantum wells in a real thermoelectric material will require much effort to reduce the barrier widths and the thermal conductivity, and to develop suitable barrier materials for the most promising 2D thermoelectrics. Because of the many trade-off constraints that govern thermoelectric performance, model calculations are especially valuable for optimizing the superlattice and materials parameters to maximize $Z_{2D}T$.

ACKNOWLEDGMENTS

The authors would like to thank T. C. Harman, P. C. Eklund, and Gang Chen for valuable discussions. The authors gratefully acknowledge support by the US Navy under Contract No. N00167-92-K-0052 (MIT), and AFOSR under URI (UCLA). Support from the

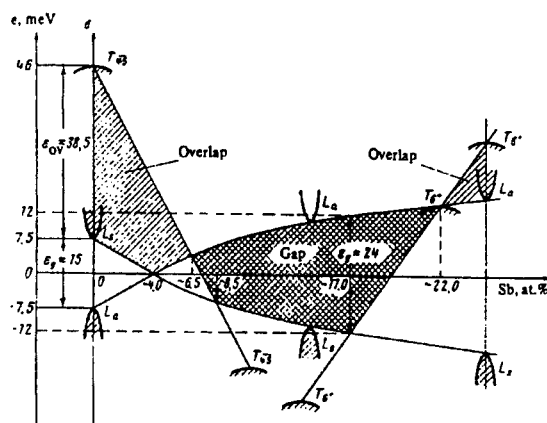


Figure 7: Bi - Sb phase diagram and the implied electronic structure. The region of the semiconducting alloys is cross hatched [26,27].

Honda Corporation for temperature dependent studies is gratefully acknowledged.

REFERENCES

- [1] H. J. Goldsmid, *Electronic Refrigeration* (Pion, London, 1986).
- [2] G. D. Mahan, in *Physics Today* **March** (1997).
- [3] G. D. Mahan, in *Solid State Physics*, edited by H. Ehrenreich and F. Spaepen (Academic Press, 1996).
- [4] G. D. Mahan, *Proc. Natl. Acad. Sci. USA* **93**, 7436-7439 (1996).
- [5] G. A. Slack and V. G. Tsoukala, *J. Appl. Phys.* **76**, 1665 (1994).
- [6] G. A. Slack, in *CRC Handbook of Thermoelectrics*, edited by D. M. Rowe, CRC Press, New York, 1995, page 407.
- [7] J.-P. Fleurial, in *Proceedings of the 15th IEEE International Conference on Thermoelectrics*, edited by J.-P. Fleurial, Pasadena, CA, 1996 (IEEE Catalogue Number 96TH8169).
- [8] L. D. Hicks and M. S. Dresselhaus, *Phys. Rev. B* **47**, 12727-12731 (1993).
- [9] L. D. Hicks and M. S. Dresselhaus, in *Semiconductor Heterostructures for Photonic and Electronic Applications: MRS Symposia Proceedings, Boston, volume 281*, edited by C. W. Tu, D. C. Houghton, and R. T. Tung, page 821, Materials Research Society Press, Pittsburgh, PA, 1993.
- [10] L. D. Hicks and M. S. Dresselhaus, *Phys. Rev. B* **47**, 16631 (1993).

-
- [11] J. O. Sofo and G. D. Mahan, Appl. Phys. Lett. **65**, 2690 (1994).
- [12] D. L. Broido and T. L. Reinecke, Phys. Rev. B **51**, 13797 (1995).
- [13] D. L. Broido and T. L. Reinecke, Appl. Phys. Lett. **67**, 1170 (1995).
- [14] Lyndon D. Hicks, *The effect of quantum-well superlattices on the thermo-electric figure of merit*, PhD thesis, Department of Physics, Massachusetts Institute of Technology, June 1996.
- [15] L. D. Hicks, T. C. Harman, and M. S. Dresselhaus, Appl. Phys. Lett. **63**, 3230 (1993).
- [16] L. D. Hicks, T. C. Harman, X. Sun, and M. S. Dresselhaus, Phys. Rev. B **53**, R10493-R10496 (1996).
- [17] Shu Yuan, H. Krenn, G. Springholz, and G. Bauer, Phys. Rev. B **47**, 7213 (1993).
- [18] G. Springholz, G. Ihninger, G. Bauer, M. M. Oliver, J. Z. Pastalan, S. Romaine, and B. B. Goldberg, Appl. Phys. Lett. **63**, 2908 (1993).
- [19] G. Springholz and G. Bauer, Appl. Phys. Lett. **62**, 2399 (1993).
- [20] T. C. Harman, D. L. Spears, and M. J. Manfra, J. Electron. Mater. **25**, 1121 (1996).
- [21] X. Sun, M. S. Dresselhaus, K. L. Wang, and M. O. Tanner, in *Thermoelectric Materials - New Directions and Approaches: MRS Symposia Proceedings, San Francisco, volume 478*, edited by T. M. Tritt, G. Mahan, H. B. Lyons, Jr., and M. G. Kanatzidis, Materials Research Society Press, Pittsburgh, PA, 1997.
- [22] R. Dornhaus, G. Nimtz, and B. Schlicht, *Narrow-Gap Semiconductors* (Springer-Verlag, Berlin, 1985). Springer Tracts in Modern Physics, Volume 98.
- [23] R. T. Isaacson and G. A. Williams, Phys. Rev. **185**, 682 (1969).
- [24] M. S. Dresselhaus, in *Proceedings of the Conference on the Physics of Semimetals and Narrow Gap Semiconductors*, edited by D. L. Carter and R. T. Bate, page 3, Pergamon Press, New York, NY, 1970.
- [25] W. M. Yim and A. Amith, Solid State Electronics **15**, 1141-1165 (1972).
- [26] N. B. Btandt, S. M. Chudinov, and V. G. Karavaev, Sov. Phys. JETP **34**, 368 (1972).
- [27] J. S. Lannin, Phys. Rev. B **19**, 2390 (1979).

THERMOELECTRIC POWER OF Bi and Bi_{1-x}Sb_x ALLOY THIN FILMS AND SUPERLATTICES GROWN BY MBE

Sunglae Cho*, Antonio DiVenere*, George K. Wong*, John B. Ketterson*, Jerry R. Meyer**, and Craig A. Hoffman**

*Department of Physics and Astronomy, Northwestern University, Evanston, IL 60208

**Code 5613, Naval Research Laboratory, Washington, D.C. 20375-5338

ABSTRACT

We have measured the thermoelectric power (TEP) of MBE-grown epitaxial Bi and Bi_{1-x}Sb_x alloy thin films and superlattices as a function of temperature in the range 20-300 K. We have observed that the TEP of a Bi thin film of 1 μm thickness is in good agreement with the bulk single crystal value and that the TEPs for superlattices with 400 \AA and 800 \AA Bi well thicknesses are enhanced over the bulk values. For $x=0.072$ and 0.088 in Bi_{1-x}Sb_x thin films showing semiconducting behavior, TEP enhancement was observed by a factor of two. However as Bi or Bi_{1-x}Sb_x well thickness decreases in superlattice geometry, the TEP decreases, which may be due to unintentional p-type doping.

INTRODUCTION

Bi and Sb are semimetals with rhombohedral structure which have an energy overlap between the conduction and valence bands. In bulk Bi, the thermoelectric figure of merit defined by $ZT=(S^2\sigma/\kappa)T$ (where S is the thermoelectric power (TEP) or Seebeck coefficient, σ is the electrical conductivity, and κ is the thermal conductivity) is suppressed by competing electron and hole contributions. However, Gallo *et al.* [1] pointed out quite early that Bi, which has a low bulk ZT of 0.4 at 300 K, would have the largest ambient-temperature figure of merit of any known material ($ZT\sim 1.8$) if one could somehow eliminate the hole population from the system. One way to eliminate the hole population is to grow Bi in a quantum well structure and remove the energy overlap. In a recent magneto-transport investigation of MBE-grown Bi thin films on CdTe substrates [2,3] we have observed a confinement-induced semimetal to semiconductor transition in a 200 \AA Bi thin film, with a 40 meV positive energy gap. More recently, Hicks and coworkers [4,5] proposed that ZT can be enhanced considerably in Bi-based superlattices. Even though several subsequent investigators [6-10] have pointed out that the projection by Hicks *et al.* of a 2D ZT larger than 8 for a 10 \AA well thickness is unrealistic, there is general agreement that $ZT > 1$ may be attainable in semiconducting Bi-based superlattices. (Five-times enhancement of S^2n was reported in PbTe/Pb_{0.927}Te_{0.073} superlattice system. [11])

The Bi-Sb alloys would seem to be more promising for a thermoelectric cooler, firstly because they can have a positive energy gap, resulting in a large TEP, and secondly because the lattice thermal conductivity is reduced by the formation of a solid solution. Based on transport studies, Jain [12] showed that Bi_{1-x}Sb_x alloys were

semiconducting for a range of values $x > 0.06$. Later studies by Heremans et al. [13] suggest the band structure shown in Fig. 1. At $x = 0.07$, the overlap between the conduction band at the L point and the valence band at the T point disappears and the material loses its semimetallic behavior and becomes a semiconductor. For $0.07 < x < 0.15$ ($0.15 < x < 0.22$), the material is a direct (indirect) gap semiconductor. Above $x > 0.22$, the material becomes a semimetal again.

In this paper, we discuss an experimental investigation of the temperature and thickness dependent TEP of epitaxial Bi and $\text{Bi}_{1-x}\text{Sb}_x$ thin films and superlattices grown on CdTe substrates. Based on the results obtained, we will discuss the further work that will be required to make Bi-based superlattices attractive for thermoelectric cooling devices.

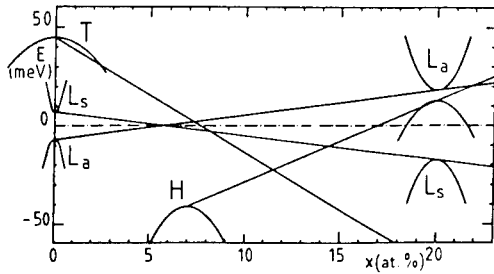


Fig. 1. Energy band structure of $\text{Bi}_{1-x}\text{Sb}_x$ alloys as a function of Sb concentration.

EXPERIMENT

The growth of Bi and $\text{Bi}_{1-x}\text{Sb}_x$ thin films and superlattices on semi-insulating (111)B CdTe substrates (0.7 % lattice mismatch) by molecular beam epitaxy (MBE) has been described in detail elsewhere [2,3,14,15]. CdTe is a semiconductor with a large energy gap (1.5 eV) and a low lattice thermal conductivity (0.06 W/cm-K), which are both prerequisites for a suitable barrier layer in superlattice thermoelectric cooling devices. The base pressure of the growth chamber was mid- 10^{-10} Torr. The growth direction of the Bi film on (111)B CdTe is parallel to the trigonal axis of Bi. We first deposited a 3000 Å CdTe buffer layer on the CdTe substrate at 250 °C, followed by deposition of the Bi layer at a rate of 0.2-0.5 Å/s. Rates were monitored by a quartz crystal balance. A 100 Å CdTe cap layer was grown on the Bi film to prevent oxidation. Reflection high-energy electron diffraction (RHEED) was used to examine the specific surface reconstruction of the deposited layers. The growth temperature of both systems was in the range of 100-150 °C. Alloy compositions were determined by Inductively Coupled Plasma (ICP) Spectroscopy.

To measure the TEP [16], we used the differential method, in which a small temperature difference is maintained across the sample to produce the thermoelectric voltage: $\Delta V = S\nabla T + b(\nabla T)^2 + \dots$, where b is a constant. In this experiment, the temperature

difference was restricted to the range of 0.1-1 °C, in order to assure that terms higher than second-order in ∇T may be ignored. To eliminate the spurious thermal voltage within the circuit, we measured the thermoelectric voltage (in the steady state) for small incremental changes in the temperature differences. The thermoelectric voltage $(\Delta V)_i$ vs. temperature difference values $(\nabla T)_i$ were plotted and from the slope of the linear region, we could determine the TEP. To measure the temperature difference across the sample, we used a differential Cu-constantan thermocouple. The thermoelectric voltage was measured by using thin copper leads and was later corrected for the TEP of the leads to obtain the final results.

RESULTS AND DISCUSSION

Figure 2 shows the temperature dependence of the TEP for Bi and $\text{Bi}_{1-x}\text{Sb}_x$ alloy thin films of 1 μm thickness. The TEP of pure Bi is seen to be in good agreement with the previous single crystal values perpendicular to the trigonal axis (open boxes), which implies that the crystal quality of Bi film is comparable to the bulk single crystal. For $x=0.072$ and 0.088 in $\text{Bi}_{1-x}\text{Sb}_x$ thin films, TEP enhancement was observed by a factor of two. This TEP enhancement may be indicative of the band structure changes occurring as Sb is added. In a magneto-transport measurement of $x=0.072$ and 0.088 $\text{Bi}_{1-x}\text{Sb}_x$ thin films, the energy gap was determined: 31 meV and 37 meV, respectively. These values are three times higher than those of bulk material (8~12 meV) [12,17]. Higher band gaps were observed in $\text{Bi}_{1-x}\text{Sb}_x$ alloy thin films grown on BaF_2 : 17 meV for $x=0.087$. Strain was suggested as the cause. [18]

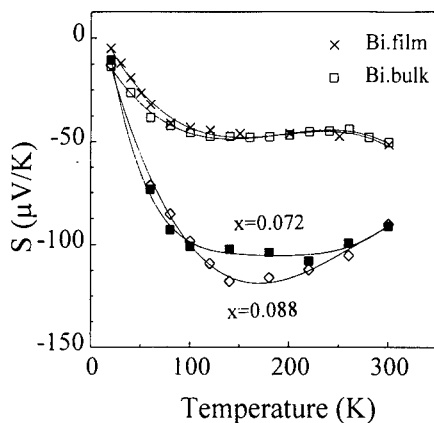


Fig. 2. The variation of the TEP as a function of temperature for Bi and $\text{Bi}_{1-x}\text{Sb}_x$ thin films of 1 μm thickness. For comparison the bulk Bi single crystal values (perpendicular to the trigonal axis as reported by Gallo *et al.* [1] in the range of 100-300 K and by Korenblit *et al.* [19] 3-80 K) are denoted by \square .

Figure 3 shows the results of temperature dependent TEP measurements on a series of Bi/CdTe superlattices. TEP values in the $(400 \text{ \AA}/100 \text{ \AA})_9$ and $(800 \text{ \AA}/100 \text{ \AA})_5$ superlattices are slightly enhanced over the bulk Bi value once temperature is greater than

200 K and 170 K, respectively. At 300 K the TEPs of the $(400 \text{ \AA}/100 \text{ \AA})_9$ and $(800 \text{ \AA}/100 \text{ \AA})_5$ superlattices are $57.69 \mu\text{V/K}$ and $56.78 \mu\text{V/K}$, respectively, compared to the bulk value (perpendicular to the trigonal axis) of $51.4 \mu\text{V/K}$. As the Bi well thickness decreases, the TEP decreases.

For films of thickness comparable or smaller than the de Broglie wavelength of the carriers, the quantum size effect dominates and the energy spectrum of the carriers in size-quantized films breaks up into subbands which influences the transport properties. In Bi with its small effective mass ($\sim 0.064 m_e$) the de Broglie wavelength is $\sim 1000 \text{ \AA}$. The theoretical calculations in the form of thin films and superlattices in the quantum size regime predict an enhanced value of the TEP as the well thickness decreases. The modest enhancement of the TEP at temperatures above 200 K in the two thickest-well superlattice samples over the $1 \mu\text{m}$ film data may in fact reflect the effects of quantum confinement. It should be first pointed out that while the enhancement is small, it is nonetheless larger than the measurement errors in the present experiment, since the TEP determinations do not require any knowledge of active-layer thickness or other quantities that are not precisely calibrated. This quantum confinement may produce a small decrease of the semimetallic overlap between the electron and hole bands, which would decrease the thermally-generated intrinsic densities and increase the TEP at a given temperature.

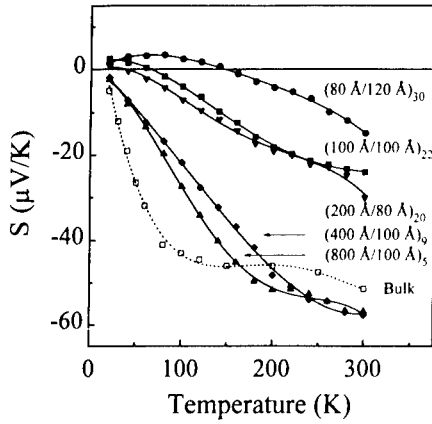


Fig. 3. TEPs of Bi/CdTe superlattices as a function of temperature. The subscript represents the number of Bi layers and the numbers in the parenthesis represent the Bi and CdTe barrier thicknesses, respectively. Bulk Bi single crystal (perpendicular to the trigonal axis) values were denoted by \square for comparison.

Figure 4 shows the results of temperature dependent TEP measurements on a series of $\text{Bi}_{0.93}\text{Sb}_{0.07}/\text{CdTe}$ superlattices. TEP values of superlattices decreases as the well thickness decreases.

For a thermoelectric material containing both electrons and holes, the total TEP may be described with the relation: $S = (\sigma_e S_e + \sigma_p S_p) / (\sigma_e + \sigma_p)$, where σ_e and σ_p are the electrical conductivities and S_e and S_p are the partial TEPs of electrons and holes, respectively. Previous magneto-transport measurements [2,3] on a series of ultrathin Bi films grown on CdTe substrates indicated heavy p-type doping: the low temperature hole

concentrations varied as $p = p_i + p_s/d$ where d is the film thickness, $p_s = 8 \times 10^{12} \text{ cm}^{-2}$ and $p_i \propto T^{3/2}$, and the electron concentrations followed $n \propto T^{3/2} e^{-E_g/k_B T}$ where $E_g = 0$ for $d \geq 300 \text{ \AA}$ and $E_g > 0$ for $d \leq 300 \text{ \AA}$. Therefore, the heavily p-type carrier concentration dominates, and the total TEP polarity becomes increasingly positive with decreasing film thickness and/or decreasing temperature. This behavior was observed in the Bi/CdTe superlattices.

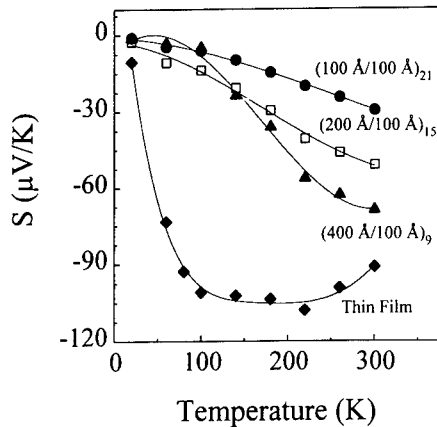


Fig. 4. TEPs of $\text{Bi}_{0.93}\text{Sb}_{0.07}/\text{CdTe}$ superlattices as a function of temperature.

For the thermoelectric cooling device application of Bi-based superlattices, one needs to improve the carrier mobility (typically in the order of $10^2 \text{ cm}^2/\text{V-s}$ for the superlattices) to increase the electrical conductivity and also prevent the unintentional p-type doping to optimize the TEP. Current work is directed toward improving interface roughness and reducing p-type doping. Te modulation doping is one strategy to improve the interface roughness and counter-dope. [20]

CONCLUSIONS

From TEP measurements on MBE grown Bi and $\text{Bi}_{1-x}\text{Sb}_x$ alloy thin films and superlattices, we observe that TEP of a Bi thin film of $1 \mu\text{m}$ thickness is in good agreement with the bulk single crystal value and as Sb is added TEP values are enhanced by a factor of two which confirms the semiconducting behavior. The TEPs for Bi/CdTe superlattices with 400 \AA and 800 \AA Bi well thicknesses are enhanced over the bulk values. However as the Bi and $\text{Bi}_{1-x}\text{Sb}_x$ well thickness in superlattices decreases, the magnitude of the TEP decreases due to unintentional p-type doping, which leads to compensation of the electron contribution and a positive sign for the TEP under some conditions. Thus, by reducing the excess hole concentration in the superlattices we may further increase the TEP value. One option would be to purposely introduce n-type impurities into the CdTe barrier layer so as to modulation dope the Bi, thereby allowing a test of the Gallo *et al.* [1] conjecture. Consequently, we were unable to confirm the prediction of Hicks *et al.*, but the results are encouraging. Current effort is concentrated

in substantially increasing the mobility. All this suggests that practical applications of Bi-based superlattices for thermoelectric cooling devices might indeed be possible.

ACKNOWLEDGEMENTS

This work was supported by ARPA under Award No. D437/00 and ONR under Document N0001496WX20241. Use was made of MRL Central Facilities supported by the National Science Foundation, at the Materials Research Center of Northwestern University, under Award No. DMR-9120521.

REFERENCES

1. C. F. Gallo, B. S. Chandrasekhar, and P. H. Sutter, *J. Appl. Phys.* **34**, 1963, 144.
2. A. DiVenere, X. J. Yi, C. L. Hou, H. C. Wang, J. Chen, J. B. Ketterson, G. K. Wong, J. R. Meyer, C. A. Hoffman, and F. J. Bartoli, *J. Vac. Sci. Technol. B* **12**, 1994, 1136.
3. C. A. Hoffman, J. R. Meyer, F. J. Bartoli, A. DiVenere, X. J. Yi, C. L. Hou, H. C. Wang, J. B. Ketterson, and G. K. Wong, *Phys. Rev. B* **48**, 1993, 11 43; *Phys. Rev. B* **51**, 1995, 5535.
4. L. D. Hicks and M. S. Dresselhaus, *Phys. Rev. B* **47**, 1993, 12 727.
5. L. D. Hicks, T. C. Harman, and M. S. Dresselhaus, *Appl. Phys. Lett.* **63**, 1993, 3230.
6. J. O. Sofo and G. D. Mahan, *Appl. Phys. Lett.* **65**, 1994, 2690.
7. G. D. Mahan and H. B. Lyon, Jr., *J. Appl. Phys.* **76**, 1994, 1899.
8. D. A. Broido and T. L. Reinecke, *Phys. Rev. B* **51**, 1995, 13 797.
9. D. A. Broido and T. L. Reinecke, *Appl. Phys. Lett.* **67**, 1995, 100.
10. P. J. Lin-Chung, and T. L. Reinecke, *Phys. Rev. B* **51**, 1995, 13 244.
11. L. D. Hicks, T. C. Harman, X. Sun, M. S. Dresselhaus, *Phys. Rev. B* **53** 10 493 (1996).
12. A. L. Jain, *Phys. Rev.* **114**, 1518 (1959).
13. J. Heremans and J.-P. Michenaud, *J. Phys. C* **18**, 6033 (1985).
14. A. DiVenere, X. J. Yi, C. L. Hou, H. C. Wang, J. B. Ketterson, G. K. Wong, and I. K. Sou, *Appl. Phys. Lett.* **62**, 1993, 2640.
15. X. J. Yi, H. C. Wang, A. DiVenere, C. L. Hou, J. Chen, J. B. Ketterson, and G. K. Wong, *Appl. Phys. Lett.* **64**, 1994, 1283.
16. S. Cho, A. DiVenere, G. K. Wong, J. B. Ketterson, J. R. Meyer and C. A. Hoffman (accepted for publication in *Solid State Communications*).
17. B. Lenoir, M. Cassart, J.-P. Michenaud, H. Scherrer and S. Scherrer, *J. Phys. Chem. Solids*, **57**, 1996, 89.
18. D. T. Morelli, D. L. Partin and J. Heremans, *Semicond. Sci. Technol.* **5**, 1990 S257.
19. I. Ya. Korenblit, M. E. Kusnetsov, and S. S. Shalyt, *Soviet Phys. JETP*, **29**, 1969, 4.
20. S. Cho, A. DiVenere, G. K. Wong, J. B. Ketterson, J. R. Meyer and C. A. Hoffman, *Bulletin of APS March Meeting*, Kansas City, MO, 1997, p273.

ENHANCEMENT IN FIGURE-OF-MERIT WITH SUPERLATTICE STRUCTURES FOR THIN-FILM THERMOELECTRIC DEVICES

R. Venkatasubramanian and T. Colpitts
Research Triangle Institute, Research Triangle Park, NC 27709, USA.

ABSTRACT

Thin-film superlattice (SL) structures in thermoelectric materials are shown to be a promising approach to obtaining an enhanced figure-of-merit, ZT , compared to conventional, state-of-the-art bulk alloyed materials. In this paper we describe experimental results on $\text{Bi}_2\text{Te}_3/\text{Sb}_2\text{Te}_3$ and Si/Ge SL structures, relevant to thermoelectric cooling and power conversion, respectively. The *short-period $\text{Bi}_2\text{Te}_3/\text{Sb}_2\text{Te}_3$ and Si/Ge SL structures appear to indicate reduced thermal conductivities compared to alloys of these materials.* From the observed behavior of thermal conductivity values in the $\text{Bi}_2\text{Te}_3/\text{Sb}_2\text{Te}_3$ SL structures, a distinction is made where certain types of periodic structures may correspond to an ordered alloy rather than an SL, and therefore, do not offer a significant reduction in thermal conductivity values. Our study also indicates that SL structures, with little or weak quantum-confinement, also offer an improvement in thermoelectric power factor over conventional alloys. We present power factor and electrical transport data in the plane of the SL interfaces to provide preliminary support for our arguments on reduced alloy scattering and impurity scattering in $\text{Bi}_2\text{Te}_3/\text{Sb}_2\text{Te}_3$ and Si/Ge SL structures. These results, though tentative due to the possible role of the substrate and the developmental nature of the 3- ω method used to determine thermal conductivity values, suggest that the short-period SL structures potentially offer factorial improvements in the three-dimensional figure-of-merit (ZT_{3D}) compared to current state-of-the-art bulk alloys. An approach to a thin-film thermoelectric device called a Bipolarity-Assembled, Series-Inter-Connected Thin-Film Thermoelectric Device (BASIC-TFTD) is introduced to take advantage of these thin-film SL structures.

INTRODUCTION

High-efficiency thermoelectric materials are key to efficient solid-state refrigeration, cooling of electronic components such as high-density, high-power integrated circuits, superconducting devices, infra-red detectors etc. and for thermoelectric power conversion. The performance of a thermoelectric device at an absolute temperature T is related to ZT , given by the expression $(\alpha^2\sigma/K)T$, where α is the Seebeck coefficient, σ is the electrical conductivity, and K is the sum-total of lattice and electronic components of thermal conductivity. $(\alpha^2\sigma)$ is also referred to as the power factor. Currently, several approaches are being investigated, including novel bulk materials such as skutterudites [1], thin-film quantum-wells [2,3], and superlattices [4] to increase ZT across various temperature regimes. Some of the early results with these efforts have been reviewed recently [5]. In this paper, we present our experimental results describing the thermoelectric properties of thin-film SL structures in the $\text{Bi}_2\text{Te}_3/\text{Sb}_2\text{Te}_3$ and Si/Ge material systems.

WHY SL STRUCTURES WITH WEAK OR NO QUANTUM-CONFINEMENT?

Recent research on thin-film thermoelectric materials have pursued two approaches. One involves the use of *quantum-wells*, as in the n-type $\text{PbTe}/\text{PbEuTe}$ system [3], where the electrons in a 10 to 20Å PbTe quantum-well are confined in two-dimensions by a 400-to-500Å thick

PbEuTe layer. The PbEuTe layer provides nearly a 200 meV potential barrier in the conduction band to obtain the quantum-confinement of electrons. With this approach, the *carrier and heat transport* (in a thermoelectric device) are expected to be in a direction *parallel to the quantum-well interfaces*. Here the parasitic thermal transport through the barrier, which is typically much thicker relative to the quantum-well, can degrade the overall ZT of the composite, quantum-well plus barrier structure [6].

At RTI, we have pursued [7] an entirely different approach to the development of engineered, low-dimensional, structured thermoelectric materials. Our approach involves the use of short-period SL structures, with negligible quantum-confinement, for the *reduction of lattice thermal conductivity* resulting from the various phonon scattering mechanisms unique to periodic structures. First of all, the vibrational discontinuities at an SL interface can enhance phonon scattering rates. Both the bond energies and elastic constants are usually different for the constituents of the SL system, for example, the lighter mass of Sb compared to Bi (in a $\text{Bi}_2\text{Te}_3/\text{Sb}_2\text{Te}_3$ SL) would imply that comparable phonon modes would have a higher frequency in Sb_2Te_3 . Reduction in phonon group velocities as a result of possible gaps in the phonon frequency spectrum in a periodic SL structure can reduce thermal conductivity in SL structures. In an SL, compared to a continuous and uniform-composition alloy, the minimum phonon energies required to produce Umklapp scattering processes (momentum-destroying scattering processes) are reduced relative to those of an alloy. In addition, phonon-wave reflection (as in optical etalons) has been observed at SL interfaces, where selective reflection of phonons occurs when the phonon wavelength fulfills the Bragg condition [8].

We had initially predicted using a simple boundary-scattering model for phonon scattering by SL interfaces [7] and later demonstrated experimentally that the $\text{Bi}_2\text{Te}_3/\text{Sb}_2\text{Te}_3$ SL structures [4] and, more recently in collaboration with Cahill of University of Illinois, the Si/Ge SL structures [9] indicate thermal conductivity values below that of their corresponding solid-solution alloys. In contrast to the quantum-well structures, when the SL structures are used predominantly for thermal conductivity reduction, the *carrier and heat transport would be perpendicular to the SL interfaces* in a thermoelectric device. From the standpoint of making practical thermoelectric devices using thin-films, the choice of making carrier transport (and the heat transport) perpendicular to the SL interfaces, and therefore along the growth direction of the thin-films, appears to offer engineering advantages [10]. If so, we need to consider the efficiency of electrical transport perpendicular to the SL interfaces.

Shown in Figure 1 are the schematics of ideal, heterostructure band diagrams in the two SL material systems, $\text{Bi}_2\text{Te}_3/\text{Sb}_2\text{Te}_3$ and Si/Ge, discussed in this paper. In Fig. 1(a), using reported bandgaps of Bi_2Te_3 and Sb_2Te_3 and assuming that the small bandgap difference of 0.07 eV gets equally divided between a conduction-band and a valence-band offset, we observe that the potential barrier for carrier transport perpendicular to the SL interfaces should be ~ 0.035 eV. Also, the thickness of the Sb_2Te_3 layer (with the larger bandgap) in the SL is made comparable to that of the Bi_2Te_3 layer. The small barrier plus the comparable thickness of the two SL component layers would lead to negligible quantum-confinement effects. For a potential thermoelectric cooling device using such a SL material system and operating near 300K, the ~ 0.035 eV barrier for carrier transport perpendicular to the SL interfaces would be comparable to the average thermal energy of carriers. This barrier can be reduced further by optimized doping of the individual Bi_2Te_3 and Sb_2Te_3 layers, if necessary, for the overall optimization of the power factor perpendicular to SL interfaces. In fact, the small barrier could potentially act as an energy-filter for the “less-efficient”, low-energy (with respect to the band-edges) carriers for improved thermo-electric energy transport [11]. Thus, we believe, efficient power factors are achievable with current and heat transport perpendicular to the $\text{Bi}_2\text{Te}_3/\text{Sb}_2\text{Te}_3$ SL interfaces.

The measured through-thickness current-voltage (I-V) characteristic of a 150-period, p-type $\text{Bi}_2\text{Te}_3/\text{Sb}_2\text{Te}_3$ SL at 300K is shown in Figure 2. This SL structure is similar to a $30\text{\AA}/30\text{\AA}$ $\text{Bi}_2\text{Te}_3/\text{Sb}_2\text{Te}_3$ SL with a low measured thermal conductivity discussed in a subsequent section. We note the linearity of the I-V characteristic near zero-bias and at high current density levels of as much as 20 Amps/cm^2 . This suggests no effect of any significant potential barrier, if present, to hole transport across the Bi_2Te_3 and Sb_2Te_3 SL interfaces.

Fig. 1(b) shows an ideal heterostructure band diagram for the n-type Si/Ge SL, based on the known bandgaps of Si and Ge and the anticipated conduction band offset in this material system [12]. Here again, the thickness of the Si and Ge layers in the SL are similar, thus reducing effective quantum-confinement effects in the Ge layer. In the n-type Si/Ge SL, the potential barrier for carrier transport perpendicular to the SL interfaces should be less than 0.1 eV at 300K. As noted above, the effective barrier to carrier transport perpendicular to the SL interfaces can be further reduced through optimized doping levels in the Si and Ge layers, for the overall optimization of power factor. We also observe that this barrier would become comparable to the average thermal energy of carriers at elevated temperatures such as 600K, as in a power generation device.

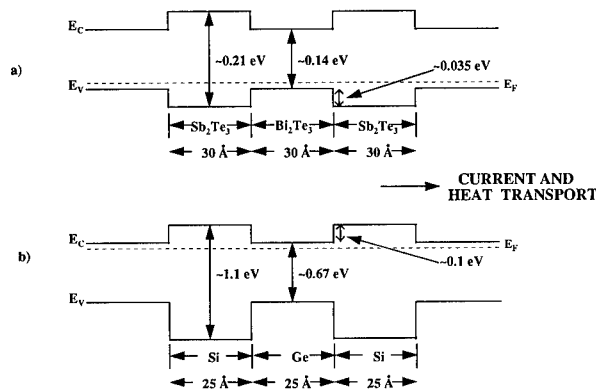


Figure 1. Ideal band-diagram of a) a p-type $\text{Bi}_2\text{Te}_3/\text{Sb}_2\text{Te}_3$ SL b) an n-type Si/Ge SL

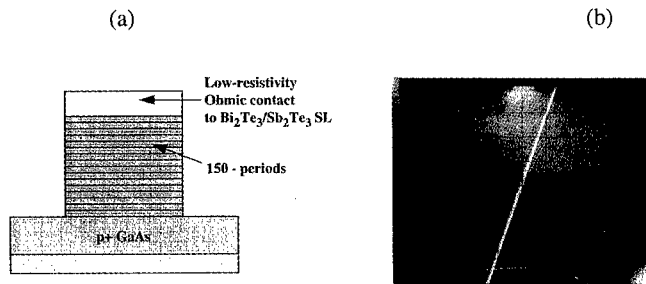


Figure 2. a) P-type, $\text{Bi}_2\text{Te}_3/\text{Sb}_2\text{Te}_3$ SL structure with low-resistivity contacts on top of SL structure and substrate b) I-V data between the top and bottom contacts ($H: 0.1\text{ Volt}, V: 0.2\text{ A}$)

In essence, we note that SL structures with negligible or weak confinement are chosen to allow efficient carrier transport perpendicular to the SL interfaces. Doing so, we can take advantage of the potential strong reduction in lattice thermal conductivity perpendicular to the SL interfaces. However, as our early results on in-plane transport properties suggest, these SL structures are also likely to offer improved electrical transport properties from a reduction or elimination of alloy scattering; note that we use periodic structures to reduce lattice thermal conductivity rather than the conventional solid-solution alloying. In the case of Si/Ge SL structures, reduction of impurity scattering leading to improved transport properties is suggested.

EXPERIMENTAL

The focus of this paper is to present experimental results on short-period SL structures to elucidate the above aspects of our approach for using short-period SL structures with weak or negligible quantum-confinement. We specifically discuss results on thermal conductivity reduction perpendicular to the SL interfaces in both the $\text{Bi}_2\text{Te}_3/\text{Sb}_2\text{Te}_3$ and Si/Ge SL material systems. A recently developed 3- ω technique for thin-films [13] was used to measure the thermal conductivity of the thin-film SL structures. This technique, originally developed for non-conducting thin-films, has recently been confirmed to work for conducting thin-films (specifically SiGe alloy films and Si/Ge SL structures [9] by Cahill with measurements carried out at the University of Illinois).

The measurement of electrical resistivity perpendicular to the SL interfaces in thin-films is complicated, unlike the ease with which they can be measured in the plane of the SL structures utilizing van der Pauw Hall-effect methods. Direct measurements of the electrical resistivity and the power factor perpendicular to the SL interfaces are being attempted in our laboratory and would be published in future. In this paper, however, we present power factor and electrical transport data in the plane of the SL interfaces that provide preliminary basis for our arguments on reduced alloy scattering and impurity scattering in $\text{Bi}_2\text{Te}_3/\text{Sb}_2\text{Te}_3$ and Si/Ge SL structures.

The $\text{Bi}_2\text{Te}_3/\text{Sb}_2\text{Te}_3$ and the Si/Ge SL structures, whose thermoelectric properties are described in this paper, were grown on semi-insulating GaAs substrates. The use of semi-insulating GaAs substrates is ideal for determining the resistivity of the thin-films by the van der Pauw Hall method and the determination of the in-plane Seebeck coefficients of the epi layers. These measurements were used to estimate the power factors in the plane of the SL structures.

Growth of SL Structures

The p-type $\text{Bi}_2\text{Te}_3/\text{Sb}_2\text{Te}_3$ SL structures and the comparable alloys reported in this study were grown by metallorganic chemical vapor deposition (MOCVD). Details of the growth process for obtaining high-quality SL structures in this material system are described elsewhere [5,14]. High-resolution double-crystal X-ray diffraction (XRD) measurements and transmission electron microscopy (TEM) data taken on $\text{Bi}_2\text{Te}_3/\text{Sb}_2\text{Te}_3$ SL structures have indicated that the SL structures are of good quality. The Si/Ge SL structures and SiGe alloy thin-films reported in this study were grown by chemical vapor deposition (CVD), and were intentionally doped n-type with Arsenic. Shown in Figure 3 is the scanning electron microscopy cross-section (XSEM) view of a Si/Ge SL structure, with a periodicity of $\sim 200\text{\AA}$ and a total layer thickness of $\sim 4.5\text{ }\mu\text{m}$. In extending the Si/Ge SL periods below $\sim 100\text{ }\text{\AA}$, we developed an angle-lapped scanning electron microscopy (ALSEM) technique. Here, a cross-sectioned short-period SL is angle-lapped at a known small angle of about 5° and then the sample is examined by SEM in plan-view to determine the SL periods; ALSEM view of a $35\text{\AA}/35\text{\AA}$ Si/Ge SL is shown in Fig.4.

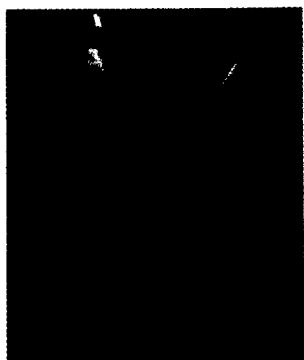


Figure 3 XSEM of a 4.5-micron-thick, 200Å-period Si/Ge SL structure

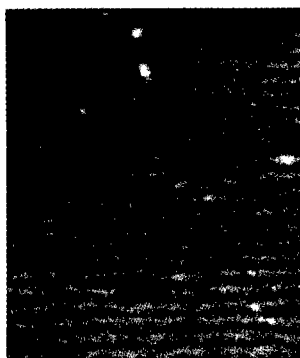


Figure 4 ALSEM view of a 35Å/35Å Si/Ge SL structure

THERMOELECTRIC PROPERTIES OF SL STRUCTURES

Bi₂Te₃/Sb₂Te₃ SL Structures

Thermal Conductivity Reduction

Figure 5 shows the observed thermal conductivity values, as a function of the SL dimension, in Bi₂Te₃/Sb₂Te₃ SL structures where the layer thickness of the Bi₂Te₃ layer is same as that of the Sb₂Te₃ layer. We see a small, but measurable, reduction in the thermal conductivity with a shorter SL dimension (one half of the SL period) in the range of ~200Å to 30Å. We also observe an apparent minimum thermal conductivity when the SL dimension approaches ~30Å; the measured thermal conductivity is as low as ~1.3 mW/cm-K. This represents nearly a factor of seven reduction in thermal conductivity compared to that measured in a BiSbTe₃ alloy thin-film, also by the 3- ω method, as indicated in Figure 6. Note that the 3- ω value of ~10.7 mW/cmK measured in the BiSbTe₃ thin-film is comparable to that measured in bulk alloys of similar composition [15].

We also observe in Figure 5 that there is a rapid rise in the measured thermal conductivity, almost approaching that of the thin-film alloy, when the SL dimension becomes smaller than ~30Å, approximately the unit-cell dimension in these materials. We note that the sub-unit cell dimension, and therefore a minimum repeat distance possible in a periodic structure, in the Bi₂Te₃ material system along the "c" growth direction is ~10 Å [16]. *A periodic structure in which the repeat distance is below a unit-cell dimension can be thought of as being an ordered alloy rather than an SL structure.* This may explain the rise in the measured thermal conductivity values of such SL structures from a minimum of ~1.4 mW/cm-K, rapidly approaching that of the alloy. This further points to the efficacy of the periodic SL structure in reducing thermal conductivity compared to alloyed materials.

A similar behavior of thermal conductivity reduction with smaller SL dimension was observed in another set of Bi₂Te₃/Sb₂Te₃ SL structures, where the Bi₂Te₃ layer thickness was kept constant at ~10Å and the Sb₂Te₃ SL dimension was varied continuously in steps of ~10Å. The observed thermal conductivity data for this set is shown in Figure 6. We notice several apparent minima in the measured thermal conductivity, when the sum of thickness of the Bi₂Te₃

and Sb_2Te_3 layers are $\sim 30\text{\AA}$, $\sim 60\text{\AA}$ and $\sim 90\text{\AA}$, representing integer multiples of the unit cell dimension of about 30\AA . We believe that the structures in which the bi-layer period does not correspond to an integer multiple of the unit cell dimension are more akin to an ordered alloy rather than a periodic SL. Thus these structures may not offer the substantial reduction in the lattice thermal conductivity compared to alloys.

In Figure 6, we observe that the $10\text{\AA}/20\text{\AA}$ $\text{Bi}_2\text{Te}_3/\text{Sb}_2\text{Te}_3$ SL structure offers a thermal conductivity of ~ 2.4 mW/cm-K. Similarly, the $10\text{\AA}/50\text{\AA}$ $\text{Bi}_2\text{Te}_3/\text{Sb}_2\text{Te}_3$ SL structure indicates thermal conductivity of 2.5 to 2.7 mW/cm-K. These values are a factor of nearly seven smaller than the thermal conductivity of ~ 16 mW/cm-K, typically observed in conventional bulk $\text{Bi}_{0.5}\text{Sb}_{1.5}\text{Te}_3$ alloys. In Fig. 6, the locus of the apparent minima in thermal conductivities is shown by the dashed line, indicating a slow increase with the SL dimension as seen in Figure 5.

An important point to note here is that the observed thermal conductivity values in the optimized $\text{Bi}_2\text{Te}_3/\text{Sb}_2\text{Te}_3$ SL structures are apparently [17] lower than the predicted minimum thermal conductivity values for the BiSbTe_3 alloy films. The minimum thermal conductivity values are based on the concept that the minimum phonon free-path is at least equal to [18] or about half of [19] the average wavelength of the Debye phonon waves. A possible exception to this rule may be an SL with a periodic structure, in which the propagation of the low-frequency phonons are hindered through an optical-etalon-like mechanism [8] or through a limited propagation distance mechanism due to “scattering” at the SL interfaces [20]. In the latter argument, depending on the frequency of the phonon wave, its propagation is assumed halted at the SL interface before an exchange of thermal energy can occur between one volume element of the extent of the phonon wave to a neighboring volume element. The concept of exchange of thermal energy between adjacent volume elements, in bulk material, was proposed in Ref. 19. Thus we believe, if the 3ω measurements of thermal conductivity values are accurate, the “scattering” of the “heat-conducting” low-frequency phonon waves at SL boundaries could reduce the thermal conductivity below the ideal minimum thermal conductivity values.

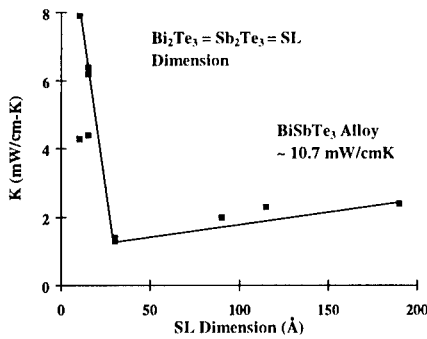


Figure 5. Thermal conductivity variation with SL dimension in the $\text{Bi}_2\text{Te}_3/\text{Sb}_2\text{Te}_3$ SL system where layer thickness of Bi_2Te_3 and Sb_2Te_3 are same.

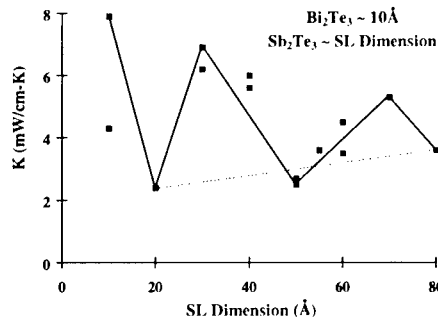


Figure 6. Thermal conductivity variation in $\text{Bi}_2\text{Te}_3/\text{Sb}_2\text{Te}_3$ SL structures where Bi_2Te_3 layer is $\sim 10\text{\AA}$. The dashed line is the locus of the apparent minima in K.

Mobility Enhancement

One of the advantages of an SL structure compared to an alloy film is the ability to obtain higher carrier mobilities through a reduction of the alloy scattering of carriers [4]. In Table I, we

compare the in-plane Hall-mobility of some p-type $\text{Bi}_x\text{Sb}_{2-x}\text{Te}_3$ alloy films and their equivalent SL structures. We observe for all the SL structures, the hole mobility in the p-type $\text{Bi}_2\text{Te}_3/\text{Sb}_2\text{Te}_3$ SL is higher than that in a corresponding $(\text{Bi}_x\text{Sb}_{2-x})\text{Te}_3$ alloy of identical electrical conductivity. Also, the ratio of improvement in the mobility of SL structures over alloy films is highest when the mole fraction of Bi is equal to that of Sb in the $\text{Bi}_x\text{Sb}_{2-x}\text{Te}_3$ alloy; this is to be anticipated as the alloy scattering of carriers would be a maximum for this composition.

In addition, from the nominal band structure indicated in Figure 1a, the periodic SL structure would lead to a larger displacement (in energy) of the holes from the acceptor states, at least by the valence band offset in the SL system. Even if this offset is only small, not enough to alloy and in turn on the bandstructure difference between the alloy and the SL. A full theoretical provide quantum confinement, the larger displacement can reduce impurity scattering to improve the carrier mobilities. The ratio of improvement in hole mobility of the SL structures over comparable alloy films would depend on the bandgap (and hence the composition). The treatment of carrier transport in such SL structures with negligible or weak quantum-confinement needs to be developed.

Seebeck coefficient and Power factor Enhancement

The *improved carrier mobilities in the SL structures*, for nearly the same electrical conductivity as in respective alloy films, also lead to *lower measured free-carrier levels and therefore, a higher measured Seebeck coefficient (α) in the SL structures*. This effect can be explained as follows. The Seebeck coefficient (α) of a p-type material is given by:

$$\alpha = \frac{k}{e} \left(\frac{\int_{E=E_v}^{\infty} E^* \sigma(E) dE}{\int_{E=E_v}^{\infty} \sigma(E) dE} - E_f^* \right)$$

where σ is the electrical conductivity, E^* is the reduced energy of holes in the valence band, and E_f^* is the reduced Fermi-energy. A lower carrier concentration, for about the same effective band gap, would lead to a lower hole E_f^* ; this would enhance α in the SL structure compared to the alloy film. The SL structure is also expected to increase the average E^* , albeit only by a small amount than possible with strong quantum-confinement, which would lead to a slight enhancement in α . The improved α , for approximately the same electrical conductivity as in the alloy, leads to a larger power factor for the SL. We have recently verified power factors in $10\text{\AA}/50\text{\AA}$ $\text{Bi}_2\text{Te}_3/\text{Sb}_2\text{Te}_3$ SL structures of as much as $\sim 57 \mu\text{W}/\text{cm}\cdot\text{K}^2$. The typical best power factor in optimized bulk alloy $\text{Bi}_x\text{Sb}_y\text{Te}_3$ ($x + y = 2$ and $x/y \sim 0.25$) is $\sim 36 \mu\text{W}/\text{cm}\cdot\text{K}^2$ [21]. Thus the SL structures appear to offer nearly 58% improvement in the in-plane power factor compared to the state-of-the-art bulk alloys. In addition, the MOCVD-grown thin alloy films and the $\text{Bi}_2\text{Te}_3/\text{Sb}_2\text{Te}_3$ SL structures offer higher power factors at lower temperatures (150K) than at 300K, in a significant variation from commercial bulk $\text{Bi}_{0.4}\text{Sb}_{1.6}\text{Te}_3$ alloys. We attribute this behavior partly to the relatively higher purity of the MOCVD-grown thin-film alloy leading to a greater carrier mobility, because impurity scattering dominates carrier transport at lower temperatures. However, the $\text{Bi}_2\text{Te}_3/\text{Sb}_2\text{Te}_3$ SL structure shows a larger improvement in power factor of as much as 106% at 150K compared to its power factor at 300K. This behavior of the SL structures near cryogenic temperatures, vis-a-vis both bulk alloy and the alloy thin-film, is probably related to the absence of alloy scattering effects in an SL [20].

Table I In-plane hole mobility enhancement in SL structures compared to alloy films, for identical electrical conductivity

Alloy Material	Equivalent SL Structure	Hole Mobility in Alloy Film (cm ² /Vsec)	Hole Mobility in SL Structure (cm ² /Vsec)	Ratio of Improvement in Mobility with SL Structures
Bi _{0.5} Sb _{1.5} Te ₃	15Å/45Å	384	603	1.57
Bi _{1.0} Sb _{1.0} Te ₃	30Å/30Å	88	432	4.91
Bi _{1.5} Sb _{0.5} Te ₃	30Å/10 Å	32	102	3.18

Potential ZT in Bi₂Te₃/Sb₂Te₃ SL Structures

The power factors in the Bi₂Te₃/Sb₂Te₃ SL structures have been measured parallel to the SL interfaces. However, the 3- ω technique [13] measures thermal conductivity values perpendicular to the SL interfaces. Further, unlike GaAs and AlAs materials, Bi₂Te₃ and Sb₂Te₃ materials exhibit anisotropic thermal conductivities; so determining ZT values of the Bi₂Te₃/Sb₂Te₃ SL structures is not straightforward. Measurement of vertical power factors in the Bi₂Te₃/Sb₂Te₃ SL structures would enable the determination of ZT. Preliminary estimates of ZT, with a correction for potential anisotropy in electrical conductivities and power factors, indicate that Bi₂Te₃/Sb₂Te₃ SL structures would offer at least a factor of three to four improvement in ZT at 300K compared to those obtainable with bulk Bi_{0.4}Sb_{1.6}Te₃ alloys.

Si/Ge SL Structures

Thermal Conductivity Reduction

We have studied the thermal conductivity of Si/Ge SL structures for a near constant SL period but varying electron concentration, as measured by Hall-effect. In these samples, the thermal conductivity increases with electron concentration for a constant SL period. Also, the increase in thermal conductivity with carrier concentration is higher at smaller SL periods. This behavior suggests reduced lattice thermal conductivity contribution to the total thermal conductivity with a shorter SL period. The reduced total thermal conductivity with a smaller SL period is also evident in the data of Fig. 7 under the limit where lattice thermal conductivity is small with short SL periods, the intercepts are a function of the carrier levels. We also observe that for large SL periods, at $n=3+1.3 \text{ E}18 \text{ cm}^{-3}$, the thermal conductivity values are extremely low. A similar result for large-period Si/Ge SL structures has been attributed to disruption of lattice vibrations by defects during lattice-mismatched, large-period, Si/Ge SL growth [9].

Mobility Enhancement

Shown in Figure 8 is the observed dependence of in-plane electron mobility, as determined by Hall-effect, on SL period for a range of free-carrier levels. We clearly observe that the electron mobility improves with smaller period in the Si/Ge SL structures, at $n=3\pm1.3\text{E}18 \text{ cm}^{-3}$. This behavior can be understood by a qualitative model as follows.

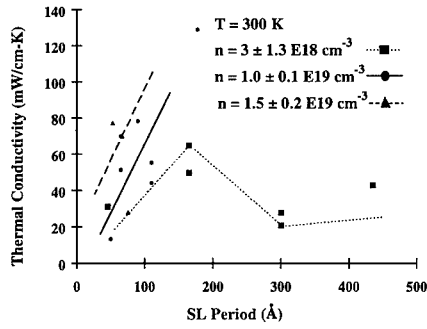


Figure 7. Variation of thermal conductivity with SL period for a range of free carrier levels.

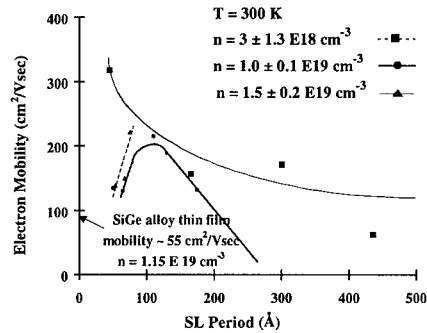


Figure 8. Variation of electron mobility with SL period for a range of free-carrier levels.

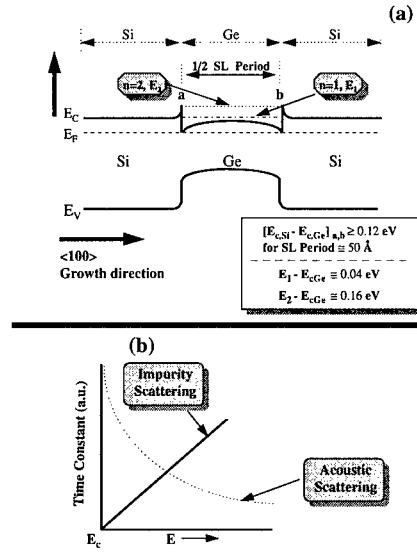


Figure 9. (a) Heterostructure band diagram at the Si/Ge SL interface and (b) the nature of time constants associated with impurity scattering and acoustic scattering

A Si/Ge SL heterostructure band diagram is shown in Figure 9(a) for an SL period $\cong 50 \text{ \AA}$ under ideal conditions and assuming that the conduction band offset is equal to the electron affinity difference between Ge and Si, ignoring possible increase in bandgap of the Si layer from uniaxial expansion along the $\langle 100 \rangle$ growth direction. Also, the energies of the $n=1$ and $n=2$ quantum levels indicated in the Ge layer are simple estimations ignoring mini-banding effects [22]. For the n-type doped Si/Ge materials and for doping levels of $\sim 3 \text{ E18 cm}^{-3}$ and above, impurity scattering of carriers is expected to significantly affect carrier mobility at 300K. Note that even in weakly-confined Si/Ge SL structures, for low-carrier densities, most of the electrons would be in the Ge layer of the SL from energetic considerations. At very high free-carrier levels, the electrons would be distributed in both the Si and Ge layers depending on their respective effective density of states. The general dependence of time constants associated with impurity scattering and acoustic scattering of electrons in the conduction band of Ge, as a function of energy separation from the conduction band edge of Ge, is shown in Figure 9 (b). In the Si/Ge SL, the average energy of electrons in the Ge layer is expected to be higher with respect to the conduction band edge of Ge as the SL period decreases. This would be the case

even if there is only weak confinement of electrons in the Ge layer of the Si/Ge SL and mini-banding effects are active. The higher energy of the electrons with smaller SL periods implies less impurity scattering, and therefore larger mobility of electrons, from the dependence of impurity scattering time constant on the energy of carriers. Further, the Si/Ge SL structures are expected to offer reduced alloy scattering of carriers compared to that of a SiGe alloy material; this would improve the carrier mobilities as well.

In Figure 8, a similar behavior of increasing electron mobility with shorter SL period is observed for $n \sim 1.0 \pm 0.1 \times 10^{19} \text{ cm}^{-3}$ till $\sim 100 \text{ \AA}$. For smaller SL periods, the mobility falls with increasing electron density as well. This fall in mobility has not been clearly understood at the present time. It is possible that at high carrier levels, significant conduction occurs in the Si layer of the SL—typically mobilities are smaller in Si compared to that in Ge. Further, the electrons in the Si layer would not benefit from above-described reduced impurity scattering. In any case, as shown in Figure 8, we note that for similar free-carrier levels, the mobility of all the Si/Ge SL structures are significantly higher than that of a comparably doped SiGe alloy epitaxial film. The improved mobility is primarily attributed to minimizing impurity scattering as well as avoiding any possible alloy scattering. The electrical resistivity of Si/Ge SL structures as a function of the SL period and free-carrier level mimic the behavior of electron mobility shown in Fig. 8 [20].

Seebeck Coefficient and Power Factor Enhancement

Shown in Figure 10 is the variation of the in-plane Seebeck coefficient in the Si/Ge SL structures as a function of SL period, at different free-carrier levels. For all the free-carrier levels, we observe that the Seebeck coefficient increases significantly with a shorter SL period. As discussed in the previous section, conduction electrons in the Ge layer of a Si/Ge SL are expected to be energetically higher (with respect to the conduction band edge of Ge) as the SL period decreases. If the Fermi level (E_f) is held close to the conduction band edge of Ge, due to doping degeneracy, the higher energy of the carriers (with respect to E_f) would lead to higher Seebeck coefficients with smaller SL periods. These results qualitatively indicate that it is possible to obtain a substantial improvement in the Seebeck coefficient, even if only weak quantum-confinement effects are present. The combination of lower electrical resistivity from improved electron mobilities for short-period ($< 150 \text{ \AA}$) Si/Ge SL structures and the improved Seebeck coefficients for short-period ($< 75 \text{ \AA}$) Si/Ge SL structures, all lead to a significant improvement in power factors of the SL structures with smaller periods. This is indicated in Figure 11. We note from this data, in the free-carrier range of 3×10^{18} to $1.5 \times 10^{19} \text{ cm}^{-3}$, that there is a significant improvement in the power factor with shorter-periods even at higher free-carrier levels. The typical power factor for state-of-the-art SiGe bulk alloy is $\sim 20 \text{ } \mu\text{W/cm-K}^2$. The power factor measured on a SiGe alloy thin-film (for reference) was $\sim 14 \text{ } \mu\text{W/cm-K}^2$. Thus the best measured power factors in Si/Ge SL structures are about a factor of 5 better than that of bulk SiGe alloys and as much as a factor of 8 better than SiGe alloy films. We attribute this increase in in-plane power factor to an enhanced mobility from reduced impurity scattering in contrast to the strong quantum confinement effects [3] invoked for the PbTe/PbEuTe quantum wells.

Potential ZT in Si/Ge SL Structures

The power factors in the Si/Ge SL structures have been measured parallel to the SL interfaces. However, the 3- ω method measures thermal conductivity perpendicular to the SL interfaces. Although, unlike Bi_2Te_3 or Sb_2Te_3 , Si and Ge do not have strong intrinsic anisotropic

properties, determining the ZT values of these SL structures would require the measurement of vertical power factors. Preliminary estimates suggest that the optimized Si/Ge SL structures would offer at least a factor of five improvement in ZT at 300K compared to bulk SiGe alloys.

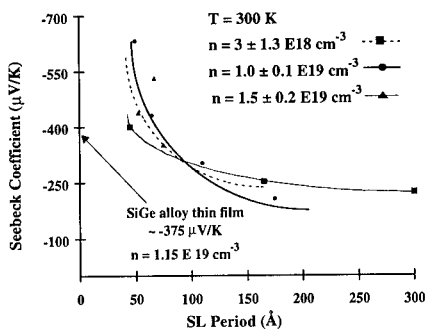


Figure 10. Seebeck coefficient as a function of SL period for various free-carrier levels.

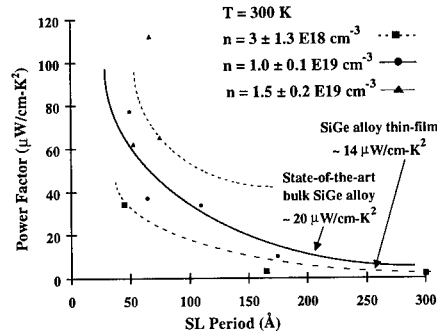


Figure 11. Variation of power factor with SL period for a range of free carrier levels.

APPROACH TO THIN-FILM THERMOELECTRIC DEVICES

A schematic of a thin-film thermoelectric device, called Bipolarity-Assembled, Series-Inter-Connected Thin-Film Thermoelectric Device (BASIC-TFTD) using the thin film SL structures, is shown in Figure 12. Here, the individual thin-film thermoelements are electrically in series and thermally in parallel. The advantages of such a thin-film device include the ability to use low-cost power supplies, simple microelectronic processing, automation for large-volume, low-cost device manufacturing, and multi-staging for improved performance. A detailed description of the fabrication sequence of such a device is presented elsewhere [10].

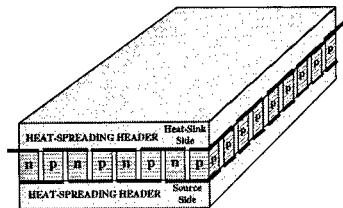


Figure 12. Schematic of a BASIC-TFTD structure for using the thin-film SL structures

CONCLUSIONS

The thermoelectric properties of $\text{Bi}_2\text{Te}_3/\text{Sb}_2\text{Te}_3$ and Si/Ge SL structures suggest that it may be possible to break the traditional, conflicting material requirements for obtaining high electrical conductivity and low thermal conductivity, encountered in bulk thermoelectric materials. SL structures could reduce alloy and impurity scattering of carriers for enhanced mobilities; yet the SL structures reduce thermal conductivity below those of solid-solution alloys. The short-period $\text{Bi}_2\text{Te}_3/\text{Sb}_2\text{Te}_3$ and Si/Ge SL structures potentially offer factorial improvements in ZT_{3D} over current state-of-the-art bulk alloys. More definitive measurements of ZT_{3D} in these SL materials are needed, including measurement of power factors perpendicular to the SL

interfaces. The development of a practical thermoelectric device technology with these SL materials would be valuable for a variety of cooling and power conversion applications.

ACKNOWLEDGMENTS

The work on $\text{Bi}_2\text{Te}_3/\text{Sb}_2\text{Te}_3$ SL structures was supported by the Office of Naval Research with Dr. John Pazik as the technical monitor. We would like to acknowledge the assistance of Mr. D. Malta of RTI for ALSEM, Dr. T. Harman of MIT Lincoln Laboratories for verification of the Seebeck coefficients in $\text{Bi}_2\text{Te}_3/\text{Sb}_2\text{Te}_3$ SL structures and Dr. Lee Danielson of Lockheed-Martin for verification of the Seebeck coefficients in Si/Ge SL structures.

REFERENCES

1. B.C. Sales, D. Mandrus, and R.K. Williams, *Science* **272**, 1325 (1996).
2. L.D. Hicks, T.C. Harman, X. Sun, and M.S. Dresselhaus, *Proc. of XV International Conf. on Thermoelectrics*, IEEE Catalog No. 96TH8169, 450 (1996); T.E. Whall and E.H. C. Parker, *Proc. of 1st Euro. Conf. on Thermoelectrics*, 51 (1987).
3. T.C. Harman, D.L. Spears, and M.J. Manfra, *J. Elec. Materials* **25**, 1121 (1996).
4. R. Venkatasubramanian, T. Colpitts, E. Watko, and J. Hutchby, *Proc. of XV International Conf. on Thermoelectrics*, IEEE Catalog No. 96TH8169, 454 (1996).
5. Special Issue on Thermoelectrics, *Naval Research Reviews*, Published by the Office of Naval Research, Ed. J. Pazik, USA, (1996).
6. G.D. Mahan and H.B. Lyon, *J. Appl. Phys.*, **76**, 1899 (1994).
7. R. Venkatasubramanian, *Proceedings of the 1st National Thermogenic Cooler Workshop*, Sept. 17, 1992, Fort Belvoir, VA; R. Venkatasubramanian, M.L. Timmons and J. A. Hutchby, *Proc. of the 12th Inter. Conf. on Thermoelectrics*, Yokohama, H. Mastubara Ed., 322 (1994).
8. V. Narayanamurthi, H. Stormer, M. Chin, A.C. Gossard and W. Wiegmann, *Phys. Rev. Lett.*, **43**, 2012 (1979).
9. S.-M. Lee, D.G. Cahill and R. Venkatasubramanian, "Thermal conductivity of Si-Ge superlattices", *Appl. Phys. Lett.*, in press (1997).
10. RTI US Patent Provisional Application No. 2025-117-20.
11. L.W. Whitlow and T. Hirano, *Proc. of the 12th International Conf. on Thermoelectrics*, Yokohama, H. Matsubara Ed., 39(1994).
12. A.G. Milnes and D.L. Feucht, *Heterojunctions and Metal-Semiconductor Junctions*, Academic Press, NY (1972).
13. D.G. Cahill, M. Katiyar, and J.R. Abelson, *Phys. Rev. B*, **50**, 6077 (1994).
14. R. Venkatasubramanian, T. Colpitts, E. Watko, M. Lamvik and N. El-Masry, *J. Crystal Growth* **170**, 817 (1997).
15. F.D. Rosi and E.G. Ramberg, "Evaluation and Properties of Materials for Thermoelectric Applications", in *Thermoelectricity*, Ed. Egli, John Wiley, NY (1960).
16. B.I. Boltaks and N.A. Fedorovich, in *Thermoelectric Properties of Semiconductors*, Ed. by V.A. Kutasson, Consultants Bureau, NY, 4 (1964).
17. G.A. Slack, Private Communication.
18. G.A. Slack, *Sol. State Phys.*, Ed. Seitz and Turnbull (Academic, NY, 1979), Vol. 34, p.13.
19. D.G. Cahill and R.O. Pohl, *Phys. Rev. B*, **35**, 4067 (1987).
20. R. Venkatasubramanian, Unpublished work in progress.
21. H. Scherrer and S. Scherrer, *Proc. of the 12th Inter. Conf. on Thermoelectrics*, Yokohama, H. Matsubara Ed., 90 (1994).
22. R.C. Miller, D.A. Kleinmann, and A.C. Gossard, *Phys. Rev. B*, **29**, 7085 (1984).

THERMAL CONDUCTIVITY AND HEAT TRANSFER IN SUPERLATTICES

G. CHEN, M. NEAGU, and T. BORCA-TASCIUC
Department of Mechanical Engineering and Materials Science
Duke University, Durham, NC27708, gchen@acpub.duke.edu

ABSTRACT

Understanding the thermal conductivity and heat transfer processes in superlattice structures is critical for the development of thermoelectric materials and devices based on quantum structures. This work reports progress on the modeling of thermal conductivity of superlattice structures. Results from the models established based on the Boltzmann transport equation could explain existing experimental results on the thermal conductivity of semiconductor superlattices in both in plane and cross-plane directions. These results suggest the possibility of engineering the interfaces to further reduce thermal conductivity of superlattice structures.

INTRODUCTION

Studies over the last few years have demonstrated that the thermoelectric power factor of quantum well structures can be increased significantly due to the quantum size effects [1]. To realize an overall increase in the thermoelectric figure of merit, thermal conductivity of these structures must be taken into consideration.

Few experimental studies have reported the thermal conductivity of semiconductor superlattices, including GaAs/AlAs [2-5], Si/Ge [6], and Bi₂Te₃/Sb₂Te₃ [7]. These experiments show that the thermal conductivity of these structures are generally lower than the values calculated from the thermal conductivity of their constituent single crystal materials according to the Fourier heat conduction theory. In several cases, the reported thermal conductivities of the superlattice structures are even smaller than those of their corresponding alloys [2,6,7]. Theoretically, Ren and Dow [8] modeled the thermal conductivity of ideal superlattice structures by combining Callaway's model [9] with a quantum mechanical treatment of the scattering rate. The predicted reduction in thermal conductivity from their model, however, is too low to explain the orders of magnitude reduction in the measured thermal conductivity of some superlattice structures. We have established models on the in-plane and cross-plane thermal conductivity of superlattices [10,11]. These models could explain the observed reduction on the thermal conductivity of GaAs/AlAs superlattice structures and suggest that diffuse interface scattering plays a significant role in the observed thermal conductivity reduction. A similar model for the in-plane thermal conductivity of superlattices has also been established independently by Mahan's group [12].

This work extends our previous work on thermal conductivity of superlattices to include the effects of specularly reflecting interfaces for transport in the cross-plane direction and presents modeling results on Si/Ge superlattices.

THEORETICAL MODELS AND ANALYSIS

Details of our models have been reported in two previous publications [10,11]. The models are based on solving the Boltzmann transport equation (BTE) for phonon propagation in periodic structures [13,14],

$$v_{xi} \frac{\partial I_{\omega i}}{\partial x_i} + v_{zi} \frac{\partial I_{\omega i}}{\partial z_i} = - \frac{I_{\omega i} - I_{\omega oi}}{\Lambda_{\omega i}} \quad (1)$$

where $I_{\omega i}$ is the spectral dependent phonon intensity of the i th layer and $I_{\omega oi}$ the equilibrium phonon intensity; the in-plane and cross-plane heat flow directions are denoted by x and z coordinates, respectively; v is the phonon group velocity; and $\Lambda_{\omega i}$ is the phonon mean free path at angular frequency ω in the i th layer.

In-Plane Direction

For heat conduction in the in-plane direction, BTE has been solved by assuming that the interfaces reflect and transmit phonons partially diffusely and partially specularly [10]. The effective thermal conductivity in this direction is given by

$$k_e = \sum_{i=1}^2 \chi_i \sum_p k_{pi} = \sum_{i=1}^2 \chi_i \sum_p \left\{ k_{bpi} - \frac{1}{2d_i} \int_0^{\omega_{mpi}} v_{pi} C_{\omega pi} \Lambda_{\omega pi}^2 [p G_{si}(\xi_1, \xi_2) + (1-p) G_{di}(\xi_1, \xi_2)] d\omega \right\} \quad (2)$$

where k_{bpi} is the contribution to the bulk thermal conductivity due to p-polarized (one longitudinal and two transverse) phonons in the i th layer; p is the specularity parameter that represents the fraction of specularly reflected and transmitted phonons; $C_{\omega pi}$ is the volumetric specific heat of phonons with frequency ω ; $\chi_i = d_i/(d_1+d_2)$ is the relative thickness of the i th layer; $\xi_i (=d_i/\Lambda_{\omega i})$ is the nondimensional thickness of the i th layer; and G_{di} and G_{si} are integrals given by

$$G_{si}(\xi_1, \xi_2) = \left[1 - \frac{\Lambda_{\omega 2} v_2}{\Lambda_{\omega 1} v_1} \right] \int_0^1 t_{12} \mu_1 (1 - \mu_1^2) (1 - e^{-\xi_1/\mu_1}) (1 - p e^{-\xi_2/\mu_2}) \frac{d\mu_1}{N} \quad (3)$$

$$G_{di}(\xi_1, \xi_2) = \int_0^1 \mu_1 (1 - \mu_1^2) (1 - e^{-\xi_1/\mu_1}) \left[1 - p \left(r_{21} - t_{12} \frac{\Lambda_{\omega 2} v_2}{\Lambda_{\omega 1} v_1} \right) e^{-\xi_2/\mu_2} \right] \frac{d\mu_1}{N} \quad (t_{12} \neq 0) \quad (4)$$

$$G_{di}(\xi_1) = \int_0^1 \frac{\mu_1 (1 - \mu_1^2) (1 - e^{-\xi_1/\mu_1}) (1 + p e^{-\xi_1/\mu_1})}{1 - p^2 e^{-2\xi_1/\mu_1}} d\mu_1 \quad (t_{12}=0) \quad (5)$$

$$N = 1 - p \left(r_{12} e^{-\xi_1/\mu_1} + r_{21} e^{-\xi_2/\mu_2} \right) + p^2 (r_{12} r_{21} - t_{12} t_{21}) e^{-\xi_1/\mu_1 - \xi_2/\mu_2} \quad (6)$$

and G_{s2} , G_{d2} can be obtained by subscript index permutation. In the above equations, r and t represent the specular reflectivity and transmissivity, respectively; and the order of their subscripts denotes the direction of phonon propagation. They are calculated according to the well established acoustic phonon mismatch theory for different incident angle [15]. The directional cosine is denoted by μ . Equation (5) is valid for the special cases when total internal reflection occurs and when the frequency of the incident phonon is larger than the maximum frequency of the corresponding polarization in the adjacent layer. This later treatment neglects the possibility of inelastic scattering at the interface.

To evaluate the thermal conductivity of real superlattice structures requires appropriate models on the bulk relaxation time of the constituting materials. We extended Holland's model [16] on bulk semiconductor materials. In this model, different relaxation time expressions are used for low and high frequency transverse phonons to account for the flattening of the phonon dispersion curve near the Brillouin zone boundary. The total bulk relaxation time for phonons of each polarization is

$$\tau^{-1} = \tau_i^{-1} + \tau_p^{-1} + \tau_d^{-1} \quad (7)$$

where τ_i^{-1} and τ_p^{-1} are inverse relaxation time due to impurity scattering and three-phonon scattering processes, respectively, and can be found in Holland's paper. The last term in Eq. (7) is the inverse relaxation time due to dislocation scattering. We use here a simplified expression for all forms of dislocations [17],

$$\tau_d^{-1} \approx \sigma \gamma^2 b^2 \omega \quad (8)$$

where σ is the dislocation density; γ is the Gruneisen number, and b the magnitude of the Burgers vector of the dislocations. When compared with experimental data, Eq. (8) is often found to be too small by a factor of 4 to 6, and for some materials systems such as LiF, it is a factor of 100 too small [17]. Our modeling results presented later are based on multiplying Eq. (8) by a factor of 6.

Another extension we made on Holland's model is to approximate the phonon dispersion relation by a sine function that is valid for one-dimensional lattice. This approximation is closer to real crystal phonon dispersion relations than the often used Debye model and impacts the modeling results in two ways: one through the phonon density of states and the other through the phonon group velocity.

Equation (2) can be simplified if the gray-medium assumption is introduced, i.e., the mean-free-path is frequency independent. Details of the simplified equations can be found in reference [10].

Cross-Plane Direction

For transport in the direction perpendicular to the superlattice plane, no analytical solution of the BTE could be obtained and numerical solutions are sought instead. To establish the appropriate boundary conditions for periodic structures, it is important to realize that although the phonon intensity is not periodic due to temperature variation along this direction, the deviation of phonon intensity from the equilibrium should be periodic [11]. This condition allows the solution of the BTE only within two adjacent layers. Numerical solution for diffuse interface scattering of phonons in GaAs/AlAs superlattices has been reported. Although partially specular and partially diffuse interface could be similar treated, our numerical approach has been troubled by the stability issue. This work reports modeling results for specular interfaces and compare them with results obtained for diffuse interfaces. Due to computational difficulty, the modeling has been based on the gray-medium assumption, i.e., the mean-free-path is considered as frequency independent.

Although it is difficult to obtain an analytical solution for the cross-plane thermal conductivity, a simple expression can be obtained to estimate the lower limit of the thermal conductivity of superlattices in this direction. As will be shown latter, when the period is very short and scattering at the interfaces is totally diffuse, the temperature drop inside each layer is very small compared to the temperature drop at the interface. If it is assumed that all the temperature drop occurs at the interface, the effective thermal conductivity in the cross-plane direction is found to be

$$k = \frac{1}{2} \frac{C_1 v_1 t_{12} (d_1 + d_2)}{(1 + r_{12})(1 + r_{21}) - t_{12} t_{21}} \quad (9)$$

where C is the volumetric specific heat and v is the phonon group velocity. The reflectivity and transmissivity at the interface will be calculated from an expression [11] obtained by extending the diffuse phonon mismatch model [18] for thermal boundary resistance,

$$t_{12} = \frac{C_2 v_2}{C_1 v_1 + C_2 v_2} \quad r_{12} = 1 - t_{12} \quad (10)$$

and t_{21} , r_{21} can be similarly obtained by permuting subscript indices.

RESULTS AND DISCUSSIONS

Results from the above described models will be compared to available experimental data on GaAs/AlAs and Si/Ge superlattices.

Parallel Direction

Figure 1(a) shows a comparison of the calculated thermal conductivity of GaAs/AlAs superlattice structures as a function of the layer thickness with reported experimental results at

room temperature for different values of the interface scattering parameter p . Both the experiments of Yao [2] and Yu et al. [4] employed GaAs/AlAs superlattices of equal thickness for all the layers. This figure demonstrates that if the interfaces scatter phonons specularly, reduction in the thermal conductivity of the superlattices is very small. With slight increase in diffuse phonon scattering, however, thermal conductivity can be greatly reduced. There are several possible mechanisms for diffuse phonon scattering at the interfaces. Those include the atomic scale mixing and terrace formation [19], and inelastic scattering caused by the difference in the force constants between the interface atoms. At this stage, it is not clear which one or several of those mechanisms are responsible for the diffuse interface scattering.

Figure 1(a) indicates that thermal conductivity of thin period superlattices may be made smaller than its corresponding alloys, although this prediction has not been proven by experiment. The explanation lies in that scattering by mass difference fluctuation in alloys is proportional to the fourth power of frequency so that long wavelength phonons are not effectively scattered. The current model assumes that phonons are either specularly or diffusely scattered, independent of their wavelength. In the diffuse interface scattering limit, phonons of all wavelengths can be effectively scattered within this model, thus reducing the superlattice thermal conductivity below alloy values. Clearly, more work needs to be done to understand the interface scattering mechanisms. To complete the discussions here, we need to answer the following two questions that seem to contradict the above prediction: (1) do superlattices made of alloys, such as $\text{Al}_{0.25}\text{Ga}_{0.75}\text{As}/\text{Al}_{0.75}\text{Ga}_{0.25}\text{As}$, have larger thermal conductivity than GaAs/AlAs superlattices of equal periodicity? and (2) what happens when the superlattice period become so short such that the whole structure is already an alloy? To answer the first question, it is realized that mass difference scattering in alloys only reduces the mean free path of high frequency phonons. By using superlattice structures, the low frequency phonons are further scattered at interfaces and the thermal conductivities of alloy superlattices could be made even smaller than those of their corresponding bulk alloys as well as smaller than those of comparable superlattices made of pure crystalline layers. An answer of the second question should trace back to the wave characteristics of phonons. When the layer becomes very thin, tunneling of phonons between layers will increase the lattice thermal conductivity. In the limit that the superlattices become effectively alloys, phonon waves will not be effectively reflected and the model will no longer be valid.

There are no reported data on the thermal conductivity of Si/Ge superlattices in the in-plane direction. Figure 1(b) shows results obtained from our model for Si/Ge superlattice systems. Two different sets of curves are presented: those including the effect of dislocations and those without dislocation scattering. In using Eq. (8), the dislocation density is taken as 10^{12} cm^{-2} [20], which represents an upper limit of high density threading dislocations. It should be pointed out that the effect of strain on phonon relaxation time has not been included in the model. This figure again shows that specular interfaces do not cause much change in thermal conductivity. When the dislocation density is high, however, the superlattice thermal conductivities are reduced by orders of magnitude due to dislocation scattering and become independent of layer thickness. It is

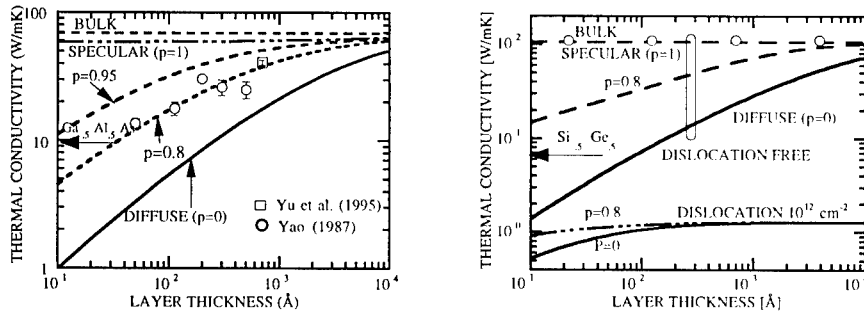


Figure 1 Room temperature thermal conductivity of superlattices in the in-plane direction as a function of the period thickness (equal thickness assumed for each layer) (a) GaAs/AlAs superlattices and (b) Si/Ge superlattices. Parameter p represents the fraction of specularly scattered phonons.

interesting to note that a recent measurement on the thermal conductivity of a 1550 Å free-standing single crystalline Si film observed a thermal conductivity ~ 2.2 W/mK [21].

Cross-Plane Direction

For heat transfer in the cross-plane direction, all calculations are performed by assuming that the phonon mean-free-path is frequency independent (gray medium assumption). Figure 2 shows the calculated effective temperature distribution inside Si/Ge superlattice structures for the case when the interface is assumed to be diffuse. This figure shows that most temperature drop occurs at the interface when the period is very short, and thus justifies the assumptions made for Eq. (9). It should be pointed out that phonons inside each layer are at highly nonequilibrium states and the temperature as used here loses its conventional meaning as an equilibrium concept [11].

Figure 3 compares the calculated thermal conductivity of Si/Ge superlattice with some recent measurements by Lee et al. [6]. The model based on diffuse interface scattering could explain the orders of magnitude reduction in thermal conductivity observed in these systems. Above certain thickness, the experimental data drops and approaches a constant. This is attributed to the dislocation formation [6]. Although a gray medium model based on the bulk medium mean free path cannot capture such a phenomenon, the modeling results for thermal conductivity in the in-plane direction may explain the observed flattening after the critical thickness. Figure 1(b) suggests that above the critical thickness, dislocations may become the dominant scattering sources and interface scattering is no longer important. Also shown in Fig. 3 is the approximate solution given by Eq. (9) and it agrees well with BTE solution in the very thin layer limit. In this limit, the mean free path of the bulk medium does not influence the superlattice thermal conductivity in the cross-plane direction. This is different from the in-plane direction, for which the limit solution of very thin films still depends on the phonon mean free path [14].

Figure 3 also gives the solution of the BTE when the interfaces scatter phonons specularly. In this case, the predicted reduction in thermal conductivity is not as strong as the prediction obtained by assuming diffuse interface scattering. It should be pointed out that solutions of the BTE for the specular interface scattering case strongly depend on the mismatches in acoustic impedance and phonon velocity between two layers. These mismatches are larger in SiGe superlattices than in GaAs/AlAs superlattices. Correspondingly, the effectively thermal conductivity calculated from the specular interface assumption for a 100 Å period GaAs/AlAs superlattice is only 55.3 W/mK, a very small reduction compared to the effective bulk value of 58.7 W/mK for such a structure.

In comparing with results obtained for in-plane direction, the following question must be answered: why the in-plane thermal conductivity can be explained by assuming partially diffuse and partially specular interfaces while a total diffuse scattering interface assumption seems to be

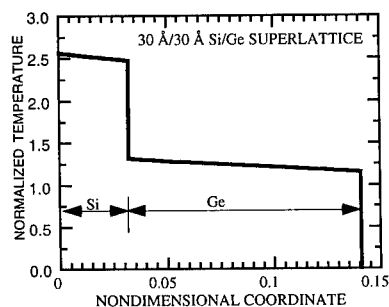


Figure 2 Nondimensionalized temperature distribution ($=C_2 v_2 T/4q$, where q is the heat flux) in one period of a Si/Ge superlattice (coordinate normalized to the average phonon mean free path within each layer). This figure shows that majority of temperature drop occurs at interfaces.

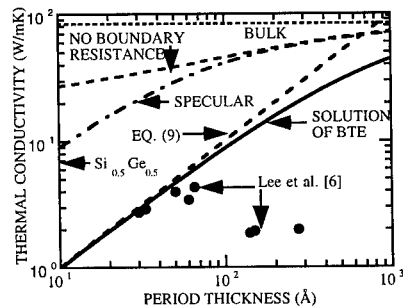


Figure 3 Cross-plane thermal conductivity of Si/Ge superlattices. This figure shows bulk value calculated from Fourier heat conduction theory, exact solutions of BTE for diffuse and specular interfaces, limit solution from Eq. (9), and results obtained by neglecting thermal boundary resistance for diffuse interfaces.

able to explain cross-plane thermal conductivity? The answer to this question lies in that the cross-plane direction modeling has been based on the gray medium assumption, which does not include the phonon confinement effect. With this factor taken into consideration, we expect that phonon scattering at interfaces will be in between the diffuse and specular limits.

CONCLUDING REMARKS

Modeling results presented in this work show that available experimental data on the thermal conductivity of superlattices could be explained based on the Boltzmann transport equation. For in-plane direction, the observed reduction in the thermal conductivity of superlattices is caused by diffuse interface scattering while for the cross-plane direction, both diffuse and specular interface scattering processes contribute to the thermal conductivity reduction. There are several issues that must be answered before a final understanding of the thermal conductivity can be reached. These issues are: what causes the diffuse phonon scattering at the interfaces and what are the effect of phonon wave interference and tunneling on the thermal conductivity of superlattices.

ACKNOWLEDGMENTS

G.C. would like to thank Dr. D. Cahill for sending him a preprint of their work on Si/Ge superlattices and acknowledges helpful discussions with Drs. K.L. Wang and M.S. Dresselhaus on thermoelectricity, and with Dr. T.-Y. Tan on dislocations. This work is supported by an National Science Foundation Young Investigator Award to G. C.

REFERENCES

- [1] L.D. Hicks, and M.S. Dresselhaus, *Phys. Rev. B*, **47**, p. 12727-12731 (1993).
- [2] T. Yao, *Appl. Phys. Lett.*, **51**, p. 1798-1800 (1987).
- [3] G. Chen, C.L. Tien, X. Wu, and J.S. Smith, *J. Heat Transf.* **116**, p. 325-331 (1994).
- [4] X.Y. Yu, G. Chen, A. Verma, and J.S. Smith, *Appl. Phys. Lett.*, **67**, p. 3553-3556 (1995).
- [5] W.S. Capinski and H.J. Maris, *Physica B*, **219&220**, p. 699-701 (1996).
- [6] S.-M. Lee, D. Cahill, and R. Venkatasubramanian, private communication (1997).
- [7] R. Venkatasubramanian, *Naval Research News*, **XLVIII**, 31-43 (1996).
- [8] S.Y. Ren and J.D. Dow, *Phys. Rev. B*, **25**, p. 3750-3755 (1982).
- [9] J. Callaway, *Phys. Rev.*, **113**, p. 1046-1051 (1959).
- [10] G. Chen, in *ASME Proc. 31st National Heat Transf. Conf.*, **HTD-323**, p. 121-129 (1996), more details to appear in *J. Heat Transf.*
- [11] G. Chen, in *Micro-Electro-Mechanical-Systems (Proc. ASME Int. Mech. Eng. Congress)*, **DSC-59**, p. 13-24 (1996).
- [12] P. Hyldgaard and G.D. Mahan, in *Thermal Conductivity 23*, edited by K.E. Wilkes, R.B. Dinwiddie, and R.S. Graves Technomic Publishing Co., Inc., 1996, p. 172-182.
- [13] A. Majumdar, *J. Heat Transf.*, **115**, p. 7-16 (1993).
- [14] G. Chen and C.L. Tien, *J. Thermophys. Heat Transf.*, **7**, p. 311-318 (1993).
- [15] W.A. Little, *Can. J. Phys.*, **37**, p. 334-349 (1959).
- [16] M.G. Holland, *Phys. Rev.*, **A**, **134**, p. 471-480 (1964).
- [17] P. Curruthers, *Rev. Mod. Phys.*, **33**, p. 92-138 (1961).
- [18] E.T. Swartz and R.O. Pohl, *Rev. Mod. Phys.*, **61**, p. 605-668 (1989).
- [19] M.H. Bode and A. Ourmazd, *J. Vac. Sci. Techn.*, **B**, **10**, p. 1787-1792 (1992).
- [20] F.K. LeGoues, B.S. Meyerson, J.F. Morar, and P.D. Kirchner, *J. Appl. Phys.*, **71**, p. 4230-4243 (1992).
- [21] X.Y. Zheng, S.Z. Li, M. Chen, and K.L. Wang, in *Micro-Electro-Mechanical-Systems (Proc. ASME Int. Mech. Eng. Congress)*, **DSC-59**, p. 93-98 (1996).

STUDIES OF BULK MATERIALS FOR THERMOELECTRIC COOLING

Jeff W. Sharp, George S. Nolas and Edward H. Volckmann
Marlow Industries, Inc., 10451 Vista Park Rd., Dallas, TX 75238-1645

ABSTRACT

We discuss ongoing work in three areas of thermoelectric materials research: 1) broad band semiconductors featuring anion networks, 2) filled skutterudites, and 3) polycrystalline Bi-Sb alloys. Key results include: a preliminary evaluation of a previously untested ternary semiconductor, KSnSb ; the first reported data in which Sn is used as a charge compensator in filled antimonide skutterudites; the finding that Sn doping does not effect polycrystalline $\text{Bi}_{1-x}\text{Sb}_x$ as it does single crystal samples.

INTRODUCTION

This paper reports recent developments in the three main thrusts of our experimental research. Section I relates the first testing of two new candidate thermoelectric materials derived from a systematic search: BaSb_3 and KSnSb . Section II describes our exploration of filled skutterudites, a first attempt at creating a "phonon-glass, electron-crystal." Section III conveys the current state of our efforts to approach single crystal performance in polycrystalline $\text{Bi}_{1-x}\text{Sb}_x$.

I. POLYANIONS

In another paper in these proceedings, we describe a selection process used to define new thermoelectric candidates. In this section, we report the initial exploration of two compounds thus selected. Both are anisotropic materials whose structures consist of extended anion networks (polyanions) that accommodate electrons contributed by alkali cations. Our initial experiments have been aimed at learning if the compounds have a low lattice thermal conductivity, $\lambda_{\text{Lattice}} \leq 3 \text{ W m}^{-1} \text{ K}^{-1}$, and an adequate band gap, $E_g \geq 0.1 \text{ eV}$.

For transport property measurements, the samples were electroplated with nickel if they would not solder directly. Resistance measurements were made using either true 4-point measurements or a pseudo-4 wire technique in which the voltage difference measured is that of copper caps attached to the sample. Probing of the voltage across the sample/copper cap interface showed that the contact resistance was negligible for high resistivity (ρ) samples. The Seebeck coefficient, S , and thermal conductivity, λ , were measured by direct methods. A nickel-coated alumina chip was used to create 3 to 5 °C temperature differentials across the sample and two thermal conductivity standards located above and below the sample in a column to calibrate heat flow. The standards were calibrated by using thermoelectric materials as the sample. Relative to Z-meter data, errors are less than $\pm 3\%$ and $\pm 10\%$ for S and λ respectively. The properties can be measured from 77 to 400 K.

BaSb₃

The crystal structure of BaSb₃ [1] is similar to that of elemental Sb (see **Table I** and **Fig. 1**). One-third of the Sb has three Sb neighbors, and the remainder has two Sb neighbors. Bond angles in the Sb sublattice range from 97° to 113°. Barium is irregularly coordinated and has 10 Sb neighbors. Also, each Ba atom has one Ba neighbor at 4.30 Å, about the same as in the element, but this is not considered a bond since Ba will be reduced in size by electron transfer to the Sb network. The covalent Sb network, high average mass of the constituents, and highly coordinated Ba make BaSb₃ one of only a handful of unexplored binaries that, in our view, are attractive thermoelectric candidates.

Table I. Lattice description and interatomic distances for BaSb₃.

Lattice	Interatomic Distances (Å)	
Monoclinic a = 10.807 Å b = 8.519 Å c = 6.471 Å β = 112.66° C2/m space group 16 atoms per cell	Sb1-Sb1	2.844 (x1)
	Sb1-Sb2	2.849 (x2)
	Sb1-Ba	3.589 (x1)
		4.050 (x1)
	Sb2-Sb2	2.844 (x2)
	Sb2-Ba	3.485 (x1)
		3.578 (x1)
		3.710 (x1)
		3.794 (x1)

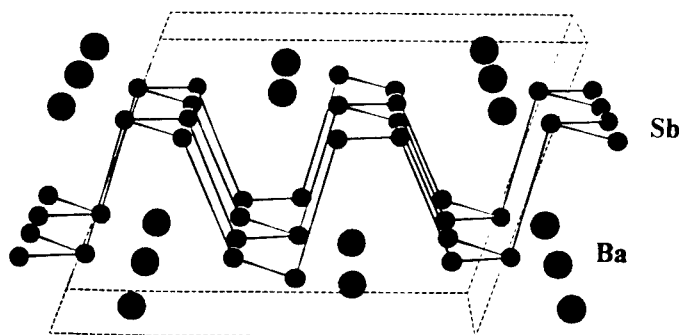


Figure 1. Crystal structure of BaSb₃, viewed from slightly off the b axis. The dominant structural feature is the two dimensional Sb net, which is similar to that in elemental Sb.

The Ba-Sb phase diagram has not been mapped, but the Sr-Sb system may be a useful guide since compounds with the same stoichiometries occur in the two systems. The Sr-Sb compounds

are SrSb_3 , SrSb , Sr_3Sb_2 and Sr_2Sb with melting points of 680 °C, 935 °C, 880 °C and 840 °C [2]. All except SrSb melt incongruently.

Synthesis of phase pure BaSb_3 has been prevented so far by violent reaction between the constituents and reaction with/adhesion to vessels. In this case, the problem of violent reactions is made acute by the high and comparable melting points of Sb (631 °C) and Ba (729 °C). Solid Sb and Ba in contact with one another react quite slowly until a temperature of approximately 600 °C is reached, at which point the liberated heat rapidly liquefies and agitates both constituents. The frozen Ba-Sb melts adhere strongly to graphite, alumina, tungsten and quartz. Graphite (or graphite foil) may be an especially poor choice of container material since Ba intercalates graphite. A third problem with this particular system is that the other known compounds, Ba_2Sb , Ba_3Sb_3 and Ba_5Sb_4 , [3] probably have melting points in the vicinity of 900 °C, per the Sr-Sb phase. High temperatures are required to eliminate these phases.

To allow the reaction to begin at a lower temperature and to occur more gradually, we replaced one sixth of the Sb with Bi. In terms of amount of second phase present, our best sample to date was obtained by heating $\text{BaSb}_{2.5}\text{Bi}_{0.5}$ from 450 to 600 °C over a few hours, holding at 800 °C for 15 hours, quickly cooling to room temperature, then annealing at 450 °C for 30 hours. During the initial ramp to 600 °C, the elements react and spray liquid onto the walls of the quartz tube. (Since the reaction tube tends to crack while cooling to room temperature, it is advantageous to place it within a second tube.) A micrograph and x-ray data for this sample are shown in **Figs. 2 and 3**. A small amount of a second phase is apparent in **Fig. 2**. The x-ray data are consistent with identifying this phase as Sb, though many Sb peaks overlap with those of BaSb_3 , so a definite determination by x-rays may not be feasible. The diffraction peaks of our sample are shifted toward larger cell dimensions relative to BaSb_3 , as is expected for incorporation of Bi. Also, there is no evidence of BaBi_3 in the x-ray pattern. Differential thermal analysis indicates that the main phase in this sample decomposes into solid and liquid at ~ 540 °C, and becomes completely molten at ~ 630 °C. If it is true that only the desired phase and Sb are present in the end product, then it may be possible to synthesize BaSb_3 of adequate quality by the procedure outlined above if a small excess of Ba is used. The room temperature ρ of the sample shown in **Fig. 2** is 0.35 m Ω -cm, and λ is 3.5 W m⁻¹ K⁻¹. S at room temperature is +17 $\mu\text{V K}^{-1}$, and is proportional to the temperature down to at least 200 K, indicating metallic behavior. If we assume full degeneracy to subtract the electronic thermal conductivity, then $\lambda_{\text{Lattice}} = 1.3 \text{ W m}^{-1} \text{ K}^{-1}$. This value is reasonable, considering that we have made an alloy, but the cracks apparent in **Fig. 2** may contribute to the low λ measured.

KSnSb

As with BaSb_3 , the crystal structure of KSnSb [4], shown in **Fig. 4**, is easily understood with reference to elemental Sb. Sn and Sb are believed to be well ordered on opposite sides of the two-layer leaves that make up the covalent anion sublattice. The bond angle in the anion net is 97°. K lies between these leaves, occupying a layer across which there are no covalent bonds. The main interatomic distances are given in **Table II**. Calculations suggest that KSnSb is a small band gap, multivalley semiconductor [5].



Figure 2. Micrograph (300X as seen here) of a sample with starting composition $\text{BaSb}_{2.3}\text{Bi}_{0.5}$. The minority phase, light patches, is believed to be mainly Sb, perhaps alloyed with Bi. X-ray data for this sample is presented in **Fig. 3**.

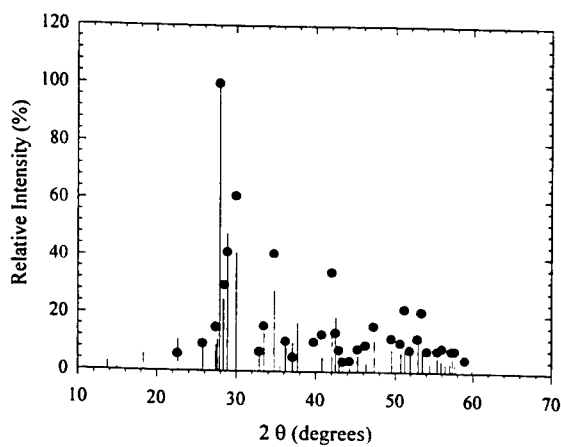


Figure 3. X-ray diffraction peaks of the sample shown in **Fig. 2**. The lines are literature values for BaSb_3 (JCPDS file, data from ref. 1), and solid circles represent our data. A LaB_6 standard was used to correct the peak positions. Our data is shifted toward larger lattice constants (lower 2θ), presumably due to incorporation of Bi. The only definite impurity phase peak is near $2\theta = 40^\circ$, and is close to a peak for Sb.

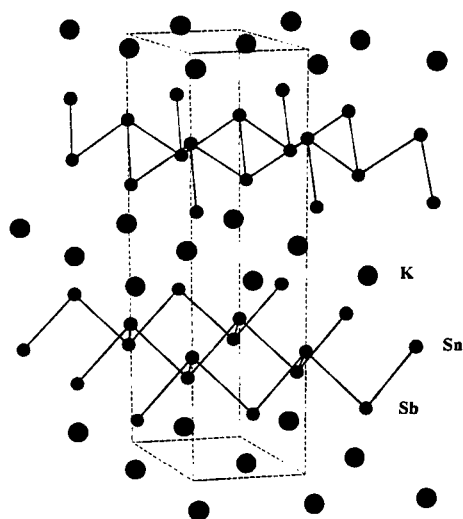


Figure 4. Hexagonal crystal structure of KSnSb, emphasizing the covalent, two dimensional Sn-Sb leaves. K contributes an electron to fill the valence band formed predominantly from Sn and Sb *p* orbitals.

Table II. Lattice description and interatomic distances for KSnSb.

Lattice	Interatomic Distances	
Hexagonal	Sb-Sn	2.925 (x3)
a = 4.359	Sb-K	3.505 (x3)
c = 13.150	Sn-K	3.650 (x3)
P6 ₃ mc space group		
6 atoms per cell		

To make KSnSb, we followed Lii and Haushalter [4] by first reacting K (99.95%) and Sn (99.999%) (K:Sn = 1.02:1.00) at 250 to 300 °C for 1 hour in a N₂ atmosphere. After synthesis of nominally 20 g of KSn in a glazed ceramic cup, the mass of the cup was unchanged to within 1 mg, so reaction between K and the vessel was negligible. The KSn was subsequently mixed stoichiometrically with Sb (99.9999%) using a Sn:Sb basis.

In one scenario, 5 grams of the mixed powders were cold pressed at 60,000 psi using tool steel die and punches. The compacts were then sintered in evacuated and argon-backfilled quartz tubes. Tungsten foil was used to avoid contact between the sample and tube. As these compacts are heated, a significant amount of melting occurs at approximately 500 °C. Since the melting points of KSn and Sb are 576 °C and 631 °C respectively, it is apparent that these constituents begin to combine quickly, and via one or more lower melting point intermediates.

Alternatively, the KSn and Sb powders were fused (650 °C for 10 minutes) in an alumina crucible lined with tungsten foil, cooled to 510 °C over approximately 1 hour, and held at that temperature for 13 hours. This procedure produced a more dense sample (83% of the x-ray density of KSnSb) suitable for transport property measurements. The measured properties are presented in Fig. 5.

Both S and λ data show the beginning of a transition from extrinsic to intrinsic behavior in the 250 to 300 K range. S peaks at 300 K and begins to decrease as minority carriers, holes in this case, are thermally excited. The usual T^{-1} fall of λ , which is entirely λ_{Lattice} at the lower temperatures in Fig. 5, is halted by the rise of the bipolar electronic contribution. The ρ data are not as easily interpreted.

It is noteworthy that an extremum of S was found in the measured temperature range, since the band gap can be estimated from these data ($E_g \approx 2eS_{\text{peak}}T_{\text{peak}}$ where e is the electron charge) [6]. The value obtained is 0.33 or 0.23 eV, depending on whether one assumes lattice scattering or point defect scattering respectively. The latter is probably more consistent with the fact that ρ rises in the extrinsic range on the low T side of the Seebeck peak. Since x-ray data on this sample show broad humps with a few weak peaks, the presence of point defect scattering is understandable. The λ data clearly show the sample is not amorphous, leading us to deduce that it has very fine crystallinity. It is expected that a sample with a good x-ray pattern will also exhibit a much higher carrier mobility, leading to a higher S^2/ρ ratio, which is what we are now seeking to show.

The results so far encourage us to continue investigations of polyanions, many of which are Zintl phases (i.e., contain alkali metal or alkali earth cations). It is worth noting, though, that powdered KSnSb becomes gummy in air, and may ignite if ground in air (so far, this is a sporadic event and may be associated with a minority phase). Also, an epoxy used for metallography reacted with a solid piece of the KSnSb sample. No such problems were encountered with BaSb₃, which is stable in water for hours, even as a coarse powder. Apparently we will encounter a range of chemical stability as we explore Zintl phases.

II. FILLED SKUTTERUDITES

The pursuit of a “phonon-glass, electron crystal” for thermoelectric applications has begun with exploration of filled skutterudites. The logic behind this approach is that such materials would possess electronic properties normally associated with good semiconductor single crystals and thermal properties normally associated with amorphous materials. In the skutterudite systems, for example, with electronic properties as good as those measured on CoSb₃ [7] crystals and $\lambda_{\text{Lattice}} = \lambda_{\text{min}} = 0.3 \text{ W m}^{-1} \text{ K}^{-1}$ (calculated for CoSb₃) would have $ZT \sim 2$ at room temperature.

The binary skutterudites have the cubic $Im\bar{3}$ (T_h^5) structure and are of the form AB_3 where A represents a metal atom and B represents a pnictogen atom ($A=\text{Co, Rh, and Ir, and } B=\text{P, As, and Sb}$ for the nine binary semiconducting compounds in this group). There are eight formula units per cubic unit cell. Some of the basic conditions for high Z , as described by Slack, are met in these materials: large unit cell, heavy constituent atom masses, low electronegativity differences between the constituent atoms, and large carrier mobilities [8]. In addition, there are two voids per unit cell in the structure. The chemical formula for IrSb₃, for example, can be written as $\text{Ir}_8\Box_2\text{Sb}_{24}$ illustrating the two voids per unit cell. Skutterudites form covalent structures with low coordination numbers for the constituent atoms and so can incorporate atoms in the voids. Many

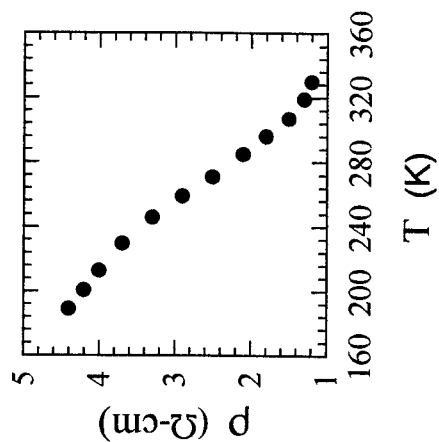
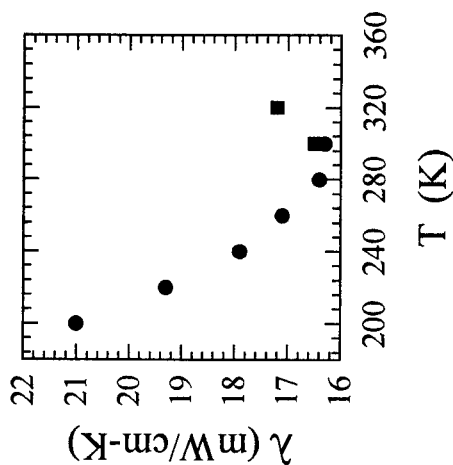
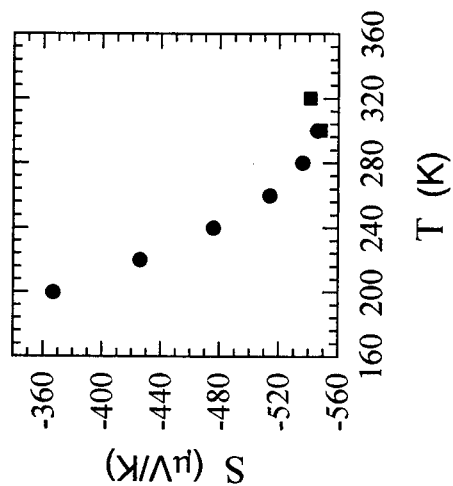


Figure 5. Thermoelectric properties of a KSnSb sample. The S and λ data represented by squares were taken after warming the sample back to room temperature. X-ray data for this sample show mainly broad humps in place of the KSnSb peaks.

different atoms have been introduced into the voids of the skutterudites, including alkali earth, lanthanide, and actinide ions.

The interest in this system for thermoelectric applications is due to the marked reduction of $\lambda_{lattice}$ of filled skutterudites as compared to the unfilled, binary skutterudites. The void-fillers “rattle” in their voids and subsequently effect phonon propagation through the lattice. This was first postulated by Slack and Tsoukala [9]. Large x-ray thermal parameters have been observed in filled skutterudites [10]. In both lanthanide-, or rare earth (RE), and alkali earth-filled skutterudites, the thermal parameter of the void-filler increases as the ratio of its radius to the radius of the void decreases. This seems to indicate that these filler ions “rattle” in the voids more easily when they have more room to do so. Nolas *et al.* [11] showed the reduction in $\lambda_{lattice}$ follows a trend similar to that of the thermal parameter for RE-filled skutterudites. The “rattling” of these ions interacts with the lattice phonons, thereby reducing their mean free paths substantially below that of the unfilled skutterudites.

The fact that filled-skutterudites possess low $\lambda_{lattice}$ values has been established. The aim now is in a more complete understanding of the phonon scattering mechanism(s) involved. Further degrading $\lambda_{lattice}$ towards that of the minimum thermal conductivity, λ_{min} , [12] is a key goal. Indeed, the potential of this material system for thermoelectric cooling applications lies in obtaining low, glass-like $\lambda_{lattice}$ values while maintaining good electronic properties. To this end more work is needed in finding the best void-filler. One candidate is Bi, with a large mass and small electronegativity difference with Sb. In addition, heavier/smaller RE ions require investigation. It seems plausible that the best candidates for void-filler would be neutral atoms or molecules. In this way scattering of phonons would result, while minimal scattering of charge carriers is realized.

If ionic void-fillers are used, more work is needed in minimizing the degradation in the electronic properties, perhaps by finding the optimum charge compensator for the void-filler ions. Up to this point, published data on only Ge and Fe as charge compensators for RE-filled-skutterudites has been investigated. We have begun work on Sn for charge compensation. A comparison of Hall data of these samples with previously published results is shown in **Table III**. As seen in **Table III**, the Sn-compensated samples have a carrier concentration, as predicted [13]. As outlined in Tritt *et al.* [14], the goal is to make filled skutterudites in which the valence electron count is exactly 72.0 for the formula units given in **Table III**. This is the proper electron count to achieve semiconductivity, as explained in Dudkin [15] and King [16]. Whether the carrier concentration in the samples shown in **Table III** is caused by a chemical imbalance (departure from the desired 1:3 RE to compensator ratio), or whether it is caused by a decrease in the band gap is not yet clear. It should be noted that all hole concentrations given in **Table III** are too high for a room temperature thermoelectric. However, decreasing the Fe to Co ratio from 3:1 has resulted in improved electronic properties [17, 18]. This has not yet been investigated for pnictogen-compensated filled skutterudites. It should be noted that it is also not clear what valence, and therefore what effect, Fe has in this system. Fe is known to possess different valences, sometimes non-integral “mixed” valences, depending on its chemical environment. Ru and Os compensation should also be investigated, however, the valence states of these in the skutterudite system is also not clear.

Table III. Room temperature hole concentration for rare-earth-filled skutterudites compensated with Ge, Fe, and Sn.

Sample	Hole concentration (10^{19} cm^{-3})	Reference
CeFe ₃ CoSb ₁₂	440	17, 18
Ir ₄ LaGe ₃ Sb ₉	88	11
LaFe ₃ CoSb ₁₂	36.5	---
Ir ₄ LaSn ₃ Sb ₉	33.5	---
Co ₄ LaSn ₃ Sb ₉	11.2	---

Experimental and theoretical results from different laboratories have shown that the skutterudite system has potential for thermoelectric applications. The good mechanical properties, the low thermal expansion, and the cubic crystal structure are all benefits of this system. The key, however, is to substantially reduce λ in this structure while minimizing the degradation in the electronic properties. Although high Z values have been reported at high temperatures, much work is still needed in order to shift these values down to the room temperature range. In addition, if this system is to be seriously considered for power generation applications, an investigation of the thermal stability of its Z values, and even its stoichiometry, is imperative.

III. POLYCRYSTALLINE Bi_{1-x}Sb_x

The polyanions discussed in Section I have anisotropic crystal structures, which is partly why they were selected for study. Maximum Z for these materials will be obtained only if the electric current is passed along the preferred axis (or axes). On the other hand, as crystals, these compounds may cleave easily in certain directions and compacted polycrystalline forms would be favored for greater durability if such material were put to use.

Bi_{1-x}Sb_x alloys provide a classic example of this problem. Parallel to the trigonal planes, Z is only 60% of the value perpendicular to the planes. However, the crystals cleave very easily along the trigonal planes making fabrication difficult and utilization risky. Polycrystalline Bi_{1-x}Sb_x that does not cleave can be made by powder metallurgy techniques. But to gain durability Z is sacrificed such that the value obtained for the polycrystalline form is only marginally better than for single crystals parallel to the trigonal planes. Acceptor doping has been reported to significantly increase Z of single crystals [19, 20]. This approach was investigated for polycrystalline Bi₈₈Sb₁₂ to see if durable material, with a higher Z , could be made.

The Bi₈₈Sb₁₂ samples were prepared by melting the desired quantities of high purity Bi, Sb and the acceptor impurity Sn in sealed quartz ampoules. The tubes were agitated to promote complete mixing of the melt, followed by a water quench to minimize segregation during solidification. 99.9999 % Bi and Sb were used after it was found that the impurities in 99.999 % raw materials produced significant variability in undoped samples. Powders were prepared by crushing the ingots via mortar and pestle so that the particles would pass through a screen with

250 μm openings. The powder was initially consolidated by cold pressing followed by a warm loading step to promote good interparticle contact. S , ρ , and λ were determined using a modified Harman method [21]. It should be noted that this technique becomes inaccurate for samples with low ZT but such samples are generally of less interest. Prior to testing from 80 to 300 K, low ohmic Ni contacts were electroplated on the ends of samples, which had typical dimensions of 3.8 mm \times 3.8 mm \times 4.8 mm.

The lower doping levels investigated, 50, 100, 300 and 600 ppm Sn, cause S to become less negative than the undoped benchmark at the lower temperatures and more negative at the higher temperatures. For these acceptor concentrations, ρ increases with concentration over the whole temperature range studied. The higher doping levels studied, 1000 and 1500 ppm Sn, produce $\text{Bi}_{88}\text{Sb}_{12}$ with p-type conductivity at the lower temperatures. Inversion from p-type to n-type conductivity occurs in these samples at intermediate temperatures because of the increasing dominance of thermally excited electrons. The resistivities of the samples with 1000 and 1500 ppm Sn exhibit maxima at the temperatures of inversion. **Figure 6** shows Z as a function of temperature for the different Sn concentrations.

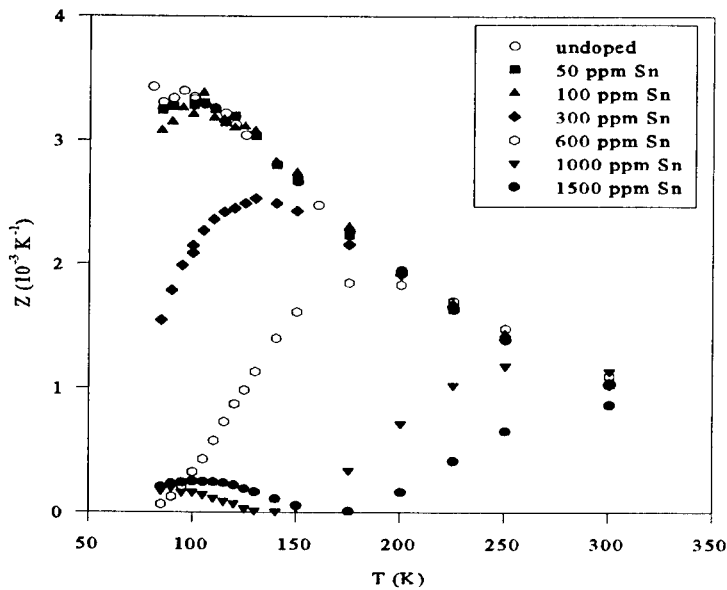


Figure 6. Temperature dependence of Z for Sn doped polycrystalline $\text{Bi}_{88}\text{Sb}_{12}$. The low temperature values of Z for the samples with 1000 and 1500 ppm Sn are for p-type material. For these samples, Z passes through 0 as the material changes to n-type with rising temperature.

The general effect of adding the acceptor impurity Sn to polycrystalline $\text{Bi}_{88}\text{Sb}_{12}$ is to shift the Fermi energy towards the valence bands. The magnitude of the partial S of the electrons increases while the partial S of the light holes decreases with increasing Sn concentrations. If the mobilities were not adversely affected by the Sn additions, then Z would be enhanced by such shifts in the partial S. However the mobility, both of the electrons and the holes, sharply decreases with increasing Sn concentration. As a result, no improvements of Z were observed with increasing Sn concentration. It is interesting that Z of n-type $\text{Bi}_{1-x}\text{Sb}_x$ single crystals can be significantly improved with doping, as reported in the literature, but that no improvement is observed in the polycrystalline material. It may be that while acceptor additions cause marked reductions in the carrier mobilities in the polycrystalline samples, this is avoided along the trigonal axis of single crystals. A more promising approach to improving Z of polycrystalline $\text{Bi}_{1-x}\text{Sb}_x$ would be to manipulate the grains so that the trigonal axes of the grains are aligned. This approach is currently under investigation.

To achieve both near maximum performance and durability in anisotropic thermoelectrics, well oriented polycrystalline forms are needed. For polycrystalline $\text{Bi}_{1-x}\text{Sb}_x$ this means that the synthesis method must produce a strong degree of texture so that the trigonal axes of the grains are nearly parallel.

ACKNOWLEDGEMENTS

We thank Prof. Julian Goldsmid for his contributions, particularly in regard to interpretation of polycrystalline Bi-Sb data. We also extend our thanks to NASA/DARPA for their support (contract NAS9-19358).

REFERENCES

1. K. Deller and B. Eisenmann, *Z. Naturfor. B* **33**, p. 676 (1978).
2. Moffatt's Handbook of Binary Phase Diagrams, edited by J. H. Westbrook (Genium, Schenectady, 1995).
3. Pearson's Handbook of Crystallographic Data for Intermetallic Phases, P. Villars and L.D. Calvert (Amer. Soc. Metals, Metals Park, OH, 1985), pp. 1413-1414.
4. K. H. Lii and R. C. Haushalter, *J. Sol. St. Chem.* **67**, p. 374 (1987).
5. P. C. Schmidt, D. Stahl, B. Eisenmann, R. Kniep, V. Eyert and J. Kübler, *J. Sol. St. Chem.* **97**, p. 93 (1992).
6. H. J. Goldsmid and J. W. Sharp, in preparation.
7. T. Caillat, A. Borshchevsky and J.-P. Fleurial, *J. Appl. Phys.* **80**, p. 4442 (1996).
8. G.A. Slack, in CRC Handbook of Thermoelectrics, edited by D.M. Rowe (CRC Press, Boca Raton, FL, 1995), p. 407.

-
9. G.A. Slack and V.G. Tsoukala, *J. Appl. Phys.* **76**, p. 1665 (1994).
 10. C.B.H. Evers, W. Jeitschko, L. Boonk, D.J. Braun, T. Ebel, U.D. Scholz, *J. Alloys Comp.* **224**, p. 184 (1995), and references therein.
 11. G.S. Nolas, G.A. Slack, D.T. Morelli, T.M. Tritt and A.C. Ehrlich, *J. Appl. Phys.* **79**, p. 4002 (1996).
 12. G.A. Slack, in *Solid State Physics*, edited by H. Ehrenreich, F. Seitz, and D. Turnbull (Academic Press, New York, 1979), Vol. 34, p. 1.
 13. D.J. Singh, private communication.
 14. T.M. Tritt, G.S. Nolas, G.A. Slack, D.T. Morelli, A.C. Ehrlich, D.J. Gillespie, and J.L. Cohen, *J. Appl. Phys.* **79**, p. 8412 (1996).
 15. L. D. Dudkin, *Sov. Phys. Tech. Phys.* **3**, p. 216 (1958).
 16. R.B. King, *Inorg. Chem.* **23**, p. 3048 (1988).
 17. B.C. Sales, D.G. Mandrus, and R.K. Williams, *Science* **272**, p. 1325 (1996).
 18. B. Chen, J. Xu, C. Uher, D.T. Morelli, G.P. Meisner, J.-P. Fleurial, T. Caillat, and A. Borshchevsky, *Phys. Rev. B* **55**, p. 1476 (1997).
 19. R. B. Horst and L. R. Williams, Proc. Internatl. Conf. Thermoelectrics III, Arlington, TX, p. 139 (1980).
 20. P. Jandl and U. Birkholz, *J. Appl. Phys.* **76**, p. 7351 (1994).
 21. T. C. Harman, *J. Appl. Phys.* **29**, p. 1373 (1958).

THERMAL CONDUCTIVITY OF $\text{Zn}_{4-x}\text{Cd}_x\text{Sb}_3$ SOLID SOLUTIONS

T. CAILLAT, A. BORSHCHEVSKY, J. -P. FLEURIAL

Jet Propulsion Laboratory/California Institute of Technology, 4800 Oak Grove Drive, Pasadena, CA 91109

ABSTRACT

$\beta\text{-Zn}_4\text{Sb}_3$ was recently identified at the Jet Propulsion Laboratory as a new high performance p-type thermoelectric material with a maximum dimensionless thermoelectric figure of merit ZT of 1.4 at a temperature of 673K. A usual approach, used for many state-of-the-art thermoelectric materials, to further improve ZT values is to alloy $\beta\text{-Zn}_4\text{Sb}_3$ with isostructural compounds because of the expected decrease in lattice thermal conductivity. We have grown $\text{Zn}_{4-x}\text{Cd}_x\text{Sb}_3$ crystals with $0.2 \leq x < 1.2$ and measured their thermal conductivity from 10 to 500K. The thermal conductivity values of $\text{Zn}_{4-x}\text{Cd}_x\text{Sb}_3$ alloys are significantly lower than those measured for $\beta\text{-Zn}_4\text{Sb}_3$ and are comparable to its calculated minimum thermal conductivity. A strong atomic disorder is believed to be primarily at the origin of the very low thermal conductivity of these materials which are also fairly good electrical conductors and are therefore excellent candidates for thermoelectric applications.

INTRODUCTION

As part of a broad search for new, more efficient thermoelectric materials conducted at the Jet Propulsion Laboratory, $\beta\text{-Zn}_4\text{Sb}_3$ was recently identified as a new high performance p-type material [1,2]. $\beta\text{-Zn}_4\text{Sb}_3$ has interesting thermoelectric properties in the 473-673K temperature range and a maximum dimensionless thermoelectric figure of merit ZT of 1.4 was obtained at a temperature of 400°C. One of the features of $\beta\text{-Zn}_4\text{Sb}_3$ is its remarkably low thermal conductivity with a room temperature lattice thermal conductivity of 6.5 mW/cmK. Formation of solid solutions is a well known approach for lowering the lattice thermal conductivity and most state-of-the-art thermoelectric materials are, in fact, solid solutions. The performance of a thermoelectric material can be improved if thermal conductivity can be reduced without a strong degradation in electrical properties. We started to investigate the possibility of alloying $\beta\text{-Zn}_4\text{Sb}_3$ with the only known isostructural compound, Cd_4Sb_3 . This compound forms a complete series of solid solution with $\beta\text{-Zn}_4\text{Sb}_3$ [3]. As a first step to assess the usefulness of $\text{Zn}_{4-x}\text{Cd}_x\text{Sb}_3$ solid solutions for thermoelectric applications, we have grown crystals and measured their thermal conductivity from 10 to 500K.

EXPERIMENT

$\text{Zn}_{4-x}\text{Cd}_x\text{Sb}_3$ crystals with $0.2 \leq x \leq 1.2$ were grown by the Bridgman gradient freeze technique. Zinc (Zn) shots (99.9999% pure), cadmium (Cd) powder shots (99.999% pure) and antimony (Sb) shots (99.999% pure) in stoichiometric ratio were loaded into carbon coated quartz ampoules with pointed bottom. The ampoules were subsequently evacuated and sealed (10^{-5} Torr). They were then introduced in a vertical two-zone furnace and remained stationary during

the growth. A gradient of about 50K/cm and a growth rate of about 0.7K/hour were used in the experiments. Details about the growth process can be found elsewhere [4]. Crystals of about 6 mm in diameter and up to 2 cm long were obtained by this technique. Some crystals were ground for x-ray diffractometry (XRD) analysis which showed that the samples were single phase with a structure corresponding to β -Zn₄Sb₃. Microprobe analysis (MPA) also showed that the samples were single phase and homogeneous in composition. Details about microstructure analysis techniques can be found elsewhere [4]. Changes in the Zn to Cd ratio along the grown ingots, inherent to the growth process used, were found by MPA. Samples often presented macro-cracks due the phase transformation from γ -Zn₄Sb₃ to β -Zn₄Sb₃ occurring upon cooling around 765K. These two phases presumably have different coefficient of expansion, resulting in stresses during cooling and causing the cracks formation. Large grains, isolated from the ingots, were used for thermal conductivity and electrical resistivity measurements. The samples were analyzed by MPA prior to the measurements to determine their composition.

Between room temperature and 500K, the thermal conductivity of samples cut perpendicularly to the growth axis were measured by a flash diffusivity technique which has been described elsewhere [5]. The error in the measurements was estimated at about 10%. From 10 to 300K, thermal conductivity measurements was carried out by the four-probe steady-state technique which has been described in [6]. For these measurements, samples of several mm long were cut in the shape of parallelepipeds with a heat flow along the longest axis. The error for these measurements was estimated at about 15% at room temperature and decreases at lower temperatures and is about 5% below 200K because the radiation losses, which is the main source of error, become negligible at low temperatures. The electrical resistivity was measured from 10 to 500K using the van der Pauw technique as described before [6,7].

RESULTS

The thermal conductivity of p-type Zn_{4-x}Cd_xSb₃ samples is shown in Fig. 1 and is compared to β -Zn₄Sb₃ and some state-of-the-art thermoelectric materials. Zn_{4-x}Cd_xSb₃ alloys have the lowest thermal conductivity in the 50-500K temperature range. The substitution of Cd atoms for Zn significantly lower the thermal conductivity in the alloys. At room temperature the thermal conductivity of β -Zn₄Sb₃ is 9 mW/cmK whereas the values for Zn_{4-x}Cd_xSb₃ samples range from 5.5 to 7 mW/cmK depending on the value of x. Between 10 and 300K, the thermal conductivity of the alloys is nearly temperature independent, a signature of strong phonon scattering by point defects. The phase transformation occurring at 263 K [2] does not appear to result in changes in thermal conductivity values whereas it seemed to alter the electrical resistivity values [9]. The low thermal conductivity values make these p-type materials potentially interesting for optimization of their thermoelectric properties at low temperatures.

The effect of mass and volume fluctuations on the lattice thermal conductivity of β -Zn₄Sb₃ can be evaluated for Zn_{4-x}Cd_xSb₃ alloys using the model proposed by Callaway and von Baeyer [10]. Details of the calculation can be found in [11]. Experimental data for Zn₄Sb₃ needed for the calculations such as the Debye temperature, sound velocity and average volume per atom in the crystal can be found in [2]. The model also requires to determine, in the case of volume fluctuations, a strain parameter for the substituted sites which was adjusted by considering the experimental lattice thermal conductivity of the alloys. They were calculated using the

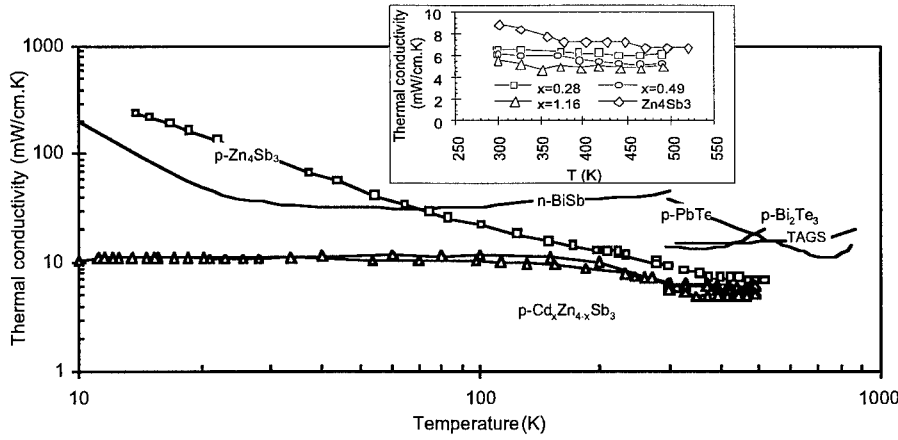


FIG. 1. Thermal conductivity vs. temperature for p-type β - Zn_4Sb_3 and p-type $\text{Zn}_{4-x}\text{Cd}_x\text{Sb}_3$ alloys. The thermal conductivity for some state-of-the-art thermoelectric materials is also shown for comparison.

Wiedemann-Franz law and the measured electrical resistivity (in the order of 2 to 3.5 $\text{m}\Omega\text{cm}$ for all samples). A Lorenz number of $2.2 \times 10^{-8} \text{ V}^2/\text{deg}^2$ was assumed for all samples and was calculated according to the doping level of the samples. The strain parameter (ϵ_{tm}) value was calculated for the Zn site by considering the lattice thermal conductivity of the $\text{Zn}_{2.84}\text{Cd}_{1.16}\text{Sb}_3$ sample at 300K. The best match was achieved for a value of $\epsilon_{\text{tm}}=43$. The results of the calculations are shown in Fig. 2 and compared to several experimental values.

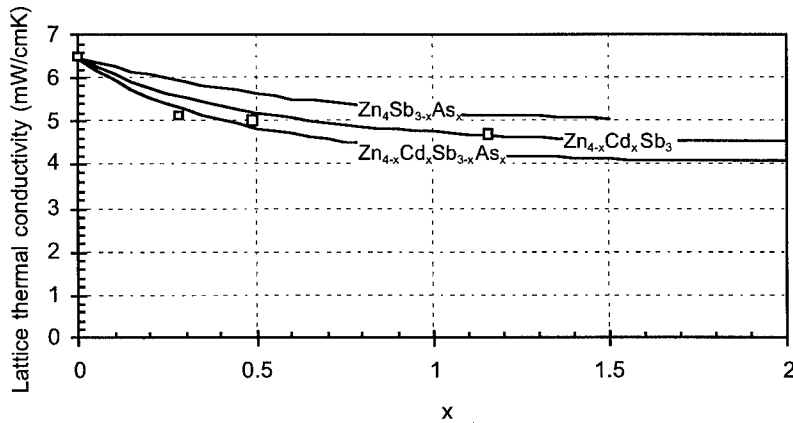


FIG. 2. Effect of alloy scattering on the room temperature lattice thermal conductivity of β - Zn_4Sb_3 . The values were calculated as a function of the fraction x on the Zn site and also on the Sb site. The symbol \square denotes experimental data for $\text{Zn}_{4-x}\text{Cd}_x\text{Sb}_3$ alloys.

A maximum decrease of about 30% in lattice thermal conductivity is predicted for a $\text{Zn}_2\text{Cd}_2\text{Sb}_3$ composition compared to $\beta\text{-Zn}_4\text{Sb}_3$. For $x=0.5$, a 25% decrease is already obtained. In the light of these results, it seems that efforts should primarily focus on the optimization of the electrical properties of $\text{Zn}_{4-x}\text{Cd}_x\text{Sb}_3$ solid solutions with $0.5 \leq x \leq 1$ to determine maximum ZT values.

Using the same formalism, we have also calculated the impact of substituting As for Sb in hypothetical $\text{Zn}_4\text{Sb}_{3-x}\text{As}_x$ solid solutions. We have assumed the same strain parameter of $\epsilon_{\text{tm}}=43$ on the Sb site in the calculations. The results, shown in Fig 2., indicate that the reduction in lattice thermal conductivity is smaller than for $\text{Zn}_{4-x}\text{Cd}_x\text{Sb}_3$ alloys, essentially because of the smaller number of sites substituted considering that mass and volume fluctuations are basically the same between Zn and Cd, and Sb and As. Fig 2. also shows the calculated lattice thermal conductivity when substitution occurs on both sites. The lowest calculated lattice thermal conductivity is nearly 4 mW/cmK for 50% of Cd and As substituted for Zn and Sb, respectively.

We have calculated the lattice thermal conductivity as a function of the temperature using the Wiedemann-Franz law using again a Lorenz number of $2.2 \times 10^{-8} \text{ V}^2/\text{deg}^2$. The results are shown in Fig 3. The lattice thermal conductivity is low and approaches glass-like thermal properties. It was interesting to compare the experimental values to the calculated minimum thermal conductivity, a concept first proposed by Slack [12] and later developed by Cahill et al. based on a model due to Einstein [13]. The minimum thermal conductivity is expressed as a sum of three Debye integrals by [13]:

$$\lambda_{\text{min}} = \left(\frac{\pi}{6}\right)^{1/3} k_B n^{2/3} \sum_i v_i \left(\frac{T}{\theta_i}\right)^2 \int_0^{\theta_i/T} \frac{x^3 e^x}{(e^x - 1)^2} dx \quad (1)$$

The sum is taken over the three sound modes (two transversal and one longitudinal) with speeds of sound v_i . k_B is the Boltzmann's constant, n the atomic density, T the temperature in K and $\theta_i = v_i (h/2\pi k_B) (6\pi^2 n)^{1/3}$. We calculated the minimum thermal conductivity for $\beta\text{-Zn}_4\text{Sb}_3$ using the speed of sound and atomic density values in [2]. The results are shown in Fig. 3. The minimum lattice thermal conductivity for $\beta\text{-Zn}_4\text{Sb}_3$ at room temperature is 4.2 mW/cmK which is only a third lower than the experimental value of 6.5 mW/cmK. For the $\text{Zn}_{2.84}\text{Cd}_{1.16}\text{Sb}_3$ alloy, the experimental value is close to the calculated minimum value at room temperature and is lower for higher temperatures reaching a minimum of 2.5 mW/cmK at 500K. At 100K, the lattice thermal conductivity of the alloy is about three times larger than the calculated minimum. Glass-like thermal conductivity have been observed in highly disordered materials and crystals containing loosely bonded atoms such as filled skutterudite materials [14-17]. In contrast, simple monoatomic substitution cannot lead to glass-like thermal conductivity. Therefore, it is remarkable that $\text{Zn}_{4-x}\text{Cd}_x\text{Sb}_3$ materials possess thermal conductivity similar to glass-like materials which we believe is due to a highly disordered structure. Indeed, the crystal structure of these materials requires disorder on one of the Sb sites for the stoichiometry [18]. In addition, Auger electron spectroscopy performed on $\beta\text{-Zn}_4\text{Sb}_3$ crystals revealed localized deviations from the exact stoichiometry [19] which suggests the presence of structural defects such as vacancies which can produce strong phonon scattering as it has been observed, for example, in In_2Te_3 , [20]. Further evidence of the atomic disorder for $\text{Zn}_{4-x}\text{Cd}_x\text{Sb}_3$ materials was given by optical absorption and reflection measurements performed on $\beta\text{-Zn}_4\text{Sb}_3$ materials crystals [19].

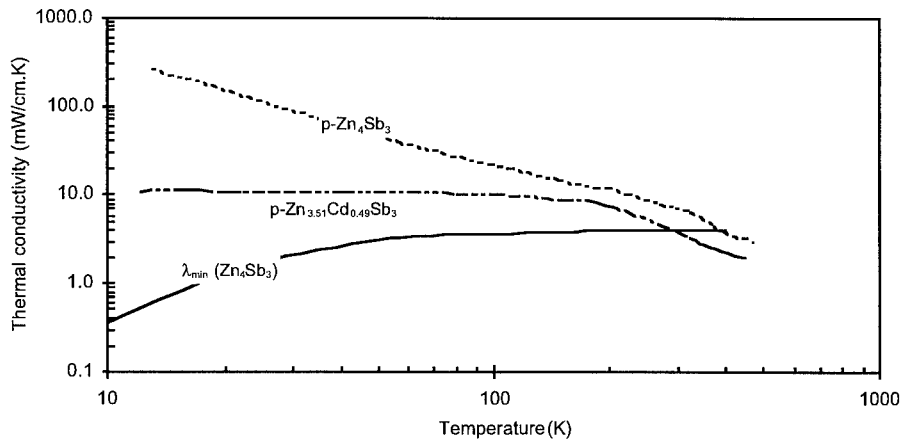


FIG. 3. Lattice thermal conductivity vs. temperature for p-type β - Zn_4Sb_3 and p-type $\text{Zn}_{3.51}\text{Cd}_{0.49}\text{Sb}_3$ alloy. The solid line is the calculated lattice thermal conductivity for β - Zn_4Sb_3 using equation (1).

CONCLUSIONS

We have measured the thermal conductivity of $\text{Zn}_{4-x}\text{Cd}_x\text{Sb}_3$ materials with $0.2 \leq x \leq 1.2$ between 10 and 500 K. The results show that these materials exhibit very low thermal conductivity comparable to the calculated minimum thermal conductivity of β - Zn_4Sb_3 around room temperature. It is believed that a high atomic structural disorder is essentially responsible for these low values. Most of the materials having glass-like thermal conductivity are poor electrical conductors and therefore are of little interest for thermoelectric applications. In contrast, $\text{Zn}_{4-x}\text{Cd}_x\text{Sb}_3$ materials are fairly good electrical conductors with electrical resistivity in the 2 to 3.5 m Ω cm range and appear to be excellent candidates for thermoelectric applications. Future efforts will focus on the investigations and optimization of their electrical properties.

ACKNOWLEDGMENTS

The work described in this paper was carried out at the Jet Propulsion Laboratory/California Institute of Technology, under contract with the National Aeronautics and Space Administration. The authors would like to thank D. Singh for stimulating discussions, A. Zoltan and D. T. Morelli for thermal conductivity measurements, Paul Carpenter for microprobe analyses, and Jim Kulleck for XRD analyses. This work was supported by the Defense Advanced Research Projects Agency, Grant No. E407.

REFERENCES

1. T. Caillat, J.-P. Fleurial, and A. Borshchevsky in Proceedings of the XV International Conference on Thermoelectrics, edited by T. Caillat (IEEE Catalog No. 96TH8169, Pasadena,

- CA 1996) pp. 151-154.
2. T. Caillat, J.-P. Fleurial, and A. Borshchevsky, *J. Phys. Chem. Solids*, in press (1997).
 3. Ya. A. Ugai, T. A. Marshakova, V. Ya. Shevchenko, and N. P. Demina, *Inorganic Materials* **5**, 1180 (1969).
 4. T. Caillat, J.-P. Fleurial, and A. Borshchevsky, *J. Cryst. Growth* **166**, 722 (1996).
 5. J. W. Vandersande, C. Wood, A. Zoltan, and D. Whittenberger, *Thermal Conductivity*, Plenum Press, New York, p. 445 (1988).
 6. D. T. Morelli, *Phys. Rev.* **44**, 5453 (1991).
 7. T. Caillat, J. -P. Fleurial, and A. Borshchevsky, *J. Appl. Phys.* **11**, 8419 (1996).
 8. V. Tydlitát, *Czech. J. Phys.* **9**, 638 (1959).
 9. V. Ya. Shevchenko, V. A. Skirpin, Ya. A. Ugai, and T. A. Marshakova, *Inorganic Materials* **4**, 1193 (1968).
 10. J. Callaway and H. C. Von Baeyer, *Phys. Rev.* **120**, 4, 1149 (1960).
 11. A. Borshchevsky, T. Caillat, and J.-P. Fleurial, and in Proceedings of the XV International Conference on Thermoelectrics, edited by T. Caillat (IEEE Catalog No. 96TH8169, Pasadena, CA 1996) pp. 112-116.
 12. G. A. Slack, in *Solid State Physics*, edited by F. Seitz and D. Turnbull (Academic, New York, 1979), Vol. 34, p. 1.
 13. D. G. Cahill, S. K. Watson, and R. O. Pohl, *Phys. Rev.* **46**, 6131 (1992).
 14. D. T. Morelli and G. P. Meisner, *J. Appl. Phys.* **77**, 3777 (1995).
 15. G. S. Nolas, G. A. Slack, D. T. Morelli, T. M. Tritt, and A. C. Ehrlich, *J. Appl. Phys.* **79**, 4002 (1996).
 16. B. C. Sales, D. Mandrus, and R. K. Williams, *Science* **272**, 1352 (1996).
 17. B. Chen, J. -H. Xu, C. Uher, D. T. Morelli, G. P. Meisner, J. -P. Fleurial, T. Caillat, and A. Borshchevsky, *Phys. Rev. B* **55**, 1476 (1997).
 18. H. W. Mayer, I. Mikhail, und K. Schubert, *Journal of the Less-Common Metals* **59**, 43 (1978).
 19. M. Tapiero, S. Tarabichi, J. G. Gies, C. Noguét, J. P. Zielinger, M. Joucla, J. Loison, M. Robino, and J. Henrion, *Solar Energy Materials* **12**, 257 (1985).
 20. I. Zaslavskii, V. M. Sergeeva, and I. A. Smirnov, *Soviet Physics Solid State* **2**, 11, 2565 (1961).

A New Class of Materials with Promising Thermoelectric Properties: $M\text{NiSn}$ ($M = \text{Ti, Zr, Hf}$)

H. Hohl*, A. P. Ramirez*, W. Kaefer**, K. Fess**, Ch. Thurner**, Ch. Kloc**, and E. Bucher*,**

*Lucent Technologies, Bell Laboratories, 700 Mountain Avenue, Murray Hill, NJ 07974

**University of Konstanz, Faculty of Physics, P.O. Box 5560, D-78457 Konstanz, Germany

Abstract

TiNiSn , ZrNiSn and HfNiSn are members of a large group of intermetallic compounds which crystallize in the cubic MgAgAs -type structure. Polycrystalline samples of these compounds have been prepared and investigated for their thermoelectric properties. With thermopowers of about $-200 \mu\text{V/K}$ and resistivities of a few $\text{m}\Omega\text{cm}$, power factors S^2/ρ as high as $38 \mu\text{W/K}^2\text{cm}$ were obtained at 700 K. These remarkably high power factors are, however, accompanied by a thermal conductivity which is too high for applications. In order to reduce the parasitic lattice thermal conductivity, solid solutions $\text{Zr}_{1-x}\text{Hf}_x\text{NiSn}$, $\text{Zr}_{1-x}\text{Ti}_x\text{NiSn}$, and $\text{Hf}_{1-x}\text{Ti}_x\text{NiSn}$ were formed. The figure of merit of $\text{Zr}_{0.5}\text{Hf}_{0.5}\text{NiSn}$ at 700 K ($ZT = 0.41$) exceeds the end members ZrNiSn ($ZT = 0.26$) and HfNiSn ($ZT = 0.22$).

Introduction

There are a number of ternary intermetallic compounds with equiatomic composition ABX where A is a transition metal from the left side of the periodic table (titanium or vanadium group elements), B a transition metal from the right side of the periodic table (iron, cobalt or nickel group elements), and X is one of the main group elements Sn, Sb, or Ga [1]. Of the 39 compounds known so far, 24 crystallize in the cubic MgAgAs -type structure, whereas the others exhibit a hexagonal FeP_2 -type structure [2,3].

TiNiSn , ZrNiSn and HfNiSn have attracted attention during the past years due to their unusual transport properties. The compounds crystallize in the cubic MgAgAs -type structure (space group $F\bar{4}3m$) with lattice parameters of 5.94 Å, 6.11 Å and 6.08 Å, respectively [1]. The unit cell of ZrNiSn is shown in Fig. 1. It contains four Zr atoms in the $4b$ positions ($1/2, 1/2, 1/2$), four Sn atoms in the $4a$ positions ($0, 0, 0$), and four Ni atoms in the $4c$ positions ($1/4, 1/4, 1/4$). The structure, therefore, consists of four interpenetrating fcc-lattices: a lattice of Zr atoms and a lattice of Sn atoms forming a rock salt structure, a lattice of Ni atoms occupying the centers of every other cube, and an ordered lattice of vacancies [4]. When the lattice of vacancies is filled up with additional Ni atoms one obtains ZrNi_2Sn , a "Heusler compound" with a cubic MnCu_2Al -type structure.

Aliev et al. investigated the temperature dependence of the resistivity of $M\text{NiSn}$ compounds ($M = \text{Ti, Zr, Hf}$) and found them to be narrow band gap semiconductors with band gaps of $E_g \approx 0.12 \text{ eV}$, 0.18 eV and 0.22 eV , respectively [6]. The compounds were also found [7] to exhibit large thermopowers, making them promising candidates for thermoelectric applications.

In an earlier study [8] we have grown single crystals of TiNiSn and ZrNiSn from a tin flux and measured their thermoelectric properties. The ZrNiSn single crystal achieves

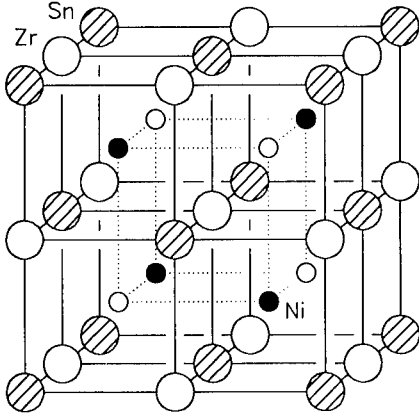


Fig. 1. Cubic unit cell of ZrNiSn. The small empty circles represent vacancies.

a power factor of $S^2/\rho = 35 \mu\text{W/K}^2\text{cm}$ at 400 K, but its thermal conductivity ($\kappa = 17 \times 10^{-2} \text{ W/Kcm}$ at 360 K) does not allow for a thermoelectric figure of merit

$$Z = \frac{S^2}{\rho \kappa} \quad (1)$$

which is large enough for thermoelectric applications.

Significantly lower lattice thermal conductivities are to be expected when polycrystalline samples are used instead of single crystals. The lattice thermal conductivity in a given class of solids also tends to be lower, the higher the mean atomic weight is. And even lower lattice thermal conductivities are to be expected when solid solutions of two or more compounds are formed.

With these guiding principles in mind, we prepared polycrystalline samples of TiNiSn, ZrNiSn and HfNiSn as well as quasi-binary solid solutions of the compounds. The thermoelectric properties of the samples will be discussed.

Experiment

Samples of composition $M\text{NiSn}$ ($M = \text{Ti, Zr, Hf}$), $\text{Zr}_{1-x}\text{Hf}_x\text{NiSn}$ ($x = 0.15, 0.3, 0.5$), $\text{Zr}_{1-x}\text{Ti}_x\text{NiSn}$ ($x = 0.15, 0.3, 0.5$) and $\text{Hf}_{1-x}\text{Ti}_x\text{NiSn}$ ($x = 0.5$) were prepared by melting together the following elements in an arc furnace under a zirconium-gettered argon atmosphere: Ti (Teledyne Wah Chang, 5N, RRR = 350), Zr (Teledyne Wah Chang, 3N4, RRR = 420), Hf (Teledyne Wah Chang, 3N4), Ni (MRC, grade v.p., RRR = 60), and Sn (Cominco, 5N). Samples were turned over and remelted several times to ensure homogeneity. The resulting buttons were wrapped in tantalum foil and annealed at 850 °C for two days in evacuated quartz ampoules. Bars with dimensions $0.6 \times 1.1 \times 8 \text{ mm}^3$ were cut from the center portions of the buttons with a diamond wheel saw.

Powder diffraction patterns of the samples were recorded on a Philips PW-1710 powder diffractometer. LaB_6 was used as standard. The thermopower was measured with an MMR SB-100 Seebeck controller in the range 85–500 K. Four-wire set-ups were used for the resistivity measurements at low (5–360 K) and at elevated (300–700 K) temperatures.

Thermal conductivities were measured in the range 85–360 K using a steady-state method (axial heat flow apparatus). Silver epoxy was used to attach contacts to the samples in all measurements.

Results

MNiSn ($M = \text{Ti, Zr, Hf}$): The ZrNiSn and HfNiSn samples were single phase with lattice parameters of $a = 6.113(1) \text{ \AA}$ and $6.079(1) \text{ \AA}$, respectively. A lattice parameter of $5.927(1) \text{ \AA}$ was found for TiNiSn, with traces of Ti_2Ni visible in the powder diffraction pattern.

The thermopowers and resistivities of the samples are shown in Fig. 2. All of the samples exhibit negative thermopowers (n-type behavior) with room temperature values of $-238 \mu\text{V/K}$ (TiNiSn), $-143 \mu\text{V/K}$ (ZrNiSn), and $-124 \mu\text{V/K}$ (HfNiSn). The thermopowers can be well described by second degree polynomials in the temperature ranges indicated by dashed lines in Fig. 2. The temperature dependence of the resistivities are typical of impurity conduction below room temperature. They turn into an intrinsic semiconducting behavior

$$\rho = \rho_0 \exp\left(\frac{E_g}{2k_B T}\right) \quad (2)$$

above $\sim 400 \text{ K}$. The band gap parameters of TiNiSn, ZrNiSn and HfNiSn are found to be $E_g \approx 0.15 \text{ eV}$, 0.13 eV and 0.19 eV , respectively.

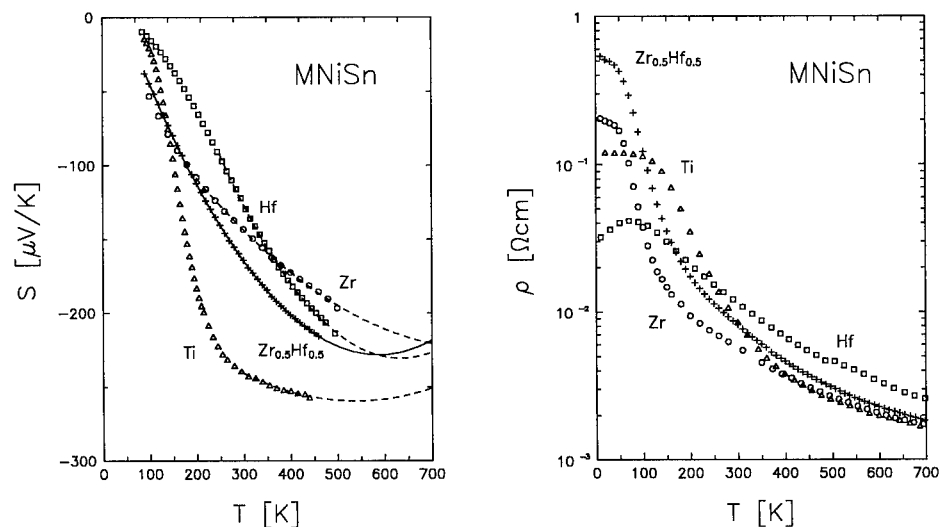


Fig. 2. Thermopowers S and resistivities ρ of MNiSn ($M = \text{Ti, Zr, Hf}$) compounds and of the $\text{Zr}_{0.5}\text{Hf}_{0.5}\text{NiSn}$ alloy. Dashed and solid lines in the left figure represent least squares fits of second order polynomials to the data.

The power factors S^2/ρ and thermal conductivities κ of $M\text{NiSn}$ compounds are shown in Fig. 3. The power factors increase monotonically with increasing temperature and achieve values of $38 \mu\text{W}/\text{K}^2\text{cm}$ (TiNiSn), $28 \mu\text{W}/\text{K}^2\text{cm}$ (ZrNiSn), and $20 \mu\text{W}/\text{K}^2\text{cm}$ (HfNiSn) at 700 K. The temperature dependence of the thermal conductivities can be described by

$$\kappa = \frac{a}{T} + b \quad (3)$$

with temperature independent parameters a and b between 85 K and room temperature. This behavior is typical of the lattice thermal conductivity κ_L of semiconductors above the Debye temperature. Slight positive deviations from this behavior become apparent above room temperature, indicating that electronic contributions κ_e to the thermal conductivity gain in importance at higher temperatures.

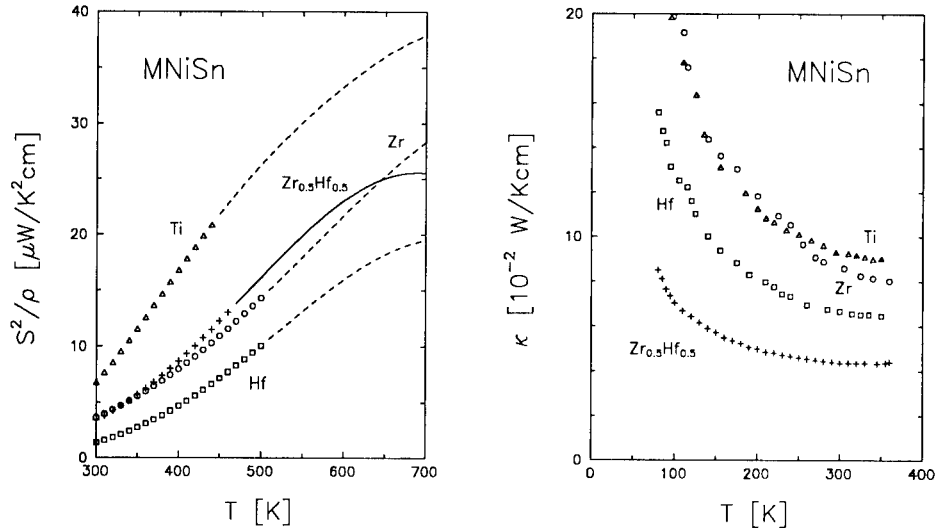


Fig. 3. Power factors S^2/ρ and thermal conductivities κ of $M\text{NiSn}$ ($M = \text{Ti, Zr, Hf}$) compounds and of the $\text{Zr}_{0.5}\text{Hf}_{0.5}\text{NiSn}$ alloy. Dashed and solid lines in the left figure are based on extrapolations of thermopowers as shown in Fig. 2.

If, for simplicity, the thermal conductivities at 360 K are used to estimate the figures of merit, values of $ZT \approx 0.29$ (TiNiSn), 0.26 (ZrNiSn), and 0.22 (HfNiSn) are obtained at 700 K.

$\text{Zr}_{1-x}\text{Hf}_x\text{NiSn}$ ($x = 0.15, 0.3, 0.5$): The powder diffraction patterns of these alloys exhibit distinct and narrow diffraction peaks. There are no impurity phases visible in the patterns. The lattice parameters of the alloys, $6.104(1) \text{ \AA}$, $6.100(1) \text{ \AA}$ and $6.095(1) \text{ \AA}$, respectively, vary smoothly between the end members, indicating the formation of a solid solution. The powder diffraction pattern of $\text{Zr}_{0.5}\text{Hf}_{0.5}\text{NiSn}$ is shown in Fig. 4.

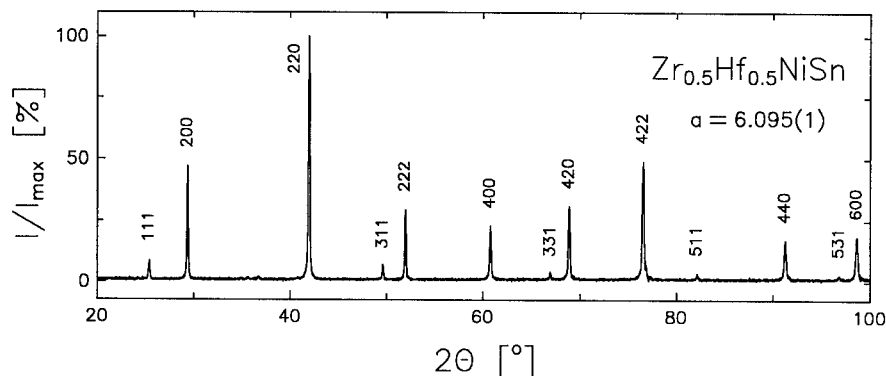


Fig. 4. Powder diffraction pattern of the $\text{Zr}_{0.5}\text{Hf}_{0.5}\text{NiSn}$ alloy, recorded with $\text{CuK}\alpha$ radiation.

The thermopowers and the resistivities of the alloys don't show a marked dependence on composition. The thermal conductivities of the alloys, however, are significantly lower than those of the end members. The room temperature thermal conductivities of the alloys are shown in Fig. 5. A minimum thermal conductivity of $\kappa_{300} = 4.38 \times 10^{-2} \text{ W/Kcm}$ is found for $x = 0.5$. The temperature dependence of the thermoelectric parameters of $\text{Zr}_{0.5}\text{Hf}_{0.5}\text{NiSn}$ are also shown in Figs. 2 and 3. The resistivity of the alloy obeys Eq. (2) with a band gap of $E_g \approx 0.16 \text{ eV}$ above 400 K.

The power factor of $\text{Zr}_{0.5}\text{Hf}_{0.5}\text{NiSn}$, $26 \mu\text{W/K}^2\text{cm}$ at 700 K, is slightly less than that of ZrNiSn . But due to its lower thermal conductivity an improved thermoelectric figure of merit is achieved: $ZT \approx 0.41$ at 700 K.

$\text{Zr}_{1-x}\text{Ti}_x\text{NiSn}$ ($x = 0.15, 0.3, 0.5$) and $\text{Hf}_{1-x}\text{Ti}_x\text{NiSn}$ ($x = 0.5$): The powder diffraction patterns of these samples differ from the $\text{Zr}_{1-x}\text{Hf}_x\text{NiSn}$ alloys in that the diffraction peaks are rather broad. It is not clear at the moment whether this behavior is caused by a structural distortion or if the alloys are two-phase mixtures of ZrNiSn (or HfNiSn) and TiNiSn . Some of the samples exhibit room temperature thermopowers as high as $-370 \mu\text{V/K}$, accompanied, however, by relatively high resistivities. The thermal conductivities of the alloys are significantly lower than those of the end members (Fig. 6). The thermoelectric figures of merit of $\text{Zr}_{0.5}\text{Ti}_{0.5}\text{NiSn}$ and $\text{Hf}_{0.5}\text{Ti}_{0.5}\text{NiSn}$ at 700 K are $ZT \approx 0.25$ and 0.34 , respectively.

Conclusions

Polycrystalline samples of TiNiSn , ZrNiSn , and HfNiSn have been prepared by arc melting. The samples show n-type behavior with room temperature thermopowers around $-200 \mu\text{V/K}$. The compounds are narrow band gap semiconductors with $E_g = 0.13\text{--}0.19 \text{ eV}$. The thermal conductivities of the compounds are dominated by the lattice contributions and can be lowered significantly by alloying. Formation of a quasi-binary solid solution is observed between ZrNiSn and HfNiSn . The figure of merit of $\text{Zr}_{0.5}\text{Hf}_{0.5}\text{NiSn}$ at 700 K ($ZT = 0.41$) exceeds the end members ZrNiSn ($ZT = 0.26$) and HfNiSn ($ZT = 0.22$).

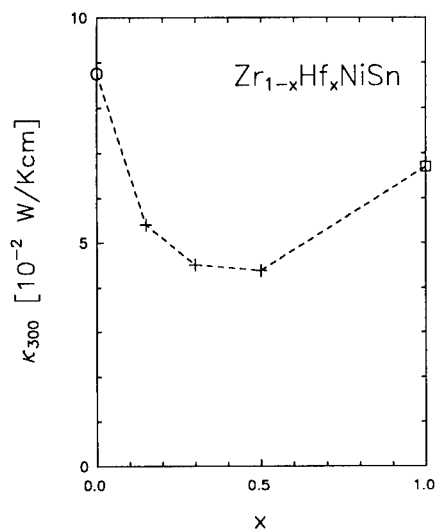


Fig. 5. Thermal conductivities of $\text{Zr}_{1-x}\text{Hf}_x\text{NiSn}$ alloys at room temperature. The dashed line is a guide for the eye.

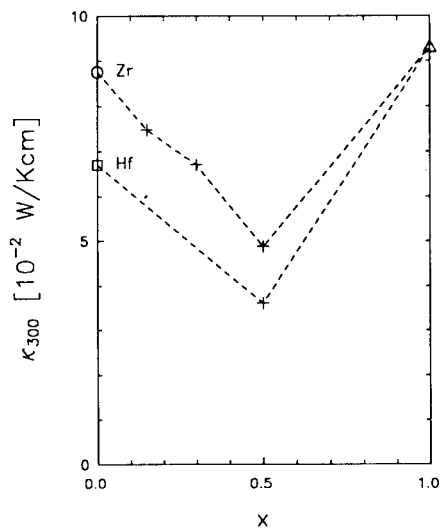


Fig. 6. Thermal conductivities of $\text{Zr}_{1-x}\text{Ti}_x\text{NiSn}$ (top) and $\text{Hf}_{1-x}\text{Ti}_x\text{NiSn}$ (bottom) alloys at room temperature.

Acknowledgments

We would like to thank Teledyne Wah Chang (Albany, OR) for generously providing us with high purity titanium, zirconium and hafnium crystal bars.

References

1. W. Jeitschko, *Metall. Trans.* **1**, 3159 (1970).
2. P. Villars and L. D. Calvert, *Pearson's Handbook of Crystallographic Data for Intermetallic Phases*, 2nd ed., Vol. 1-4 (ASM International, Ohio, 1991).
3. L. D. Dudkin, Z. M. Dashevskii, and R. V. Skolozdra, *Inorg. Mater.* **29**, 249 (1993).
4. A statistical distribution of occupied sites is found in the (1/4, 1/4, 1/4) and the (3/4, 3/4, 3/4) sublattices of TiNiSn , TiCoSn , and TiIrSn [5].
5. Yu. V. Stadnyk, L. A. Mykhailiv, V. V. Kuprina, and R. V. Skolozdra, *Inorg. Mater.* **24**, 1196 (1989).
6. F. G. Aliev, N. B. Brandt, V. V. Moshchalkov, V. V. Kozyrkov, R. V. Skolozdra, and A. I. Belogorokhov, *Z. Phys. B* **75**, 167 (1989).
7. F. G. Aliev, V. V. Kozyrkov, V. V. Moshchalkov, R. V. Skolozdra, and K. Durezewski, *Z. Phys. B* **80**, 353 (1990).
8. Ch. Kloc, K. Fess, W. Kaefer, K. Friemelt, H. Riaz-Najad, and E. Bucher, in *Proc. XV International Conference on Thermoelectrics, ICT96, March 26-29, 1996, Pasadena, CA*, pp. 155-158.

DEVELOPMENT OF BI-SB-TE TERNARY ALLOY WITH COMPOSITIONALLY GRADED STRUCTURE

A.YAMAMOTO, T.OHTA

Energy Fundamentals Division, Electrotechnical Laboratory, AIST, MITI,
Umezono 1-1-4 Tsukuba Ibaraki 305, Japan a.yamamoto@etl.go.jp

ABSTRACT

Compositionally graded p-type Bi-Sb-Te thermoelectric material was synthesized by PIES (Pulverized and Intermixed Elements Sintering) method. The materials consisted of three segmented regions of different alloy composition, i.e. $y = 0.8/0.825/0.9$ in $(\text{Bi}_2\text{Te}_3)_{1-y}(\text{Sb}_2\text{Te}_3)_y$ system. It was found that the electrical power output of the compositionally graded material was larger than that of the best single composition material when the temperature difference was the designed value.

INTRODUCTION

Bi-Sb-Te ternary alloy is one of the best material for thermoelectric application in temperature range from 300K to 500K. Over the past thirty years a considerable number of studies have been carried out on the related alloys and up today the highest figure of merit $ZT = 0.96$ has been achieved for p-type single crystal[1]. Further improvement seems to be difficult by optimizing the alloy composition and quality of the crystal. On the other hand, from the viewpoint of application, thermoelectric materials are usually used under large temperature difference. The ZT value of the material should be large in wide temperature range, i.e. the average ZT value has to be large. The ZT value of Bi-Sb-Te based alloy, however, strongly depends on temperature and has a maximum value at a certain temperature.

In order to average the peaky ZT value some concepts for materials designing such as Functionally Graded Materials have been proposed in earlier studies[2, 3]. These proposals were concluded in promising prospect of introducing these materials, but they did not consider the negative aspects due to interfaces which are inevitably incorporated in the material and it seems difficult to argue about the enhancement in the performance without experimental data.

In this study compositionally graded Bi-Sb-Te ternary alloy was fabricated by PIES method to demonstrate the effect of graded structures. Three different alloy powders were compacted together and hot-pressed so that harmful interfaces were eliminated. Experimental results on output power characteristics of the material under large temperature differences were compared with the theoretical estimation of it.

EXPERIMENT

PIES method

PIES method (Pulverized and Intermixed Elements Sintering method) is one of the most promising sample preparation techniques for mass production of thermoelectric materials. Figure 1 shows the flow diagram of sample preparation by PIES method. The method consists of two simple processes. The first one is ball-milling process where raw powder elements are intermixed and pulverized by mechanical energy input. In this process, the powder forms a solid solution without any temperature increment. The second one is sequent sintering process where the powder is compacted in a temperature much below its melting point by using hot-pressing (HP), hot isostatic pressing (HIP) or plasma activated sintering (PAS). Samples made by PIES method usually have very fine grains which favor a reduction in the thermal conductivity and an enhancement in the mechanical strength. PIES method does not require an intricate process such as sealing in a quartz ampoule, melting in Rocking furnace and grinding and sieving which all are used in conventional melt techniques. A series of measurements on p-type Bi-Sb-Te alloy prepared by PIES method has already proved its high potential, i.e. ZT values are the same level as conventional melt samples. The process has been employed in many other materials[4-8].

In this study 99.999% purity Bi, Sb and Te powdered elements were used as starting materials. Hot pressing method was employed as a sintering process. Hot pressing conditions were 753K, 400kgf/cm², for one hour. Typical sizes of hot-pressed specimen were 10mm ϕ x 5mm and specimens were sliced into 1mm thick disk shape. The density of specimen measured by Archimedes' method were more than 98% of the ideal value.

Measurement

The Seebeck coefficients were calculated from measured thermoelectric power with temperature difference of 10K. The electrical resistivity measurements and Hall measurements were performed by van der Pauw method. The thermal conductivities were calculated from the thermal diffusivity, the specific heat and the density. The thermal diffusivities and the specific heats were measured by laser flash method and differential scanning calorimeter (DSC), respectively.

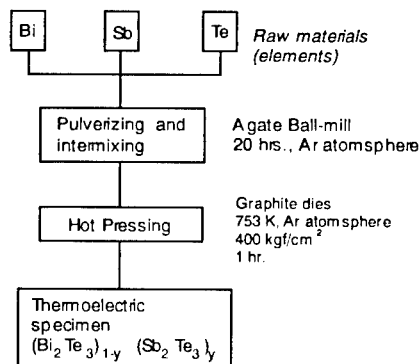


Figure 1. Procedure of sample preparation by PIES method

Compositionally Graded Sample

In this study compositionally graded samples were fabricated to prove the enhancement in output characteristics. Through the study on a compositional dependence of thermoelectric properties, segmentation structure of $y = 0.80 / 0.825 / 0.9$ was selected where y indicated the Sb_2Te_3 fraction in $(\text{Bi}_2\text{Te}_3)_{1-y}(\text{Sb}_2\text{Te}_3)_y$ system.

In the experiment compositionally graded samples were prepared by piling the alloyed powders of different composition at a charge process into graphite dies before hot-pressing. This technique was performed quite well since no cracking was observed at the interfaces inside the sample and there were not any unfavorable effects on the mechanical strength. Sample dimensions were $2\text{mm} \times 2\text{mm} \times 5\text{mm}$. The sample was hold between nickel electrodes which applied a temperature difference to the sample. Current leads and voltage leads were also attached to nickel electrodes and the $V-I$ characteristic of the sample was measured by varying an external load.

RESULTS

Thermoelectric Properties of PIES samples

The compositional dependence of carrier density of PIES sample has been reported in earlier work[5]. The results showed that the carrier density strongly depended on the composition and samples of Sb_2Te_3 fraction $y > 0.7$ showed p-type conduction while those of $y < 0.7$ showed n-type conduction. This result is quite different from the results of typical Bi-Sb-Te alloy which is made by melt process[9]. Here we focus on the p-type region for further consideration.

Figure 2, 3 and 4 are the temperature dependence of Seebeck coefficient, resistivity and thermal conductivity as a function of composition. The lines in Figure 2 and 3 vary in order of composition y and clearly each peak of line shifts to higher temperature range as composition y

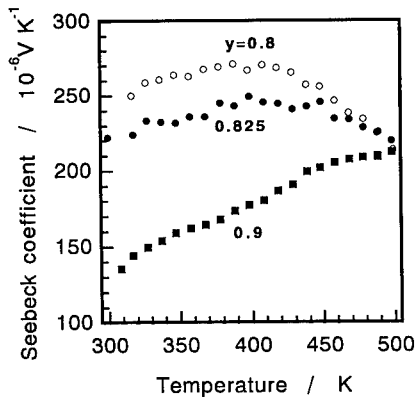


Figure 2. Temperature dependence of Seebeck coefficient

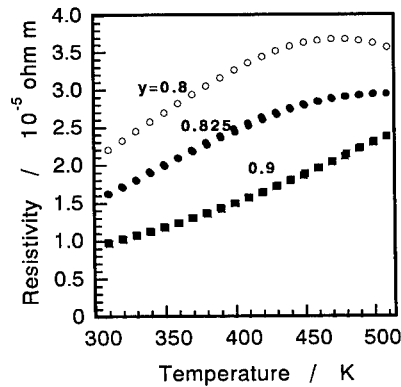


Figure 3. Temperature dependence of resistivity

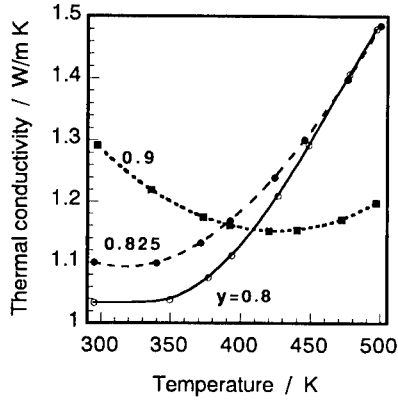


Figure 4. Temperature dependence of thermal conductivity.

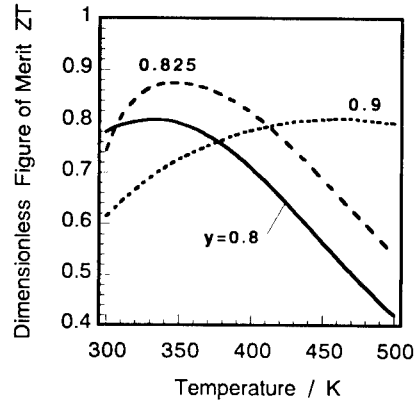


Figure 5. Temperature dependence of figure of merit.

increase. This peak shift may account for change of the carrier density which strongly depend on the alloy composition y .

Figure 5 shows the temperature dependence of dimensionless figure of merit ZT values which are calculated from data shown in Figure 2, 3 and 4. The highest figure of merit value 0.88 is obtained at 340K in sample of $y = 0.825$. There are overlaps between each temperature dependence. This means a possibility of an enhancement in conversion efficiency through graded sample. For example, a compensative combination of curves of $y=0.825$ and $y=0.9$ in Figure 5 will produce larger average ZT value in the temperature range from 300K to 500K.

Compositionally Graded Sample

Compositionally graded sample consisted of three segments, $y = 0.8, 0.825$ and 0.9 . It was 5mm in height and its cross section area was $5 \times 5 \text{ mm}^2$. The sample was designed so that each segmented region had the same thickness for design simplification, however, it was not the best compositional distribution. Compositional distributions were confirmed by Energy Dispersive X-ray spectroscopy as shown in Figure 6. Figure 7 shows the expected distributions of resistivity and Seebeck coefficient along the temperature gradient in the sample under conditions of $T_H=500\text{K}$ and $T_L=300\text{K}$, i.e. $\Delta T=200\text{K}$.

First the output power values of the compositionally graded and single composition samples were calculated numerically from the value of the total electrical resistance and thermoelectric power of them. The electrical resistance R_i and thermoelectric power E are given by

$$R_i = \frac{1}{A} \int_0^l \rho(T) dx \quad E = \int_{T_L}^{T_H} \alpha(T) dT \quad (1)$$

$\rho(T)$ and $\alpha(T)$ are given by figure 2 and 3 for the single composition samples and figure 7 for the

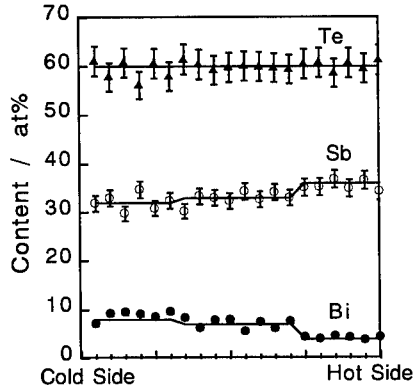


Figure 6. Bi, Sb and Te contents in compositionally graded sample measured by Energy Dispersive X-ray spectroscopy.

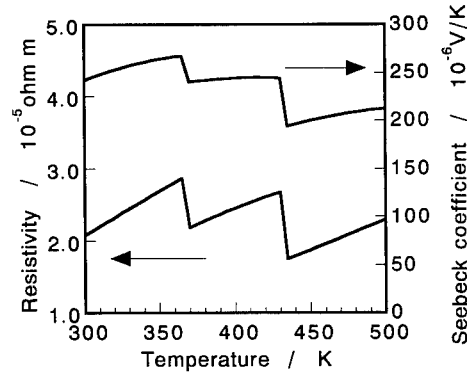


Figure 7. Distributions of the resistivity and Seebeck coefficient of the graded sample.

graded sample. The maximum electrical power output is given by

$$P_{\max} = \frac{E^2}{4(R_i + R_{\text{contact}})} \quad (2)$$

where R_{contact} is the contact resistance at the interfaces between nickel electrodes and the sample. The results of calculation are summarized in Table I. Output Power of the graded sample is larger than those of single composition samples at $\Delta T=200\text{K}$ in which condition the graded one is designed. This is due to the positive effect of the compositionally graded structure.

Second we measured the output power P as a function of current I for respective samples listed in Table I. The results are shown in Figure 8. The existence of R_{contact} influences the output power directly and it seems to be the main reason that all the values in Figure 8 are lower than the estimated values listed in Table I. In the figure output power of the graded sample is larger than those of single composition samples at temperature difference of 200K, i.e. $T_H=500\text{K}$. On the other

Table I. Calculated maximum output power under conditions : $T_L=300\text{K}$, $R_{\text{contact}}=0$.

ΔT (K)	Electrical Output (mW)			
	Graded sample		Single composition samples	
	$y=0.8/0.825/0.9$	$y=0.8$	$y=0.825$	$y=0.9$
100	5.103	5.091	5.513	4.165
150	11.19	10.49	11.50	9.423
200	19.11	16.70	18.72	16.51

hand output power of $y=0.825$ sample is the largest and the positive effect is not observed in the graded sample when the temperature difference is 150K and 100K. These results are consistent with the calculation which is based on respective data shown in Figure 2 and 3.

As shown in Figure 8 the maximum power output produced by the graded sample was 11.6mW which was 8.6% larger than that of $y=0.825$ sample at the designed temperature difference ($\Delta T=200K$). Thus the validity of compositionally graded designing in p-type Bi-Sb-Te alloy was indicated experimentally.

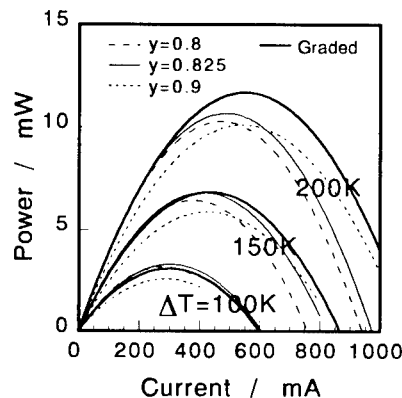


Figure 8. Output power characteristics of $y=0.8, 0.825, 0.9$ single composition samples and compositionally graded sample. $T_L=300K$.

CONCLUSIONS

In this paper preparation and characterization of compositionally graded thermoelectric material of $(Bi_2Te_3)_{1-y}(Sb_2Te_3)_y$ system were discussed. The preparation of compositionally graded materials and of several homogeneous materials was successfully performed by using PIES method and the figure of merit showed a maximum value of $ZT = 0.88$ for $y = 0.825$ at 340K.

Output power of the compositionally graded material was measured under temperature difference of 100, 150 and 200K. The electrical power output of the graded sample was 8.6% larger than that of the best single composition sample at designed temperature difference of 200K. The enhancement in output power is caused by the compositionally graded structure of the material and the validity of it was indicated experimentally.

REFERENCES

1. T. Caillat et al., Mat. Res. Soc. Symp. Proc. Vol. 234, p.189 (1991).
2. L. W. Whitlow et al., The 11th Proc. Int. Conf. on Thermoelectrics, p.244 (1992).
3. Anatychuk L. I. et al., The 14th Proc. Int. Conf. on Thermoelectrics, p.7 (1995).
4. T. Ohta et al., The 8th Proc. Int. Conf. on Thermoelectrics, p.7 (1989).
5. T. Ohta et al., The 13th Proc. Int. Conf. on Thermoelectrics, p.267 (1994).
6. T. Ohta et al., The 14th Proc. Int. Conf. on Thermoelectrics, (1995), p.24 (1995).
7. T. Caillat et al., The 11th Proc. Int. Conf. on Thermoelectrics, p.240 (1992).
8. B. A. Cook et al., The 9th Proc. Int. Conf. on Thermoelectrics, p.234 (1990).
9. J. Shim et al., The 9th Proc. Int. Conf. on Thermoelectrics, p.27 (1990).

THERMOELECTRIC PROPERTIES OF P-TYPE $(\text{Bi}_{1-x}\text{Sb}_x)_2\text{Te}_3$ FABRICATED BY MECHANICAL ALLOYING PROCESS

BOO YANG JUNG*, JAE SHIK CHOI*, TAE SUNG OH*, AND DOW-BIN HYUN**

*Depart. of Metall. and Mater. Sci., Hong Ik Univ., Seoul, Korea, ohts@wow.hongik.ac.kr

**Metals Division, Korea Institute of Science and Technology, Seoul 136-791, Korea

ABSTRACT

Thermoelectric properties of polycrystalline $(\text{Bi}_{1-x}\text{Sb}_x)_2\text{Te}_3$ ($0.75 \leq x \leq 0.85$), fabricated by mechanical alloying and hot pressing methods, have been investigated. Formation of $(\text{Bi}_{0.25}\text{Sb}_{0.75})_2\text{Te}_3$ alloy powder was completed by mechanical alloying for 5 hours at ball-to-material ratio of 5 : 1, and processing time for $(\text{Bi}_{1-x}\text{Sb}_x)_2\text{Te}_3$ formation increased with Sb_2Te_3 content x . When $(\text{Bi}_{0.25}\text{Sb}_{0.75})_2\text{Te}_3$ was hot pressed at temperatures ranging from 300°C to 550°C for 30 minutes, figure-of-merit increased with hot pressing temperature and maximum value of $2.8 \times 10^{-3}/\text{K}$ could be obtained by hot pressing at 550°C. When hot pressed at 550°C, $(\text{Bi}_{0.2}\text{Sb}_{0.8})_2\text{Te}_3$ exhibited figure-of-merit of $2.92 \times 10^{-3}/\text{K}$, which could be improved to $2.97 \times 10^{-3}/\text{K}$ with addition of 1 wt% Sb as acceptor dopant.

INTRODUCTION

Thermoelectric modules have been widely utilized to cool electronic devices such as integrated circuit packages, laser diodes and IR detectors, because quick and precise control of temperature is possible with almost no noise during operation [1,2]. As p-type materials for Peltier coolers used near room temperature, single crystal and polycrystalline $(\text{Bi,Sb})_2\text{Te}_3$ alloys have been extensively investigated and thermoelectric figure-of-merit of $(\text{Bi,Sb})_2\text{Te}_3$ alloys was optimized with composition near $(\text{Bi}_{0.25}\text{Sb}_{0.75})_2\text{Te}_3$ [1-4].

As a new processing technique, mechanical alloying has been applied to prepare polycrystalline thermoelectric materials in recent years [4-6]. Mechanical alloying is a technique in which intermetallic compound or alloy powders are fabricated from elemental powders through a sequence of collision events inside a high energy ball mill. Since mechanical alloying occurs near room temperature, this technique can be a cost-saving process for the production of polycrystalline thermoelectric materials compared to the conventional "vacuum melting/grinding" process where a long processing time, and high temperature and large scale facilities are required [4-6]. Also vaporization of calcogenide elements, such as Te, and segregation of dopants may be prevented in powders produced by mechanical alloying, as melting process is not involved during powder processing [5,7].

In this paper, thermoelectric properties of polycrystalline $(\text{Bi}_{1-x}\text{Sb}_x)_2\text{Te}_3$ ($0.75 \leq x \leq 0.85$), fabricated by mechanical alloying and hot pressing have been investigated with variation of Sb_2Te_3 content x , hot pressing temperature and the amount of excess Sb addition, as acceptor dopant.

EXPERIMENTAL PROCEDURE

High purity (> 99.99%) Bi, Sb, and Te granules were washed with 10% nitric solution, acetone, and distilled water to remove the surface oxide layer. The appropriate amounts of Bi, Sb and Te were weighed for $(\text{Bi}_{1-x}\text{Sb}_x)_2\text{Te}_3$ ($0.75 \leq x \leq 0.85$) compositions and charged in a hardened tool steel vial with steel balls as milling media under Ar atmosphere. Ball-to-material weight ratio was held 5 : 1. Mechanical alloying was conducted by shaking the vial at ~1200 rpm using a Spex mixer/mill. After the vibro-milling process, X-ray diffraction (XRD) analysis was performed to characterize the crystalline phases and lattice parameters of $(\text{Bi}_{1-x}\text{Sb}_x)_2\text{Te}_3$ formed by mechanical alloying. DTA was conducted in Ar ambient at a scan rate of 5°C/min for the as-mixed and mechanically alloyed powders.

$(\text{Bi}_{1-x}\text{Sb}_x)_2\text{Te}_3$ powders, fabricated by mechanical alloying, were cold pressed at 325 MPa to form 5 mm × 5 mm × 10 mm compacts. Hot pressing was conducted in vacuum at

temperatures ranging from 300°C to 550°C for 30 minutes. Seebeck coefficient α of the hot pressed specimens was measured at room temperature by applying temperature difference of 10°C at both ends of a specimen using a sub-heater. Electrical resistivity ρ and thermal conductivity κ were measured at room temperature using Harman method [8] in vacuum of 10^{-5} torr to minimize thermal conduction through convection. Figure-of-merit Z was characterized using the equation $Z = \alpha^2/\rho\kappa$.

RESULTS and DISCUSSION

XRD patterns of the as-mixed and mechanically alloyed powders, shown in Fig. 1, clearly illustrated the formation of $(\text{Bi}_{0.25}\text{Sb}_{0.75})_2\text{Te}_3$ alloy from elemental Bi, Sb and Te powders by mechanical alloying at room temperature.

DTA curves of the as-mixed and mechanically alloyed $(\text{Bi}_{0.25}\text{Sb}_{0.75})_2\text{Te}_3$ powders were shown in Fig. 2. For the as-mixed powder, endothermic peaks were observed at 272°C, 423°C and 617°C due to the melting of Bi, Te-rich Bi-Te eutectic, and $(\text{Bi}_{0.25}\text{Sb}_{0.75})_2\text{Te}_3$. Exothermic peak at 531°C was due to the reaction of Bi-Te melt with solid Sb to form $(\text{Bi}_{0.25}\text{Sb}_{0.75})_2\text{Te}_3$. Such peaks except one at 617°C disappeared in DTA for mechanically alloyed powder, which indicated the formation of $(\text{Bi}_{0.25}\text{Sb}_{0.75})_2\text{Te}_3$ by mechanical alloying. Endothermic peak at 417°C was due to the melting of Te-rich second phase. Melting point of Te-rich eutectic was 413°C and 425°C for Bi-Te and Sb-Te, respectively [9].

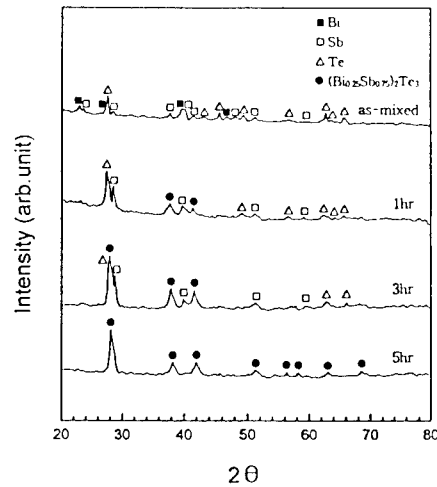


Fig. 1 XRD patterns of $(\text{Bi}_{0.25}\text{Sb}_{0.75})_2\text{Te}_3$ powders with mechanical alloying time.

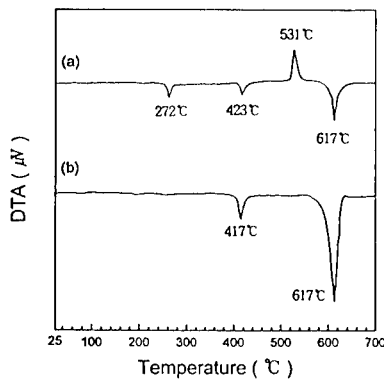


Fig. 2 DTA curves of (a) as-mixed (Bi, Sb, Te) powder and (b) mechanically alloyed $(\text{Bi}_{0.25}\text{Sb}_{0.75})_2\text{Te}_3$ powder.

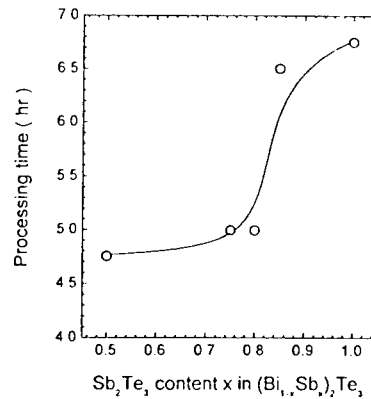


Fig. 3 Processing time for the complete formation of $(\text{Bi}_{1-x}\text{Sb}_x)_2\text{Te}_3$ by mechanical alloying with Sb_2Te_3 content x .

As shown in Fig. 3, processing time for the complete formation of $(\text{Bi}_{1-x}\text{Sb}_x)_2\text{Te}_3$ by mechanical alloying was increased with Sb_2Te_3 content x . Such retardation of the mechanical alloying process with increasing Sb_2Te_3 content might be due to the bonding characteristics between Bi_2Te_3 and Sb_2Te_3 . Enthalpy of formation ΔH_{mix} for Sb_2Te_3 and Bi_2Te_3 is -56.48 kJ/mol and -77.40 kJ/mol, respectively [10], and Sb-Te bond is weaker than Bi-Te bond [11].

Seebeck coefficient, electrical resistivity, thermal conductivity and figure-of-merit of $(\text{Bi}_{0.25}\text{Sb}_{0.75})_2\text{Te}_3$, mechanically alloyed and hot pressed at temperatures ranging from 300°C to 550°C , were illustrated in Fig. 4. Seebeck coefficient of mechanically alloyed $(\text{Bi}_{0.25}\text{Sb}_{0.75})_2\text{Te}_3$ was increased with hot pressing temperature up to 450°C and then decreased with further increase of hot pressing temperature. Electrical resistivity of $(\text{Bi}_{0.25}\text{Sb}_{0.75})_2\text{Te}_3$ was decreased with hot pressing temperature. In p-type $(\text{Bi,Sb})_2\text{Te}_3$ alloys, carriers are mainly generated by anti-structure defects (Sb or Bi substitution into Te site) [12]. With increasing the hot pressing temperature, thus, composition became more Te-deficient and anti-structure defects were formed more heavily, resulting in reduction of the electrical resistivity. Comparing Seebeck coefficient and electrical resistivity, it could be suggested that transition from intrinsic to extrinsic conduction in mechanically alloyed $(\text{Bi}_{0.25}\text{Sb}_{0.75})_2\text{Te}_3$ occurred at hot pressing temperature of 450°C . Lattice thermal conductivity κ_{ph} , illustrated in Fig. 4(c), was obtained by calculating κ_{el} with Lorentz factor of $\pi^2/3$ and subtracting κ_{el} from κ_{tot} . Lattice thermal conductivity of the mechanically alloyed and hot pressed $(\text{Bi}_{0.25}\text{Sb}_{0.75})_2\text{Te}_3$ was below 0.7 W/m·K, which is lower than the reported value for as-grown ingot (about 1 W/m·K) [13] due to the fine grain size of the mechanically alloyed and hot pressed samples.

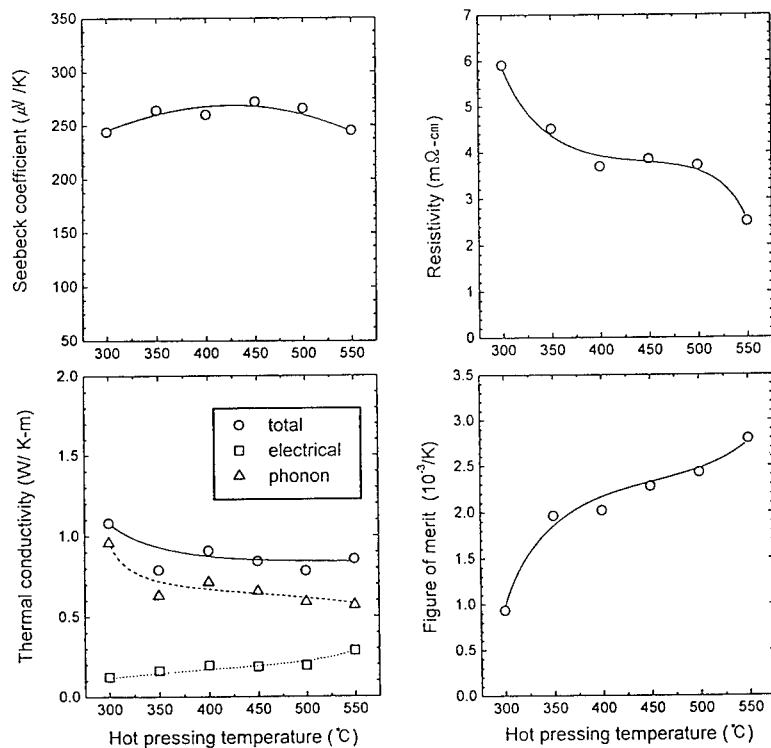


Fig. 4 (a) Seebeck coefficient, (b) electrical resistivity, (c) thermal conductivity and (d) figure-of-merit of mechanically alloyed $(\text{Bi}_{0.25}\text{Sb}_{0.75})_2\text{Te}_3$ with hot pressing temperature.

As shown in Fig. 4(d), figure-of-merit of the mechanically alloyed $(\text{Bi}_{0.75}\text{Sb}_{0.25})_2\text{Te}_3$ was increased with hot pressing temperature, and maximum value of $2.8 \times 10^{-3}/\text{K}$ was obtained by hot pressing at 550°C .

$(\text{Bi}_{1-x}\text{Sb}_x)_2\text{Te}_3$ ($0.75 \leq x \leq 0.85$) powders were fabricated by mechanical alloying (Fig. 3), and hot pressed at 550°C . Seebeck coefficient, electrical resistivity, thermal conductivity and figure-of-merit of $(\text{Bi}_{1-x}\text{Sb}_x)_2\text{Te}_3$ were illustrated in Fig. 5 with variation of Sb_2Te_3 content x . Seebeck coefficient of $(\text{Bi}_{1-x}\text{Sb}_x)_2\text{Te}_3$ was decreased from $245 \mu\text{V}/\text{K}$ to $170 \mu\text{V}/\text{K}$ with increasing Sb_2Te_3 content x from 0.75 to 0.85. As carrier concentration increased with increasing Sb_2Te_3 content in $(\text{Bi},\text{Sb})_2\text{Te}_3$ solid solutions, electrical resistivity of mechanically alloyed $(\text{Bi}_{1-x}\text{Sb}_x)_2\text{Te}_3$ was decreased from $2.51 \text{ m}\Omega\text{-cm}$ to $0.78 \text{ m}\Omega\text{-cm}$ with increasing Sb_2Te_3 content. Although total thermal conductivity of $(\text{Bi}_{1-x}\text{Sb}_x)_2\text{Te}_3$ increased with Sb_2Te_3 content x , lattice thermal conductivity exhibited almost constant value of $\sim 0.5 \text{ W}/\text{K}\text{-m}$ for $0.75 \leq x \leq 0.85$. For single crystal Bi_2Te_3 - Sb_2Te_3 , lattice thermal conductivity κ_{ph} reached a minimum at $\sim 70\%$ Sb_2Te_3 . κ_{ph} has been also reported to change a little in the composition range from $\sim 60\%$ to 80% Sb_2Te_3 , and then increase abruptly with Sb_2Te_3 content higher than 80% [2]. Comparing this report with the result in Fig. 5(c), it could be suggested that actual Sb_2Te_3 content in mechanically alloyed and hot pressed $(\text{Bi}_{1-x}\text{Sb}_x)_2\text{Te}_3$ were less than the weighed composition x . As shown in Fig. 5(d), figure-of-merit of $(\text{Bi}_{1-x}\text{Sb}_x)_2\text{Te}_3$ exhibited the maximum of $2.92 \times 10^{-3}/\text{K}$ at $x = 0.8$ composition.

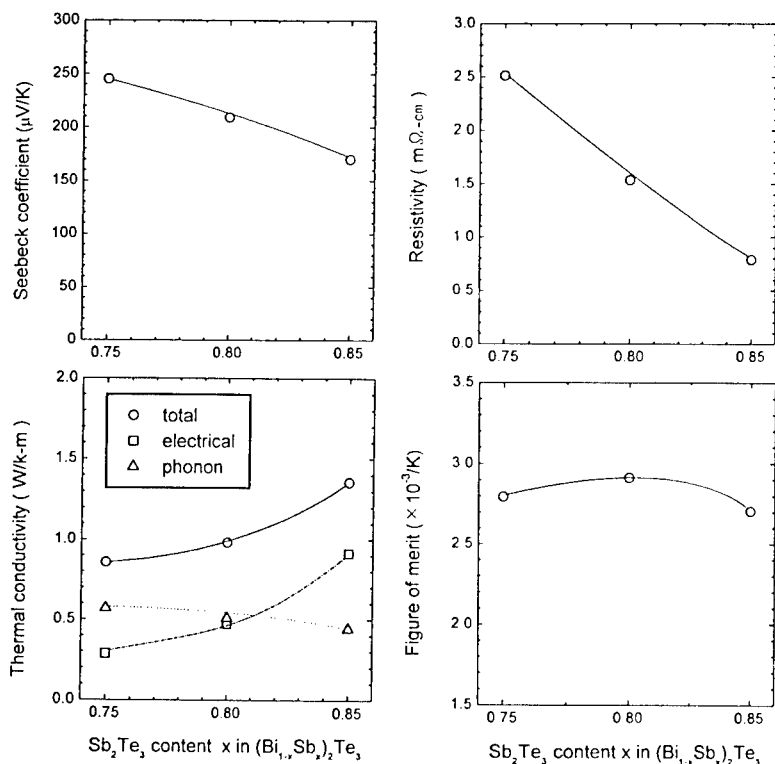


Fig. 5 (a) Seebeck coefficient, (b) electrical resistivity, (c) thermal conductivity and (d) figure-of-merit of $(\text{Bi}_{1-x}\text{Sb}_x)_2\text{Te}_3$ with Sb_2Te_3 content x .

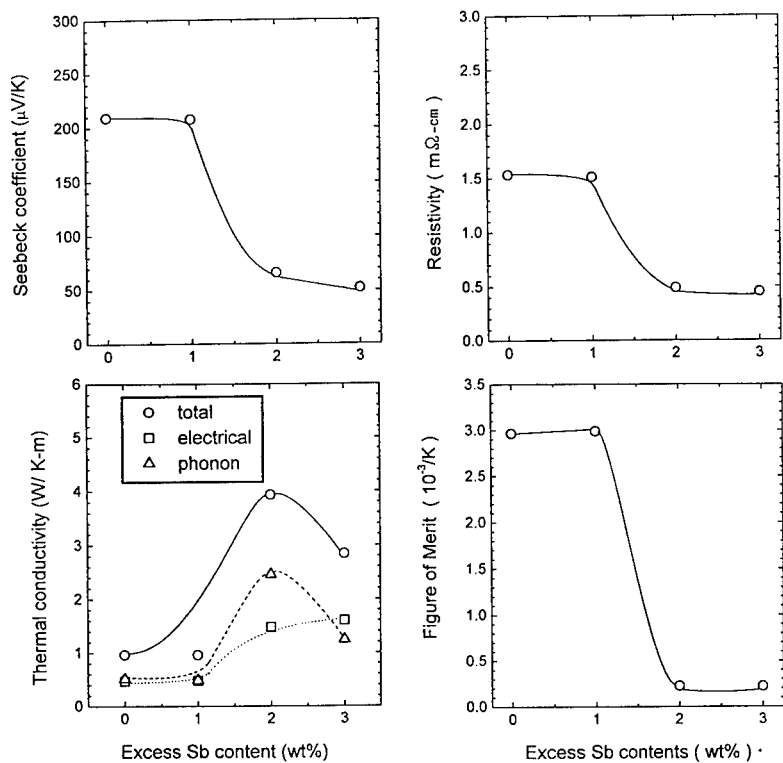


Fig. 6 (a) Seebeck coefficient, (b) electrical resistivity, (c) thermal conductivity and (d) figure-of-merit of $(\text{Bi}_{0.2}\text{Sb}_{0.8})_2\text{Te}_3$ with the amount of excess Sb.

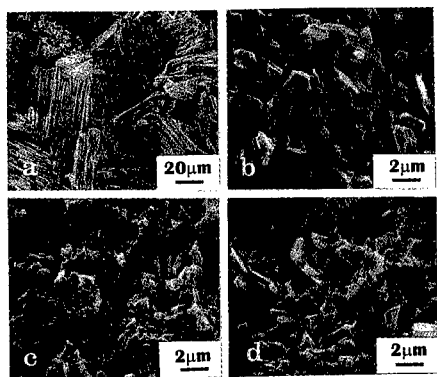


Fig. 7 SEM micrographs on the fracture surfaces of $(\text{Bi}_{0.2}\text{Sb}_{0.8})_2\text{Te}_3$ with addition of (a) 0 wt%, (b) 1 wt%, (c) 2 wt%, and (d) 3 wt% excess Sb, as acceptor dopant.

For Bi_2Te_3 based thermoelectric materials, Seebeck coefficient of $210 \sim 220 \mu\text{V/K}$ and electrical resistivity of $\sim 1.0 \text{ m}\Omega\text{-cm}$ are required to optimize figure-of-merit [2]. To improve the figure-of-merit of $(\text{Bi}_{0.2}\text{Sb}_{0.8})_2\text{Te}_3$ by lowering electrical resistivity, excess Sb up to 5 wt% was added as acceptor dopant to Bi, Sb and Te elemental powders. Then, powders were mechanically alloyed for 5 hours and hot pressed at 550°C for 30 minutes.

Thermoelectric properties of $(\text{Bi}_{0.2}\text{Sb}_{0.8})_2\text{Te}_3$ were illustrated in Fig. 6 with variation of the amount of excess Sb. Seebeck coefficient of $(\text{Bi}_{0.2}\text{Sb}_{0.8})_2\text{Te}_3$ decreased abruptly to $\sim 50 \mu\text{V/K}$ with addition of excess Sb more than 2 wt%, and variation of the electrical resistivity of $(\text{Bi}_{0.2}\text{Sb}_{0.8})_2\text{Te}_3$ exhibited the same behavior as Seebeck coefficient. Thermal conductivity of $(\text{Bi}_{0.2}\text{Sb}_{0.8})_2\text{Te}_3$ increased from 1 W/K-m to 4 W/K-m with addition of 2 wt% excess Sb. As shown in Fig. 7(d), figure-of-merit was slightly improved from $2.92 \times 10^{-3}/\text{K}$ to $2.97 \times 10^{-3}/\text{K}$ with addition of 1 wt% excess Sb, and then decreased abruptly to $\sim 0.5 \times 10^{-3}/\text{K}$ with further addition of Sb. As illustrated in SEM micrographs on the fracture surface of $(\text{Bi}_{0.2}\text{Sb}_{0.8})_2\text{Te}_3$, refinement of plate-like grains occurred with increasing the amount of excess Sb addition (Fig. 7).

SUMMARY

Formation of $(\text{Bi}_{0.2}\text{Sb}_{0.75})_2\text{Te}_3$ thermoelectric materials was completed by mechanical alloying of elemental Bi, Sb, Te granules of $\sim 4 \text{ mm}$ diameter for 5 hours at ball-to-material weight ratio of 5 : 1. Processing time for the complete formation of $(\text{Bi}_{1-x}\text{Sb}_x)_2\text{Te}_3$ by mechanical alloying increased with Sb_2Te_3 content x , which might be due to the bonding characteristics between Bi_2Te_3 and Sb_2Te_3 . When $(\text{Bi}_{0.2}\text{Sb}_{0.75})_2\text{Te}_3$ was hot pressed in vacuum for 30 minutes, figure-of-merit, measured at room temperature, increased from $0.93 \times 10^{-3}/\text{K}$ to $2.8 \times 10^{-3}/\text{K}$ with increasing hot pressing temperature from 300°C to 550°C . When hot pressed at 550°C for 30 minutes, $(\text{Bi}_{0.2}\text{Sb}_{0.8})_2\text{Te}_3$ and $(\text{Bi}_{0.15}\text{Sb}_{0.85})_2\text{Te}_3$ exhibited figure-of-merit of $2.92 \times 10^{-3}/\text{K}$ and $2.68 \times 10^{-3}/\text{K}$, respectively. Figure-of-merit of $(\text{Bi}_{0.2}\text{Sb}_{0.8})_2\text{Te}_3$ was slightly improved to $2.97 \times 10^{-3}/\text{K}$ with addition of 1 wt% excess Sb, and then decreased abruptly to $\sim 0.5 \times 10^{-3}/\text{K}$ with further addition of excess Sb.

ACKNOWLEDGMENTS

This work was supported by the Institute of Information Technology Assessment in Electronics and Telecommunication Research Institute of Korea.

REFERENCES

1. D. M. Rowe, CRC Handbook of Thermoelectrics, CRC Press, Inc., Boca Raton (1995).
2. W. M. Yim and F. D. Rosi, *J. Solid State Electronics*, **15**, 1121 (1972).
3. I. J. Ohsugi, T. Kojima and I. A. Nishida, *J. Appl. Phys.*, **68**, 5692 (1990).
4. K. Hasezaki, M. Nishimura, M. Umata, H. Tsukuda and M. Araoka, *Proc. 12th ICT*, 307 (1993).
5. B. A. Cook, B. J. Beaudry, J. L. Harringa and W. J. Barnett, *Proc. 9th ICT*, 234 (1990).
6. D. M. Rowe, V. S. Shukla and N. Savvides, *Nature*, **290**, 765 (1981).
7. A. Yanagitani, S. Nishikawa, Y. Kawai, S. Hayashimoto, N. Itoh and T. Kataoka, *Proc. 12th ICT* (1993) 281.
8. T. C. Harman, J. H. Cahn and M. J. Logan, *J. Appl. Phys.*, **30**, 9 (1959).
9. N. Kh. Abrikosov, V. F. Bankina, L. V. Poretskaya, L. E. Shelimova and E. V. Skudnova, *Semiconducting II-VI, IV-VI, and V-VI Compounds*, Plenum Press, New York (1969).
10. I. Barin, *Thermochemical Data of Pure Substances*, VCH, New York (1989).
11. G. R. Miller and C. Y. Li, *J. Phys. Chem. Solids*, **26**, 173 (1965).
12. J. Horak, K. Cermak and L. Koudelka, *J. Phys. Chem. Solid*, **47**, 805 (1986).
13. H. P. Ha, Y. W. Cho, J. Y. Byun and J. D. Shim, *Proc. 12th ICT*, 105 (1993).
14. J. Jaklovsky, R. Ionescu, N. Nistor and A. Chiculita, *Phys. Status Solidi(A)*, **27**, 329 (1975).

MICROSTRUCTURAL AND THERMOELECTRIC PROPERTIES OF P-TYPE Te-DOPED $\text{Bi}_{0.5}\text{Sb}_{1.5}\text{Te}_3$ AND N-TYPE SbI_3 -DOPED $\text{Bi}_2\text{Te}_{2.85}\text{Se}_{0.15}$ COMPOUNDS

J. SEO,* K. PARK,** C. LEE,* J. KIM***

*Department of Metallurgical Engineering, Inha University, Incheon 402-751, Korea

**Department of Materials Engineering, Chung-ju National University, Chungju, Chungbuk 380-702, Korea

***Advanced Manufacturing Processing Division, Korea Academy of Industrial Technology, Siheung, Kyunggi-do 429-450, Korea

ABSTRACT

The p-type Te-doped $\text{Bi}_{0.5}\text{Sb}_{1.5}\text{Te}_3$ and n-type SbI_3 -doped $\text{Bi}_2\text{Te}_{2.85}\text{Se}_{0.15}$ thermoelectric compounds were fabricated by hot pressing in the temperature range of 380 to 440 °C under 200 MPa in Ar. Both the compounds were highly dense and showed high crystalline quality. The grains of the compounds were preferentially oriented and contained many dislocations through the hot pressing. The fracture path followed the transgranular cleavage planes, which are perpendicular to the c-axis. In addition, with increasing the pressing temperature, the figure of merit was increased. The highest values of figure of merit for the p- and n-type compounds, which were obtained at 420 °C, were $2.69 \times 10^{-3}/\text{K}$ and $2.35 \times 10^{-3}/\text{K}$, respectively.

INTRODUCTION

Bi_2Te_3 -based compounds are well known to be good materials for the thermoelectric devices near room temperature. The crystal structure of Bi_2Te_3 at room temperature is rhombohedral ($a=0.438$ nm and $c=3.049$ nm) [1]. The crystal structure is composed of atomic layers in the order of $\text{Te/Bi/Te/Te/Bi/Te/Bi/Te/Te}/\dots$ along the c-axis. The Te/Te layers are considered to be weakly bound with van der Waal forces [2]. Also, the crystal has distinct (111) cleavage planes perpendicular to the c-axis. Owing to the cleavage features, the crystal has low mechanical properties and poor ability in micro-processing for fabricating the miniature thermoelectric modules. Many attempts were made to fabricate the thermoelectric materials without cleavage features by means of sintering. However, sintering technique is not effective because the figure of merit of sintered compounds is lower than that of single crystals. In this work, we fabricated the p-type Te-doped $\text{Bi}_{0.5}\text{Sb}_{1.5}\text{Te}_3$ and n-type SbI_3 -doped $\text{Bi}_2\text{Te}_{2.85}\text{Se}_{0.15}$ compounds by the hot pressing and then investigated the microstructure and thermoelectric properties of the compounds.

EXPERIMENTAL

To fabricate the p-type 4.0 wt% Te-doped $\text{Bi}_{0.5}\text{Sb}_{1.5}\text{Te}_3$ and n-type 0.1 wt% SbI_3 -doped $\text{Bi}_2\text{Te}_{2.85}\text{Se}_{0.15}$ compounds, the starting powders with >99.99 % purity were mixed. The mixture was placed into SiO_2 tube with 25 mm diameter and 330 mm length. Then, the tube was evacuated below 10^{-4} torr and sealed. The powders mixture was heated at 700 °C to make a melt. The melt in the tube was stirred under a frequency of 5 times/min at 700 °C for 6 hours using a rocking furnace to make a homogeneous melt without segregation. The tube containing the melt was cooled to room temperature in furnace. The solidified ingot was crushed into fine flakes using Al_2O_3 bowl. The resulting flakes were ball milled for 12 hours and then sieved to prepare powders with 45-74 μm size. To remove the oxygen developed during the crushing and ball milling, the resulting powders for the p- and n-type compounds were reduced in hydrogen atmosphere at 380 and 360 °C, respectively, for 4 hours. The powders were compacted by the hot pressing in the temperature range 380 to 440 °C at steps of 20 °C under 200 MPa in Ar to produce the billets with 30 mm diameter and 6 mm length.

The density of the hot-pressed compounds was measured by pycnometer (Micrometric Co.). The preferred orientation of grains was investigated by X-ray diffraction (XRD). Detailed microstructural information on the compounds was obtained

from transmission electron microscopy (TEM). TEM specimens were prepared by mechanical grinding, dimpling, and ion milling. Ion milling was performed under 1 mA current and 3 kV Ar ions at an incident angle of 12° with liquid nitrogen to minimize ion-induced damage. The microstructure of the specimens was investigated using a Philips CM20 transmission electron microscope.

The thermoelectric properties were measured at room temperature along the direction perpendicular to the pressing direction. The specimens with dimensions of 2×2×15 mm and of 4×4×4 mm were cut out of the compounds for the measurements of the Seebeck coefficient α and thermal conductivity κ and of the electrical resistivity ρ , respectively. Then, their surfaces were polished with a series of SiC polishing paper of up to #2000 and further polished on a polishing cloth impregnated with Al₂O₃ powders of 0.3 μ m size. To measure the Seebeck coefficient α , heat was applied to the specimen which was placed between the two Cu discs. The thermoelectric electromotive force E was measured upon applying small temperature difference ($\Delta T < 2$ °C) between the both ends of the specimen. The Seebeck coefficient α of the compounds was determined from the $E/\Delta T$. The electrical resistivity ρ was measured by the four-probe technique. The repeat measurement was made rapidly with a duration smaller than one second to prevent errors due to the Peltier effect. The thermal conductivity κ was measured by the static comparative method using a transparent SiO₂ ($\kappa=1.36$ W/Km at room temperature) as a standard sample in 5×10^{-5} torr.

RESULTS AND DISCUSSION

P-type 4.0 wt% Te-doped Bi_{0.5}Sb_{1.5}Te₃

It was found that the p-type Bi_{0.5}Sb_{1.5}Te₃ compounds were highly dense. The powders of the Bi_{0.5}Sb_{1.5}Te₃ compounds are flaky so that the flat faces of the powders are contacted by the hot pressing. The bonding between the powders became strong with increasing the pressing temperature, resulting in an increase in the density. The densities of the compounds hot pressed at 380, 400, and 420 °C were 98.0, 98.3, and 99.0 % of theoretical density, respectively. High quality compounds were not obtained at 440 °C because of the local melting of the powders.

To investigate the preferred orientation of grains, XRD analyses from the perpendicular and parallel sections to the pressing direction were made. Figures 1(a) and (b) show the XRD patterns obtained from the perpendicular and parallel sections, respectively, for the compounds hot pressed at 380, 400, and 420 °C. The intensity of the (0 0 15) and (0 0 18) planes from the perpendicular section is much stronger than that from the parallel section. Also, the intensity of (0 0 6) plane is only observed at the perpendicular section. The (0 0 6), (0 0 15), and (0 0 18) planes are perpendicular to the c-axis. This indicates that the grains are preferentially oriented through the hot pressing. It is also important to note that the intensity of the (0 0 6), (0 0 15), and (0 0 18) planes from the perpendicular section increased with the pressing temperature, strongly indicating that the degree of preferred orientation increased with the pressing temperature. It is thus expected that with increasing the pressing temperature, the increase in density and preferred orientation causes to an improvement in the thermoelectric properties. It has previously been reported that the preferred orientation of grains is observed in unidirectionally solidified materials, in which the growing direction is perpendicular to the c-axis [3]. Fig. 2 shows the TEM bright field image from the perpendicular section to the pressing direction for the compounds hot pressed at 420 °C. The grain size was found to be ~30 μ m. The compounds contain many dislocations within grains. The crystalline defects such as stacking faults and microtwins were not observed.

Table 1 shows the thermoelectric properties of the p-type compounds hot pressed at various temperatures. With increasing the hot pressing temperature, the carrier concentration n_c is decreased, whereas the carrier mobility μ is significantly increased. The increase in mobility results from the porosity decrease. At this time, the reason for the decrease in carrier concentration is unidentified. Also, as the pressing temperature is increased, the Seebeck coefficient α is slightly increased because of the decrease in carrier concentration. The relationship between the α and n_c can be expressed as follows: $\alpha \approx r - \ln n_c$, where r is the scattering factor [4]. The electrical resistivity ρ

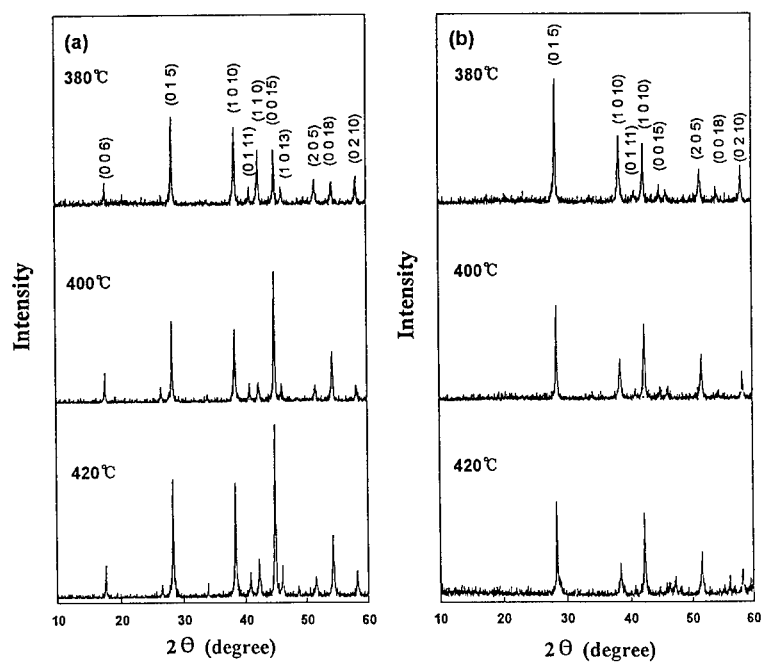


Fig. 1. XRD patterns from the (a) perpendicular and (b) parallel sections to the pressing direction for the p-type $\text{Bi}_{0.5}\text{Sb}_{1.5}\text{Te}_3$ compounds hot pressed at 380, 400, and 420 °C.

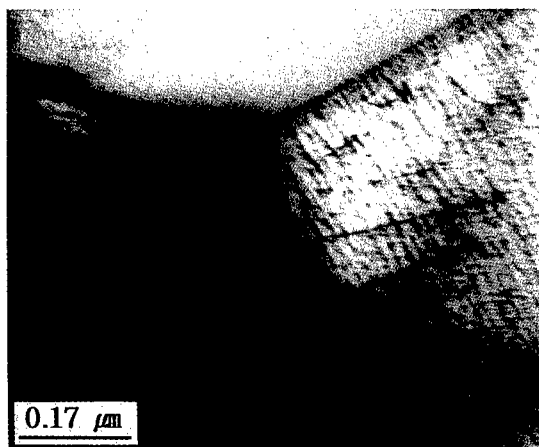


Fig. 2. TEM bright field image from the perpendicular section to the pressing direction for the p-type $\text{Bi}_{0.5}\text{Sb}_{1.5}\text{Te}_3$ compounds hot pressed at 420 °C.

Table 1. Thermoelectric properties of the p-type $\text{Bi}_{0.5}\text{Sb}_{1.5}\text{Te}_3$ compounds hot pressed at various temperatures

	Hot pressing temperature ($^{\circ}\text{C}$)		
	380	400	420
$n_e (\times 10^{23}/\text{m}^3)$	1.17	1.06	0.97
$\mu (\times 10^{-2} \text{m}^2/\text{Vs})$	2.07	2.83	3.77
$\alpha (\mu\text{V}/\text{K})$	218.4	224.3	232.2
$\rho (\times 10^{-9} \Omega \text{m})$	2.85	1.89	1.71
$\kappa (\text{W}/\text{Km})$	0.95	1.09	1.17
$Z (\times 10^{-4}/\text{K})$	1.76	2.44	2.69

of the compounds decreased with increasing the temperature. The electrical resistivity can be expressed as the following relationship: $\rho = 1/n_e e \mu$. Thus, two competing factors, carrier concentration and mobility, determine the resistivity. The decrease in resistivity would result from the significant increase in mobility and the decrease in carrier concentration. The thermal conductivity κ is slightly increased with the pressing temperature probably because of the density increase. The figure of merit Z was calculated using the following equation: $Z = \alpha^2 / \rho \kappa$. The figure of merit increased with the pressing temperature. This is because with increasing the pressing temperature, the Seebeck coefficient is slightly increased and the electrical resistivity is decreased, although the thermal conductivity is slightly increased. The compounds hot pressed at 420°C show the highest figure of merit ($Z = 2.69 \times 10^{-4}/\text{K}$).

N-type SbI_3 -doped $\text{Bi}_2\text{Te}_{2.85}\text{Se}_{0.15}$

The n-type SbI_3 -doped $\text{Bi}_2\text{Te}_{2.85}\text{Se}_{0.15}$ compounds were highly dense. The density increased with increasing the pressing temperature because of an improvement in the bonding between the powders. The densities of the compounds pressed at 380 , 400 , and 420°C were 97.9 , 98.5 , and 99.2% of theoretical density, respectively. Fig. 3 shows the



Fig. 3. TEM bright field image from the perpendicular section to the pressing direction for the n type $\text{Bi}_2\text{Te}_{2.85}\text{Se}_{0.15}$ compounds hot pressed at 420°C .

TEM bright field image from the perpendicular section to the pressing direction for the n-type compounds hot pressed at 420 °C. Many dislocations are present within the grains.

Figures 4(a) and (b) show the XRD patterns obtained from the perpendicular and parallel sections, respectively, for the compounds hot pressed at 420 °C. The intensity of (0 0 6), (0 0 15), and (0 0 18) planes, which are perpendicular to the c-axis, is only observed at the perpendicular section. This indicates that the grains are preferentially oriented through the hot pressing. The preferred orientation contributes to an improvement in the thermoelectric properties.

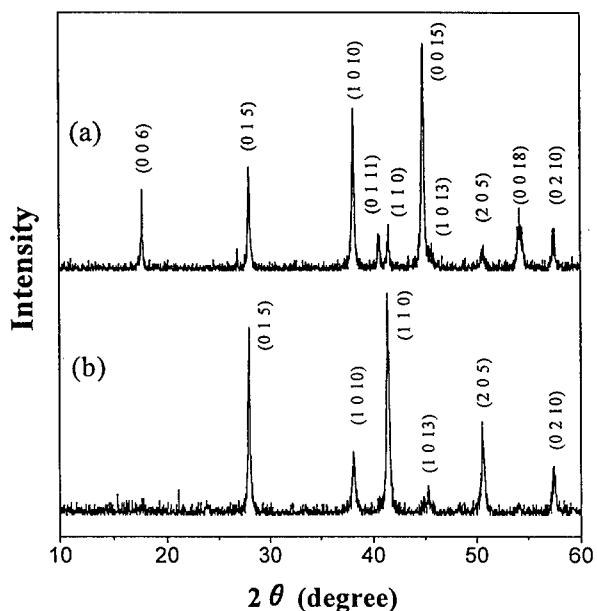


Fig. 4. XRD patterns obtained from the (a) perpendicular and (b) parallel sections to the pressing direction for the n-type $\text{Bi}_2\text{Te}_{2.85}\text{Se}_{0.15}$ compounds hot pressed at 420 °C.

Table 2 shows the thermoelectric properties of the n-type compounds pressed at various temperatures. As the pressing temperature is increased, the carrier concentration n_c is slightly decreased, whereas the mobility μ is increased due to the density increase. Also, with increasing the pressing temperature, the absolute value of Seebeck coefficient α is slightly increased due to the decrease in carrier concentration. The electrical resistivity ρ is slightly decreased with increasing the temperature because of the increase in mobility and the slight decrease in carrier concentration. In addition, the thermal conductivity κ is slightly increased with the temperature probably because of the density increase. The figure of merit, which was calculated using $Z = \alpha^2 / \rho \kappa$, increased with the pressing temperature. This is due to the fact that with increasing the temperature, the absolute value of Seebeck coefficient is slightly increased and the electrical resistivity is slightly decreased, although the thermal conductivity is slightly increased. The compounds hot pressed at 420 °C show the highest figure of merit ($Z = 2.35 \times 10^{-3} / \text{K}$).

Table 2. Thermoelectric properties of the n-type $\text{Bi}_2\text{Te}_{2.85}\text{Se}_{0.15}$ compounds hot pressed at various temperatures

	Hot pressing temperature ($^{\circ}\text{C}$)		
	380	400	420
n_c ($\times 10^{21}/\text{m}^3$)	5.16	5.08	4.50
μ ($\times 10^{-2} \text{m}^2/\text{Vs}$)	1.31	1.43	1.77
α ($\mu\text{V}/\text{K}$)	-150.3	-155.3	-161.9
ρ ($\times 10^{-3} \Omega\text{m}$)	0.92	0.86	0.79
κ (W/Km)	1.36	1.39	1.42
Z ($\times 10^{-3}/\text{K}$)	1.80	2.02	2.35

CONCLUSIONS

The hot-pressed p-type Te-doped $\text{Bi}_{0.5}\text{Sb}_{1.5}\text{Te}_3$ and n-type Sb₁₃-doped $\text{Bi}_2\text{Te}_{2.85}\text{Se}_{0.15}$ thermoelectric compounds were highly dense and showed high crystalline quality without any stacking faults and microtwins. The hot pressing gave rise to the preferred orientation of grains and the formation of many dislocations. It was also found that the figure of merit of both the compounds increased with increasing the pressing temperature. The values of figure of merit for the p- and n-type compounds hot pressed at 420°C were $2.69 \times 10^{-3}/\text{K}$ and $2.35 \times 10^{-3}/\text{K}$, respectively.

ACKNOWLEDGEMENTS

We would like to thank the support from the University Basic Research Support Fund (96-146) of Korea Ministry of Information and Communication.

REFERENCES

1. R. W. G. Wyckoff, Crystal Structure, Vol. 2, Interscience Publishers, New York, 1964.
2. J. R. Weise and L. Muller, J. Phys. Chem. Solids **15**, 13 (1960).
3. J. P. Fleurial, L. Gailliard, R. Triboulet, H. Scherrer, and S. Scherrer, J. Phys. Chem. Solids **49**, 1237 (1988).
4. K. Uemura and I. Nishida, Thermoelectric Semiconductors and Their Application, Nikkan-Kogyo Shinbun Press, Tokyo, Japan, 1988.

THE ENHANCEMENT OF THERMOELECTRIC POWER AND SCATTERING OF CARRIERS IN $\text{Bi}_{2-x}\text{Sn}_x\text{Te}_3$ SINGLE CRYSTALS

V.A. Kulbachinskii*, H. Negishi**, M. Sasaki**, Y. Giman**, M. Inoue**

*Low Temperature Physics Department, Physics Faculty, Moscow State University, 119899, Moscow, Russia

**Department of Material Science, Hiroshima University, Higashi-Hiroshima 739, Japan

ABSTRACT

Thermoelectric power, electrical resistivity, and Hall effect of p-type $\text{Bi}_{2-x}\text{Sn}_x\text{Te}_3$ ($0 < x < 0.03$) singlecrystals have been measured in the temperature range 4.2-300K. By doping of Sn atoms into the host Bi_2Te_3 lattice, the enhancement in the thermoelectric power is observed in the intermediate temperature range 30-150 K for $x \leq 0.0075$. The activation type behaviour of Hall coefficient and resistivity are found which corresponds to the Sn-induced impurity band located above the second lower valence band.

INTRODUCTION

Bismuth telluride Bi_2Te_3 is a typical layered semiconductor. Its valence and conduction bands (band gap $E_g \approx 0.18$ eV at $T=300$ K and $E_g \approx 0.23$ eV at $T=4.2$ K) are known to have many valley structures of six general ellipsoids in each case, with each ellipsoid centred on a one of a mirror plane of the Brillouin zone [1,2]. The occupation of Te lattice position by Bi atoms (antistructural defects) makes this material a p-type conductor. In addition, electronic properties of Bi_2Te_3 with incorporation of foreign atoms, such as Ge [3-5], Pb [6] and Sn [7-9] have been studied. Such Bi_2Te_3 -based compounds are widely used for practical applications to thermoelectric devices because of high figure of merit [10]. We have recently carried out conventional galvanomagnetic as well as pulsed laser induced "transient thermoelectric effect" (TTE) measurements for the $\text{Bi}_{2-x}\text{Sn}_x\text{Te}_3$ crystals [11]. Detailed analysis of the experimental results [7-9,11] have revealed that Sn is an acceptor and by doping Sn atoms in Bi_2Te_3 the Fermi energy of the upper valence band (UVB) is increased and Sn-induced impurity band (IB) is additionally formed near the top of the lower valence band (LVB) lying by about 15 meV below the top of the UVB (fig. 1).

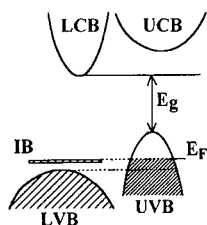


Fig. 1

Schematic band structure for $\text{Bi}_{2-x}\text{Sn}_x\text{Te}_3$. IB - impurity band, UCB - upper conduction band, LCB - lower conduction band.

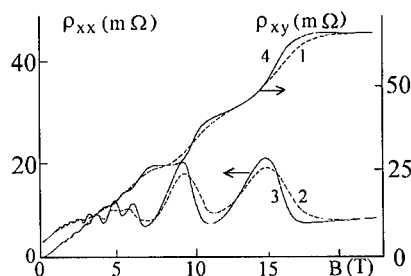


Fig. 2

Quantum Hall like oscillations of Hall resistivity ρ_{xy} and ρ_{xx} in $\text{Bi}_{2-x}\text{Sn}_x\text{Te}_3$ at $T=4.2$ K (1,2) and $T=1.5$ K (3,4).

Impurity band with high density of states fixes the Fermi level in $\text{Bi}_{2-x}\text{Sn}_x\text{Te}_3$ which leads to the oscillations of Hall resistance at low temperatures - fig. 2. However, the thermoelectric power for samples with a small addition of Sn atoms was not carried out. In order to get an insight into the effect of Sn substitution on the electronic properties of Bi_2Te_3 , we have carried out measurements of the thermoelectric power along C_2 axis, Hall effect, electrical resistivity for $\text{Bi}_{2-x}\text{Sn}_x\text{Te}_3$.

EXPERIMENT

Samples

Single crystals of p-type $\text{Bi}_{2-x}\text{Sn}_x\text{Te}_3$ ($0 < x < 0.03$) were grown by a modified Bridgman technique from polycrystalline materials synthesized from 5N purity elements in a conical quartz ampoule; the value of x correspond to the stoichiometry of the starting mixture. The crystals were easily cleaved perpendicular to the trigonal C_3 axis. Samples for transport measurements were cut from cleaved single crystal plates by a spark erosion machine (typical dimensions: $4 \times 1 \times 0.8 \text{ mm}^3$) and electrical leads were soldered by Bi-Sb alloys with a flux (glycerin + NH_4OH). The resistivity and Hall effect measurements were carried out using a conventional dc potentiometric method with dc current along the C_2 direction in magnetic fields up to 8 T applied along the C_3 axis (perpendicular to the layers) over the temperature range 4.2-300K. The temperature dependence of the Hall coefficient R_{H1} was obtained at fixed magnetic field $B \approx 0.2 \text{ T}$. Thermoelectric power was measured by a conventional method with a temperature difference between both ends of a sample less than 1 K and with reference to a Cu leads wire.

Experimental results

The temperature dependence of the resistivity ρ along the C_2 axis for $\text{Bi}_{2-x}\text{Sn}_x\text{Te}_3$ with different Sn content is shown in fig. 3. As the temperature is lowered, the resistivity ρ of undoped samples decreases almost linearly at high temperatures and tends to level off to residual resistivity ρ_0 , showing a metallic behaviour. It should be noted that the ρ -T curves for the $\text{Bi}_{2-x}\text{Sn}_x\text{Te}_3$ exhibit a shoulder or a maximum near 60 K, and the values of ρ_0 are increased with Sn concentration x . The similar behaviour has been reported earlier in the case of In doped samples [5]. The Hall coefficient R_{H1} of the undoped samples increases with increasing magnetic field, while those of Sn doped samples are strongly magnetic field dependent and oscillate.

With decreasing temperature the values of R_{H1} for undoped samples are decreased slowly below 200 K and approach to a constant value at lower temperatures. On the other hand, the Sn doped samples show quite different temperature dependence, in which the values of R_{H1} are increased remarkably with decreasing temperatures. Fig. 4 illustrates the semilogarithmic plots of R_{H1} versus $1/T$, showing the activation-energy type behaviour in the temperature range approximately 77 - 150 K of the form $R_{H1} \sim \exp(E_a/kT)$, where the slopes give the activation energy E_a ; $E_a \approx 10 \text{ meV}$ for $x = 0.0025 - 0.0125$ above 77 K. In this temperature range the same an activation behaviour was also observed in ρ (T) dependence - see fig. 3.

The Fermi energy evaluated from the period of Shubnikov de Haas oscillations (solely observed in lightly doped samples $x < 0.02$ [8,9]) and the observed Hall coefficient at low temperature $T = 4.2 \text{ K}$ (where these values are almost constant for $x < 0.0075$) show a characteristic variation with Sn content, which we shall discuss later. The temperature dependence of the Hall mobility $\mu_{H1} = R_{H1}/\rho$ is shown in logarithmic scales in fig. 5. With

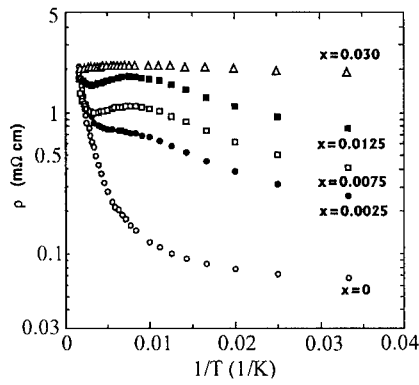


Fig. 3

The semilogarithmic plot of the resistivity ρ versus $1/T$, showing the activation-type behaviour in $\text{Bi}_{2-x}\text{Sn}_x\text{Te}_3$ in the temperature range approximately 77 - 150 K

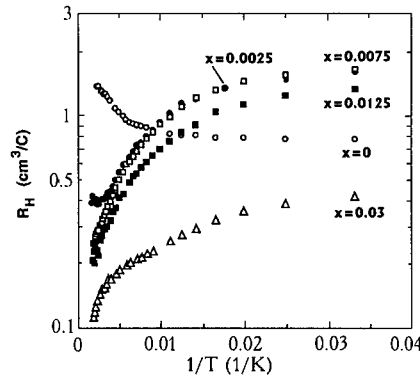


Fig. 4

The semilogarithmic plot of the Hall coefficient R_H versus $1/T$, showing the activation-type behaviour in $\text{Bi}_{2-x}\text{Sn}_x\text{Te}_3$ in contrast to Bi_2Te_3 .

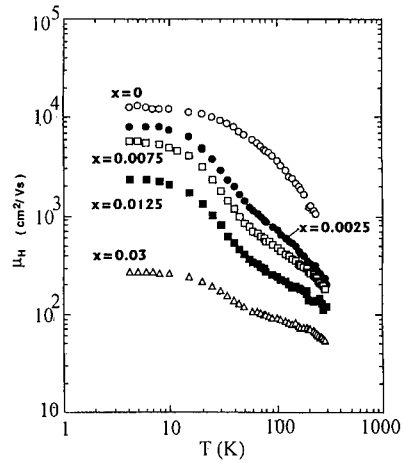


Fig. 5

Temperature dependence of the observed Hall mobility $\mu_H = R_H/\rho$ for $\text{Bi}_{2-x}\text{Sn}_x\text{Te}_3$.

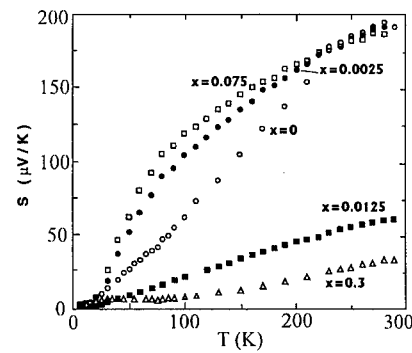


Fig. 6

Temperature dependence of the observed thermopower S for $\text{Bi}_{2-x}\text{Sn}_x\text{Te}_3$.

lowering temperature, the Hall mobilities for Bi₂Te₃ are increased obeying the power law, $\mu_H = T^{-m}$, with $m=1.5-2.2$ above 100 K, and approach constant values of the order of 10^4 cm²/Vs at low temperatures. The magnitude of the exponent m indicates that the intervalley scattering by polar optical and acoustic phonons are dominant above 100 K. With increasing Sn content x , the magnitudes of μ_H and the exponent m decreased, while sharp changes in the slopes of the μ_H - T curves are noticed at the intermediate temperature range 30- 70 K, corresponding to the anomalies in the ρ - T curves, which are in contrast to the case of Ge-doped samples of Bi₂Te₃, where the Ge atoms serve as weak acceptors [3-5]. Fig. 6 shows the temperature dependence of the thermopower S . The undoped Bi₂Te₃ has a value of 190 μ V/K at room temperature and it shows almost a linear decrease with decreasing T ; the values of S/T are nearly constant ($=0.70 \pm 0.05$ μ V/K²) above 100K. Bi_{2-x}Sn_xTe₃ crystals with low Sn content $x=0.0025$ and 0.0075 have nearly the same values as the undoped one at room temperature but the S - T curves show a more convex change with larger values in the intermediate temperature range 30-200 K compared to that of the undoped sample. For heavily doped samples with $x=0.0125$ and 0.03 , the thermopowers are reduced appreciably to almost a quarter or one fifth of the undoped value, showing nearly a linear dependence on T .

DISCUSSION

For a discussion of the foregoing transport data, we will use a band model for p-type Sn doped Bi₂Te₃ crystals [7-9,11] with reference to the host Bi₂Te₃, as shown schematically in fig. 1. In the host Bi₂Te₃ there exist a number of antistructural defects (ASD), which donates conduction holes into the UVB (or accept electrons from the UVB) up to a Fermi energy E_F ; the number of the ASD depend on the crystal growth. With increase of the number of ASDs, the hole Fermi energy is increased to fill up to the lower LVB. The activation behaviour of ρ (fig. 3) and the Hall coefficient (fig. 4) in the temperature range $77 < T < 150$ K indicates the existence of the Sn-induced acceptor level located by about 10 meV above the top of the LVB or an impurity band that lies below the top of UVB by 15 meV as it is shown in fig. 1.

Thus it is inferred that at intermediate temperatures we observe the activation of holes to the impurity band. The number of states in the impurity band increases when the Sn content increases, thus the impurity band fix the Fermi level up to high Sn content. For temperature range $10 < T < 50$ K the Hall coefficient still shows the activation on temperature, while the resistivity shows the metallic behaviour. According to our opinion such dependencies may be explained by a redistribution of carriers in this temperature range between different valleys due to different rate with temperature.

In a model of two degenerate hole gases the Hall coefficient R_H should always decrease with increasing of magnetic field when the influence of a geometrical factor in R_H for the second type of holes is neglected. The experimental results at $T=4.2$ K show an increase of R_H with magnetic field in the host Bi₂Te₃. Such dependence of the R_H on B may be explained if we take into account the anisotropy factor for the two types of hole (two and four ellipsoids in C_2 direction respectively). This procedure was done in [5] which explained the observed increase of the R_H in magnetic field. The oscillatory magnetic field dependence of R_H was observed for Sn doped samples - see fig. 2.

The impurity band with a high density of states fixes the Fermi level. In magnetic field the energy spectrum of UVB ("light holes") is quantized, while for the "heavy holes" in LVB magnetic field is still weak due to difference in effective masses. The degeneracy of the Landau levels in magnetic field increases and if the Fermi level is fixed in impurity band, holes flow from impurity band to UVB and, hence, the Hall coefficient or Hall resistance will strongly oscillate (like in Quantum Hall effect) as it was observed (see fig. 2).

The thermopower S in the impurity conduction region is given by

$$S(T) = (k/e) \left[(2r+5)/(2r+3) \{ F_{r+3/2}(\xi)/F_{r+1/2}(\xi) - \xi \} \right] \quad (1)$$

where

$$F_r(\xi) = \int_0^\infty (x^r / e^{x-\xi}) dx \quad (2)$$

is the Fermi integral and $\xi = E_F/kT$ is the reduced Fermi energy, r is a parameter characterising the scattering mechanism [12]; $r = -1/2$ for the acoustic phonon scattering and $1/2$ for polar optical phonon one. Using the value of $S = 190 \mu V/K$ at room temperature and $r = 1/2$ which is very close to the calculated from experimental data value of r [13] in Bi_2Te_3 for polar optical scattering, E_F is evaluated to be near 20 meV, which is of comparable order of magnitude but less of the value obtained from the Hall concentration. These results indicate that in Bi_2Te_3 holes in the UVB can not be treated as a completely degenerate nor nondegenerate system around room temperature; in fact, we should note that Bi_2Te_3 has an exceptionally large dielectric constant $\epsilon = 94$ [14] compared to normal value of the order of 5-20 for usual semiconductors, such as Si, Ge, GaAs.

Moreover, for lightly doped samples $x < 0.0075$, we have found an appreciable enhancement in S in the intermediate temperature range 30-200 K by Sn-doping (Fig. 6). Now the thermopower S for multi-scattering centres is given by

$$S = \sum (\rho_i S_i / \rho), \quad \rho = \sum \rho_i \quad (3)$$

where ρ_i and S_i are the resistivity and thermopower for the i -th scattering centres (i =neutral, ionized impurity scattering, and phonon scattering), respectively. Thus corresponding to the contribution of ionized impurity scattering term $\rho_{(ion)}$ to the resistivity and to the Hall mobility (scattering parameter $r=3/2$), the $\rho_{(ion)} S_{(ion)}$ term play a dominant role in the total thermopower in $Bi_{2-x}Sn_xTe_3$, compared to those of the neutral impurity terms. On the other hand, for heavily doped samples with $x > 0.0125$, the S - T curve is nearly linear and the magnitude S decreases with x , which suggest that the hole system is degenerate and the carriers in the impurity band play a dominant role at high temperatures.

For further quantitative discussion for $Bi_{2-x}Sn_xTe_3$, we need more detailed calculations based on the multicarrier model consisting of the two valence and six-ellipsoidal pockets (UVB, LVB) and Sn induced impurity band by taking account of the degeneracy or screening of the holes in each band of this material with the large dielectric constant. Fitting the data of Fig. 6 with eq.(1) at each temperature yields to the temperature dependence of the r .

Our data shows that near $T=100$ K the scattering in $Bi_{2-x}Sn_xTe_3$ changes from phonon to impurity scattering. The intervalleys scattering also plays an important role at the intermediate temperature range in this complex many valleys material with impurity band. Indeed, the observed Hall mobility μ_H for $Bi_{2-x}Sn_xTe_3$ may be the sum of each contribution from the charged impurity scattering centres, as well as phonon scattering. At low temperatures the Hall mobilities for all samples are constant, which is regarded as a temperature-independent scattering term $\mu_{(neutral)}$ due to some neutral centres.

Then in addition to this contribution, the total Hall mobility $\mu_H(T)$ may be determined by temperature-dependent phonon $\mu_{(ph)}$ and ionized impurity scattering $\mu_{(ion)}(T)$, which we express, as

$$1/\mu_H(T) = 1/\mu_{(ph)}(T) + 1/\mu_{(ion)}(T) + 1/\mu_{(neutral)}(T) \quad (4)$$

Then the temperature-dependent term $\mu(T)$ can be obtained by subtracting the temperature-independent $\mu(\text{defect})$ from the total mobility $\mu_{\text{it}}(T)$, as

$$1/\mu(T) = 1/\mu_{\text{it}}(T) - 1/\mu_{\text{(neutral)}}(T) = 1/\mu_{\text{(ph)}}(T) + 1/\mu_{\text{(ion)}}(T) \quad (5)$$

The temperature dependence of $\mu(T)$ for Bi_2Te_3 follows approximately the power law, as $\mu_{\text{it}} = T^{-m}$ with $m=1.6$, while for the $\text{Bi}_{2-x}\text{Sn}_x\text{Te}_3$, the mobility $\mu(T)$ is decreased with increasing Sn content x and obeys the power law a large value $m=(2-2.6)$ at low temperatures and a smaller value $m=1/2-1$ at higher temperatures. There is apparently indication for intermediate temperatures of the contribution from the intervalley scattering and no indication of the contribution from conventional ionized impurity scattering that depends on T as a power law with $m=3/2$. These results indicate that in both Bi_2Te_3 and $\text{Bi}_{2-x}\text{Sn}_x\text{Te}_3$ crystals, phonon scatterings dominate, such as acoustic, optical phonon, or piezoelectric scattering. In this respect, $\text{Bi}_{2-x}\text{Sn}_x\text{Te}_3$ system is a unique material, where Sn atoms substitute partially the Bi atoms within their layers that donate conduction holes to the Bi_2Te_3 valence band, leading to the formation of Sn-induced impurity band. This band may be strongly coupled with the host UVB and thus these impurity centres may subject to nearly the same lattice vibrations as the host ones; for further details, lattice dynamical studies of these materials will be required.

CONCLUSION

In summary, the transport properties and thermopower along the C_2 axis of the $\text{Bi}_{2-x}\text{Sn}_x\text{Te}_3$ are understood by considering the formation of Sn-induced impurity band near the main valence bands. Thermal excitation of holes in the Sn-induced impurity centres leads to an increase in the number of ionized impurity centres and holes in the impurity band, which give rise to the enhancement in the thermopower, the resistivity, and Hall effect of this unique material system.

REFERENCES

1. A. von Middendorf A., and G. Lanwehr G., Sol. State Com. **11**, p.203 (1972).
2. H. Kohler H., Phys. Stat. sol. (b) **74**, p.591 (1976).
3. H. Tamura, Jpn. J. Appl. Phys. **5**, p.1169 (1966).
4. M. Predota, and L. Benesh, Phys. stat. sol. (a) **100**, p.401 (1987).
5. N.B. Brandt, and V.A. Kulbachinskii, Semicond. Sci. Technol. **7**, p.907 (1992).
6. S. Biswas, and R. Bhattacharya, phys. stat. sol. (b) **151**, p.193 (1989).
7. V.A. Kulbachinskii, N.E. Klokova, S.Ya. Skipidarov, J. Horak. P. Lostak. and S.A. Azou, Vestnik Moskovskogo Universiteta, Fizika, 30, N3, p.68 (1989) , (for English translation see: Sov. Phys. Vestnik MGU, Physics, **30**, (1989)).
8. V.A. Kulbachinskii, N.B. Brandt, P.A. Cheremnykh, et al. phys. stat. sol. (b) **150**, p.247, (1988).
9. V.A. Kulbachinskii, N.E. Klokova, J. Horak. P. Lostak, S.A. Azou, G.A. Mironova, Fiz. Tverd. Tela (Leningrad) **31**, p.2218 (1989); (for English translation see: Sov. Phys. Solid State **31**, (1989)).
10. H.J. Goldshmitt, Adv. Phys. **14**, p.273, (1965).
11. V.A. Kulbachinskii, M. Inoue, M. Sasaki, H. Negishi, W.X. Gao, K. Takase, Y. Giman, P. Lostak, and J. Horak, Phys. Rev. B, **50**, p.16921 (1994).
12. K. Seeger, Semiconductor Physics, Springer-Verlag, New York 1973.
13. V.A. Kulbachinskii, H. Negishi, M. Sasaki, et al., phys. stat. sol. (b) **199**, p.505, (1997).
14. R. Sehr, and L.R. Testardi, J. Phys. Chem. Solids **23**, p.19 (1962).

MICROSTRUCTURE, MECHANICAL PROPERTIES, AND THERMOELECTRIC PROPERTIES OF HOT-EXTRUDED P-TYPE Te-DOPED $\text{Bi}_{0.5}\text{Sb}_{1.5}\text{Te}_3$ COMPOUNDS

K. PARK,* J. SEO,** C. LEE**

*Department of Materials Engineering, Chung-ju National University, Chungju, Chungbuk 380-702, Korea

**Department of Metallurgical Engineering, Inha University, Incheon 402-751, Korea

ABSTRACT

The p-type $\text{Bi}_{0.5}\text{Sb}_{1.5}\text{Te}_3$ compounds with Te dopant (4.0 and 6.0 wt%) and without dopant were fabricated by hot extrusion in the temperature range of 300 to 510 °C under an extrusion ratio of 20:1. The undoped and Te doped compounds were highly dense and showed high crystalline quality. The grains contained many dislocations and were fine equiaxed ($\sim 1.0 \mu\text{m}$) owing to the dynamic recrystallization during the extrusion. The hot extrusion gave rise to the preferred orientation of grains. The bending strength and the figure of merit of the undoped and Te doped compounds were increased with increasing the extrusion temperature. The Te dopant significantly increased the figure of merit. The values of the figure of merit of the undoped and 4.0 wt% Te-doped compounds hot extruded at 440 °C were $2.11 \times 10^{-3}/\text{K}$ and $2.94 \times 10^{-3}/\text{K}$, respectively.

INTRODUCTION

Bismuth telluride (Bi_2Te_3) compounds have been used as thermoelectric cooling and heating materials, since they have the high figure of merit at room temperature. The compounds have a rhombohedral structure ($a=0.438 \text{ nm}$ and $c=3.049 \text{ nm}$) and belong to space group $R\bar{3}m$ [1]. The electrical and mechanical properties along the direction parallel to the (111) cleavage plane are better than those along the direction perpendicular to the plane, i.e., the c-axis [2, 3]. Since the compounds have the cleavage features, they have difficulty for the mass production of small thermoelectric modules. It has been reported that the phonons for SiGe alloys are scattered at the grain boundaries. The scattering gives rise to a decrease in the thermal conductivity, resulting in an increase in the thermoelectric performance [3, 4]. One way of increasing the scattering is by refining the grain size. The grain refinement can be achieved by hot extrusion. In this work, we fabricated the p-type undoped and Te doped $\text{Bi}_{0.5}\text{Sb}_{1.5}\text{Te}_3$ compounds by hot extrusion and then investigated the thermoelectric properties of the compounds.

EXPERIMENTAL

To fabricate the hot-extruded p-type undoped and Te (4.0 and 6.0 wt%) doped $\text{Bi}_{0.5}\text{Sb}_{1.5}\text{Te}_3$ compounds, the mixture of starting powders with >99.99 % purity was heated at 700 °C to make a melt. The solidified ingot was crushed into fine flakes using Al_2O_3 bowl. The resulting flakes were ball milled for 12 hours and then sieved to prepare powders with 45–74 μm size. The powders were compacted by hot pressing at 420 °C under 200 MPa in Ar to produce the billets with 30 mm diameter and 6 mm length. Subsequently, the compacted billets were hot extruded in the temperature range 300 to 510 °C at steps of 70 °C under an extrusion ratio of 20:1 and a ram speed of 50 mm/min.

The microstructure of the compounds was investigated by transmission electron microscopy (TEM) and X-ray diffraction (XRD). TEM specimens were prepared by mechanical grinding, dimpling, and ion milling. The microstructure of the specimens was investigated using a Philips CM20 transmission electron microscope. The thermoelectric properties of the hot-extruded compounds were measured at room temperature along the direction parallel to the extrusion direction. To measure the Seebeck coefficient α , heat was applied to the specimen which was placed between the two Cu discs. The thermoelectric electromotive force E was measured upon applying small temperature difference ($\Delta T < 2 \text{ }^\circ\text{C}$) between the both ends of the specimen. The Seebeck coefficient α of the compounds was determined from the $E/\Delta T$. The electrical resistivity ρ was

measured by the four-probe technique. The repeat measurement was made rapidly with a duration smaller than one second to prevent errors due to the Peltier effect. The thermal conductivity κ was measured by the static comparative method using a transparent SiO_2 ($\kappa=1.36$ W/Km at room temperature) as a standard sample in 5×10^{-5} torr.

RESULTS AND DISCUSSION

Microstructure

High-quality extruded bars without any defects such as tearing, orange peel, and blister were obtained in the hot extrusion temperatures of 300-440 °C. However, hot cracks were developed during the hot extrusion at 510 °C. This would result from the local melting due to the heat formed by the friction between the billet and die. The density of the compounds increased with increasing the extrusion temperature. This increase arises due to an improvement in the bonding between the powders. The highest density was obtained at 440 °C and its value was 99.6 % of theoretical density.

The bending strength of the hot extruded compounds increased with increasing the extrusion temperature due to the porosity decrease. The bending strength of the compounds hot extruded at 440 °C was 92 MPa. The fractograph of the compounds hot extruded at 440 °C is shown in Fig. 1. It is apparent that the fractograph represents the transgranular cleavage features. The fracture path follows the transgranular cleavage planes. The orientation change from grain to grain is also found. The grain size estimated from this fractograph is $\sim 1.0 \mu\text{m}$.

The XRD patterns obtained from the compounds hot extruded at 440 °C are shown in Fig. 2. Figures 2(a) and (b) show the XRD patterns obtained from the perpendicular and parallel sections to the extrusion direction, respectively. The intensity of (0 0 6), (0 0 15), and (0 0 18) planes, which are perpendicular to the c-axis, is only observed at the parallel section. This indicates that the hot extrusion gave rise to the preferred orientation of grains. The preferred orientation contributes to an improvement in the thermoelectric properties.

Figures 3(a) and (b) show the TEM bright field images from the perpendicular and parallel sections to extrusion direction, respectively, for the compounds hot extruded at 440 °C. It is evident that the grains are fine equiaxed ($\sim 1.0 \mu\text{m}$) and contain many dislocations. This leads to the suggestion that dynamic recrystallization (DRX) occurred during the hot extrusion. The DRX is important for increasing the ductility during the extrusion and refining the grains. Also, the DRX significantly improves the product mechanical strength and toughness. The crystalline defects such as stacking faults and microtwins are not found.

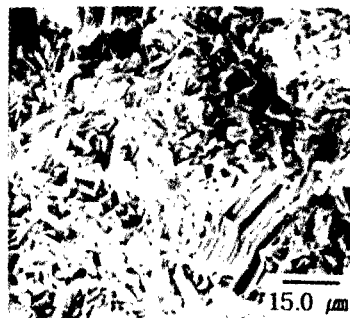


Figure 1. Fractograph of the compounds hot extruded at 440 °C.

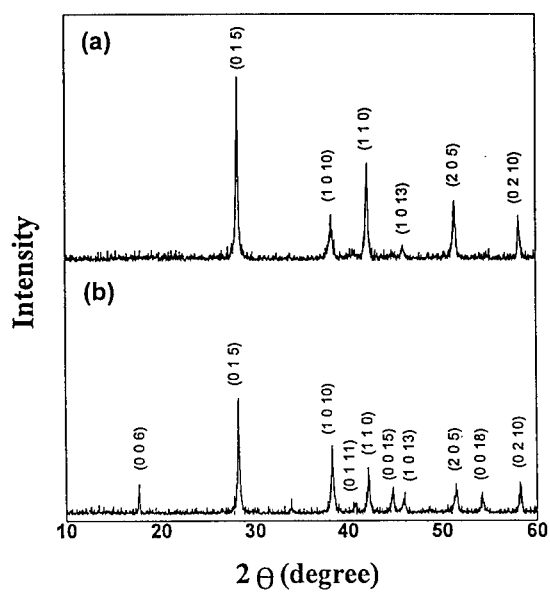


Figure 2. XRD patterns obtained from the (a) perpendicular and (b) parallel sections to the hot extrusion direction for the compounds hot extruded at 440 °C.

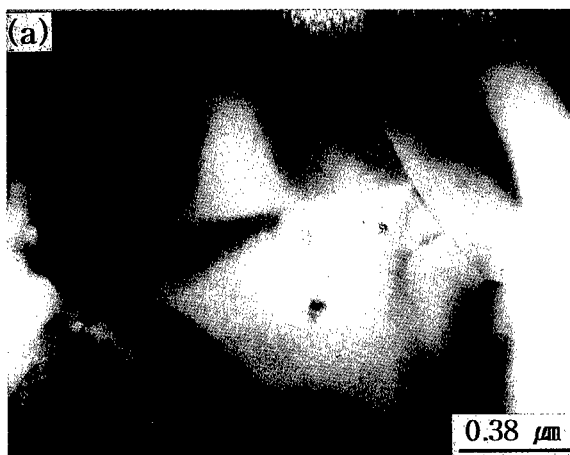




Figure 3. TEM bright field images obtained from the (a) perpendicular and (b) parallel sections to the extrusion direction for the compounds extruded at 440 °C.

Effect of Extrusion Temperature on Thermoelectric Properties

Table 1 shows the thermoelectric properties of the 4.0 wt% Te-doped compounds hot extruded at various temperatures. As the extrusion temperature is increased, the carrier concentration n_c is decreased and the mobility μ is significantly increased. The significant increase in mobility arises due to the porosity decrease. At present, we do not know the origin of the decrease in carrier concentration. The Seebeck coefficient α increased with increasing the extrusion temperature because of the decrease in carrier concentration. As the hot extrusion temperature is increased, the electrical resistivity ρ is significantly decreased. The electrical resistivity can be expressed as the following relationship: $\rho = 1/n_c e \mu$. Thus, the decrease in electrical resistivity would result from the significant increase in mobility and the decrease in carrier concentration. Also, the thermal conductivity κ increased with increasing the temperature. The increase in thermal conductivity would result from the decrease in porosity and the decrease in phonon-grain boundary scattering. The figure of merit Z was calculated using the following equation: $Z = \alpha^2 / \rho \kappa$. The figure of merit increased with the extrusion temperature. This is due to the fact that with increasing the extrusion temperature, the Seebeck coefficient is increased and the electrical resistivity is significantly decreased, although the thermal conductivity is increased. The compounds hot extruded at 440 °C show the highest figure of merit ($Z = 2.94 \times 10^{-3} / \text{K}$).

Effect of Te dopant contents on thermoelectric properties

Table 2 shows the variation of thermoelectric properties with Te dopant contents for the compounds hot extruded at 440 °C. The Te dopants are excited so that they become cations and release the electrons, thus decrease the holes. Consequently, with increasing the Te contents, carrier concentration n_c is decreased, giving rise to the increase in the Seebeck coefficient α . The electrical resistivity ρ increased with increasing the dopant contents because of the increase in scattering by the carriers. In addition, the thermal conductivity κ decreased with the dopant contents because the phonons were scattered by the ionized Te impurity. The value of figure of merit Z shown in Table 2 was

calculated using $Z = \alpha^2 / \rho \kappa$. This table represents that the Te dopant significantly increased the figure of merit. The figure of merit of the undoped and 4.0 wt% Te-doped $\text{Bi}_{0.5}\text{Sb}_{1.5}\text{Te}_3$ compounds are $2.11 \times 10^{-3}/\text{K}$ and $2.94 \times 10^{-3}/\text{K}$, respectively.

Table 1. Thermoelectric properties of the 4 wt% Te-doped $\text{Bi}_{0.5}\text{Sb}_{1.5}\text{Te}_3$ compounds hot extruded at various temperatures

	Hot extrusion temperature ($^{\circ}\text{C}$)		
	300	370	440
n_c ($\times 10^{20}/\text{m}^3$)	1.23	0.98	0.85
μ ($\times 10^{-2} \text{m}^2/\text{Vs}$)	0.73	1.68	3.96
ρ ($\times 10^{-9} \Omega \text{m}$)	6.92	3.79	1.85
α ($\mu\text{V}/\text{K}$)	145.8	207.1	231.1
κ (W/Km)	0.46	0.69	0.98
Z ($\times 10^{-3}/\text{K}$)	0.67	1.63	2.94

Table 2. Thermoelectric properties as a function of Te dopant content for the compounds hot extruded at 440°C

	Te dopant content (wt %)		
	0.0	4.0	6.0
n_c ($\times 10^{20}/\text{m}^3$)	1.16	0.85	0.81
μ ($\times 10^{-2} \text{m}^2/\text{Vs}$)	3.29	3.96	3.53
ρ ($\times 10^{-9} \Omega \text{m}$)	1.63	1.85	2.18
α ($\mu\text{V}/\text{K}$)	204.3	231.1	238.1
κ (W/Km)	1.21	0.98	0.94
Z ($\times 10^{-3}/\text{K}$)	2.11	2.94	2.76

CONCLUSIONS

The p-type undoped and Te doped $\text{Bi}_{0.5}\text{Sb}_{1.5}\text{Te}_3$ compounds were highly dense. The grains were fine equiaxed ($\sim 1.0 \mu\text{m}$) and contained many dislocations due to the dynamic recrystallization during the extrusion. The grains were also preferentially oriented through the hot extrusion. The high density and fine grains contributed to an increase in the bending strength and figure of merit. The bending strength and figure of merit were increased with increasing the extrusion temperature. Also, the Te dopant significantly increased the figure of merit. The bending strength and the figure of merit of the 4.0 wt% Te doped compounds hot extruded at 440°C were 92 MPa and $2.94 \times 10^{-3}/\text{K}$, respectively. The high bending strength can improve the bonding strength between the thermoelectric materials and metal electrode during soldering for the fabrication of thermoelectric modules.

ACKNOWLEDGEMENTS

We would like to thank the support from the University Basic Research Support Fund (96-146) of Korea Ministry of Information and Communication.

REFERENCES

1. R. W. G. Wyckoff, Crystal Structure Vol. 2, Interscience Publishers, New York, 1964.
2. Y. M. Yim and F. D. Rosi, Solid State Electronics **15**, 1121 (1972).
3. D. M. Rowe, Applied Energy **24**, 139 (1986).
4. H. J. Goldsmid and A. Penn, Phys. Lett. **27A**, 523 (1986).

THERMOELECTRIC PROPERTIES OF ZnSb FILMS GROWN BY MOCVD

R. Venkatasubramanian, E. Watko and T. Colpitts
Research Triangle Institute, Research Triangle Park, NC 27709, USA.

ABSTRACT

The thermoelectric properties of ZnSb films grown by metallorganic chemical vapor deposition (MOCVD) are reported. The growth conditions necessary to obtain stoichiometric ZnSb films and the effects of various growth parameters on the electrical conductivity and Seebeck coefficients of the films are described. The as-grown ZnSb films are p-type. It was observed that the thicker ZnSb films offer improved carrier mobilities and lower free-carrier concentration levels. The Seebeck coefficient of ZnSb films was found to rise rapidly at approximately 160°C. The thicker films, due to the lower doping levels, indicate higher Seebeck coefficients between 25 to 200°C. A short annealing of the ZnSb film at temperatures of ~ 200°C results in reduced free-carrier level. Thermal conductivity measurements of ZnSb films using the 3- ω method are also presented.

INTRODUCTION

ZnSb, with a stoichiometry of Zn:Sb=1:1, has long been considered to offer high figure-of-merit (ZT) for power generation applications [1]. ZnSb, an intermetallic compound, has a high Seebeck coefficient compared to other phases of the alloy due to the ionic character of the compound. ZnSb, with the desired 1:1 stoichiometry, has been difficult to prepare in bulk form without the formation of other eutectic phases of the alloy, Zn₄Sb₃ and Zn₃Sb₂, from a peritectic reaction of the Zn-Sb melt. The presence of other phases reduces the overall Seebeck coefficient and ZT of the ZnSb material.

However, certain thin-film deposition techniques which take place under non-thermal equilibrium conditions, and are driven instead by kinetic limitations, allow the growth of films with desired stoichiometry. Ion cluster beam (ICB) process is one such technique and ZnSb thin films grown by the ICB process have indicated Seebeck coefficients as high as 600 μ V/K at 550K [1]. These ZnSb films had appreciable electrical conductivity, as high as 5E2 $\text{ohm}^{-1} \text{cm}^{-1}$. The ZnSb thin-films were p-type with carrier mobilities of ~ 22 cm^2/Vsec . Even so, assuming that the thermal conductivity of the ZnSb thin films were comparable to bulk samples, a ZT of ~5 was estimated at 520K by Koyanagi et. al [1].

In this paper we report that MOCVD-grown ZnSb films, with a stoichiometry of Zn:Sb=1:1, also offer high Seebeck coefficients. We also provide some experimental justification of the assumption that the thermal conductivity of the thin-films are indeed comparable to those of bulk ZnSb crystals.

MOCVD OF ZnSb

The ZnSb crystal has a primitive orthorhombic structure, a distorted form of cubic structure, as shown in Figure 1. Hence, we attempted to grow these films on commonly available, face-centered cubic-structured, GaAs. Si and Ge, also have cubic crystal structures; however, these were not chosen as substrate materials for they cannot be made non-conducting or semi-insulating to enable the transport property measurements of the ZnSb films.

The ZnSb thin films were deposited on semi-insulating GaAs substrates using diethylzinc (DEZn) and trisdimethylaminoantimony (TDMASb). Under optimal growth conditions, the desired stoichiometry was reproducible for a wide ratio of flow rates of these growth precursors, DEZn and TDMASb. The stoichiometry values were determined by energy dispersive X-ray analysis. X-ray diffraction studies indicate that the ZnSb films grown on GaAs substrates are single-crystalline with the dominant orientation of the film along the growth direction being $\langle 2,2,-4,1 \rangle$.

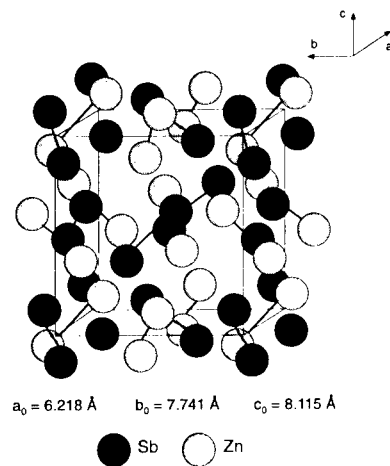


Figure 1 Orthorhombic Crystal structure of ZnSb

PROPERTIES OF ZnSb FILMS

Here, we first discuss the electrical transport properties of ZnSb films measured by the van der Pauw Hall method. Next, the Seebeck coefficient (α) measured in the films at 300K, the variation of α with temperature, and the effect of various growth conditions on α , are discussed. The thermal conductivity values in a select set of ZnSb films at 25 °C and 150 °C, measured by the 3- ω method are presented [2,3].

Electrical Transport Properties

The as-grown ZnSb films by MOCVD were found to be p-type, similar to the ZnSb films [1] grown by the ICB process. Shown in Figure 2 is the effect of increased layer thickness of the epitaxial ZnSb film on the residual p-doping level and hole mobility in the layer. The significant reduction in the residual doping level in the film, in conjunction with an increase in mobility, is indicative of reduced defects, possibly Sb vacancies as discussed in the following sections. Growth of ZnSb films thicker than $\sim 1.35 \mu\text{m}$ was not attempted in this study. We note that the best carrier mobility ($\sim 23.5 \text{ cm}^2/\text{Vsec}$) of a micron-thick MOCVD-grown film is comparable to

the best value of 22.8 cm²/Vsec, observed in ICB-grown ZnSb films. The electrical conductivities of the films were in the range of 1E3 ohm⁻¹cm⁻¹.

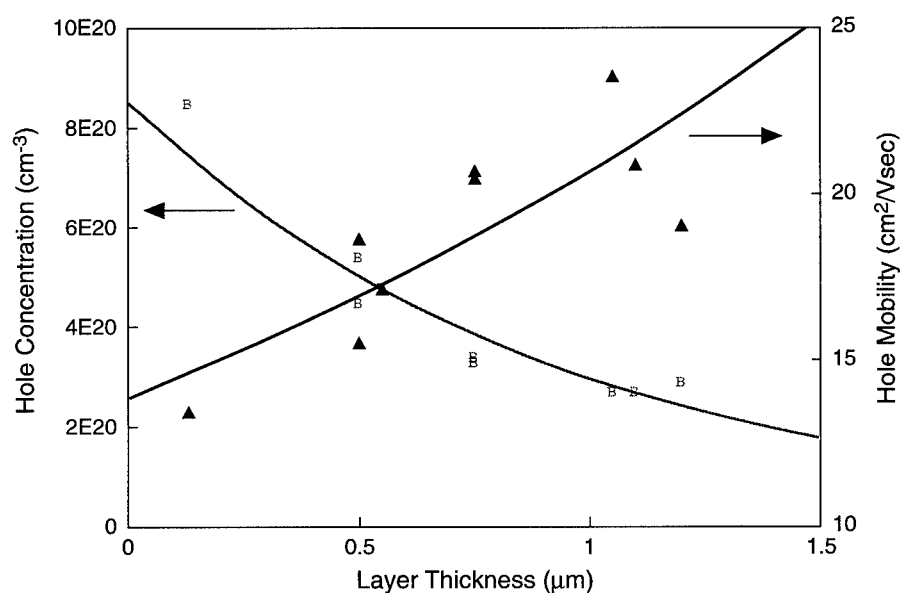


Figure 2 Effect of ZnSb layer thickness on residual doping level and hole mobility at 25 °C

The high residual p-doping level in the ZnSb films, especially in the thinner films, is attributable to native Sb vacancies. With thicker films i.e., larger growth time, we believe, at the growth temperature and with an over-pressure of the Sb-growth precursor, the Sb vacancies get thermally annealed out. Note that Sb vacancies are expected to behave as acceptors. Te, a Group-VI atom, is expected to occupy the Sb site as a donor and so Te-doping would reduce the residual p-doping level. In fact, there has been a published work on the use of Te doping in bulk CdSb to reduce the p-doping level [4]. So we investigated Te doping in ZnSb films and the initial results are shown in Table I.

For a constant layer thickness of ~ 0.5 μm, we did notice a drop in the residual p-type carrier level with Te doping. At higher concentrations of the Te-dopant, we observed that the ZnSb films become polycrystalline (based on x-ray data) and even though the residual doping falls dramatically over two orders of magnitude, the hole mobility becomes very low due to the polycrystalline nature of the films.

Seebeck Coefficients in ZnSb Films

The Seebeck coefficients (α) in the ZnSb films were measured between 25 °C to 200 °C. Shown in Figure 3 is the variation of α with temperature, for two ZnSb samples of different thickness. We observe that the thicker film, due to the lower residual doping level, indicates a significantly higher α through out the temperature range of measurement.

Table I Effect of Te doping on properties of ZnSb films

Sample #	Thickness t(μm)	Te-Doping (Torr)	x-ray Data	p (cm ⁻³)	μ (cm ² /Vsec)
7-235	0.5	---	Single Crystalline	4.5E20	18.6
7-244	0.5	3.5 x 10 ⁻⁴	Single Crystalline	3.6E20	20.0
7-245	0.47	7.0 x 10 ⁻⁴	Single Crystalline	3.1E20	16.2

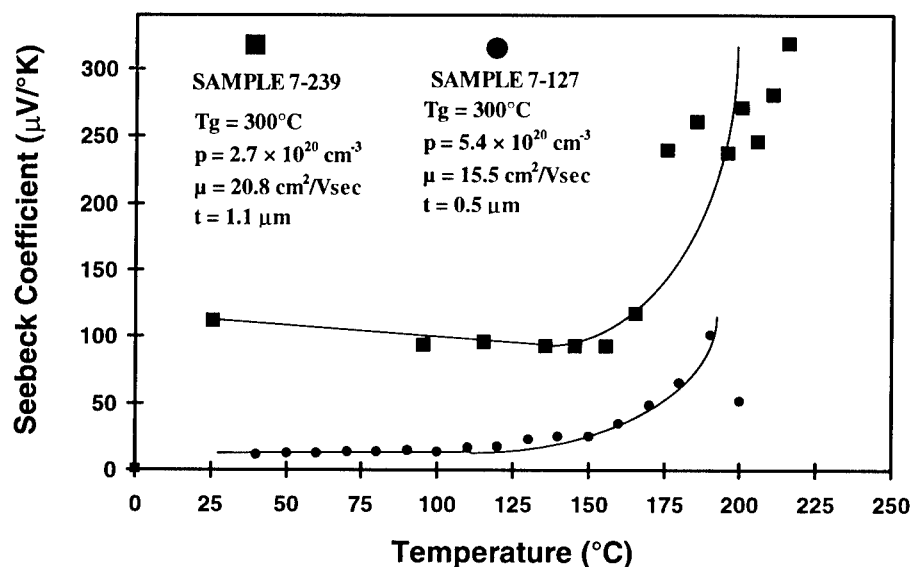


Figure 3 Seebeck coefficients of ZnSb films

We also observe a rather sharp rise in α near 175 $^\circ\text{C}$ for both the samples; this is similar to the observed α .vs. T behavior of ZnSb films grown by the ICB process [1]. The near-constant Seebeck coefficient between 25 $^\circ\text{C}$ to ~160 $^\circ\text{C}$ is also indicative of near-constant electrical conductivity and absence of any significant chemical or structural changes in the film. The ZnSb films may be undergoing defect annealing near and above 160 $^\circ\text{C}$ [5]. We have observed a reduction in carrier concentration and an increase in the electrical resistivity of the ZnSb films at 25 $^\circ\text{C}$, after an exposure to ~200 $^\circ\text{C}$ (Table II). The reduction in carrier concentration is attributable to quenching of Sb-vacancies, possibly by a mechanism such as Sb displacement from an interstitial site to a substitutional site.

Table II Hall-Data of ZnSb samples before and after 200°C exposure

Sample #	Thickness (μm)	Before 200°C Exposure			After 200°C Exposure		
		μ (cm ² /vs)	P (cm ⁻³)	Resistivity (ohm-cm)	μ (cm ² /vs)	P (cm ⁻³)	Resistivity (ohm-cm)
7-127	0.5	15.5	5.4E20	7.4E-4	15.7	3.0E20	1.3E-3
7-127-a	0.5	9.0	4.8E20	1.45E-3	9.3	2.5E20	2.7E-3

Thermal Conductivity of ZnSb Films

Measurements of the thermal conductivity (K) of ZnSb films were carried out using the 3-ω method [2,3]. Shown in Table III are the K values at 25°C for two ZnSb films, with different carrier concentration levels. It is interesting to note that, for the as-grown films, the thermal conductivity decreases at lower carrier levels. This suggests that a significant portion of the thermal conductivity may be due to transport of heat by the high-density of free carriers. It is worth observing that Sample 7-240, which had the lowest free-carrier level but was polycrystalline due to the larger Te-doping level, offers the lowest thermal conductivity at 25°C. This is consistent with the polycrystalline grain-boundary scattering of phonons in addition to a lower electronic contribution to the overall thermal conductivity.

Table III Thermal conductivity of ZnSb films at 25 °C determined by the 3-ω method

Sample #	Thickness (μm)	Carrier Concentration (cm ⁻³)	Te Doping	K (W/cm-K)
7-248	0.9	4.0E20	--	0.033
7-247	1.05	2.4E20	--	0.011
7-240	0.33	2.0E18	Yes; Polycrystalline	0.008

As noted in the previous section, the Seebeck coefficient of ZnSb films remain fairly stable up to 160°C and so we considered the measurement of thermal conductivity of the films at ~150°C for estimating ZT at higher temperatures. The 3-ω data on a set of ZnSb samples are shown in Table IV. For single-crystal films, the thermal conductivity (K) falls slowly in going from 25°C to 150°C. This is consistent with the observed variation of K with temperature in CdSb bulk crystals [4]. However, the polycrystalline ZnSb film shows an increasing K with temperature, consistent with reduced phonon-scattering at grain boundaries at higher temperatures.

SUMMARY

We have demonstrated that ZnSb single-crystalline films with a stoichiometry of Zn:Sb=1:1 can be grown by MOCVD. The residual doping level in these films was rather high, although decreasing monotonically from 8.5E20 cm⁻³ for layer thickness of 0.13 μm to

$2.7 \times 10^{20} \text{ cm}^{-3}$ for layer thickness of $1.1 \text{ }\mu\text{m}$. The preliminary values of Seebeck coefficients of these films were found to be as high as $372 \text{ }\mu\text{V/K}$ at $\sim 150^\circ\text{C}$. The 3ω -measured K values of ZnSb films at $\sim 150^\circ\text{C}$ are ~ 0.01 to 0.02 W/cm K , in agreement with typical values seen in bulk ZnSb crystals [1] at such temperatures. These results suggest that ZnSb films does offer potentially higher ZT values, larger than current state-of-the-art power conversion materials, for low-temperature, low-grade-heat, thermoelectric power generation.

Table IV Comparison of thermal conductivity of ZnSb films at 25°C and 150°C

Sample #	Thickness (μm)	Crystallinity	K_{25} (W/cmK)	K_{150} (W/cmK)
7-248	0.9	Single-crystalline	0.033	0.021
7-247	1.05	Single-crystalline	0.011	0.009
7-240	0.33	Polycrystalline	0.008	0.020

REFERENCES

1. T. Koyanagi et.al, Proc. of the XII International Conf. on Thermoelectrics, Yokohama, Japan, 340(1994).
2. D.G. Cahill and R.O. Pohl, Phys. Rev. B, **35**, 4067 (1987) and D.G. Cahill, H.E. Fischer, T. Klitsner, E.T. Swartz, and R.O. Pohl, J. Vac. Sci. and Technol. **A7**, 1259 (1989).
3. D.G. Cahill, M. Katiyar, and J.R. Abelson, Phys. Rev. B, **50**, 6077 (1994).
4. S.V. Airapetyants, Thermoelectric Properties of Semiconductors, Ed. by V.A. Kutasov, Consultants Bureau, New York, 1964.
5. J. Sharp, Marlow Industries, Private Communication.

THERMOELECTRIC PROPERTIES OF N-TYPE $\text{Bi}_2(\text{Te}_{1-x}\text{Se}_x)_3$ FABRICATED BY MECHANICAL ALLOYING AND HOT PRESSING

HEE-JEONG KIM*, JAE-SHIK CHOI* TAE-SUNG OH* AND DOW-BIN HYUN**

*Depart. of Metall. and Mater. Sci., Hong Ik Univ., Seoul, Korea, ohts@wow.hongik.ac.kr

**Metals Division, Korea Institute of Science and Technology, Seoul 136-791, Korea

ABSTRACT

Thermoelectric properties of polycrystalline $\text{Bi}_2(\text{Te}_{1-x}\text{Se}_x)_3$ ($0.05 \leq x \leq 0.25$), fabricated by mechanical alloying and hot pressing, have been investigated. Formation of n-type $\text{Bi}_2(\text{Te}_{0.9}\text{Se}_{0.1})_3$ alloy powders was completed by mechanical alloying for 3 hours at ball-to-material ratio of 5 : 1, and processing time for $\text{Bi}_2(\text{Te}_{1-x}\text{Se}_x)_3$ formation increased with Bi_2Se_3 content x. Figure-of-merit of $\text{Bi}_2(\text{Te}_{0.9}\text{Se}_{0.1})_3$ was markedly increased by hot pressing at temperatures above 450°C, and maximum value of $1.9 \times 10^{-3}/\text{K}$ was obtained by hot pressing at 550°C. With addition of 0.015 wt% Bi as acceptor dopant, figure-of-merit of $\text{Bi}_2(\text{Te}_{0.9}\text{Se}_{0.1})_3$, hot pressed at 550°C, could be improved to $2.1 \times 10^{-3}/\text{K}$. When $\text{Bi}_2(\text{Te}_{1-x}\text{Se}_x)_3$ was hot pressed at 550°C, figure-of-merit increased from $1.14 \times 10^{-3}/\text{K}$ to $1.92 \times 10^{-3}/\text{K}$ with increasing Bi_2Se_3 content x from 0.05 to 0.15, and then decreased to $1.30 \times 10^{-3}/\text{K}$ for x = 0.25 composition.

INTRODUCTION

Thermoelectric materials have been widely investigated to apply for Peltier cooling modules for electronic devices such as integrated circuit packages, laser diodes and IR detectors, because quick and precise control of temperature is possible [1,2]. Single crystal and polycrystalline Bi_2Te_3 - Bi_2Se_3 alloys of 5% ~ 25% Bi_2Se_3 have been utilized as n-type materials for Peltier coolers [1-4].

As a new processing technique, mechanical alloying has been applied to prepare polycrystalline thermoelectric materials in recent years [4-6]. Mechanical alloying is a technique in which intermetallic compound or alloy powders are fabricated from elemental powders through a sequence of collision events inside a high energy ball mill. Since mechanical alloying process occurs near room temperature, this technique can be a cost-saving alternative for the production of polycrystalline thermoelectric materials to the conventional "vacuum melting/grinding" process where a long processing time, and high temperature and large scale facilities are required [4-6]. Also vaporization of chalcogenide elements, such as Te and Se, and segregation of dopants may be prevented in powders produced by mechanical alloying, as melting process is not involved during powder fabrication processing [5,7].

In this paper, thermoelectric properties of polycrystalline $\text{Bi}_2(\text{Te}_{1-x}\text{Se}_x)_3$ ($0.05 \leq x \leq 0.25$), fabricated by mechanical alloying and hot pressing have been investigated with variation of Bi_2Se_3 content x, hot pressing temperature and the amount of excess Bi addition, as acceptor dopant.

EXPERIMENTAL PROCEDURE

High purity (> 99.99%) Bi, Te, and Se granules of ~4 mm diameter were washed with 10% nitric solution, acetone, and distilled water to remove the surface oxide layer. The appropriate amounts of Bi, Te and Se were weighed for $\text{Bi}_2(\text{Te}_{1-x}\text{Se}_x)_3$ ($0.05 \leq x \leq 0.25$) compositions and charged in a hardened tool steel vial with steel balls as milling media under Ar atmosphere. Ball-to-material weight ratio was held to be 5 : 1. Mechanical alloying was conducted by shaking the vial at approximately 1200 rpm using a Spex mixer/mill. After the vibro-milling process for 3 hours, X-ray diffraction (XRD) analysis was performed to characterize the crystalline phases and lattice parameters of $\text{Bi}_2(\text{Te}_{1-x}\text{Se}_x)_3$ formed by mechanical alloying. DTA was conducted in Ar atmosphere at a scan rate of 5°C/min for the as-mixed and mechanically alloyed powders.

$\text{Bi}_2(\text{Te}_{1-x}\text{Se}_x)_3$ powders, fabricated by mechanical alloying, were cold pressed at 325 MPa to form 5 mm \times 5 mm \times 10 mm compacts. Hot pressing was conducted in vacuum at temperatures ranging from 300°C to 550°C for 30 minutes. DTA was also conducted for hot pressed specimens in Ar atmosphere at a scan rate of 5°C/min. Microstructure on the fracture surface of hot pressed specimens were observed using scanning electron microscopy (SEM).

Seebeck coefficient α of the hot pressed specimens was measured at room temperature by applying temperature difference of 10°C at both ends of a specimen using a sub-heater. Electrical resistivity ρ and thermal conductivity κ were measured at room temperature using Harman method [8] in vacuum of 10^{-5} torr to minimize thermal conduction through convection. Figure-of-merit Z was characterized using the equation $Z = \alpha^2/(\rho\kappa)$.

RESULTS and DISCUSSION

As shown in Fig. 1, XRD patterns of the powders, mechanically alloyed for 3 hours, clearly illustrated that formation of $\text{Bi}_2(\text{Te}_{1-x}\text{Se}_x)_3$ alloys was completed by mechanical alloying of elemental Bi, Te and Se powders at room temperature.

In Fig. 2, DTA curves of $\text{Bi}_2(\text{Te}_{0.9}\text{Se}_{0.1})_3$ and $\text{Bi}_2(\text{Te}_{0.85}\text{Se}_{0.15})_3$ powders, processed by mechanical alloying for 3 hours, were illustrated with results for specimens hot pressed at 550°C. In DTA curves of mechanically alloyed powders, only one endothermic peak was observed for compositions with Bi_2Se_3 content $x \leq 0.1$. For Bi_2Se_3 content $x > 0.15$, however, two endothermic reactions occurred at around 600°C, which might indicate that powders were composed with two different compositions of Bi_2Se_3 content. In $\text{Bi}_2(\text{Te,Se})_3$ single crystals, formation of Te-rich second phase has been also reported for compositions with Bi_2Se_3 content more than ~12 mol% [9,10]. As indicated in Fig. 2, processing time for the formation of homogeneous $\text{Bi}_2(\text{Te}_{1-x}\text{Se}_x)_3$ by mechanical alloying was increased with Bi_2Se_3 content x .

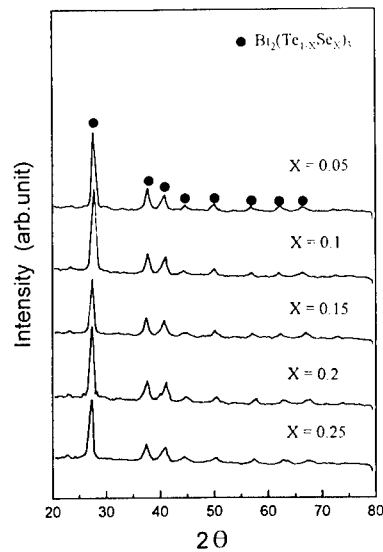


Fig. 1 XRD patterns of $(\text{Bi}_{0.25}\text{Sb}_{0.75})_2\text{Te}_3$ powders with mechanical alloying time.

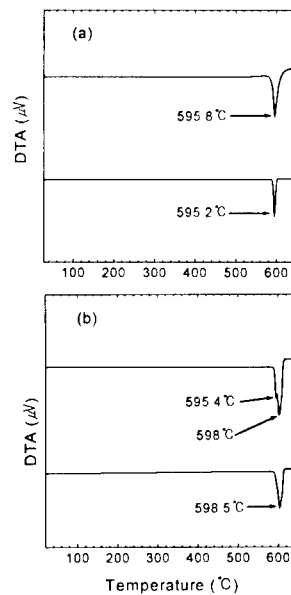


Fig. 2 DTA curves of mechanically alloyed and hot pressed $\text{Bi}(\text{Te}_{1-x}\text{Se}_x)_3$ powders for (a) $x = 0.1$ and (b) $x = 0.15$.

Seebeck coefficient, electrical resistivity, thermal conductivity and figure-of-merit of $\text{Bi}_2(\text{Te}_{0.9}\text{Se}_{0.1})_3$, mechanically alloyed and hot pressed at temperatures ranging from 300°C to 550°C, were illustrated in Fig. 3. Seebeck coefficient of $\text{Bi}_2(\text{Te}_{0.9}\text{Se}_{0.1})_3$ increased with increasing hot pressing temperature up to 450°C, and then decreased with further increase of hot pressing temperature. In Fig. 3(b), electrical resistivity was decreased with increasing hot pressing temperature up to 450°C, which might be due to densification of the microstructure. Increment of electrical resistivity of specimens, hot pressed at temperatures above 450°C, could be attributed to the reduction of electron concentration by compensation with holes generated during formation of anti-structure defects. Vaporization of Te in Bi_2Te_3 alloys and thus formation of anti-structure defects were reported to occur more severely at temperatures above 450°C [9,11]. As shown in Fig. 3(d), figure-of-merit of $\text{Bi}_2(\text{Te}_{0.9}\text{Se}_{0.1})_3$ was markedly increased by hot pressing at temperatures above 450°C, and maximum value of $1.9 \times 10^{-3}/\text{K}$ was obtained by hot pressing at 550°C.

To improve figure-of-merit of n-type $\text{Bi}_2(\text{Te}_{0.9}\text{Se}_{0.1})_3$ by increasing Seebeck coefficient, $\text{Bi}_2(\text{Te}_{0.9}\text{Se}_{0.1})_3$ powders with addition of excess Bi, as acceptor dopant, was formed by mechanical alloying for 3 hours and hot pressed at 550°C. Thermoelectric properties of $\text{Bi}_2(\text{Te}_{0.9}\text{Se}_{0.1})_3$ were shown in Fig. 4 with variation of the amount of excess Bi. With increasing the amount of excess Bi, Seebeck coefficient and electrical resistivity of $\text{Bi}_2(\text{Te}_{0.9}\text{Se}_{0.1})_3$ increased due to the formation of anti-structure defects. When excess Bi of 0.5 wt% was

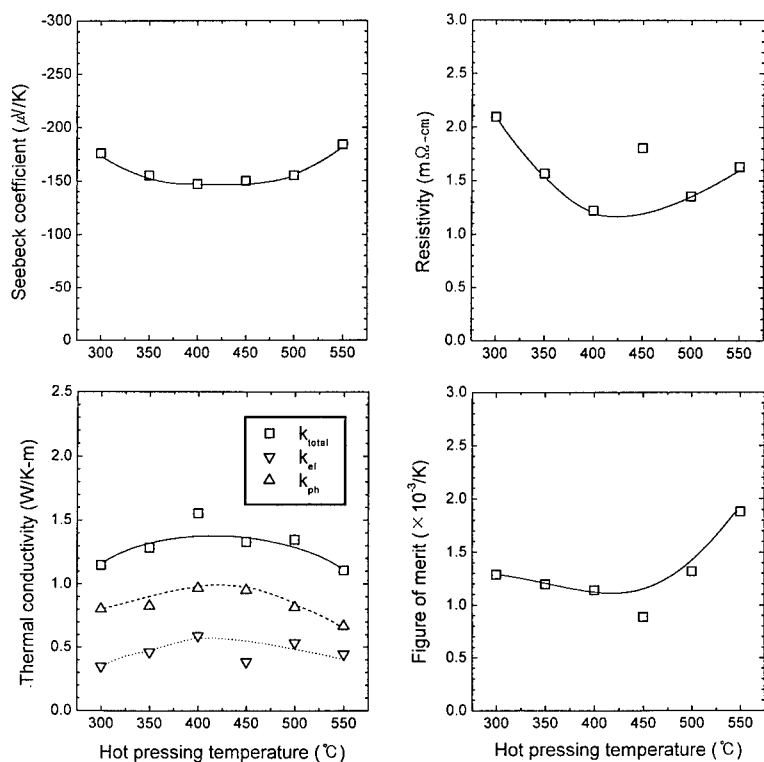


Fig. 3 (a) Seebeck coefficient, (b) electrical resistivity, (c) thermal conductivity and (d) figure-of-merit of $\text{Bi}_2(\text{Te}_{0.9}\text{Se}_{0.1})_3$ with hot pressing temperature.

added, transition to p-type conduction occurred and Seebeck coefficient exhibited a positive value of 54 $\mu\text{V/K}$. With addition of 0.015 wt% Bi, as shown in Fig. 4(d), figure-of-merit of $\text{Bi}_2(\text{Te}_{0.9}\text{Se}_{0.1})_3$ was improved to $2.1 \times 10^{-3}/\text{K}$.

Thermoelectric properties of $\text{Bi}_2(\text{Te}_{1-x}\text{Se}_x)_3$, mechanically alloyed for 3 hours and hot pressed at 550°C, were illustrated in Fig. 5. Seebeck coefficient and electrical resistivity of $\text{Bi}_2(\text{Te}_{1-x}\text{Se}_x)_3$ were increased with increasing Bi_2Se_3 content x from 0.05 to 0.15, and then decreased with further increase of Bi_2Se_3 content. As shown in Fig. 5(d), figure of merit increased from $1.14 \times 10^{-3}/\text{K}$ to $1.92 \times 10^{-3}/\text{K}$ with increasing Bi_2Se_3 content x from 0.05 to 0.15, and then decreased to $1.30 \times 10^{-3}/\text{K}$ for $x = 0.25$ composition.

As shown in Figs. 3 and 5, mechanically alloyed and hot pressed $\text{Bi}_2(\text{Te}_{1-x}\text{Se}_x)_3$ ($0.05 \leq x \leq 0.25$) exhibited negative Seebeck coefficient and thus n-type conduction without depending on Bi_2Se_3 content and hot pressing temperature. For single crystal $\text{Bi}_2(\text{Te,Se})_3$ without addition of donor dopant, however, p-type conduction has been reported for compositions with Bi_2Se_3 up to ~22% [2]. This discrepancy between single crystal and mechanically alloyed $\text{Bi}_2(\text{Te}_{1-x}\text{Se}_x)_3$ might occur due to the following two reasons : firstly, concentration of anti-structure defects related to the vaporization of Te and Se was much lower in powders fabricated by mechanical alloying process, compared to single crystal $\text{Bi}_2(\text{Te,Se})_3$ alloys. Holes were generated during formation of anti-structure defects by substitution of Bi into Te or Se sites.

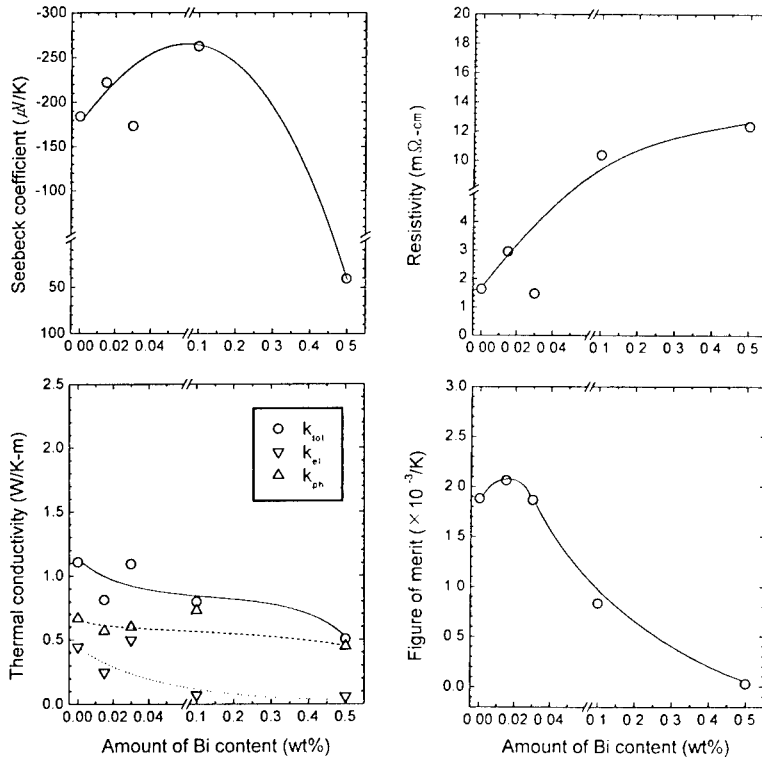


Fig. 4 (a) Seebeck coefficient, (b) electrical resistivity, (c) thermal conductivity and (d) figure-of-merit of $\text{Bi}_2(\text{Te}_{0.9}\text{Sc}_{0.1})_3$ with the amount of excess Bi addition.

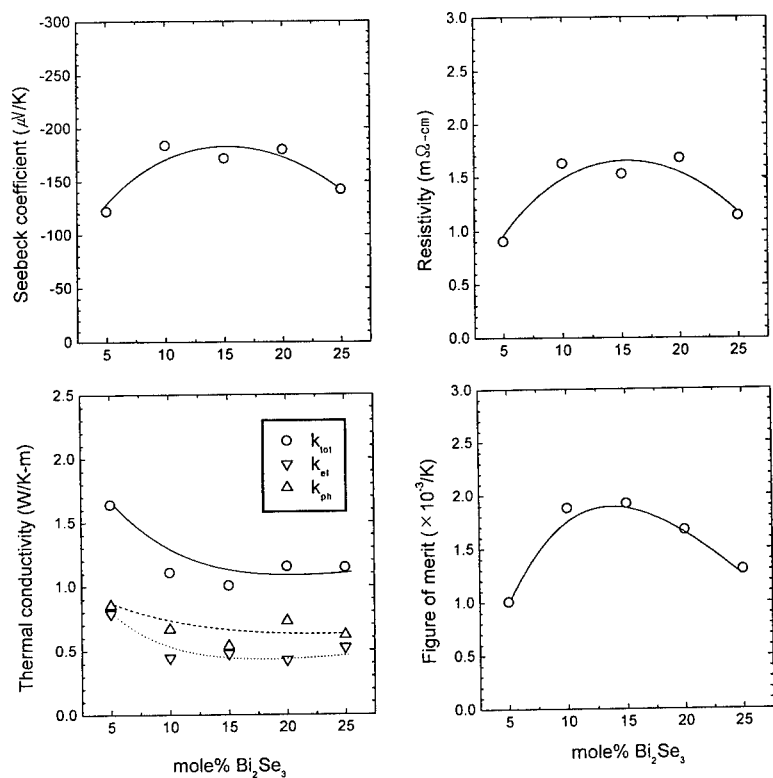


Fig. 5 (a) Seebeck coefficient, (b) electrical resistivity, (c) thermal conductivity and (d) figure-of-merit of $\text{Bi}_{12}(\text{Te}_{1-x}\text{Se}_x)_3$ with Bi_2Se_3 content x .

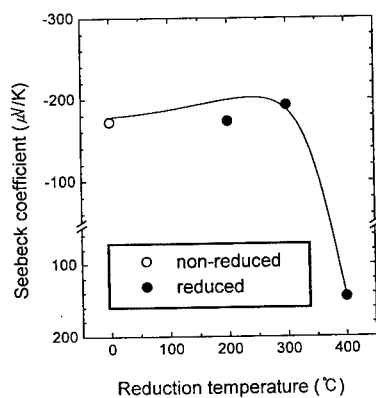


Fig. 6 Seebeck coefficient of $\text{Bi}_{12}(\text{Te}_{0.85}\text{Se}_{0.15})_3$ vs. reduction treatment temperature in H_2 atmosphere.

Secondly, the surface of powders fabricated by mechanical alloying was oxidized, and oxygen ions in the Bi_2Te_3 lattice were reported to act as donor dopant [12]. To confirm the effects of surface oxidation on n-type conduction, mechanically alloyed $\text{Bi}(\text{Te}_{0.95}\text{Se}_{0.05})_3$ powders were reduction-treated in H_2 ambient for 24 hours, and then hot pressed at 550°C . Seebeck coefficient of the reduction-treated $\text{Bi}(\text{Te}_{0.95}\text{Se}_{0.05})_3$ was illustrated in Fig. 6. When the surface oxide was effectively removed by reduction at 400°C , mechanically alloyed and hot pressed $\text{Bi}(\text{Te}_{0.95}\text{Se}_{0.05})_3$ also exhibited a positive Seebeck coefficient as reported for single crystal [2]. From results in Fig. 6, it could be also suggested that reduction treatment of mechanically alloyed Bi_2Te_3 -based powders should be conducted at 400°C .

SUMMARY

Formation of n-type $\text{Bi}_2(\text{Te}_{0.95}\text{Se}_{0.05})_3$ alloy powders was completed by mechanical alloying of elemental Bi, Te and Se granule of ~ 4 mm for 3 hours at ball-to-material weight ratio of 5 : 1. Contrary to the powders with Bi_2Se_3 content $x \leq 0.1$, $\text{Bi}_2(\text{Te}_{1-x}\text{Se}_x)_3$ powders with $x \geq 0.15$ were composed of two different compositions after mechanical alloying for 3 hours. Mechanically alloyed and hot pressed $\text{Bi}_2(\text{Te}_{1-x}\text{Se}_x)_3$ ($0.05 \leq x \leq 0.25$) exhibited negative Seebeck coefficient and thus n-type conduction without depending on Bi_2Se_3 content x and hot pressing temperature. When mechanically alloyed $\text{Bi}(\text{Te}_{0.95}\text{Se}_{0.05})_3$ powders were reduction-treated in H_2 ambient at 400°C for 24 hours and hot pressed at 550°C , Seebeck coefficient of $\text{Bi}(\text{Te}_{0.95}\text{Se}_{0.05})_3$ was changed from negative to positive value. Thus, it could be suggested that n-type conduction of mechanically alloyed $\text{Bi}_2(\text{Te}_{1-x}\text{Se}_x)_3$ was partly due to the surface oxidation of the powders. Figure-of-merit of $\text{Bi}_2(\text{Te}_{0.95}\text{Se}_{0.05})_3$ was markedly increased by hot pressing at temperatures above 450°C , and maximum value of $1.9 \times 10^{-3}/\text{K}$ was obtained by hot pressing at 550°C . With addition of 0.015 wt% Bi as acceptor dopant, figure-of-merit of $\text{Bi}_2(\text{Te}_{0.95}\text{Se}_{0.05})_3$ hot pressed at 550°C , could be improved to $2.1 \times 10^{-3}/\text{K}$. When $\text{Bi}_2(\text{Te}_{1-x}\text{Se}_x)_3$ was hot pressed at 550°C , figure-of-merit increased from $1.14 \times 10^{-3}/\text{K}$ to $1.92 \times 10^{-3}/\text{K}$ with increasing Bi_2Se_3 content x from 0.05 to 0.15, and then decreased to $1.30 \times 10^{-3}/\text{K}$ for $x = 0.25$ composition.

REFERENCES

1. D. M. Rowe, CRC Handbook of Thermoelectrics, p.605, CRC Press, Inc., Boca Raton (1995)
2. W. M. Yim and F. D. Rosi, *J. Solid State Electronics*, **15**, 1121 (1972)
3. I. J. Ohsugi, T. Kojima, and I. A. Nishida, *J. Appl. Phys.*, **68**, 5692 (1990)
4. K. Hasezaki, M. Nishimura, M. Umata, H. Tsukuda, and M. Araoka, *Proc. 12th ICT*, 307 (1993)
5. B. A. Cook, B. J. Beaudry, J. L. Harringa, and W. J. Barnett, *Proc. 9th ICT*, 234 (1990)
6. D. M. Rowe, V. S. Shukla, and N. Savvides, *Nature*, **290**, 765 (1981)
7. A. Yanagitani, S. Nishikawa, Y. Kawai, S. Hayashimoto, N. Itoh, and T. Kataoka, *Proc. 12th ICT*, 281 (1993)
8. T. C. Harman, J. H. Cahn, and M. J. Logan, *J. Appl. Phys.*, **30**, 9 (1959)
9. M. Carle, D. Perrin, T. Caillat, S. Scherrer, and H. Scherrer, *Proc. 10th ICT*, 27 (1991)
10. J. P. Hugh and W. A. Tiller, *Trans. Mat. Soc. AIME*, **215**, 651 (1959)
11. G. R. Miller and C.-Y. Li, *J. Phys. Chem. Solids*, **26**, 173 (1965)
12. D. M. Gel'fgat and Z. M. Dashevskii, *Inorg. Mat.*, **19**, 1172 (1984)

THERMOELECTRIC PROPERTIES OF $M_2Mo_6Se_6$ ($M=Ti, In$)

D. T. VEREBELYI*, J. E. PAYNE*, G. X. TESSEMA**, AND E. MENGISTU**

*South Carolina State University, Department of Physical Sciences, Orangeburg S.C.

**Clemson University, Department of Physics and Astronomy, Clemson, S.C.

ABSTRACT

We have measured the thermal conductivity of $Ti_2Mo_6Se_6$, a quasi-one dimensional conductor which belongs to the family of $M_2Mo_6X_6$ linear chain compounds. Using these results and our measurements of the Seebeck coefficient and the electrical conductivity we estimate the dimensionless figure of merit to be of the order of 0.08. This result suggest that this compound and other related compounds are good potential TE.

INTRODUCTION

In recent years, the field of thermoelectrics (TE) has been the subject of rising research activity.^[1,2] This is mainly due to the need for cryo-cooling of electronic devices, increasing environmental awareness, and the advantage for low noise refrigeration, without moving parts, for domestic as well as military purposes. Research in TE follows two directions: (1) the new direction consists in the search for novel materials with enhanced TE properties, and (2) the traditional approach which consists in the optimization of the TE properties of known materials through doping and other mechanism that would enhance the figure of merit. One of the promising type of materials for TE applications are low dimensional compounds. The purpose of this study is to investigate the potential for TE of the family of quasi-1D materials, $M_2Mo_6X_6$ ($M= Ti, K, Na, In, \dots$, and $X = Se, Te, \dots$). Most of these compounds exhibit a metal insulator transition supposedly driven by a Peierls transition.^[3-6] This paper focuses on the TE properties of the $Ti_2Mo_6Se_6$ compound. This compound is an excellent testing system for the whole family of compounds, because of its high electrical conductivity, rather high room temperature Seebeck coefficient (S) and the sensitivity of these properties to stress and doping.^[7,8]

EXPERIMENT

The structure of these compounds consists of infinite chains of Mo_6X_6 running along the hexagonal axis.^[9] The transition metals are intercalated between these chains. In addition to the other remarkable properties such as a metallic R vs. T behavior and a rather high superconducting transition temperature ($T_c = 6.5$ K) for a quasi-one dimensional compound, $Ti_2Mo_6Se_6$ has a high Seebeck coefficient, $-40 \mu V/K$ at room temperature.^[7,8,10] The resistance of these compounds, was measured using the conventional four probe technique. Figure 1 shows the metallic behavior of the electrical resistance.

For the measurement of the Seebeck coefficient, the two ends of the sample were attached to Cu wires using Ag paint. A welded Cu-(Au-Fe 0.7%) junction was used to measure the thermal gradient, ΔT , across the sample. ΔT is applied using a 45Ω heater attached to a Cu block to which both the sample and the thermocouple junction are thermally anchored. At each temperature, the linearity between the thermal voltage and ΔT was checked. The temperature dependence of the Seebeck coefficient of this compound is consistent with previously published results which we reproduce in Figure 2.^[4] For comparative reasons we also show the temperature dependence of the $In_2Mo_6Se_6$. The solid triangle and solid circles are representative points from our measurements shown to verify consistency of our results with previous publications.

Although, sufficient data already exists concerning R and S for these compounds,^[3-6] a complete characterization of the TE properties requires the knowledge of the thermal conductivity (κ). This is perhaps the most challenging problem due to the small size of the samples which have whisker-like morphology with typical dimension of $2000 \times 10 \times 10 \mu m^3$. A special experimental setup was

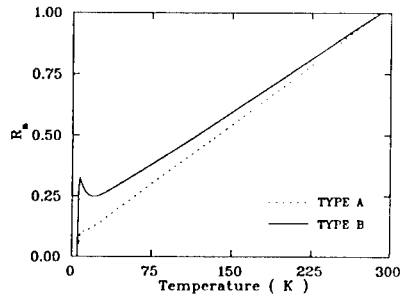


Figure 1. Resistance vs. Temperature curve showing the metallic behavior of $\text{Tl}_2\text{Mo}_6\text{Se}_6$.

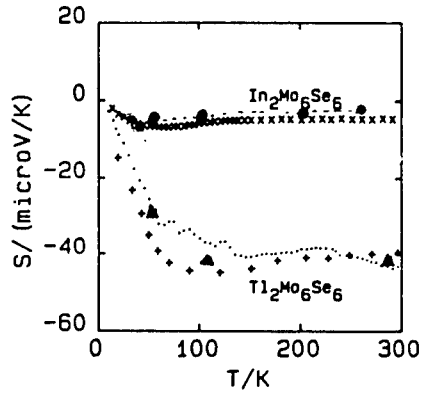


Figure 2. The thermopower of $\text{Tl}_2\text{Mo}_6\text{Se}_6$ and $\text{In}_2\text{Mo}_6\text{Se}_6$, a reproduction from Ref. 4. The solid triangle and the solid circle are our results shown to verify consistency.

developed for this purpose. The technique uses a standard Nb wire in series with the sample and provides the absolute value of κ by comparing the thermal gradients across the sample with that across the standard, for the same amount of heat flow through both. This technique is described in a separate article accepted for publication to the Journal of Scientific Instruments.^[10] Figure 3 shows the temperature dependence of κ for the Tl compound. κ is nearly T independent down to about 200 K. A broad peak is observed at around 40 K.

Based on these measurements and published results by others we calculated the room dimensionless thermoelectric figure of merit, ZT for this compound. Using $\rho = 5 \times 10^{-7} \Omega\text{m}$, $S = -40 \mu\text{V/K}$ ^[11] and our results for κ at 200 K (12 W/mK). We obtain $ZT = 0.08$. Due to the rapid drop in the Seebeck coefficient and the increase in κ at lower temperatures we expect a lower figure of merit at low temperature. This rather large figure of merit suggest that this compound or the other compounds from the same family have a real potential for TE application. Work is in progress to improve the properties through chemical doping. A factor of three in the Seebeck coefficient should be sufficient to make these materials technologically interesting or as model compounds for the design and engineering of novel low dimensional materials for TE application. Work is in progress to fully characterize the related In compound.

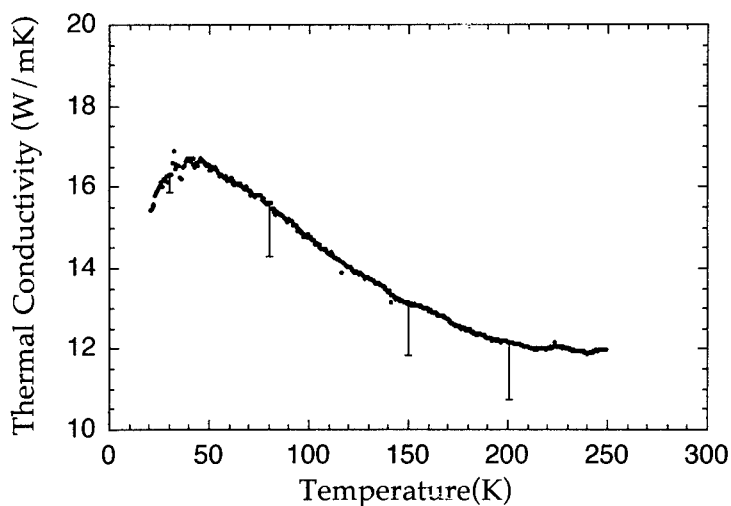


Figure 3. Temperature dependence of the thermal conductivity of $\text{Tl}_2\text{Mo}_6\text{Se}_6$.
An additional scaling factor of $\pm 25\%$ is due to size uncertainty.

Acknowledgements: The authors have benefited from the comments and discussion with T.M. Tritt. We would like to acknowledge R. Brusetti for the quality samples he so generously provided. The work at Clemson was supported by NSF # DMR9312530. The work at SCSU was supported by DOE, Basic Energy Sciences, Materials Science Division under contract number DE-FG05-93ER45493.

REFERENCES

1. T.M Tritt, Science **272**, 1276 (1996).
2. G. Mahan, Brian Sales and Jeff Sharp, Physics Today, March 1997.
3. M. Potel, R. Chevrel, M. Sergent, J.C. Armici, M Decroux, and O. Fisher, J. of Solid State Chem., **35**, 286 (1980).
4. J.C. Armici, M. Decroux, O. Fisher, M. Potel, R. Chevrel, and M. sergent, Solid State Comm. **33**, 607 (1980). T. Mori, Y. Yokogawa, A. Kobayashi, Y. Sasaki, and H. Kobayashi, Solid State Comm. **49**, 249 (1984).
5. P.H. Hor, et al. Solid State Comm. **55**, 231 (1995).
6. R. Lepetit, P. Monceau, M. Potel, P. Gougeon, and M. Sergent, J. of Low Temp. Phys. **56**, Nos3/4 (1984).
7. G.X. Tessema, Y.T. Tseng, M.J. Skove, and E.P. Stillwell, R. Brusetti, P. Monceau, M. Potel and P. Gougeon. Phys. Rev. B, **43**, 3434 (1991).
8. Y.T. Tseng, G.X. Tessema, and M.J. Skove, Sol. State Comm. **82**, 841 (1992).
9. J. Rouxel, Crystal chemistry and Properties of Materials with Quasi-One dimensional Structures (Reidel, Holland, 1986).
10. D.T. Verebelyi, accepted for publication in Review of Scientific Instruments.
11. R. Brusetti, A. Briggs, and O. Laborde, M. Potel, and P. Gougeon, Phys. Rev B. **49**, 8931 (1994).

Thermoelectric Transport in Superlattices

T. L. Reinecke* and D. A. Broido**

*Naval Research Laboratory, Washington DC 20375

**Department of Physics, Boston College, Chestnut Hill, MA 02167

ABSTRACT

The thermoelectric transport properties of superlattices have been studied using an exact solution of the Boltzmann equation. The role of heat transport along the barrier layers, of carrier tunneling through the barriers, of valley degeneracy and of the well width and energy dependences of the carrier-phonon scattering rates on the thermoelectric figure of merit are given. Calculations are given for Bi_2Te_3 and for PbTe , and the results of recent experiments are discussed.

INTRODUCTION

There has been a renewed interest in the past few years in finding new materials for potential use in cleaner more efficient cooling applications [1], and superlattice systems have been one focus of this work. The dimensionless "figure of merit" ZT , [2] provides a measure of the quality of materials for such applications. It is given by $ZT = \sigma S^2 T / \kappa$, where σ is the electrical conductivity, S is the thermoelectric power, T is the temperature, and κ is the total thermal conductivity. Even modest improvements in ZT would be quite desirable for a number of applications.

Interest in superlattices as desirable thermoelectric materials was stimulated several years ago by suggestions [3-5] that they would give greatly enhanced thermoelectric efficiencies as compared to their bulk counterparts. These suggestions were based on arguments using the densities of states for ideal two- and one-dimensional systems and did not include the effects of the finite thickness of the barriers for transport or of carrier tunneling between the layers of finite barrier heights. In subsequent work [6-10] the effects of finite barrier widths and of finite barrier heights on thermoelectric transport in superlattices systems have been studied. These two effects tend to decrease ZT at each well or wire width as compared to those for ideal two- and one-dimensional systems.

More recently, we have considered the effects of the well width and energy dependences of the scattering rates of carriers in these systems [11]. It is well known that electron scattering rates in superlattices differ qualitatively from those in bulk materials [12-14]. These effects give rise, for example, to decreasing carrier mobility with decreasing well thickness. All previous work on thermoelectric transport in superlattices has employed a constant relaxation time approximation, which assumes that the carrier scattering time is independent of carrier energy and of well or wire thickness. In addition to these effects, in all considerations of transport in confined structures, it must be kept in mind that the carriers exist in quantized subbands and that the valley degeneracy of multi-valley bulk semiconductors can be lifted by the quantum confinement.

Our interest in this area has been in developing a quantitative treatment of thermoelectric transport in realistic superlattice systems. Here we give results from the most complete treatment to date of this transport in quantum well superlattices. This treatment includes fully the elastic and inelastic carrier-phonon scattering and also the effects of multiple carrier valleys. Our multi-subband formulation provides an exact solution to the Boltzmann equation for carrier transport in the plane of quantum wells, from which we obtain the transport coefficients and ZT . Using results from this treatment, we discuss here several physical effects which are essential for a reliable understanding thermoelectric transport in superlattices.

Here quantum well superlattices with well and barrier widths, a and b , and period $d = a + b$ are considered. We focus on transport in the plane of the quantum well layers, which is the direction of interest in most work to date. A Boltzmann equation approach is used for the steady state electron transport in the presence of weak electric field E and weak temperature gradient ∇T . The electric and heat currents in the superlattice are given by

$$\mathbf{J}_e = -e \sum_{nj} \int \frac{d\mathbf{k}}{4\pi^3} \mathbf{v}_{nj} \delta f_{nj} \quad (1)$$

$$\mathbf{J}_Q = \sum_{nj} \int \frac{d\mathbf{k}}{4\pi^3} \mathbf{v}_{nj} (\epsilon - \mu) \delta f_{nj} \quad (2)$$

with δf_{nj} is the deviation from the equilibrium distribution function for the n^{th} carrier subband and j^{th} valley

$$\delta f_{nj} = \left(-\frac{\partial f_{0nj}}{\partial \epsilon} \right) \frac{\hbar \mathbf{k}_{\parallel}}{m_{j\parallel}} \cdot \left[-e\mathbf{E} \tau_{1nj}(\mathbf{k}_{\parallel}) - \frac{\nabla T}{T} \tau_{2nj}(\mathbf{k}_{\parallel}) \right] \quad (3)$$

where the scattering functions, τ_{1nj} and τ_{2nj} , are determined from the solution of the Boltzmann equation for each well thickness. Here $\epsilon = \epsilon_{nj}(\mathbf{k})$ is the energy dispersion of the carrier in the n^{th} subband, and $m_{j\parallel}$ is the mass of the j^{th} valley for motion along the quantum well. The currents are related to the transport coefficients by

$$\mathbf{J}_e = \sigma \mathbf{E} - \sigma S \nabla T \quad \mathbf{J}_Q = \sigma \text{STE} - \gamma_e \nabla T \quad (4)$$

where $\gamma_e = \kappa_e + \sigma S^2 T$, and κ_e is the electronic contribution to the thermal conductivity.

CONSTANT RELAXATION TIMES

First we use the constant relaxation time approximation (CRTA) to discuss the effects of finite barrier widths and of carrier tunneling between quantum well layers. At this point we neglect the well width and energy dependence of the scattering rates and the effect of confinement on the valley degeneracy. In this approximation to the Boltzmann equation, the transport coefficient can be expressed as [15]

$$\sigma = L_0 \quad \sigma S = -\frac{1}{eT} L_1 \quad \gamma = \frac{1}{e^2 T} L_2 \quad (5)$$

where

$$L_j = \int d\epsilon \left(-\frac{\partial f_0}{\partial \epsilon} \right) \sigma(\epsilon) (\epsilon - \zeta)^j \quad (6)$$

and

$$\sigma(\epsilon) = e^2 \tau \int \frac{d\mathbf{k}}{4\pi^3} \delta(\epsilon - \epsilon(\mathbf{k})) v_x^2 \quad (7)$$

Here τ is the relaxation time, \mathbf{k} is a three-dimensional wavevector, f_0 is the equilibrium Fermi distribution, $v_x = \hbar^{-1} \partial \epsilon(\mathbf{k}) / \partial k_x$, and μ is the chemical potential of the carriers. The transport is taken to be in the x -direction. The total thermal conductivity is composed of a phonon part in addition to the electronic contribution, $\kappa = \kappa_{ph} + \kappa_e$.

In order to treat carrier tunneling through the barriers, we use an Kronig-Penny-like model to describe their dispersion for a finite potential off-set V_0 . The carrier dispersion of the n^{th} subband then is

$$\epsilon_n(\mathbf{k}) = \epsilon_n(k_z) + \frac{\hbar^2}{2} \left(\frac{k_x^2}{m_x} + \frac{k_y^2}{m_y} \right) \quad (8)$$

Here, the superlattice axis is in the z -direction, m_x and m_y are the anisotropic effective masses in the plane of the layers, and $\epsilon_n(k_z)$ is obtained by solution of the Kronig-Penney model. For relatively weak coupling between wells, $\epsilon_n(k_z)$ can be approximated by

$$\epsilon_n(k_z) = \epsilon_{n0} + \Delta_n (1 \mp \cos k_z d) \quad (9)$$

where ϵ_{n0} is the energy at the bottom of the n^{th} subband, the overlap integrals, Δ_n , give the half-width of the subband, and the $+$ ($-$) sign corresponds to negative (positive) band dispersion. Δ_n depend on potential height V_0 , the barrier and well widths a and b and on the subband index n . For the range of parameters, a , b , and V_0 , considered here, we find that this form gives a good fit to the relevant portion of the exact Kronig-Penney band structure. Then the density of states of the superlattice then can be obtained analytically by summing over wavevectors at a given energy [16].

In order to illustrate the effects of the superlattice band structure on ZT , calculations have been made for Bi_2Te_3 superlattices. In the bulk it has the one of the highest ZT values known. The transport properties of Bi_2Te_3 are highly anisotropic. We take the x -direction to be in the quantum well plane and to be along the a_0 axis of the hexagonal unit cell. The superlattice direction z is taken to be along the b_0 axis of the unit cell, which gives [3] $m_x = 0.021$, $m_y = 0.32$ and $m_z = 0.081$ and a mobility $\mu_x = 1200 \text{ cm}^2/\text{Vsec}$. These calculations were done at room temperature, $T=300\text{K}$, and in each case the carrier density is chosen to maximize ZT . The value of the phonon contribution to the thermal conductivity is [3] $\kappa_{\text{ph}} = 0.015 \text{ W/cmK}$ for the well and barrier material. Here we have taken both the quantum well and barrier materials to be the same, and we describe a superlattice by putting a potential barrier between them. In this case in order to account for the six valleys of the conduction band of Bi_2Te_3 , σ and κ_e have been multiplied by 6 for both bulk and superlattices. For the superlattices, this is expected to be an overestimate of these quantities because the anisotropic masses partially lift the valley degeneracy.

Figure 1 gives ZT_S for the Bi_2Te_3 superlattice scaled by the bulk value, which is calculated to be $ZT_{3D}=0.53$, as a function of the thickness of the quantum well layer, a , for three different ratios of the barrier to well thickness b/a . Here the barrier height, V_0 , is taken to be 0.2 eV, a value that is typical of off-sets in semiconductor superlattices. For thicker wells, ZT_S lies below that of the bulk, and this effect is more pronounced for the larger barrier thicknesses. This behavior arises from the parasitic effects of the thermal current that flows through the barrier layers. For decreasing well widths, ZT_S increases and reaches a maximum, and then for still smaller well widths ZT_S decreases as a result of carrier tunneling through the barriers. The value of the well width at which the maximum occurs decreases for increasing barrier widths b . The maximum of ZT_S for superlattices is found to be somewhat larger than the bulk value and is nearly independent of the barrier width for this range a and b . This enhancement arises from the changes in the density of states upon electron confinement in relatively narrow wells.

Figure 2 shows the dependence of ZT_S on the barrier height, V_0 . For large periods d , ZT_S increases for decreasing V_0 and approaches the bulk value. In effect, the thermal conduction in the barriers becomes relatively less important as the carriers spread out into the barriers. For superlattice periods near the maximum of ZT_S its enhancement over the bulk value is larger for larger V_0 , which arises from greater quantum confinement manifested by flatter superlattice dispersions. This shows that the maximum in ZT_S arises from tunneling between the layers.

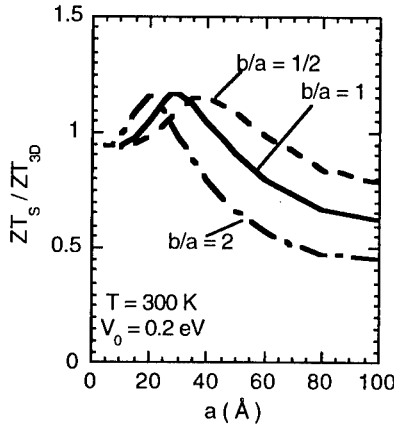


Fig. 1. The figure of merit ZT_S of Bi_2Te_3 superlattices scaled by ZT_{3D} for the corresponding bulk given as a function of the well width a for several ratios of the barrier width to well width, $b/a = 1/2$ (dashed line), 1 (solid line), and 2 (dashed - dotted line).

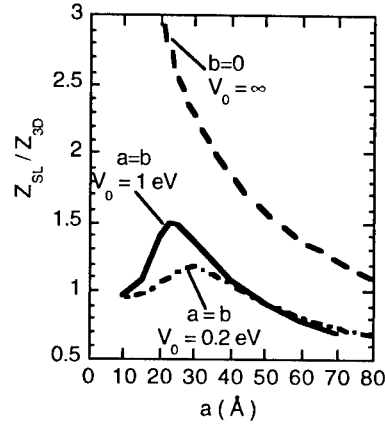


Fig. 2. The figure of merit ZT_S of Bi_2Te_3 superlattices (scaled by ZT_{3D}) as a function of the superlattice period d for potential barrier heights, $V_0 = 0.2$ eV (dashed dotted line), and 1 eV (solid line). Also shown is the ZT_S for $V_0 = \infty$ and $b=0$ (dashed line).

CONFINEMENT EFFECTS ON SCATTERING TIMES AND VALLEY DEGENERACY

The CRTA assumes that the carrier scattering time is independent of carrier energy and well thickness. It is well known that electron scattering rates in superlattices differ qualitatively from those in bulk materials [12-14]. We expect the dominant carrier scattering at room temperature to be due to quasi-elastic acoustic phonon scattering via the deformation potential interaction and inelastic polar optical phonon scattering via the Fröhlich interaction. Scattering by ionized impurities is less important at room temperature. From the results obtained above in the constant relaxation time approximation, we see that strong carrier confinement in the quantum well layers produces large ZT 's, and our interest here is in the maximum values of ZT occurring with confinement. Thus, we will consider the strong confinement limit in which the barrier height $V_0 \rightarrow \infty$. For this case, no tunneling occurs between the quantum wells. In order to solve the Boltzmann equation in this case, we use an iterative approach that was developed to treat inelastic scattering mechanisms in bulk systems [17,18]. We have extended this approach to treat the multi-subband case of a quantum well superlattice. For transport in the x direction in the plane of the well, the transport coefficients are given by

$$\sigma = \frac{e^2 k_B T}{\pi \hbar^2 d} \sum_{n_j} \int_0^\infty dx \left(-\frac{\partial f_0(\zeta_{n_j})}{\partial x} \right) \tau_{1n_j}(x) x \quad (10)$$

$$\sigma S = -\frac{ek_B}{\pi \hbar^2 d} \sum_{n_j} \int_0^\infty dx \left(-\frac{\partial f_0(\zeta_{n_j})}{\partial x} \right) \tau_{2n_j}(x) x \quad (11)$$

$$\gamma_e = \frac{k_B^2 T}{\pi \hbar^2 d} \sum_{nj} \int_0^\infty dx \left(-\frac{\partial f_0(\zeta_{nj})}{\partial x} \right) (x - \zeta_{nj}) \tau_{2nj}(x) x \quad (12)$$

Here the Fermi distribution $f_0 = 1/(\exp(x - \zeta_{nj}) + 1)$ involves the scaled chemical potential, $\zeta_{nj} = (\mu - \epsilon_{nj})/k_B T$, where ϵ_{nj} is the energy at the bottom of the n^{th} subband deriving from the j^{th} valley.

For illustration we evaluate the transport coefficients and figure of merit ZT for PbTe superlattices, which are of particular current interest experimentally. Bulk PbTe is a multi-valley semiconductor which has four parabolic anisotropic conduction band valleys along the [111] crystallographic directions. In this case we consider explicitly the lifting of the carrier valley degeneracy of multi-valley semiconductors due to confinement. The superlattice axis is along the [111] direction. We employ a two-band $\mathbf{k} \cdot \mathbf{p}$ model to obtain the band-edge masses for the j^{th}

valley as $\epsilon_j(\mathbf{k}) = \frac{\hbar^2}{2} \left(\frac{k_z^2}{m_{jz}} + \frac{k_{\parallel}^2}{m_{j\parallel}} \right)$, where m_{jz} and $m_{j\parallel}$ are the masses along the superlattice axis and

in the plane of the layers, respectively. Along the principal axes of the single longitudinal ellipsoidal valley aligned along [111] (z-direction) we find $m_{jz} = 0.35$ and $m_{j\parallel} = 0.034$. The other three oblique valleys are equivalent, and the band-edge mass for these valleys projected along the [111] direction is $m_{0z} = 0.038$. The corresponding density-of-states averaged in-plane mass is calculated to be $m_{0\parallel} = 0.076$. The parameters used in the calculations of the scattering rates are [19]

the longitudinal optical phonon energy $\hbar\omega_0 = 14$ meV, the static and high frequency dielectric constants, $\kappa_0 = 33$, $\kappa_\infty = 414$, the deformation potential constant, $D = 25$ eV, and $\rho v_1^2 = 486$ meV/Å³

where ρ is the density, and v_1 is the average speed of the longitudinal acoustic phonons. The lattice contribution to the thermal conductivity in PbTe is taken to be $\kappa_{ph} = 2W/m \cdot K$.

We begin by taking the barriers to have zero thickness and infinite potential height, which produces the highest ZT in the CRTA. Once again, the carrier density is chosen to maximize ZT . The solid line in Figure 3 gives ZT_{SL}/ZT_{Bulk} as a function of well thickness. With decreasing well thickness, ZT_{SL} first decreases and then increases for the narrowest wells. This behavior is caused by the lifting of the valley degeneracy due to the quantum confinement, which occurs because of the large difference in effective masses for longitudinal and oblique valleys along the confinement direction. As the well thickness decreases further, the ZT of the system, now with only a single contributing valley, increases modestly. ZT_{SL} remains below the bulk value for wells down to 10 Å. The dotted line is ZT_{SL} calculated in a multi-subband CRTA that uses the same constant relaxation time for each subband, which is chosen to match the bulk mobility [19], $\mu_{bulk} = 1700 \text{ cm}^2/\text{V} \cdot \text{s}$. The same trend is evident in this case. Thus, for well widths of interest in practice the increase in ZT_{SL} brought about by the strong confinement is more than offset by a decrease in ZT_{SL} arising from the lifting of the valley degeneracy.

In order to illustrate the role of an accurate treatment of the carrier scattering, we consider a model of a PbTe superlattice system in which all four valleys are degenerate with the mass of the [111] valley. The dash-dotted line in Figure 3 gives the ZT_{SL} from the CRTA with this valley degeneracy. For small well thicknesses, ZT_{SL} increases sharply, reaching a value almost 5 times the bulk value for the narrowest well considered, $a = 10$ Å. For comparison, the dashed line shows ZT_{SL} obtained with the theoretical treatment given here. It is evident that the increase in ZT_{SL} is considerably smaller than that predicted by the CRTA. This difference arises from the decrease in the scattering functions, τ_{1nj} and τ_{2nj} , with decreasing well width.

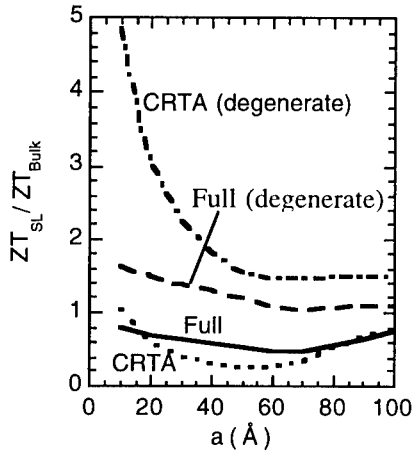


Fig. 3. ZT_{SL}/ZT_{Bulk} vs. well thickness, a , for PbTe superlattices having zero barrier thickness with and without lifting of valley degeneracy. Solid line: full treatment in text including lifting of valley degeneracy; dotted line: CRTA with lifting of valley degeneracy; Dashed line: full treatment with enforced valley degeneracy; Dash-dotted line: CRTA with enforced valley degeneracy.

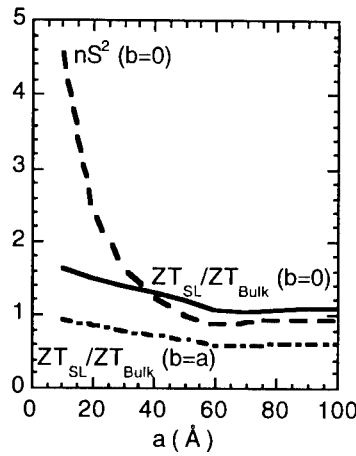


Fig. 4. ZT_{SL}/ZT_{Bulk} (solid line), P/P_{Bulk} , (dashed line) as a function of well thickness for PbTe quantum well superlattices with zero barrier thickness, and ZT_{SL}/ZT_{Bulk} with same well and barrier thickness (dash-dotted line).

Recent experimental work [20] has reported an increase in the factor, nS^2 , in PbTe/PbEuTe quantum well systems, where n is the carrier density. In the CRTA, $n \propto \sigma$, so that $nS^2 \propto P$, where $P = \sigma S^2$ is called the power factor and is proportional to the numerator of ZT . However, because the τ 's should not be constant, this proportionality should not hold. Thus it is of interest to compare the well width dependence of nS^2 with that of ZT obtained from the full theoretical treatment. In figure 4, ZT_{SL} and nS^2 , scaled by their bulk values, are plotted as functions of well thickness for PbTe quantum well superlattices with zero barrier thickness. As before, the carrier density is chosen to maximize P and ZT . With decreasing well thickness, nS^2 increases more rapidly than does ZT . These results suggest that one must exercise care in using nS^2 as a direct measure of ZT . A more reliable measure of ZT would be provided by the power factor itself because σ includes the well-thickness dependent scattering functions, whereas n does not.

Finally we consider the effects of barrier layers of non-zero thickness on ZT_{SL} . For simplicity, we neglect the electron tunneling through the barrier layers. The dash-dotted line in Figure 4 shows ZT_{SL} vs. a , for well and barrier thicknesses the same, $a=b=d/2$, and for the model PbTe superlattices discussed above having four-fold valley degeneracy. The barrier layer reduces ZT_{SL} due to the heat transport in the layer. A similar dependence on barrier layer thickness was seen in

Figures 1 and 2 for calculations in the CRTA. For non-zero barriers in PbTe superlattices ZT_{SL} lies below the bulk value for all well thicknesses shown.

ACKNOWLEDGEMENTS

This work was supported in part by the US Office of Naval Research.

REFERENCES

1. Gerald Mahan, Brian Sales and Jeff Sharp, *Physics Today* **50** (No. 3), 42 (1997)
2. Goldsmid, H. J., in *Thermoelectric Refrigeration*, Plenum Press, NY (1964).
3. L. D. Hicks and M. S. Dresselhaus, *Phys. Rev. B* **47**, 12727 (1993).
4. L. D. Hicks, T. C. Harman and M. S. Dresselhaus, *Appl. Phys. Lett.* **63**, 3230 (1993).
5. L. D. Hicks and M. S. Dresselhaus, *Phys. Rev. B* **47**, 16631 (1993).
6. J. O. Sofo and G. D. Mahan, *Appl. Phys. Lett.* **65**, 2690 (1994).
7. D. A. Broido and T. L. Reinecke, *Phys. Rev. B* **51**, 13797 (1995).
8. D. A. Broido and T. L. Reinecke, *Appl. Phys. Lett.* **67**, 100 (1995).
9. D. A. Broido and T. L. Reinecke, *Appl. Phys. Lett.* **67**, 1170 (1995).
10. P. J. Lin-Chung and T. L. Reinecke, *Phys. Rev. B* **51**, 13224 (1995).
11. D. A. Broido and T. L. Reinecke (to be published).
12. P. J. Price, *Ann. Phys. (NY)* **133**, 217 (1981).
13. B. Vinter, *Appl. Phys. Lett.* **45**, 581 (1984).
14. P. A. Knipp and T. L. Reinecke, *Phys. Rev. B* **48**, 5700 (1993).
15. N. D. Ashcroft and N. D. Mermin, *Solid State Physics*, (Saunders, Philadelphia, 1976), Chapt. 13.
16. L. Friedman, *J. Phy. C* **17**, 3999 (1984).
17. D. L. Rode, *phys. Rev. B* **2**, 1012 (1970).
18. J. O. Sofo and G. D. Mahan, *Phys. Rev. B* **49**, 4565 (1994).
19. Landholt and Bö rnstein, *Numerical Data and Functional Relationships in Science and Technology, New Series*, Vols. 17f (Springer-Verlag, Berlin, 1983) pp. 170-180.
20. L. D. Hicks, T. C. Harman, X. Sun and M. S. Dresselhaus, *Phys. Rev. B* **53**, 10493 (1996).

QUANTUM CONFINEMENT EFFECTS ON THE THERMOELECTRIC FIGURE OF MERIT IN Si/Si_{1-x}Ge_x SYSTEM

X. Sun*, M. S. Dresselhaus*, K. L. Wang**, M. O. Tanner**

*Department of Physics, Massachusetts Institute of Technology, Cambridge, MA 02139

**Department of Electrical Engineering, University of California, Los Angeles, CA 90024

ABSTRACT

The Si/Si_{1-x}Ge_x quantum well system is attractive for high temperature thermoelectric applications and for demonstration of proof-of-principle for enhanced thermoelectric figure of merit Z , since the interfaces and carrier densities can be well controlled in this system. We report here theoretical calculations for Z in this system, and results from theoretical modeling of quantum confinement effects in the presence of δ -doping within the barrier layers. The δ -doping layers are introduced by growing very thin layers of wide band gap materials within the barrier layers in order to increase the effective barrier height within the barriers and thereby reduce the barrier width necessary for the quantum confinement of carriers within the quantum well. The overall figure of merit is thereby enhanced due to the reduced barrier width and hence reduced thermal conductivity, κ . The δ -doping should further reduce κ in the barriers by introducing phonon scattering centers within the barrier region. The temperature dependence of Z for Si quantum wells is also discussed.

INTRODUCTION

Recently, it has been shown theoretically [1] that it may be possible to increase the thermoelectric figure of merit (Z) of certain materials by preparing them in the form of two-dimensional (2D) quantum-well structures. This has already been demonstrated experimentally [2] using n-type PbTe/Pb_{1-x}Eu_xTe multiple-quantum-well structures grown by molecular-beam epitaxy.

In bulk form, Si_{1-x}Ge_x is a promising thermoelectric material for high temperature applications [3, 4, 5], and has been used in radio-isotope thermoelectric generators (RTGs) on satellites and spacecraft for compositions of about Si_{0.7}Ge_{0.3} operating at ~ 1000 K [6]. Because of the large amount of expertise and information available regarding the materials science of fabricating Si/Si_{1-x}Ge_x quantum wells, it is an interesting system for the demonstration of both proof-of-principle and 2D thermoelectric device operation at high temperatures.

TWO-DIMENSIONAL THERMOELECTRICITY OF Si

The effect on Z of using materials in two-dimensional (2D) structures, such as 2D multiple-quantum-well (MQW) structures, has been studied earlier [1], and it was shown theoretically that this approach could yield a significant increase in Z over the bulk value as the quantum-well width is decreased. The proposed increase in the power factor $S^2\sigma$ arises mainly from the enhancement of the density of electron states per unit volume (near the Fermi level) that occurs for small quantum well widths. Further increase in Z is possible through the reduction of the thermal conductivity, κ , resulting from enhanced phonon scattering at the interfaces between the quantum wells and barriers.

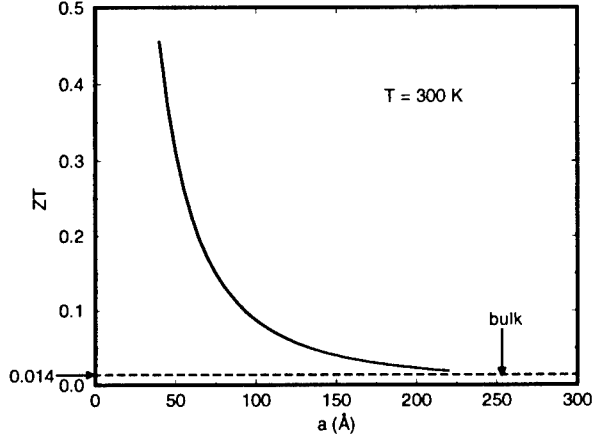


Figure 1: The calculated $Z_{2D}T(\zeta^*)$ versus layer thickness a at room temperature for a Si quantum well. The dashed line indicates the ZT for bulk Si [7].

Let the quantum well be parallel to the x - y plane and assume that the current flow is in the x direction. In the $\text{Si}/\text{Si}_{1-x}\text{Ge}_x$ quantum well structures we have investigated, the samples are grown along the $[100]$ direction and the transport measurements are performed along the principal directions of each of the six ellipsoids in the conduction band. By assuming that the conduction band is parabolic and that the electrons occupy only the lowest ($n = 1$) sub-band of the quantum well, the figure of merit for a two-dimensional system of Si can be found as [1, 7]

$$Z_{2D}T = \frac{\left(\frac{2F_1}{F_0} - \zeta^*\right)^2 F_0}{\frac{1}{B_{2D}} + 3F_2 - \frac{4F_1^2}{F_0}}, \quad (1)$$

where the Fermi-Dirac function F_i is given by

$$F_i = F_i(\zeta^*) = \int_0^\infty \frac{\eta^i d\eta}{e^{(\eta - \zeta^*)} + 1}, \quad (2)$$

and $\zeta^* = \zeta/k_B T$ is the reduced chemical potential relative to the edge of the first sub-band. The value of B_{2D} in Eq. (1) is determined by the intrinsic properties of Si and the width a of the quantum well [7]. For a given value of B_{2D} , the reduced chemical potential ζ^* in Eq. (1) is optimized to yield the maximum value of $Z_{2D}T$ within the quantum well. In the 2D case, ζ^* may be varied both by doping and by changing the layer thickness a . This extra degree of freedom of low dimensional structures provides a promising approach for increasing $Z_{2D}T$ above the characteristic $Z_{3D}T$ of the corresponding bulk materials.

Si crystallizes in the diamond structure. The conduction band is characterized by six equivalent minima along the $\langle 100 \rangle$ -axes of the Brillouin zone. The surfaces of constant energy are ellipsoids of revolution with their major axes along $\langle 100 \rangle$. The transverse and longitudinal effective masses are $m_\perp = 0.1905 m_0$ and $m_\parallel = 0.9163 m_0$. The electron mobility at room temperature for bulk Si is $\mu_n = 1447 \text{ cm}^2 \text{ V}^{-1} \text{ s}^{-1}$. The bulk phonon thermal conductivity is $\kappa_{ph} = 1.313 \text{ W cm}^{-1} \text{ K}^{-1}$ at 300 K [8].

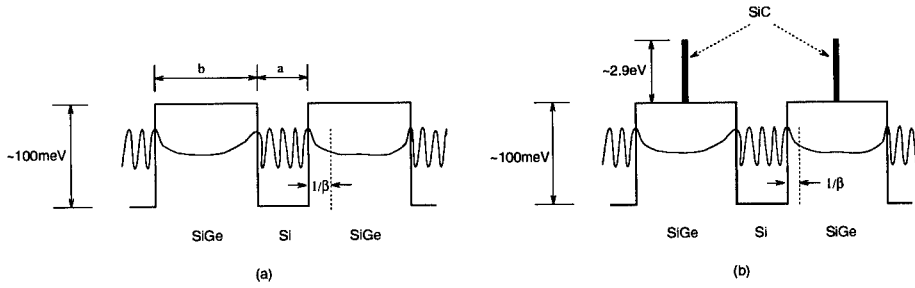


Figure 2: The δ -doping within barrier layers, using the wide bandgap material SiC. Schematic electron wavefunctions in Si/SiGe superlattices without (a) and with (b) δ -doping SiC layers, where $1/\beta$ characterizes the depth of the wavefunction penetrating into the barrier.

In a quantum-well structure, since phonons can scatter off the interfaces, the phonon thermal conductivity may be reduced relative to the bulk value which is given by

$$\kappa_{ph} = \frac{1}{3} C_v v l, \quad (3)$$

where l is the phonon mean free path, C_v is the lattice heat capacity, and v is the velocity of sound in the material. For Si, $C_v = 1.658 \text{ J K}^{-1} \text{ cm}^{-3}$ and $v = 8.4332 \times 10^5 \text{ cm/s}$, giving a value of $l = 282 \text{ \AA}$. If the layer thickness a is greater than 282 \AA , then layering does not seriously affect the mean free path l , and κ_{ph} should then be similar to its bulk value. However, if a is less than 282 \AA , then l and κ_{ph} are limited by phonon scattering off the interfaces and a rough estimate for κ_{ph} is obtained by setting $l = a$ and using Eq. (3).

The calculated $Z_{2D}T(\zeta^*)$ as a function of a for Si quantum wells at room temperature is shown in Fig. 1, together with a dashed line indicating the room temperature 3D figure of merit of $Z_{3D}T = 0.014$. The quantum well width a in the calculations is less than the phonon mean free path l , and therefore $\kappa_{ph} = \frac{1}{3} C_v v a$ is used to estimate the phonon contribution to the thermal conductivity for $a < l$. The results show a significant increase in the thermoelectric figure of merit for a quantum well width a below 100 \AA .

QUANTUM CONFINEMENT IN THE PRESENCE OF δ -DOPING

The quantum confinement of carriers within a quantum well is crucial to get high mobility carriers and to achieve two-dimensional transport. In order to get high thermoelectric performance in the Si quantum well, one has to use a relatively large barrier width. This reduces the overall thermoelectric performance because of the thermal conductivity of the barrier region. Simply reducing the barrier width will destroy the quantum confinement, hence bringing the system back to the three-dimensional case.

Fig. 2 shows a strategy to improve quantum confinement with thinner barrier layers by employing δ -doping layers within the barriers which form very thin sheets of a wide band gap semiconductor. We have performed theoretical modeling with SiC, which is a wide band gap semiconductor, as the δ -doping layer. The effect of δ -doping can be taken into account by introducing a potential, $V(z) = V\delta(z - z_0)$, into the Schrödinger equation for electrons

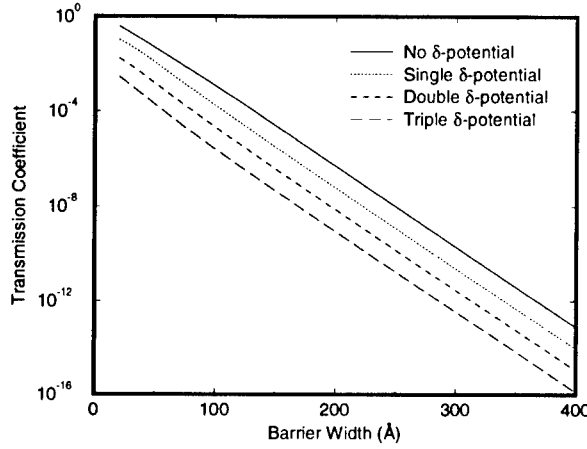


Figure 3: The transmission coefficient as a function of barrier width for different δ -doping schemes in Si/SiGe superlattices.

in the framework of a semiclassical theory [9], where z_0 is the position of the δ -doping layer and V is the product of the barrier height and the width for the δ -doping layer. For δ -doping by SiC, we have considered a δ -doping layer with a width of 2\AA , so that $V = 2.9\text{eV} \times 2\text{\AA}$.

The quantum confinement in the quantum well can be characterized by the wavefunction leakage into the barrier layer which is defined as

$$\text{leakage} = \frac{\int_{\text{barrier}} |\Psi(z)|^2 dz}{\int_{\text{well+barrier}} |\Psi(z)|^2 dz}. \quad (4)$$

Numerical calculations show that for barrier widths less than 200\AA , the wavefunction leakage is decreased significantly in the presence of the SiC δ -potential. The wavefunction leakage defined in Eq. (4) is not the only factor affecting the electronic states within the superlattice. Carrier tunneling across the barrier layers should also be avoided and therefore should be considered, especially in the case of thin barriers. The transmission coefficient D through a barrier potential $U(z)$ can be found generally as

$$D = D_0 e^{-\frac{2}{\hbar} \int \sqrt{2m^*[U(z)-E]} dz}, \quad (5)$$

where E is the energy eigenvalue of the electronic state, and D_0 , which corresponds to the transmission coefficient for a freely propagating wave, is approximately equal to one for all practical purposes. Fig. 3 shows the numerical calculations for the transmission coefficient as a function of barrier width for several cases, including a single δ -potential at the mid-point of the barrier as well as two and three δ -potentials within the barrier layer. Since the suppression of the wavefunction within the barrier layers is more significant if we put δ -potentials of the same size closer to the interface between the quantum well and barrier, the optimum position was found for the placement of two δ -potentials within the barrier. In the case of three δ -potentials, one of the δ -layers is placed at the center of the barrier. In Fig. 3 we observe that while maintaining the same transmission coefficient, the barrier

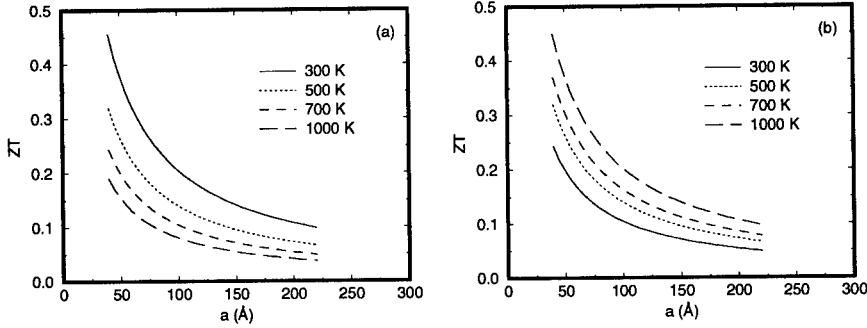


Figure 4: The calculated $Z_{2D}T(\zeta^*)$ versus layer thickness a at various temperatures for a Si quantum well. The electron mobility is determined empirically as (a) $\mu_n = 1.43 \times 10^9 T^{-2.42} \text{ cm}^2/\text{Vs}$ (T in K) for intrinsic Si, and (b) $\mu_n = 2.11 \times 10^5 T^{-1} \text{ cm}^2/\text{Vs}$ (T in K) for an n-type Si with carrier concentration of 10^{18} cm^{-3} .

width can be reduced significantly by introducing one or more δ -doping layers within the barrier region.

TEMPERATURE DEPENDENCE OF ZT

Since $\text{Si}/\text{Si}_{1-x}\text{Ge}_x$ is a system aimed at high temperature operation (up to 1000 K), it is interesting to investigate the thermoelectric performance of $\text{Si}_{1-x}\text{Ge}_x$ quantum well systems at elevated temperatures. Since the power factor for $\text{Si}_{1-x}\text{Ge}_x$ materials generally increases with increasing T above room temperature [3, 4], the power factor as well as the thermoelectric figure of merit for the quantum well are expected to show even greater enhancement above 300 K.

In calculating the figure of merit using Eq. (1), we found that the value of $Z_{2D}T$ for quantum wells is very sensitive to the carrier mobility. This implies that carrier mobility is one of the most important factors in determining thermoelectric performance. With increasing temperature, it is well known that the carrier mobility for Si decreases exponentially in the temperature range between 300 K and 1000 K, which can be written empirically as

$$\mu_n = \mu_0 T^{-\lambda}, \quad (6)$$

where $\lambda = 2.42$ for intrinsic electron carriers. If we use Eq. (6) with $\lambda = 2.42$ to calculate the temperature dependent figure of merit for Si quantum wells, we will find that $Z_{2D}T$ is not favorable at high temperatures because of the rapid decrease of carrier mobility, as shown in Fig. 4(a). However, in the case of 2D Si quantum wells for thermoelectric application, the optimal and feasible carrier concentration is on the order of $4 \times 10^{18} \text{ cm}^{-3}$. For such heavily doped n-type bulk Si, the exponent λ in Eq. (6) can be approximated using existing experimental data [10] to obtain $\mu_n = 2.11 \times 10^5 T^{-1} \text{ cm}^2/\text{Vs}$ (T in K). This weaker temperature dependence has a large effect on $Z_{2D}T$ as a function of quantum well width at elevated temperatures, as shown in Fig. 4(b). These results suggest that $Z_{2D}T$ for $\text{Si}/\text{Si}_{1-x}\text{Ge}_x$ quantum wells is very favorable at higher temperatures.

CONCLUSION

Theoretical modeling of the thermoelectric figure of merit for Si/Si_{1-x}Ge_x quantum well structures suggests that an increase in the thermoelectric figure of merit over bulk values in the Si/Si_{1-x}Ge_x quantum well system should be possible. In order to enhance the overall thermoelectric performance, it should be possible to decrease the barrier width by introducing one or more δ -doping layers in the barrier layers while maintaining the same level of carrier quantum confinement. Further enhancement in $Z_{2D}T$ for Si/Si_{1-x}Ge_x quantum well structures is expected at elevated temperatures through both quantum confinement and phonon interface scattering effects. Numerical calculations suggest that $Z_{2D}T$ is favorable at elevated temperatures in the heavy doping regime.

ACKNOWLEDGMENTS

The authors thank Drs. G. Dresselhaus, T. C. Harman, C. B. Vining and Professors Gang Chen, P. C. Eklund for valuable discussions. The authors gratefully acknowledge support by the US Navy under Contract No. N00167-92-K-0052 (MIT) and AFOSR under URI (UCLA), and the Honda Motor Co., Ltd. for the temperature dependent studies.

REFERENCES

- [1] L. D. Hicks and M. S. Dresselhaus, Phys. Rev. B **47**, 12727 (1993).
- [2] L. D. Hicks, T. C. Harman, X. Sun, and M. S. Dresselhaus, Phys. Rev. B **53**, R10493 (1996).
- [3] G. A. Slack and M. A. Hussain, J. Appl. Phys. **70**, 2694 (1991).
- [4] C. B. Vining, in *CRC Handbook of Thermoelectrics*, edited by D. M. Rowe (CRC Press, New York, 1995) p. 329.
- [5] G. D. Mahan, in *Solid State Physics*, edited by H. Ehrenreich and F. Spaepen (Academic Press, 1996).
- [6] C. Wood, Rep. Prog. Phys. **51**, 459 (1988).
- [7] X. Sun, M. S. Dresselhaus, K. L. Wang, and M. O. Tanner, in *Advances in Microcrystalline and Nanocrystalline Semiconductors - 1996*, edited by P. M. Fauchet, R. W. Collins, P. A. Alivisatos, I. Shimizu, T. Shimada, and J.-C. Vial (Mater. Res. Soc. Proc. 452, Pittsburgh, PA, 1997) p. 261.
- [8] *Landolt-Börnstein Numerical Data and Functional Relationships in Science and Technology*, New Series, edited by K.-H. Hellwege (Springer-Verlag, Berlin, 1982), Vol. 17a, pp. 43-87.
- [9] N. W. Ashcroft and N. D. Mermin, in *Solid State Physics* (Holt, Rinehart and Winston, New York, 1976), chap. 13.
- [10] S. S. Li, NBS Special Publication **400-33**, 13 (1977).

LOW THERMAL CONDUCTIVITY SKUTTERUDITES

J.-P. FLEURIAL*, T. CAILLAT AND A. BORSHCHEVSKY
Jet Propulsion Laboratory/California Institute of Technology,
4800, Oak Grove Drive, MS 277-207, Pasadena, CA 91109
*jean-pierre.fleurial@jpl.nasa.gov

ABSTRACT

Recent experimental results on semiconductors with the skutterudite crystal structure show that these materials possess attractive transport properties and have a good potential for achieving ZT values substantially larger than for state-of-the-art thermoelectric materials. Both n-type and p-type conductivity samples have been obtained, using several preparation techniques. Associated with a low hole effective mass, very high carrier mobilities, low electrical resistivities and moderate Seebeck coefficients are obtained in p-type skutterudites. For a comparable doping level, the carrier mobilities of n-type samples are about an order of magnitude lower than the values achieved on p-type samples. However, the much larger electron effective masses and Seebeck coefficients make n-type skutterudites promising candidates as well. Unfortunately, the thermal conductivities of the binary skutterudite compounds are too large, particularly at low temperatures, to be useful for thermoelectric applications.

Several approaches to the reduction of the lattice thermal conductivity in skutterudites are being pursued: heavy doping, formation of solid solutions and alloys, study of novel ternary and filled skutterudite compounds. All those approaches have already resulted in skutterudite compositions with substantially lower thermal conductivity values in these materials. Recently, superior thermoelectric properties in the moderate to high temperature range were achieved for compositions combining alloying and "filling" of the skutterudite structure. Experimental results and mechanisms responsible for low thermal conductivity in skutterudites are discussed.

INTRODUCTION

Thermoelectric generators and cooling devices present several advantages compared to other energy conversion technologies: they are reliable, can operate unattended in hostile environments, and are also environmentally friendly. However, their application has been limited up to now because of the relatively low conversion efficiency of traditional thermoelectric materials used in the devices. New more efficient materials are needed. A systematic search for advanced thermoelectric materials was initiated at JPL several years ago and resulted in the discovery of a new family of promising semiconducting materials with the skutterudite crystal structure [1].

The unit cell of the skutterudite structure (cubic, space group Im3, prototype CoAs_3) contains square radicals $[\text{As}_4]^{4-}$. This anion, located in the center of the smaller cube, is surrounded by 8 Co^{3+} cations. The unit cell was found to consist of 8 smaller cubes (octants) described above but two of them do not have the anions $[\text{As}_4]^{4-}$ in the center. This is necessary to keep the ratio $\text{Co}^{3+}:[\text{As}_4]^{4-} = 4:3$. Thus, a typical coordination structure results with $\text{Co}_8[\text{As}_4]_6 = 2\text{Co}_4[\text{As}_4]_3$ composition and 32 atoms per cell, as depicted in Figure 1.

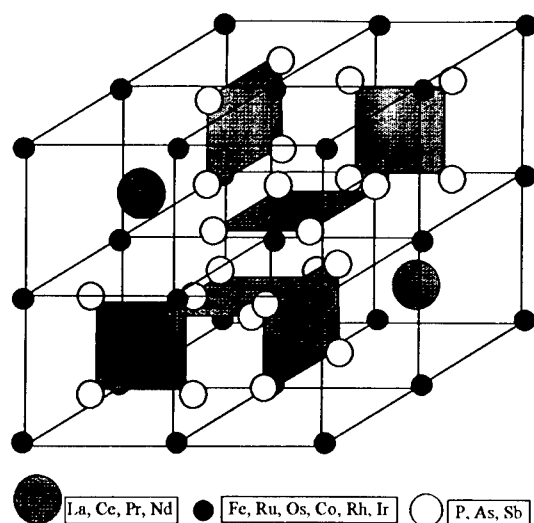


Figure 1: Skutterudite crystal structure. The unfilled structure has 32 atoms: a cubic frame with 8 transition metals, 24 pnictogens distributed in six square radicals and located in six of the eight octants, and two empty octants. Two rare earth elements located in the two remaining octants form a completely filled structure.

A low lattice thermal conductivity and a high carrier mobility are desirable for improved figures of merit in new thermoelectric materials. High carrier mobility values are usually found in crystal structures with a high degree of covalency. It has been shown that the bonding is predominantly covalent in the skutterudite structure and high hole mobility values have been measured on several skutterudite compounds: IrSb_3 , RhSb_3 , CoSb_3 , CoAs_3 , RhAs_3 and RhP_3 [2]. The unit cell is relatively large and complex, indicating that low lattice thermal conductivity values might be possible.

For state-of-the-art thermoelectric materials, the number of isostructural compounds is limited and the possibilities to optimize their properties for maximum performance at different temperatures of operation are also very limited. This is not the case for the skutterudite family of materials, where eleven binary compounds and many solid solutions and related phases are known to exist [2]. These materials cover a large range of decomposition temperatures and bandgaps which offers the possibility to adjust composition and doping level for a specific temperature range of application.

However, the room temperature thermal conductivity of binary skutterudites ($100\text{--}150 \text{ mWcm}^{-1}\text{K}^{-1}$) was found to be too high to result in high ZT values. Substantial reductions in the lattice thermal conductivity must be obtained to achieve values comparable to those of state of the art thermoelectric materials ($10\text{--}40 \text{ mWcm}^{-1}\text{K}^{-1}$).

Several approaches were recently considered to reduce the lattice thermal conductivity of these materials. Such reductions have been observed in heavily doped n-type binary compounds, solid solutions, ternary compounds, and also filled skutterudites. This paper presents recent thermal conductivity experimental data obtained on several skutterudite materials and briefly discusses the various phonon scattering mechanisms. It is shown that low thermal conductivity

skutterudites can be obtained and high ZT values are possible, which can lead to a significant improvement in the thermal-to-electric conversion efficiency of thermoelectric devices.

LATTICE THERMAL CONDUCTIVITY REDUCTION IN SKUTTERUDITES

The dimensionless thermoelectric figure of merit ZT is inversely proportional to the thermal conductivity. As a consequence, efficient thermoelectric materials have low thermal conductivity values such as Bi₂Te₃-alloys (15 to 20 mWcm⁻¹K⁻¹), PbTe-alloys (10 to 20 mWcm⁻¹K⁻¹) and Si-Ge alloys (40 to 50 mWcm⁻¹K⁻¹). The contribution of the crystal lattice, through heat conduction by phonons, to the total thermal conductivity can be reduced by effectively scattering the phonons. Several scattering mechanisms are of interest to reduce the lattice thermal conductivity of skutterudites: electron-phonon scattering in heavily doped samples, mass and strain fluctuation scattering in solid solutions and alloys, electron charge transfer scattering in mixed-valence ternary compounds, and void filler scattering in filled skutterudite compounds [3].

Heavily Doped CoSb₃

The thermal conductivity of heavily doped n-type CoSb₃ sample was recently measured [4]. The thermal conductivity data are shown in Figure 2. For lightly doped samples, the lattice thermal conductivity at 100°C is about 80 mWcm⁻¹K⁻¹ but for more heavily doped samples, the value decreases to about 44 mWcm⁻¹K⁻¹ (1x10²⁰ cm⁻³) and can be as low as 32 mWcm⁻¹K⁻¹ (1x10²¹ cm⁻³).

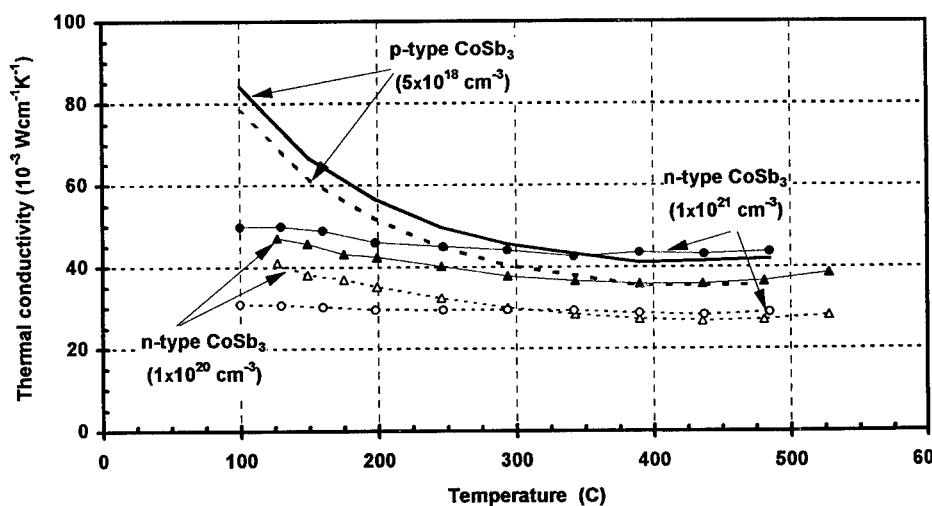


Figure 2: Lattice (dotted lines) and total (plain lines) thermal conductivity as a function of temperature for CoSb₃ samples with various doping levels.

The total thermal conductivity of the most heavily doped sample is actually higher than the one doped at 1x10²⁰ cm⁻³ because of the large electronic contribution (proportional to the electrical conductivity). The temperature dependence of the lattice thermal conductivity

becomes weaker for more heavily doped samples, indicating that electron-phonon scattering is responsible for the large decrease in lattice thermal conductivity. This is an interesting finding because charge carrier phonon scattering would scatter the phonons with low frequency and if coupled with point defect scattering could result in very low lattice thermal conductivity values. The combination of point defects and charge carrier scattering was utilized in Si-Ge alloys [5]. Because of lower carrier concentrations, this scattering mechanism has not been identified yet in p-type samples.

Skutterudite Solid Solutions

All state-of-the-art thermoelectric materials are solid solutions between two or more isostructural binary compounds or phases. The mass and strain fluctuations brought by point defects in solid solutions is a well known approach to reduce the lattice thermal conductivity. However, point defects not only scatter phonons but also scatter charge carriers, resulting in some decrease in carrier mobility. Thus, improvements in the thermoelectric properties can be obtained if the ratio of the carrier mobility to the lattice thermal conductivity is larger for the solid solutions.

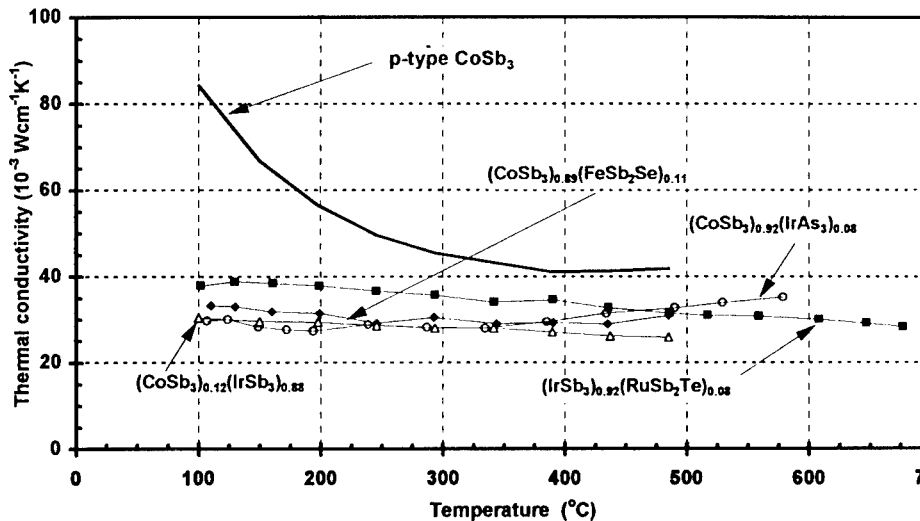


Figure 3: Thermal conductivity as a function of temperature for CoSb₃- and IrSb₃-based solid solutions. Results are compared to those obtained for lightly doped CoSb₃.

The existence of several solid solutions between skutterudite compounds were reported in the literature [6-9]. More recent studies showed that many more solid solutions can be formed and initial results demonstrated that a reduction in lattice thermal conductivity can be obtained [10]. For example, a room temperature lattice thermal conductivity of 33 mWcm⁻¹K⁻¹ was obtained for a lightly-doped, single phase, homogeneous and fully dense p-type (CoSb₃)_{0.75}(IrSb₃)_{0.25} solid solution. This represents a 70% reduction compared to either one of the end members in this system. The corresponding reduction in carrier mobility was only about 46%. Results

obtained for $a(\text{RhSb}_3)_{0.5}(\text{IrSb}_3)_{0.5}$ solid solution showed that its room temperature lattice thermal conductivity was decreased by about 45% [8]. The smaller reduction in this latter sample can be attributed to the fact that the decrease is only due to mass fluctuations in this system and that there is no strain fluctuation (the atomic volumes of Rh and Ir are almost identical). Some of the high temperature experimental results on several lightly doped solid solutions are shown in Figure 3. The results are compared to the experimental data on CoSb_3 and demonstrate the sharp reduction and near temperature-independent variation of the thermal conductivity of solid solutions.

In order to help selecting the most promising solid solutions systems, the effect of mass and strain fluctuation scattering of phonons was calculated for skutterudites using the theory developed by Callaway and Von Baeyer [11]. The calculation requires computing an alloy scattering parameter Γ which is a function of the variations in atomic masses and volumes introduced by the presence of different atoms located on the same sublattice. For compositions where volume fluctuations are becoming important, an adjustable strain parameter used in calculating Γ can be determined by fitting experimental data [10]. The result of the calculations conducted for CoSb_3 -based solid solutions are shown in Figure 4.

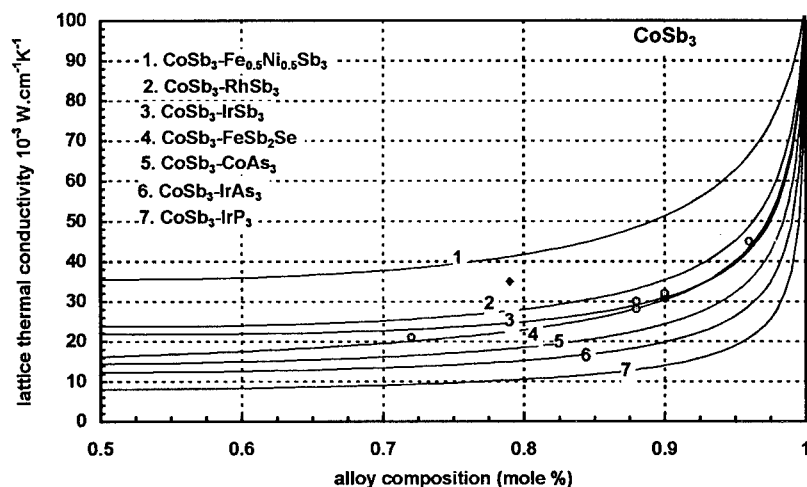


Figure 4: The calculated lattice thermal conductivity of CoSb_3 -based solid solutions at 300K as a function of solid solution composition. Experimental data are reported for $\text{CoSb}_3\text{-IrSb}_3$ (○), $\text{CoSb}_3\text{-FeSb}_2\text{Se}$ (■) and $\text{CoSb}_3\text{-Fe}_{0.5}\text{Ni}_{0.5}\text{Sb}_3$ (◆).

The major findings of these theoretical calculations are that: a) skutterudite solid solutions with small mass and volume fluctuations (such as $\text{CoSb}_3\text{-Fe}_{0.5}\text{Ni}_{0.5}\text{Sb}_3$, $\text{IrSb}_3\text{-RhSb}_3$ and $\text{IrSb}_3\text{-RuSb}_2\text{Te}$) exhibit relatively small decreases in lattice thermal conductivity; b) solid solutions between ternary and binary skutterudites do not result in lower thermal conductivity values compared to those obtained for optimum binary skutterudite alloys and; c) the lowest thermal conductivity values are achieved for alloys maximizing mass and volume fluctuations, such as $\text{CoSb}_3\text{-IrP}_3$ with $8 \text{ mWcm}^{-1}\text{K}^{-1}$ for a 50 mole% concentration.

These calculations show that point defect scattering alone can be a very efficient phonon scattering mechanism in some skutterudite solid solutions. More work is needed to determine the

solubility limit of some of these solid solutions and efforts are currently underway to prepare samples of the most promising systems and compare the experimental data with the theoretical predictions.

Ternary Compounds

Skutterudite related phases can be formed by substitution by neighboring atoms for the anion or the cation in binary skutterudite compounds, the condition being that the valence-electron count remains constant. This is similar to the diamond-like family of semiconductors. The substitution can occur on the anion site or on the cation site. Structurally related skutterudite phases can also be formed by partial substitution of the cation and the anion. Nine ternary skutterudite related phases have been reported in literature [2]. Based on x-ray diffraction analyses, fourteen new compositions were discovered at JPL. A number of isostructural quaternary and more complex complex compositions have also been identified.

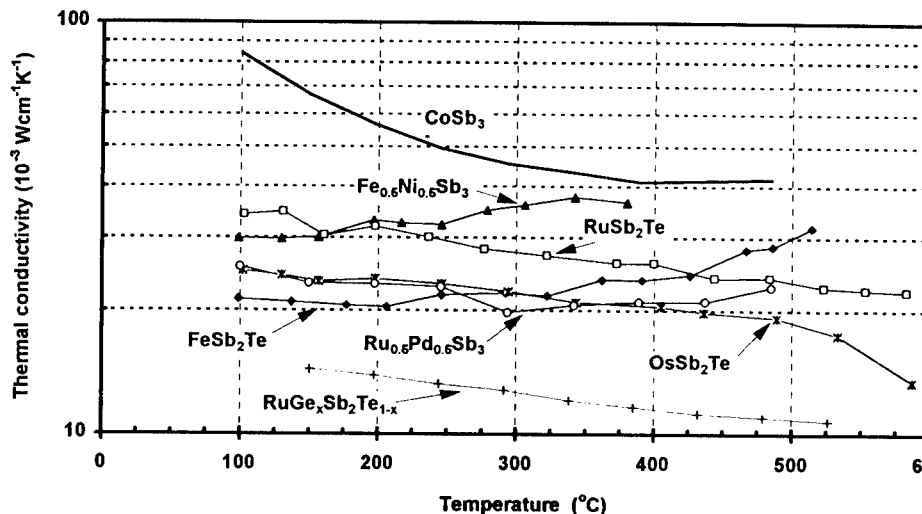


Figure 5: Thermal conductivity as a function of temperature for several ternary skutterudite compounds. Results are compared to those obtained for lightly doped CoSb_3 .

The electrical properties of the ternary skutterudites can vary substantially from the results obtained on the binary compounds. P-type conductivity samples were obtained for $\text{Ru}_{0.5}\text{Pd}_{0.5}\text{Sb}_3$, FeSb_2Te and RuSb_2Te , with typical carrier concentrations of $1 \times 10^{20} \text{ cm}^{-3}$, $5 \times 10^{20} \text{ cm}^{-3}$, and $8 \times 10^{18} \text{ cm}^{-3}$ respectively. N-type conductivity $\text{Fe}_{0.5}\text{Ni}_{0.5}\text{Sb}_3$ samples were also prepared but characterized by mixed conduction effects near room temperature. These results indicate that significant changes in band structure and doping behavior were brought by changes in the atomic and electronic structure. In particular, fluctuations in the valence of the transition metal atoms could be imposed by the need to conserve the skutterudite crystal structure. Understanding and controlling these changes is a key step in designing a skutterudite composition with superior thermoelectric properties.

The experimental data on the high temperature thermal conductivity of five ternary compounds, FeSb_2Te , RuSb_2Te , OsSb_2Te , $\text{Fe}_{0.5}\text{Ni}_{0.5}\text{Sb}_3$ and $\text{Ru}_{0.5}\text{Pd}_{0.5}\text{Sb}_3$ are plotted in Figure 5

[3, 12]. The results are compared to the data on lightly doped CoSb₃. The lattice contribution to the thermal conductivity is greatly reduced in these materials, with room temperature values ranging from 15 to 30 mW.cm⁻¹K⁻¹. The low thermal conductivity values of these compounds, while very encouraging, are nevertheless a bit surprising considering that the atomic mass and volume differences introduced by the substituting anion/cation are fairly small. This indicates that additional mechanisms must be involved.

A possible explanation for the unusually high phonon scattering rate could be that transition metal elements have mixed valence states and electrons are transferred between the different ions, thus scattering the phonons in this process [3, 13]. In a study of the thermal conductivity of Fe₃O₄, Slack [14] has shown that the phonon scattering caused by interaction of the phonons by local disorder in the magnetic lattice was significant. The binary compound CoSb₃ can be described by its ionic formula: Co³⁺Sb₃⁻¹. For example, when considering the stoichiometric Ru_{0.5}Pd_{0.5}Sb₃ composition, it is assumed that the valence state of Ru, Pd, and Sb would be Ru²⁺, Pd⁴⁺, and Sb⁻¹, respectively. Systematic shifts from the stoichiometric Ru_{0.5}Pd_{0.5}Sb₃ were revealed by microprobe analysis [12]. Results indicate that the Ru:Pd atomic ratio can vary substantially from the expected 1:1 value and that there is a significant number of vacancies on the transition metal sublattice. To compensate for the Pd deficit and excess Sb in the samples, the Ru must adopt a mixed valence state, *i.e.*, Ru²⁺ and Ru⁴⁺. Such valence fluctuations were recently confirmed by x-ray absorption near-edge structure analysis [13].

In addition to Ru_{0.5}Pd_{0.5}Sb₃, other ternary skutterudites such as RuSb₂Te also show significant stoichiometric deviations. Experimental data for Fe_{0.5}Ni_{0.5}Sb₃, Ru_{0.5}Pd_{0.5}Sb₃, FeSb₂Te, RuSb₂Te, OsSb₂Te and RuGe_xSb₂Te_{1-x} samples prepared at JPL are presented in Table 1. Based on electron microprobe analysis, we have recalculated each composition to conform to the T³⁺X₃⁻¹ stoichiometry, adding vacancies to the metal sublattice when needed. The valence ratio *v* of the mixed valence transition metal (for example [Ru²⁺]/[Ru⁴⁺]) was then determined from the ionic formula. The lattice thermal conductivity calculated from the measured thermal conductivity at room temperature using the Wiedmann-Franz law is also reported in this table.

Table 1: Valence Fluctuations in Low Thermal Conductivity Ternary Skutterudites, where *v* is the valence ratio (e.g. [Ru²⁺]/[Ru⁴⁺]) and λ_L is the lattice thermal conductivity in 10⁻³ W/cmK.

Compound	Composition (at%)	Ionic Formula	<i>v</i>	λ _L
Fe _{0.5} Ni _{0.5} Sb ₃	Fe _{12.8} Ni _{11.9} Sb _{75.2}	Fe ²⁺ _{0.51} Ni ⁴⁺ _{0.49} Sb ⁻¹ ₃	--	29
Ru _{0.5} Pd _{0.5} Sb ₃	Ru _{12.3} Pd _{10.6} Sb _{77.1}	[Ru ²⁺ _{0.11} Ru ⁴⁺ _{0.28} Pd ⁴⁺ _{0.20} Sb ⁻¹ _{0.41}]	1.4	15
FeSb ₂ Te	Fe _{25.1} Sb _{52.0} Te _{22.9}	Fe ²⁺ _{0.91} Fe ³⁺ _{0.09} Sb ⁻¹ _{2.1} Te ⁰ _{0.9}	10.4	23
RuSb ₂ Te	Ru _{22.4} Sb _{49.7} Te _{25.3}	[Ru ²⁺ _{0.10} Ru ⁴⁺ _{0.79} Sb ⁻¹ _{0.11} Te ⁰ _{1.98}]	7.2	28
OsSb ₂ Te	Os _{24.6} Sb _{50.5} Te _{24.9}	[Os ²⁺ _{0.02} Os ⁴⁺ _{0.98} Sb ⁻¹ _{0.02} Te ⁰ _{2.03}]	32.3	25
RuGe _x Sb ₂ Te _{1-x}	Ru _{24.0} Ge _{4.7} Sb _{50.6} Te _{20.7}	[Ru ²⁺ _{0.05} Ru ⁴⁺ _{0.75} Ge ⁻² _{0.18} Sb ⁻¹ _{2.0} Te ⁰ _{0.82}]	3.7	14

From Table 1, it can be seen that Ru_{0.5}Pd_{0.5}Sb₃ and RuGe_xSb₂Te_{1-x} possess high concentrations of Ru⁴⁺ (and vacancies), resulting in *v* values approaching 1, for which the scattering rate of phonons by the electron exchange mechanism is maximized. Those two compositions have the lowest lattice thermal conductivity values. For FeSb₂Te, RuSb₂Te and

OsSb₂Te, the ν values are much larger than 1, but the lattice thermal conductivities are still much lower than the values obtained for CoSb₃, RhSb₃ and IrSb₃. However, as is the case in some arsenopyrites [15], short-range disorder on the pnictogen sublattice could also lead to substantial valence fluctuations for the transition metals (and thus lower values of ν) trying to compensate for localized variations in the Sb:Te atomic ratio of 2. It is also likely that the substitution of Te by Ge in RuSb₂Te imposes a much higher Ru⁴⁺ concentration, which results in a 50% decrease in lattice thermal conductivity. As to Fe_{0.5}Ni_{0.5}Sb₃, it is likely that Fe and Ni are of valence 2+ and 4+ respectively since the valence of Fe in the corresponding arsenopyrite, Fe_{0.5}Ni_{0.5}Sb₂, was determined as close to 2+ [15]. However the presence of some small amount of Fe³⁺ and Ni³⁺ could also result in strong electron exchange scattering of the phonons and explain the low lattice thermal conductivity.

Although ternary compounds have rather low thermal conductivity values, it is difficult to control their electrical properties. When doping ternary skutterudites, and supposing that the electron exchange mechanism is indeed present, changes in carrier concentration are not easy to achieve because dopants can be compensated by small fluctuations in the overall valence of the transition metals.

Filled Skutterudites

Finally, the last approach which is now under consideration for reducing the lattice thermal conductivity of skutterudite materials is to fill the voids present in the skutterudite structure with rare earth elements (see Figure 1). Slack first suggested that the “rattling” of the rare earth element would produce a significant phonon scattering and reduce the thermal conductivity, but with minimal decrease in carrier mobility [16]. A large number of materials with a filled skutterudite crystal structure has already been synthesized [17]. The composition of these types of compounds can be represented by the formula LnT₄Pn₁₂ (Ln = La, Ce, Pr, Nd, Sm, Eu, Gd, Th and U; T = Fe, Ru, Os; Pn = P, As, Sb). In these compounds, the empty octants of the skutterudite structure which are formed in the T₄Pn₁₂ framework are filled with a rare earth element. Because the T₄Pn₁₂ groups using Fe, Ru or Os are electron-deficient (by 4 e⁻) relative to the skutterudite electronic structure (using Co, Rh or Ir), the introduction of the rare earth atom compensates this deficiency by adding free electrons. However, the number of valence electrons given up by the rare earth atoms is generally insufficient: for example, La has a 3+ oxidation state, Ce can be 3+ or 4+. This means that most of these compounds behave as metals, or very heavily doped p-type semimetals.

To conserve the excellent semiconducting behavior of the unfilled binary skutterudites, it is necessary to introduce a “compensating” atom for the addition of the “filling” atom into the structure. The ratio of compensating atoms to filling atoms is determined exclusively from the number of valence electrons of the filling atom. Thus, if Ce (the most stable valence number is 3) is introduced into the two empty octants of the 32 atoms CoSb₃ unit cell, 6 atoms of Fe (each providing one acceptor per atom) will have to be substituted for Co: CoSb₃ (or Co₈Sb₂₄) will become Ce₂Fe₆Co₂Sb₂₄ (or CeFe₃CoSb₁₂). This composition is very close to the compound CeFe₄Sb₁₂ whose existence was previously reported. The same approach can be applied with other atoms. Moreover, the doping level and conductivity type might be controlled by changing the compensating to filling atomic ratio. Also, the introduction of compensating atoms can bring a substantial increase in phonon scattering (mass and volume differences) and carrier scattering (ionized impurity, disorder) rates. Experimental evidence of this enhanced phonon scattering has since been published in the literature [18-23]. It also has been demonstrated that Ce is nearly trivalent at temperatures higher than 100K [23].

This approach seems to be particularly promising in light of recent results obtained on p-type $\text{CeFe}_{4-x}\text{Co}_x\text{Sb}_{12}$ materials [21-23]. The high temperature thermal conductivity data of some of these compositions are shown in Figure 6. The thermal conductivity of those materials is much lower than for CoSb_3 . The $\text{CeFe}_4\text{Sb}_{12}$ sample has a room temperature thermal conductivity of about $24 \times 10^{-3} \text{Wcm}^{-1}\text{K}^{-1}$ at room temperature and increasing up to $27 \times 10^{-3} \text{Wcm}^{-1}\text{K}^{-1}$ at 575°C . Based on the low electrical resistivity value ($0.5 \times 10^{-3} \Omega\text{cm}$), the lattice contribution to the thermal conductivity was estimated at $12 \times 10^{-3} \text{Wcm}^{-1}\text{K}^{-1}$. This demonstrates that the combination of the “rattling” atom and very high carrier concentration ($5 \times 10^{21} \text{cm}^{-3}$) very effectively scatter the phonons, and results in an extremely low lattice thermal conductivity. However, it is difficult to quantify the two scattering mechanisms, void-filling and electron-phonon. Experiments on a series of $\text{CeFe}_{4-x}\text{Co}_x\text{Sb}_{12}$ samples have shown that the amount of Ce filling decreases with increasing substitution of Fe by Co. Despite this reduction, a decrease in carrier concentration and increase in electrical resistivity and Seebeck coefficient was observed with increasing Co content, indicative of a more semiconducting behavior [23].

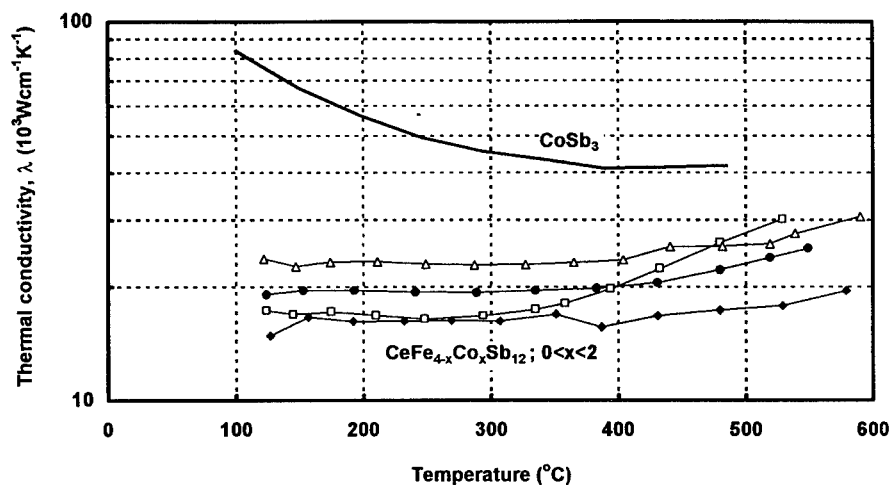


Figure 6: Thermal conductivity as a function of temperature for several CoSb_3 -based filled skutterudite compositions. Results are compared to those obtained for lightly doped CoSb_3 .

We can rewrite those compositions with the following formula, $\text{Ce}_f\text{Fe}_{4-x}\text{Co}_x\text{Sb}_{12}$, where f represent the fraction of Ce filling ($f=1$ represents complete filling). In addition to Co, substitution of Fe by Ni and Ru has also been investigated recently. The variations of the filling fraction f as a function of x have been plotted in Figure 7 for the three different ranges of compositions. When Fe is totally replaced by Co, only a very small amount of Ce remains in the sample ($f=0.065$) while completely filled $\text{CeRu}_4\text{Sb}_{12}$ can be prepared ($f=1$). This is attributed to the fact that Ru and Fe are isoelectronic. The dotted line was calculated based on a $\text{CeFe}_4\text{Sb}_{12}$ - $\text{Ce}_{0.065}\text{Co}_4\text{Sb}_{12}$ range of “solid solution” compositions. $\text{Ce}_f\text{Fe}_{4-x}\text{Ni}_x\text{Sb}_{12}$ compositions with $x > 1.5$ have not yet been synthesized, but it is clear that at equivalent concentrations, Ni substitution results in less Ce filling than Co substitution. However, because Ni donates two electrons instead of only one for Co when replacing Fe, the decrease in carrier concentration and

corresponding change in properties with increasing x is much stronger for $\text{Ce}_7\text{Fe}_{4-x}\text{Ni}_x\text{Sb}_{12}$. A more detailed study of the transport properties of these samples will be given elsewhere.

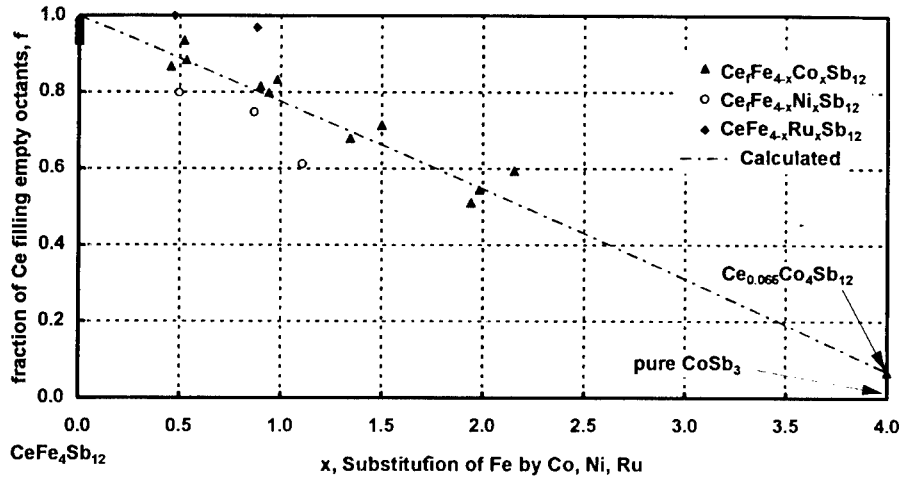


Figure 7: Ce filling fraction (f) for $\text{Ce}_7\text{Fe}_{4-x}\text{M}_x\text{Sb}_{12}$ samples as a function of Fe substitution by M (x) with $\text{M} = \text{Co}, \text{Ni}$ and Ru . No decrease in Ce filling is observed for $\text{Ce}_7\text{Fe}_{4-x}\text{Ru}_x\text{Sb}_{12}$ samples.

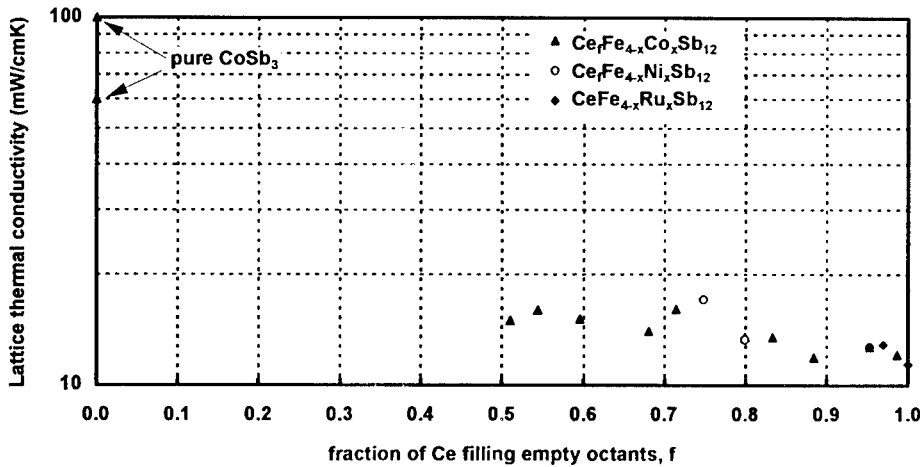


Figure 8: Room temperature lattice thermal conductivity as a function of the Ce filling fraction (f) for $\text{Ce}_7\text{Fe}_{4-x}\text{M}_x\text{Sb}_{12}$ compositions with $\text{M} = \text{Co}, \text{Ni}$ or Ru . Results for lightly doped p-type and heavily doped n-type CoSb_3 samples are also reported at $f = 0$.

The lattice thermal conductivity λ_l of $\text{Ce}_7\text{Fe}_{4-x}\text{M}_x\text{Sb}_{12}$ samples, where $\text{M} = \text{Co}, \text{Ni}$ or Ru , was calculated from the total thermal conductivity using the Wiedman-Franz law. Calculations show that the lattice thermal conductivity increases slowly with increasing Co or Ni content, but is left

unchanged for Ru substitution, even for $x = 0.9$. The room temperature values of λ_L is plotted as a function of the Ce filling fraction f in Figure 8. The weak dependence of $\lambda_L(f)$ for samples of $\text{Ce}_f\text{Fe}_{4-x}\text{Co}_x\text{Sb}_{12}$ suggests that void filling phonon scattering could be effective even at low values of f . It also appears that because of the very high carrier concentrations, electron-phonon scattering accounts for most of the variations in λ_L . Indeed, a typical carrier concentration value of $5 \times 10^{21} \text{ cm}^{-3}$ is obtained for $\text{CeFe}_4\text{Sb}_{12}$ at 300K, while a carrier concentration of $4 \times 10^{20} \text{ cm}^{-3}$ was measured for both $\text{Ce}_{0.51}\text{Fe}_{2.1}\text{Co}_{1.9}\text{Sb}_{12}$ and $\text{Ce}_{0.75}\text{Fe}_{3.1}\text{Ni}_{0.9}\text{Sb}_{12}$ compositions. The Co-based sample has 51% of its voids filled with Ce while the Ni-based sample has 75% of filled voids, but their lattice thermal conductivity is nearly identical, 16 to $17 \times 10^{-3} \text{ Wcm}^{-1}\text{K}^{-1}$, to be compared with a value of $12 \times 10^{-3} \text{ Wcm}^{-1}\text{K}^{-1}$ for $\text{CeFe}_4\text{Sb}_{12}$.

Another interesting result is the fact that no decrease in lattice thermal conductivity was observed when Ru was substituted for Fe. It seems that the point defects generated by a Ru atom on the Fe site do not contribute any further to the overall scattering rate, possibly because void fillers (Ce) already scatter phonons in a wide frequency domain.

The combination of the low electrical resistivity, moderate Seebeck coefficient and low thermal conductivity resulted in high ZT values at temperatures above 400°C . A maximum ZT value of 1.4 has been achieved to date at a temperature of 600°C [21]. If current data is extrapolated to higher temperatures, it appears that even higher ZT would be obtained, provided that those materials were determined to remain stable. High ZT values at lower temperatures, as well as n-type conductivity samples might be obtained by controlling the composition and doping levels to increase the Seebeck coefficient and achieve a more semiconducting behavior. For example, this might be achieved by increasing the Co (or Ni) to Fe atomic ratio, or combining substitutions of both Fe and Sb, or filling the voids with a tetravalent atom.

CONCLUSION

The properties of binary skutterudite compounds are very attractive for thermoelectric applications. However, their lattice thermal conductivity values are too high, in particular at low temperatures. Several approaches to significantly reduce the thermal conductivity of skutterudites have been identified: heavy doping, solid solution formation, valence fluctuations, and void filling. Ultimately, a combination of these approaches should be employed to reach a lattice thermal conductivity close to the theoretical minimum. Recent results have shown that high ZT values substantially larger than 1.0 can be achieved for some skutterudite solid solutions and filled compositions. Efforts are currently underway to pursue these various approaches, both experimentally and theoretically, and demonstrate that they can lead to a significant improvement in the thermal-to-electric conversion efficiency of thermoelectric devices.

ACKNOWLEDGMENTS

The work described in this paper was carried out at the Jet Propulsion Laboratory/California Institute of Technology, under contract with the National Aeronautics and Space Administration. The authors would like to thank Donald T. Morelli and Greg P. Meisner of the General Motors Research & Development Center for their contribution in the preparation and measurement of some of the skutterudite samples, as well as Glen A. Slack of the Rensselaer Polytechnic Institute for many challenging discussions. This work is supported by the U.S. Office of Naval Research, Grant No. N00014-95-F-0068.

REFERENCES

1. T. Caillat, A. Borshchevsky, and J.-P. Fleurial, Proceedings, 7th International Conference on Thermoelectrics, ed. K. Rao, University of Texas at Arlington, p. 98 (1993).
2. J.-P. Fleurial, T. Caillat, and A. Borshchevsky, Proceedings, 14th International Conference on Thermoelectrics, ed. M. Vedernikov, Ioffe Physico-Technical Institute, p. 231 (1995).
3. G. A. Slack, J.-P. Fleurial, and T. Caillat, Naval Research Reviews, Vol. XLVIII, 23-30 (1996).
4. T. Caillat, A. Borshchevsky, and J.-P. Fleurial, J. Appl. Phys. 80 (8) 4442-4449 (1996).
5. J. P. Dismukes, L. Eskström, E. F. Steigmeier, I. Kudman, and D. S. Beers, J. Appl. Phys., vol. 35, p. 2899 (1964).
6. N. Mandel, and J. Donohue, Acta Cryst., B27, p. 2288 (1971).
7. H. D. Lutz, and G. Kliche, Journal of Solid State Chemistry, vol. 40, p. 64 (1981).
8. G. Slack, and V. G. Tsoukala, J. Appl. Phys. 76, 1665 (1994).
9. A. Borshchevsky, J.-P. Fleurial, E. Allevato, and T. Caillat, *Proceedings, 13th International Conference on Thermoelectrics*, ed. B. Mathiprakasam and P. Heenan (AIP Conference 316, New York), p. 31 (1995).
10. A. Borshchevsky, J.-P. Fleurial, and T. Caillat, *Proceedings, 15th International Conference on Thermoelectrics*, ed. T. Caillat (IEEE Catalog 96TH8169), p. 112 (1996).
11. T. Callaway, and H. C. Von Baeyer, Phys. Rev., vol. 120, p. 1149 (1960).
12. T. Caillat, J. Kulleck, A. Borshchevsky, and J.-P. Fleurial, J. Appl. Phys. vol. 79, 11, 1141 (1996).
13. G.S. Nolas, V.G. Harris, T.M. Tritt and G.A. Slack, J. Appl. Phys. 80 (11) 6304-6308 (1996).
14. G. A. Slack, Phys. Rev, vol. 126, p. 427 (1962).
15. G. Brostigen and A. Kjekshus, Acta Chem. Scand. 24 (8) 2993-3012 (1970).
16. G. A. Slack, Thermoelectric Handbook, ed. by M. Rowe (Chemical Rubber, Boca Raton, FL), p. 407 (1995).
17. G. P. Meisner, M. S. Torikachvili, K. N. Yang, M. B. Maple, R. P. Guertin, J. Appl. Phys., 57, vol. 1, p. 3073 (1985).
18. D. T. Morelli, and G. P. Meisner, J. Appl. Phys. vol. 77, p. 3777 (1995).
19. G. S. Nolas, G. A. Slack, T. M. Tritt, and D. T. Morelli, Proceedings, 14th International Conference on Thermoelectrics, ed. M. Vedernikov, Ioffe Physico-Technical Institute, p. 236 (1995).
20. G. S. Nolas, G. A. Slack, T. Caillat, and G. P. Meisner, J. Appl. Phys, Vol. 79, 5, p. 2622 (1996).
21. J.-P. Fleurial, A. Borshchevsky, and T. Caillat, D. T. Morelli, and G. P. Meisner, *Proceedings, 15th International Conference on Thermoelectrics*, ed. T. Caillat (IEEE Catalog 96TH8169), p. 91 (1996).
22. B.C. Sales, D. Mandrus and R.K. Williams, Science, Vol. 22, 1325-1328 (1996)
23. B. Chen, J.H Xu, C. Uher, D.T. Morelli, G.P. Meisner, J.-P. Fleurial, T. Caillat and A. Borshchevsky, Phys. Rev. B. 55 (3) 1476-1480 (1997)

COMPUTATIONAL STUDIES OF NOVEL THERMOELECTRIC MATERIALS

D.J. SINGH¹, I.I. MAZIN², S.G. KIM³, L. NORDSTROM⁴

¹Code 6691, Naval Research Laboratory, Washington, DC 20375

²CSI, George Mason University and Code 6691 NRL, Washington, DC 20375

³UES Inc. and Code 6691 NRL, Washington, DC 20375

⁴Physics Department, Uppsala University, Box 530, S-75121 Uppsala, Sweden

ABSTRACT

The thermoelectric properties of La-filled skutterudites and β -Zn₄Sb₃ are discussed from the point of view of their electronic structures. These are calculated from first principles within the local density approximation. The electronic structures are in turn used to determine transport related quantities. β -Zn₄Sb₃ is found to be metallic with a complex Fermi surface topology, which yields a non-trivial dependence of the Hall concentration on the band filling. Calculations of the variation with band filling are used to extract the carrier concentration from the experimental Hall number. At this band filling, which corresponds to 0.1 electrons per 22 atom unit cell, we calculate a Seebeck coefficient and temperature dependence in good agreement with the experimental value. The high Seebeck coefficients in a metallic material are remarkable, and arise because of the strong energy dependence of the Fermiology near the experimental band filling. Virtual crystal calculations for La(Fe,Co)₄Sb₁₂ show that the system obeys almost perfect rigid band behavior with varying Co concentration, and has a substantial band gap at a position corresponding to the composition LaFe₃CoSb₁₂. The valence band maximum occurs at the Γ point and is due to a singly degenerate dispersive (Fe,Co)-Sb band, which by itself would not be favorable for TE. However, very flat transition metal derived bands occur in close proximity and become active as the doping level is increased, giving a non-trivial dependence of the properties on carrier concentration and explaining the favorable TE properties.

INTRODUCTION

There has been a recent revival of activity in the search for improved thermoelectric (TE) materials, with an emphasis on novel materials concepts [1]. The utility of a material for TE applications is measured by its dimensionless figure of merit, $ZT = \sigma S^2 T / \kappa$, where T is temperature, σ is the electrical conductivity, S is the Seebeck coefficient and κ is the thermal conductivity, which contains both electronic and lattice contributions, κ_e and κ_l , respectively.

Good TE materials should have high Seebeck coefficients combined with low thermal conductivity and reasonable electronic conductivity. Since the same electrons contribute to σ and κ_e , the ratio $\sigma T / \kappa$ cannot in general be increased arbitrarily, and has a maximum near that given by the Wiedemann-Franz "law". This maximum is achieved when the lattice thermal conductivity is small compared to the electronic component. If Wiedemann-Franz holds, $S = 160 \mu\text{V/K}$ is required for the state-of-the-art value $ZT = 1$. Much TE research over the past 40 years has focussed on covalent semiconducting compounds and alloys, composed of 4th and 5th row elements, with a view to finding low thermal conductivity materials that have reasonable carrier mobilities and high band masses. Most current generation TE materials are of this type, e.g. Bi₂Te₃, Si-Ge, PbTe. Despite research efforts spanning three decades, little progress in increasing

ZT has been achieved, and in particular $\text{Bi}_2\text{Te}_3/\text{Sb}_2\text{Te}_3$ has remained the material of choice for room temperature applications.

Recently, three new materials with $\text{ZT} \geq 1$ have been reported [2-4], and these do not clearly fall in the same class as previous TE materials. $\beta\text{-Zn}_4\text{Sb}_3$, with reported $\text{ZT} \approx 1.3$ at temperatures relevant to waste heat recovery, has a large region of linear temperature dependence of the resistivity, suggestive of a metallic rather than semiconducting material, but unlike normal metals this is accompanied by high thermopowers. $\text{CeFe}_4\text{Sb}_{12}$ both by itself and doped with Co shows high values of ZT combined very low thermal conductivities, and depending on the composition can show either metallic-like or semiconducting temperature dependencies of the resistivity. At low temperature $\text{CeFe}_4\text{Sb}_{12}$ displays properties reminiscent of heavy Fermion materials [5]. Band structure calculations [6] for $\text{CeFe}_4\text{X}_{12}$, $\text{X}=\text{P,As,Sb}$ show that the Ce f-states contribute significantly to the electronic structure near the Fermi energy, leading the enhanced band masses, favorable for TE, and producing band gaps via hybridization with the valence states. This would imply a rather different electronic structure for $\text{LaFe}_4\text{Sb}_{12}$. However, $\text{La}(\text{Fe,Co})_4\text{Sb}_{12}$ does have $\text{ZT} \approx 1$ for appropriate conditions, although ZT for pure $\text{LaFe}_4\text{Sb}_{12}$ is apparently lower than for pure $\text{CeFe}_4\text{Sb}_{12}$. Here we report first principles calculations, within the local density approximation (LDA), similar to our previous calculations for binary and Ce-filled skutterudites [6-8]. These are aimed at understanding the transport properties of $\beta\text{-Zn}_4\text{Sb}_3$ and $\text{La}(\text{Fe,Co})_4\text{Sb}_{12}$.

METHOD

The self-consistent LDA calculations presented here were performed using the general potential linearized augmented planewave (LAPW) method [9]. This method makes no shape approximations to either the potential or charge density and uses flexible basis sets in all regions of space. As such it is well suited to materials with open crystal structures and low site symmetries like those treated here. Well converged basis sets were used. The contained approximately 2100 functions for $\beta\text{-Zn}_4\text{Sb}_3$ and coincidentally the same number for $\text{La}(\text{Fe,Co})_4\text{Sb}_{12}$, which has fewer atoms in the unit cell, but some shorter bond lengths requiring the use of smaller LAPW spheres (2.45 vs. 2.50 a.u.). Local orbital extensions to the basis set were used to relax linearization errors generally and to include the upper core states of La consistently with the valence states.

The calculations were based on the experimental crystal structures of $\text{LaFe}_4\text{Sb}_{12}$ and $\beta\text{-Zn}_4\text{Sb}_3$, except a stoichiometric structure was used for $\beta\text{-Zn}_4\text{Sb}_3$ was used in which the mixed Sb site, which is reported to have approximately 10% Zn and 90% Sb in the actual material, was taken as a pure Sb site, yielding a formula Zn_6Sb_5 with 22 atoms per rhombohedral unit cell. This was then corrected in a rigid band way by adjusting the Fermi level upwards, as discussed below. The electronic structures of $\text{La}(\text{Fe,Co})_4\text{Sb}_{12}$ alloys were calculated as for $\text{LaFe}_4\text{Sb}_{12}$ using the virtual crystal method, i.e. self-consistent LAPW calculations were performed using average ions with fractional charges intermediate between Fe and Co. This approximation includes the average ionic charge and band filling, but is known to distort the electronic structure for alloys when the scattering properties of the ions being alloyed differ substantially. Calculations were performed for 0%, 25% and 50% Co substitution.

Transport properties relevant to TE were determined from the calculated band structures using standard kinetic theory as given by Ziman and others [10,11]. For the electrical conductivity, the Bloch-Boltzmann kinetic equation in lowest order is (similarly for the other Cartesian directions)

$$\sigma_x(T) = e^2 \int d\epsilon N(\epsilon) v_x^2(\epsilon) \tau(\epsilon, T) \left(-\frac{\partial f(\epsilon)}{\partial \epsilon} \right) \quad (1)$$

Here $N(\epsilon)$ is the density of electronic states at the energy ϵ per unit volume, τ is the scattering rate for electrons, and the quantity $v_x^2(\epsilon)$ is defined by:

$$N(\epsilon) v_x^2(\epsilon) = (2\pi)^{-3} \int v_x^2 \frac{dS_\epsilon}{v_\epsilon} \quad (2)$$

$$N(\epsilon) = (2\pi)^{-3} \int \frac{dS_\epsilon}{v_\epsilon} \quad (3)$$

Here the integrations are over the iso-energy surface defined by $E=\epsilon$. For $E=E_F$, the Fermi energy, the integral is over the Fermi surface and v_ϵ is the Fermi velocity. In this case the quantity is the square of the plasma frequency $\omega_{px}^2 = 4\pi e^2 N(E_F) v_x^2(E_F)$, which is proportional to the optical carrier concentration $(n/m)_{\text{eff}} = N(E_F) v_x^2(E_F)$. We note that unless the bands are parabolic this quantity is not simply related to the Hall concentration or the electron count (i.e. doping level). In fact, even these later two quantities are also not simply related in general since the Hall concentration is determined by the average curvature of the Fermi surface while the doping level is given by the volume enclosed by the Fermi surface.

For isotropic scattering, which is often a reasonable approximation, the relaxation time does not enter the expression for the Hall concentration, which is [11,12]:

$$n_H = -\sigma^2 / e \sigma_H \quad (4)$$

with

$$\sigma_H = \frac{e^3}{12} \int d\epsilon N(\epsilon) v(\epsilon) \cdot [Tr(\mathbf{m}^{-1}) - \mathbf{m}^{-1}] v(\epsilon) \tau^2(\epsilon, T) \left(-\frac{\partial f(\epsilon)}{\partial \epsilon} \right) \quad (5)$$

where for simplicity we have given the expression for cubic symmetry. Here \mathbf{m} is the \mathbf{k} -dependent effective mass tensor, defined as

$$m_{\alpha\beta}^{-1} \equiv \hbar^{-1} \frac{\partial v_\alpha}{\partial k_\beta} \equiv \hbar^{-2} \frac{\partial^2 \epsilon_k}{\partial k_\alpha \partial k_\beta} \quad (6)$$

Provided that the Fermiology does not vary strongly on the scale of kT , the derivatives of the Fermi distribution in the above expressions may be replaced by the $T=0$ limit, which is the delta function, thereby suppressing the energy integrals. This simplification was employed in the calculations of the Hall concentrations in this paper. This approximation is, however, inadequate for the Seebeck coefficient, S , since, unlike the Hall concentration, we wish to obtain its value up to fairly high temperatures in order to compare with experimental values and T dependencies.

The usual kinetic theory expression for S is:

$$S(T) = \frac{e}{T\sigma(T)} \int d\epsilon N(\epsilon) v_x^2(\epsilon) \epsilon \tau(\epsilon, T) \left(-\frac{\partial f(\epsilon)}{\partial \epsilon} \right) = \frac{1}{eT\sigma(T)} \int d\epsilon \epsilon \sigma(\epsilon, T) \left(-\frac{\partial f(\epsilon)}{\partial \epsilon} \right) \quad (7)$$

where we have introduced the usual notation, $\sigma(\epsilon) = N(\epsilon)v_x^2(\epsilon)\tau(\epsilon, T)$; as mentioned, the actual conductivity is $\sigma(E_F)$. In the lowest order in T , the above expression becomes proportional to the logarithmic energy derivative of the conductivity evaluated at E_F .

$$S(T) = \frac{\pi^2 k^2 T}{3e\sigma} \frac{d\sigma}{d\epsilon} \Big|_{E=E_F} \quad (8)$$

This equation implies a linear relation between S and T , which is the low temperature form of $S(T)$. However, in general, $d\sigma/d\epsilon$ varies with energy much more strongly than $\sigma(\epsilon)$, so that this lowest order in T approximation for $S(T)$ breaks down at lower T than the corresponding expressions for σ and σ_{II} . In order to compare with the experimental temperature dependence, the results in this paper were calculated using the full eqn. 7, yielding deviation of $S(T)$ from linear behavior as T is increased.

The formula for $\sigma(\epsilon)$ contains two energy dependent factors: an energy dependent square plasma frequency Nv^2 and the relaxation time τ . Ordinarily, the first term is the most energy dependent, but there are exceptions [13], e.g. Pd metal where E_F occurs near a very sharp feature in $N(\epsilon)$ and Kondo systems where there is resonant scattering [11]. Since neither $\text{La(Fe,Co)}_4\text{Sb}_{12}$ or $\beta\text{-Zn}_4\text{Sb}_3$ show indications of such behavior, we have approximated the energy dependence of σ using only the Nv^2 term.

$\text{LaFe}_4\text{Sb}_{12}$

Skutterudites and modifications to these compounds have been regarded as promising potential TE materials for the last few years based on experimental measurements of the transport properties of binary skutterudites, particularly IrSb_3 and CoSb_3 and general considerations. For example, Slack and Tsoukala found reasonably high Seebeck coefficients (nearly linear in T over the measured range with $S=72 \mu\text{V/K}$ at 300K) combined with very high hole mobilities in a sample with a doping level of $1.1 \times 10^{19} \text{ cm}^{-3}$. This high mobility is consistent with the highly covalent electronic structure implied by chemistry of Ir and Sb, the crystal structure, which is dominated by near tetrahedral coordination of Sb including both Sb-Sb and Co-Sb bonds and first principles calculations [7]. Unfortunately, measured values of κ for the binary skutterudites proved to be much higher than estimates of the minimum thermal conductivity for this crystal structure [14,15]. Within the Slack's classification, the binary Skutterudites are good electron crystals with high power factors, but they are not close enough to being phonon glasses to make good TE materials.

The strategy suggested by these considerations is to seek modifications of the binary skutterudites that have lower lattice κ with minimal modification to the electronic properties. Among the modifications tried were alloying on the transition metal and/or pnictogen sites [16,17] and filling of the large voids in the skutterudite structure with heavy atoms [3-5] that might have soft anharmonic Einstein like phonon modes and thereby reduce the thermal conductivity. Both of these are successful in that they result in considerably reduced values of κ , and as mentioned in $\text{Ce(Fe,Co)}_4\text{Sb}_{12}$ and $\text{La(Fe,Co)}_4\text{Sb}_{12}$ high values of ZT have been achieved. This may be rationalized by electron counting, although as will be shown below the resulting picture is misleading. In any case, the argument is as follows: CoSb_3 is a semiconductor with a

high power factor but poor thermal properties. $\text{LaFe}_4\text{Sb}_{12}$ and $\text{CeFe}_4\text{Sb}_{12}$ are known metallic compounds with considerably lower thermal conductivities, presumably due to the "rattling ion" model of Slack. In the highly covalent band structures of these materials, each Fe atom should contribute one less electron than a Co atom in the CoSb_3 , while the additional trivalent La should contribute three electrons, resulting in a net deficiency of one electron per formula unit. Accordingly, the composition $\text{LaFe}_3\text{CoSb}_{12}$ may be electronically similar to CoSb_3 providing the desired combination of high power factor and κ . There is strong evidence that Ce is trivalent in these compounds, leading to a similar argument, although there are complications due to heavy fermion/valence fluctuation effects at low temperature. In fact, as synthesized $\text{La}(\text{Fe},\text{Co})_4\text{Sb}_{12}$ forms La deficient so that the actual Co concentration needed to obtain compensation is higher than 25%.

One complication is that first principles calculations for CoSb_3 [7], show a small band gap with a highly non-parabolic, quasi-linear valence band dispersion. This result, which now has experimental support [18-20], combined with the kinetic transport theory above, implies that in p-type CoSb_3 the doping level, n , dependence of S and σ will differ from that of a semiconductor with parabolic bands. In particular, in the constant scattering time, degenerate regime, $S \propto n^{-1/3}$ and $\sigma \propto n^{2/3}$ instead of the usual $S \propto n^{-2/3}$ and $\sigma \propto n$. This means that the power factor, σS^2 will be less dependent on doping level than in a conventional case and that it will be more difficult to optimize ZT by adjusting n (but note that κ has an electronic component proportional to σ).

From a TE point of view it would perhaps be preferable if the band structure of $\text{La}(\text{Fe},\text{Co})_4\text{Sb}_{12}$ were different from CoSb_3 since this would allow more efficient optimization.

This in fact is the case. The calculated band structure of $\text{LaFe}_4\text{Sb}_{12}$ is shown in Fig. 1. This band structure shows an indirect Γ -N gap of 0.60 eV at a position above E_F corresponding to a band filling of one more electron. This is qualitatively different from the band structure of CoSb_3 . The direct gap at Γ is 0.76 eV. Both the conduction and valence band edges are formed from parabolic bands with hybridized Fe/Co-Sb character. In addition there are some rather flat (heavy mass) primarily Fe/Co d derived bands near but not at the band edge both above and below the gap.

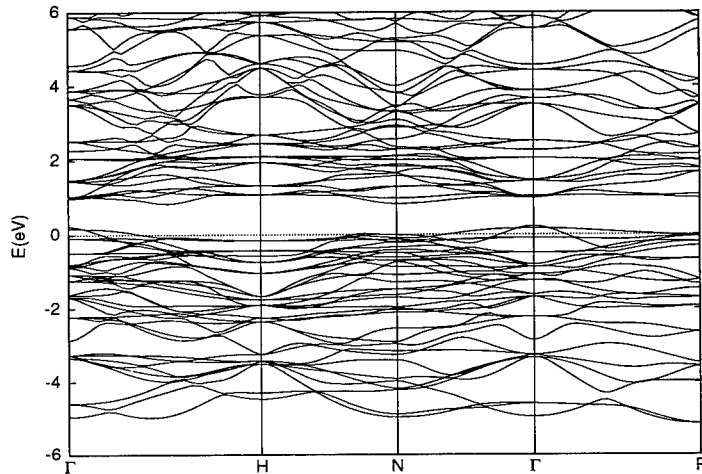


Figure 1 Calculated band structure of bcc $\text{LaFe}_4\text{Sb}_{12}$. The Fermi energy is denoted by the dotted horizontal line at 0 eV.

The projected electronic density of states (DOS) corresponding to this band structure is shown in Fig. 2. Although the DOS is highly covalent, it is less so than IrSb_3 and is closer in

shape to CoSb_3 . In particular, the Co d contribution is peaked in the region from -1 eV to 0 eV relative to E_F and is concentrated in the energy region around the gap. In contrast in IrSb_3 the Ir d contribution is spread more uniformly over the valence band region from -6 eV to well above E_F . The peaked structure of the DOS in $\text{LaFe}_4\text{Sb}_{12}$ corresponds to the flat Fe/Co-d derived bands seen in Fig. 1 and results in the fact that E_F lies on the edge of a very sharp

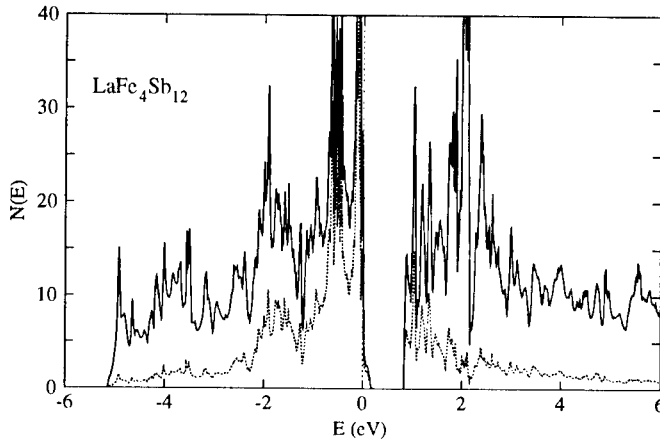


Figure 2 Projected DOS of $\text{LaFe}_4\text{Sb}_{12}$ on a per formula unit basis. The solid line is the total DOS and the dotted line is the Co d contribution. The Fermi energy is at 0 eV.

decrease in the DOS. This leads to an expectation that high values of S may occur in the $\text{La}(\text{Fe},\text{Co})_4\text{Sb}_{12}$ system, as observed and quantitatively determined below. However, before proceeding to calculate the transport properties for $\text{La}(\text{Fe},\text{Co})_4\text{Sb}_{12}$ it is necessary to determine to what extent its band structure is similar to that of $\text{LaFe}_4\text{Sb}_{12}$. In order to address this issue we have performed virtual crystal approximation calculations for this material with 25% and 50% replacement of Fe by Co.

In the calculations we have held the structure fixed at the $\text{LaFe}_4\text{Sb}_{12}$ structure and have kept the La concentration stoichiometric. The calculations show good rigid band behavior. This is illustrated in Figs. 3, which shows the total DOS for the three different Co concentrations and Fig. 4 which is the band structure near E_F for the semiconducting 25% Co composition. The main variation near the gap as the Co concentration is increased is due to a small upward shift of the lighter mass band forming the valence band edge at Γ , relative to the Fe/Co d derived flat bands. This leads to a gradual narrowing of the band gap with increasing Co concentration.

Given rigid band behavior calculation of the transport properties as a function of doping level amounts to calculating the properties with fixed band structure for various positions of the Fermi level. For this purpose we used the virtual crystal band structure calculated with 25% Co. A blow-up of this band structure near the gap is shown in Fig. 4.

As in $\text{LaFe}_4\text{Sb}_{12}$ the gap of 0.56 eV is indirect with a valence band maximum at Γ . The conduction band minimum is along the Γ -H and coincidentally is virtually degenerate with the lowest band at N. Although these multiple minima in the zone provide a favorable arrangement for TE in n-type material, we note that n-type $\text{La}(\text{Fe},\text{Co})_4\text{Sb}_{12}$ apparently cannot be made without substantial La deficiency, which would modify the band structure. The direct gap at Γ is 0.66 eV.

The valence band structure is also interesting from a TE point of view. The valence band edge is derived from a singly degenerate light mass ($m \approx 0.2 m_e$) band of hybridized Sb p character, which disperses downwards away from the Γ point. However, immediately below this band is a much flatter band ($m \approx 3 m_e$) of primarily Fe/Co-d character [21]. With increasing hole doping, starting with undoped material, the Fermi energy initially moves into the light band.

However, at a band filling of only 0.005 e/cell ($1.3 \times 10^{19} \text{ cm}^{-3}$), corresponding to a Fermi energy of 0.1 eV relative to the VBM, the second band is reached. This heavy band shows strong onsets in $N(E)$, $v_x^2(E)$ and related quantities, resulting in a strong energy dependence in σ , and high values of S . Reported samples [3] show Hall numbers above 10^{20} cm^{-3} implying that both the light and

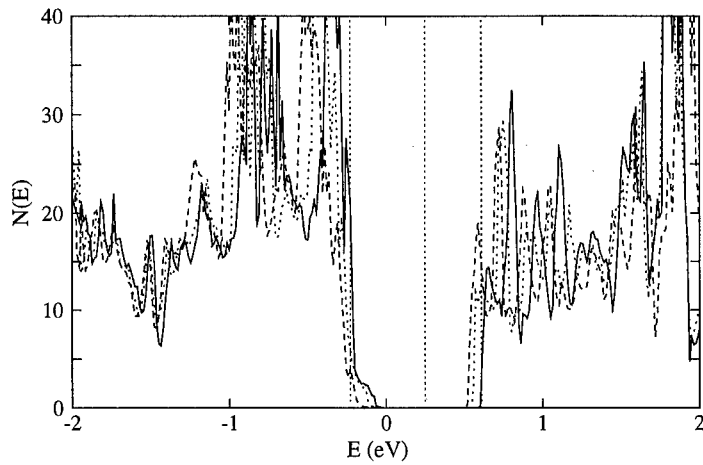


Figure 3 Total DOS for $\text{La}(\text{Fe,Co})_4\text{Sb}_{12}$ with 0% (solid), 25% (dotted) and 50% (dashed) Co. The valence band edges are fixed at 0 eV. The values of E_F are denoted by the dotted vertical lines.

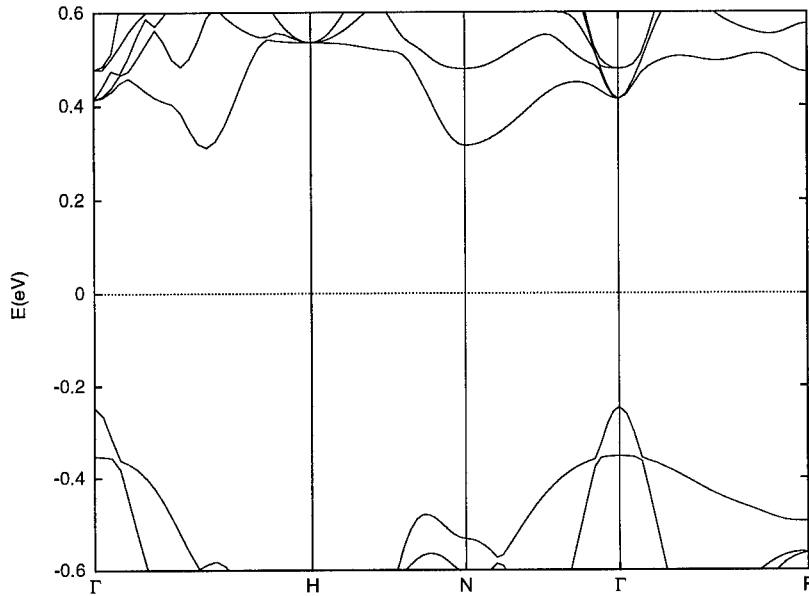


Figure 4 Band structure of $\text{La}(\text{Fe,Co})_4\text{Sb}_{12}$ with $x_{\text{Co}}=0.25$.

heavy bands are active in transport.

In order to understand the transport more quantitatively, we have performed calculations of transport properties as a function of hole doping away from the gap based on the 25% Co

virtual crystal band structure of Fig. 4. The Hall number, carrier concentration (doping level), and thermopower at 600K are shown as a function of E_F in Fig. 5. Over almost all of the range shown the Hall number is lower than the doping level. This deviation, which increases with band filling, reflects deviations from parabolic band behavior. Although the presence of the heavy band is responsible for the high thermopower of this materials, S at 600K does not show

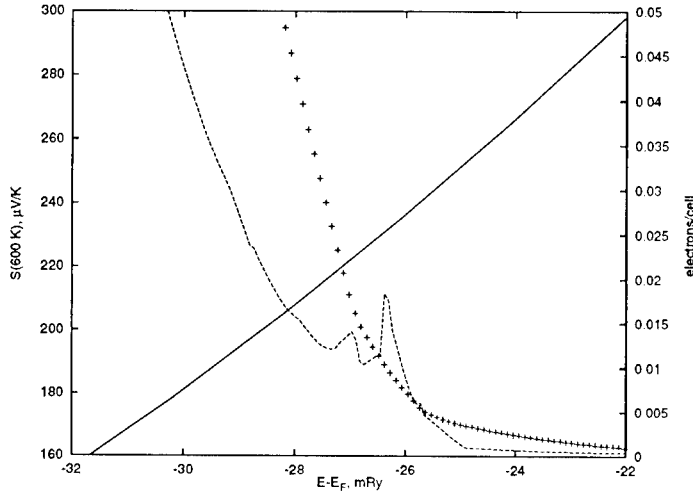


Figure 5 Hole concentration (+), Hall number (dashed) and thermopower at 600K (solid) vs. chemical potential in $\text{La}(\text{Fe},\text{Co})\text{Sb}_3$. The onsets of the light and heavy bands are at -18 mRy and -26 mRy, respectively.

any noticeable structure near -26 mRy, which is the onset of the heavy band. This is because the form of Eqn. 7 has strong contributions at energies up to 2-3 kT from the chemical potential [22] and because kT at 600K is 3.7 mRy. Thus the heavy band contributes to S over the entire range of Fig. 5. However, the carrier concentration increases sharply below the onset of the second band, reflecting its sharp dispersion. This provides a mechanism for pinning the Fermi level near the onset, providing high thermopowers even though the carrier concentration is apparently difficult to control in these materials.

Although the Hall number is not reported, the sample shown by Sales, Mandrus and Williams [3] has $S(600\text{K}) \approx 180 \mu\text{V/K}$. Comparing with our calculations, this corresponds to a chemical potential of -30 mRy, or 4 mRy below the onset of the heavy band. This corresponds to a doping level of 0.08 holes per cell and a Hall number of .045 holes per cell. The Hall concentration of 1.2×10^{20} holes per cm^{-3} is consistent with the reported lower end of the range of Hall concentrations reported in Ref. [3] for various samples ($1 \times 10^{20} \text{ cm}^{-3}$). As discussed below the best TE properties are anticipated at lower doping levels, and the TE properties of the sample shown are apparently near the best that were measured.

The temperature dependence of S at a chemical potential -30.3 mRy (matching the experimental value of S at 500K) is shown in Fig. 6. The agreement is only semi-quantitative, and is clearly not as good as was obtained for binary skutterudites, particularly in view of the fact that the Seebeck coefficient was used in the present case to fix the carrier density, while in the binaries it was determined from independent measurements of the Hall number. The implication is that either the approximation of neglecting the energy dependence of τ is inadequate, as could be the case in the light band near the onset of the heavy band, or the calculated band structure is distorted relative to the sample. The latter possibility is not readily discounted. We note the fact that the actual, as measured, material is La deficient, and based on

our results La strongly modifies the valence band structure. Specifically La-Fe-Sb hybridization [23] determines the relative positions of the heavy and light bands, which is an important ingredient in determining the temperature dependence of S .

Related to this it should be noted that the thermal conductivity for this sample in the temperature range above 500K is roughly 1/3 electronic and 2/3

lattice in origin. As mentioned κ_i is strongly reduced from κ_i of CoSb_3 by La addition, but most of this effect is expected to occur at fairly low La concentrations within the rattling ion framework of Slack and Cahill, Watson and Pohl [15], and supported by measurements in the $\text{Ce(Fe,Co)}_4\text{Sb}_{12}$ on samples with different Ce concentrations [4]. Because of the strong interaction between the valence bands and La, La vacancies should strongly scatter electrons reducing the electrical conductivity. This is consistent with the wide range in hole mobilities ($2\text{--}30\text{ cm}^2/\text{Vs}$) measured for the various samples. Based on this we conjecture that samples with higher La filling, if they can be made, would have higher mobilities and higher values of σ at a fixed band filling. Because of the Wiedemann-Franz relation, this would also lead to higher κ_e . In that case, the value of S would become the most important factor determining ZT at a given temperature. We speculate it may be quite feasible to increase ZT substantially in this material if the La concentration could be made stoichiometric near 25% Co concentration. In this case, the doping level for maximum ZT will occur at lower carrier concentrations than any of the reported samples. We speculate that depending on how much the mobility can be improved by La filling, it may be possible to obtain high values ZT at lower temperatures by doping so that the chemical potential is roughly kT above the onset of the heavy band (i.e. in the 10^{19} cm^{-3} range).

$\beta\text{-Zn}_4\text{Sb}_3$

$\beta\text{-Zn}_4\text{Sb}_3$, like $\text{La(Fe,Co)}_4\text{Sb}_{12}$ appears to be a low carrier concentration metal with a very low lattice thermal conductivity. For example, the resistivity [2] increases linearly with T over a wide range. The Hall number, $n_H = 9 \times 10^{19}\text{ cm}^{-3}$ for the reported high ZT sample, which although small for a metal may be too large to allow analysis of the transport in terms of usual semiconductor formulae. Our first principles calculations, discussed below, show that the n_H is not simply related to the actual doping level defined by band filling again characteristic of a metal. Also like the skutterudite, the crystal structure of $\beta\text{-Zn}_4\text{Sb}_3$ is dominated by both metal-Sb and Sb-Sb bonds, implying a high degree of covalency, which is also apparent from the

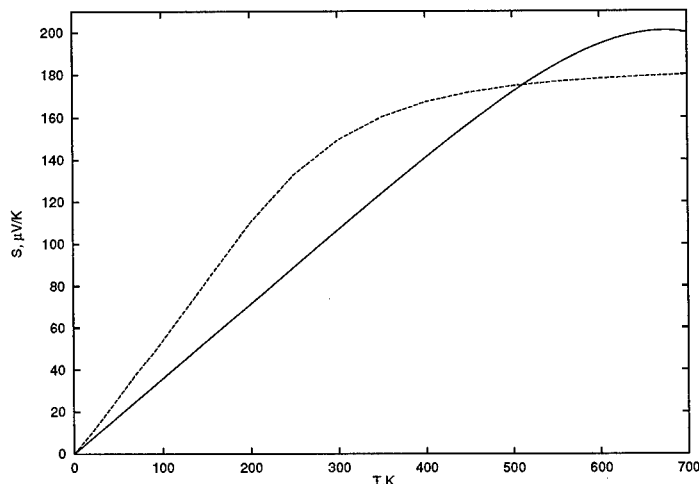


Figure 6 Calculated (dashed, see text) and experimental (solid) $S(T)$ for La(Fe,Co)Sb_{12} .

calculations. This strongly covalent network may be a key ingredient in obtaining reasonable conductivities in a material with high S , as has been previously noted by several authors for semiconductor TE materials where a combination of high effective mass and high mobility is sought.

The calculated DOS of $\beta\text{-Zn}_4\text{Sb}_3$ is shown in Fig. 7. As mentioned this was obtained for the stoichiometric composition.

The actual E_F was determined within a rigid band approximation, by matching the calculated and

measured values of n_H . This rigid band approximation is expected to be very good in this material because of the strong covalency and the similar bonding of Sb and the additional Zn in this compound as implied by the existence of the mixed site.

The measured n_H is approximately 0.05 holes per unit cell. Matching this with our calculations of n_H we find an upward shift of E_F by 24 mRy with respect to the stoichiometric E_F . This places E_F 8 mRy below the band gap, and corresponds to a doping level of 0.1 holes/cell. As mentioned n_H and band filling are often not simply related in metals. In $\beta\text{-Zn}_4\text{Sb}_3$ this occurs because of the topology of the Fermi surface, which is complex, highly non-parabolic and anisotropic. Particularly, it has both hole like and electron like sections and varies strongly near the actual E_F . The complexity of the Fermi surface near the actual E_F leads to rapid variation of the Fermi velocities, v , with energy. This leads to an enhancement of the energy dependence of σ , which according to the kinetic theory discussed above leads to high thermopowers. This suggests the investigation of other low carrier density metals with strongly energy dependent Fermi surface topologies and low lattice thermal conductivities as possible TE materials.

At the actual band filling the calculated plasma frequency is 0.22 eV, which is in the low end of the metallic regime. With this band filling we obtain S (averaged over direction to compare with non-oriented samples) in good agreement with experimental measurements, which strongly supports the present band structure model. The temperature dependence of S is shown in Fig. 8 along with the experimental data of Ref. 2. As may be noted the agreement is excellent, particularly considering that only the independently measured n_H was used to fix E_F . Calculations at other doping levels are also plotted illustrating the strong dependence of S on doping level in this material at temperatures where ZT is large.

The experimentally measured thermal conductivity [2] is extremely low and close to the Wiedemann Franz value for the reported sample. Although Wiedemann-Franz depends on a number of approximations that can be violated in real materials the implication is that the lattice component of the κ is extremely low, and that for the reported sample κ_c dominates. In such a regime, ZT is roughly proportional to S^2 , meaning that increasing S should lead to increases in

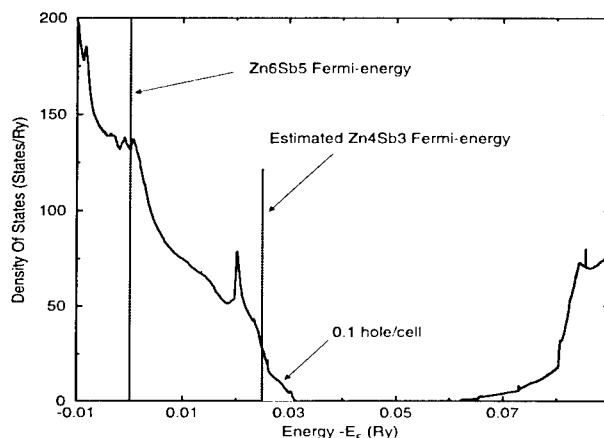


Figure 7 DOS of $\beta\text{-Zn}_4\text{Sb}_3$. The calculations were performed for the stoichiometric composition (E_F at lower vertical line). The actual Fermi energy is given by the upper marker.

ZT, despite the fact that σ may decrease. The calculations show that S increases with increasing E_F , and this corresponds to increasing the amount of Zn on the mixed Sb-Zn site. It would be interesting to determine the effect of this on ZT if samples with higher Zn concentrations can be made.

SUMMARY

First principles calculations of band structures and transport properties of $\text{La}(\text{Fe},\text{Co})_4\text{Sb}_{12}$ and $\beta\text{-Zn}_4\text{Sb}_3$ are reported. In both cases high ZT and large thermopowers have been reported on materials that may be reasonably described as metallic, both from the point of view of experimental measurements and the calculated band structures. The electronic structure of $\text{La}(\text{Fe},\text{Co})_4\text{Sb}_{12}$ is strongly distorted from that of the corresponding binary, CoSb_3 implying a non-trivial role for La. The results suggest that samples with higher La filling, and lower hole concentrations may have better TE properties. In $\beta\text{-Zn}_4\text{Sb}_3$, higher Zn concentrations on the mixed site will favor lower hole concentrations, which may also be favorable for obtaining higher ZT.

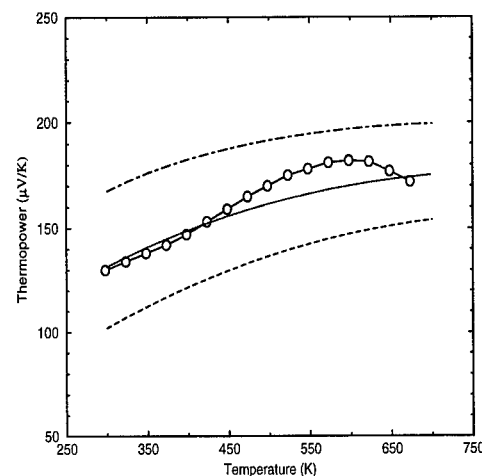


Figure 8 Calculated (short dashes) and experimental (solid line) $S(T)$ for $\beta\text{-Zn}_4\text{Sb}_3$. $S(T)$ for doping levels of 0.15 and 0.04 holes/cell are given by the curves below and above those for the actual doping level.

ACKNOWLEDGEMENTS

This work was supported by the ONR and DARPA. Computations were performed using the DoD HPCMO facilities at the NAVO and ASC. We are grateful for helpful discussions with W.E. Pickett, J.L. Feldman, T. Caillat, J.P. Fleurial, T. Tritt, D.T. Morelli and G.A. Slack.

REFERENCES

1. G. Mahan, B. Sales and J. Sharp, *Physics Today* **50** #3, 42 (1997).
2. T. Caillat, J.P. Fleurial and A. Borshchovsky in *Proceedings ICT'96* edited by T. Caillat, A. Borshchovsky and J.P. Fleurial (IEEE Press, Piscataway, 1996), pp. 151-154.
3. B.C. Sales, D. Mandrus and R.K. Williams, *Science* **272**, 1325 (1996).
4. J.P. Fleurial, A. Borshchovsky, T. Caillat, D.T. Morelli and G.P. Meisner in *Proceedings ICT'96* edited by T. Caillat, A. Borshchovsky and J.P. Fleurial (IEEE Press, Piscataway, 1996), pp. 91-95.

5. D.T. Morelli and G.P. Meisner, J. Appl. Phys. **77**, 3777 (1995).
6. L. Nordstrom and D.J. Singh, Phys. Rev. B **53**, 1103 (1996).
7. D.J. Singh and W.E. Pickett, Phys. Rev. B **50**, 11235 (1994).
8. J.L. Feldman and D.J. Singh, Phys. Rev. B **53**, 6273 (1996); **54**, 712 (1996).
9. D.J. Singh, Planewaves, Pseudopotential and the LAPW Method, Kluwer, Boston, 1994.
10. J.M. Ziman, Principles of the Theory of Solids, Cambridge University Press, Cambridge, 1972.
11. C.M. Hurd, The Hall effect in Metals and Alloys, Plenum, New York, 1972.
12. W.W. Schulz, P.B. Allen and N. Trivedi, Phys. Rev. B **45**, 10886 (1992).
13. A.E. Karakozov, I.I. Mazin and Y.A. Uspenski, Sov. Phys. Doklady **277**, 848 (1984).
14. G.A. Slack in Solid State Physics edited by F. Seitz and D. Turnbull (Academic, New York, 1979), Vol. 34, p. 1
15. D.G. Cahill, S.K. Watson and R.O. Pohl, Phys. Rev. B **46**, 6131 (1992).
16. T. Caillat, J. Kulleck, A. Borshchevsky and J.P. Fleurial, J. Appl. Phys. **79**, 8419 (1996).
17. G.S. Nolas, G.A. Slack, D.T. Morelli, T.M. Tritt and A.C. Ehrlich, J. Appl. Phys. **79**, 4002 (1996).
18. D.T. Morelli, T. Caillat, J.P. Fleurial, A. Borshchevsky, J. Vandersande, B. Chen and C. Uher, Phys. Rev. B **51**, 9622 (1995).
19. D. Mandrus, A. Migliori, T.W. Darling, M.F. Hundley, E.J. Peterson and J.D. Thompson, Phys. Rev. B **52**, 4926 (1995).
20. T. Caillat, A. Borshchevsky and J.P. Fleurial, J. Appl. Phys. **80**, 4442 (1996).
21. The inverse effective mass tensor is not fully isotropic especially for the heavier band. This is symmetry allowed because of the missing mirror planes in the spacegroup.
22. In metals convergence is usually obtained with an energy range of $\pm 5kT$, but because of the strong variation of σ due to the band onsets we used $\pm 10kT$ in the present calculations.
23. The light band is derived from the Sb p states directed perpendicular to the plane of the Sb₄ rings. These hybridize strongly with Co 4p like states that mix with the La 4f resonance. This resonance, which is above the gap, pushes the light band down.

**FILLED SKUTTERUDITE ANTIMONIDES: VALIDATION OF THE
ELECTRON-CRYSTAL PHONON-GLASS APPROACH
TO NEW THERMOELECTRIC MATERIALS**

D. MANDRUS*, B. C. SALES*, V. KEPPENS*, B. C. CHAKOUMAKOS*, P. DAI*, L. A. BOATNER*, R. K. WILLIAMS**, J. R. THOMPSON*, T. W. DARLING***, A. MIGLIORI***, M. B. MAPLE****, D. A. GAJEWSKI****, AND E. J. FREEMAN****

*Solid State Division, Oak Ridge National Laboratory, Oak Ridge, TN 37831

**Metals and Ceramics Division, Oak Ridge National Laboratory, Oak Ridge, TN 37831

***Materials Science and Technology Division, Los Alamos National Laboratory, Los Alamos, NM 87545

****Department of Physics and Institute for Pure and Applied Physical Sciences, University of California, San Diego, La Jolla, CA 92093

ABSTRACT

After a brief review of the transport and thermoelectric properties of filled skutterudite antimonides, we present resonant ultrasound, specific heat, and inelastic neutron scattering results that establish the existence of two low-energy vibrational modes in the filled skutterudite $\text{LaFe}_3\text{CoSb}_{12}$. It is likely that at least one of these modes represents the localized, incoherent vibrations of the La ion in an oversized atomic "cage." These results support the usefulness of weakly bound, "rattling" ions for the improvement of thermoelectric performance.

INTRODUCTION

One of the most promising new ideas in the field of thermoelectrics is the "electron-crystal, phonon-glass" (ECPG) concept originally proposed by Slack.¹ In this picture a loosely bound atom with a large thermal parameter scatters phonons much more strongly than electrons, thus permitting a "glasslike" thermal conductivity to coexist with the high electron mobilities found in crystals. Very recently, Sales, Mandrus, and Williams² reported a high thermoelectric figure of merit (ZT) in $\text{LaFe}_3\text{CoSb}_{12}$, which was primarily due to a drastic reduction in the lattice component of the thermal conductivity of this material compared to its unfilled analogue. Similar results have been reported by others.^{3,4} Although it was hypothesized in Ref. 2 that the reason for the large ZT in filled skutterudites was the incoherent "rattling" of the rare earth ions, no evidence for a low frequency local mode existed at that time. Here we present resonant ultrasound, specific heat, and inelastic neutron scattering results that support the existence of a local mode in $\text{LaFe}_3\text{CoSb}_{12}$ and validate the ECPG approach to new thermoelectric materials.

EXPERIMENTAL DETAILS

Polycrystalline samples were synthesized by sealing the starting materials in silica tubes, heating above the liquidus temperature, quenching, annealing, and hot-pressing. All samples were more than 90% dense, and single phase by powder x-ray diffraction. Single crystals were grown using a modified Bridgman method and an Sb-rich melt.

Resonant Ultrasound Spectroscopy (RUS) is a dynamic modulus measurement technique developed by Migliori *et al.* and reviewed at length in Ref. 5. The technique employs tiny LiNbO_3 transducers and a sensitive heterodyne receiver to measure the free-body resonances of a small ($2 \times 2.5 \times 3 \text{ mm}^3$) sample shaped in the form of a rectangular parallelepiped. Once the free-body resonances are known, non-linear optimization methods are employed to extract the elastic constants.

The neutron experiments were conducted at ORNL's High Flux Isotope Reactor. The single-crystal refinements were performed using a 4-circle neutron diffractometer. The inelastic neutron experiments were performed on a triple axis spectrometer using both pyrolytic graphite and Be energy analyzers.

Standard methods were used for the specific heat and resistivity measurements.

RESULTS AND DISCUSSION

A brief review of some important crystal-chemical and transport properties of filled skutterudites will be given first. A diagram of the cubic filled skutterudite crystal structure (space group $Im\bar{3}$, 34 atoms per unit cell) appears in Figure 1. There are two interesting aspects to this structure. First, the rare earth ion sits in an oversized atomic "cage." A typical ionic radius for a rare earth is about 1.4 \AA , whereas the radius of the "hole" in the skutterudite structure is about 2.0 \AA . This suggests that the rare earth ion is weakly bound and may have a large thermal parameter. That this is in fact the case may be seen in Figure 2, which illustrates the large difference in thermal parameters between the rare earth ion and the other ions in $\text{LaFe}_3\text{CoSb}_{12}$. The second interesting feature in the skutterudite structure is the presence of four-membered Sb rings. These rings suggest that the octet principle may in fact be fulfilled in skutterudites if the Sb-Sb bonds are properly taken into account. In fact, if we apply a slightly modified form of the octet rule known as the generalized 8-N rule⁶, we find that the valence electron concentration per anion (VEC) for skutterudites is 6. For example, in CoSb_3 each Co contributes 9 electrons and each Sb contributes 3 electrons; this gives 18 valence electrons per formula unit, and a VEC of 6. This implies that skutterudites can be viewed as simple valence compounds if the two Sb-Sb bonds per Sb are taken into account. Therefore, the generalized 8-N rule predicts that any skutterudite with a $\text{VEC} = 6$ should be a semiconductor, as is CoSb_3 . In semiconducting $\text{LaFe}_3\text{CoSb}_{12}$, for example, the $\text{VEC} = 6$ and the rule is obeyed. Although these

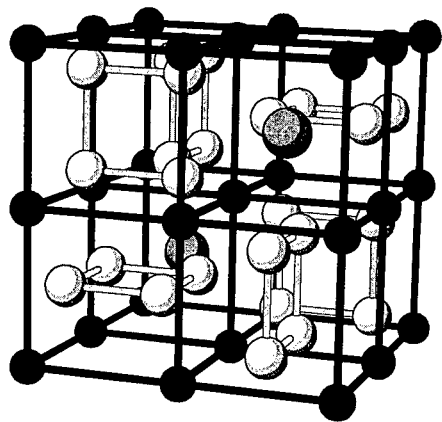


Figure 1. Diagram of the filled skutterudite structure. For $\text{LaFe}_3\text{CoSb}_{12}$ the two large balls represent La ions, the small dark gray balls represent Fe or Co ions, and the light gray balls represent Sb ions. Note the four-membered Sb rings, and the large "cage" in which the La resides.

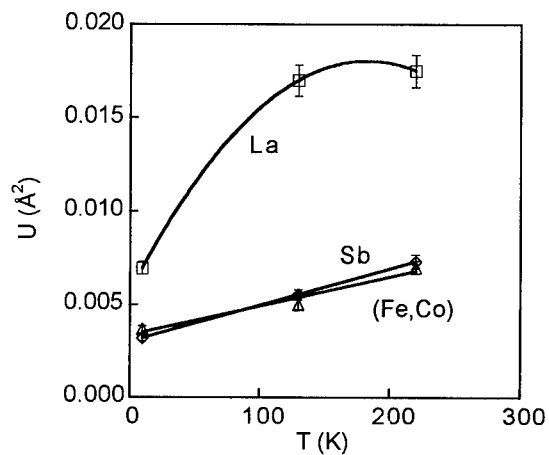


Figure 2. Refined atomic displacement parameters obtained on a single crystal of $\text{La}_{0.75}\text{Fe}_3\text{CoSb}_{12}$ using a 4-circle neutron diffractometer. The crystal was approximately 2 mm on a side. The large value of the atomic displacement parameter for the La ion is consistent with a large amplitude vibratory motion, although static disorder can also lead to a large value of U . Solid lines are guides to the eye.

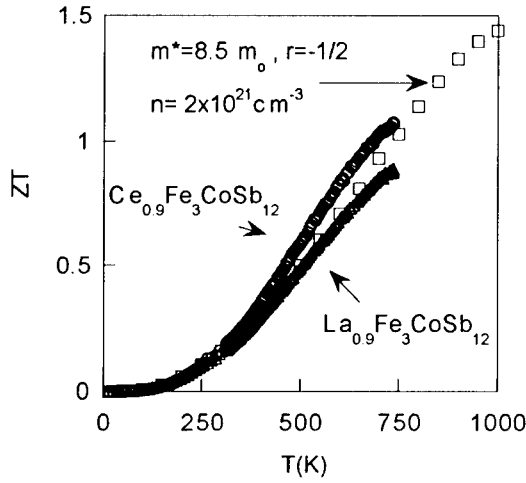


Figure 3. ZT vs. temperature for two filled skutterudite antimonides and a model calculation assuming transport occurs in a single parabolic band. The calculation was performed assuming the relaxation-time approximation, with the energy dependence of the relaxation time given by $\tau = \tau_0 E^r$. For acoustic phonon scattering, $r = -1/2$.

simple electron counting arguments are no substitute for detailed electronic structure calculations, they are often useful guides to the synthesis of new materials.⁷

In Figure 3 we plot ZT vs. temperature for two filled skutterudite antimonides. We also plot a model calculation for ZT using generalized Fermi-Dirac statistics and assuming that transport occurs in a single parabolic band. At high temperatures the achievable thermopowers and resistivities of the filled and unfilled materials are not dramatically different, but as we illustrate in Figures 4 and 5 the lattice component of the thermal conductivity of the filled compounds is an order of magnitude smaller than that of the unfilled at room temperature. Also in Figure 5 we plot the minimum thermal conductivity as calculated by the prescription of Cahill, Watson, and Pohl⁸ using sound velocities obtained by RUS. To reach minimum thermal conductivity, heat transport in a material should occur as a random walk of thermal energy between neighboring atoms vibrating with random phases. This implies a mean free path on the order of an interatomic spacing, and is nearly impossible to achieve in real materials. Glasses, for example, have a mean free path of about 10 Å. We can estimate the mean free path in $\text{La}_{0.75}\text{Fe}_3\text{CoSb}_{12}$ as follows. If we write $\kappa = 1/3 C_v \langle v \rangle \Lambda$, where C_v is the heat capacity per unit

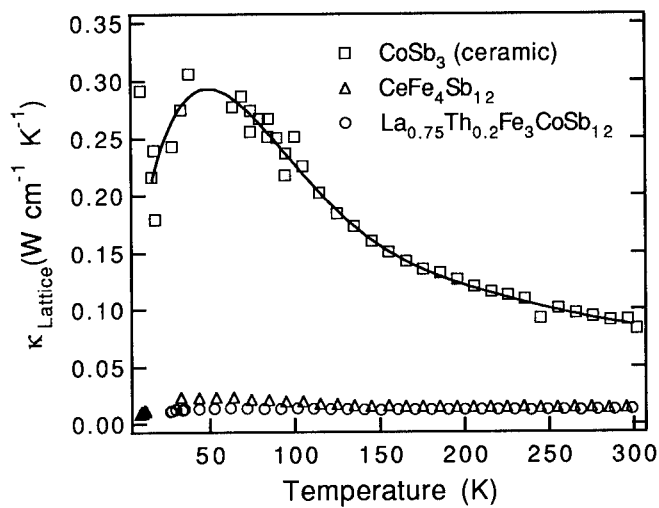


Figure 4. Lattice component of thermal conductivity of CoSb_3 and two filled skutterudites vs. temperature. The reduction in thermal conductivity achieved by filling the rare-earth site is truly remarkable.

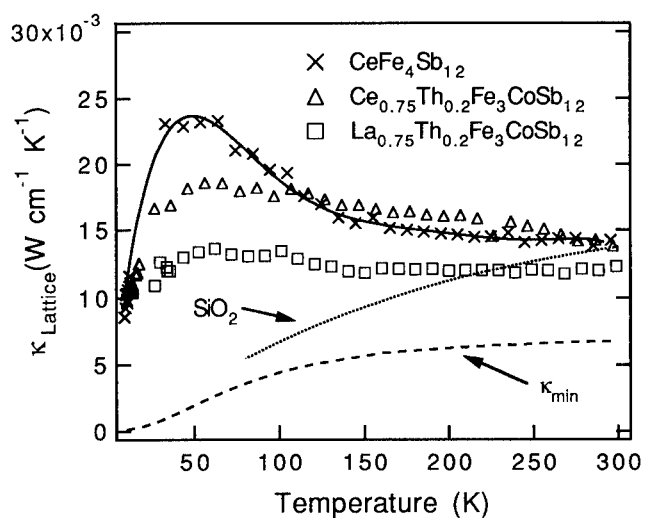


Figure 5. Lattice component of the thermal conductivity of three filled skutterudites and vitreous silica vs. temperature. Also plotted is the minimum thermal conductivity for a filled skutterudite antimonide calculated using Eq. 17 of Ref. 8.

volume, $\langle v \rangle =$ is the average sound velocity, and Λ the phonon mean free path, we find that for $\text{LaFe}_3\text{CoSb}_{12}$ we have $\Lambda = 8.2 \text{ \AA}$. This is comparable to the 7.9 \AA distance between the rare earth ions, and is consistent with the notion that phonons are scattered by incoherently vibrating La ions.

In order to better characterize the lattice dynamics of filled skutterudites, RUS measurements were performed on both CoSb_3 and $\text{La}_{0.75}\text{Fe}_3\text{CoSb}_{12}$ from 5 to 300 K. The results appear in Figure 6 and in Table 1. The solid line through the CoSb_3 data is a model calculation using the function $c(T) = c_0 - s/(e^{T/\Theta} - 1)$; this function, which has some theoretical justification, was shown by Varshni⁷ to describe the temperature dependence of the elastic constants of many simple substances and in effect defines “normal” elastic behavior in much the same way that the Debye model defines “normal” specific heat behavior. It is immediately apparent from Figure 6 that although CoSb_3 is well-defined by the Varshni function, the elastic response of $\text{La}_{0.75}\text{Fe}_3\text{CoSb}_{12}$ is quite unusual. The large change in c_{44} at low temperatures is immediately suggestive of a low energy mode that couples strongly to acoustic phonons, and the two well-defined peaks in the ultrasonic attenuation of $\text{La}_{0.75}\text{Fe}_3\text{CoSb}_{12}$ suggest that two low-energy modes may be present. Although a complete understanding of the elastic response of $\text{La}_{0.75}\text{Fe}_3\text{CoSb}_{12}$ is not yet available, we can begin to understand the data by considering the elastic response of a two-level system (TLS). First, we recall that the elastic constants are given by the second derivative of the free energy with respect to strain, $c = \partial^2 F / \partial \epsilon^2$. The Helmholtz free energy of a TLS is given by $F = -k_B T \ln(1 + e^{-\Delta/T})$, where Δ is the level spacing. If we assume that strain couples to the system as $\Delta = \Delta_0 + d\epsilon$, where d is a coupling constant, it is a simple matter to calculate the two-level contribution to the elastic response. As illustrated in Figure 7, we find that we can model the data reasonably well by including 2 TLS's with level spacings of 50 K and 200 K.

To further characterize the unusual thermodynamics of filled skutterudites, specific heat measurements were performed on a sample of $\text{La}_{0.9}\text{Fe}_3\text{CoSb}_{12}$ from 2 K to 45 K. The results appear in Figure 8. In addition to the standard $C_p = \gamma T + \beta T^3$, two Einstein oscillators of the form $C_{\text{Einstein}} = (\theta_E/T)^2 e^{\theta_E/T} / (e^{\theta_E/T} - 1)^2$ were required in order to successfully model the data. The Einstein temperatures of the two oscillators were $\theta_{E1} = 70 \text{ K}$, and $\theta_{E2} = 157 \text{ K}$. It is tempting to ascribe the lower energy oscillator to the “rattling” of the La ions because the magnitude of the 70 K oscillator contribution is about what we expect. At high temperature we expect each mole of Einstein oscillators to contribute $3R = 24.94 \text{ J/K}$ to the heat capacity. Since only about 1/17 of the atoms are “rattlers,” we expect a contribution of about $(1/17)*3R = 1.47 \text{ J/mol-K}$. This is very close to the fitted value of 1.21 J/mol-K .

Localized lattice vibrations such as we have been discussing are expected to produce narrow peaks in the phonon density of states (DOS).¹⁰ In Figure 9 we present a measurement of the phonon DOS using inelastic neutron scattering. These measurements were performed at 11 K

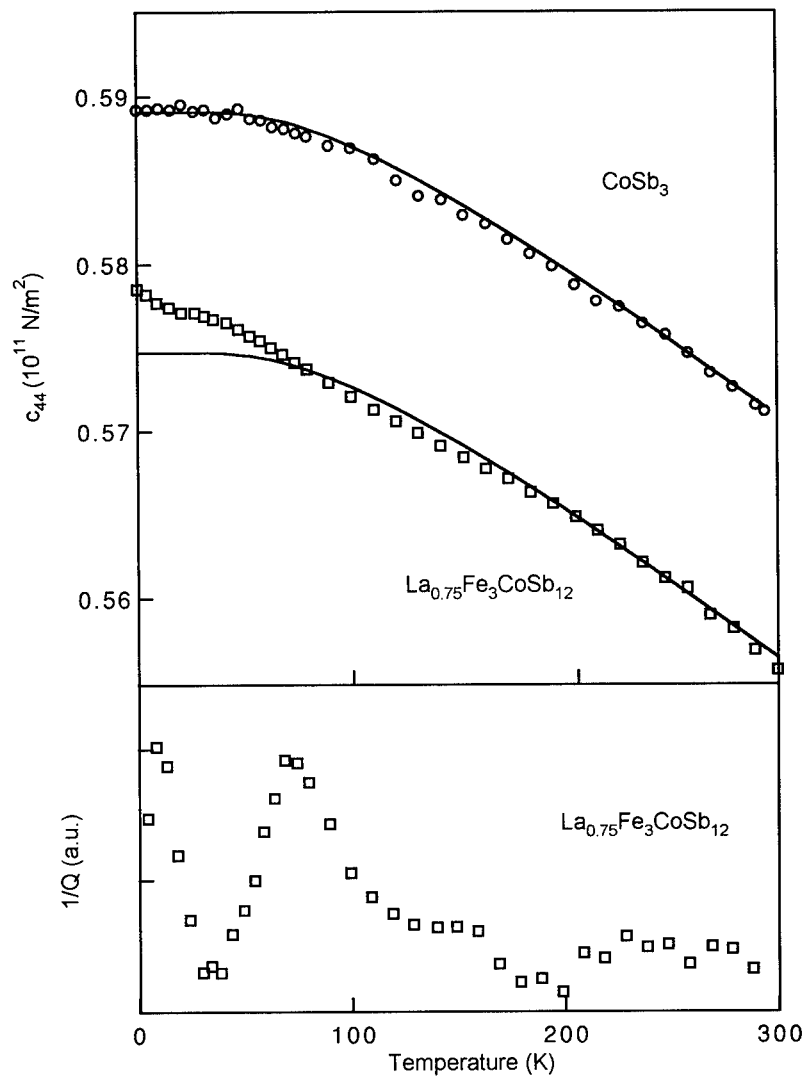


Figure 6. Upper panel. Shear modulus c_{44} vs. temperature for CoSb₃ and La_{0.75}Fe₃CoSb₁₂. The solid line through the CoSb₃ data is a fit to the function $c(T) = c_0 - s/(e^{t/T} - 1)$. The fitting parameters used were $c_0 = 0.589 \times 10^{11} \text{ N/m}^2$, $s = 0.0275 \times 10^{11} \text{ N/m}^2$, and $t = 265 \text{ K}$. The solid line through the La_{0.75}Fe₃CoSb₁₂ data is the fit to CoSb₃ displaced downwards by $0.0144 \times 10^{11} \text{ N/m}^2$. Lower panel. $1/Q$ vs. temperature for a sample of La_{0.75}Fe₃CoSb₁₂. Q is the quality factor for a free-body resonance of the sample, and $1/Q$ is proportional to the ultrasonic absorption.

Table 1. Density, elastic constants, bulk modulus, longitudinal and transverse sound velocity, and Debye temperature of CoSb_3 and $\text{La}_{0.75}\text{Fe}_3\text{CoSb}_{12}$. These values were obtained from room temperature RUS measurements.

	CoSb_3	$\text{La}_{0.75}\text{Fe}_3\text{CoSb}_{12}$
$\rho_{\text{theor.}} (\text{g/cm}^3)$	7.64	7.78
$\rho_{\text{exp.}} (\text{g/cm}^3)$	7.29	7.64
$c_{11} (10^{11} \text{ N/m}^2)$	1.58	1.57
$c_{44} (10^{11} \text{ N/m}^2)$	0.57	0.55
$B (10^{11} \text{ N/m}^2)$	0.82	0.84
$v_l (\text{m/s})$	4650	4530
$v_t (\text{m/s})$	2800	2680
$\theta_D (\text{K})$	319	310

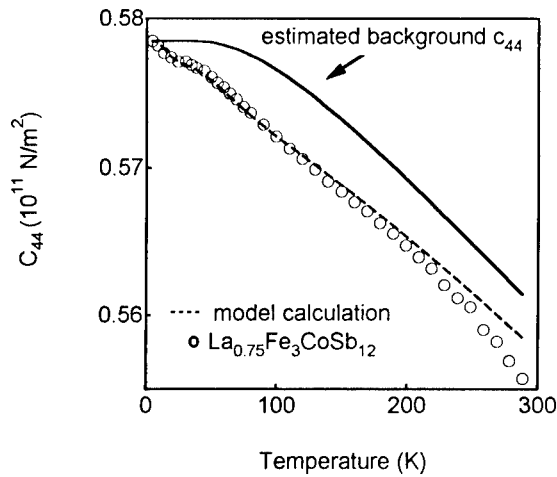


Figure 7. Open circles: shear modulus c_{44} vs. temperature for a sample of $\text{La}_{0.75}\text{Fe}_3\text{CoSb}_{12}$. Solid line: estimated background c_{44} obtained from the function $c(T) = c_0 - s/(e^{T/t} - 1)$ taking s and t from the fit to CoSb_3 (see Figure 6) and choosing $c_0 = 0.5785 \times 10^{11} \text{ N/m}^2$ to agree with the data at low temperature. Dotted line: two-level system (TLS) model calculation obtained by taking $c_{44}(\text{model}) = c_{44}(\text{background}) + c_{44}(\text{TLS \#1}, \Delta=50 \text{ K}) + c_{44}(\text{TLS \#2}, \Delta=200 \text{ K})$.

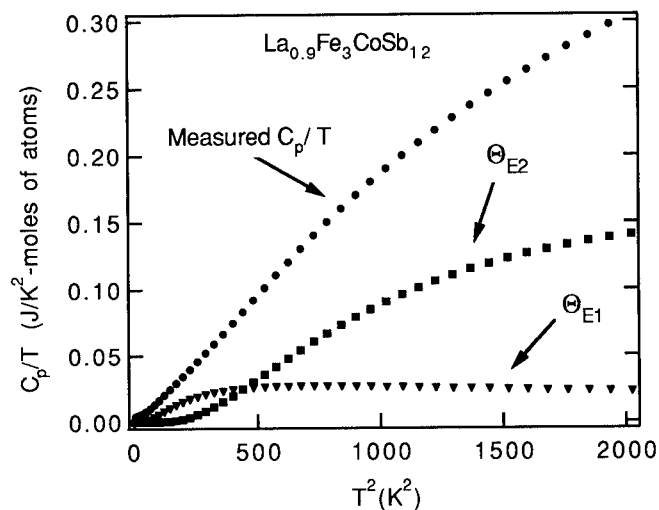


Figure 8. Specific heat C_p divided by temperature vs. temperature squared for $\text{La}_{0.9}\text{Fe}_3\text{CoSb}_{12}$. The contributions of the two fitted Einstein oscillators are also shown. A fit to the equation $C_p(\text{J/K-mole-atoms}) = \gamma T + \beta T^3 + A C_{E1}(T) + B C_{E2}(T)$ yielded the following values for the fitting parameters: $\gamma = 0.0037 \text{ J/mol-K}^2$, $\beta = (12/5)\pi^4 k_B N_A / \Theta_D^3 = 6.86 \times 10^{-5} \text{ J/mol-K}^4$, $\Theta_{E1} = 70 \text{ K}$, $A = 1.21 \text{ J/mol-K}$, $\Theta_{E2} = 157 \text{ K}$, $B = 16.00 \text{ J/mol-K}$. The Debye temperature Θ_D obtained from this fit is $\Theta_D = 302 \text{ K}$. This is in excellent agreement with the Debye temperature of 310 K obtained using RUS (see Table 1).

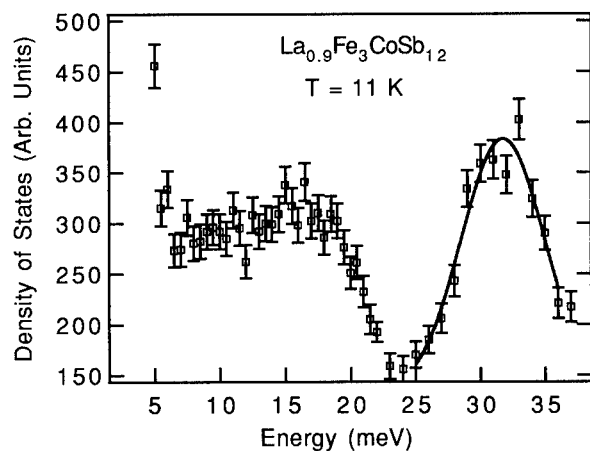


Figure 9. Phonon density of states for $\text{La}_{0.9}\text{Fe}_3\text{CoSb}_{12}$ obtained using inelastic neutron scattering and a pyrolytic graphite analyzer. The intensity below 5 meV is from elastic scattering.

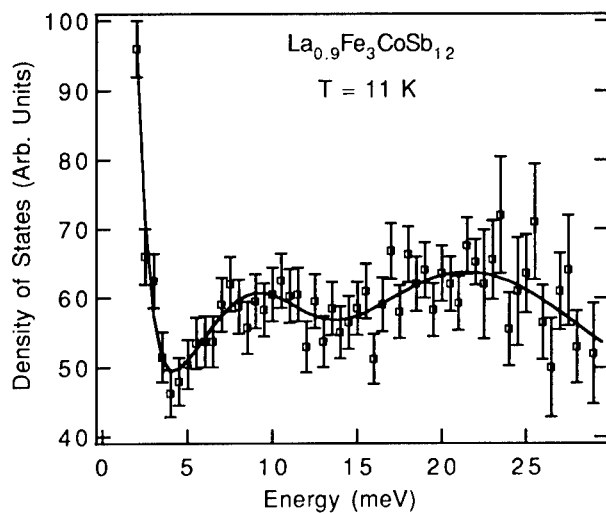


Figure 10. Phonon density of states for $\text{La}_{0.9}\text{Fe}_3\text{CoSb}_{12}$ obtained using inelastic neutron scattering and a high resolution Be analyzer. The intensity below 4 meV is from elastic scattering.

on a 30 g polycrystalline sample of $\text{La}_{0.9}\text{Fe}_3\text{CoSb}_{12}$. Using a high resolution Be analyzer and 4 days of counting time, two low energy peaks were visible, one at 100 K and one at 240 K. Although the energies of these peaks are close to the vibrational energies observed in the ultrasound and specific heat experiments, it is important to note that a calculation of the phonon DOS of CoSb_3 by Feldman and Singh¹¹ predicts a double peak structure somewhat similar to the one observed in $\text{La}_{0.9}\text{Fe}_3\text{CoSb}_{12}$. Given that RUS has shown that the lattice dynamics of CoSb_3 and $\text{La}_{0.9}\text{Fe}_3\text{CoSb}_{12}$ are very different, it is unclear how much weight to attach to these calculations in the evaluation of data on the filled materials. Measurements of the phonon DOS of CoSb_3 are presently underway, and these should help us determine the source of the peaks in the phonon DOS of $\text{La}_{0.9}\text{Fe}_3\text{CoSb}_{12}$.

In conclusion, the filled skutterudite antimonides appear to represent excellent examples of electron-crystal, phonon-glass materials in which the incoherent “rattling” of loosely bound ions greatly reduces the lattice component of the thermal conductivity while only modestly degrading the electronic transport properties. Resonant ultrasound, specific heat, and inelastic neutron measurements have indicated the existence of two low-energy vibrational modes in $\text{La}_{0.9}\text{Fe}_3\text{CoSb}_{12}$ that do not appear to be present in CoSb_3 . It is likely that one, or both, of these modes are associated with the vibrations of the La ion in a shallow potential well.

ACKNOWLEDGMENTS

Oak Ridge National Laboratory is managed by the Lockheed Martin Energy Research Corporation for the U.S. Department of Energy under contract No. DE-AC05-96OR22464. Work at Los Alamos was performed under the auspices of the U.S. Department of Energy. Research at UCSD was supported by the U.S. Department of Energy under grant No. DE-FG03-86ER-45230 and the National Science Foundation under grant No. DMR-94-08835.

REFERENCES

1. G. A. Slack in Thermoelectric Handbook, CRC Press, Boca Raton, FL, 1995.
2. B. C. Sales, D. Mandrus, and R. K. Williams, *Science* **272**, p. 1325 (1996).
3. J.-P. Fleurial, A. Borshchevsky, T. Caillat, D. T. Morelli, and G. P. Meisner in Proceedings of the Fifteenth International Conference on Thermoelectrics, Pasadena, CA (IEEE, New York, NY 1996), p. 91.
4. B. X. Chen, J. H. Xu, C. Uher, D. T. Morelli, G. P. Meisner, J. P. Fleurial, T. Caillat, A. Borshchevsky, *Phys. Rev. B* **55**, p. 1476 (1997).
5. A. Migliori, J. L. Sarrao, W. M. Visscher, T. M. Bell, M. Lei, Z. Fisk, and R. G. Leisure, *Physica B* **183**, p. 1 (1993).
6. For a lucid exposition see U. Müller, Inorganic Structural Chemistry, John Wiley, New York, 1993, pp. 116-126.
7. It is in fact surprising that the generalized 8-N rule appears to work in skutterudites because calculations by D. J. Singh and W. E. Pickett, *Phys. Rev. B* **50**, p. 11235 (1994) indicate little static charge transfer between the pnictogen and the transition metal.
8. D. G. Cahill, S. K. Watson, and R. O. Pohl, *Phys. Rev. B* **46**, p. 6131 (1992).
9. Y. P. Varshni, *Phys. Rev. B* **2**, p. 3952 (1970).
10. A. D. Caplain and L. K. Nicholson, *J. Phys. F* **8**, p. 51 (1978).
11. J. L. Feldman and D. J. Singh, *Phys. Rev. B* **53**, p. 6273 (1996).

SYNTHESIS OF NEW THERMOELECTRICS USING MODULATED ELEMENTAL REACTANTS

MARC D. HORNBOSTEL, HEIKE SELLINSCHEGG, and DAVID C. JOHNSON

Department of Chemistry and Materials Science Institute
University of Oregon, Eugene, OR 97403

ABSTRACT

A series of new, metastable ternary crystalline compounds with the skutterudite crystal structure have been synthesized using modulated elemental reactants. The initial reactants are made up of multiple repeats of a $\sim 25\text{\AA}$ thick unit containing elemental layers of the desired ternary metal, iron and antimony. Low temperature annealing (150°C) results in interdiffusion of the elemental layers to form amorphous reaction intermediates. Annealing these intermediates at temperatures between 200°C and 250°C results in exothermic crystallization of the desired skutterudite crystal structure. Most of the new compounds prepared are only kinetically stable, decomposing exothermically to form thermodynamically more stable mixtures of binary compounds and elements. Low angle x-ray diffraction studies show that the resulting films are exceedingly smooth. These films have an ideal geometry for measuring properties of importance for thermoelectric devices—the Seebeck coefficient and the electrical conductivity. Thermal conductivity can be measured using a modification of the 3ω technique of Cahill. Samples can be produced rapidly, allowing for systematic screening and subsequent optimization as a function of composition and doping levels.

INTRODUCTION

Recently there has been a resurgence of interest in thermoelectrics because of the discovery of new materials and the development of new approaches to this old problem. The efficiency of a thermoelectric device is given by the component materials' figure of merit, $ZT = TS^2\sigma/\kappa$, where T is the temperature, S is the Seebeck coefficient, σ is the electrical conductivity and κ is the thermal conductivity. The best, currently used materials have figures of merit near 1. If the figure of merit was increased to 2 to 4, thermoelectric coolers would begin to compete with compressor based refrigeration. The development of new materials with higher figures of merit would replace fluorocarbon compounds used in compressors with Peltier refrigerators, enable power generation from heat sources which are currently considered "waste" heat, and enable the cooling of electrical circuits, including those containing superconducting oxide electronics[1,2].

Optimizing the figure of merit involves balancing several factors which have resulted in the development of some general guidelines. One wants as high a Seebeck coefficient as possible. High Seebeck coefficients result from a large density of states. Materials with high densities of states at the Fermi level include heavily doped semiconductors and heavy fermion materials. In addition to a high Seebeck coefficient, one desires the greatest possible ratio of electrical to thermal conductivity. Since thermal conductivity from carriers and electrical conductivity are linked by the Weidemann-Franz relationship, the best one can do is make the thermal conductivity from lattice phonons as small as possible. To obtain low phonon conductivity, one wants large, complex unit cells and/or a misfit between a lattice site and a cation. In the latter case, the random thermal displacement of the cation results in a high scattering rate for the lattice phonons resulting in a low thermal conductivity. To maintain good electrical conductivity in such a material, one wants the elements with states at the Fermi level to be part of a rigid covalent network, with little contribution from the orbitals of the vibrating cation.

Since there are several factors which need to be tuned to optimize these properties, one needs chemical flexibility within a structure. Thus improved thermoelectric materials are likely to be ternary or quaternary compounds. An example of one such promising new ternary

material for thermoelectric applications are the filled skutterudites. These materials, of general formula $MFe_{4-x}Co_xSb_{12}$ where $M = La, Ce, Nd$ and $0 < x < 4$, have been found to have unoptimized figures of merit near 1[2]. This promising figure of merit is a result of several contributing factors. First, these compounds have a reasonably high Seebeck coefficient resulting from a complex structure at the Fermi energy. In addition, they have a very low lattice thermal conductivity as a result of effective phonon scattering by the lanthanide cation. The lanthanide cations have a very large vibrational amplitude as a result of the large coordination site formed by the iron-antimony framework.

Synthetic problems have prevented optimization of the properties of the filled skutterudites. The synthesis of ternary and quaternary compounds using traditional solid-state synthesis techniques often results in mixed phase products. Unfortunately, this is the case in the synthesis of the "filled" skutterudite antimonides[3,4]. The traditional synthesis of solid state compounds is limited because high temperatures are needed to overcome low solid state diffusion rates[5,6]. This limits the products to the thermodynamically most stable compounds. In a compound such as the filled skutterudites, the misfit between lattice site and ternary cation results in a lower lattice energy than would be expected. The lattice energy can be increased by substitution of a larger cation, but this would result in an increase in the lattice thermal conductivity. One would actually like to prepare filled skutterudites with smaller cation such as lutetium, resulting in hopefully lower lattice thermal conductivity but also less lattice stability. This is not possible using conventional approaches, since the mixture of binary compounds is more stable than the desired ternary compound.

This synthesis problem is particularly problematic when one is trying to scan a large group of compounds for improved properties. For scanning purposes, one needs clean, single phase materials with controllable dopant levels. Even when it is possible to discover a set of reaction conditions to produce a particular compound, this usually requires considerable effort which often must be repeated for each new trial composition.

Our solution to this synthesis problem is the use of modulated elemental reactants. These reactants overcome diffusion limitations by making diffusion lengths on the order of angstroms. By using reactants with short enough diffusion lengths, one can form amorphous intermediates through a solid state amorphization reaction[7]. Nucleation then becomes the rate limiting step in forming a crystalline compound[8]. This ability to control reaction intermediates is important because one can now avoid binary compounds as intermediates during the synthesis of higher order compounds[9]. This makes it possible to kinetically access compounds which are thermodynamically unstable with respect to binary compounds[10]. The products of this synthesis are phase pure films of several thousand angstrom thickness. Physical properties can be easily measured on these films. The films can be patterned during deposition making them ideal for measuring conductivity and Seebeck coefficients. Thermal conductivity can be measured using a modification of the 3ω technique of Cahill[11,12].

EXPERIMENTAL

The multilayer reactants were prepared in a high-vacuum evaporation system which has been described in detail elsewhere[13]. Briefly, the elements were sequentially evaporated under high vacuum ($\sim 3 \times 10^{-7}$ torr) under the control of a personal computer. Elements were deposited at rates of 0.5 Å/sec using either electron-beam guns or Kundsens cells. Deposition rates of each element were monitored using independent quartz crystal thickness monitors. Deposition was done simultaneously on several different substrates.

Different substrates were used for different applications. A polished silicon wafer was used to characterize the deposited multilayer and investigate the interdiffusion of the reactants using low-angle x-ray diffraction[14]. Multilayer composites deposited on PMMA coated wafers are floated free from the substrate by dissolving the PMMA with acetone, then collected for

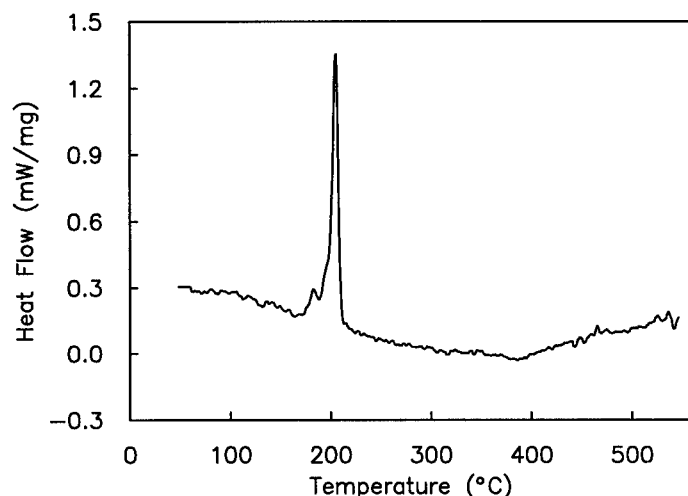


Figure 1: Differential scanning calorimetry data for a representative Y-Fe-Sb sample. The exotherm at 200°C is due to crystallization of $Y_{1-x}Fe_4Sb_{12}$. The sample decomposed with no obvious exotherms, by 550°C.

differential scanning calorimetry (DSC) studies. The total mass of each sample collected from the PMMA coated wafers was ~ 2 –3mg.

The stoichiometry of the samples was determined by electron microprobe analysis. Samples were annealed in a differential scanning calorimeter under a nitrogen atmosphere. Measured exotherms were correlated with x-ray diffraction data to identify and track the interdiffusion of the elements and the crystallization of any compounds. Samples on native oxide coated silicon substrates were annealed in a nitrogen glove box with less than a part per million of oxygen and water.

RESULTS AND DISCUSSION

We have successfully applied this synthesis approach to the synthesis of new skutterudites with the goal of optimizing their figure of merit. Figure 1 shows the calorimetry trace of a modulated elemental reactant with alternating layers of yttrium, iron and antimony with an overall composition ratio near 1:4:12. An exotherm is observed at 200°C. Diffraction data collected after this exotherm and after heating to 550°C, shown in figure 2, indicate that the exotherm is from nucleation and growth of a new filled skutterudite compound YFe_4Sb_{12} . By 550°C, this new compound decomposes into a thermodynamically more stable mixture of Sb, $FeSb_2$ and non-crystalline material. *Therefore, this new compound could not have been made using conventional synthesis since it is thermodynamically unstable with respect to binary compounds which are reaction intermediates in the conventional synthesis.* The $FeSb_2$ impurity is due to this particular sample having and Fe:Sb ratio of slightly greater than 1:3. Samples with stoichiometric ratios of iron to antimony show no $FeSb_2$ impurities. We are therefore able to control impurity levels using the average composition of the starting multilayer. Using this synthesis approach we have replaced the lanthanum cation with a vacancy forming the new binary compound $FeSb_3$, a tetravalent cation, hafnium, forming $Hf_{1-x}Fe_4Sb_{12}$, and the divalent cation tin. In addition, we have replaced the lanthanum with all the lanthanides as well as group IIIB metals. Phase pure materials are obtained by low temperature annealing above the

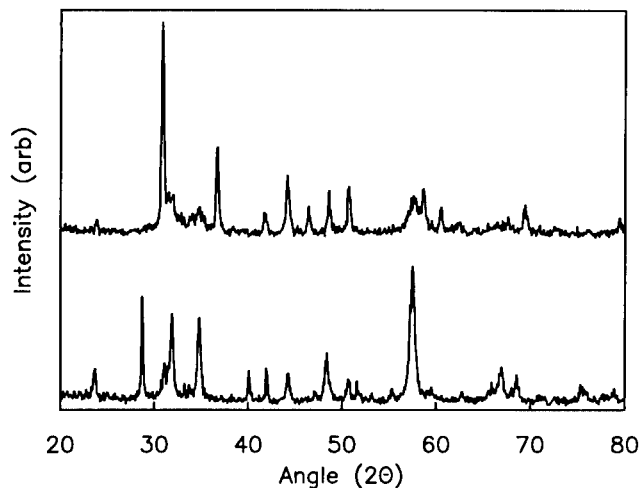


Figure 2: X-ray diffraction scans taken on the Y-Fe-Sb sample shown in figure 1 after heating to 250°C (top) and 550°C (bottom). The top diffraction pattern is that of $Y_{1-x}Fe_3Sb_{12}$ with a small amount of $FeSb_2$ impurity. The bottom diffraction is that of a mixture of Sb and $FeSb_2$.

formation exotherm[15–17].

The synthesis approach we are using provides rapid access to these various compounds as well as solid solutions of these compounds because up to 20 different samples can be produced with a single deposition chamber per day. This synthesis approach also gives unprecedented control over important synthetic parameters. In addition to simple solid solutions, it is possible to controllably dope samples, prepare samples with composition gradients, and prepare crystalline superlattices containing interwoven layers. Electrical conductivity and Seebeck coefficients can be measured on samples deposited directly on insulating substrates. For thermal conductivity measurements, the samples have been deposited directly on thin poly-imide sheets. The formation temperature is low enough that the samples can be crystallized without damaging the plastic substrate. With this process, samples can be produced rapidly and reliably enough that the scanning of materials is limited by the measurement of physical properties, not by the sample synthesis.

We have just begun the process of optimizing these materials for use in thermoelectric devices. Figure 3 shows the electrical conductivity of the new metastable binary compound $FeSb_3$. This compound, which contains 4 fewer electrons than the semiconducting compound $CoSb_3$, is metallic as expected from a rigid band model. The first step in the optimization of the properties is to prepare a series of compounds with each ternary cation in which the ratio of iron to cobalt is controlled to form a semiconducting material. Preliminary data on substitution of cobalt for iron in these systems indicates that the decomposition temperature is raised by alloying iron and cobalt skutterudites. The synthesis of these compounds is currently underway.

Once a semiconducting material is made with each ternary metal, we need to measure the thermal conductivity. We will be using a modification of the 3ω technique developed by Cahill. Briefly, the sample is deposited and annealed on a very thin ($7\mu m$) poly-imide film to form a continuous, smooth skutterudite film. A thin line of silver metal is then evaporated onto the back of the poly-imide foil. The silver is used as both heater and temperature sensor. The temperature oscillations of the metal line are measured by the third harmonic of the voltage

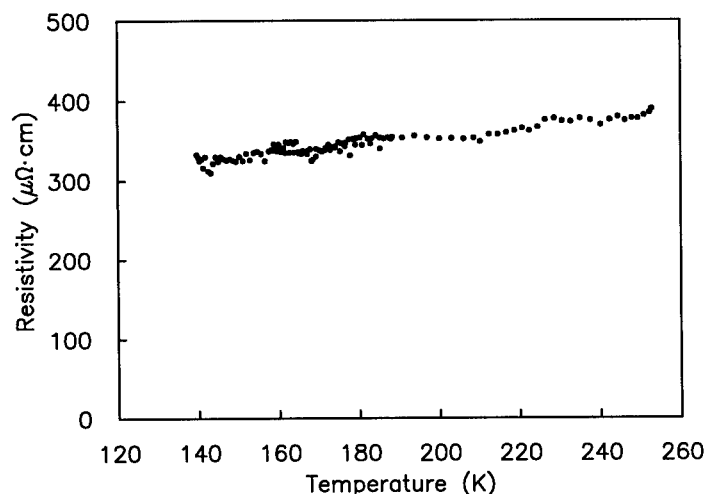


Figure 3: The electrical conductivity of a FeSb₃ film as a function of temperature.

across the line. Both the amplitude and phase shift of the temperature oscillations as a function of frequency are used to deconvolute the thermal conductivity of the substrate as well as the film. Measurements on substrates with skutterudite films are now underway.

Once a semiconducting compound with a low lattice thermal conductivity is obtained in the iron-cobalt solid solution, the next step is to optimize the Seebeck coefficient. In the currently used materials, this was accomplished by heavily doping these semiconductors resulting in a large density of states. The ternary skutterudites provide three potential crystallographic sites for dopants: the ternary metal can be replaced or its stoichiometry altered, the transition metal site can be doped with another transition metal to either add or remove electrons, and the antimony site can be substituted with, for example, selenium as an n-type dopant or germanium for p-type doping.

CONCLUSION

Elementally modulated reactants provide a new tool for solid state chemists to rationally control the synthesis of kinetically stable compounds. Its strength is in the ability to quickly explore composition space and rationally optimize the properties for particular applications. The low temperature synthesis of Y_{1-x}Fe₄Sb₁₂ illustrates this ability. Elementally modulated reactants are useful as an exploratory technique to probe both the chemistry and physical properties of otherwise inaccessible compounds.

ACKNOWLEDGEMENTS

Acknowledgement is made to the donors of the Petroleum Research Fund, administered by the ACS for partial support of this research. The support of the National Science Foundation (DMR-9308854 and DMR-9510562) is also gratefully acknowledged.

REFERENCES

- [1] G. Mahan, B. Sales, J. Sharp, *Physics Today*, **50**, 42-47 (1997)

-
- [2] B. C. Sales, D. Mandrus, R. K. Williams, *Science*, **272**, 1325-1328 (1996)
- [3] D. J. Braun, W. Jeitschko, *J. Less-Common Metals*, **72**, 147-156 (1980)
- [4] W. Jeitschko, D. Braun, *Acta. Cryst.*, **B33**, 3401-3406 (1977)
- [5] F. J. DiSalvo, *Science*, **247**, 649-655 (1990)
- [6] A. Stein, S. W. Keller, T. E. Mallouk, *Science*, **259**, 1558-1564 (1993)
- [7] L. Fister, D. C. Johnson, *J. Am. Chem. Soc.*, **114**, 4639-4644 (1992)
- [8] M. Fukuto, M. D. Hornbostel, D. C. Johnson, *J. Am. Chem. Soc.*, **116**, 9136-9140 (1994)
- [9] L. Fister, D. C. Johnson, *J. Am. Chem. Soc.*, **116**, 629-633 (1993)
- [10] T. Novet, D. C. Johnson, *J. Am. Chem. Soc.*, **113**, 3398-3403 (1991)
- [11] D. G. Cahill, M. Katiyar, J. R. Abelson, *Phys. Rev. B*, **50**, 6077-6081 (1994)
- [12] D. G. Cahill *Rev. Sci. Instr.*, **61**, 802-808 (1990)
- [13] L. Fister, X. M. Li, T. Novet, J. McConnell, D. C. Johnson, *J. Vac. Sci. Technol. A*, **11**, 3014-3019 (1993)
- [14] T. Novet, J. M. McConnell, D. C. Johnson, *Mater. Res. Soc. Symposium Ser.*, **238**, 581-586 (1992)
- [15] M. D. Hornbostel, E. J. Hyer, J. H. Edvalson, D. C. Johnson, *Inorg. Chem.*, submitted (1997)
- [16] M. D. Hornbostel, E. J. Hyer, J. Thiel, D. C. Johnson, *J. Am. Chem. Soc.*, accepted, (1997)
- [17] S. L. Stuckmeyer, H. Sellinschegg, M. D. Hornbostel, D. C. Johnson, *Ang. Chem.*, submitted (1997)

PROPERTIES OF CoSb₃ FILMS GROWN BY PULSED LASER DEPOSITION

Hans-Martin Christen*, David G. Mandrus, David P. Norton, Lynn A. Boatner, and
Brian C. Sales

Oak Ridge National Laboratory, Solid State Division, Oak Ridge, TN 37831

*Present address: Neocera, Inc., 10000 Virginia Manor Road, Suite 300, Beltsville,
MD 20705-4215

Abstract

Polycrystalline CoSb₃ films were grown on a variety of electrically insulating substrates by pulsed laser ablation from a stoichiometric hot-pressed target. These films are fully crystallized in the skutterudite structure, and the grains exhibit a strongly preferred alignment of the cubic [310]-axis perpendicular to the substrate surface. The film quality is studied for different single-crystal substrates and as a function of growth temperature and background gas.

Hall measurements show that the films are *p*-type semiconducting with a room-temperature carrier density of 3×10^{20} holes/cm³. The Hall mobility is found to be 50 to 60 cm²/Vs, which is high for such a heavily-doped material. The Seebeck coefficient and the resistivity are measured as a function of temperature and are compared to bulk measurements.

Introduction

CoSb₃ is a narrow-gap semiconductor with excellent electronic properties including high values for the hole mobility μ , the electrical conductivity σ and the Seebeck coefficient S . The thermal conductivity κ of CoSb₃ is relatively large, however, for an optimum thermoelectric material (see [1] and references therein). In bulk CoSb₃ alloys, the experimentally achieved values of the dimensionless figure of merit $ZT = S^2 \times \sigma \times T / \kappa$, typically fall in the range of $ZT \leq 0.5$ and thus remain below the values required for most practical applications.

Recent efforts to obtain a higher ZT have been focused on decreasing the lattice thermal conductivity κ_{lattice} . In the "filled" skutterudites LaFe₃CoSb₁₂ and CeFe₃CoSb₁₂, a κ_{lattice} has been measured which is an order of magnitude lower than that of the isoelectronic CoSb₃ [2]. In an alternate approach to reduce κ_{lattice} , one could attempt to "fill" the empty cage in the CoSb₃ lattice with a noble gas, thus incorporating a "rattler", i.e. a phonon scatterer, without affecting the excellent electronic properties of the material.

Unfortunately, a noble gas cannot be incorporated into the lattice by an equilibrium process. In a thin film, however, such a "rattler" may possibly be added either through diffusion or ion implantation.

Pulsed Laser Deposition (PLD), a process in which the material is ablated from a stoichiometric target by the focused beam of an excimer laser and deposited onto a heated substrate, may offer yet another way to incorporate impurities. PLD is a

fast growth method in which non-equilibrium phenomena can be exploited. The use of background gases or ion sources can easily be incorporated, and it is hoped that new meta-stable phases can be synthesized by such processes.

Further motivation for the growth of thin films is derived from the necessity of their use in device integration and the hope that epitaxial layers will lend themselves to fundamental studies that would otherwise have to be performed on difficult-to-obtain single crystals.

While it was demonstrated earlier that polycrystalline CoSb_3 can be grown on $\text{Si}(100)$ and quartz substrates using magnetron rf-sputtering [3], this research shows for the first time that thin, strongly textured polycrystalline films of CoSb_3 can be grown by PLD on a wide variety of substrates, and the thermoelectric properties of these films are reported.

Experimental

For the preparation of targets, a stoichiometric mixture of high purity Sb and Co pieces were melted together in a carbonized silica tube at 1050 °C for 24 h, quenched into a water bath, and then annealed at 700 °C for 30 h. The resulting material was ball

milled in an argon atmosphere, and hot pressed (10^7 Pa) at 700 °C into a 1" diameter pellet. X-ray diffraction shows that only the skutterudite phase is present in the target.

A detailed description of PLD can be found elsewhere [4]. In our setup, the CoSb_3 target is placed in a vacuum chamber 7 cm from the surface of the substrate, which is mounted (using silver paste) on a heated stainless-steel plate. The beam of a pulsed KrF excimer laser ($\lambda = 248$ nm) is focused onto a 1mm \times 6mm spot on the surface of the rotating target and is scanned across the target to avoid excessive patterning of the target surface. Argon is used as a background gas with a typical pressure of 80 mTorr, and the focused laser energy density is between 1.5 and 3 J/cm² at a repetition rate of 4 Hz.

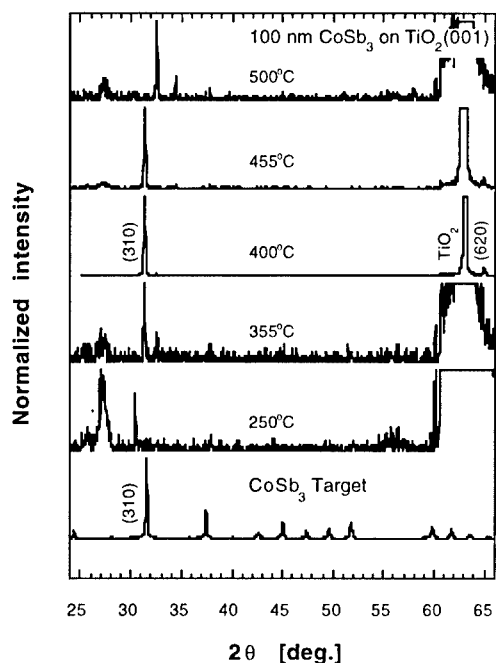


Figure 1: X-ray diffraction patterns (θ - 2θ scans) for 100 nm thick CoSb_3 films on (001)-oriented TiO_2 for substrate temperatures between 250°C and 500°C, and for the target material. The curves are normalized with respect to the strongest film reflection. The TiO_2 reflection (at 62.95°) is visible on all film scans.

Experimental results

At substrate temperatures above 550°C, no film growth occurs; i.e. the ablated material either does not condense onto the substrate or re-evaporates completely. Films grown between 500°C and 550°C show a significant deficiency in Sb (as observed with the EDX). The X-ray diffraction patterns for 100 nm thick films grown on 001-oriented TiO_2 substrates at various temperatures between 250°C and 500°C are shown in Fig. 1 and compared to the diffraction pattern of the target material. The curves are normalized with respect to the strongest film reflection. The substrate peak at 62.95° is clearly observed. The in-plane structure of the substrate is a quadratic lattice with $a = 4.59 \text{ \AA}$; half of the cubic lattice constant of CoSb_3 is only 2% smaller. Despite this lattice match, no epitaxy is observed. Instead, the films grow with a distinct (310)-texture, consistent with the previous report by Anno et al. [3]. Omega-scans show a FWHM of 2.5° for the (310)-reflection, indicating strong alignment of the grains in the film.

This texturing of the films is seen to be independent of the substrate material. Fig. 2 compares the X-ray patterns for films grown on silicon, CaF_2 , sapphire, SrTiO_3 , and TiO_2 . In all samples the (310)-reflection is the most intense. Different grain

orientations or secondary phases are present on all but the TiO_2 and SrTiO_3 substrates.

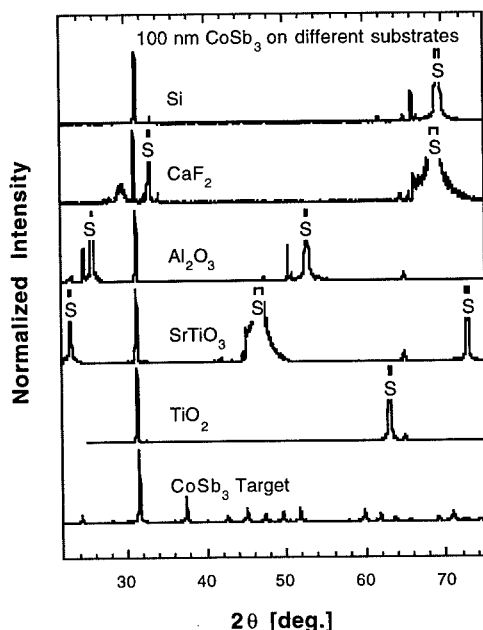


Figure 2: X-ray diffraction patterns (θ - 2θ scans) for 100 nm thick CoSb_3 films grown at 400°C on various substrates (silicon, CaF_2 , Al_2O_3 , SrTiO_3 , and TiO_2). The curves are normalized with respect to the strongest film reflection. Substrate peaks are marked with "S". The diffraction pattern of the target material is shown for comparison.

The reason no epitaxy is found even in the case of the lattice-matched TiO_2 seems to lie in the very weak bonding between the film and the substrate. Note that the covalent bonding within the intermetallic compound is significantly different from that of the predominantly ionic TiO_2 . Evidence of weak adhesion of the film to the substrate is found when a film is intentionally scratched and then analyzed in the SEM; the film in fact delaminates in micron-sized flakes.

Fig. 3 illustrates the influence of the background gas during film growth. As before, the film grown in 80 mTorr of argon exhibits only the (310) and the (620) X-ray reflections. In contrast,

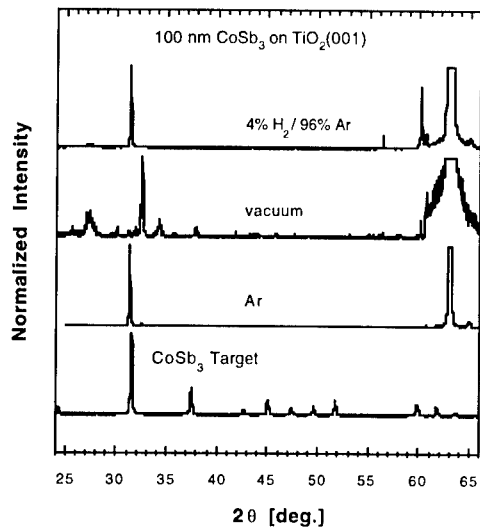


Figure 3: X-ray diffraction patterns (θ - 2θ scans) for 100 nm thick CoSb_3 films deposited in argon, vacuum, and a 4% H_2 /96% Ar mixture. All films were grown at 400°C on (001)-oriented TiO_2 substrates. The curves are normalized with respect to the strongest film reflection. The diffraction pattern of the target material is shown for comparison.

samples obtained in 80 mTorr of forming gas (4% H_2 in Ar) and those grown in vacuum show a number of additional reflections.

Hall measurements on 100 nm thick CoSb_3 films on TiO_2 reveal *p*-type conductivity with a carrier mobility of 50 to $60 \text{ cm}^2/\text{Vs}$ at room temperature and $190 - 200 \text{ cm}^2/\text{Vs}$ at 77K. The corresponding carrier densities are $3 \times 10^{20} \text{ cm}^{-3}$ and $1.2 \times 10^{19} \text{ cm}^{-3}$ at room temperature and 77 K, respectively.

Finally, the 4-probe resistivity and the Seebeck coefficient were measured simultaneously at temperatures between 20K and 720K. The results are displayed in Fig. 4. For comparison purposes, the

corresponding results for the target material are shown in the inserts.

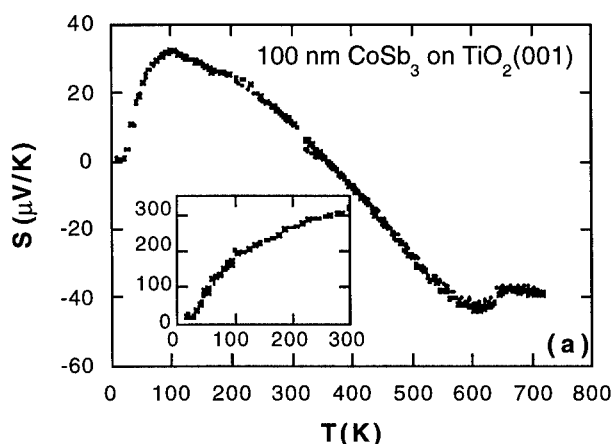
Discussion

In comparing the transport properties of the films with those of the target, it is apparent that the films are extrinsically doped. This could be due to impurities or to defects generated during the deposition process. The target material itself exhibits a remarkably low carrier density of $1.2 \times 10^{17} \text{ cm}^{-3}$. Dopants in the target material which may have segregated to grain boundaries during the sintering process would not necessarily contribute to electrical conduction, and may thus be "invisible" in our measurements on the target material. In the process of PLD, however, such impurities would necessarily become evenly spread throughout the film without having the opportunity to segregate to grain boundaries, thus becoming electrically active. However, it seems unlikely that the very large difference in carrier concentrations between the target and the films can be explained solely by this phenomenon.

In bulk samples, Sb deficiency (one of the more likely defects in the films) generally results in *n*-type conductivity. Hall measurements on the films indicate *p*-type conductivity, but the change of sign in the Seebeck coefficient indicates that the material is doped extrinsically both with electrons and holes, making Hall data difficult to interpret.

The increase in the resistivity below room temperature appears to be due to the freeze-out of extrinsic carriers, since the mobility also increases below 300 K. Above 600 K, the resistivity drops again, which can be attributed to the onset of intrinsic conduction.

Summary and Outlook



We have shown that highly textured, single-phase films of CoSb_3 can be grown by PLD. The film's properties differ from the bulk values mainly in the larger carrier concentration and, consequently, the lower electrical resistivity.

Reduction of the carrier concentration would require a better control of the stoichiometry.

This could be achieved, for example, by the use of slightly off-stoichiometric targets to compensate for any Sb-loss.

Alternatively, charge compensation by intentional doping may also be considered.

Despite the close lattice match between the CoSb_3 and the TiO_2 substrate, no epitaxy is obtained, most likely due to the different type of chemical bonding within the substrate and within the film material. Potential ways to obtain epitaxial films include grapho-epitaxy (utilizing features such as

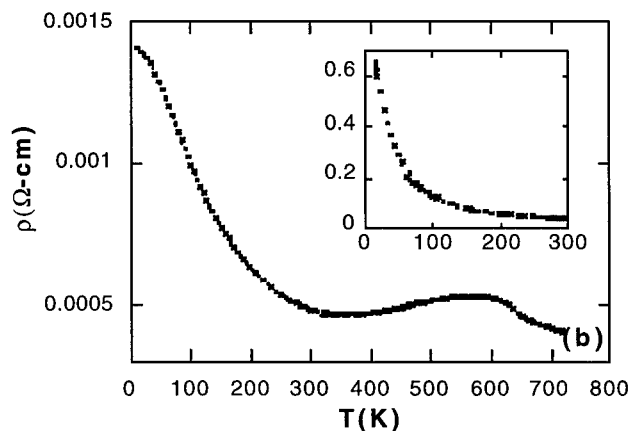


Figure 4: a) The Seebeck coefficient of a 100 nm thick CoSb_3 film grown in argon on (001)-oriented TiO_2 as a function of temperature. The data below room temperature was measured first. The insert shows the data for the target material.

b) Resistivity data obtained simultaneously with the Seebeck coefficient of Fig. 4 a. The insert shows the data obtained for the target material.

atomic steps in the substrate surface to provide a preferred growth direction) or ion-beam assisted growth (selective removal of grains with a certain orientation by ion-beam sputtering).

In addition, incorporation of "rattler" dopants should be possible by ablating from a doped target (not necessarily single-phase, i.e. the dopant may have segregated to grain boundaries) or using a secondary source during growth, such as an ion beam or a background gas. Alternatively, thin films should lend themselves well to post-growth incorporation of dopants by diffusion or ion-beam implantation.

Acknowledgments

J. A. Kolopus is acknowledged for the preparation of the TiO₂ substrates. This research was sponsored by the Division of Materials Sciences, U.S. Department of Energy under Contract No. DE-AC05-96OR22464 with Lockheed Martin Energy Research Corp., and in part by an appointment to the Oak Ridge National Laboratory Postdoctoral Research Associates Program administered jointly by the Oak Ridge National Laboratory and the Oak Ridge Institute for Science and Education.

References

1. G. Mahan, B. Sales, and J. Sharp, *Physics Today*, March 1997, 42.
2. B. C. Sales, D. Mandrus, R. K. Williams, *Science* **272** 1325 (1996).
3. H. Anno, K. Matsubara, Y. Notohara, T. Sakakibara, K. Kishimoto, and T. Koyanagi, *Proc. XV Int. Conf. on Thermoelectrics*, Pasadena, CA, March 26-29, 1996.
4. D. B. Chrisey and G. K. Hubler (Eds.), Pulsed Laser Deposition of Thin Films (John Wiley & Sons, Inc., New York, 1994).

RARE EARTH THERMOELECTRICS

G.D. Mahan

Department of Physics and Astronomy, University of Tennessee, Knoxville,
TN 37996-1200, and Solid State Division, Oak Ridge National Laboratory,
Oak Ridge, TN, gmahan@utk.edu

ABSTRACT

A review is presented of the thermoelectric properties of rare earth compounds. A discussion is presented of the prospects for future improvements in the figure of merit.

INTRODUCTION

Metals are generally unsuitable for thermoelectrics because the figure of merit is low. The Seebeck coefficient (S) is low and the thermal conductivity (K) is high. Thus the value of $Z = \sigma S^2/K$ is small, where σ is the electrical conductivity. An exception to this general behavior is in *mixed valent* compounds, where the Seebeck coefficient can be relatively large[1-7]. The phrase "mixed valent" applies to compounds where one of the ions has two possible valence states of similar energy. This local ion has a valence which fluctuates in time. These fluctuations cause a peak in the electronic density of states near to the chemical potential, which is the origin of the large value of the Seebeck coefficient[8-11].

So far the metals with the largest value of S have been in compounds which contain either cerium (Ce) or ytterbium (Yb). In Ce the $4f$ state fluctuates between zero and one electron. In Yb the $4f$ hole fluctuates between zero and one. We will review the properties of these compounds. The best Ce compounds so far is CePd₃ in which the Seebeck coefficient reaches values of [1,4-6] 80-120 $\mu\text{V/K}$: the value is sensitive to stoichiometry. The best Yb compounds are YbPd (with $S = 105\mu\text{V/K}$ at 250 K[7]) and YbAl₃ (with $S = 90\mu\text{V/K}$ at 200K[2]).

Many theoretical papers have calculated the properties of Ce and Yb compounds[9-11]. They generally predict that the Seebeck coefficient has a peak value of around $100\mu\text{V/K}$. This value is in good agreement with the highest experimental values for these compounds. No one has yet calculated the theoretical value for mixed valent compounds with more than one $4f$ electron or hole: the case where the state $(4f)^n$ varies between $n = L$ and $n = L \pm 1$. The theoretical maximum Seebeck coefficient for these cases is not yet known.

In metals the Seebeck coefficient is the important factor in the figure of merit. The electronic part of the thermal conductivity is usually given accurately by the Wiedemann-Franz Law[12]

$$K_e = \frac{\pi^2}{3} \sigma T \left(\frac{k_B}{e} \right)^2 \quad (1)$$

where k_B is Boltzmann's constant and e is the charge of the electron. Both theory[13] and experiment[14] suggest that the Wiedemann-Franz Law remains valid in a mixed valent metal. The total thermal conductivity $K = K_L + K_e$ is the sum of the lattice part (K_L) and the electronic part. For metals the electronic part is usually much larger than the lattice part. In this case, a very simple expression is obtained for the dimensionless figure of merit

$$ZT = \frac{\sigma T S^2}{K_e + K_L} \approx \frac{\sigma T S^2}{K_e} \quad (2)$$

$$ZT \approx \left(\frac{S}{S_0} \right)^2 \quad (3)$$

$$S_0 = \frac{\pi}{\sqrt{3}} = 156 \mu V/K \quad (4)$$

The factors of σT cancel in numerator and denominator, and the value for ZT depends only upon the Seebeck coefficient. Values of $ZT > 1$ require that $S > 156 \mu V/K$. This value has not yet been achieved in mixed valent compounds. As noted above, the largest value of S so far is around $120 \mu V/K$. Both theory and experiment suggest that Ce and Yb compounds have a maximum value for S of about $100 \mu V/K$.

Increasing the Seebeck coefficient in mixed valent compounds seems to require that one consider rare earth compounds composed of atoms other than Ce or Yb. There are several problems with this approach: (1) Few mixed valent compounds, of rare-earths, have been found for atoms other than Ce or Yb, (2) The ones that exist have Seebeck coefficients smaller than $100 \mu V/K$, and (3) There is no theory which suggests that higher values of S can be achieved. Nevertheless, we believe research should be done to find mixed-valent materials in compounds with $(4f)^n$ and $13 > n > 1$. We are presently calculating the Seebeck coefficient for this case. These materials generally have large values of the power factor (σS^2) at room temperatures and below. They seem to be the best prospect for new thermoelectric materials which operate below room temperatures.

ANDERSON MODEL

Theoretical work on these compounds have mostly employed a Hamiltonian suggested originally by P.W. Anderson. It is for a single atom with local $(4f)^n$ states in a metal with conduction states labeled by ε_k . We generally neglect cooperative effects between different rare earth atoms. The Anderson model Hamiltonian is [8]

$$H = H_0 + V \quad (5)$$

$$H_0 = \sum_k \varepsilon_k C_k^\dagger C_k + \varepsilon_f \sum_\mu n_\mu + U \sum_{\nu > \mu} n_\nu n_\mu \quad (6)$$

$$n_\nu = f_\nu^\dagger f_\nu \quad (7)$$

$$V = \frac{1}{N_f} \sum_{k\nu} V_k [C_k^\dagger f_\nu + f_\nu^\dagger C_k] \quad (8)$$

The symbols C_k, f_ν refer to the lowering operators for band and f -electrons. The interaction V represents the hybridization of the conduction states and the local electrons. It is responsible for the mixed valent behavior. This Hamiltonian is inadequate to discuss states in actual metals. It ignores things such as the spin-orbit interaction which causes the splitting of the f -states. We correct this deficiency later.

As a first step, consider the solutions to this Hamiltonian for the case that $V = 0$. An f -electron has a degeneracy of $N_f = 14$ including both orbital and spin. The energy of a state $(4f)^n$ is E_n and the partition function is

$$E_n = n\varepsilon_f + \frac{n(n-1)}{2}U \quad (9)$$

$$Z = \sum_{n=0}^{N_f} \binom{N_f}{n} e^{-\beta E_n} \quad (10)$$

The Green's function is calculated using the formalism for nonzero temperature[8]. The imaginary part of its retarded function ($ip \rightarrow \omega + i\eta$) gives the spectral function $A_f(\omega)$. These functions are

$$\mathcal{G}_f(ip) = -\sum_{\mu} \int_0^{\beta} d\tau e^{ip\tau} \langle T_{\tau} f_{\mu}(\tau) f_{\mu}^{\dagger}(0) \rangle \quad (11)$$

$$= \frac{1}{Z} \sum_n \binom{N_f}{n} (N_f - n) \frac{e^{-\beta E_n} + e^{-\beta E_{n+1}}}{ip + E_n - E_{n+1}} \quad (12)$$

$$A_f(\omega) = 2\pi \frac{1}{Z} \sum_n \binom{N_f}{n} (N_f - n) [e^{-\beta E_n} + e^{-\beta E_{n+1}}] \delta(\omega + E_n - E_{n+1}) \quad (13)$$

This series appears rather complicated. A simple result is obtained if we assume that the lowest eigenvalue E_n occurs for $n = L$. Then the above series has just two terms which are not negligible

$$A_f(\omega) = 2\pi \{ (N_f - L) \delta(\omega + E_L - E_{L+1}) + L \delta(\omega + E_{L-1} - E_L) \} \quad (14)$$

The spectral function has just two peaks. From the ground state L the system can go to either $L \pm 1$. The peak at $\omega = E_{L+1} - E_L$ occurs at positive energy and has a weighting factor of $(N_f - L)$. The peak at $\omega = -(E_{L-1} - E_L)$ occurs at negative energies and has a weight of L . Mixed valent behavior is obtained whenever $E_L - E_{L\pm 1}$ is a small energy difference; typically less than one electron volt. The eigenvalue ε_f is negative while U is positive. The lowest eigenvalue E_n occurs at $n = L$ when $-LU < \varepsilon_f < -(L-1)U$. Mixed valent behavior occurs whenever ε_f equals either $-LU + \delta$ or $-\delta - (L-1)U$ where δ is a small energy value.

Next consider the role of the hybridization interaction V . It changes the spectral function $A_f(\omega)$ in several important ways. First, it introduces a new energy parameter which is defined as

$$\Delta = \frac{\pi}{N} \sum_k V_k^2 \delta(\varepsilon_k) \quad (15)$$

For rare-earths, this has a typical value of $\Delta = 0.1$ eV. The hybridization causes Lorentzian broadening of the two peaks in $A_f(\omega)$. The lower energy peak is broadened by $(N_f + 1 - L)\Delta$ while the peak at positive frequency is broadened by $(L + 1)\Delta$. From the point of view of the Seebeck coefficient, these peaks are quite broad. If one arranges that either $E_L - E_{L+1}$ or $E_L - E_{L-1}$ are close to zero energy, and calculates the Seebeck coefficient, the resulting values are not very large[11]. Having the mixed valent peaks near to zero energy does not give a large Seebeck coefficient. Note that most calculations have been done for the case that $L = 1$.

The Hybridization interaction V causes another important feature in the spectral function $A_f(\omega)$. A third peak occurs in the spectral function. It has a very narrow energy width $\delta \ll \Delta$ so that it appears to be very sharp. The center of the peak is quite close to the chemical potential. This peak is called the "Kondo Resonance". It is this third peak which causes the high value of the Seebeck coefficient. So far this peak has only been calculated for the case that $L = 1$. Several of its important features are[9-11]:

1. For the symmetric case that $N_f = 2$ and $E_{L-1} = E_{L+1}$ the peak is centered on the chemical potential and is perfectly symmetric in frequency. In this case the Seebeck coefficient is identically zero.
2. For the case that $N_f > 2$ the center of the peak moves slightly away from the chemical potential. In this case the Seebeck coefficient is nonzero.
3. The maximum value of S is obtained with the maximum value of N_f .
4. The Kondo resonance is very temperature dependent, and decreases rapidly with increasing temperature.

How the spectral function $A_f(\omega)$ is used in the calculation of S and σ is described elsewhere[15].

HUND'S RULES

The above theory assumed that the degeneracy of the state with n f -electrons was given by the binomial coefficient $\binom{N_f}{n}$. The actual degeneracy is far less, because of Coulomb and spin-orbit interactions. The state with one f -electron or hole is divided in two by the spin-orbit interaction. The state with two f -electrons has thirteen different energy levels[16-17]. Usually only the ground state is important, and only the ground state contributes to the

Kondo resonance. Of course, the ground state configuration is given according to Hund's Rules. We reproduce the well-known table for the lanthanides. Each state with nf -electrons now is divided into sublevels denoted by ℓ . The magnetic quantum number is m_ℓ , degeneracy is $(2J_\ell + 1)$, and energy is $E_{n\ell}$.

3+	nf	S	L	J	2J+1
Ce	1	1/2	3	5/2	6
Pr	2	1	5	4	9
Nd	3	3/2	6	9/2	10
Pm	4	2	6	4	9
Sm	5	5/2	5	5/2	6
Eu	6	3	3	0	0
Gd	7	7/2	0	7/2	8
Tb	8	3	3	6	13
Dy	9	5/2	5	15/2	16
Ho	10	2	6	8	17
Er	11	3/2	6	15/2	16
Tm	12	1	5	6	13
Yb	13	1/2	3	7/2	8

Table 1: Ground state degeneracy $(2J+1)$ for 3+ rare earths according to Hund's Rules

We mentioned earlier that the Seebeck coefficient increased with the value of N_f for the case that $L = 1$. This has been interpreted as having the Seebeck coefficient increase with the value of the degeneracy of the ground state. If this interpretation is correct, then larger values of the Seebeck coefficient are obtained when the ground state has the largest value of $(2J + 1)$. According to the table, this value can be as large as 17 for Ho^{3+} . This is the argument for having larger Seebeck coefficients for mixed valent materials with $1 < L < 13$.

We discuss the theory for the case that the hybridization V is zero. The partition function is

$$Z = \sum_{n=0}^{N_f} \sum_{\ell} (2J_\ell + 1) e^{-\beta E_{n\ell}} \quad (16)$$

In order to define the Green's function and spectral function we need to define the matrix element $W_u(n\ell, m_\ell; n+1, \ell', m_{\ell'})$

$$W_u(n\ell, m_\ell; n+1, \ell', m_{\ell'}) = \langle n+1, \ell', m_{\ell'} | f_\mu^\dagger | n\ell, m_\ell \rangle \quad (17)$$

$$\begin{aligned} G_f(ip) &= \frac{1}{Z} \sum_{n\mu} \sum_{\ell m_\ell} \sum_{\ell' m_{\ell'}} W_\mu(n\ell, m_\ell; n+1, \ell', m_{\ell'})^2 \\ &\times \frac{e^{-\beta E_{n\ell}} + e^{-\beta E_{n+1, \ell'}}}{ip + E_{n\ell} - E_{n+1, \ell'}} \end{aligned} \quad (18)$$

We assume that for $n = L$ the lowest state ($\ell = 0$) is occupied and then we find for the spectral function

$$A_f(\omega) = 2\pi \sum_{\ell' m_{\ell'} \mu} \{W_{\mu}(L00; L+1, \ell', m_{\ell'})^2 \delta(\omega + E_{L0} - E_{L+1, \ell'}) + W_{\mu}(L-1, \ell', m_{\ell'}; L00)^2 \delta(\omega + E_{L-1, \ell'} - E_{L0})\} \quad (19)$$

Now the spectral function has a series of many peaks. The ground state $\ell = 0$ for L electrons can go to neighboring states $(L+1, \ell')$ or $(L-1, \ell')$. Mixed valent behavior is found whenever either $E_{L0} - E_{L+1,0}$ or $E_{L0} - E_{L-1,0}$ have a small value in energy. Such cases will obviously have a Kondo resonance. Its magnitude is yet unknown. The properties are not known for the case that $L \neq 1$ and the hybridization $V \neq 0$.

CONCLUSIONS

We have outlined the features which make rare-earth compounds attractive thermoelectric materials. Not all compounds have high Seebeck coefficients. Only those which show mixed valent behavior have high values of S . So far the best ones have either cerium or ytterbium as the rare earth element. More compounds $(4f)^n$ need to be found which have mixed valent behavior with $13 > n > 1$. They have the possibility of having larger values of the figure of merit.

ACKNOWLEDGEMENTS

I thank Dr. Brian Sales for many useful discussions regarding rare-earth compounds. Research support is acknowledged from the University of Tennessee, from the U.S. Department of Energy, and from Applied Research Projects Agency through contract DOD-ARPA-MDA972-95-1-0021 MAHN.

REFERENCES

1. R.J. Gambino, W.D. Grobman and A.M. Toxen, Appl. Phys. Lett. **22**, 506 (1973)
2. P.B. van Aken, H.J. van Daal and K.H.J. Buschow, Phys. Lett. **49A**, 201 (1974)
3. D. Jaccard and J. Sierro, in Valence Instabilities, edited by P. Wachter and J. Boppart (North-Holland, New York, 1982) pg 409
4. H. Sthiol, D. Jaccard and J. Sierro, in Valence Instabilities, edited by P. Wachter and J. Boppart (North-Holland, New York, 1982) pg 443
5. J.R. Thompson, S.T. Sekula, C.K. Loong and C. Stassis, J. Appl. Phys. **53**, 793 (1982)

-
6. M.J. Besnus, J.P. Kappler and A. Meyer, J. Phys. F **13**, 597 (1983)
 7. R. Potts, W. Boksich, G. Leson, B. Politt, H. Schmidt, A. Freimuth, K. Keulerz, J. Langen, G. Neumann, F. Oster, J. Rohler, U. Walter, P. Weidner, and D. Wohlleben, Phys. Rev. Lett. **55**, 481 (1985)
 8. G.D. Mahan, Many-Particle Physics, Second edition (Plenum, New York, 1990) Chapter 11
 9. N.E. Bickers, D.L. Cox and J.W. Wilkins, Phys. Rev. B **36**, 2036 (1987)
 10. N.E. Bickers, Rev. Mod. Phys. **59**, 845 (1987)
 11. A.C. Hewson, The Kondo Problem to Heavy Fermion (Clarendon Press, Cambridge, 1993)
 12. G. Wiedemann and R. Franz, Ann. Phys. **9**, 497 (1853)
 13. A.K. Bhattacharjee and B. Coqblin, Phys. Rev. B **38**, 338 (1988)
 14. E. Bauer, in Transport and Thermal Properties of f -Electron Systems, edited by G. Oomi (Plenum, New York, 1993)
 15. G.D. Mahan, in Solid State Physics, edited by H. Ehrenreich and F. Spaepen (Academic Press, New York, in press)
 16. S. Hufner, Optical Spectra of Transparent Rare Earth Spectra (Academic Press, New York, 1978)
 17. Z.B. Goldschmidt, in Handbook on the Physics and Chemistry of Rare Earths, Vol. 1, edited by K.A. Gschneider and L. Eyring (North-Holland, New York, 1978) page 1

OPTIMIZATION OF MATERIALS FOR THERMOMAGNETIC COOLING

A. MIGLIORI, T.W. DARLING, F. FREIBERT, S. A. TRUGMAN, E. MOSHOPOULOU,
J.L.SARRAO

Los Alamos National Laboratory, Los Alamos, NM 87545

ABSTRACT

We review thermoelectric transport in a magnetic field. The key physical effect for thermomagnetic cooling is the Ettingshausen effect. We describe the design principles, measurement difficulties and areas where more work can prove fruitful in an exploration of cryogenic refrigeration based on this effect. New principles are discussed to guide the search for new materials and their development.

INTRODUCTION

Our intent in this paper is to provide a basic review of thermomagnetic cooling, and to indicate new directions for the development of materials in this old and extensively studied area of electronic transport in solids. The basic physical effects required for an understanding are the Peltier effect, the process in zero magnetic field that is used by all modern thermoelectric coolers, and the Ettingshausen effect, a somewhat obscure but powerful refrigeration process that, combined with the Peltier effect, completes the description of heat transport by charge carriers in solids. Because of the extensive literature on these processes, the review here will be brief--the major emphasis will be to sketch carefully that which is new or previously overlooked. We begin with an historical perspective outlining briefly why there is some motivation to revisit this old problem.

Because the $\text{Bi}_{(1-x)}\text{Sb}_x$ system has especially light charge carriers, these alloys have been the mainstay for use in thermomagnetic refrigerators. Early studies of the unusual electrical properties of single crystalline $\text{Bi}_{(1-x)}\text{Sb}_x$ were performed by Jain [1], and inspired by the large magneto-thermoelectric figure of merit data (we shall discuss in some detail the figure of merit below) of Smith [2] and of Cuff, et al.[3], $\text{Bi}_{(1-x)}\text{Sb}_x$ became the key thermomagnetic material. The orientation of the applied magnetic field with respect to crystal axes played an important role in optimizing $\text{Bi}_{(1-x)}\text{Sb}_x$ alloys because the behavior of the thermopower in a transverse magnetic field is very different for different orientations [4,5]. However, little has been published before this work to rationalize physically this fact in terms of a microscopic picture. Goldsmid has attempted to justify a preferred magnetic field orientation based on purely phenomenological predictions for the infinite-field thermomagnetic figure of merit [6] as derived from experimentally determined physical parameters for single crystal Bi. This orientation has become the orientation used in almost every measurement since. However the apparent lack of understanding of the relationship between the band structure of Bi and its alloys with Sb, and the physics of thermoelectric and thermomagnetic effects leaves an interesting approach open, to be described below, that may provide substantially improved materials for Ettingshausen cooling.

REVIEW OF THERMOELECTRIC TRANSPORT

The root of all thermoelectric effects is the small variation of the energy and momentum distribution of charge carriers caused by temperature gradients. Such variations produce, among other

things, a non-zero electric field inside electrical conductors-the Seebeck effect-and it is the coupling between this electric field and electric current \vec{j} that provides thermoelectric power generation or refrigeration (the Peltier effect). The size of the effect is dependent on the energy scales and temperature of the solid. In a degenerate metal, where only a few charge carriers near the Fermi energy ϵ_f are out of their ground state (for Cu, ϵ_f/k_b is of order 30,000K), the effects are small. In semiconductors and semimetals where only a few charge carriers are present (Bi has 10^6 fewer charge carriers than Cu, and ϵ_f/k_b is ~ 1000 K) and very few in the ground state, the effects are large.

All thermoelectric devices, meaning systems composed of materials in which thermoelectric effects are of sufficient strength to be of practical importance, employ charge carriers (quasiparticles) of both negative (e or electron-like) and positive (h or hole-like) charge. Of course, there are really only electrons, but holes in the electronic distribution act just like real particles with positive charge-that is they move in a direction opposite to electrons in an electric field. It is this "reverse" motion that enables large thermoelectric effects because by using both electrons and holes in a device, electric current can be made to circulate, while "particle" current remains unidirectional, and it is the particle current that carries heat.

To compute the performance of thermoelectric devices, we begin with a pair of simple definitions valid for both thermomagnetic and thermoelectric systems:

$$\vec{j} = \sigma(\vec{E} - S\nabla T) \quad (1)$$

$$\vec{j}_q = \sigma S T \vec{E} - (\sigma S^2 T + K)\nabla T \quad (2)$$

where \vec{j}_q is the heat flux, \vec{j} is the electrical current, σ is the electrical conductivity tensor, K the thermal conductivity tensor, \vec{E} the electric field, S the thermopower tensor and T temperature. The thermal conductivity has two important components, K_p the phonon thermal conductivity and K_e the electronic thermal conductivity. The third equation of importance to a phenomenological understanding is

$$\nabla \cdot \vec{j}_q - \vec{E} \cdot \vec{j} = 0 \quad (3)$$

which is a continuity equation for a time-independent temperature distribution inside a device, expressing the necessity for a balance between the difference between energy (heat) flows into and out of a small volume (first term) and the electrical energy consumed in that volume (second term).

For a one-dimensional Peltier system where \vec{j} is necessarily independent of position and using (1)-(3) we obtain

$$Tj \frac{dS}{dx} - \frac{d}{dx} K \frac{dT}{dx} - \frac{j^2}{\sigma} = 0 \quad (5)$$

from which all the important quantities can be calculated. Note first that the second derivative of temperature is a critical piece, meaning that no matter how short the Peltier device is, if it is operating in a useful region, we cannot neglect the variation of the temperature gradient. Second, in the usual treatments [6] the first term is neglected. This term is basically the Thomson heat, and for the cryogenic refrigerators our work is focused on where T varies substantially, it can be of comparable size to the other terms and should not be neglected. For example, in a simple metal, S is proportional to T while in semiconductors it can vary between $\Delta/(eT)$ at low temperatures (where Δ is the semiconducting gap and e is the electronic charge) to a constant at high temperatures. The usual treatment is, however, to neglect these variations, as well as the temperature dependences of all the other material properties. This has the seductive effect of making (5) integrable so that closed-form solutions can be obtained. These solutions are somewhat unphysical even in an attempt to obtain a

feel for the problem because $K_e/(\sigma T)$ is typically independent of temperature for most high-carrier-density systems (this is the Wiedemann-Franz law-see below), and in many materials used for Peltier coolers, the electronic thermal conductivity K_e dominates, making the Wiedemann-Franz law applicable. Thus K_e and σ cannot be reasonably taken as independent of temperature in an attempt to obtain a simple differential equation because such an approximation changes the *form* of the equation. Some numerical studies have shown that such approximations produce errors in calculated performance of order 10% [6] for coolers operating near room temperature. When one considers that in the last 30 years, improvements in thermoelectric materials have been of order 10%, such an error is unacceptable. For cryogenic refrigeration, where T may vary by a factor of two, the errors are certain to be much worse.

Nevertheless, the usual approach is to integrate (5), apply appropriate boundary conditions and then find the minimum temperature assuming all transport properties are constant which gives

$$T_h - T_{c0} = \frac{\sigma S^2}{2K} T_{c0}^2 \quad (6)$$

where T_{c0} is the minimum possible temperature. Also from the same solution, if T_c is close to T_h (and greater than the minimum temperature), the best coefficient of performance (COP) is less than $\frac{1}{2}$ for maximum heat pumped.

It is seen that everything depends more or less on the dimensionless (and strongly temperature dependent) quantity, $\sigma S^2 T/K$, historically called ZT , a particularly unhelpful appellation. Much more revealing is to note that $K/\sigma T_c$ has units of thermopower squared $(\mu V/K)^2$ so that a critical thermopower S_0 can be defined such that

$$S_0 = \sqrt{\frac{K}{\sigma T_c}} \quad (7)$$

which expresses a value for the thermopower that must be achieved for any reasonable thermoelectric material. If the material were such that the phonon thermal conductivity could be neglected, the quantity inside the square root is the Lorenz number $L=(155\mu V/K)^2$, a constant that comes from the Wiedemann-Franz law, a very general relationship between the electronic thermal conductivity and the electrical conductivity [7]. Thus any material with a thermopower less than about $155\mu V/K$ is not going to be a good candidate for a Peltier refrigerator, especially if K_p is not negligible. S_0 , computed from measured properties, is then a simple-to-measure break point for material searches.

ETTINGSHAUSEN COOLERS

We are, however, not working on Peltier coolers, but on the more complex Ettingshausen cooler. The complexities come in because the material properties *must* be treated as tensors and the analysis is more difficult. In figure 1 we show a schematic of what the charge carriers must do. Referring to figure 1 it can be seen that the idea is to use a single material in which both electrons and holes are present. An electric field in the y -direction makes the holes travel roughly downward and the electrons roughly upward. The magnetic field B , however, deflects both carriers to the positive x -direction, and it is this effect that, exactly analogous to Peltier cooler, pumps heat. Notice that just as in a Peltier cooler, the x -component of electric current carried by holes is opposite in direction to that carried by electrons but there is a net flow of particles toward the hot end.

To get a feel for Ettingshausen cooling, let's proceed under the assumption that we have

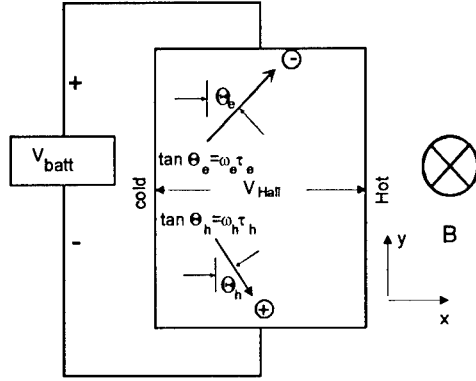


Figure 1. Shown is an Ettingshausen refrigerator. The angles will be discussed below.

electrons and holes with the same masses, numbers, and with the same mean free path—that is, perfect e-h symmetry (this will be justified below). Equations (1)-(3) are still valid except that there is no ordinary thermopower and no Hall effect. This is expressed as follows

$$\sigma = \begin{pmatrix} \sigma_{11} & 0 \\ 0 & \sigma_{11} \end{pmatrix} \text{ and } S = \begin{pmatrix} 0 & S_{12} \\ -S_{12} & 0 \end{pmatrix} \quad (8)$$

where σ_{11} , S_{12} are the non-zero components of the resistivity and thermopower tensors. We shall assume K to be a scalar. Noting that $j_x = E_x = dT/dy = 0$, we can obtain two more equations

$$j_y = \sigma_{11} \left(E_y + S_{12} \frac{dT}{dx} \right) \quad (9)$$

and

$$j_{qx} = \sigma_{11} S_{12} T E_y - (K - \sigma_{11} S_{12}^2 T) \frac{dT}{dx}$$

except that the current j_y is not independent of position, while E_y is. Thus (9) is not of the same form as (5), as is occasionally stated [6]. Another key point is that now $\sigma_{11} S_{12}^2 T/K$ cannot exceed unity because if it did, heat would flow from cold to hot with no energy input to the system. This thermodynamic boundary of unity on a set of parameters not obviously constrained by physics is another key difference between the two refrigeration processes. The resulting differential equation for an Ettingshausen refrigerator, and its solution are

$$-E_y^2 \sigma_{11} = E_y T \frac{d(\sigma_{11} S_{12})}{dx} + \frac{d}{dx} \left[(K - \sigma_{11} S_{12}^2 T) \frac{dT}{dx} \right] \quad (10)$$

where we dropped all terms arising from departures from e-h symmetry.

Unlike the Peltier case, the use of a temperature-independent thermal conductivity is a little better justified because the magnetic field greatly reduces the electronic thermal conductivity which is usually proportional to temperature, leaving only the phonon term. However, approximations to

the temperature dependence of the transport properties, just as in the Peltier case, are dangerous as they change the form of the resulting solutions in as yet unexplored ways.

Because E and j are perpendicular to the heat flows, two or more Ettingshausen coolers (EC) in series can make electrical contact between the hot end of the smaller stage and the cold end of the larger stage, making it possible to produce a sequence of staged coolers simply by machining the correct shape from the bar of single material. Therefore, in a properly engineered EC, there is no obvious minimum temperature, T varies strongly with length, and a set of formulae like those for the Peltier cooler is not very useful. Nevertheless, it is interesting to note that (10) can be solved for the minimum temperature if materials properties are independent of temperature and the material is shaped as a rectangular bar. The solutions are

$$\frac{T_{c0}}{T_H} = 1 - \frac{T_H}{2T_0} \text{ where} \quad (11)$$

$$T_0 = \frac{K}{\sigma_{11}\sigma_{12}^2} > T_H \text{ and } E_{y0} = \frac{S_{12}T_c}{l}.$$

Because of the form of (11) one must be very cautious about defining a figure of merit, but using T_0 as a parameter is at least simple. However, for the rectangular Ettingshausen cooler with uniform electric field and temperature independent transport properties, the minimum value of $T_{c0}/T_H = 1/2$ when $T_0 = T_H$ [9] (the limit imposed by the second law of thermodynamics). At present there is no microscopic argument for this limit. However, if no approximations about temperature dependence are made, it is only important that everywhere $T_0 > T$, a much less restrictive limit.

As is obvious, no really simple direct comparison can be made because the Peltier figure of merit can be unbounded while the Ettingshausen equations apply only to an unrealistically simple geometry. Furthermore, the equations are fundamentally different, even though some authors attempt to map the EC problem onto the Peltier problem by using different definitions for K and σ [6]. Such attempts are no help to the materials scientist who is interested only in how well the refrigerator can be made to work. The best approach to evaluating an EC material is to use measured values of the

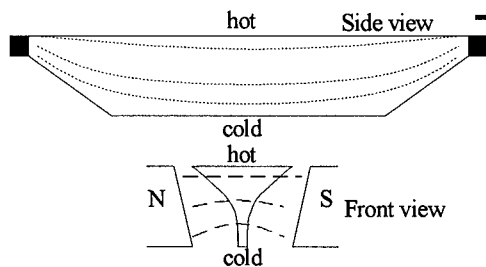


Figure 2. Shown is a front and side view of an Ettingshausen cooler. Dotted lines are the electric field, dashed are the magnetic field. It is clear that this is a very complex, fully 3 dimensional optimization problem and that, judging from previous work, a well-thought-out numerical solution could produce very substantially improved performance.

conductivity tensor, the thermopower tensor and the thermal conductivity, and the complete version of (10) to optimize the shape and driving electric and magnetic fields. To see how complex this problem is, we show in figure 2 a schematic of the general problem. As can be seen, electrical leads are attached at the hot end only, using the shape of the material and temperature dependences of the transport properties to allow current to flow in a fully three-dimensional manner, thereby mitigating some of the end effects and thermal conduction of electrical contacts. Note also that the pole pieces for the permanent magnets can be shaped to optimize performance. A simple symmetry argument shows that the leading term in the field dependence of S_{12} is B . Work by Horst et al. [10] show that at large fields, S_{12} drops rapidly with B , and a first pass at a simple microscopic calculation by us [11] confirms this. Thus there is a best magnetic field at a given temperature. Hence a varying field is important.

Finally we point out that the exponential shape reported as optimum by other authors [12] is based on unrealistic temperature dependences and, as with other refrigeration processes, small errors in the analysis of entropy production at the cold end of a cryogenic refrigerator can have drastic consequences at the hot end. For example, with a cold end 1/13 the width of the hot end, an exponential shape produced a 50% greater temperature drop than a rectangular one. Neither was optimal [13]. Thus optimization of geometry without a full numerical approach is likely to introduce substantial inefficiencies. It is our belief that a proper numerical simulation of an EC based on measured material properties has never been done as well as it is possible to do, that the simple computations are seriously flawed and that the real potential of EC's has not yet been realized [8].

OPTIMIZATION OF MATERIALS

In order to proceed with the development of new materials for an Ettingshausen cooler, one is faced with an enormous task because the temperature *and* magnetic field dependence of the key physical parameters must be known. The addition of the magnetic field variable utterly destroys any reasonable chance of success based on unfocussed searches. Theoretical guidance is crucial, and developing such guidance has been of central importance to our research program. Even without a complete solution to (10), there are very good ways to attack the material development problem based on a) the search for e-h symmetry, b) the need to minimize the effective mass, and c) the need to minimize quantum effects in a magnetic field. We discuss here some viable approaches to these problems.

In what follows, we shall consider systems with several parabolic bands in which the energy ϵ of the electron or hole is $p^2/(2m_i)$ where p is the momentum and m_i is the effective mass of the i^{th} carrier, as well as systems for which this is not true. A parabolic band makes charge carriers have the same relationship between energy and momentum as a free particle.

Band structure, e-h symmetry and effective mass

It is clear that one quality of importance is to maximize the total number of particles moving toward the hot end. If the number and velocity component of electrons did not equal the same quantity for holes in the direction of heat flow, then very quickly, charge would pile up at the hot and cold ends, creating a voltage (the Hall voltage) that would reduce (or stop if only one carrier were present) the flow of the majority carriers, degrading refrigeration. Therefore, the ideal Ettingshausen material must have equal numbers of electrons and holes with equal mobility. This is called 'e-h

symmetry'. Such a system has *zero* thermopower and would produce no temperature drop if used in a Peltier cooler.

In addition to e-h symmetry, because we are looking to pump heat, and because the Ettingshausen effect is present only in a magnetic field, it is clear that materials whose transport properties are strongly affected by magnetic fields are required. For any practical device, a strong magnetic field must be of order 1T, a field achievable with modern permanent magnets. For this to be true, the effective mass of the carriers must be low and the mean free path must be large. This is because the angles in figure 1 between the applied electric field and the direction the carriers move under conditions where there is no Hall voltage is $\theta_i = \tan^{-1}(\omega\tau)$, where $\omega = qB/(m_i^*c)$ is the cyclotron frequency, c is the speed of light, m_i^* the effective mass of the carrier, q its charge, τ the mean time between collisions and i refers to either electrons or holes. For example, in a typical metal (like Cu) at 300K with an effective mass of about one electron mass, θ_i is of order 0.3×10^{-6} at $B=1$ T, while for Bi at 4K with some carriers having a mass of order 10^{-3} electron masses θ_i is of order unity at the same magnetic field. Thus a low effective mass is critical. Therefore one key guide for materials searches is the electronic band structure because the band structure tells us the number, mass and type of charge carriers that will participate in the important physical processes.

The electron band, a parabola (or maybe a different shape) facing up and the hole band, a parabola facing down, can overlap (the top of the hole parabola, or hole band edge, is above the bottom of the electron parabola or electron band edge) or not. If the bands overlap at the Fermi energy ϵ_F the material is a semi-metal. If they do not overlap, the material is a semiconductor (figure

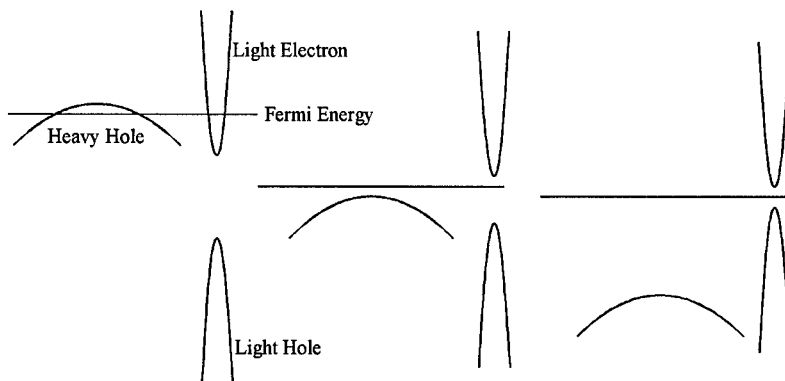


Figure 3. Shown is a schematic of the band structure of a hypothetical 3-band semi-metal somewhat like Bi. The horizontal lines are the Fermi energies. At any particular temperature, the two bands closest to the Fermi energy dominate, so the system can change its character completely, depending on the position of the Fermi energy and on temperature. On the left is a semi-metal with a heavy hole and a light electron crossing the Fermi energy and producing a non-electron-hole-symmetric system, in the center is a semiconductor with a heavier hole just below the Fermi energy and a light electron just above it, making its properties also not electron-hole symmetric, and on the right a semiconductor with nearly perfect electron-hole symmetry at temperatures low enough that the carriers from the heavier hole are never thermally excited.

i). In both cases, ϵ_f lies between the band edges, its exact location dependent on the band masses m_e and temperature. The number of electrons available for conduction is the total number below ϵ_f , and for holes it is the number above ϵ_f . In a semi-metal like Bi, ϵ_f crosses the two bands at a level such that there are exactly the same number of holes as electrons, but because the curvature of the parabolas (which determines the effective mass) is not the same, the masses are different, and so are the mobilities (left, figure 3), and therefore e-h symmetry is not present, leading one to hope for better.

It is clear from figure 3 that it is very difficult to get e-h symmetry in Bi as it is. However, Bi is a low symmetry metal so that in certain symmetry directions the bands can cross or nearly cross at ϵ_f . This is illustrated in one of the best band structure calculations for Bi, done by Liu and Allen [13], where we show in figure 4 the very unusual, non-parabolic near-intersection of the light electron band with a normally unoccupied, perfectly symmetric light hole. If this light hole could be occupied equally with the light electron, nearly perfect e-h symmetry would result, with carrier masses of order 10^{-4} that of an electron (because of the shape of the bands, the masses vary strongly as the e-h symmetry point is approached). This has never been exploited, even though it is well known that the addition of Sb to Bi moves the heavy hole (the hole discussed above, which is normally the only hole present) down and out of the way, forming a semiconductor above 4%-7% Sb (somewhat like the right side of figure 3). As Sb is added to Bi, the heavy hole moves away, the Sb scatters phonons well (its mass is very different from Bi), reducing the phonon thermal conductivity, and has a minimum effect on τ (it does nothing to the electron density), keeping the Hall angle large. However, as the hole moves down and out of the way, the electron pockets shrink to zero. This might seem to be a problem, and it would be if the cooler were operated at a few K, but at 100K or so, thermal excitations produce a good supply of e-h pairs, comparable in number to the number present in pure Bi at 0K, and, of course, the pairs are symmetric. A little doping (which we compute from the band structure) will produce a system in which the very light electron and its symmetric hole are present

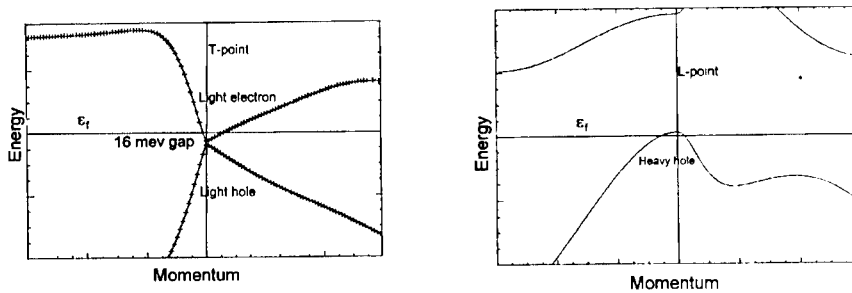


Figure 4. Shown are expanded views of the band structure of Bi near the heavy hole at the L-point and the light electron/light hole at the T-point. These calculations were provided by R.E. Allen and are the same values used in a recent publication [12].

in equal numbers. An excess of the heavy hole is also present but has little effect on the EC because these carriers don't move much. It is just the right balance of Sb and doping that our present work is aimed toward. There is almost no systematic study of this region of the concentration space [14] so much new data must be taken, especially in orientations not usually studied, but described in the next section.

Directions for \vec{B} , \vec{I} and ∇T

We can provide a proper basis for the historical orientation of \vec{B} , \vec{E} , and \vec{I} in a Bi-based EC cooler using simple arguments, and indicate new orientations as well. In figure 5 we show the Fermi surfaces of Bi in the first Brillouin zone, which is why the ellipsoids are cut in half. This set of surfaces is the intersection of ϵ_f with the dispersion curves of the electrons and holes. Even though there are several electron surfaces, the total number of electrons equals the number of holes. Where the surfaces are narrow, the dispersion curves have a lot of curvature (for non-parabolic bands the mass is found by fitting a parabola tangent to the dispersion curve at the Fermi energy), yielding low effective masses. Remembering that one goal is to maximize the total flux of heat-carrying particles, can we find a rule that will tell us what directions \vec{B} , \vec{E} , and \vec{I} must be in? If all the surfaces were spherical, then any direction is as good as another because the masses (inverse of the curvature) would all be the same. However, in a low-symmetry metal like the rhombohedral Bi, the electron masses vary with direction by a factor of 30, and the hole masses somewhat less. If we consider what happens when simple resistive transport occurs we find that for one of the carriers,

$$\begin{pmatrix} \frac{m_1}{ne^2\tau} & \frac{B}{nec} \\ \frac{B}{nec} & \frac{m_2}{ne^2\tau} \end{pmatrix} \begin{pmatrix} j_x \\ j_y \end{pmatrix} = \begin{pmatrix} E_x \\ E_y \end{pmatrix} \quad (12)$$

where n is the number of electrons (or holes), e the charge on an electron, B is the magnetic field, τ is the mean time between scattering events, m_1 the carrier mass in the x -direction, m_2 in the y -

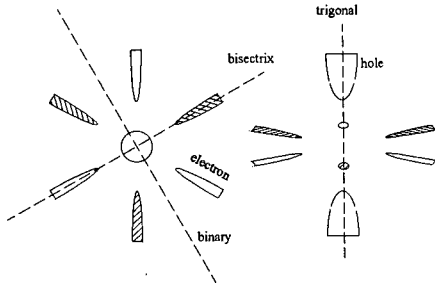


Figure 5. Shown is the Fermi surface of Bi. Under some doping conditions, it may be possible to eliminate the hole in the middle, so that at temperatures of order 100K, both electrons and holes would be where only the electron pockets are now.

direction. The low mass would apply to particles traveling across a narrow direction of the Fermi surface. A second version of (12) for the other carrier would look the same except that the signs of off-diagonal matrix elements are reversed. We can find the overall response by adding current densities linearly for the electrons and holes. What we are after is a very large positive value of j_x for one carrier and a large negative value for the other, summing the electric current to zero but maintaining a large particle flux toward the hot end. If we have a system in which e-h symmetry is present, i.e. a good EC material, then when the full problem is solved, E_x would be zero and so would the total j_x . We can, therefore, solve each of the two version of (12) separately to maximize j_x/j_y -that is we want the maximum possible transverse component of current for each carrier separately for a given current drawn from the battery. However, we know that E_x will be zero when both carrier contributions are summed, so we set it to zero in (12) to obtain

$$\frac{j_x}{j_y} = \frac{eB\tau}{m_1c} = (\omega\tau)_1 \quad (13)$$

where ω is the cyclotron frequency. This remarkable result shows that the particle current in the heat-carrying direction depends on the effective mass in that direction alone (figure 1), and that the angle that the current makes with the electric field is the Hall angle $\Theta = \tan(\omega\tau)$, the angle that the x- and y-components of the electric field would make with each other if only one carrier were present and $j_x=0$ (figure 1).

Maximizing (13) is a very important priority but one cannot simply increase the magnetic field (if $\omega\tau$ is of order unity the magnetic field is considered strong) because if B exceeds 1T or so, permanent magnets can't be used and the system becomes a laboratory curiosity. Thus it is important for the effective mass to be very small, typically 0.01 or less than that of a bare electron. We can, however, keep electronic scattering down (and hence τ up) by minimizing alloy elements that change the electron count, and we can make sure that the temperature gradient points in the direction of lowest mass. Applying this to the Bi-Sb system we find that because the electron masses are much less than the hole masses, the hole pocket forces the temperature gradient to be perpendicular to the trigonal axis. Next, note that in a magnetic field, electron orbits shift and re-quantize with an energy spacing $\hbar\omega$ (\hbar is Planck's constant) so it is important that the magnetic field not align perpendicular to the low-mass direction or else large gaps will form in the energy spectrum (Landau levels), affecting the ability to get e-h symmetry because usually only one carrier will align with the field and appreciably suffer such quantum effects. Thus the electrons, which are very light must not have the long axis of their pockets along B . Therefore B must be along the binary axis, leaving \bar{j} along the bisectrix, as shown in figure 5, and in agreement with experiment.

Applying the same rules to the doped Bi-Sb system described above, where e-h symmetry is approximately present produces the surprising result that ∇T must be along the trigonal axis, \bar{j} along a bisectrix axis and B along a binary. This orientation has not been studied in optimally doped and alloyed Bi-Sb, and has the added advantage that all the light e-h pockets contribute optimally, unlike the traditional orientation.

MEASUREMENTS

In order to explore carefully new alloys of doped Bi-Sb, a very tedious collection of somewhat difficult measurements must be made. These must include the resistivity tensor, the thermopower tensor and the thermal conductivity for many alloys over a broad temperature range in varying magnetic field. In addition, the measurement techniques are non-trivial. The difficulty arises because

a good thermoelectric material (Peltier or Ettingshausen) generates huge thermoelectric voltages and substantial temperature gradients when current is passed through it, mixing up thermopower and resistivity signals in a nearly impossible-to-unscramble way.

If we start with a uniform temperature and magnetic field in a sample to be measured, and drive a constant current through it, electric potentials are set up almost immediately, and then, with some time constant, thermal gradients develop which may change measured voltages. The measured voltage may be a strong function of time, with time constants less than 1s. The constant voltage measured after a long time, when the gradients are stable, is called the adiabatic value. Measurements made quickly give the isothermal values. Figure 6 shows a typical measurement of the time dependence of the longitudinal voltage on a Bi-Sb alloy, and static results for a doped alloy where the Hall voltage vanishes as e-h symmetry is reached in the remarkable low field of 0.4T. The curved region of the time dependent data arises from a compounding of the Ettingshausen effect and the Nernst effect. The isothermal value of the voltage, combined with the known drive current, yields the resistance while the difference between isothermal and adiabatic voltages, combined with the thermal conductivity, yields the Nernst (or Ettingshausen) coefficient. This also provides a direct measure of the critical thermopower and T_0 in the material [15]. The static data is necessary also because the time-dependent effects, though accurately tracking the key properties, degrade at small fields as B^2 and also degrade for systems that are poor EC materials, requiring the use of static measurements to map out the full transport parameters.

These measurements were made using two fast, ultra low noise amplifiers in a differential instrumentation amplifier configuration designed by us. The output of the amplifiers is digitized at rates near 1 kHz to measure over a time scale of approximately 800ms, by which time the voltage approaches a steady value. The timing of the current switch is controlled by a PC over a GPIB bus and the timing of the digitization cycle is adjusted to catch the voltage level before the current is switched on. Fitting a simple exponential growth to the curve gives a time constant of $\tau \sim 150$ ms, although the time dependence is not expected to be exactly exponential [15]. Such measurements,

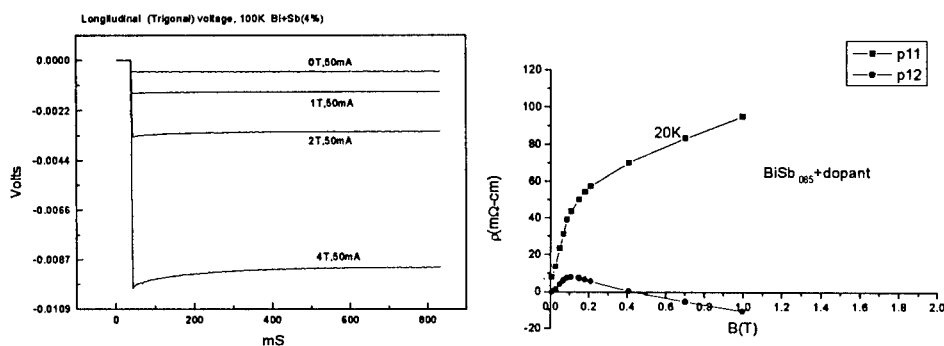


Figure 6. Left, the response of a sample of Bi_{0.96}Sb_{0.04} alloy to the application of a constant current. The current turns on at the beginning of the trace, about 40ms after the start of recording. Right, a BiSb_{0.05} doped alloy showing the change in sign of the Hall voltage, marking e-h symmetry, and the strong variation in properties at fields below 0.5T.

combined with static measurements of thermal conductivity, are required to predict the performance of a material used in an EC cooler.

SUMMARY

We have reviewed the Peltier and Ettingshausen effects, discussed accurate phenomenological equations to describe the Ettingshausen cooler and indicate how the Ettingshausen cooler can provide better performance for the same effective material properties than a Peltier cooler via geometry optimization. Rules are described for determining the best directions to use in Ettingshausen materials, and the key difficulties with measurements are reviewed.

ACKNOWLEDGEMENTS

This work was supported by the U.S. Department of Energy, Advanced Energy Projects. The authors wish to thank R.E.Allen for providing us with the data files used to produce figure 5 which is certainly the best band structure calculation on Bi to date.

REFERENCES

- 1) A. L. Jain, Phys. Rev. **114**, 1518 (1959).
- 2) G. E. Smith, Phys. Rev. Lett. **9**, 489 (1962).
- 3) K. F. Cuff, R. B. Horst, J. L. Weaver, S. R. Hawkins, C. F. Kooi, and G. M. Enslow, Appl. Phys. Lett. **2**, 145 (1963).
- 4) E. Gruneisen and J. Gielessen, Ann. Physik. **27**, 243 (1936).
- 5) R. Wolfe and G. E. Smith, Phys. Rev. **129**, 1086 (1963).
- 6) H. J. Goldsmid, *Electronic Refrigeration* (Pion Limited, London, 1986).
- 7) N. W. Ashcroft and N. D. Mermin, *Solid State Physics* (W. B. Saunders Co., Philadelphia, 1976).
- 8) C. F. Kooi, R. B. Horst, K. F. Cuff, and S. R. Hawkins, J. Appl. Phys. **34**, 1735 (1963).
- 9) C. F. Kooi, R. B. Horst, and K. F. Cuff, J. Appl. Phys. **39**, 4257 (1968).
- 10) R.B. Horst and L. R. Williams, *Proceedings, Third International Conference on Thermoelectric Energy Conversion*, Arlington, TX (New York:IEEE)p. 183 (1980)
- 11) S.A.Trugman, A. Migliori, F. Frieber, T.W.Darling, in preparation.
- 12) B.J. Obrien and C.S. Wallace, J. Appl Phys. **29**,1010 (1958).
- 13) Y. Liu and R. E. Allen, Phys. Rev. B **52**, 1566 (1995).
- 14) N. B. Brandt and E. A. Svistova, J. Low Temp. Phys. **2**, 1 (1970).
- 15) G. L. Guthrie and R. L. Palmer, J. Appl. Phys. **37**, 90 (1966).

THERMOELECTRIC BEHAVIOR OF CONDUCTING POLYMERS: ON THE POSSIBILITY OF "OFF-DIAGONAL" THERMOELECTRICITY

N. Mateeva, H. Niculescu*, J. Schlenoff**, and L. Testardi
TecOne, Inc., 1803 Sageway Drive, Tallahassee, FL 32303

* Also at The Florida A&M Univ./Florida State Univ. College of Engineering.

** Also at The Chemistry Department of Florida State Univ.

ABSTRACT

Non-cubic materials, when structurally aligned, possess sufficient anisotropy to exhibit thermoelectric effects where the electrical and thermal currents are orthogonal ("off-diagonal" thermoelectricity). We discuss the benefits of this form of thermoelectricity for devices and describe a search for suitable properties in the air-stable conducting polymers polyaniline and polypyrrole. We find the simple and general correlation that the logarithm of the electrical conductivity scales linearly with the Seebeck coefficient on doping but with proportionality in excess of the conventional prediction for thermoelectricity. The correlation is unexpected in its universality and unfavorable for thermoelectric applications. A simple model suggests that mobile charges of both signs exist in these polymers, and this leads to reduced thermoelectric efficiency. We also briefly discuss non air-stable polyacetylene, where "ambipolar" transport does not appear to occur, and where properties seem more favorable for thermoelectricity.

INTRODUCTION

The Seebeck coefficient S , like the electrical conductivity σ and the thermal conductivity κ , is an anisotropic property in structurally ordered materials with symmetry less than cubic. Thus the performance of any such material as a thermoelectric element is also anisotropic. However, it is necessary, in this case, to further define the anisotropy by consideration of the directions of the electrical and thermal currents in an anisotropic thermoelectric medium.

The ordinary form of thermoelectricity can be referred to as "diagonal thermoelectricity" (DTE). In DTE, the electrical and thermal currents flow parallel. DTE utilizes the diagonal components of S in its matrix representation. DTE can occur in any material irrespective of its crystallographic symmetry. All thermoelectric devices in use today use DTE. The name "anisotropic thermoelectricity" is sometimes used to mean ordinary thermoelectricity (DTE) but implemented in different crystallographic directions for a crystal.

There is another form of thermoelectricity, which we refer to as "off diagonal thermoelectricity" (ODTE), where anisotropy leads to new configurations because the electrical and thermal current flows are not parallel¹. ODTE utilizes the off-diagonal components of S in its matrix representation. This can lead to substantial improvements in the ease and efficiency of thermoelectric implementation. ODTE, which is rooted in anisotropy, only occurs in non-cubic materials with oriented structures, and, depending on the symmetry, only in certain directions.

ODTE allows independent control of the electrical & thermal impedances via the element shape, and has the potential for flexible device implementation. Figure 1 shows the differences in device geometry & possible applications for flexible ODTE.

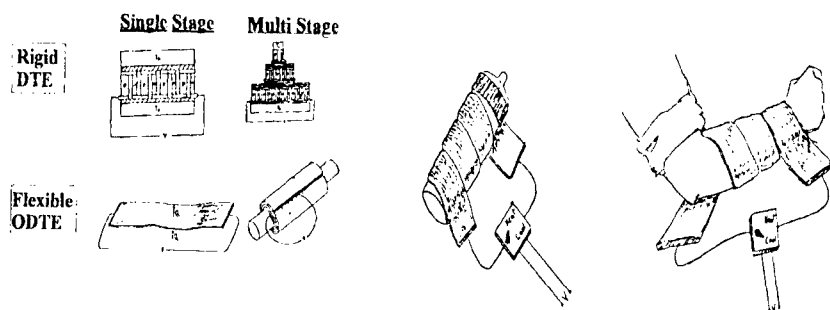


Figure 1: DTE & ODTE device geometries & possible applications for flexible ODTE.

Conducting polymers are cheap, flexible, lightweight and easily made anisotropic (e.g., by stretching) which makes them attractive for ODTE. Their main disadvantage is a low thermoelectric efficiency index ZT . However, most research in these materials centers on achieving the state of maximum electrical conductivity. It is necessary, however, to investigate conducting polymers which are more lightly doped than those pursued in current research on conducting polymers to determine their potential for thermoelectric applications. A further disadvantage is that some conducting polymers are not air-stable.

The only study we are aware of which has reported two of the relevant thermoelectric parameters - σ and S - over a sufficiently wide doping range in conducting polymers is the 1985 work of Reynolds, Schlenoff and Chien² who measured these properties for non air-stable polyacetylene. Their results, replotted in figure 2 in the form to be used in this paper, show a linear relation between $\log \sigma$ and S over a wide range in doping and with a proportionality given by $-\beta(e/k)$ where (e/k) is the elementary charge divided by Boltzmann's constant, and the number $\beta = 1$. This is the behavior expected for a material having mobile charge of one sign only (see below).

We have calculated the doping dependence of ZT in polyacetylene using the RSC² data and assuming, for the unmeasured thermal conductivity, a constant value of 0.01 W/cmK . These results show that the maximum ZT has a value of only slightly greater than 10^{-3} there, nearly 3 orders of magnitude below the value for the best thermoelectric materials today. In the past 10 years, however, there have been a number of reports³ of polyacetylene with σ larger by 10^3 or more than that found by RSC². This increase has been the result of new dopants and new preparation methods. If $\beta = 1$ for these materials, then they would have $ZT > 1$ at 300K, a value larger than that for any known material. However, no report of the $\sigma - S$ behavior of these high σ materials in a more lightly doped state has appeared.

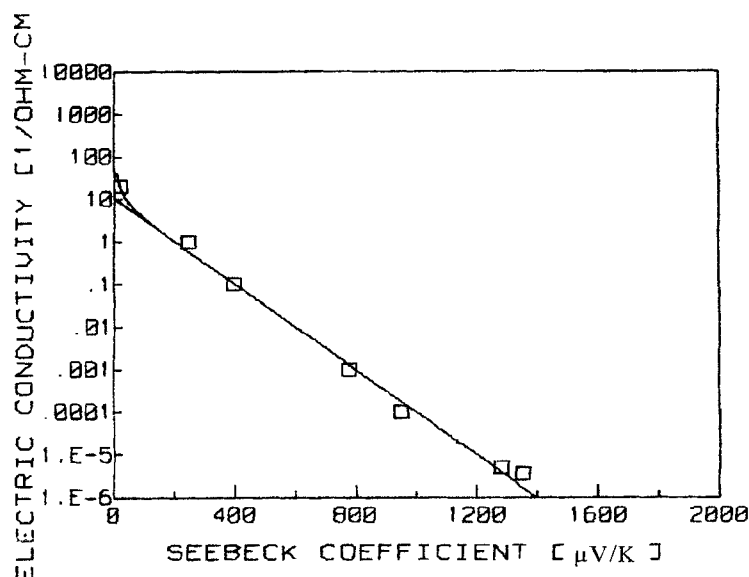


Figure 2. Log (σ) vs S for polyacetylene (from Reynolds, Schlenoff and Chien²).

EXPERIMENT

We chose not to investigate these new forms of conducting polyacetylene because they are neither air-stable nor easily manufactured. We have, instead, measured the thermoelectric properties of air-stable polyaniline and, to lesser extent, polypyrrole. Our samples of polyaniline were synthesized according to the methods of Adams et. al.¹, and MacDiarmid et. al.³, and stretched, in some cases, to develop anisotropy. We also investigated polypyrrole by dedoping polypyrrole coated Milliken Contex Fabric.

Figure 3 shows the σ - S relation found for our polyaniline samples which were stretched to $\sim 3X$ their original length and subsequently doped with oxalic acid. The data for parallel-to-pull and perpendicular-to-pull samples both follow the relation $\log_e(\sigma/\sigma_{\max}) = -\beta (e/k) S$ where $\beta_{\parallel} = 9$ and $\sigma_{\max_{\parallel}} = 33[\text{S/cm}]$ for the parallel-to-pull case and $\beta_{\perp} = 15$ and $\sigma_{\max_{\perp}} = 2.7[\text{S/cm}]$ for the perpendicular-to-pull case. The line just above the data gives the approximate σ - S relation found in polyacetylene by RSC². The upper most line gives the approximate σ - S relation found in the best thermoelectric materials for room temperature applications today. Note that the horizontal scale in Figure 3 (& Figure 4) is 10X smaller than that in Figure 1.

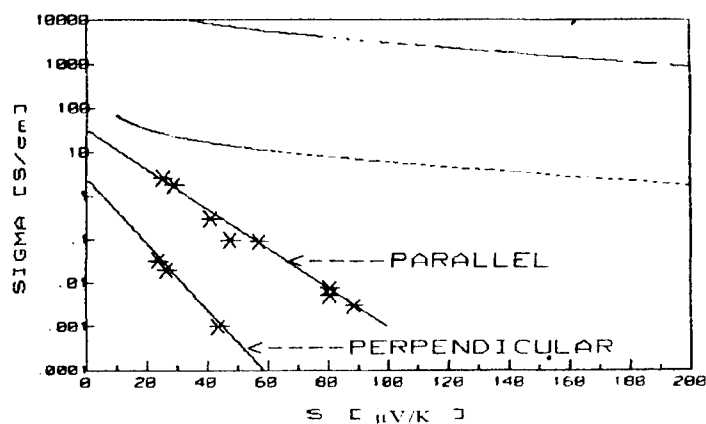


Figure 3. Log (σ) vs S for stretched polyaniline doped with oxalic acid.

The value of β depends on the chemical nature of the dopant in the unstretched (isotropic) state as well as in the stretched (anisotropic) state. The largest values of β in isotropic polyaniline occurred for camphor sulphonic acid (CSA) doping, where β was ~ 45 , and HCl electrochemically deposited and doped material, where β was ~ 17 . Typical values for polyaniline (and, with less data, for polypyrrole) were $\beta \sim 9$. Figure 4 shows the σ - S data for over 150 samples.

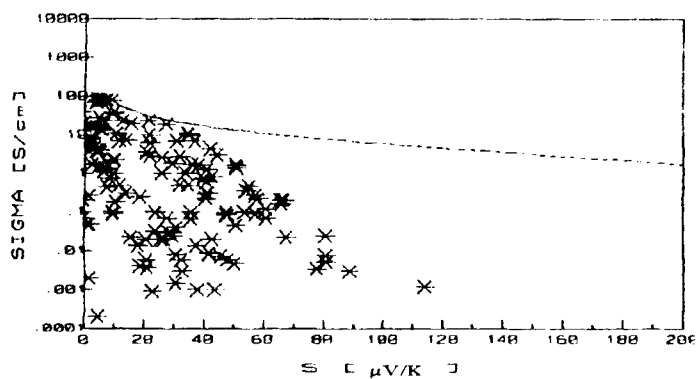


Figure 4. Log (σ) vs S coefficient for all data.

These data are derived from 2 base materials (polyaniline and polypyrrole), 13 different dopants, stretch-oriented & unoriented forms, serially & individually doped and dedoped, and chemically & electrochemically synthesized/doped, though not in all combinations. One can discern the linear trends in the plot for the different dopants some of whose details have been revealed in the previous graph. The common results of these doping studies are that i) a correlation exists between σ and S such that $\log_e(\sigma/\sigma_{\max}) = -\beta (e/k) S$, ii) the value of β depends on the chemical nature of the dopant but is always $\gg 1$, and iii) the values of β and σ_{\max} are anisotropic in a stretched sample. The conclusions above hold whenever we have sufficient data to test them.

When the thermoelectric efficiency index⁶ $ZT = S^2 \sigma T / \kappa$ is combined with the empirical $\sigma - S$ relation, adding the assumption of a constant κ , one finds the maximum ZT will be $ZT(\max) \approx \sigma_{\max} [S/\text{cm}] / (8 \times 10^5 \kappa \beta^2)$ at 300K. The major conclusion of these results, then, is that the occurrence of the empirical $\sigma - S$ correlation with $\beta \gg 1$ is very detrimental to thermoelectric application potential. With $\beta \sim 10$, as in our polyaniline and polypyrrole, one needs electrical conductivities which are $\sim 100X$ greater for applications than in the case where $\beta = 1$, other parameters being equal. This conclusion is independent of the basis for the $\sigma - S$ correlation.

Since the off-diagonal terms in S rarely exceed the diagonal terms by great amounts, the failure to achieve large DTE ZT 's (because of the large β) makes further analysis for ODTE of little value.

ON THE RELATION BETWEEN ELECTRICAL CONDUCTIVITY AND SEEBECK COEFFICIENT

When current passes between two dissimilar materials, heat is evolved or absorbed at the interface at a rate which is proportional to the current (the Peltier effect). The proportionality constant Π is thus the heat of transport per unit electric charge e , and S is thus the entropy of transport per unit electric charge. For a simple system of particles where the fraction of occupied current carrying states is c , we expect $S = (k/e) \log_e[c/(1-c)]$. The electrical conductivity σ of such a system is given by $\sigma = \sigma_{\max} * c * (1-c)$ where, when $c \ll 1$, σ_{\max} is the "apparent" maximum conductivity (at $c = 1$) and is proportional to the mobility of the charge carriers. For an electrically neutral material there will be contributions from the equal number of both + and - charge carrier types to σ , which simply add, and to S , which add with a weighting proportional to their σ 's. Under the additional restraint that $c \ll 1$ (the "light doping" limit), this leads to the final result $\log_e(\sigma/\sigma_{\max}) = -\beta (e/k) S$ where the number $\beta = (r+1)/(r-1)$, and $r = \text{mobility}(+)/\text{mobility}(-)$.

In conventional semiconductors r is $\gg 1$ (p-type conduction) or $\ll 1$ (n-type conduction) because of the very large mass difference between the electron and the parent ionized dopant atom, and because the ionized dopant atom is chemically "locked in place" due to the substitutional nature of the inclusion. These conditions may not apply with such force to the current carrying charge in disordered polymers made conducting by doping with ionizable molecules.

Relevant to the usual interpretations of conducting polymer electrical behavior, neither the Mott theory⁷ nor the Efros-Shklovskii theory⁸ of transport in disordered materials leads to a linear relation between $\log(\sigma)$ and S unless $\log(\sigma/\sigma_{\max}) * [d \log N(E)/d(E/kT)]_{E=E_F} = \text{constant}$ with varying dopant concentration. $N(E)$ is the density of charge carrying states as a function of energy E , and E_F is the Fermi Energy. Such a constraint appears unexpected.

CONCLUSIONS

Our central result, that $\beta \gg 1$ in polyaniline and polypyrrole, thus leads to the conclusion that there are mobile charge carriers of both signs in these doped polymers. Our experiments cannot, however, determine if these carriers are electrons & holes or anions & cations. For $\beta \approx 9$, which characterizes many of our samples in the isotropic (unstretched) state, we would further conclude that the mobilities are in the ratio $r = \text{mobility}(+)/\text{mobility}(-) = 1.25$. This leads to a substantial “internal short-circuiting” of the Seebeck effect ($\beta \gg 1$) and much reduced thermoelectric efficiency. The near parity of the charge mobilities does not, however, occur in polyacetylene according to this interpretation, and the data of RSC².

A fuller account of this work will be published elsewhere and can be obtained from TecOne, Inc., Tel: 904-562-9789 (voice), 904-514-3109 (FAX), or ltestard@phy.fsu.edu (e-mail).

ACKNOWLEDGMENTS

The authors wish to thank Dr. Andrew Child of Milliken Research Corporation for kindly providing samples of Milliken Context Fabric, and The Advanced Energy Projects Division of The Department of Energy for their support of this work.

REFERENCES

1. For a further discussion of the “off-diagonal” thermoelectric effects see “Physical Properties of Crystals”, J.F. Nye, Chapter XII, Clarendon Press, (1985). For references to recent experimental observations, see L. R. Testardi, *Appl Phys Lett*, **64**, 2347 (1994).
2. J. R. Reynolds, J. B. Schlenoff, and C. W. Chien, *J. Electrochem Soc* **132**, 1131 (1985).
3. See, for example, “Physical Properties of Polymers Handbook”, edited by James Mark, chapter 34 by R. S. Kohlman, J. Joo and A. J. Epstein, American Institute of Physics, (1996).
4. P. L. Adams, J. Laughlin and A. P. Monkman, *Synth Met*, **76**, 157 (1996). A. P. Monkman, P. N. Adams, P. J. Laughlin and E. R. Holland, *Synth Met*, **69**, 183 (1995).
5. A. G. MacDiarmid, J. C. Chiang, A. F. Richter, N. L. D. Somasiri and A. J. Epstein in “Conducting Polymers”, Alcacer, L., Editor, Reidel Dordrecht (Netherlands), 105 (1987).
6. See, for example, “Thermoelectricity: Science and Engineering”, edited by R. Heikes and R. Ure, chapter 11 by R. W. Ure and R. R. Heikes, Interscience Publishers, N.Y., (1961), and “CRC Handbook of Thermoelectrics”, edited by D. M. Rowe, chapter 5 by C. M. Bhandari and D. M. Rowe, CRC Press, Boca Raton, (1995).
7. See, for example, “Electronic Processes in Noncrystalline Materials”, N. F. Mott and E. A. Davis, Oxford University Press, London, (1979).
8. See, for example, “Electronic Properties of Doped Semiconductors”, B. I. Shklovskii and A. L. Efros, Springer, Berlin, (1979).

ELECTRICAL TRANSPORT PROPERTIES OF THE PENTATELLURIDE MATERIALS HfTe_5 AND ZrTe_5

T. M. TRITT,^{1,3} M. L. WILSON,¹ R. L. LITTLETON, JR.,¹ C. FEGER,² J. KOLIS,^{2,3}
A. JOHNSON,¹ D. T. VEREBELYI,¹ S. J. HWU,^{2,3} M. FAKHRUDDIN,¹ and F. LEVY⁴

1. DEPARTMENT OF PHYSICS AND ASTRONOMY

2. DEPARTMENT OF CHEMISTRY

3. MATERIALS SCIENCE AND ENGINEERING DEPARTMENT

CLEMSON UNIVERSITY, CLEMSON, SC 29634 USA

4. INSTITUT DE PHYSIQUE APPLIQUEE, LAUSSANNE, SWITZERLAND

Abstract:

We have measured the resistivity and thermopower of single crystals as well as polycrystalline pressed powders of the low-dimensional pentatelluride materials: HfTe_5 and ZrTe_5 . We have performed these measurements as a function of temperature between 5K and 320K. In the single crystals there is a peak in the resistivity for both materials at a peak temperature, T_P where $T_P \approx 80\text{K}$ for HfTe_5 and $T_P \approx 145\text{K}$ for ZrTe_5 . Both materials exhibit a large p-type thermopower around room temperature which undergoes a change to n-type below the peak. This data is similar to behavior observed previously in these materials. We have also synthesized pressed powders of polycrystalline pentatelluride materials, HfTe_5 and ZrTe_5 . We have measured the resistivity and thermopower of these polycrystalline materials as a function of temperature between 5K and 320K. For the polycrystalline material, the room temperature thermopower for each of these materials is relatively high, $+95 \mu\text{V/K}$ and $+65 \mu\text{V/K}$ for HfTe_5 and ZrTe_5 respectively. These values compare closely to thermopower values for single crystals of these materials. At 77 K, the thermopower is $+55 \mu\text{V/K}$ for HfTe_5 and $+35 \mu\text{V/K}$ for ZrTe_5 . In fact, the thermopower for the polycrystals decreases monotonically with temperature to $T \approx 5\text{K}$, thus exhibiting p-type behavior over the entire range of temperature. As expected, the resistivity for the polycrystals is higher than the single crystal material, with values of $430 \text{ m}\Omega\text{-cm}$ and $24 \text{ m}\Omega\text{-cm}$ for HfTe_5 and ZrTe_5 respectively, compared to single crystal values of $0.35 \text{ m}\Omega\text{-cm}$ (HfTe_5) and $1.0 \text{ m}\Omega\text{-cm}$ (ZrTe_5). We have found that the peak in the resistivity evident in both single crystal materials is absent in these polycrystalline materials. We will discuss these materials in relation to their potential as candidates for thermoelectric applications.

Introduction:

Large research efforts have been performed on materials based on the Bi_2Te_3 and $\text{Si}_{1-x}\text{Ge}_x$ systems for thermoelectric (TE) applications.¹⁻³ These materials have been extensively studied and optimized for their use in thermoelectric refrigeration and power generation applications and remain the current state-of-the-art materials. Despite this comprehensive investigation of the traditional TE materials there is still substantial room for improvement. The need for improvement in properties is particularly acute in the lower temperature regime given that most of the conventional TE materials show optimal performance at room temperature and above.

Recently there has been renewed interest in the investigation of new and/or significantly more efficient TE materials. This enhanced interest has been driven by the need for much higher

performance and new temperature regimes for TE devices in many applications. Applications utilizing TE materials are demanding higher performance room temperature materials than exist presently. In addition, as the field of "cryoelectronics" and "cold computing" grows the need for lower temperature (100 - 200 K) TE materials has become necessary. The advantages of "cold computing" are discussed in a recent article by Sloan,⁴ where he states that "speed gains of 30% - 200% are achievable in some CMOS computer processors" and that "cooling is the fundamental limit to electronic system performance." While there are a considerable number of applications in the high temperature regime, there are even greater potential device applications for refrigeration at lower temperatures, between 80 and 400K. Materials of both n-type and p-type are necessary if a thermoelectric device is to be fabricated.

Thermoelectric energy conversion utilizes the Peltier heat generated when an electric current is passed through a thermoelectric material to provide a temperature gradient with heat being absorbed on the cold side and rejected at the sink, thus providing a refrigeration capability. Conversely, an imposed ΔT will result in a voltage or current, i.e. small scale power generation.⁵ For a material to be a good candidate for thermoelectric applications it needs to possess a high figure of merit, Z , where $ZT = \alpha^2 \sigma T / \lambda$, where α is the Seebeck coefficient, σ the electrical conductivity and λ the total thermal conductivity ($\lambda = \lambda_L + \lambda_E$; the lattice and electronic contributions respectively). The most promising materials are typically semiconductors with carrier concentrations of approximately 10^{19} carriers/cm³. The power factor, $\alpha^2 \sigma$, can be optimized through doping to give the largest Z . High mobility carriers are most desirable so as to have the highest electrical conductivity. For all the current state of the art materials, the dimensionless figure of merit, $ZT \approx 1$.

It is apparent that at this time the field of thermoelectrics is undergoing a rapid rebirth. This rebirth is not driven primarily by dramatic new discoveries, but rather by existing technologies greatly desiring higher performance materials. As such, many new materials, new classes of compounds and new synthesis techniques are being investigated and some of these are showing promising results.⁶⁻¹³ One area of investigation that is sorely lacking in this rebirth concerns lower temperature ($80K < T < 200K$) thermoelectric materials. The most promising manner in which to search for a potential thermoelectric materials at these temperatures ($T \approx 100$ K) is to investigate systems which exhibit more exotic electrical transport than standard metal or semimetal transport. One candidate is a material exhibiting a sharp density of states ($n(E)$) near the Fermi energy (E_F) that could lead to a large thermoelectric power. The electrical conductivity is proportional to $n(E)$ while the thermopower is proportional to the logarithmic derivative of $n(E)$ $\{(1/n) * dn/dE\}$ with E evaluated at $E = E_F$. Low-dimensional systems are known to be very susceptible to van Hove singularities (or cusps) in their density of states. A number of systems that are candidates for such low temperature thermoelectric materials are heavy fermion materials, Kondo systems and low-dimensional materials. Low dimensional materials are specifically susceptible to electronic phase transitions and exotic transport properties (e.g. charge density wave materials). Doping effects are typically very strong in these types of materials and can drastically change their electronic transport. Quantum well systems take advantage of this low dimensional character through physical confinement in thin film structures to enhance the electronic properties of the material (i. e. the power factor, $\alpha^2 \sigma$).⁶

Results and Discussion

We have performed some preliminary investigations of a very interesting class of low-dimensional materials known as the pentatellurides, HfTe_5 and ZrTe_5 . In Figure 1, we show resistivity and thermopower for HfTe_5 and ZrTe_5 as a function of temperature. This is data for a bundle of single crystal fibers, approximately $100\text{ }\mu\text{m}$ in diameter and approximately 5 mm long. This data agrees well with previously reported single crystal data.¹⁴⁻²¹ The resistivity for HfTe_5 increases as the temperature is decreased from room temperature and exhibits a peak ($\rho(T_p) \approx 3\rho(300\text{K})$) at around $T_p \approx 80\text{K}$ after which the resistivity falls rapidly as the temperature is further reduced. The ZrTe_5 material behaves in a similar manner except the peak occurs at a higher temperature, $T_p \approx 145\text{K}$. The room temperature electrical conductivity of these materials is $2.9 \times 10^3 (\Omega\text{-cm})^{-1}$ for HfTe_5 and $1 \times 10^3 (\Omega\text{-cm})^{-1}$ for ZrTe_5 which is comparable to the best known thermoelectric materials. However, the most interesting property of these materials, in regards to thermoelectrics, concerns the low temperature thermopower near the peak. At temperatures above the peak the thermopower is very high, on the order of $120\text{ }\mu\text{V/K}$ for HfTe_5 and $110\text{ }\mu\text{V/K}$ for ZrTe_5 . Near T_p the thermopower exhibits a strong temperature dependence and changes sign to a comparable negative thermopower ($\approx -100\text{ }\mu\text{V/K}$ for each). Thus, these materials exhibit both large n-type ($T < T_p$) and p-type ($T > T_p$) behavior depending on the temperature.

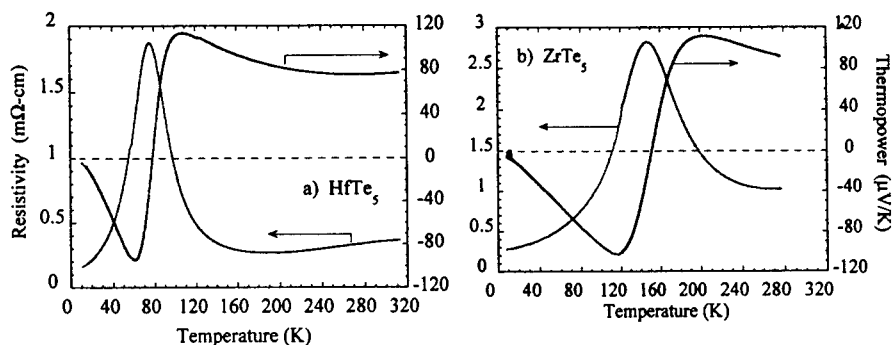


Figure 1. The absolute thermopower, α , and the resistivity, ρ , as a function of temperature for single crystal (a.) HfTe_5 and (b.) ZrTe_5 .

The electrical transport properties of these materials was studied some 15 years ago, albeit not in relation to the materials' properties for applications in thermoelectrics.¹⁴⁻²¹ The transition or peak was first thought to be evidence of a charge density wave (CDW) peak but no evidence of a CDW transition or CDW behavior was found. These materials were being investigated just before the breakthrough of high temperature superconductivity and many of the researchers working on these systems turned their research in that direction. From the early work, the transition in the pentatellurides appears to be an electronic phase transition and not a structural phase transition, thus the electronic properties of this system should be very susceptible to doping. DiSalvo et al.¹⁵ performed Zr and Ta substitution for Hf in the HfTe_5 material and found the doping and

substitutions were able to change the peak temperature, while also affecting the magnitude of the resistivity of these materials. The thermopower was not reported. The magnitude of the thermopower has been found to very sample dependent,¹⁴ probably due to small amounts of trace impurities or differences in growth conditions, so in doped materials the electronic properties should be very susceptible to optimization.

Dramatic pressure effects¹⁶ have also been observed in the pentatelluride materials with the thermopower below the peak, the n-type, being changed by 150% or more to values of approximately $-240 \mu\text{V/K}$ in ZrTe_5 at $T = 120\text{K}$ and $P = 12 \text{ kbar}$. The resistivity (conductivity) is reduced (increased) by a factor of four at these pressures and temperatures. The thermopower, as well as the conductivity, for ZrTe_5 is increased with pressure, effectively increasing the power factor for this material by a factor of ten or more at these pressures and temperatures. Smaller changes, yet still substantial, are also observed in HfTe_5 at similar pressures. These materials are also very sensitive to external stress.²¹ Uniaxial stress shifts the peak in resistance for ZrTe_5 and effects a change in magnitude more strongly in HfTe_5 . Thus, the possibility of dramatically changing the thermopower towards more desirable values has already been shown to be possible. A very sharp variation of the density of states ($n(E)$) near the Fermi energy (E_F) is predicted from a calculation of the density of states by Bullett¹⁸ for one of these materials, ZrTe_5 . As discussed previously, this provides the possibility for a large thermoelectric power through various dopings to manipulate the Fermi level in these materials. One could assume a similar density of states exists for the HfTe_5 system.

The pentatellurides have three small pieces of Fermi surface, two electron-type and one hole-type. The larger of the three pieces is the hole-type surface.¹⁹⁻²¹ The magnetotransport of these materials is also somewhat unusual. Very large magnetoresistance was observed even at relatively high temperatures for large magnetotransport effects ($T \approx 100\text{K}$).¹⁷ Also the mobility is quite large, $\mu \approx 3000 \text{ cm}^2/\text{V-sec}$ for HfTe_5 above the peak ($T \approx 200\text{K}$). This is three times the mobility for Bi_2Te_3 . The crystal structure is also very complex for these materials, with a large number of atoms per unit cell. This coupled with the low-dimensional nature of the materials makes the material likely to have a relatively low thermal conductivity and to the best of our knowledge this quantity has never been reported. We have measured the thermal conductivity of a similar system, NbTe_4 and found it to be on the order of 10 watts/m-K . This was a larger crystal than these fibers, thus easier to measure the thermal conductivity. We are in the process of developing apparatus to perform the thermal conductivity measurements on the pentatellurides.²² A thermal conductivity of 10 watts/m-K would be too large for a good thermoelectric and this parameter may be the limiting factor for the potential of these materials for TE applications.

A TE module is typically composed of an n-type and a p-type material connected through electrical contact pads.⁵ Thus, it is most desirable to have both an n-type and a p-type material to be able to build a thermoelectric module. At the low temperatures ($T < 90\text{K}$) a superconductor could be used as one leg, not for the heat transport but to get the current to return to the other leg without joule heating.²³ These pentatelluride materials, depending on temperature, as shown for a bundle of single crystal materials in Figure 1, exhibit both n-type and p-type behavior. This makes the possibility of fabricating a thermoelectric device for this temperature range even more possible. Most of the current research concerns materials that can be utilized at room temperature and above. The only material, to my knowledge, that can be utilized at lower temperatures ($T \approx 100\text{K}$) is the

$\text{Bi}_{1-x}\text{Sb}_x$ system (only n-type) requiring approximately a 2 Tesla magnetic field to enhance the properties to an acceptable ZT value.²⁴ Each pentatelluride material is p-type above the peak and could be used in conjunction with the n-type BiSb.

We have also investigated polycrystalline pressed powders of these pentatelluride materials and the resistivity and thermopower is shown in Fig 2.a and 2.b for HfTe_5 and ZrTe_5 respectively. The resistivity, which is very anisotropic for the single crystals, is much larger in the polycrystals ($\rho \geq 25 \text{ m}\Omega\text{-cm}$) as expected, since we are averaging over the low electrical conductivity direction as well as the high electrical conductivity direction. However, the thermopower remains quite high and of comparable value to the single crystal material but it is p-type over the entire temperature range investigated. It appears that pressed pellets will not be interesting for potential thermoelectric applications due to the large resistivity. However a fiber matrix or fiber-composite matrix method for the single crystals much like is performed with carbon fibers is feasible. The device could be fabricated with an inherent pressure to improve the thermoelectric properties of these materials if this is favorable.

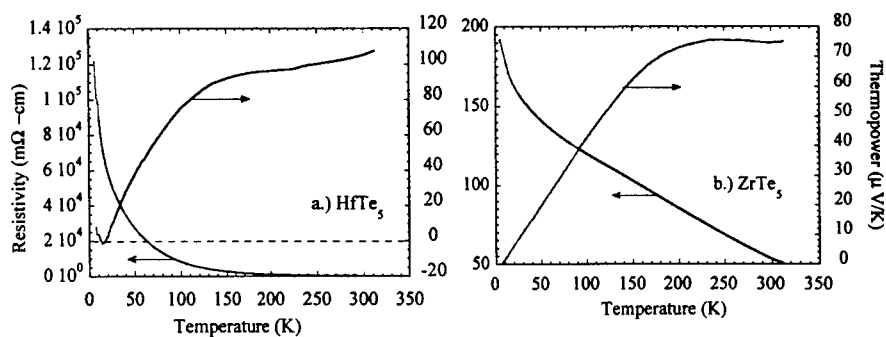


Figure 2. The absolute thermopower, α , and the resistivity, ρ , as a function of temperature for polycrystalline pressed powders (a.) HfTe_5 and (b.) ZrTe_5 .

In Figure 3, we show a plot of the numerator of the figure of merit ($\alpha^2\sigma T$) or essentially the power factor times the temperature for each material. HfTe_5 exhibits a very large $\alpha^2\sigma T$ at $T \approx 100\text{K}$ and if a low thermal conductivity is found for these materials then there is definitely potential for utilizing them for thermoelectric applications. In summary, we have performed preliminary measurements on a promising system to investigate for lower temperature thermoelectric properties. The doping possibilities are very broad in these pentatelluride systems, with substitutions of Hf or Zr by Ti, Nb, Ta etc. possible as well as replacing Te by S, Se etc. Much more work needs to be done, including as we stated extensive doping studies, thermal conductivity measurements and pressure studies of the properties.

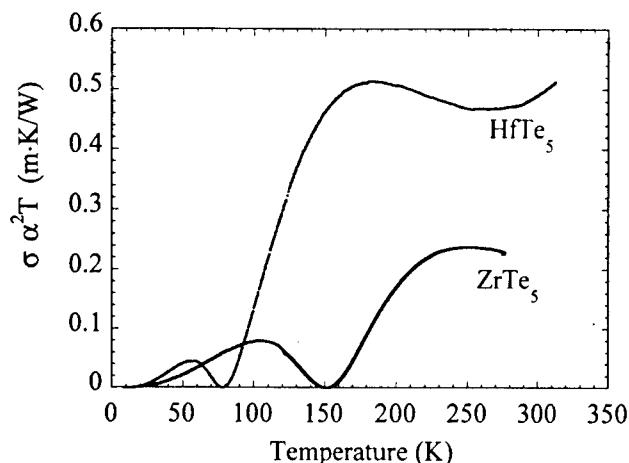


Figure 3. The numerator of ZT ($\alpha^2\sigma T$) vs. the temperature for HfTe₅ and ZrTe₅.

REFERENCES

- 1.) H. J. Goldsmid, *Electronic Refrigeration*, (Pion Limited Publishing, London, (1986)
- 2.) *CRC Handbook of Thermoelectrics*, edited by D. M. Rowe, CRC Press, Boca Raton (1995)
- 3.) C. W. Wood, Rep. Prog. Phys. **51**, 459-539 (1988)
- 4.) J. Sloan, Superconductor Industry, Fall 1996, p30 (1996)
- 5.) Terry M. Tritt, Science, **272**, 1276 (1996)
- 6.) L. D. Hicks and M. S. Dresselhaus, Phys. Rev. B., **47**, 12727 (1993)
- 7.) J. P. Fleuriet, T. Calliet and A. Borshchevsky, Proc. of the XIII International Conference on Thermoelectrics, AIP, p 40-44 (1995)
- 8.) B. C. Sales, D. Mandrus and R. K. Williams, Science, **272**, 1325 (1996)
- 9.) D. T. Morelli et. al., Phys. Rev. B, **51**, 9622 (1995)
- 10.) Glen A. Slack and V. G. Toukala, Jour. Appl. Phys., **76**, 1635 (1994)
- 11.) G. Nolas, G. Slack, D. T. Morelli, T. M. Tritt and A. C. Ehrlich, Jour. Appl. Phys., **79**, 4002 (1996)
- 12.) T. M. Tritt et. al., Jour. Appl. Phys., **79**, 8412 (1996)
- 13.) G. Nolas, G. Slack, V. G. Harris and T. M. Tritt, Jour. Appl. Phys., **80**, 6304 (1996)
- 14.) T. E. Jones et. al., Solid St. Comm., **42**, 793 (1982)
- 15.) F. J. DiSalvo, R. M. Fleming and J. V. Waszczak, Phys. Rev. B., **24**, 2935 (1981)
- 16.) W. W. Fuller et. al., Journal de Physique, **C3**, 1709 (1983)
- 17.) M. Isumi, et. al., Solid State Comm., **42**, 773 (1982)
- 18.) D. W. Bullett, Solid State Comm., **42**, 691 (1982)
- 19.) G. N. Kamm et. al., Phys. Rev. B., **35**, 1223 (1987)
- 20.) G. N. Kamm et. al., Phys. Rev. B., **31**, 7617 (1985)
- 21.) E. P. Stillwell, A. C. Ehrlich, G. N. Kamm and D. J. Gillespie, Phys. Rev. B., **39**, 1626 (1989)
- 22.) D. T. Verebelyi, accepted for publication, Rev. Sci. Instrum.
- 23.) Hylan Lyons, private comm., H. J. Goldsmid et. al., Jour. of Phys. D, **21**, 344 (1988)
- 24.) W. M. Yim and A. Amith, Solid State Electronics, **15**, 1141 (1972)

THERMOPOWER, ELECTRICAL AND HALL CONDUCTIVITY OF UNDOPED AND DOPED IRON DISILICIDE SINGLE CRYSTALS

A. HEINRICH *, G. BEHR *, H. GRIESSMANN *, S. TEICHERT ** AND H. LANGE ***

*Institut für Festkörper- und Werkstofforschung Dresden, Helmholtzstr.20, D-01069 Dresden, Germany

**Technische Universität Chemnitz-Zwickau, Institut für Physik, D-09107 Chemnitz, Germany

***Hahn-Meitner Institut Berlin GmbH, Abt. Photovoltaik, Rudower Chaussee 6, D-12489 Berlin, Germany

ABSTRACT

The electrical transport properties of β -FeSi₂ single crystals have been investigated in dependence on the purity of the source material and on doping with 3d transition metals. The transport properties included are electrical conductivity, Hall conductivity and thermopower mainly in the temperature range from 4K to 300K. The single crystals have been prepared by chemical transport reaction in a closed system with iodine as transport agent. In undoped single crystals prepared with 5N Fe both electrical conductivity and thermopower depend on the composition within the homogeneity range of β -FeSi₂ which is explained by different intrinsic defects at the Si-rich and Fe-rich phase boundaries. In both undoped and doped single crystals impurity band conduction is observed at low temperatures but above 100K extrinsic behaviour determined by shallow impurity states. The thermopower shows between 100K and 200K a significant phonon drag contribution which depends on intrinsic defects and additional doping. The Hall resistivity is considered mainly with respect to an anomalous contribution found in p-type and n-type single crystals and thin films. In addition doped single crystals show at temperatures below about 130K an hysteresis of the Hall voltage. These results make former mobility data uncertain. Comparison will be made between the transport properties of single crystals and polycrystalline material.

INTRODUCTION

The compound β -FeSi₂ belongs to the group of semiconducting silicides formed by the transition metals Cr, Mn, Fe, Ru, Re, Os and Ir in the Si rich part of the corresponding phase diagrams [1]. Within this group of silicides the three compounds β -FeSi₂, MnSi_{1.75} and Ru₂Si₃ with energy gaps of 0.85eV, 0.46eV and 0.9eV, respectively, are considered as promising thermoelectric materials for medium and high temperature applications [2,3]. Many efforts have been made to find suitable doping elements and doping levels for high efficient n-type and p-type compounds. The most extensive investigations have been carried out over about thirty years on β -FeSi₂. Both bulk material [2-13] and thin films [14-20] have been considered. The continuous interest in the thermoelectric properties of this compound is mainly connected with the availability of its components, its chemical stability and compatibility with Si technology.

In recent years β -FeSi₂ has found increasing interest as possible candidate also for optoelectronic and photovoltaic applications [1]. In this connection the preparation of high quality epitaxial films was achieved by molecular beam epitaxy [21] and chemical beam epitaxy [22]. New metastable disilicide phases have been found but single crystalline films could not be prepared [21]. The optical properties have been investigated from the infrared range to interband transitions up to 24eV and compared with recent electron band structure calculations [23,24].

Despite the great interest in thermoelectric and optoelectronic applications many of the transport properties of β -FeSi₂ are still not understood: Transport measurements on epitaxially

grown β -FeSi₂ thin films have shown high mobilities [21,25] never measured in polycrystalline material. A strong non-linear Hall resistivity was found and explained by different models. The main scattering mechanisms are not known which limit the mobility, unclear is the role of polaron formation in n-type material, uncomplete is the knowledge of defect formation and impurity levels. As a consequence it remained an open question whether β -FeSi₂ can be modified to give improved thermoelectric properties in comparison with the state of the art material.

To get more insight into the fundamental properties of β -FeSi₂ also single crystals have been investigated in recent years [19,26-30]. Undoped and doped single crystals have been prepared by chemical transport reaction and their transport properties have been measured at low and high temperatures. According to their high structural order and defined stoichiometry the β -FeSi₂ single crystals should be considered as basis for applied research. It was found that the purity of the source material can have a substantial effect on the transport properties [30]. Using highly purified source material information should be obtained also about intrinsic defects.

It is the aim of this paper to discuss aspects of the current understanding of the transport properties of β -FeSi₂ single crystals. The transport properties considered include electrical conductivity, thermopower and Hall resistivity and with that all parameters which determine the thermoelectric power factor. Special emphasis will be laid on correlations between the purity of the source material and the transport behaviour. But first a short summary will be given of transport data of polycrystalline β -FeSi₂ and the preparation will be described of β -FeSi₂ single crystals of ultra-high purity.

POLYCRYSTALLINE β -FeSi₂

In the first paper on thermoelectric properties of β -FeSi₂ [4] p-type and n-type material was obtained by doping with Al and Co, respectively. In the following investigations mainly initiated by Birkholz [5,8,11,13] and Nishida [2,7,9] the doping levels have been optimized and further doping elements were tested, Ni, Pt, Rh and Pd for n-type and Mn and Cr for p-type compounds. It is now well established that doping with transition metals from the right side of Fe in the Periodic Table yields n-type conductivity but from the left p-type conductivity. Al also acts as an acceptor by replacing Si.

Usually the thermoelectric properties of β -FeSi₂ depend also on the preparation technique and purity of the source material and with that on unintentional doping. In standard powder technology β -FeSi₂ is prepared from the metallic high temperature phase α -FeSi_{2+x} which has a broad temperature dependent homogeneity range $0.24 < x < 0.64$ [31]. Therefore, after the $\alpha \rightarrow \beta$ transition one has an excess of Si which can have an additional doping effect. At the same level of intentional doping the transport properties can be quantitatively quite different. Fig.1 shows as an example the thermopower at room temperature

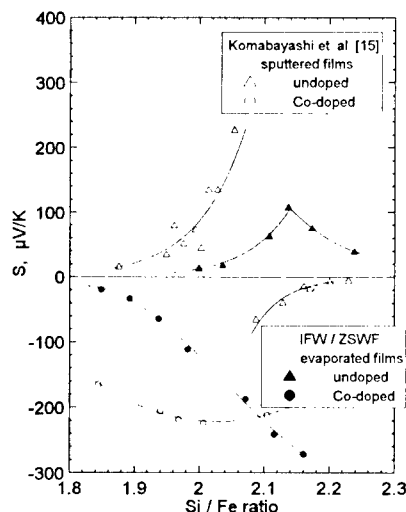


Fig.1 Thermopower $S(300K)$ of polycrystalline β -FeSi₂ thin films

of undoped and Co-doped polycrystalline β -FeSi₂ thin films in dependence on the deviation x from stoichiometry. Compared are results obtained on sputtered [19] and evaporated films [15].

Taking into account the role of unintentional doping the thermoelectric properties of β -FeSi₂ have been optimized by several authors. Very efficient n-type β -FeSi₂ was developed by partial compensation of Co with Al [13]. This compensation produces an increase of the efficiency by 10% in comparison with uncompensated material. A generator modul consisting of this β -FeSi₂ as n-leg and MnSi_{1.75} as p-leg gives an efficiency $\eta=3\%$ at $\Delta T=600\text{K}$ [13]. Efficient n-type β -FeSi₂ was also found by alloying with Ru [32]. Also the use of unconventional doping elements as oxygen [16] or of sophisticated preparation techniques as plasma processing of the starting powder can give improved material [33].

In Table I characteristic transport properties at room temperature of β -FeSi₂ are summarized which have been obtained by different authors with polycrystalline bulk material and thin films. The maximum efficiencies Z were obtained in the temperature range from 670K to 870K, for Co-doped β -FeSi₂ values have been achieved of 2.3 to 5.2 10^{-4} K^{-1} and for Mn-doped material 1.3 10^{-4} K^{-1} . Also Al-doped material reaches ZT values of 0.2 at 800K.

Table I
Room temperature electrical and thermoelectrical data for doped polycrystalline β -FeSi₂

dopant	σ (Ωcm) ⁻¹	S $\mu\text{V/K}$	μ cm^2/Vs	$S^2\sigma$ $\mu\text{W/cmK}^2$	λ W/mK	E_A meV	Ref.
Co	40 ... 150	-150 ... -250	0.3	2.2 ... 3.5	4 ... 10	25 ... 80	5,7,9,10,15
Co	500	-100 ... -270		11	5		12
Co + Al	230	-190		8.3	4.5		13
Ni	13	-110		0.17		140	14
Pt	110	-200		4.9		20	14
Mn	5 ... 10	280 ... 450	8	0.4 ... 1.5	6	110	7,9,10,12,15
Cr	30 ... 35	220 ... 300		1.4 ... 3.0	12	70 ... 130	12,14,15,
Al	190	170	1.6 ... 4	6	6	60	5,11

PREPARATION OF β -FeSi₂ SINGLE CRYSTALS

To achieve high-purity semiconductor grade β -FeSi₂ single crystals it is necessary to use high-purity starting materials and to optimize the whole preparation process to maintain the purity. Ultra-high-purity silicon was used as source material. High-purity iron was prepared by a multistep process starting from technological iron powder. After chlorination of the iron a vacuum distillation of FeCl₂ over lumpy sponge iron to separate the nickel from the ferrous chloride was performed. The reduction of the ferrous chloride was performed with hydrogen on a resistance-heated pure iron deposition wire. The typical experimental conditions were described in [34,35]. The chemical composition of the highly pure iron is shown in Table II.

According to the phase diagram of the Fe-Si system the orthorhombic β -FeSi₂ phase does not coexist with the melt and decomposes during heating at 1255K into FeSi and α -FeSi₂, which has a composition different from β -FeSi₂ [31]. The α -FeSi₂ phase is stable above 1210K. Therefore, the growth of β -FeSi₂ single crystals must be carried out in the temperature region below 1210K, and chemical transport reactions or flux growth may be used. To avoid impurity incorporation from the flux the chemical transport reaction in closed silica ampoules was used with a mixture of iron (5 N) and silicon (5 N) as source materials (about 1.5g in total) and I₂ as the transport medium. In most cases the composition of the starting material was equal to the atomic ratio Fe/Si = 2 of the disilicide. But the ratios 2.5 and 1.5 were chosen for deposition of



Fig. 2: As grown β -FeSi₂ single crystals

Table II
Impurities of Fe and β -FeSi₂ detected by MS

Element	Fe-Wire (mass ppm)	β -FeSi ₂ (mass ppm)
B	< 1	< 1
S	< 1	< 0.1
P	< 1	< 1
Na	< 1	2
Ba	< 1	< 0.1
Cl	2	< 1
Br	< 1	< 0.1
K	< 1	< 1
Ca	< 0.1	2
Ti	< 1	< 1
Cr	< 1	7
Mn	< 1	< 0.1
Co	1	1
Pb	< 1	< 0.1
W	< 1	< 0.1
Ni	2	11
Cu	5	2
Zn	< 1	< 1
Ga	1	1
Zr	1	1
Nb	< 0.1	< 1
Sb	< 1	< 0.1
Sn	< 1	< 0.1
As	< 1	< 0.1
Mo	< 2	< 0.1
Ag	< 0.1	1
I	< 0.1	19
Ta ¹⁾	13	19
C ²⁾	10	- ³⁾
O ²⁾	9	- ³⁾
N ²⁾	6	- ³⁾
H	< 6	- ³⁾

¹⁾ MS-sample holder consists of Ta

²⁾ 70% of the contents of C, O, N are bound on the surface [19]

³⁾ not determined

crystals with the upper and the lower boundaries of the homogeneity range of β -FeSi₂, too. The chemical vapour transport was performed in a horizontal configuration and proceeded from the source at a temperature T_2 (1323 K) to the crystallization zone kept at a lower temperatures T_1 of 100 to 300 K below T_2 . Usually, after a 24 hours preheating in a reversal temperature gradient $T_2 < T_1$, the ampoule was kept for about 10 days at the experimental temperatures T_1 and T_2 . Special attention must be paid to the maintenance of the purity of the starting agents. This demands the use of high-purity iodine. Furthermore, a special heat treatment of the silica tubes used in chemical transport reactions is necessary to exclude oxygen and water.

The single crystals obtained (Fig. 2) have a needle-like shape with dimensions of (5 - 10) × 2 × 0.5 mm³. The crystal structure was checked by X-ray diffraction. The measured peaks were correlated only to the orthorhombic β -FeSi₂ phase, no traces of α -FeSi₂ were found. Only at crystallization temperatures T_1 of 1223 K plate-like crystals of the α -FeSi₂ phase were obtained. The habit of the crystals does not change if different source compositions and different temperatures in the crystallization zone of the transport ampoule are used. In contrast to the crystals reported in literature before [26], selected crystals have a flat surface indicating that the usual twinning can be avoided in the material of higher purity. Further efforts are necessary to find optimum conditions for this type of crystal growth.

The analyses of impurities in the single crystals (Table II) displays no significant increase in comparison with the starting materials but a decrease in the elements which will not be transported by iodine. Only the concentration of the transport agent iodine is increased in the single crystals to 19 wt. ppm.

ELECTRICAL RESISTIVITY

Undoped β -FeSi₂ Single Crystals

Undoped single crystals grown with source material of a purity of 4N and less show irregular behaviour [19]. Therefore, single crystals were grown with 5N source material described above to look for intrinsic defects and for the dependence of the transport behaviour on the deviation from strict stoichiometry within the homogeneity range. The investigated samples can be divided according to their composition into three groups:

1. crystals with composition of the Si-rich phase boundary (source material Si/Fe=2.5)
2. crystals with undefined composition within the homogeneity range (source material Si/Fe=2.0)
3. crystals with composition of the Fe-rich phase boundary (source material Fe/Si=1.5).

In Table III preparation parameter and transport data at room temperature are summarized of samples which are discussed in the following.

In Fig.3 the electrical resistivity $\rho(T)$ of characteristic samples is shown in the temperature range from 80K to 400K. There is a clear dependence of $\rho(T)$ on the deviation from strict stoichiometry. From the Fe-rich phase boundary to the Si-rich phase boundary the resistivity ratio ρ_{80}/ρ_{300} increasing from 2 to 200. This strong increase of the resistivity ratio is an evidence of a finite width of the homogeneity range despite the approximately constant resistivity $\rho(300K) = (20 \dots 100)\Omega\text{cm}$. The activation energy of the shallow donor is 25meV at the Fe-rich boundary but more than 60meV at the Si rich phase boundary. This different values are a strong indication that different intrinsic defects are formed at the both phase boundaries.

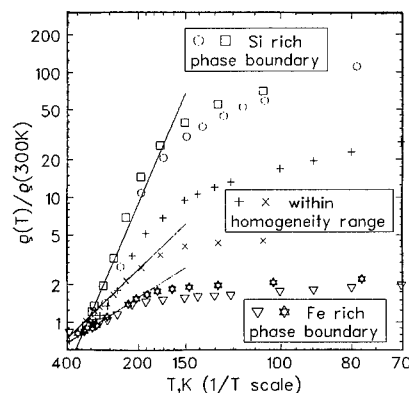


Fig.3 Resistivity of undoped β -FeSi₂ single crystals with different composition

Below 100K the slope of $\rho(T)$ decreases and reaches in samples with excess of Fe very small values as known from impurity band conduction. We have found a constant activation energy in the meV range (Table III), within the considered temperature range down to 4K there is no variable range hopping conduction. This is in contrast to the behaviour of undoped polycrystalline β -FeSi_{2+x} thin films which show Mott hopping in the same temperature range.

At high temperatures $T > 450\text{K}$ the activation energy increases in all samples from the value of the shallow donor to about 0.4eV indicating the onset of intrinsic conduction [30].

Doped β -FeSi₂ Single Crystals

Doping of highly pure β -FeSi₂ single crystals should give information on the relation between intrinsic and extrinsic defects. But up to now doping experiments were carried out on single crystals only which were undefined with respect to their stoichiometry (ratio Si/Fe=2.0 of the

source material). It remains a problem for further work to dope single crystals prepared at the phase boundaries of the homogeneity range.

Doping experiments were carried out with 3d transition metals using 4N Fe for Cr, Mn and Ni [29] and 5N Fe for Co. In [36] it was proved by ESR measurements that the above mentioned metals are incorporated into the lattice in most cases on both inequivalent Fe sites. In Table III transport parameter at 300K are given of doped samples.

Despite the different magnitude at 300K the resistivity $\rho(T)$ shows the same general temperature dependence as in undoped single crystals. Below room temperature $\rho(T)$ strongly increases until 100K...150K and changes to a much weaker temperature dependence below about 100K (Fig.4). The activation energy in the first temperature range is attributed to the corresponding dopant, see Table III.

Table III

Electrical parameter of doped β -FeSi₂ single crystals prepared with 4N and 5N Fe, resp.

Symbol	dopant / at% source mat.	ρ / Ωcm (300 K)	S / $\mu\text{V/K}$ (300 K)	E_A / meV (300 K)	T_{hopp} / K
+	Cr 1	0.22	490	80	-
×	Mn 0.3	3.3	500	50	-
△	Co 1	0.9	-600	40	38
▽	Co 3	1.1	-650	50	80
□	Ni 2	6.7	-600	95	-
◇	Ni 5	0.45	-620	60	-

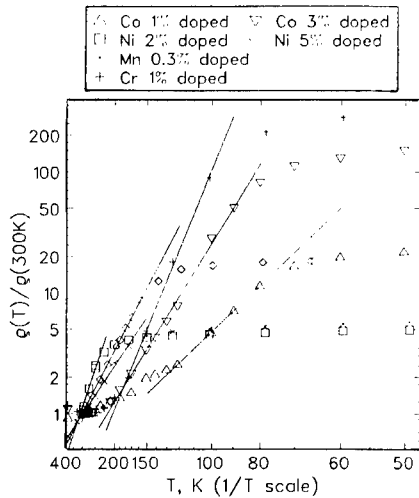


Fig.4 Resistivity of doped β -FeSi₂ single crystals (straight lines: $\ln\rho \propto E_A/kT$)

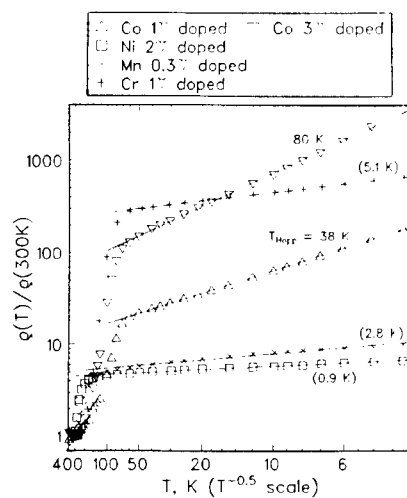


Fig.5 Low temperature resistivity of doped β -FeSi₂ single crystals in the plot of variable range hopping

The low temperature behaviour is characterized by straight lines in the plot $\ln\rho$ vs. $T^{-1/2}$, see Fig.5. But only the Co-doped single crystals follow the corresponding variable range hopping law $\ln\rho(T) \propto (T_{\text{hopp}}/T)^{-1/2}$ in the presence of a Coulomb gap [37]. This law can only be applied if the

hopping temperature T_{Hopp} is larger than the measuring temperature T . The small hopping temperatures in the Co-doped crystals are an indication of a high impurity concentration close to the metal-insulator transition within the impurity band. In all other samples we have an impurity band with delocalized states and metallic characteristic. At high temperatures intrinsic conduction is observed above 600K [30] i.e. at much higher temperatures than in undoped single crystals.

THERMOPOWER

Undoped β -FeSi₂ Single Crystals

Fig.6 shows the unexpected result, that the thermopower of undoped β -FeSi₂ changes sign with increasing purity of the source material for the crystal growth. Single crystals prepared with 4N Fe show a positive thermopower, but those prepared with 5N Fe negative thermopower. The samples of Fig.6 have been prepared with stoichiometric source material. p-type conductivity is usually found also in undoped polycrystalline β -FeSi₂ thin films and bulk material made by commercially available Fe of 4N or less purity. The p-type conductivity of undoped β -FeSi₂ is obviously caused by unintentional doping and not by intrinsic defects. According to Fig.6 intrinsic defects are expected to be donors.

The magnitude as well as the general temperature dependence of the thermopower $S(T)$ is obviously independent of the conductivity type. At low temperatures $S(T)$ remains very small near zero up to about 70K, increases sharply up to values of $|S| = 500 \dots 800 \mu\text{V/K}$ at 150K and shows a weak temperature dependence up to room temperature. Room temperature values are usually within $450 \mu\text{V/K}$ and $900 \mu\text{V/K}$ and with that much larger than in most polycrystalline material (see Table I and Fig.1).

In Fig.7 the thermopower $S(T)$ is compared of undoped single crystals prepared with excess of Si and Fe, respectively. The two groups of crystals exhibit different magnitudes and temperature dependences of $S(T)$. In samples of the Si-rich phase boundary the thermopower increases with decreasing temperature to a maximum between 100 and 150K or increases further up to values $|S| > 2000 \mu\text{V/K}$ at 100K. These large values of the thermopower can not be explained by an usual diffusion thermopower. Phonon drag effects should play an important role [44]. The slope of the increase of $|S(T)| \propto T^n$ below 300K is given by $n = -0.8 \dots -1.2$.

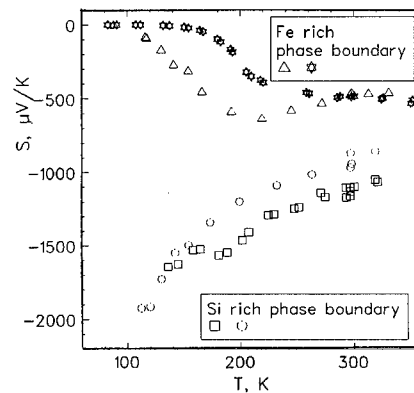
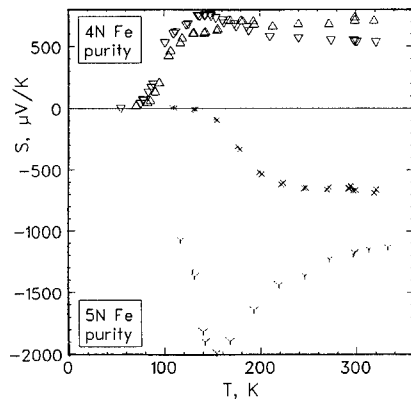


Fig.6 Thermopower of undoped β -FeSi₂ single crystals prepared with 4N and 5N Fe

Fig.7 Thermopower of undoped β -FeSi₂ single crystals prepared with excess of Fe and Si

The different behaviour of $S(T)$ of the both groups of crystals corresponds to the different behaviour of the resistivity (Fig.3): (i) Below room temperature the thermopower $|S|$ increases or remains approximately constant as long as the resistivity increases according to the activation energy of the shallow donor. (ii) The small thermopower is found in the temperature range of the impurity band conduction.

In this picture the strong change of the thermopower in the range between 100K and 150K is the result of the transition from usual band conduction to impurity band conduction.

Doped β -FeSi₂ Single Crystals

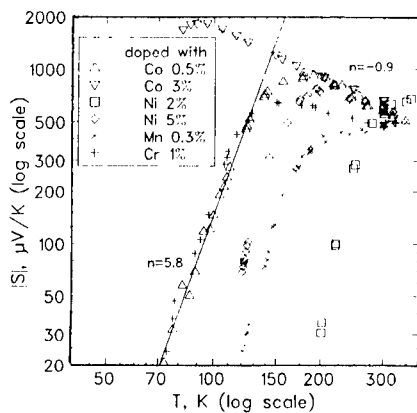


Fig.8 Absolute value of the thermopower of doped β -FeSi₂ single crystals

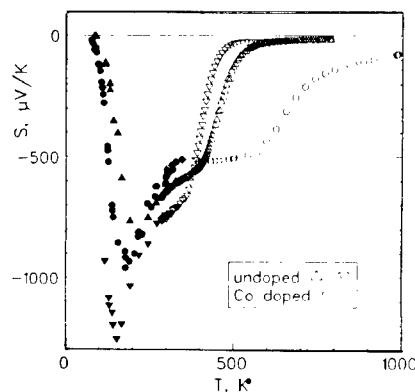


Fig.9 Thermopower of undoped and Co-doped β -FeSi₂ single crystals

The thermopower in doped β -FeSi₂ single crystals exhibit the same general features as in undoped crystals. In agreement with the behaviour of polycrystalline material doping with Co and Ni yielded n-type and doping with Cr and Mn p-type crystals. Common characteristics of $S(T)$ can be derived from Fig.8. Independent of the doping element and of the conductivity type the strong increase of $S(T)$ from 70K to 150K can be described by $|S| \propto T^n$ with $n \approx 6$. Also the temperature dependence of $S(T)$ below 300K is similar in most samples and given by the same exponent $n \approx -0.9$ as in undoped crystals. Therefore, the low temperature maximum seems to be a general characteristic of high quality β -FeSi₂ single crystals. But it can be suppressed e.g. by intrinsic defects as in undoped samples of the Fe-rich phase boundary. The most pronounced maximum was found in the Co-doped crystal with $c_{Co} = 0.5\text{at}\%$ prepared with 5N Fe.

At temperatures above 300K the thermopower remain approximately constant until the onset of intrinsic conduction at $T \approx 400$ in undoped and $T \approx 600$ K in doped single crystals (Fig.9).

HALL MEASUREMENTS

Hall Mobility

The hitherto existing Hall measurements on β -FeSi₂ give an inconsistent picture. In polycrystalline β -FeSi₂ the hole mobility at room temperature was found to lie between 2 and $8\text{cm}^2/\text{Vs}$ [5,7,10,22,38], but hole mobilities up to $100\text{cm}^2/\text{Vs}$ were measured in epitaxial films of

high structural order deposited onto Si single crystals [25,39]. These high mobility values are very probably caused by the substrate which has a sheet resistance in the same order of magnitude as the β -FeSi₂ film. For the electron mobility much smaller values of 0.26 to 0.31 cm²/Vs have been found [5,7,10] which were explained by small polaron conduction. In polycrystalline bulk material the hole mobility decreases for $T > 300\text{K}$ according to $\mu \propto T^{-n}$ with $n \approx 2$ and the electron mobility was found to remain approximately constant [7,10].

The present controversial discussion of the Hall mobility of β -FeSi₂ is the result of different conclusions which were drawn from the observed field dependence of the Hall resistivity in both polycrystalline and single crystalline samples. Hall measurements on p-type single crystals [28] have been analysed considering both a shallow and deep acceptor level. Hole mobilities were found at room temperature of about 20 cm²/Vs which increase with decreasing temperature according to $\mu \propto T^{-n}$ with $n > 3$, reach a maximum below 100K and then decrease. The position and absolute height of the maximum depend on the crystal quality. A maximum value of 1200 cm²/Vs was found at about 80K. In [29] similar results on p-type single crystals were obtained: hole mobilities $\mu(300\text{K})$ up to 30 cm²/Vs, an exponent n between 2 and 3.6 depending on the purity of the basis material, maximum values $\mu \approx 450\text{ cm}^2/\text{Vs}$ at 150K. The strong temperature dependence of $\mu(T)$ can only be described by phonon scattering if optical phonons dominate. Because of the large number of low energy optical phonons in β -FeSi₂ this should be possible also at low temperatures.

Also the electron mobility of β -FeSi₂ single crystals was found to be much larger than in polycrystalline samples. On the basis of a two band model to account for the observed non-linear dependence of the Hall voltage on the magnetic field electron mobilities of 1.6 to 3.6 cm²/Vs at 300K were calculated [27].

Non-linear Hall Resistivity

A non-linear dependence of the Hall voltage on the magnetic field was observed in n-type single crystals and thin films below room temperature as well as in p-type thin films below 250K and p-type single crystals below 200K [27,29,40-42]. The non-linear Hall resistivity $\rho_H(B)$ has been analysed in [40] assuming the existence of an anomalous Hall effect due to magnetic ordering at low temperatures. Both the normal and anomalous Hall coefficients R_0 and R_1 decrease with increasing temperature. Their ratio R_1/R_0 also decreases from about 10 at 20K to zero at 250K. These values range between the extrema for ferromagnetic semiconductors and metals. But in [27] the non-linearity was explained using a two-band model.

Systematic investigations of the non-linear Hall resistivity on thin films and single crystals [41,42] revealed characteristic similarities in the general behaviour of both types of samples but a more pronounced non-linearity in single crystals. In Fig. 10 the results obtained on thin

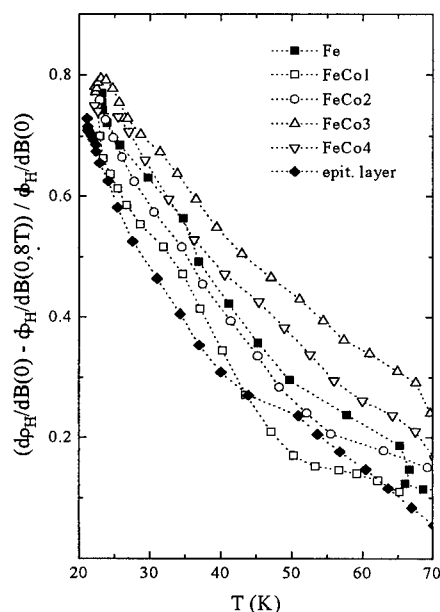


Fig. 10 Average curvature of the Hall resistivity in β -FeSi₂ thin films

films are summarized: the curvature of $\rho_H(B)$ as a measure of the non-linearity decreases with increasing temperature in all films in the same manner independent of doping and disorder [42]. The Hall resistivity of doped single crystals is shown in Fig.11. Non-linear behaviour is found in both n-type and p-type crystals almost up to room temperature, but in n-type crystals the effect is stronger and shows a more complicated field dependence. Especially a negative Hall constant was only observed at high fields and high temperatures.

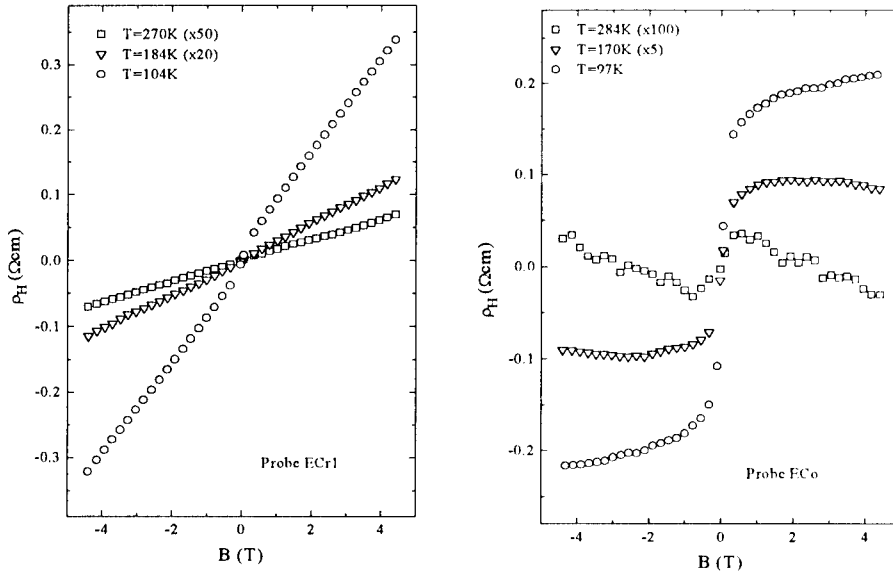


Fig.11 Hall resistivity of a p-type Cr-doped and a n-type Co-doped β -FeSi₂ single crystal (note the scaling factor of the data)

In doped single crystals in addition to the non-linear behaviour of $\rho_H(B)$ a strong hysteresis effect was found below 130K. This hysteresis was observed in both n-type and p-type crystals [1,41,42]. The width of the hysteresis loop decreases with increasing temperature and vanishes above 130K. This result suggests that a remanent magnetization exists in the field direction at low temperatures and that the non-linearity at higher temperatures is also caused by an anomalous Hall effect.

But first magnetization and magnetic susceptibility measurements [43] did not confirm this suggestion. There is a hint for an antiferromagnetic interaction in β -FeSi₂ but not for a strong remanent magnetization. On the other hand the explanation of the non-linear Hall resistivity by a two band model is inconsistent with the experimental data [42]. Further work is necessary to solve this problem. But mobility values and carrier concentrations are questionable which were derived from Hall measurements without taking into account the non-linear Hall resistivity. Hall data above room temperature are scarce [5,7] and still not known from β -FeSi₂ single crystals.

CONCLUSIONS

The thermoelectric properties of polycrystalline β -FeSi₂ have been optimized by several authors with basis material of 4N purity or less in case of Fe. Efficient material was obtained by doping with Co (n-type) and Al and Mn (p-type). But unintentional doping has a strong influence

on the transport behaviour. It was shown that the investigation of β -FeSi₂ single crystals can help to avoid unintentional doping and to provide a basis for further applied research provided that very pure source material is used.

It has been shown that in undoped single crystals prepared with 5N Fe both electrical conductivity and thermopower depend on the composition within the homogeneity range of β -FeSi₂ which is explained by different intrinsic defects at the Si-rich and Fe-rich phase boundaries. In both undoped and doped single crystals impurity band conduction is observed at low temperatures and extrinsic behaviour determined by shallow impurity states above 100K. The thermopower shows between 100K and 200K a significant phonon drag contribution. Much larger values of the thermopower have been obtained as known from polycrystalline material.

A serious still unsolved problem is the non-linear Hall resistivity found below room temperature in single crystalline and polycrystalline, undoped and doped β -FeSi₂. The explanation of this non-linearity by an anomalous Hall effect is mainly based on a low temperature hysteresis effect. But new results on the magnetic susceptibility does not confirm this assumption.

The chemical vapour transport was successfully used to obtain undoped and doped single crystals of high purity and defined stoichiometry within the homogeneity range of β -FeSi₂.

ACKNOWLEDGEMENTS

This work was in part supported by the Bundesministerium für Forschung und Technologie (contract number 03 N 1018 B5) and the Dr. Wilhelm Heinrich und Else Heraeus Foundation (Germany).

REFERENCES

1. H. Lange, in *Silicide Thin Films-Fabrication, Properties and Applications*, edited by R. T. Tung, K. Maex, P.W. Pellgrini, and L.H. Allen (Mater. Res. Soc. Proc. **402**, Pittsburgh, PA, 1996), p. 307.
2. I. Nishida, J. Mater. Sci. Soc. Jap. **15**, 72 (1978).
3. C. B. Vining, in *CRC Handbook of Thermoelectrics*, edited by D. M. Rowe (CRC Press, Boca Raton, 1995) p. 277; in *Proc. IX. Int. Conf. Thermoelectrics*, edited by C.B. Vining (JPL, Pasadena, CA, 1990) p. 249.
4. R.M. Ware and D.J. McNeill, Proc. IEE **111**, 178 (1964).
5. U. Birkholz and J. Schelm, phys. stat. sol. (a) **27**, 413 (1968).
6. I.D. Ivanova, N.Kh. Abrikosova, E.I. Elagina and V.D. Khostikova, Izv. Akad. Nauk SSSR, Neorg. Mater. **5**, 1933 (1969).
7. I. Nishida, Phys. Rev. B **7**, 2710 (1972).
8. G. Waldecker, H. Meinhold and U. Birkholz, phys. stat. sol. (a) **15**, 143 (1973).
9. Y. Isoda, T. Ohkoshi, I. Nishida and H. Kaibe, J. Mater. Sci. Soc. Jap. **25**, 311 (1989).
10. T. Kojima, phys. stat. sol. (a) **111**, 233 (1989).
11. U. Stöhrer, R. Voggesberger, G. Wagner and U. Birkholz, En. Conv. Mgmt. **20**, 143 (1990).
12. T. Tokiai and T. Uesugi, J. Am. Ceram. Soc. **78**, 1089; J. Ceram. Soc. Jap. **103**, 661 (1995).
13. E. Groß, M. Riffel and U. Stöhrer, J. Mater. Res. **10**, 34 (1995).
14. M. Komabayashi, K. Hijikata, S. Ido, Jap. J. Appl. Phys. **29**, 1118 (1990); **30**, 331 (1991).
15. M. Komabayashi and S. Ido, Jap. J. Appl. Phys. **30**, 2883 (1991); J. Ceram. Soc. Jap. **100**, 21 (1992).
16. K. Matsubara, H. Kuno, Y. Okuno, H. Takaoka and T. Takagi, Proc. ISIAT'83 & IPAT'83, (Kyoto 1983) p. 1221.
17. M. Powalla and K. Herz, Appl. Surf. Science **70/71**, 593 (1993).

18. K. Matsubara, K. Kishimoto, K. Nagao, O. Ueda, T. Miki, T. Koyanagi and I. Fujii, in *Proc. XII. Int. Conf. Thermoelectrics*, edited K. Matsuura (IEE Japan, Yokohama, 1993) p.223; Y. Isoda, M.A. Okamoto, T. Ohkoshi and I.A. Nishida, *ibid.*, p. 192.
19. A. Heinrich, C. Gladun, A. Burkov, Y. Tomm, S. Brehme and H. Lange, in *Proc. XIV. Int. Conf. Thermoelectrics*, edited by M. Vedernikov (St. Petersburg, 1995) p. 259.
20. S. Teichert, R. Kilper, T. Franke, J. Erben, P. Häussler, W. Henrion, H. Lange and D. Paknin, *Appl. Surf. Science* **91**, 56 (1995).
21. H.v. Känel, U. Kafader, P. Sutter, N. Onda, H. Sirringhaus, E. Müller, U. Kroll, C. Schwarz and Goncalves-Conzo, *Mat. Res. Soc. Proc.* **320**, 73 (1994).
22. J.L. Regolini, F. Trincat, I. Berberzier and Y. Shapira, *Appl. Phys. Lett.* **60**, 956 (1992).
23. A.B. Filonov, D.B. Migas, V.L. Shaposhnikov, N.N. Dorozhkin, G.V. Petrov, V.E. Borisenko, W. Henrion and H. Lange, *J. Appl. Phys.* **79**, 7708 (1996).
24. H. Lange, *phys. stat. sol. (b)* **201**, No1 (1997).
25. K. Rademacher, PhD Thesis, RTWH Aachen, 1994.
26. Ch. Kloc, E. Arushanov, M. Wendl, H. Hohl, U. Malang and E. Busher, *J. Alloys Comp.*, **219**, 93 (1995).
27. E. Arushanov, Ch. Kloc, H. Hohl and E. Bucher, *J. Appl. Phys.* **75**, 5106 (1994).
28. E. Arushanov, Ch. Kloc and E. Bucher, *Phys. Rev. B* **50**, 2653 (1995); E. Arushanov, E. Bucher, Ch. Kloc, O. Kulikowva, L. Kulyuk and A. Siminel, *ibid.*, **52**, 20 (1995).
29. S. Brehme, L. Ivanenko, Y. Tomm, G.-U. Reinsperger, P. Strauß and H. Lange, in *Silicide Thin Films - Fabrication, Properties and Applications*, edited by R.T. Tung, K. Maex, P.W. Pellgrini and L.H. Allen (Mater. Res. Soc. Proc. 402, Pittsburgh, PA, 1996), p. 355.
30. A. Heinrich, AS. Burkov, C. Gladun, G. Behr, K. Herz, J. Schumann and H. Powalla, in *Proc. XV. Int. Conf. Thermoelectrics*, edited by T. Caillat (JPL, Pasadena, CA, 1996) p. 57.
31. O. Kubaschewski, in *Iron-Binary Phase Diagrams* (Springer, Berlin, 1982), p. 136.
32. H. Takizawa, P.F. Mo, T. Endo and M. Shimida, *J. Mat. Science* **30**, 4199 (1995).
33. T. Miki, Y. Matsui, K. Matsubara, K. Kishimoto, K. Nagao and I. Fujii, in *Proc. XII. Int. Conf. Thermoelectrics*, edited K. Matsuura (IEE Japan, Yokohama, 1993), p. 29.
34. G. Weise and G. Oswian, *Kristall und Technik* **11**, 729 (1976).
35. G. Behr, J. Werner, G. Weise, A. Heinrich, A. Burkov and C. Gladun, *phys. stat. sol. (a)* **160** (1997) in press.
36. K. Irmscher, W. Gelhoff, Y. Tomm, H. Lange and V. Alexs, *Phys. Rev. B* **55**, 4417 (1997).
37. B.I. Shklovskii and A.L. Efros, *Electronic Properties of Doped Semiconductors* (Springer, Berlin, 1984), p. 240.
38. C.A. Dimitriadis, J.H. Werner, S. Logothetidis, M. Stutzmann, J. Weber and R. Nesper, *J. Appl. Phys.* **68**, 1726 (1990).
39. D.H. Tassis, C.L. Mitsas, T.T. Zorba, C.A. Dimitriadis, O. Valassiades, D.I. Siapkias, M. Angelakeris, P. Poulpoulos and N.K. Flevaris, *J. Appl. Phys.* **80**, 962 (1996).
40. O. Valassiades, C.A. Dimitriadis and J.H. Werner, *J. Appl. Phys.* **70**, 890 (1991).
41. S. Teichert, G. Beddies, Y. Tomm, H.-J. Hinneberg and H. Lange, *phys. stat. sol. (a)* **152**, K15 (1995).
42. S. Teichert, PhD Thesis, Technical University Chemnitz, 1996.
43. E. Arushanov, M. Respaud, J.M. Broto, Ch. Kloc, J. Leotin and E. Bucher, *Phys. Rev. B* **53**, 5108 (1996).
44. C. Herring, *Phys. Rev.* **96**, 163 (1954).

FABRICATION OF p- β -Fe_{1-x}Mn_xSi₂ / n-Si HETEROSTRUCTURE DIODE AND THEIR ELECTRICAL AND OPTICAL PROPERTIES

T. Takada ^{a,b)}, H. Katsumata^{a,b)}, Y. Makita ^{a)}, N. Kobayashi ^{a)}, M. Hasegawa ^{a)}, S. Uekusa^{b)}

^{a)} Electrotechnical Laboratory, 1-1-4 Umezono, Tsukuba, Ibaraki 305, Japan.

^{b)} Meiji University, 1-1-1 Higashi-mita, Tama, Kawasaki, Kanagawa 214, Japan

Abstract

We report on the fabrication of p-type β -FeSi₂ layers on n-type Si(100) substrates and the investigation of their p-n diode characteristics. Since our undoped β -FeSi₂ layers have typically shown n-type conductivity, the p-type layers were formed by the introduction of Mn impurity into β -FeSi₂ layers using two types of doping methods; one is an Electron-Beam-Deposition (EBD) procedure of Fe_{1-x}Mn_xSi₂ ($X < \sim 0.1$) at room temperature and subsequent annealing at 900 °C for 1-120 min, where FeSi₂ ingots added with Mn (~10 %) were used as starting materials. The other is a ⁵⁵Mn⁺-implantation into β -FeSi₂ layers formed by EBD and subsequent annealing at 850 °C for 1-120 min.

From van der Pauw measurements, p-type β -Fe_{1-x}Mn_xSi₂ layers with the resistivity of 0.0036-0.031 $\Omega \cdot \text{cm}$ and hole mobility of 11.9-89.0 $\text{cm}^2/\text{V} \cdot \text{sec}$ were found to be successfully formed on n-Si substrates by both doping methods. The p-n diode characteristics of these heterostructure diodes were investigated by I-V and C-V measurements. The results indicate that the carrier distribution does not agree with either ideal one-side step or one-side slop junctions, although optical transmittance and reflectance measurements indicate that the silicide/Si interface is of good quality.

Introduction

Transition-metal silicides with low electrical resistivity and high chemical stability have recently been of great importance as materials for contacts and gates to Si in VLSI devices. On the other hand, nine types of silicides with semiconducting properties are currently known : CrSi₂, MnSi_{1.7}, β -FeSi₂, RuSi₂, ReSi₂, OsSi₂, Os₂Si₃ and Ir₃Si₅, which have band-gap energies from 0.12 to 2.30 eV [1]. Among them, β -FeSi₂ has attracted increasing attention as a new material for (1) thermoelectric device [2] because of relatively large Seebeck coefficient and (2) optoelectronic devices such as solar cell and infrared detector due to its chemical stability at higher temperatures, non-toxicity, low cost and a strong optical absorption coefficient (about 10^5 cm^{-1} near 1 eV [3]-[5]). In recent reports on the electrical characterizations of thin films fabricated by SPE (Solid Phase Epitaxy) [6], MBE (Molecular Beam Epitaxy) [7], and CVD (Chemical Vapor Deposition) [8], low hole mobility of 2-10 $\text{cm}^2/\text{V} \cdot \text{sec}$ and high carrier concentration in the range of 10^{18} - 10^{19} cm^{-3} were demonstrated, and the former low hole mobility was suggested to be due to the influence of electron phonon scattering effect [9][10]. These values are typical for β -FeSi₂ layers [11]. There are, however, several exceptional data that high hole mobilities of 107 and 128 $\text{cm}^2/\text{V} \cdot \text{sec}$ were observed from IBS- and MBE- grown β -FeSi₂ layers [11], and the reason for this observation remains uncertain. In addition, most of these β -FeSi₂ layers mentioned above showed p-type conductivity. Nevertheless, our β -FeSi₂ layers fabricated on n-Si(100) substrates using EBD have typically shown n-type conductivity, which also remains unresolved.

The purpose of this study is 1) to make p-type β -Fe_{1-x}Mn_xSi₂ layers on n-type Si(100), 2) to investigate their p-n diode characteristics and 3) to clarify the origin of n-type conductivity observed from our undoped β -FeSi₂ layers. Their electrical and optical properties were investigated by van der

Pauw, reflectance, transmittance and Raman scattering measurements, and the diode characteristic was measured by I-V and C-V techniques.

Experimental

$\text{Fe}_{1-x}\text{Mn}_x\text{Si}_2$ layers were grown on (100)-oriented single-crystal Si wafers having a thickness of about 380 μm with resistivity $\rho > 10^3 \Omega\cdot\text{cm}$. Introduction of Mn atoms into FeSi_2 layers was performed by using two different types of doping methods. One is an all electron beam deposition procedure of $\text{Fe}_{1-x}\text{Mn}_x\text{Si}_2$ ([all-EBD]). The other is Mn^+ implantation into FeSi_2 layers that were prepared by EBD ([EBD+ I^2]). The Si substrates were first degreased with organic solvents. After being rinsed in high-purity water, they were etched in diluted solution for 10 min ($\text{HF}:\text{H}_2\text{O} = 1:50$) before being loaded into the evaporation chamber with the base pressure of about 5×10^{-7} Torr. For a fabrication of [all-EBD] samples, $\text{Fe}_{1-x}\text{Mn}_x\text{Si}_2$ layers ($X \sim 0.1$) were then deposited on the Si substrates at room temperature (R.T.) by evaporating FeSi_2 ingots added with $\sim 10\%$ Mn flakes using a single electron-gun evaporation system, which gives an estimated silicide thickness of about 500 nm. These samples were subsequently annealed at $T_a = 900^\circ\text{C}$ for $t_a = 1$ -120 min using an infrared gold image furnace under constant high purity Ar^+ gas flow. For comparison, $\text{Fe}_{1-x}\text{Mn}_x\text{Si}_2$ layers ($X \sim 0.03$) with thickness of 300 nm, defined as [EBD+ I^2] samples, were fabricated by 400 keV $^{55}\text{Mn}^+$ ion-implantation [Mn^+ dose $1.6 \times 10^{16} \text{ cm}^{-2}$] into the EBD-grown FeSi_2 layers, which were annealed at 800°C for 1 min before implantation and at

$T_a = 850^\circ\text{C}$ for $t_a = 1$ -120 min after implantation. The total samples used for this study, labeled as A-I with different fabrication procedures and different annealing procedures are listed in Table. 1.

Table. 1 Nine samples labeled as A-I prepared by two types of fabrication methods; $\text{Fe}_{1-x}\text{Mn}_x\text{Si}_2$ layers were formed on Si(100) either by (1) conventional EBD method and subsequent annealing at 900°C for 1-120 min or (2) Mn^+ ion implantation into the EBD-grown FeSi_2 layers and subsequent annealing at 850°C for 1-120 min, where FeSi_2 layers were first annealed at 800°C for 1 min before implantation.

Sample	Method	T_a [$^\circ\text{C}$]	t_a [min]
A	all-EBD	as - grown	
B	all-EBD	900	1
C	all-EBD	900	30
D	all-EBD	900	60
E	all-EBD	900	120
F	EBD+ I^2	850	1
G	EBD+ I^2	850	30
H	EBD+ I^2	850	60
I	EBD+ I^2	850	120

For the phase determination of silicide layers, X-ray diffraction (XRD) measurements were carried out, where the incident angle of the $\text{CuK}\alpha$ source radiation was maintained at 2.83° to the surface so as to obtain a Si (311) diffraction as a reference. Raman scattering measurements were performed at R.T. in backscattering geometry using the 514.5 nm line of an Ar^+ laser to investigate the crystalline quality of the $\text{Fe}_{1-x}\text{Mn}_x\text{Si}_2$ layers. Transmittance and reflectance measurements were performed in the range of 0.4-1.1 eV with DA8 FT-spectrometer, using a double-polished Si substrate and Au reflecting mirror as a reference, respectively. Their electrical conductivity, carrier concentration and mobility were measured by van der Pauw technique in magnetic fields of 10k gauss. Ohmic contact electrodes were formed by placing small Indium shot on the silicide films and by alloying them with supersonic solder. The p-n diode characteristic was investigated using conventional I-V and C-V techniques.

Results and Discussion

Figure 1 shows the annealing time dependence of XRD spectra obtained from four samples B-E fabricated using [all-EBD] procedures, which were isothermally annealed at 900 °C. By comparing these spectra, we can recognize that polycrystalline β -Fe_{0.9}Mn_{0.1}Si₂ thin films are formed, although the as-grown

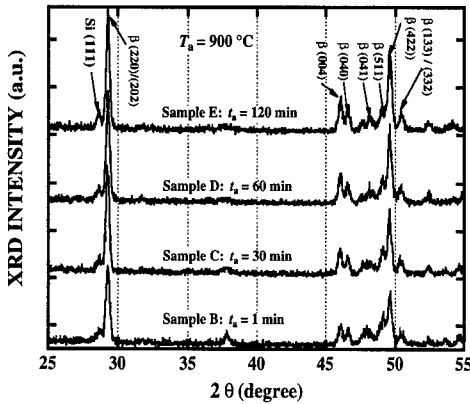


Fig. 1 Annealing time dependence of XRD spectra obtained from four samples, B with $t_a = 1$ min, C with $t_a = 30$ min, D with $t_a = 60$ min and E with $t_a = 120$ min, which were all annealed at 900 °C.

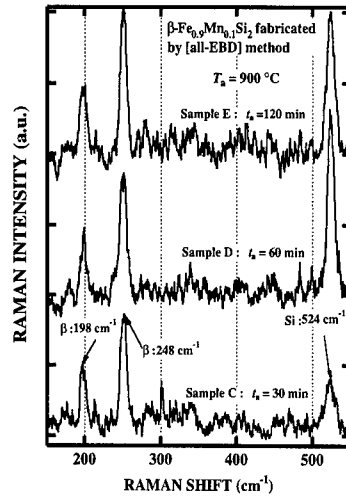


Fig. 2 Raman scattering spectra obtained from samples, C with $t_a = 30$ min, D with $t_a = 60$ min, E with $t_a = 120$ min, which were annealed at 900 °C.

sample exhibits an amorphous structure. In this figure, the signal from Si (111) due to the Si agglomeration in the β -Fe_{0.9}Mn_{0.1}Si₂ thin films by the high temperature annealing is also observed [4].

Figure 2 shows Raman scattering spectra of the same samples C-E as those used in Fig. 1. In Fig. 2, two intense signals due to Fe-Si vibrational mode are observed from each spectrum at 198 and 248 cm⁻¹, indicating that β -Fe_{0.9}Mn_{0.1}Si₂ layers obtained are of good crystalline quality. On the other hand, the other signal observed at 524 cm⁻¹ is attributed to Si-Si bonding, suggesting that the Si agglomeration discussed above was formed in the β -Fe_{0.9}Mn_{0.1}Si₂ layers.

Near-infrared reflectance and transmittance spectra for the β -Fe_{0.9}Mn_{0.1}Si₂ layers obtained from two samples B and E are shown in Fig. 3. For photon energies below 0.9 eV, the reflectance spectra show constructive and destructive interferences, which are caused by the multiple internal reflections between the surface and the β -Fe_{0.9}Mn_{0.1}Si₂/n-Si interface. An occurrence of these interferences in thin films indicates that the interfaces are of good quality, i.e., flat interfaces, from an optical point of view [12]. The interferences running in these samples become weakened with increasing annealing time, indicating that the long-time annealing degrades the flatness of the interface. The optical absorption spectra (α) can be calculated from both measured reflectance and transmittance data using eq.(1);

$$\alpha \times d = \ln [(1-R/T)] \quad (1)$$

where d is the thickness of silicide layers, R and T are the measured reflectance and transmittance data, respectively. The linear part in the relation $(\alpha \times d)^2$ of two samples B and E as a function of photon

energy $h\nu$ indicated a direct transition. By the extrapolation of the linear part to x-axis, a direct band gap of $E_g = 0.86\text{--}0.87$ eV was determined. These values are in good agreement with those previously reported on $\beta\text{-FeSi}_2$ thin films fabricated by deposition technique [4]. Optical absorption coefficients of these samples near the absorption edge are estimated to be about 10^5 cm⁻¹ from eq.(1), suggesting that these silicide layers have a potential feature for the fabrication of solar cell and IR detector.

Although our $\beta\text{-FeSi}_2$ layers fabricated on n-type Si substrates without doping of Mn have so far shown n-type conductivity, $\beta\text{-Fe}_{0.9}\text{Mn}_{0.1}\text{Si}_2$ thin films formed on n-Si substrates using two types of doping methods were successfully converted to p-type conductivity. Figures 4(a) and 4(b) show the annealing time dependence of the hole mobility, μ_h and the hole concentration, n_h for samples B-I, which were doped with Mn using solely EBD (Fig. 4(a)) or ion implantation (Fig. 4(b)). These data were obtained using van der Pauw technique at R.T.. Between two Figs 4(a) and 4(b), no significant change in hole mobility and hole concentration is observed. In both figures, however, the decrease of hole concentration and the increase of hole mobility can be seen in the range of t_a from 30 to 120 min. This reason is considered to be due to the compensation of hole carrier by residual donor impurity diffused from Si (100) substrate, where the donor is confirmed to be phosphorus from photoluminescence measurements. The typical hole concentration of samples prepared in this work is in agreement with that (1.6×10^{19} cm⁻³) of $\text{Fe}_{0.99}\text{Mn}_{0.01}\text{Si}_2$ layers formed by ion beam synthesis (IBS) [11]. The strong discrepancy of two doping methods lies in the activation ratio of Mn impurity. In [all-EBD]-grown samples, the hole carriers ($7.5\text{--}34.0 \times 10^{18}$ cm⁻³) activated in these silicide layers are considerably lower than the initial amount of Mn impurity (2.5×10^{21} cm⁻³) corresponding to the component ratio of $X=0.1$. One possible explanation for the observed low activation ratio is due to the formation of Manganese silicide in $\beta\text{-Fe}_{0.9}\text{Mn}_{0.1}\text{Si}_2$ layers. The concentration and the distribution of Mn doped in $\beta\text{-Fe}_{0.9}\text{Mn}_{0.1}\text{Si}_2$ layers are not clear, and thus, they are still open to investigation using SIMS and RBS. In contrast, the activation ratio of [EBD+I²]-grown samples is a few tens times higher than those of [all-EBD]-grown samples.

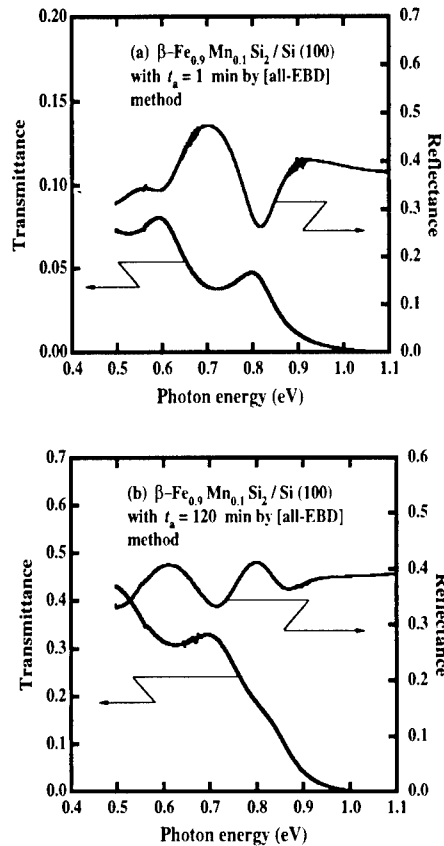
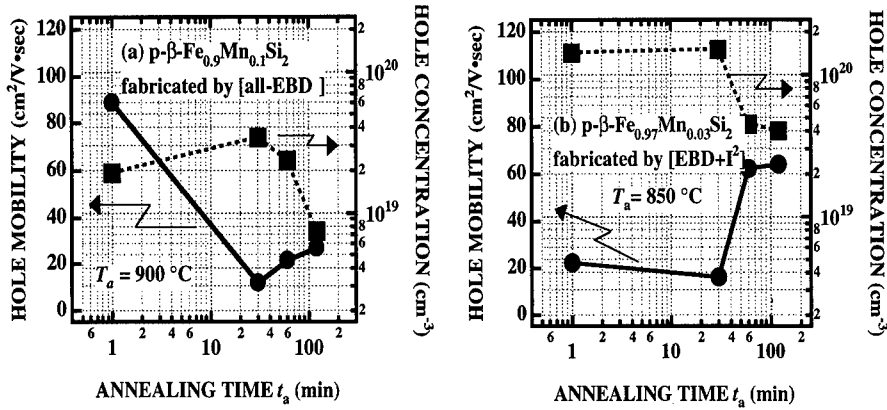


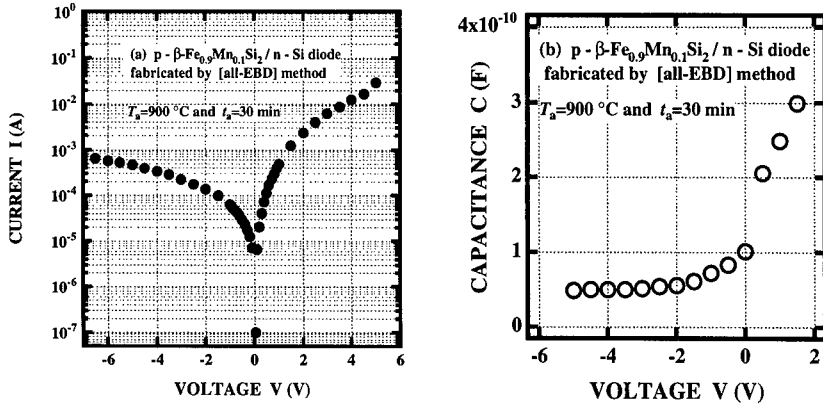
Fig. 3 Near-infrared transmittance and reflectance spectra obtained from two samples. B with $t_a = 1$ min shown in Fig. 3 (a) and E with $t_a = 120$ min shown in Fig. 3 (b), which were annealed at 900 °C.



Figs. 4(a) and 4(b) Annealing time dependence of the hole mobility and the hole concentration in β-Fe_{1-x}Mn_xSi₂ layers prepared by [all-EBD] (4a) or [EBD+I₂] (4b) procedure with T_a = 900 °C and 850 °C, respectively.

Figure 5(a) shows I-V characteristic on p-β-Fe_{0.9}Mn_{0.1}Si₂/n-Si heterostructure diode for sample C, which was prepared by [all-EBD] procedure with T_a = 900 °C and t_a = 30 min. The rectification property, which is of great importance in p-n junction, can be seen from this figure, indicating that p⁺-n junction diode is formed. Such a rectification property is also seen from the result of C-V measurement on p-β-Fe_{0.9}Mn_{0.1}Si₂/n-Si diode as shown in Fig. 5(b). The voltage dependence of junction capacitance for an ideal junction is typically given by eq.(2)

$$C \propto (V_{bi} - V)^{-n} \quad (2)$$



Figs. 5(a) and 5(b) I-V characteristic (5(a)) and C-V characteristic (5(b)) of p-β-Fe_{0.9}Mn_{0.1}Si₂/n-Si heterostructure diode fabricated using [all-EBD] procedure with T_a = 900 °C and t_a = 30 min.

In eq.(2), V_{bi} denotes built-in voltage and exponent n typically equals to 2 in the case of an ideal one-side step junction and to 3 in the case of an ideal one-side slope junction. The relations of $1/C^2$ and $1/C^3$ as a function of reverse voltage are not linear, indicating that the impurity distribution in obtained junction is not ideal in spite of the good quality of the $\beta\text{-Fe}_{0.9}\text{Mn}_{0.1}\text{Si}_2/\text{n-Si}$ interfaces, which were suggested from the optical measurements. This problem is also open to studying in the future.

Conclusions

Polycrystalline p-type $\beta\text{-Fe}_{1-x}\text{Mn}_x\text{Si}_2$ ($x < 0.1$) layers were fabricated on n-Si(100) substrates using two types of Mn-doping methods followed by thermal annealing up to $T_a = 900^\circ\text{C}$: [all-EBD] procedure and Mn^{+} -implantation into EBD-grown $\beta\text{-FeSi}_2$ layers. In both cases, the decreases of hole concentration with increasing annealing time, t_a were observed in the range of $t_a = 30\text{--}120$ min. This was interpreted by the compensation of residual donor impurity diffused from Si substrates, which could be the reason of n-type conductivity typically observed from undoped $\beta\text{-FeSi}_2$ layers on n-Si substrates.

I-V and C-V characteristics of the p- $\beta\text{-Fe}_{0.9}\text{Mn}_{0.1}\text{Si}_2$ / n-Si heterostructure diode with $T_a = 900^\circ\text{C}$ and $t_a = 30$ min showed a rectification property. This shows that thermal controlling devices and solar cells fabricated using $\beta\text{-FeSi}_2$ can assemble into a Si integrated circuit. The dependences of $1/C^2$ and $1/C^3$ on the reverse voltage were not linear, suggesting that the carrier distribution does not agree with either ideal step junction or ideal slope junction, although reflectance measurements indicated that the silicide/n-Si interfaces were of good quality.

References

- [1] H. Lange, Mat. Res. Soc. Symp. Proc. **402** (1996) 307.
- [2] T. Tsunoda, M. Mukaida, A. Watanabe, Y. Imai, J. Mater. Res. **11** (1996) 1.
- [3] H. Katsumata, H.L. Shen, N. Kobayashi, Y. Makita, M. Hasegawa, H. Shibata, S. Kimura, A. Obara, and S. Uekusa, Proc. of the 9th Int. Conf. on Ion Beam Modification of Materials, (1995) 943.
- [4] H. Katsumata, Y. Makita, H. Shibata, N. Kobayashi, M. Hasegawa, S. Kimura, A. Obara, Contributed paper to XV INTERNATIONAL CONFERENCE ON THERMOELECTRICS (Pasadena, California, USA).
- [5] N. Kobayashi, H. Katsumata, H.L. Shen, M. Hasegawa, Y. Makita, H. Shibata, S. Kimura, A. Obara, and S. Uekusa, and T. Hatano, Thin Solid Films **270** (1995) 406.
- [6] J. Nishida, Phys. Rev. B **7** (1973) 2710.
- [7] A. Rizzi, B.N.E. Rosen, D. Freundt, Ch. Dieker and H. Luth, Phys. Rev. B **51**, (1995) 17780.
- [8] J. L. Regolini, F. Tricat, I. Sagnes, Y. Shapira, G. Bremond, and D. Bensahel, IEEE Trans. Electron Devices **39** (1992) 200.
- [9] N. E. Christensen, Phys. Rev. B **42** (1990) 7148.
- [10] C. Giannini, S. Lagomarsino, F. Scarinci, and P. Castrucci, Phys. Rev. B **45** (1992) 8822.
- [11] K. Rademacher, R. Carius and S. Mantl, Nucl. Instr. & Meth. B **84** (1994) 163.
- [12] M.C. Bost and John E. Mahan, J. Appl. Phys. **64** (1988) 2034.

STRUCTURAL AND OPTICAL PROPERTIES OF β -FeSi₂/Si(100) PREPARED BY LASER ABLATION METHOD

H.Kakemoto^{a,b}, Y.Makita^a, A.Obara^a, Y.Tsai^c, S.Sakuragi^c, S.Ando^b and T.Tsukamoto^b

^a Electrotechnical Laboratory, 1-1-4 Umezono, Tsukuba, Ibaraki 305, Japan

^b Science University of Tokyo, 1-3 Kagurazaka, Shinjuku, Tokyo 162, Japan

^c Union Material, 1620 Oshido-kyodai, Tonemachi, Ibaraki 270-12, Japan

ABSTRACT

β -FeSi₂ is a promising material for the application of various electronic, optoelectronic and energy devices. We present here the semiconducting properties of β -FeSi₂ films on Si(100) substrate prepared by laser ablation method. Samples were grown using poly-crystalline bulk β -FeSi₂ prepared by horizontal gradient freeze method. For the monitoring of growth, in-situ observation of ablation plume was made through fluorescence spectroscopy. Reflection of high-energy electron beam diffraction (RHEED) was also made *in-situ* to see the surface morphology. Characterization of the films by X-ray diffraction presented purely β (220) orientation. Raman scattering measurements at room temperature also indicated that the grown films are semiconducting β -FeSi₂. Optical absorption spectra at room temperature showed absorption coefficient higher than 10^5 cm^{-1} above the band-gap ($\sim 1.2 \text{ eV}$). It was revealed that high quality semiconducting β -FeSi₂ films can be fabricated by laser ablation method without post-annealing.

INTRODUCTION

Recently, much attention has been directed to β -FeSi₂ thin films grown on Si substrates as a next generation versatile semiconductor material. Among multiple intermetallic Fe-Si alloys, β -FeSi₂ ($a=9.863$, $b=7.791$, $c=7.833$, orthorhombic: D_{2h}) exhibits semiconducting behaviors with direct band-gap (E_g) of $\sim 0.875 \text{ eV}$ [1-2]. Optical absorption coefficient of β -FeSi₂ which is induced resonance absorption from localized Fe(d) electron-LO phonon interaction attains to be higher than $\sim 10^5 \text{ cm}^{-1}$. This high optical absorption coefficient and the above value of direct band-gap energy are attractive features for the fabrication of optoelectronic and energy devices [3]. The system of Fe-Si alloys involves α , β , γ and ϵ -phases. The tetragonal α -phase (Fe_2Si_5) is metallic and stable between 937°C and 1220°C . ϵ -FeSi is a dilute magnetic metal (Kondo insulator) [4]. The mixture between rare earth element (RE) and Fe-Si alloy such as $\text{RE}_2\text{Fe}_3\text{Si}_5$ [5] behaves as a superconducting material and in addition it shows negative magnetoresistance effect, reflecting the existing localized electrons in the lattice [6]. It is therefore of great importance to investigate β -FeSi₂ in order to elucidate a variety of interesting physical properties. Large-size homogeneous β -FeSi₂ bulk crystal is normally difficult to be grown due to the complicated phase diagram [7]. The difficulties are attributed to the presence of eutectic reaction, peritectic reaction and Daltonide type stoichiometric width of Fe-Si system. High-quality β -FeSi₂ bulk crystal can be used not only as a target material for laser ablation (LA) but also a standard sample for the measurements of optical absorption spectra in the low absorption coefficient regime. Further if single crystal of β -FeSi₂ is obtained, it can be used also as a substrate for epitaxial growth. We performed the growth of the β -FeSi₂ bulk crystals by horizontal gradient freeze (HGF) method using molten material [8]. Compared with various thin film growth methods, LA method has several unique advantages such as capability of high stoichiometry control, possibility of low growth-temperature, crucible free technology which avoids the contamination from crucible materials. Using the above polycrystalline bulk β -FeSi₂, we prepared single-phase β -FeSi₂ thin films by LA method [9]. We present here the structural and optical properties of β -FeSi₂ films grown on Si(100) substrates.

EXPERIMENTAL

The schematic diagram of LA apparatus used in our study is shown in Fig.1. LA apparatus consists of growth and preparation chambers and their pressure were 5.0×10^{-9} Torr and 5.0×10^{-7} Torr, respectively. FZ (floating zone)-Si(100) wafers with high-resistance ($\rho = 1 \times 10^3 \Omega \text{cm}$) were used as substrates for LA experiments. Prior to growth, chemical treatment of Si substrate surface was done first by ethanol ($\text{C}_2\text{H}_5\text{OH}$) for cleaning using supersonic cleaner, then by HF ($\text{HF} : \text{H}_2\text{O} = 1 : 50$) for etching and finally by pure water for rinsing. By this treatment, hydrogen terminated Si substrate surface was confirmed to be formed. After this treatment, Si substrate was introduced into preparation chamber for evacuation and de-gassing and then transferred into growth chamber. Poly-crystalline $\beta\text{-FeSi}_2$ targets grown by HGF method were also transferred into growth chamber and were placed at multi-target holder. Target materials were rotated at 10 rpm under ultra high vacuum (UHV).

The self-emission from laser-ablated $\beta\text{-FeSi}_2$ plume was collected by quartz lens and quartz fiber through quartz window equipped with the LA growth chamber. The focused light from excimer laser (Lambda Physik EMG 201, ArF : $\lambda = 193 \text{ nm}$, laser power = 80 mJ, repetition frequency = 5 Hz) that produces LA plume was introduced at irradiation angle of 45 degree (power density = 1 J/cm^2) to the normal of the substrate. The self-emission from LA plume was observed by photospectrometer (Hamamatsu Photonics PMA - 11). *In-situ* observation of deposited $\beta\text{-FeSi}_2$ surface was made by reflection high energy electron-beam diffraction (RHEED) at 30 kV. Under this condition, LA growth of samples were performed for 2 hrs.

Crystallographical characterization of the films was carried out by X-ray diffraction (XRD). Raman scattering measurements were made at room temperature (R.T.) using 1-m focal length double-monochromator (JASCO) and the 514.5 nm line of Ar^+ laser. In order to determine the band-gap energy and the type of optical transition, optical absorption measurements were performed at R.T. with Bomem - DA 8 spectrometer using a quartz halogen lamp as a light source.

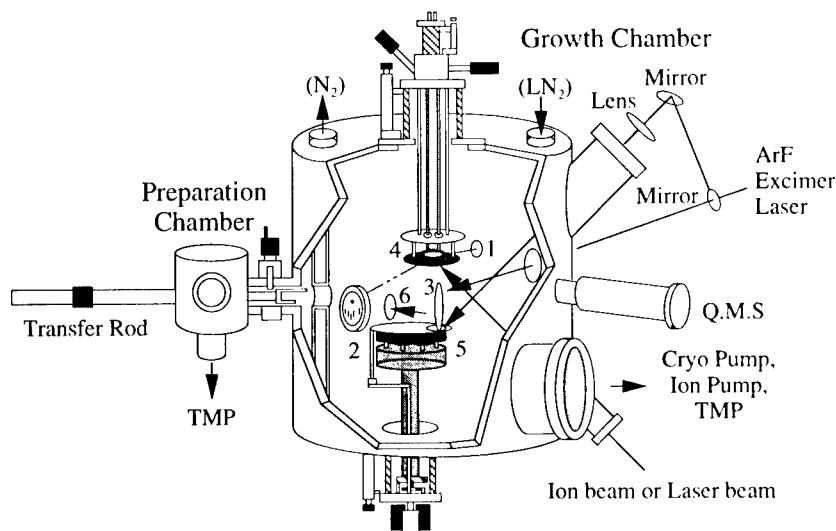


Figure 1. Schematic diagram of LA apparatus. 1. RHEED electron gun, 2. RHEED screen, 3. LA plume, 4. electric bombardment-type substrate heating holder, 5. multi-target holder, 6. plume light and preparation chamber.

RESULTS AND DISCUSSION

A. Diagnosis of laser ablated plume

Laser ablated particles in the plume are classified into three species. The first species having the smallest mass and fastest velocity (kinetic energy and potential energy excited by laser beam are 2~3 eV and 1~40 eV, respectively) [10] form super-sonic molecular beams and are normally used for obtaining high quality LA films. Figure 2 shows the self-emission spectra from β -FeSi₂ particles in the LA plume under UHV condition [11]. Several signals from the first species were observed in the ultra-violet energy range (> 3.0 eV). It is known that laser ablated particles are ordinarily ionized and present light emission. In our configuration as is shown in Fig.1, the temperature elevation of the target material due to the radiation from the heated substrate holder can be minimized by a sufficient separation of the target from the latter. It is expected the change of self-emission spectra deriving from LA plume is generated due to the temperature variation of the LA target material. Emissions, A, D, E and F are particles of Fe atoms or molecules which are dissolved by laser beam and the remaining emissions (B, C, G) are shows Fe-Si related particles.

B. Thermal cleaning of Si substrate surface

In order to remove the hydrogen-terminated surface of Si substrate, the temperature of substrate was raised as high as 1250 °C using electron-bombardment method. RHEED measurements indicated that thermally cleaned Si surface shows streaky (2x1) pattern, however, subsequently, RHEED image of sample showed SiC pattern which is produced by the contamination of gas molecules generated from growth chamber during thermal cleaning.

Table 1. Emissions and assignments in Fig.2

Emission	λ (nm)	Assignments
A	251.25	Fe
B	259.54	Si or Fe-Si
C	262.23	Si or Fe-Si
D	273.99	Fe
E	283.44	Fe
F	287.3	Fe
G	387.16	Fe-Si

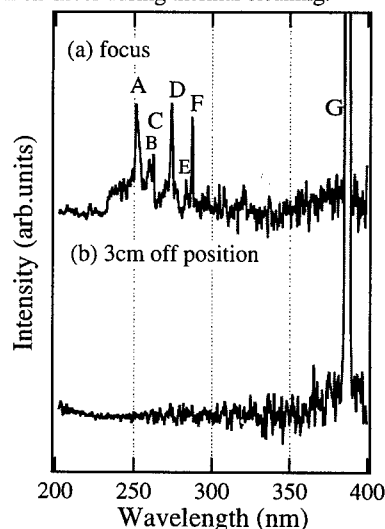


Figure 2. LA plume spectroscopy of β -FeSi₂ bulk crystal target at (a) focused position and (b) 3cm off position from focused one, respectively.

C. Deposition of β -FeSi₂ film on Si(100)

When the growth substrate temperature, T_g was kept at 550~650°C (sample A) and 650 °C~750 °C (sample B), (2x1) surface of β -FeSi₂ was identified in the RHEED pattern. Figure 3 shows RHEED pattern of β -FeSi₂ film on Si(100) substrate. The heteroepitaxial relationship, β -FeSi₂(100)/Si(001) with β -FeSi₂[100] \parallel Si<110> is often defined as type A (T_g =300~550 °C)

and type B ($T_g \sim 750^\circ\text{C}$) [12]. In our experiments, the RHEED pattern of type A and type B were not yet observed. XRD measurements were made to identify the formation of β -phase in the LA-deposited sample. Most of XRD measurements were done for Si(311) plane at incidence angle of 2.83 degree. Figure 4 shows XRD signals for two samples; (a) powdered β -FeSi₂ bulk crystal grown by HGF method used as LA target and (b) β -FeSi₂ film prepared by LA method. In Fig.4 (a), multiple peaks are observed, suggesting that the bulk β -FeSi₂ is poly crystalline-like. In Fig.4 (b), however, a signal at the diffraction angle reflecting β (220) orientation is uniquely notified, implying that LA-grown sample is highly oriented and the promotion of epitaxial crystal growth from well-defined surface lattice of Si substrate is practiced by the LA method. The precise value of the β (220) diffraction angle in Fig.4 (b) is slightly shifted from the standard one for bulk β -FeSi₂. This feature shows the lattice pseudomorphic effect between β -FeSi₂ film and Si substrate with lattice mismatch of $\sim +1.5\%$ by expanding a-b plane and shorting c axis of β -FeSi₂ crystal structure. We calculated the pressure between β -FeSi₂ film and substrate using the XRD datum (d) shown in Fig.4 (b), the standard datum (d_o) and Young's modulus (E) and Poisson's ratio (ν) for bulk β -FeSi₂ crystal [13]. We obtained a stress about 0.2 GPa for the LA-grown β -FeSi₂ film shown in Fig. 4 (b).

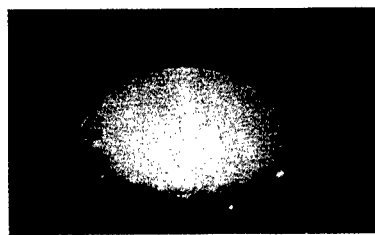


Figure 3. RHEED image of laser ablation grown β -FeSi₂ on Si(100) [110] azimuth using β -FeSi₂ bulk crystal target (sample A). RHEED pattern showed spotty pattern suggesting poly crystalline specimen.

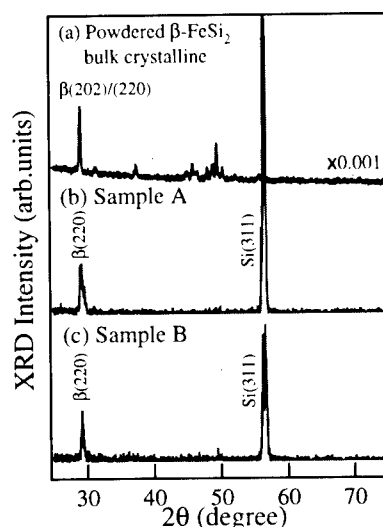


Figure 4. XRD pattern of (a) powdered β -FeSi₂ bulk crystalline, (b) LA grown β -FeSi₂ on Si(100), $T_g=550\text{--}650^\circ\text{C}$: sample A and (c) $T_g=650\text{--}750^\circ\text{C}$: sample B. LA growth samples showed diffraction angle β (220) orientation.

D. Raman scattering

Figure 5 shows Raman scattering spectrum at R.T. for the LA-grown β -FeSi₂ film. In Fig.5 (a), Raman signals are clearly identified at 171.52 cm^{-1} , 190.65 cm^{-1} , 200.6 cm^{-1} and 250.44 cm^{-1} , however, in Fig.5 (b), Raman intensities are low and only half of those in Fig.5 (a) and signal at 171.52 cm^{-1} was not observed. All of these signals are derived from β -FeSi₂ [14]. The predominant signal at 250 cm^{-1} is in good agreement with the theoretical calculation of Raman allowed modes for bulk β -FeSi₂, suggesting that the LA-grown film has a fairly good crystal quality. It is important to note that the energy positions of the Raman signals in Fig.5 are nearly

identical to those obtained theoretically [14], although all experimental signals are slightly shifted towards lower energies (red shift about 0.96 cm^{-1} ~ 4.78 cm^{-1}) compared with the theoretical ones (179 cm^{-1} , 197 cm^{-1} , 206 cm^{-1} and 253 cm^{-1}). This red shift (phonon-softening) implies that the force constants decrease and proclaims that the generation of tensile strain can be ruled out since the red shift (the shift of Raman signal towards lower frequencies) are generally associated with lower lattice parameters. We consider that this effect is due to an increase of the bond length in the vicinity of Fe vacancies or stress existing pseudomorphically in LA grown sample. This situation produces the expansion of lattice constant, which decreases the oscillator strength of the Si-Fe bonds and necessarily leads to the red shift of Raman signals.

E. Optical absorption

The optical absorption spectrum is important to determine the type of optical transition and its energy gap. Figure 6 presents the absorption coefficient (α) versus photon energy ($h\nu$) in which the onset of absorption occurs at $\sim 0.84 \text{ eV}$. In this figure one notes that the sample attains absorption coefficient as high as $3.5 \times 10^4 \text{ cm}^{-1}$ for $h\nu$ above 1.0 eV . Direct and indirect optical absorption are expressed as Eq. (1) and (2).

$$\alpha_{dir} = A(h\nu - E_g^{dir})^{1/2} \quad (1)$$

$$\alpha_{indir} = B(h\nu - E_g^{indir})^2 \quad (2)$$

where E_g^{dir} is the direct and E_g^{indir} is indirect band-gap. From the $(\alpha h\nu)^{1/2}$ versus $(h\nu)$ plots using (1), we obtained a direct band-gap energy E_g^{dir} of $\sim 0.81 \text{ eV}$. The fitting constants of optical absorption A (direct) and B (indirect) were determined to be $1.0685 \times 10^6 \text{ (cm}^{-1} \text{ eV}^{-1/2})$ and $7.71 \times 10^5 \text{ (cm}^{-1} \text{ eV}^{-2})$, respectively. The results of recent band structure calculation [2] have shown that the experimental optical data in the energy region indicated in Fig.6 the direct band-edge is located in the vicinity of the Δ point of the Brillouin zone, whereas the first interband transition of appreciable oscillator strength takes place at the Y point with an energy of 0.85 eV , in agreement with the experimental data for samples prepared by other methods [15]. However we can not

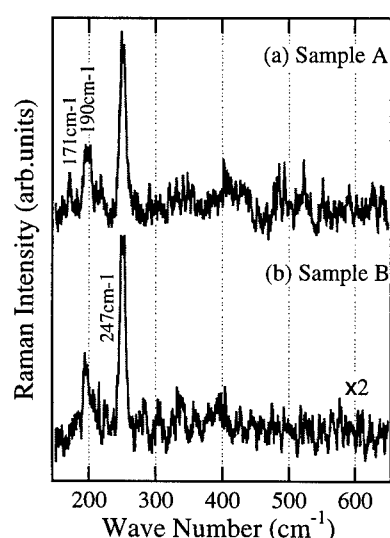


Figure 5. Raman scattering spectra from LA grown β -FeSi₂ on Si(100). (a) $T_g=550\sim 650 \text{ }^\circ\text{C}$: sample A, and (b) $T_g=650\sim 750 \text{ }^\circ\text{C}$ sample B : showed several signals shifting low energy from poly crystalline β -FeSi₂ film.

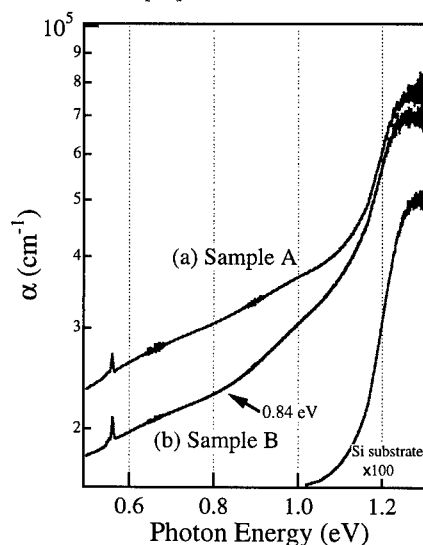


Figure 6. Optical absorption coefficient of (a) $T_g=550\sim 650 \text{ }^\circ\text{C}$: sample A and (b) $T_g=650\sim 750 \text{ }^\circ\text{C}$: sample B at band-edge of poly crystalline β -FeSi₂ film in plots appropriate for direct and indirect transitions.

clearly recognize this onset of the optical absorption in Fig.6 since our samples exhibit strong optical absorption tail on the lower energy side (presumably Urbach tail). The observation of the tail is ascribed to the existing defects and strain in the samples which are previously discussed in the analysis of XRD and Raman scattering measurements.

CONCLUSION

Under ultra-high vacuum ambient, laser ablation growth of stoichiometrically well-controlled β -FeSi₂ film on Si(100) substrate was for the first time fabricated using β -FeSi₂ bulk poly-crystal as a target material. The bulk β -FeSi₂ crystal was prepared by horizontal gradient freeze (HGF) method. Judging from RHEED and XRD measurements, samples grown at substrate temperature 550 °C - 750 °C showed poly-crystalline features and the surface was mostly β (220) oriented. Raman signals from laser-ablated samples showed red energy-shift, suggesting that vacancy and/or stress are existing between grown film and Si substrate. The onset of optical absorption for laser-ablated β -FeSi₂ films were found to take place in photon energy of ~ 0.84 eV. Using the theoretical expressions for direct and indirect optical transitions, the band-gap energy E_g was determined to be 0.81 eV and 0.96 eV for the former and the latter transitions, respectively. These results revealed that β -FeSi₂ is quasi direct band-gap induced by zone-folding effect.

ACKNOWLEDGMENTS

Authors would like to acknowledge F. Watanabe for the design and the fabrication of the electron-bombardment type substrate heating-holder. They also wish to express their gratitude to H.Katsumata, H.Shibata, N.Tsukada, N.Kobayashi, T.Iida, C.Stauter, S.Uekusa, M.Hasegawa, Y.Ishii, T.Tsunoda, S.Kimura, S.Okamura and Y.Takano for helpful discussion.

REFERENCE

- [1] N.E.Christensen, Phys. Rev. **B 42**, (1990) 7148
- [2] A.B.Filonov, D.B.Migas, V.L.Shaposhnikov, N.N.Dorozhkin, G.V.Petrov, V.E.Borisenko, W.Henrion and H.Lange, J. Appl. Phys. **79**, (1996) 7708
- [3] H. Kakemoto, Y. Makita, H. Katsumata, T. Iida, C. Stauter, A. Obara, H. Shibata, Y. Tsai, S. Sakuragi, N. Kobayashi, M. Hasegawa, S. Uekusa and T. Tsukamoto SPIE **2888** 6-7 Nov, (1996) Beijing, China
- [4] Z.Schlesinger, Z.Fisk, Hai-Tao Zhang, M.B.Maple, J.F.DiTuas and G.Aeppli, Phys.Rev.Lett. **71**, (1993) 1748
- [5] A.R.Moodenbaugh, D.E.Cox, C.B.Vining, and C.U.Segre, Phys. Rev. **B 29**, (1983) 271
- [6] C.H.Olk, S.M.Yalisove, J.P.Heremans, and G.L.Doll, Phys. Rev. **B 52**, (1995) 4643
- [7] O.Kubaschewski: Iron-Binary Phase Diagram, Springer-Verlag, New York, (1982) 136
- [8] H.Kakemoto, Y.Tsai, A.C.Beye, H.Katsumata, S.Sakuragi, Y.Makita, A.Obara, N.Kobayashi, H.Shibata, S.Uekusa, T.Tsukamoto, T.Tsunoda, and Y.Imai, Mat. Res. Soc. Symp. Proc. **402**, (1996) 331
- [9] C.H.Olk, S.M.Yalisove and G.L.Doll Phys. Rev. **B 52**, (1995) 1692
- [10] H.Fukumura, H.Nakaminami, S.Eura, H.Masuhara, and T.Kawai, Jpn. J. Appl. Phys. **28**, (1988) L4412
- [11] N.Inoue, S.Kashiwabara, S.Toshima and R.Fujimoto, Proc. of LAMP '92, Nagaoka (June, 1992) 1105
- [12] K.M.Geib, John E.Mahan, Robert G.Long, Menachem Nathan and G.Bai, J. Appl. Phys. **70**, (1991) 1730
- [13] A. Kinbara and H. Haraki, Jpn. J. Appl. Phys. **4**, (1965) 243
- [14] K.Lefki, P.Muret, E.Bustarret, N.Boutarek, R.Madar, J.Chevrier, J.Derrien, and M.Brunel, Solid State Commun **80**, (1991) 791
- [15] H.Lange, W.Henrion, B.Selle, G.-U.Reinsperger, G.Oertel, and H.von Känel, Appl. Surf. Sci. **102**, (1996) 169

THERMOELECTRIC COOLING CONTAINER FOR MEDICAL APPLICATIONS

A.A. AIVAZOV*, Y.I. SHTERN*, B.G. BUDAGUAN*, K.B. MAKHRACHEV*,
M. PASTOR**

* Moscow Institute of Electronic Technology, 103498 Moscow, Russia

** NTE, 08186 Barcelona, Spain

ABSTRACT

In this work the thermoelectric cooling container for storing and transportation of the medicine, particularly for insulin, is discussed. In the working volume the temperature is supported on the level of +4°C. The container can work in two operating conditions: with the power supply and without the power supply. Two removable blocks are used for this purpose. One block (thermoelectric) is used for the work with the power supply and another (passive)-for the work without power supply.

The thermoelectric block has a 12V power supply, which is used in the automobiles, yachts and other kinds of transport. The temperature in the working volume is supported by the use of the Peltier effect. An electronic device is used in this block and stabilizes temperature on the level of +4°C and indicates information about working conditions. The thermoelectric container has a power supply block for work at 220(110)V.

The working temperature in the container can be maintained in the absence of the power supply. In this case the necessary temperature conditions are supported by melting of the crystallized salt. For this purpose the container has a hermetic volume containing this salt and contacting with the working volume.

INTRODUCTION

Thermoelectric cooling devices have found their place in various fields of human activity since A.F. Ioffe grounded half-century ago the possibility of practical application of the Peltier

effect. In a number of applications - in military equipment, medicine, laser devices, computers etc., thermoelectric method of cooling is the only acceptable method. In particular, this circumstance is connected with increasing of number of semiconductor devices and IC, where thermoelectric cooling devices (TECD) are used for cooling and temperature stabilization. Application of TECD improves essentially characteristics of electronic devices, makes their operation more reliable and stable, enhances response speed, nonstability etc.

Thermoelectric devices have a number of advantages in comparison with other systems of thermostabilization, namely: practically unlimited operating resource, absence of cryogen reliability, small dimensions and weight, low delay, noiseless operation, independence on space orientation, possibility of local cooling, accurate regulation and stabilization of temperature.

The thermoelectric method of cooling acquires the utmost topicality in the connection with the signing in the 1987 of the Montreal protocol by all leading countries, that commits them to decrease the application of freon gaseous mixtures dangerous for the ozone layer of earth's atmosphere. The main field of application for these gases is in refrigerator equipment. As was recognized by the whole world community, the only alternative today are solid-state heat pumps on semiconductor cells, using the Peltier effect.

The basic limitation, restraining the mass application of Peltier effect in cooling systems, is the insufficient efficiency of this method. The latter is determined basically by low thermoelectric figure of merit of semiconductor materials based on bismuth telluride. Unfortunately, the alternative for these materials has not been found yet.

At the same time, it is necessary to note, that the advantages of thermoelectric method of cooling haven't yet been completely used. This statement is confirmed by the permanent expansion of fields, where the Peltier effect is applied, and by enhancement of a number of new devices.

Authors of this paper performing orders of military industry during 25 years accumulated the richest experience in the field of high technologies of cool production and equipment of thermostabilisation for vital units of space and military equipment [1-3]. At the same time the number of thermoelectric devices and thermoelectric equipment of wide consumption were designed and are being designed. Some of them are following: portable and stationary refrigerators; air chillers including devices for means of transport: cooled container for the transport of vegetables, fruits, flowers; cooled container for the trade of food; coolers-heaters of liquids (drink); units for cooling and thermostabilisation of laser equipment and optoelectronic

communications lines; thermoelectric thermostats; climatic cameras; thermoelectric technological equipment, for example, the set for the checking of completeness of windows exposing in dielectric layers for the production of integrated circuits.

The Peltier effect is used in medicine for cooling instruments (ophthalmology), manufacturing of low-temperature cameras for keeping and transporting of blood and human organs.

In this work we shall consider in details the thermoelectric container for keeping and transporting of medicinal preparations and particularly insulin. This preparation must be kept at the temperature from 2 to 10°C. It is important for diabetics to keep this preparation by them during different moves and other occasions, in particular, when power sources, providing the operation of devices is absent.

RESULTS

The authors have designed the thermoelectric insulin container keeping the temperature inside its volume at 4°C. The application of this container assumes its operation in two different modes: with a power source and without it. Two removable blocks were provided for this purposes. One of them - thermoelectric (active), that operates from the electrical network +12V-supply board of car, yacht and other means of transport. The second, passive, is intended for operation without a power source. The main frame of container 1 (fig.1) consists of working space 2, where the container with preparation 3 is placed. The hermetic cylinder 4 is made coaxial to working space. The hermetic cylinder is filled by melted salt 5 with a crystallization point of 4°C. The design of the container provides good heat contact of salt with the walls of working space. The cylinder for the salt and the frame of working space are made from material with high heat conductivity. The working space and the cylinder with the salt are insulated from the external medium by the material (6) with a low heat conductivity ($\sim 0,03 \text{ W/m}^{\circ}\text{K}$). This material can be, for example, the foam. The cover 7 closes hermetically the working space and is the basis where the chamber with preparation is fastened.

Two blocks, active and passive, can be attached to the main frame depending on the situation. Blocks have centering guides 8, which are fixed reliably by pressing keepers, placed in the main frame. This design allows one to orient blocks correctly with respect to the main frame. For separation of the block from the frame, it is sufficient to press on two buttons 9, located on

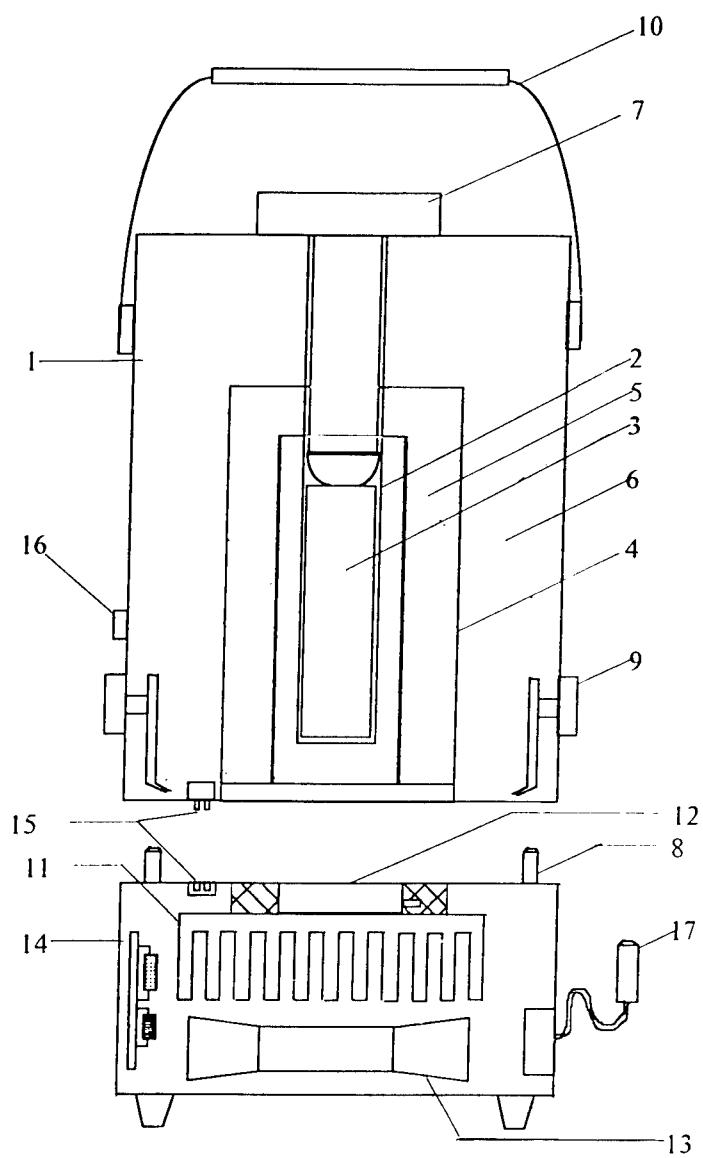


Fig.1 The scheme of the thermoelectrically cooled container for the transportation of insulin.

the lateral surface of the frame. The container is furnished by the handle 10 for the comfort of transportation. The temperature pickup is placed in the working volume near the chamber with the preparation.

The active block consists of the radiator 11, where the thermoelectric module 12 (TEM-1,4-1,5/127) is fastened. The characteristics of the module are the following: supply voltage +12V, current 4A, dimensions (40*40*4) mm. The fan 13 is also installed on the radiator. The plate with the electric circuit 14 is connected with the temperature pickup by the plug 15. The plate is intended for the control of thermoelectric module to stabilize the temperature inside the working space. LEDs 16 placed on the block indicate the mode of container operation. The active block has the plug for the connection to the board supply.

The passive block is intended for heat insulation of the working space when the active block is removed. It contains the plate 17 with electric circuits checking the temperature and the electric cell (accumulator).

The scenario of container operation depends on start conditions. The most favorable version (#1) is the following. Before being moved the container with preparation was in the stationary refrigerator at the temperature no more than 4°C. In this case the salt has been crystallized and the initial temperature in the working volume <4°C. During the movement the container is connected with the board supply and the optimal temperature is maintained in the working space by means of thermoelectric cooling. If the power supply is absent by some reasons so the temperature of 4°C is achieved due to salt melting. In this case the passive block must be attached to the main frame. Both salt mass and heat insulation of working volume were calculated to provide keeping the temperature at 4°C during 10 hours. The operating time in passive mode was calculated as:

$$\tau = Q/q,$$

where $Q = h \cdot m$ - the energy of phase transition;

h - the specific heat of melting;

m - the salt mass;

q - the heat leakage through the walls of container.

The second version differs from the first one by the initial temperature of the working volume that is the same as the temperature of surroundings. After the connection the container

with the board supply the optimal temperature is provided by means of thermoelectric cooling. The container achieves the optimal temperature in a working time of 40 min.

CONCLUSION

The thermoelectric cooled container for transportation of insulin operating from +12V electric network was designed. The operation of container in two modes (with power supply and without it) is provided by two different removable blocks attached to the main frame of the container. The optimal temperature in the working size (4°C) is achieved for 40 minutes after connection to the power supply. The method thermostabilization and heat insulation provide maintaining optimal temperature for 10 hours after the power supply is switched off.

REFERENCES

1. A.A. Aivazov, Y.I. Shtern, O.A. Baskov, Patent of USSR # 1512433 from 09.08.1989
2. A.A. Aivazov, Y.I. Shtern, O.A. Baskov, Proc. of IX International Conference on Thermoelectricity, USA, CA, Pasadena, March, 1990, p.174.
3. A.A. Aivazov, Y.I. Shtern, K.B. Makhachev, 14 Inter. Confer. on Thermoelectrics, St.Peterburg, Russia, June 1995, Abstracts p.32.

OVERVIEW OF INDUSTRY INTEREST IN NEW THERMOELECTRIC MATERIALS

H.B. LYON JR.

Thermogenics Business Team, Marlow Industries Inc. 10451 Vista Park Road, Dallas, TX
hlyon@marlow.com

ABSTRACT

The technology base for air conditioning, refrigeration, component cooling below ambient temperatures and power generation will be required to meet several new challenges. The main lines of these challenges will be presented in a way which relates them to the several new thermoelectric materials and materials engineering options being pursued by the research community. The potential benefits of thermoelectric devices are only partially met by enhancing the figure of merit ZT , the nature of the design challenge and the resulting systems approach are presented. The research and the industry are entering into a new era.

INTRODUCTION

In 1958, Abram Joffe (Ioffe) concluded his Scientific American article[1], "... thermoelectricity is unfolding before our eyes. It is only in the last two or three years that this field has been opened. Let us see what will happen in the next three to five years." In this article he referred to the performance of the best materials as being able to convert heat to electricity with an efficiency of about 10 per cent. When referring to use of thermoelectrics in the refrigeration mode he was less specific about the efficiency but did acknowledge the great disparity between thermoelectrics and the efficiency of large vapor compression systems. He also indicated some kind of parity in efficiency between thermoelectrics and very small vapor compression systems.

14 years later, the assessment "Thermoelectricity, The Breakthrough that never came"[2] reported that 64 firms had been engaged in a full-scale effort to find better materials in the period from 1958-1963. The article estimated that the resources spent totaled \$30 million (est \$130 million in \$1997). However, by 1971 there were only five firms remaining; the major firms active today can trace their roots back to those remain five.

One of the reasons Ioffe's expectations didn't materialize in the 3-5 year window was the extraordinary success of the Freon based Rankin Cycle compressors. The introduction of this technology was met with wide acceptance. Mechanical engineers were presented with a very cost effective solution that was widely embraced by society.

This magnitude of growth in the use of CFC's is one indicator of the growth in this industry, this growth is shown in **Figure 1**[3].

The introduction of refrigeration into homes, autos, factories, schools changed all of our lives; opening up new paths of regional development, new functions in the supply chains of food stuffs; these are only a few of the innumerable scenarios imbedded in the history of refrigeration and airconditioning. Ioffe's expectations were obviously aware of this growth in application. The refrigeration systems and their compressors became very inexpensive in both their acquisition costs and their life cycle costs. Their efficiency in many applications was improved until efficiencies equaled or exceeded 50% of the theoretical maximum Coefficient of Performance (COP) namely, that of Carnot efficiency.

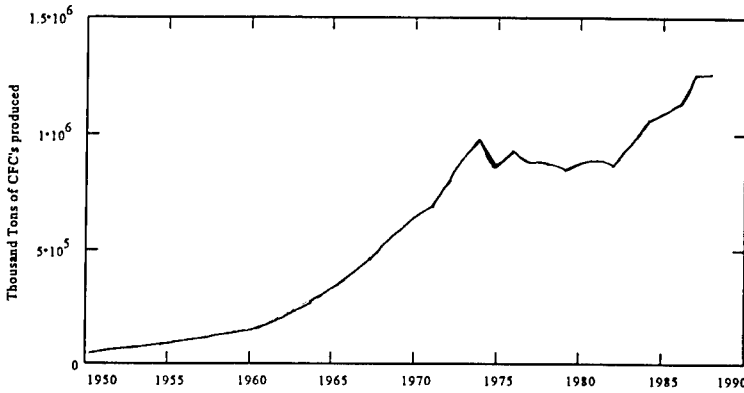


Figure 1

This maximum possible COP is the consequence of the laws of thermodynamics, and can be stated in formula as:

$$Carnot\ Efficiency = \frac{T_{cold}}{[T_{hot} - T_{cold}]} \quad (1)$$

A necessary component of an industry perspective for a refrigeration system is its Coefficient of Performance as a percentage of *Carnot Efficiency*. The Coefficient of Performance as used in this formulation is:

$$Coefficient\ of\ Performance = COP = \frac{Heat\ Pumped}{Power\ Required} = \frac{Q_{cold}}{W} \quad (2)$$

In terms of *Carnot Efficiency* (%) this becomes:

$$Carnot\ Efficiency\ (%) = \frac{Q_{cold} \cdot [T_{hot} - T_{cold}]}{W \cdot T_{cold}} \quad (3)$$

For the sake of comparison, we shall use the Carnot efficiency of a vapor compressor system and compare that with thermoelectric efficiency. To make this comparison we utilize the Carnot efficiency of a compressor in terms of the heat pumping system capacity. One representation of this is shown in **Figure 2** [4]. This reaffirms Ioffe's perception of 1958.

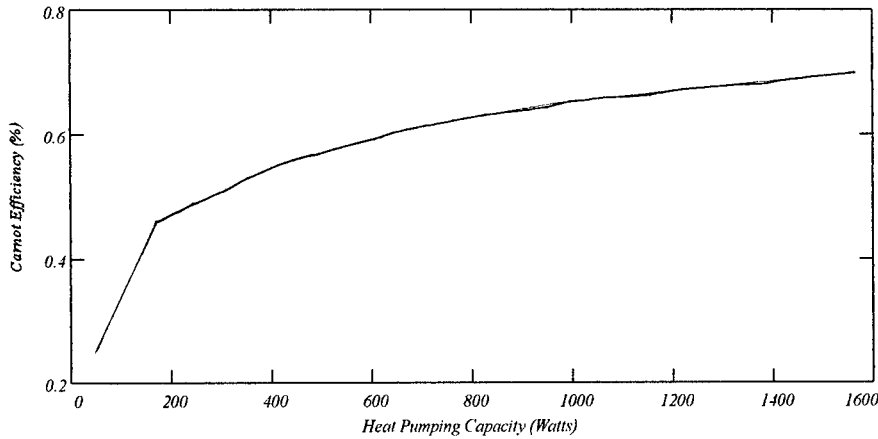


Figure 2

The beginning of the analysis starts with the formulation first presented by Altenkirch in 1911[5]. The basic equations for the heat pumped (Q_{cold}) and input power (W) are given as:

$$Q_{cold} = \alpha_{cold} \cdot i \cdot T_{cold} - \frac{1}{2} i^2 \rho_{ave} \frac{l}{A} - \lambda_{ave} \frac{A}{l} (T_{hot} - T_{cold}) \quad (4)$$

$$W = \left[i \rho \frac{l}{A} + (\alpha_{hot} T_{hot} - \alpha_{cold} T_{cold}) \right] \cdot i \quad (5)$$

When equations (4) and (5) are optimized for the maximum performance which can be obtained from a given material, the equation for the figure of merit of the material is the result. This is given as:

$$Figure\ of\ Merit = ZT = \frac{\alpha^2 T}{\rho \lambda} \quad (6)$$

Where: α = Seebeck Coefficient
 ρ = electrical resistivity
 λ = thermal conductivity

More importantly, this value of ZT when the material is operating in the extrinsic mode scales with temperature. Actual data for an average material is presented in **Figure 3**.

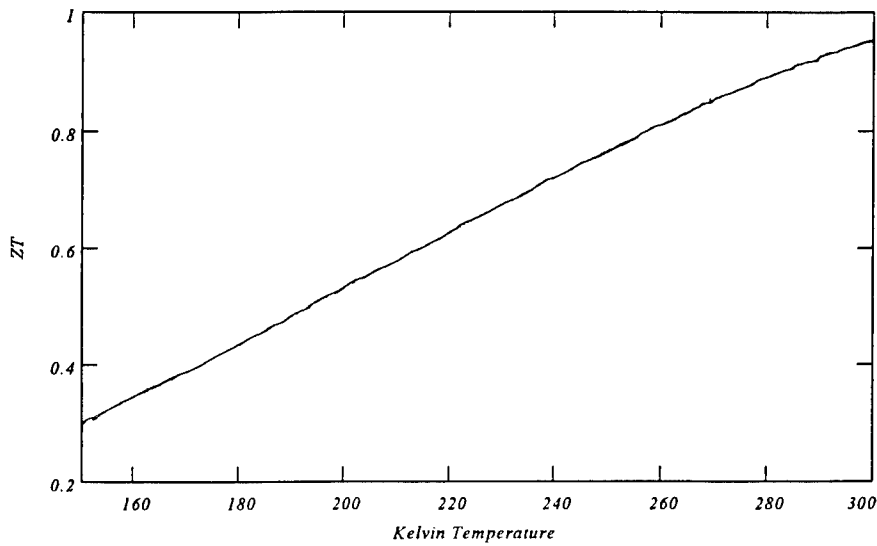


Figure 3

The data from **Figure 3** can be reduced to equation (7) .

$$ZT(T) = 0.004676 T - 0.4043 \quad (7)$$

This mathematical representation allows us to calculate parameters for comparison with the efficiencies of vapor compression systems. The equations of Altenkirch, and particularly those derived by our Russian colleagues [6] allows us to define the maximum temperature difference of a device when the heat pumped is zero in terms of ZT in equation (8).

$$\Delta T_{\max}(T) = [T_{\text{hot}} - T_{\text{cold}}] \times \left[\frac{\sqrt{ZT_{\text{ave}} + 1} - 1}{\sqrt{ZT_{\text{ave}} + 1} + 1} \right] \quad (8)$$

When various hot side temperatures are considered, the calculated value is shown in **Figure 4**. This figure is idealized and doesn't account for the radiation, convection and interconnect resistances which are clearly involved in real devices. However, even without these corrections, the quoted values listed in the literature for most of the thermoelectric manufacturers are close to the calculated values.

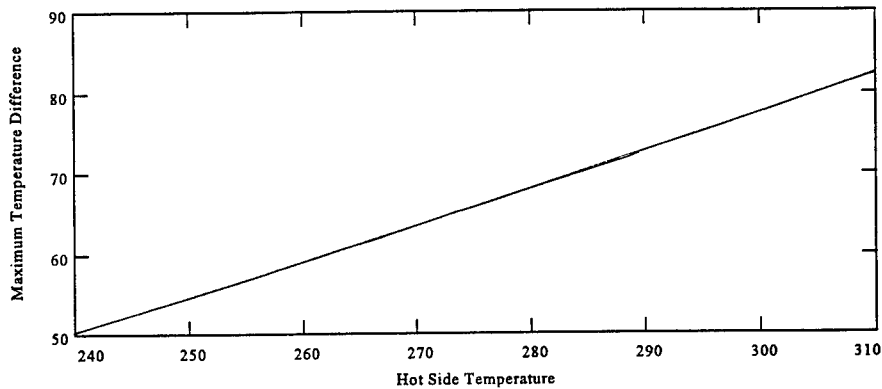


Figure 4

The parameter ΔT_{\max} in Centigrade leads to the calculation of the Coefficient of Performance and % of Carnot efficiency. This calculation uses equation (9) .

$$\text{Carnot Efficiency (\%)} = \left[\frac{\Delta T_{\max} - \Delta T_{\text{used}}}{2 \times T_{\text{cold}}} \right] \quad (9)$$

The workhorse thermoelectric material in a refrigeration setting (Temperatures between 300 K and 270 K) has a value near to 10% of Carnot Efficiency. This has remained the same for 40 years. Furthermore, the % Carnot Efficiency decreases as the ΔT_{used} is increased, nearing zero as the ΔT_{\max} is reached **Figure 5**.

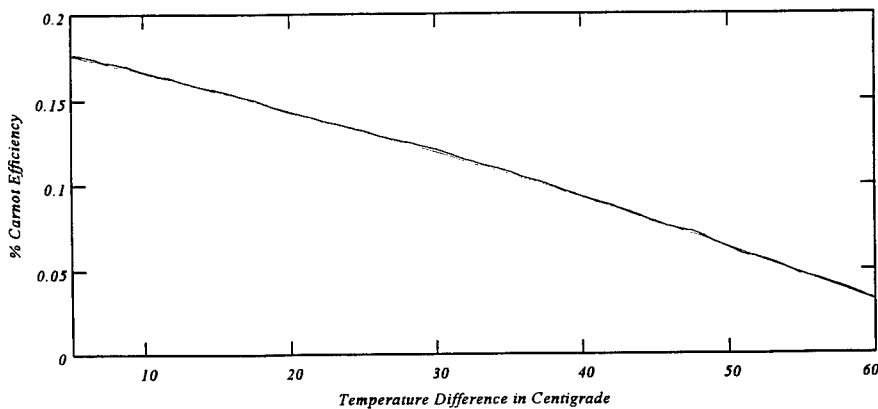


Figure 5

Comparison of this data **Figure 5**, for thermoelectrics, with **Figure 2**, for vapor compressors, establishes the basis for industries perspective of thermoelectrics for the past 40 years.

From this perspective the 10% of Carnot Efficiency provided by thermoelectric devices, leads to their being limited in application to capacities of 50 watts per device. Before leaving this analysis let us consider in **Figure 6** what would happen when we improve ZT. This chart when compared with **Figure 2** demonstrates that a ZT of 4.0 would open up vapor compressor applications for heat loads of 100 - 200 Watts per device (that is systems presently powered by $\frac{1}{2}$ and $\frac{3}{4}$ horsepower motors).

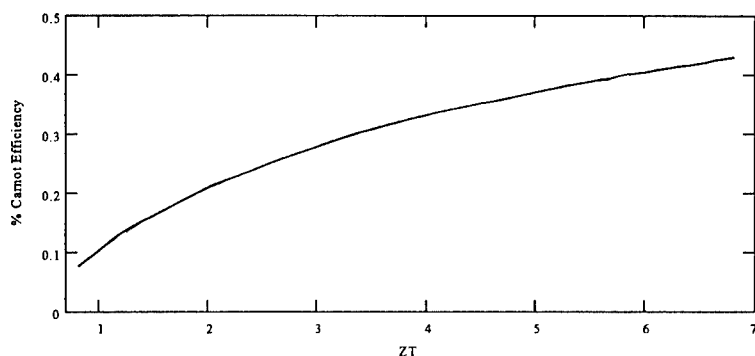


Figure 6

THE BASIC PROPOSITION

The basic proposition presented herein is that the interest of industry for thermoelectrics is defined in part by improvements in ZT. During the first era of a full scale effort to improve material performance, in the period 1958-1963, a ZT of 3.0 was the goal. Now the efficiency of alternatives is such that a ZT of 4.0 would be required for the large impact that Ioffe envisioned in 1958. Values of this magnitude do appear feasible[7][8].

Fortunately, the socket by socket replacement of vapor compressors for refrigeration is not the only route to increased usage in industry. There are numerous applications emerging which can transform even marginal improvements in materials into systems level improvements which are competitive with alternate technologies.

Therefore the other part of industries interest, which may be even larger, is tied up in systems level aspects. Therefore, a second part of the basic proposition presented herein is that, there are several attractive systems level interests which can result from incremental improvements in thermoelectric performance; but only if the other characteristics of thermoelectrics are proven. While this presentation focusses on refrigeration, a similar development and conclusion is equally applicable to power generation.

A key conclusion to this argument is that many of these systems compatibilities are tied directly to the very same material characteristics which define ZT. Example: the type of bonding which appears to contribute to good thermoelectric properties also defines a coefficient of thermal expansion which could be troublesome.

Therefore, a renewed interest by industry in thermoelectrics is emerging; it is going to be an interest in more than ZT; and will include a very sophisticated ability to evaluate what kind of systems performance will result.

To begin to build this bridge the following systems aspects will be covered: heat sinks, current for maximum efficiency or power, and aspect ratio.

Heat Sink Resistance

The importance of heat sink resistances can be shown by referring to **Figure 5**. The resistance of a heat sink is around $0.15\text{ }^{\circ}\text{C}/\text{Watt}$. For a 50 Watt load and a Coefficient of Performance of 1.0, this would mean that 100 Watts would have to be dissipated through a heat sink. This additional temperature is imposed across the thermoelectric device adding 15°C to the ΔT .

Referring to **Figure 5** would indicate the impact of adding this temperature difference to the 40°C of the refrigerator. This would reduce the Carnot Efficiency of the thermoelectric device by one-half. In this case the system level efficiency is defined as much by the passive parts of the thermal pathway as by the thermoelectric efficiency.

Current and COP optimization

The current used to obtain maximum heat pumping in thermoelectric devices is quite different from the current for maximum efficiency. This can be shown in **Figure 7** and **Figure 8** for a present design.

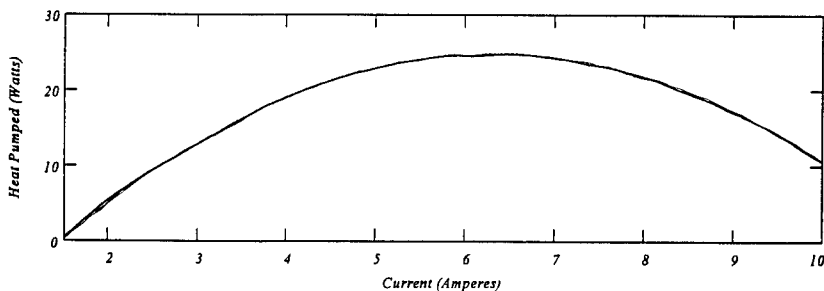


Figure 7

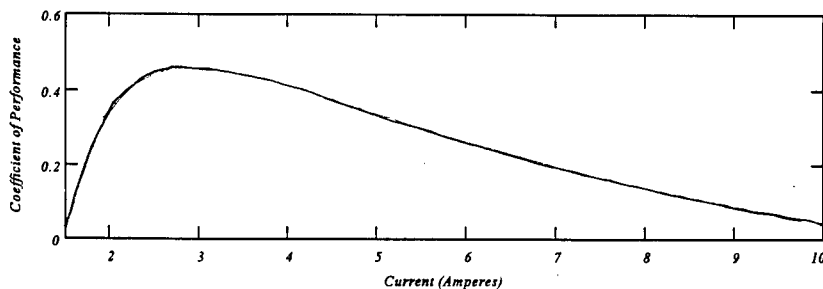


Figure 8

Comparison indicates that the maximum efficiency exists when the device is pumping about one half of the maximum heat it can pump, and that the maximum heat pumping occurs when around half of the efficiency is available.

The obvious question raised at this point in time is whether it is possible to increase the number of elements to achieve the necessary amount of heat pumping while operating at the COP maximum. The answer is that the Coefficient of Thermal Expansion, the durability of the thermoelectric material and cost factors define the maximum number of elements that can be incorporated in a device. When looking towards the future keep in mind that this same analysis indicates that the disparity between these two currents increases as ZT increases.

Aspect ratio (length/area)

One of the issues that will arise as "Engineered Material Films" are introduced is that the aspect ratio of the material will be important to the performance of the device. The COP equation yields the conditions for the optimum length/area for a device. There is one current for the optimum performance of a thermoelectric device for any given length/area. This current for maximum COP as a function of length over area can be calculated. If these dimensions are not utilized the reduction in COP as a function of COP maximum can be shown in **Figure 9**.

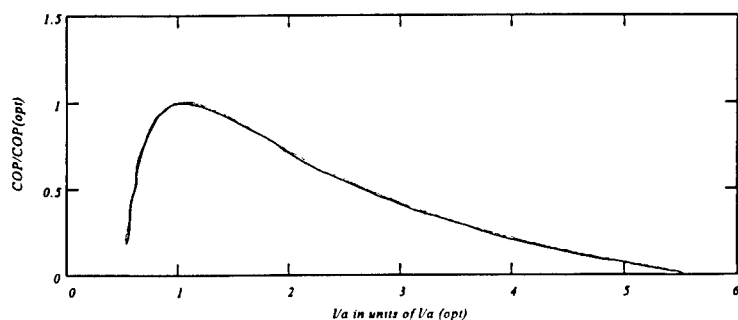


Figure 9

Quantum Wells

Device design challenges face us as we address quantum wells and superlattices. For the purpose of this discussion let us consider that the composition of a layered structures has 10,000 repeating units of multiple layers with angstrom thickness, which results in a composite element (chip) $30\mu\text{m}$ thick (0.003 cm) and 1 cm wide on each side.

When addressing Quantum Well superlattices, where the current flows in the plane of the film, we will have an l/A ratio of over 300 cm^{-1} . When addressing superlattices, where the current flows perpendicular to the plane of the film, the l/A ratio is 0.003 cm^{-1} . In both cases it is obvious that some additional replication of chips or processing of the films will be necessary to achieve an optimal l/A ratio.

MATERIALS OPTIMIZATION

40 years of research in the bismuth and bismuth telluride family of alloys have exhausted every known bulk material option that could be conceived. Thus we are not aware of any significant improvement in material performance applicable to the refrigeration and air conditioning marketplace based upon these materials in bulk form. A similar conclusion can be made for the materials applied to power generation.

However, there are four paths of departure from this stagnation which together contribute a significant new potential, particularly from systems level perspective. These paths are:

- new material systems,
- superlattices.
- renewed optimization of materials in the 100-200 kelvin region
- new instruments with which to assess material characteristics.

The industry interest will be peaked when the academic interest in material parameters is realistically evaluated from a systems perspective. ZT alone is not enough.

New Materials

The thermoelectric potential of new materials must be described in terms of two parameters: (1) weighted mobility (which includes the number of valleys) and (2) lattice thermal conductivity. The description should include the coordinates of the material on a two dimensional chart and a description as to whether those coordinates are within striking distance of ZT greater than 1.0. **Figure 10** displays the $ZT = 1.0$ solution for the β equations[9] which provide the dimensions of this description. The vertical axis is in terms weighted mobility ($\text{m}^2\text{V}^{-1}\text{sec}^{-1}$) and the horizontal axis is in terms of ($\text{Wm}^{-1}\text{K}^{-1}$).

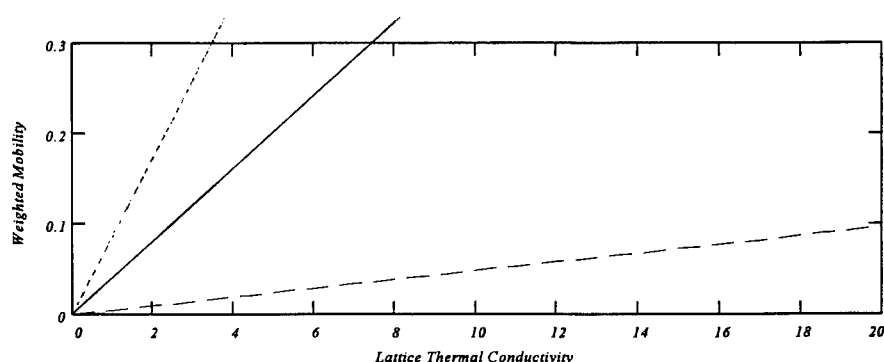


Figure 10

The left hand dotted line is the $ZT = 1.0$ line for 100 K (using a $3/2$ scattering parameter), the solid line represents $ZT=1.0$ for 300 K (using a $1/2$ scattering parameter) and the dashed line represents $ZT=1.0$ for 700 K (using a $1/2$ scattering parameter). On such descriptions it is possible to communicate the importance of minimum lattice thermal conductivity, as well as the maximum mobility that must be achieved.

At the present time experimentalists have a number of useful tools to use to enhance weighted mobility and reduce lattice thermal conductivity. It is also possible to establish[10] a well-

defined value for the minimum lattice thermal conductivity of each material. Presentations of the type proposed will enhance the communication of the potential of new materials between academia, government laboratories and industry.

One of the most exciting new concepts from this authors vantage is the emergence of "placing fillers in cage like systems". This concept first became visible by the reduction of thermal conductivity achieved by the filling of Skutterudite compounds[11]. While the concept still needs to be fully evaluated, achievement of order of magnitude reduction in lattice thermal conductivity without creating unrecoverable destruction of weighted mobility is a reasonable expectation.

Several other issues emerge when addressing industries interest in new materials however space doesn't allow more than a topical listing. The agenda includes such items as: temperature dependence of ZT in the various temperature ranges of application, material anisotropies, coefficient of thermal expansion, contact resistance, strength in tension and compression, mechanical failure modes, processing cost, and material cost.

Superlattices

Quantum confinement or phonon destruction of known thermoelectric systems through superlattices provides us with a new potential for the known bulk materials.

For Quantum wells the 2 dimensional (2D) quantum confinement with its enhancement in weighted mobility is now proven[12] for Lead Telluride. The experimental verification of a three dimensional ZT is the next milestone to be approached. This result when achieved will define the heat pumping potential of these "engineered materials" as well as demonstrate the degree to which the barrier material detracts when converting the 2D enhancement to a 3D parameter.

Superlattices containing differing layers of thermoelectric materials can achieve enhancement of ZT primarily through phonon destruction in the direction perpendicular to layers[13].

For both formats, establishing economic production of "chips" with realistic length/area ratios are the next item on the agenda. In both cases it is important to achieve epitaxial growth for 10,000 or more layers with the other thermoelectric materials.

Renewed optimization of materials in the 100-200 Kelvin region

There are several applications which require enhanced performance of materials below 200 K. This is a domain where one of the best thermoelectric materials, the BiSb alloys, has yet to become a production material. The major reason is the fragile nature of the material. Significant research in these compounds continued for about ten years after the last major effort. However, there are several applications where these and other existing thermoelectric materials can be integrated into hybrid systems with very favorable results[14]. Recently, the results of several years of investigations, and a demonstration under a NASA contract[15], resulted in the shifting of the temperature of peak Z to 175 K for p-type Bi₂Te₃ alloys **Figure 11**.

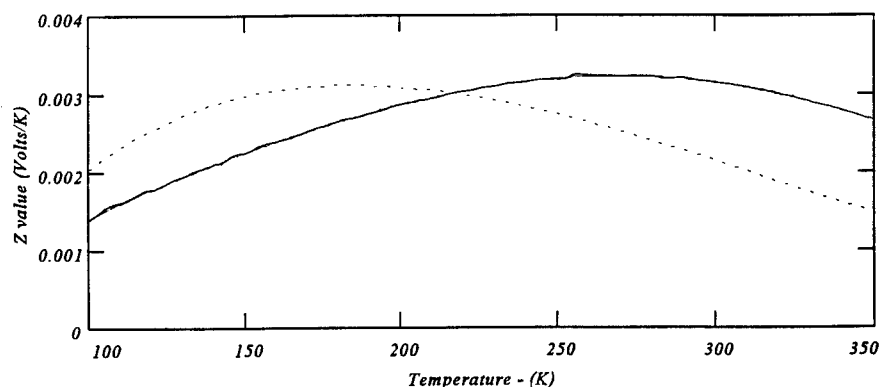


Figure 11

This material improvement resulted in the predicted increase in the performance of a device already in production. This improvement in material performance results in the potential for systems level improvements in: performance, efficiency, reduction in unit acquisition cost or reduction in life cycle costs. The choices are up to the customer as to how to optimize the tradeoffs. Industry also looks for ways to integrate thermoelectric materials into other technologies. The benefits of such hybridization are more efficient systems, enhanced ability to match cooling capacity to specific systems needs, the ability to handle large shifts in heat loads, and temperature stabilization. To accomplish this performance the ability to shift the peak performance of a material as shown in **Figure 11** becomes very important. There will be a strong interaction between the materials scientists and the systems engineer in this type of application.

New instruments with which to assess material characteristics

The answer to questions being posed by industry will require oriented (in plane and cross plane, and anisotropic) measurements of all key parameters from which weighted mobility and lattice thermal conductivity are derived, and direct measurement of the transport properties which define thermoelectric performance. These measurements need to be repeatable and confirmed by independent measurements over wide ranges of temperature. It would also be desirable if these new techniques would be independent of sample size.

CONCLUSIONS

From the vantage point of this industry observer, the application of thermoelectric materials is entering into a new era. It is an era characterized by laboratory confirmation of principles, new problems emerging which need temperature stabilization, requirements for controlling the rate of change of temperature and exciting new proposals for enhanced performance materials. The era will be characterized by: the emergence of new forms of collaboration between users and researchers, the integration of several new tools from the physics and chemistry communities, systems level evaluations of potential early in the research cycle and significant opportunities which will be open to the thermoelectric option for relatively short periods of time.

ACKNOWLEDGMENTS

The support of Marlow Industries Inc. through the Thermogenic Business Unit is acknowledged. Many aspects of the work represented in this paper resulted from effort supported by NASA and DARPA under NAS 9-19358.

REFERENCES

1. A.F. Joffe, Scientific American, **199**, 5, p. 31 Nov .(1958).
2. C.J.Lynch, "Thermoelectricity: The Breakthrough That Never Came", Innovation p. 48-57 (1971)
3. Data taken from Dupont literature.
4. Marlow Industries Inc. internal study on micro compressors.
5. E. Altenkirch, Physik. **XII**, 920 (1911)
6. B. Gol'tsman, B. Kudinov, I. Smirnov, Nauka. (1972) Translated by US Army AD 783734
7. G.A.Slack, in CRC Handbooks of Thermoelectrics , edited by D.M.Rowe (CRC Press, Boca Raton, 1994)
8. G.Mahan, B.Sales, J. Sharp, Physics Today, p. 42, (March 1997)
9. R.P.Chasmar, R. Stratton J.Electronics and Control, **7**, p. 52, (1959)
10. G.A. Slack, in Solid State Physics, Vol.34, p. 1 (1979)
11. T.M.Tritt, G.S.Nolas, G.A.Slack, D.T.Morelli, A.C.Ehrlich, D.J.Gillespi, and J.L.Cohen, J.Appl.Phys. **79**, 8412 (1996)
12. L.D.Hicks, T.C.Harman, X.Sun, M.S. Dresselhaus, in 1966 Proceedings, Fifteenth IEEE International Conference on Thermoelectrics(ICT) IEEE p. 450, (1996)
13. R. Venkatasubramanian, T. Colpitts, E. Watko, and J.Hutchby in 1966 Proceedings, Fifteenth IEEE International Conference on Thermoelectrics(ICT) IEEE p. 454. (1996)
14. H.B.Lyon Jr., J. Bierschenk, in XIV International Conference on Thermoelectrics, p. 481, (1995)
15. H.B. Lyon, Final Report, NAS 9-19358, (1997)

ADVANCED THERMOELECTRIC MATERIALS AND SYSTEMS FOR AUTOMOTIVE APPLICATIONS IN THE NEXT MILLENNIUM

DONALD T. MORELLI

Physics & Physical Chemistry Department, General Motors Research and Development
Center, 30500 Mound Road, Warren, MI 48090 dmorelli@notes.gmr.com

ABSTRACT

A combination of environmental, economic, and technological drivers has led to a reassessment of the potential for using thermoelectric devices in several automotive applications. In order for this technology to achieve its ultimate potential, new materials with enhanced thermoelectric properties are required. Experimental results on the fundamental physical properties of some new thermoelectric materials, including filled skutterudites and 1-1-1 intermetallic semiconductors, are presented.

INTRODUCTION

With the potential for new thermoelectric (TE) materials with enhanced properties on the horizon, several key applications of TE devices in the automotive industry have been identified [1]. Chief amongst these are the use of a thermoelectric generator for the conversion of waste exhaust heat to electricity and the application of TE heating and cooling systems for climate control. Prototype exhaust gas generators for both passenger cars [2,3] and diesel trucks [4] have actually been built, tested, and shown to generate very modest amounts of electrical power. As in other large scale applications of TE's, the limited conversion efficiency in power generation mode and coefficient of performance (COP) in refrigeration mode render such applications economically and technologically unfeasible. Recently, however, it has been suggested that an increase in the dimensionless thermoelectric figure of merit ZT by as much as a factor of two over that of state of the art materials might be physically attainable [5]. This rather bright prospect for the availability of materials with enhanced properties combined with a variety of environmental and economic considerations have led to a critical reassessment of the use of TE's in such applications. A TE refrigerator constructed from a material with, say, $ZT = 2$ (about a factor of two greater than that currently available) would have a COP approaching that of a conventional vapor compression air conditioner; a TE generator fabricated from such a material would be lighter and could convert heat to electricity at a higher efficiency. The exhaust gas thermoelectric generator would have the ability of relieving the automotive alternator of a portion of its load, thereby increasing the overall vehicle fuel efficiency. The fuel savings so generated not only would reduce vehicle emissions but would provide the consumer with relief for the initial cost of the generator in the form of fuel savings over several years of operation of the vehicle. It was this scenario which led to a joint General Motors/Jet Propulsion Laboratory joint program aimed at developing new thermoelectric materials of enhanced figure of merit in the Partnership for the Next Generation Vehicle (PNGV) Program.

In the next section I will discuss these two key potential automotive applications. I will then describe our research on two new materials systems with potentially interesting thermoelectric properties.

AUTOMOTIVE THERMOELECTRIC SYSTEMS

Waste Heat Thermoelectric Generator

A well known rule of thumb in internal combustion engine (ICE) power generation is the following: of the power generated by the engine, approximately one third is available for propelling the vehicle; the remaining two thirds is evolved roughly equally as waste heat in the exhaust stream and latent heat in the coolant system. This means that for a typical ICE generating 75 kW of power (approximately 100 hp), roughly 50 kW of waste heat is generated. Evidently even if only a small fraction of this can be recovered, a substantial amount of electrical power could be generated. This additional power could be used to partially unload the alternator and thereby increase the vehicle fuel economy, or alternatively could provide supplemental power for additional luxury or safety features.

The ability to convert the large amount of heat available in the exhaust and radiator streams is limited mainly by two parameters: 1) the conversion efficiency of present day thermoelectric generator materials; and 2) the efficiency of the extraction of heat from the respective fluids (the exhaust gas or the liquid coolant) by means of heat exchangers. The first of these is a problem in materials research which we will discuss in more detail below; the second is not the main subject of this paper, but represents a complex design issue which must satisfy many constraints. Here we will simply mention a few of the main limitations which must be considered in such systems:

- size and mass
- physical location
- back pressure
- system cost

The total thermal power P_T in Watts available in a flowing fluid can be characterized simply by the expression:

$$P_T = \dot{m} c_p \Delta T \quad (1)$$

where \dot{m} is the mass flow rate of the fluid in kg s^{-1} , c_p is the specific heat in $\text{J kg}^{-1} \text{K}^{-1}$, and ΔT is the available temperature difference measured in Kelvin. Thus careful estimate of the power available in the exhaust gas and coolant streams requires detailed knowledge of the fluid flow rates, heat capacities, and temperatures. For exhaust gas systems large temperature differences (as much as 1000 K) are available but the mass flow rates are modest. In coolant systems, the available temperature difference is small (tens of Kelvin) but the mass flow rates are higher. As a result, as mentioned above, the total thermal power available in the two streams is comparable, and both should be considered for potential energy conversion.

Thermoelectric Climate Control

While the driving force behind the development of thermoelectric generator systems is the production of useful electrical power from waste heat, thermoelectric climate control in automotive systems is attractive from the point of view of simplicity and environmental friendliness. The study of Molina and Rowland in 1974 [6] first suggested that chlorofluorocarbon compounds, principally R-12, or Freon (the refrigerant of choice in air conditioning systems for the last 50 years), were destroying the protective ozone layer in the stratosphere at an alarming rate. As a result, the Montreal protocol of 1987 has led to a gradual phasing out of these harmful chemicals. In their stead, non chlorine-containing fluorocarbons, such as R-134a, which do not possess the long term stability of R-12, have begun to receive widespread use as refrigerants. It was not realized until quite recently, however, that *all* fluorocarbons, including both R-12 and R-134a, can contribute to global warming [7]. This is because these gases are capable of absorbing the infrared radiation the earth emits to stabilize its temperature. The infrared-absorbing capability of a gas is measured by its Global Warming Potential (or GWP) index. The GWP index measures the absorption characteristics relative to that of CO₂, which is defined to have a GWP index of unity. The GWP indices of R-12 and R-134a are 8,500 and 1,300, respectively. In other words, one kg of R-12 and R-134a are equivalent to 8,500 and 1,300 kg of CO₂, respectively, in terms of their global warming impact. Thus even relatively small amounts of these chemicals released into the atmosphere, e.g., via leakage, can have serious consequences in the long term.

In light of these sobering facts it is natural to contemplate alternative cooling technologies which might supplant vapor compression systems containing such chemicals. Thermoelectric cooling is one such alternative which presents many advantages including all solid state operation, electronic capacity control, reversibility to provide both heating and cooling, and high reliability. In spite of these many benefits, thermoelectric cooling has not enjoyed widespread or large scale use due to the low efficiency relative to vapor compression systems.

Here, as in the case of power generation, the role of materials research comes into play. If new materials can be developed with figure of merit a factor of two greater than those available today, the performance of TC systems will approach that of vapor compression systems. We have just begun to see some progress in the development of such materials. In the following sections I will describe some of our experimental work on two promising families of materials for advanced thermoelectrics: skutterudite compounds and intermetallic semiconductors.

NEW MATERIALS FOR ADVANCED THERMOELECTRICS

Filled Skutterudite Compounds

Much of the renewed excitement in thermoelectrics was initiated by the observation of the JPL group [8] that some members of a family of compounds called skutterudites possess fundamental physical properties which favor large thermoelectric figure of merit. The

thermoelectric figure of merit is given by $Z = S^2\sigma/\kappa$, where S is the Seebeck coefficient, σ the electrical conductivity, and κ the thermal conductivity, and is optimized in heavily doped semiconductors of low lattice thermal conductivity. The skutterudite compounds, of the form AB_3 with $A = \text{Co, Rh, or Ir}$ and $B = \text{P, As, or Sb}$, were studied by Dudkin and coworkers in the late fifties and early sixties [9], and were thought to be semiconductors with band gaps on the order of 1 eV. Their potential as thermoelectric materials is derived from the observation that p-type materials such as CoSb_3 , IrSb_3 , and RhSb_3 display quite high values of hole mobility, approaching $10^4 \text{ cm}^2 \text{ V}^{-1} \text{ s}^{-1}$ at room temperature, which exceeds that of all p-type semiconductors, including Si, Ge, and GaAs. At the same time, the complex unit cell (16 atoms) and heavy atom masses provide the potential of low lattice thermal conductivity in this compound. Indeed, subsequent study of the thermoelectric properties of CoSb_3 and IrSb_3 showed that the power factor (the numerator $S^2\sigma$ entering into the figure of merit) is quite large and comparable to that of state of the art thermoelectric materials such as Bi_2Te_3 and PbTe . Singh and Pickett [10] carried out band structure calculations for these materials and showed that the skutterudites are very narrow or zero-band gap semiconductors characterized by a linearly dispersing valence band and conduction bands of large effective mass. The observed transport properties of single crystals of CoSb_3 [11] were consistent with this picture. Unfortunately, although the power factor for binary skutterudites is large, the thermal conductivity, while moderately small, is about a factor ten too high to make these compounds useful as thermoelectrics.

Interest in the use of these compounds as thermoelectric materials most likely would have ceased at this point were it not for the observation of Slack and Tsoukala [12] that the skutterudite structure is amenable to modification in the direction of a greatly reduced lattice thermal conductivity. In particular, the unit cell contains a void which can be filled by a rare earth atom. Because the radius of the rare earth atom is significantly smaller than the radius of the void, the former “rattles,” i.e., exhibits a soft phonon mode. Subsequently, Morelli and Meisner [13] provided the first experimental evidence of the reduction in lattice thermal conductivity relative to unfilled skutterudites for $\text{CeFe}_4\text{Sb}_{12}$. These results were confirmed shortly thereafter on various rare-earth filled skutterudites by Nolas, et al. [14]. Figure 1 displays the thermal conductivity of several of these filled skutterudite compounds as measured in our laboratory and it is clear that the prediction of a strong reduction in thermal conductivity upon filling up the skutterudite structure is quite convincingly demonstrated.

While void-filling can provide a strong reduction in the lattice thermal conductivity of skutterudites, the introduction of a primarily trivalent rare earth ion will no doubt influence the electronic structure and transport properties. Indeed, in $\text{CeFe}_4\text{Sb}_{12}$, from a purely crystal chemistry point of view, the substitution of Fe for Co provides 4 additional holes in the valence band, only three of which are filled by electrons from the rare earth; there is thus one additional hole per formula unit, and this material should be a p-type semimetal, in agreement with experiment [13]. Much excitement was recently demonstrated when the studies of Sales, et al. [15] and Fleurial, et al. [16] showed that by partial substitution of Co on the Fe site, the hole concentration decreases, causing an increase in the Seebeck coefficient which then gives rise to the enhanced thermoelectric properties. As a result, samples of both $\text{LaFe}_{4-x}\text{Co}_x\text{Sb}_{12}$ and $\text{CeFe}_{4-x}\text{Co}_x\text{Sb}_{12}$ display $ZT \approx 0.9\text{--}1.4$ at elevated temperatures. It was perhaps surprising that one can partially substitute

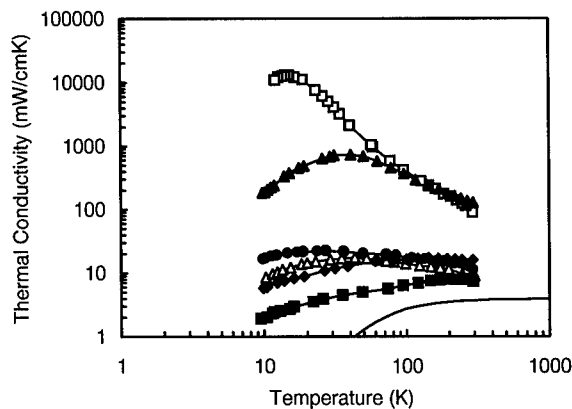


Figure 1. Thermal conductivity of several skutterudite compounds. \square : CoSb_3 single crystal; \blacktriangle : IrSb_3 polycrystal; \triangle : $\text{CeFe}_4\text{Sb}_{12}$; \bullet : $\text{LaIr}_4\text{Ge}_3\text{Sb}_9$; \blacklozenge : $\text{SmIr}_4\text{Ge}_3\text{Sb}_9$; \blacksquare : $\text{NdIr}_4\text{Ge}_3\text{Sb}_9$; solid line: minimum thermal conductivity corresponding to a phonon mean free path of one lattice spacing.

Co for Fe in $\text{CeFe}_4\text{Sb}_{12}$ (and related) filled skutterudites since it was previously thought that such compounds would not form with Co on the transition metal site. We recently [17] carried out a detailed study of $\text{Ce}_y\text{Fe}_{4-x}\text{Co}_x\text{Sb}_{12}$ with $0 < x < 2$ and showed that the amount of Ce in the voids, y , decreases strongly with Co substitution, and the resultant transport and thermoelectric properties are determined by the subtle interplay between Co doping x on the Fe site and the rare earth filling parameter y . Among the key questions that need to be addressed are: What is the valence of Ce in filled skutterudites? What is the magnetic state of Fe in these materials? What is the influence of partial rare earth filling and Fe/Co doping on the lattice thermal conductivity?

If it is assumed that the Fe in $\text{CeFe}_4\text{Sb}_{12}$ is in the Fe^{2+} state, and that the Ce is trivalent, then only three of the four additional holes created in the valence band by the Fe will be filled by electrons, and the material will be a p-type semimetal with one hole per formula unit, approximately as observed [17]. As Co is substituted for Fe, the number of valence band holes decreases, but at the same time the amount of Ce entering the voids is diminished as well. Thus, instead of reaching compensation at $x = 1$ (three holes in the valence band being completely filled by three electrons from the Ce) compensation is not reached until $x = 3$. Thus over the phase space in which $\text{Ce}_y\text{Fe}_{4-x}\text{Co}_x\text{Sb}_{12}$ forms, one can adjust the carrier concentration and type either by a) altering the amount of rare earth filling the void; or b) changing the Fe/Co ratio. Figure 2 shows the variation in electrical resistivity and Figure 3 the variation in thermoelectric power as a function of temperature for p-type samples as Co is substituted for Fe. We see that the resistivity evolves from a semimetallic behavior ($p = 5.5 \times 10^{21}$ holes cm^{-3}) for $x = 0$ to an activated one ($p = 6.0 \times 10^{20}$ holes cm^{-3}) for $x = 2$, while the room temperature Seebeck coefficient rises from

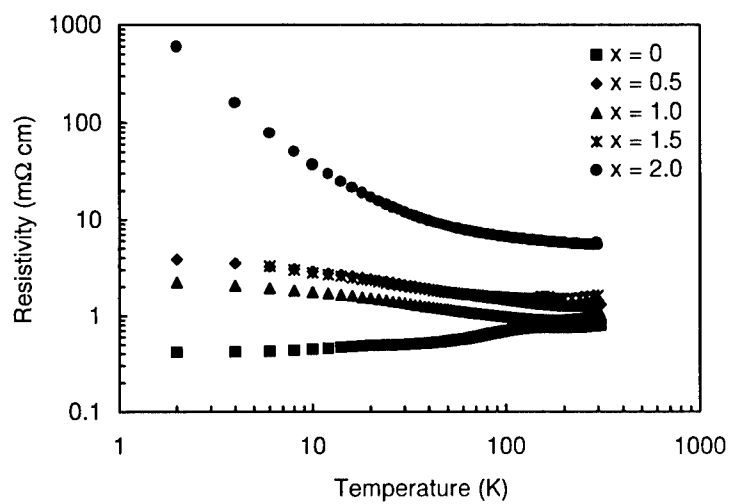


Figure 2. Resistivity as a function of temperature for $\text{CeFe}_{4-x}\text{Co}_x\text{Sb}_{12}$.

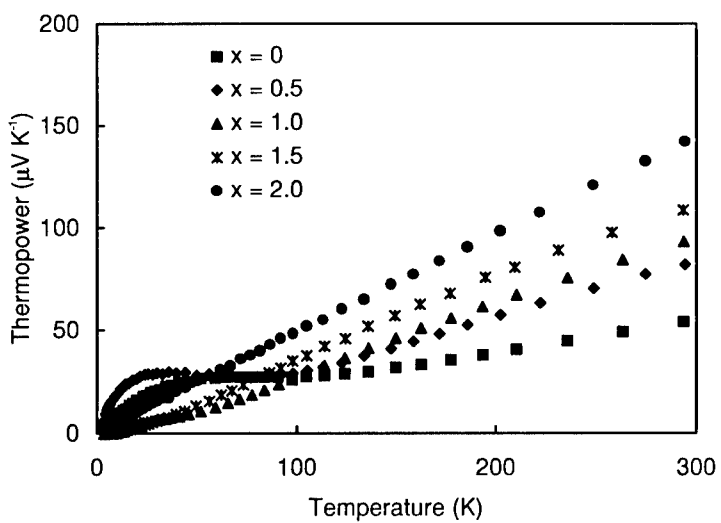


Figure 3. Thermoelectric power as a function of temperature for $\text{CeFe}_{4-x}\text{Co}_x\text{Sb}_{12}$.

approximately $50 \mu\text{VK}^{-1}$ to nearly $150 \mu\text{VK}^{-1}$. For samples containing little or no Co there occurs a hump in the Seebeck coefficient near 50 K whose origin is not understood at this time. Because this hump seems to affect the value of the Seebeck coefficient at room temperature, we make no attempt to derive an effective mass for these samples. For the $x = 2$ sample, however, the Seebeck coefficient is more well behaved as a function of temperature, and from these data and the hole concentration for this sample we derive a hole effective mass $m^* \approx 4$.

Figure 4 displays the thermal conductivity as a function of temperature for $\text{CeFe}_{4-x}\text{Co}_x\text{Sb}_{12}$ with $0 \leq x \leq 2$. For Co-containing samples the thermal conductivity is dramatically depressed relative to $\text{CeFe}_4\text{Sb}_{12}$. This is perhaps somewhat surprising since Co and Fe have very little mass and size difference. The origin of the strong phonon scattering for samples with a nonzero Co/Fe ratio is not understood at this time but is the focus of current experimental scrutiny.

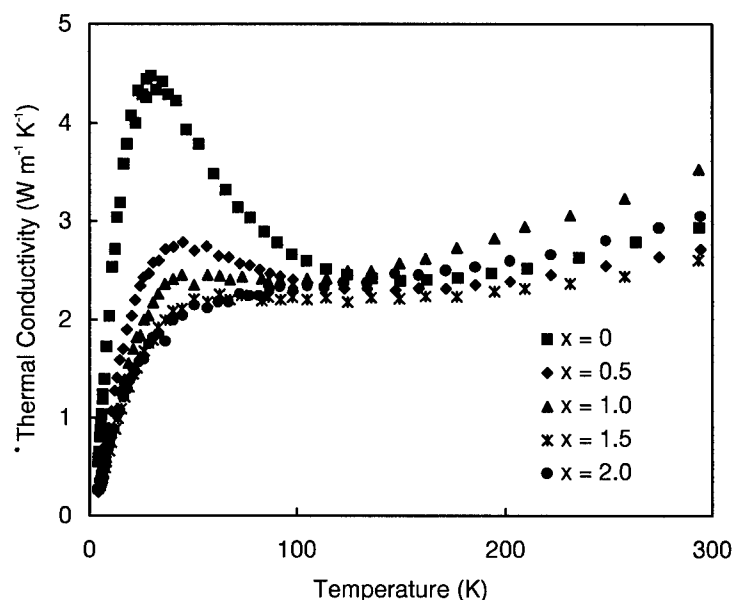


Figure 4. Thermal conductivity as a function of temperature for $\text{CeFe}_{4-x}\text{Co}_x\text{Sb}_{12}$.

We see that the origin of high thermoelectric figure of merit in Ce-filled skutterudites is the heavy carrier effective mass, giving rise to large Seebeck coefficient, and low thermal conductivity due to the combination of scattering from the soft phonon mode associated with the rare earth atom and additional phonon scattering on the Co/Fe site. Experiments

on samples with $x > 2$ are currently underway in order to probe the behavior of n-type samples. Although the electron mobility tends to be significantly lower than the hole mobility in skutterudite compounds, n-type filled skutterudites are predicted [18] to have very heavy conduction band masses which should yield large Seebeck coefficients and high Z .

1-1-1 Intermetallic Compounds

Our investigation of this interesting class of compounds began with studies of the transport properties of NdBiPt [19]. This compound is isostructural with TiNiSn and as such consists of three interpenetrating FCC sublattices with one element on each sublattice. Similar to the case of TiNiSn, the band structure of NdBiPt is expected to reflect that of NdBi but with the bands pushed apart by the presence of the symmetry-breaking Pt atom in the lattice. In this case the binary substructure compound NdBi is a good semimetal with a carrier concentration of approximately 10^{21} cm^{-3} . Figures 5 and 6 show the longitudinal and Hall resistivities of NdBiPt as a function of temperature. A precursory examination of the Hall curves reveals that the Hall resistivity changes sign as a function of both

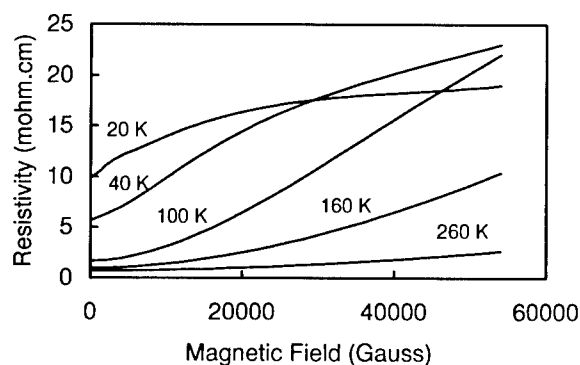


Figure 5. Longitudinal resistivity $\rho_{xx}(B)$ at selected temperatures for NdBiPt.

temperature and magnetic field. This is an indication that at least two carriers of opposite sign are active in this material. The data can be fit to a two band model consisting of holes of concentration p and mobility ν and electrons of concentration n and mobility μ . The results indicate that NdBiPt is a zero gap semiconductor or a semimetal of very small (5 meV) overlap. This is consistent with the expected band structure model in which Pt pushes the bands of NdBi apart by nearly 0.5 eV and results in a decrease in carrier concentration of three orders of magnitude. Unlike the case of TiNiSn, in which a gap actually forms, NdBiPt does not develop a gap because the binary substructure compound

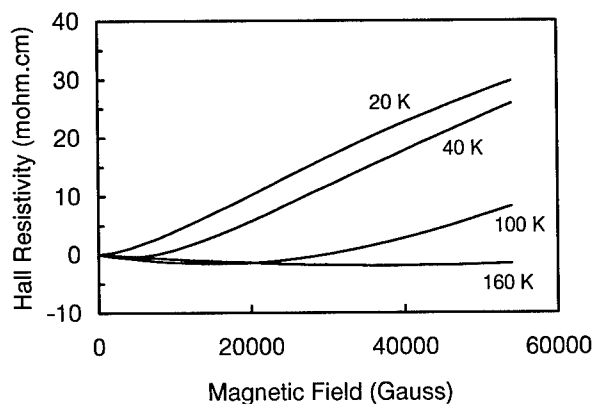


Figure 6. Transverse (Hall) resistivity $\rho_{xy}(B)$ at selected temperatures for NdBiPt.

NdBi possesses a quite large overlap. It is expected that using binary substructures with significantly smaller band overlaps relative to NdBi will lead to true semiconductor compounds when the ternary structure is formed. The rare earth-phosphide and arsenide rocksalt substructures would be a good place to start in this regard.

CONCLUSIONS

With the advent of new materials with enhanced thermoelectric properties the opportunities to apply TE devices in the automotive industry for both power generation from waste heat and heating/cooling will be many and varied. Two very promising materials systems which deserve further experimental and theoretical scrutiny are skutterudite compounds and 1-1-1 intermetallic semiconductors. The subtle interplay between rare earth filling and transition metal doping in $\text{Ce}_y\text{Fe}_{4-x}\text{Co}_x\text{Sb}_{12}$ filled skutterudites gives rise to record high values of Z at high temperature and provides a powerful tool for tailoring and optimizing the properties of this fascinating material. In the case of 1-1-1 intermetallics, such as TiNiSn and NdBiPt, the transition metals Ni and Pt play a unique role in breaking the symmetry of the lattice and forcing the substructure TiSn and NdBi bands apart to produce semiconductor-like materials with interesting transport properties. In order to gauge the ultimate potential of these and other materials for TE applications, detailed and careful experimental and theoretical studies of their fundamental physical properties are required.

ACKNOWLEDGMENTS

It is a pleasure to acknowledge collaborations with Jean-Pierre Fleurial, Thierry Caillat, Alex Borshchevsky, Ctirad Uher, Paul Canfield, George Nolas, and Glen Slack.

REFERENCES

1. D.T. Morelli, *Proc. 15th Int. Conf. Thermoelectrics* (ed. T. Caillat, Institute of Electrical and Electronics Engineers, Piscataway, NJ, 1996), p. 91.
2. E. Takanose and H. Tamakoshi, *Proc. 12th Int. Conf. Thermoelectrics* (ed. K. Matsuura, Institute of Electrical Engineers of Japan, 1994), p. 467.
3. U. Birkholz, E. Groß, U. Stöhrer, K. Voss, D.O. Gruden, and W. Wurster, *Proc. 7th Int. Conf. Thermoelectrics* (ed. K. Rao, University of Texas-Arlington, 1988), p. 124.
4. J. Bass, N.B. Elsner, and F.A. Leavitt, *Proc. 13th Int. Conf. Thermoelectrics* (ed. B. Mathiprakisam, American Institute of Physics New York, NY, 1995), p. 295.
5. G.A. Slack, in *Thermoelectric Handbook* (ed. M. Rowe, Chemical Rubber Company, Boca Raton, FL, 1995), p. 1.
6. M.J. Molina and F.S. Rowland, *Nature* **249**, 810 (1974).
7. M.S. Bhatti, *Proc. 1997 Society of Automotive Engineers Congress*, Detroit (to be published).
8. J.-P. Fleurial, T. Caillat, and A. Borshchevsky, *Proc. 13th Int. Conf. Thermoelectrics* (ed. B. Mathiprakisam, AIP Press, New York, 1995), p. 40.
9. B.N. Zobrina and L.D. Dudkin, *Sov. Phys. Sol. St.* **1**, 1688 (1960), and references therein.
10. D.J. Singh and W.E. Pickett, *Phys. Rev. B* **50**, 11235 (1994).
11. D.T. Morelli, T. Caillat, J.-P. Fleurial, J.W. Vandersande, B. Chen, and C. Uher, *Phys. Rev. B* **51**, 9620 (1995).
12. G.A. Slack and V.G. Tsoukala, *J. Appl. Phys.* **76**, 1665 (1994).
13. D.T. Morelli and G.P. Meisner, *J. Appl. Phys.* **77**, 3777 (1995).
14. G.S. Nolas, G.A. Slack, D.T. Morelli, T.M. Tritt, and A.C. Ehrlich, *J. Appl. Phys.* **79**, 4002 (1996).

15. J.-P. Fleurial, T. Caillat, A. Borshchevsky, D.T. Morelli, and G.P. Meisner, *Proc. 15th Int. Conf. Thermoelectrics* (ed. T. Caillat, Institute of Electrical and Electronics Engineers, Piscataway, NJ, 1996), p. 91.

16. B.C. Sales, D. Mandrus, and R.K. Williams, *Science* **272**, 1325 (1996).

17. B. Chen, J.-H. Xu, C. Uher, D.T. Morelli, G.P. Meisner, J.-P. Fleurial, T. Caillat, and A. Borshchevsky, *Phys. Rev. B* **55**, 1476 (1997).

18. L. Nordstrom and D.J. Singh, *Phys. Rev. B* **53**, 1103 (1996).

19. D.T. Morelli, P.C. Canfield, and P. Drymiotis, *Phys. Rev. B* **53**, 12896 (1996).

**THERMOELECTRIC APPLICATIONS AS RELATED
TO BIOMEDICAL ENGINEERING FOR NASA
JOHNSON SPACE CENTER**

C. D. Kramer, P.E.

NASA Johnson Space Center, Houston, EA5, Houston, TX 77058 Ckramer@ems.jsc.nasa.gov

ABSTRACT

This paper presents current NASA biomedical developments and applications using thermoelectrics. Discussion will include future technology enhancements that would be most beneficial to the application of thermoelectric technology.

A great deal of thermoelectric applications have focused on electronic cooling. As with all technological developments within NASA, if the application cannot be related to the average consumer, the technology will not be mass-produced and widely available to the public (a key to research and development expenditures and thermoelectric companies). Included are discussions of thermoelectric applications to cool astronauts during launch and reentry. The earth-based applications, or spin-offs, include such innovations as tank and race car driver cooling, to cooling infants with high temperatures, as well as, the prevention of hair loss during chemotherapy. In order to preserve the scientific value of metabolic samples during long-term space missions, cooling is required to enable scientific studies. Results of one such study should provide a better understanding of osteoporosis and may lead to a possible cure for the disease.

In the space environment, noise has to be kept to a minimum. In long-term space applications such as the International Space Station, thermoelectric technology provides the acoustic relief and the reliability for food, as well as, scientific refrigeration/freezers. Applications and future needs are discussed as NASA moves closer to a continued space presence in Mir, International Space Station, and Lunar-Mars Exploration.

INTRODUCTION

NASA's Vision Statement: "NASA is an investment in America's future. As explorers, pioneers, and innovators, we boldly expand frontiers in air and space to inspire and serve America and to benefit the quality of life on Earth." One portion of the NASA's Mission Statement is to, "research, develop, verify, and transfer advanced aeronautics, space, and related technologies."

From these statements, it is clear that NASA is funding research and development of state-of-the-art technologies in order to achieve the vision. Thermoelectrics is not an exception. In the Biomedical Engineering field, thermoelectrics are currently used in freezers, refrigerators, incubators, astronaut cooling, and animal and fish habitats. This is not to say that there are not more areas that could be converted, however, the key is to increase efficiency since power is a limited resource in space.

Within the vision of exploration, the Space Shuttle, International Space Station (ISS), and Mir, are not NASA's only concerns. As Dr. Akira Miyamoto wrote for the Life Sciences and Space Medicine Conference in 1995, "...the manned space program has recently changed worldwide. It has become a new era of international collaboration because it is difficult to

achieve our programs alone. In fact, we can no longer afford to do so. International cooperation among agencies is becoming more valuable, and this trend will continue in the future. This cooperation must be extended to the collection of baseline medical data.” [1]

THEORY

Astronauts suffer from a progressive and continuous negative calcium balance and associated bone metabolism disorders during spaceflight. Several studies have been made and several experiments have been conducted, but, little experience has been gained in real-time spaceflight. However, the cause of the calcium imbalances and the bone metabolic disorders are still not clear. In addition, the proper treatment for metabolic bone disease in microgravity is still obscure. It will soon be necessary to prevent progressive spaceflight bone decalcification to ensure the success of missions requiring long duration stays in space such as living on a Lunar base or a voyage to Mars [2].

The Human Research Facility (HRF) for the International Space Station objectives included: “to facilitate and implement the science efforts of the NASA and external Life Sciences communities; to contribute to the definition of critical issues which affect crew health and performance during long-duration spaceflight; and to develop and evaluate countermeasures to mitigate risk during and after spaceflight.” [3]

In March 1998, a Space Shuttle Spacelab flight will occur as a dedicated mission to study neuroscience. The mission, Neurolab, will include areas of cellular and molecular biology; developmental neurobiology; sensory and motor systems; nervous system homeostasis and adaptation; and behavior, cognition and performance. Human and animal research will be performed.

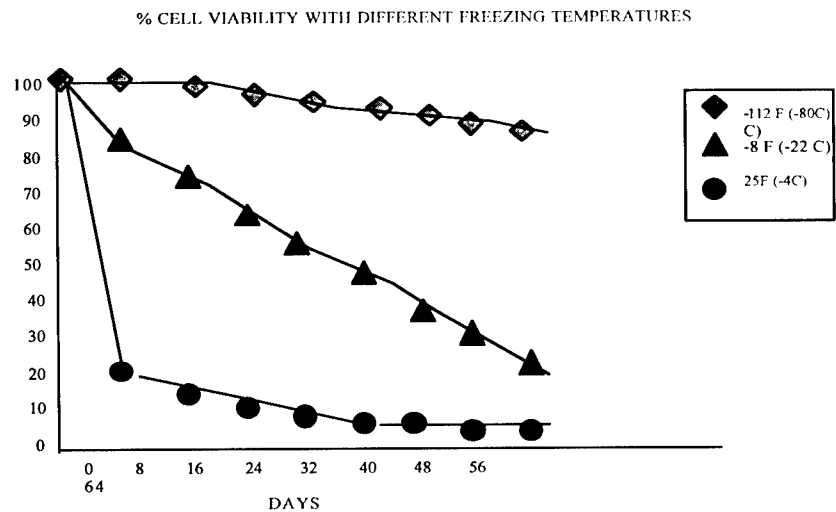


Figure 1 - Cell Viability With different Freezing Temperatures

The studies in bone density, kidney stones, bone metabolic disorders, and calcium imbalance for these missions require blood and urine samples from the crewmembers. These studies are being performed on Mir and the Space Shuttle currently. Extensive research will be performed on the International Space Station, as well as, any Lunar or Mars exploration. These studies require refrigeration (4° C), and freezing (-22° C, -80° C). As seen in Figure 1, cell viability is dependent on temperature and time.

Thermoelectric refrigerators and freezers (-20° C) are currently being utilized on the Space Shuttle and Mir. Issues of acoustic noise and reliability have been resolved, however, have been more taxing on the available power than vapor compression.

Furthermore, as seen in Figure 1, due to the lengthy stays, there is a requirement from the science community for an International Space Station -80° C freezer. Without the efficiency, this at present time, cannot be thermoelectric. In both the -22° C and the -80° C cases, 5 ml samples must be able to be frozen within 30 minutes.

Science for the International Space Station also requires a -183° C freezer for use in studying protein crystal growth (see Figure 2). This commercially backed science opens the way for understanding protein structure for pharmaceuticals development of drugs to combat diseases such as cancer. The -183° C freezer also provides a means to accomplish genetic studies not achievable with the -80° C or -22° C freezers.

REFRIGERATOR/FREEZER NEEDS FOR ISS

Temperature	Operational Need	Science Need
$\pm 4^{\circ}\text{C} \pm 3^{\circ}$ must stay above freezing	Food & Drinks includes fresh fruits and vegetables for resupply	Prechill biological specimens before centrifuge Defrosting samples Reagents & metabolic kits Cells for Biotechnology
-26° C $\pm 3^{\circ}$ -26° C down to -40° C but needs to be very stable at holding temp.	Frozen Foods* Provides water/food for ISS crew members	Biological specimens Blood, urine, saliva, animal tissues, plants, cells Protein crystal growth studies
-60 to -90° C		Quick freeze for animal tissues Long-term stowage of biological specimens
-190° C		Protein crystal growth

- Industrial Standards:
 - 40° C Warehousing and transportation of frozen foods
 - 15-20° C Grocery store shelves frozen foods
 - 26° C Compromised from design constraints
 - 20-70° C Standard for all biological specimens. Above -20° C generally considered too warm.

Figure 2 - Refrigeration/Freezer Needs for ISS

Presently, astronauts' launch and entry suits are cooled with water, using thermoelectrics. Water flows through small tubes that line an undergarment in the crew escape suits and then circulated for cooling through the thermoelectric device (Figure 5). Food freezers are being developed for the International Space Station that must be able to maintain food for up to 90 days (4 crewmembers). The request was industry standards of -40°C , the technology today for maximum food volume with minimal stowage mass is -20°C . This is indeed still a challenge due to power constraints and a power-off requirement of 6.5 hours without food loss with an ambient temperature of 49°C .

Many incubators are required for animal and materials study. These technologies are using thermoelectrics for the range of 4°C to 40°C for very small quantities. One such facility is the Avian Development Facility (Figure 3) which is a fully programmable, closed environment system that maintains optimal incubation conditions for embryos from day 0 until hatch.

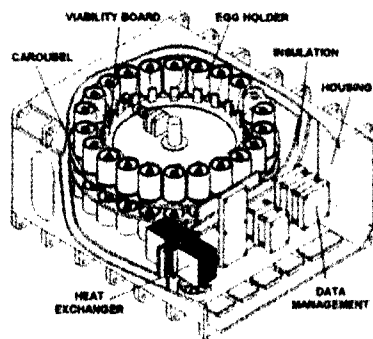


Figure 3 - Avian Development Facility - *Space Flight Prototype*

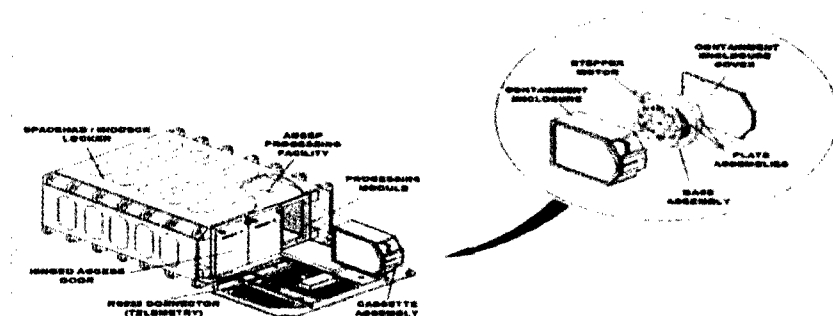


Figure 4 - Advanced SEPARation (ADSEP) - *Space Flight Processing Facility*

This system maintains optimal incubation conditions for embryos from day 0 until hatch. This facility provides a snapshot of embryogenesis in space using Japanese quail or chicken eggs.

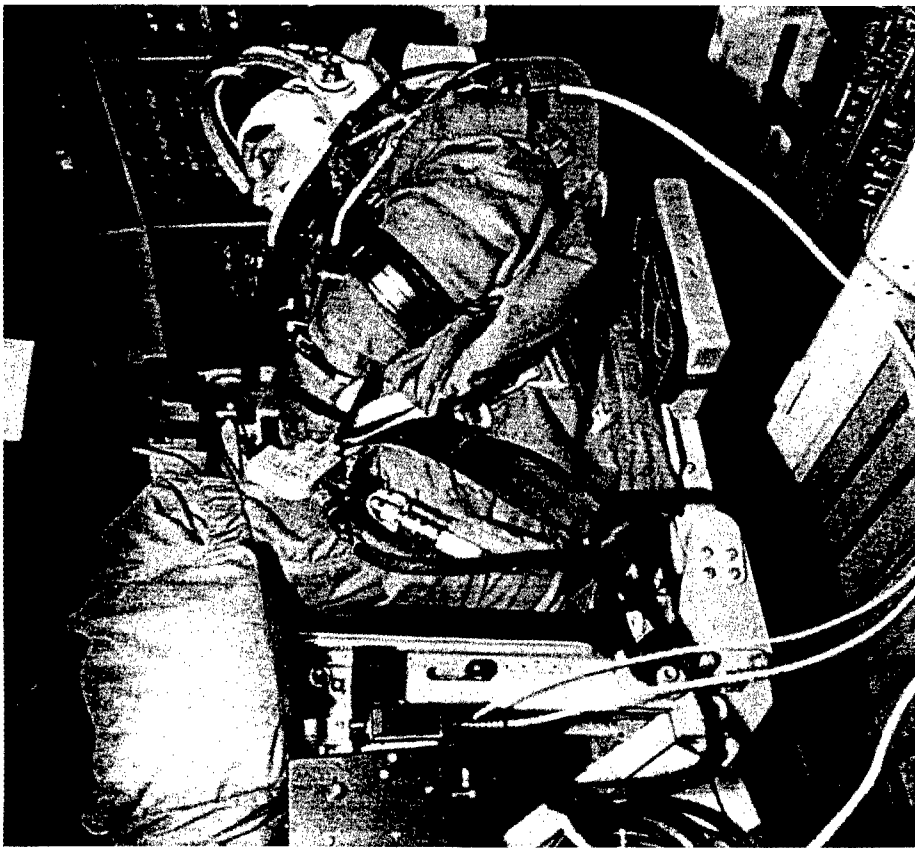


Figure 5 - Launch Entry Suit

Another example of a space flight processing facility requiring controlled temperature between 4-40° C is the Advanced Separations (ADSEP) Facility (Figure 4). It separates living cells, cellular particles, and proteins using aqueous two-phase partitioning.

CONCLUSION

Commercial spin-offs are unlimited to those with imagination. A device similar to the liquid cooling garment used by astronauts was developed in the early 1980's as a scalp cooling mechanism to prevent drug induced alopecia [5] during chemotherapy. This successful device used ice as a cooling mechanism. Liquid cooling garments for hot environments such as tank

and race car drivers have been requested. These garments can be used for other thermo-regulatory disorders in infants, as well as, adults. Firefighters breathing systems and suits need cooling. A tube chiller developed by the Biomedical Hardware Development and Engineering Office is used to transport blood samples from donor to hospital without loss of critical data.

In conclusion, for biomedical needs, thermoelectrics have to become more efficient (a better figure of merit) systems engineering is required to produce the most efficient unit. The developer of the engine has to be included in the product design systems engineering team to understand all constraints and limitations the chip will see. NASA Johnson Space Center is supporting thermoelectric research in the hope of achieving the more efficient thermoelectric devices.

[1] Akira Miyamoto, M.D., Chiaki Mukai, M.D., Tadasha Murai, M.D., and Chihara Skekiguchi, M.D. "IML-2 Baseline Data Collection as an Example of future International Cooperation." *Life Sciences and Space Medicine Conference '95*, P. 235, AIAA, USA, 1995.

[2] Akira Miyamoto, M.D., Chiaki Mukai, M.D., Tadasha Murai, M.D., and Chihara Skekiguchi, M.D. "IML-2 Baseline Data Collection as an Example of future International Cooperation." *Life Sciences and Space Medicine Conference '95*, P. 235 AIAA, USA, 1995.

[3] Susan M. Fortney, Ph.D. "Human Research Facility for Space Station Alpha." *Life Sciences and Space Medicine Conference '95*, P. 17, AIAA, USA, 1995.

[4] Helen Lane, Ph.D. "Cell Viability With Different Freezing Temperatures." *Refrigerator/Freezer Development and Use Presentation*, NASA, October 1996.

[5] Catherine D. Forshage and Robert W. Kramer. "Prevention of Drug-Induced Alopecia by Scalp Cooling in Patients with Cancer." In Patients with Cancer, *Proceedings of the Tenth Annual Northeast Bioengineering Conference*, P. 109, IEEE, USA, March 1982.

TRANSPORT PROPERTIES OF PARTIALLY-FILLED $\text{Ce}_y\text{Co}_4\text{Sb}_{12}$

C. UHER*, B. CHEN*, S. HU*, D.T. MORELLI**, G.P. MEISNER**

*Department of Physics, University of Michigan, Ann Arbor, MI 48109, cuher@umich.edu

**Physics and Physical Chemistry Department, General Motors Research and Development Center, Warren, MI 48090

ABSTRACT

We have investigated the magnetic and transport properties of $\text{Ce}_y\text{Co}_4\text{Sb}_{12}$ filled skutterudites with the filling fraction $y \leq 0.1$. These compounds are n-type materials that develop a magnetic moment upon the presence of trivalent cerium. Cerium has a strong influence on all transport properties and even in small amounts it drastically reduces the lattice thermal conductivity. The resulting figures of merit are comparable to the values established previously for the p-type filled skutterudites.

INTRODUCTION

Much effort has recently been focused on the synthesis and physical properties of the class of solids called skutterudites. The interest stems chiefly from their promise as novel thermoelectric materials [1,2]. In their simple (unfilled) form with a generic formula AB_3 where A is any one of Co, Ir or Rh, and B stands for a pnictogen element such as As, P or Sb, the skutterudites display very high mobility and large thermopower, making the so-called power factor $P = \sigma S^2$ among the highest ever measured. Unfortunately, the thermal conductivity of these unfilled skutterudites is too high and the figure of merit $Z = \sigma S^2/\kappa$ is not competitive with the state-of-the-art thermoelectric materials based on Bi_2Te_3 , PbTe, or Si-Ge alloys. However, thanks to its open structure with voids (or "cages") that are large enough to accommodate foreign atoms, the prospect of these materials for thermoelectric applications is considerably enhanced. The atoms in the cages of such filled skutterudites are weakly bound and their vibration ("rattling") impedes the heat flow so much that the resulting thermal conductivity is depressed to values not too different from those observed on amorphous solids [3]. At the same time, by filling the voids, the favorable electronic properties do not appear to be totally washed out. The overall outcome is a record-high thermoelectric figure of merit [4].

In our previous work we have studied the low temperature transport properties of both simple CoSb_3 [5] and the Ce-filled skutterudites [6] based on $\text{Ce}_y\text{Fe}_{4-x}\text{Co}_x\text{Sb}_{12}$. Specifically, we have shown that Co substitution at the Fe sites suppresses hole transport and, at high Co content, results in an n-type material. Furthermore, we have demonstrated that the Ce filling fraction depends very sensitively on the Co concentration. For instance, while the cages of the $x = 0$ compound are essentially all occupied by Ce ($y \approx 0.98$), at the other extreme of no Fe present ($x = 4$) the cages are only sparsely populated with Ce ($y \leq 0.07$). The excess of Ce apparently nucleates as a minute amount of a second phase the trace of which is detected in the x-ray structural analysis and magnetic susceptibility.

In this study we focus on the compounds with 100% Co content, i.e. $x = 4$, and low level of Ce doping. The aim here is to explore the domain of n-type transport, and to inquire how large a fractional occupancy is needed in order to drastically reduce the thermal conductivity.

RESULTS AND DISCUSSION

Samples and Techniques

The object of the study are samples of $\text{Ce}_y\text{Co}_4\text{Sb}_{12}$ with Ce filling fractions y comparable to or smaller than the critical filling fraction $y \approx 0.07$ established for this compound previously from the microprobe measurements [6]. The nominal Ce compositions together with the relevant transport parameters of the samples are summarized in Table I. Samples in the form of parallelepipeds were prepared by the method described in Ref. 6 and their x-ray analysis confirmed a single-phase nature of the material. Magnetic studies were made using a Quantum Design SQUID Magnetometer, and the electrical and thermal transport measurements were carried out using a 4-probe potentiometric technique and the longitudinal steady-state method, respectively.

Table I. Room temperature parameters for the samples under study.

Composition	Carrier density (10^{20}cm^{-3})	Hall mobility ($\text{cm}^2\text{V}^{-1}\text{s}^{-1}$)	Effective mass m^*	Curie constant (emu K g^{-1})	Fig. of merit ZT
CoSb_3	0.0067	72	3.8	-	0.008
$\text{Ce}_{0.05}\text{Co}_4\text{Sb}_{12}$	0.6	55	1.8	2.43×10^{-5}	0.11
$\text{Ce}_{0.075}\text{Co}_4\text{Sb}_{12}$	1.4	41	2.4	1.85×10^{-5}	0.16
$\text{Ce}_{0.100}\text{Co}_4\text{Sb}_{12}$	2.8	25	4.7	4.50×10^{-5}	0.20

Structural Studies

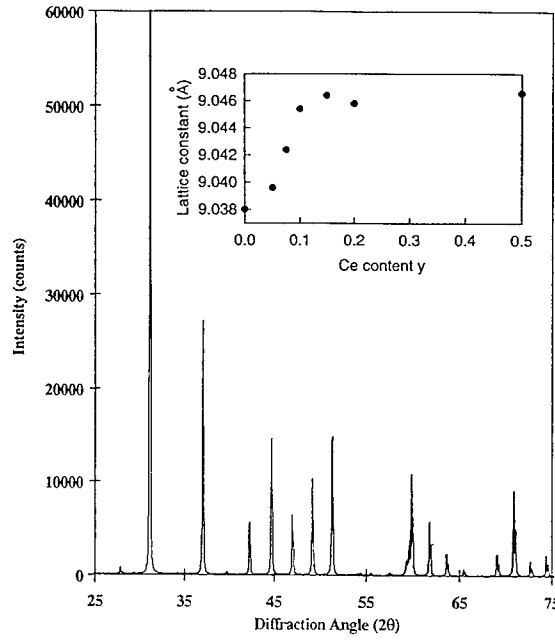
The inset in Fig. 1 displays the lattice constant of $\text{Ce}_y\text{Co}_4\text{Sb}_{12}$ as a function of Ce concentration. A linear functional dependence is seen to persist up to about $y \approx 0.1$. Beyond this filling fraction, the lattice constant is essentially independent of Ce content. The data, in conjunction with the microprobe measurements, indicate that up to the limit of $y \approx 0.1$, Ce is incorporated in the cages of this skutterudite structure. At larger concentrations of Ce the cages are saturated (although filled to only about 10%) and the excess Ce participates in the formation of an impurity phase. This conjecture is supported by the x-ray diffraction data which, for $y \leq 0.1$, show only peaks corresponding to the filled skutterudite structure (see Fig.1) while at high Ce content additional small peaks are evident.

Magnetic Susceptibility

Magnetic susceptibility was measured over the temperature range 6-300K and the data are shown in Fig.2. Due to the formation of a hybridized d^3sp^2 bond between Sb and one of Co d-electrons, the remaining d-electrons of Co are paired up resulting in a nonmagnetic d^6 configuration. Thus, CoSb_3 should be a diamagnetic compound and the behavior of its susceptibility indeed confirms this. Compounds containing Ce develop magnetic moments and the Curie-Weiss character of susceptibility is clearly evident. We analyze the susceptibility data using the expression

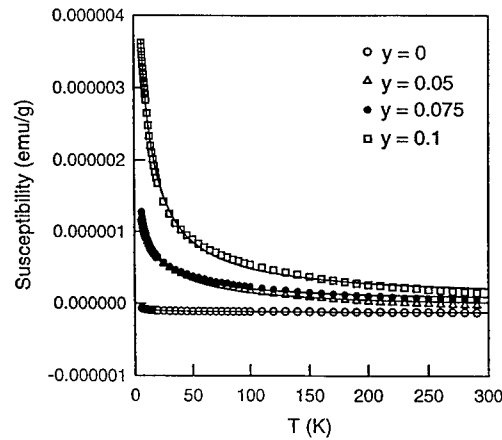
$$\chi = C/(T - \theta) + \chi_0 \quad (1)$$

Figure 1: X-ray diffraction data for $\text{Ce}_{0.1}\text{Co}_4\text{Sb}_{12}$ sample. Variation of the lattice constant with Ce content is shown in the inset.



where C is the Curie-Weiss constant, θ is the Curie temperature, and χ_0 stands for the background, temperature independent contribution. The fits to the data are shown in Fig.2 as solid lines, the Curie-Weiss constants are given in Table I, and the Curie temperatures for the three Ce containing samples are, in order of the increasing Ce content, 30.2K, 20.2K, and 10.6K, respectively. From the values of the Curie-Weiss constant we deduce an effective moment per Ce atom of 2.58, 1.84, and 2.48 Bohr magnetons, respectively, consistent with the theoretical value of 2.54 for trivalent cerium.

Figure 2: Temperature dependence of magnetic susceptibility. Solid curves are fits using Eq.1.



Resistivity and Thermopower Measurements

All samples in this study, including the undoped CoSb₃, are n-type conductors with the room temperature values of the carrier density and Hall mobility given in Table I. The temperature dependence of the resistivity is shown in Fig.3.

The n-type nature of transport is also clearly reflected in the negative sign of the thermopower. The undoped CoSb₃ displays a huge negative thermopower, see Fig.4, with values in excess of 650 $\mu\text{V/K}$ near room temperature. With increasing electron concentration the thermopower rapidly diminishes but remains at respectable values of $\sim 170 \mu\text{V/K}$. These values are comparable to the data on n-type single crystals [7] and large magnitudes of the thermopower are presumably due to the large electron effective mass predicted for these compounds [8]. The experimental effective masses, obtained with the aid of Eqs. 2 and 3,

$$S = \pm \frac{k_B}{e} \left(\frac{2F_1(\eta)}{F_0(\eta)} - \eta \right) \quad (2)$$

$$n = \frac{4}{\sqrt{\pi}} \left(\frac{2\pi m^* k_B T}{h^2} \right)^{3/2} F_{1/2}(\eta) \quad (3)$$

where $\eta = \frac{E_F}{k_B T}$ and F_x is a Fermi integral of order x , are given in Table I.

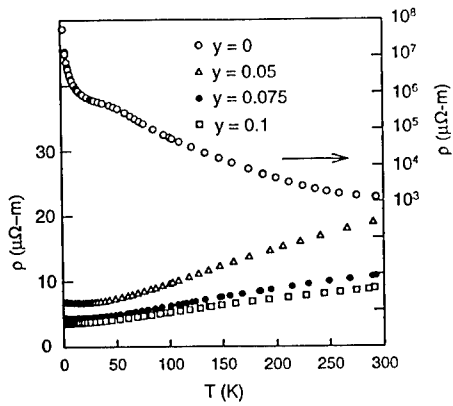


Figure 3: Temperature dependence of the electrical resistivity. Right-hand scale for CoSb₃, left-hand scale for the Ce-doped samples

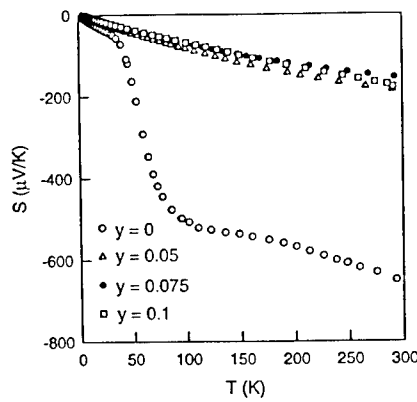


Figure 4: Thermopower as a function of temperature for the investigated samples.

Thermal Conductivity

Temperature dependence of the thermal conductivity of our samples is displayed in Fig.5. The corresponding electronic thermal conductivity contributions calculated using the resistivity data of Fig.3 and assuming the validity of the Wiedemann-Franz law represent a fraction of a percent of the total thermal conductivity at 300K for CoSb_3 but reach about 16% for $\text{Ce}_{0.10}\text{Co}_4\text{Sb}_{12}$. The undoped CoSb_3 shows a typical dielectric behavior with a dominant peak near 30K followed by a gradually decreasing thermal conductivity as phonon-phonon umklapp scattering takes over at higher temperatures. For comparison, the solid line in Fig. 5 shows the data for a single crystal of CoSb_3 reported on previously [5]. While the grain boundary scattering degrades the thermal conductivity in the vicinity of its peak value, there is little difference between the polycrystalline and single crystal specimens at room temperatures.

The presence of Ce in the structure has a profound influence on the thermal conductivity at all temperatures. Not only is the peak dramatically suppressed but the room temperature value of the conductivity is also strongly depressed. These data further substantiate previous observations [3,9] of a marked reduction in the thermal conductivity upon filling the cages of skutterudites. In fact, the present results indicate that surprisingly little Ce is needed to strongly scatter phonons and gain a significant advantage from the reduction of the thermal conductivity.

Thermoelectric Figure of Merit

The data of Figs.3-5 serve as a basis for calculation of the dimensionless figure of merit ZT and the room temperature values are entered in Table I. Clearly, these values do not compete favorably with the room temperature figure of merit of Bi_2Te_3 -based compounds. However, the numbers for the n-type Ce-doped samples are very similar to those measured on p-type filled skutterudites at comparable temperatures [4,10]. Assuming that the temperature dependence above 300K would be similar for both n-type and p-type filled skutterudites, the compounds under study would appear as very competitive for the n-type leg of the high

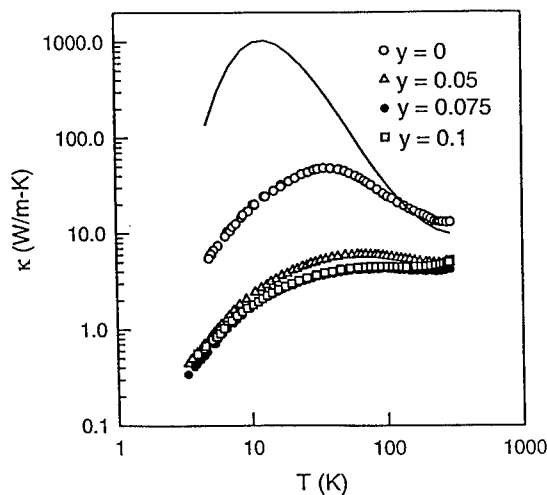


Figure 5: Temperature dependence of thermal conductivity. Solid line represents the data for a single crystal of CoSb_3 from Ref. 5.

temperature thermoelectric couple. The material compatibility of the n-type and p-type branches would be a distinct advantage in the manufacture of thermoelectric power generators.

CONCLUSIONS

The cages of the CoSb_3 structure can accommodate Ce up to a filling fraction of $y \sim 0.1$. The presence of Ce leads to an n-type character of transport and to a development of a magnetic moment that reflects a trivalent state of Ce. While the thermal conductivity of Ce-filled skutterudites is very strongly suppressed, the mobility remains reasonably large. These features result in the figure of merit that is comparable or even exceeds the values reported for the p-type filled skutterudites at room temperature. The availability of both n-type and p-type filled skutterudites with high figures of merit is an encouraging step forward in the quest to develop an efficient thermoelectric power generation capability.

ACKNOWLEDGMENTS

This work was supported by the ONR Grant N00014-96-1-0181.

REFERENCES

1. T. Caillat, A. Borshchevsky, and J.-P. Fleurial, in Proceedings of the XIth International Conference on Thermoelectrics, edited by K. R. Rao (University of Texas at Arlington Press, Arlington, 1993), p.98-102.
2. G. A. Slack and V. G. Tsoukala, *J. Appl. Phys.* **76**, p. 1665 (1994).
3. D. T. Morelli and G. P. Meisner, *J. Appl. Phys.* **77**, p. 3777 (1995).
4. B. C. Sales, D. Mandrus, and R. K. Williams, *Science* **272**, p. 1325 (1996).
5. D. T. Morelli, T. Caillat, J.-P. Fleurial, A. Borshchevsky, J. Vandersande, B. Chen, and C. Uher, *Phys. Rev.* **B51**, p. 9622 (1995).
6. B. Chen, J.-H. Xu, C. Uher, D. T. Morelli, G. P. Meisner, J.-P. Fleurial, T. Caillat, and A. Borshchevsky, *Phys. Rev.* **B55**, p. 1476 (1997).
7. T. Caillat, A. Borshchevsky, and J.-P. Fleurial, *J. Appl. Phys.* **80**, p. 4442 (1996).
8. D. J. Singh and W. E. Pickett, *Phys. Rev.* **B50**, p. 11235 (1994).
9. G. S. Nolas, G. A. Slack, D. T. Morelli, T. M. Tritt, and A. C. Ehrlich, *J. Appl. Phys.* **79**, p. 4002 (1996).
10. J.-P. Fleurial, T. Caillat, A. Borshchevsky, D. T. Morelli, and G. P. Meisner, 15th Int. Conf. Thermoelectrics (IEEE, Pixataway, 1996), p. 91.

MEASUREMENT OF THE THERMOELECTRIC PROPERTIES OF QUASICRYSTALLINE AlPdRe AND AlCuFe ALLOYS.

M.L. WILSON^a, S. LeGAULT^b, R.M. STROUD^c and T.M. TRITT^a

^aDepartment of Physics and Astronomy, Clemson University, Clemson SC

^bMcGill University, Department of Physics and Astronomy, Montreal Canada

^cNaval Research Laboratory, Washington D.C.

ABSTRACT

We report the measurement of the thermal conductivity, electrical resistivity, and thermoelectric power on two quasicrystalline compounds, $\text{Al}_{70}\text{Pd}_{20}\text{Re}_{10}$ and $\text{Al}_{62.5}\text{Cu}_{25}\text{Fe}_{12.5}$. These materials are found to possess a thermal conductivity of order 1 W/m-K, while retaining their semimetallic conductivity. These features coupled with moderately large thermopowers, up to 55 $\mu\text{V/K}$, imply that the general class of quasicrystalline compounds warrants careful investigation for their potential as new thermoelectric materials.

INTRODUCTION

The recent surge of interest in potential applications for thermoelectric (TE) materials has driven a new surge of interest and research into the discovery of new thermoelectric materials. In the mid 1960's a great deal of research was undertaken to find new and better TE materials. While this research had early successes with Bi_2Te_3 , and $\text{Si}_{1-x}\text{Ge}_x$, researchers rapidly ran out of new classes of compounds in which to search for better TE properties and the research subsided. The recent surge in research in TE materials is partly related to the great strides that have been made in materials synthesis in the last 20 years. Dozens of new classes of compounds have been discovered which show promise as good TE materials. The main question lies in what classes show the best promise and therefore should be examined.

The primary input into which materials should be examined lies in the three material dependent properties entering the thermoelectric figure of merit ZT :

$$ZT = \frac{\sigma \alpha^2 T}{\kappa} \quad (1)$$

where σ is the electrical conductivity, α is the thermopower, κ is the thermal conductivity and T is temperature. What is desired when searching for a promising class of compounds is to find systems with two good properties and a key as to how to improve the third. For instance, typically a material having high electrical conductivity has high crystallinity. Low thermal conductivity on the other hand requires a large unit cell, a glassy structure, or very weakly bound atoms 'rattling' inside the lattice. The thermoelectric power is less predictable since it relies on the derivative of the density of states at the Fermi level. Given this, it is most straightforward to begin a search examining classes having high crystallinity and large unit cells. Quasicrystals represent the extreme limit of this type of a material.

QUASICRYSTALS

Quasicrystals are the name given to any compound which displays a 'forbidden' structural symmetry. The most common quasicrystals have either a 5-fold or a 10-fold axis of rotation, in addition, compounds with 8- and 12-fold axes are also known.^{1,2,3} 5-fold symmetric crystals have icosahedral symmetry, and as such are called icosahedral quasicrystals. A 5-fold axis cannot occur in a traditional translationally ordered solid because a 2-dimensional tiling of pentagons cannot fill all space. Hence, true quasicrystals have no translational long range order, rather, the unit cell size is the size of the entire crystal. Quasicrystals do, however, have long range positional order.

Quasicrystals are argued to grow by means of local matching rules governing the orientation of new atoms. By using a particular set of local matching rules for the addition of new atom clusters, a crystal can be formed in which the position of all atoms in the lattice is uniquely determined, yet no repeating pattern exists. This positional order gives rise to sharp x-ray diffraction lines similar to those of conventional single crystals.¹

The icosahedral quasicrystals form the largest family of quasicrystalline materials with about 60 members known.³ Of these systems 12 can be grown as single domain macroscopic crystals of large enough size to perform 'intrinsic' transport measurements. For this reason we will discuss results on these stable quasicrystalline phases.

Most icosahedral quasicrystals are composed of icosahedral metal clusters known as Pauling triacontahedra (containing 44 atoms) or MacKay icosahedra (containing 54 atoms). These clusters are then arranged with additional linking atoms in a non-repeating pattern to form a quasicrystal. In some cases these clusters are arranged in a repeating pattern, these systems are known as quasicrystalline approximants. Most of the understanding of electronic and phonon structure and precision knowledge of atomic positions in quasicrystalline materials are actually determined from measurements on and calculations of stable approximant phases. One such approximant Al_3CuLi_3 is a bcc lattice of Pauling triacontahedra and containing a total of 180 atoms per unit cell. This is actually a small approximant lattice since phases with lattice constants of up to 100 Å, containing about 50,000 atoms per cell, are known.¹ These approximants are interesting in their own right but due to space they will not be discussed.

EXPERIMENTAL

Due to the essentially infinite unit cell size of a true quasicrystal, the thermal conductivity is extremely low when compared to other crystalline materials composed of metal atoms. Figure 1 shows thermal conductivity data for three quasicrystalline materials, $\text{Al}_{62.5}\text{Cu}_{25}\text{Fe}_{12.5}$, $\text{Al}_{70}\text{Pd}_{20}\text{Re}_{10}$, and $\text{Al}_{70}\text{Pd}_{20}\text{Mn}_{10}$. The presented thermal conductivities are all around 1 W/mK at 150 K. This is a factor of 2 lower than typical doped Bi_2Te_3 materials. This thermal conductivity is low enough to fall into the range commonly found for amorphous glasses.⁴ In the thermoelectric figure of merit one divides by κ . Hence, these low values of κ greatly enhance the potential for TE application of quasicrystalline materials. While few studies of the thermal conductivity have been made on stable quasicrystalline compounds, most materials examined have κ_{phonon} below about 3 W/mK at temperatures below 150 K.

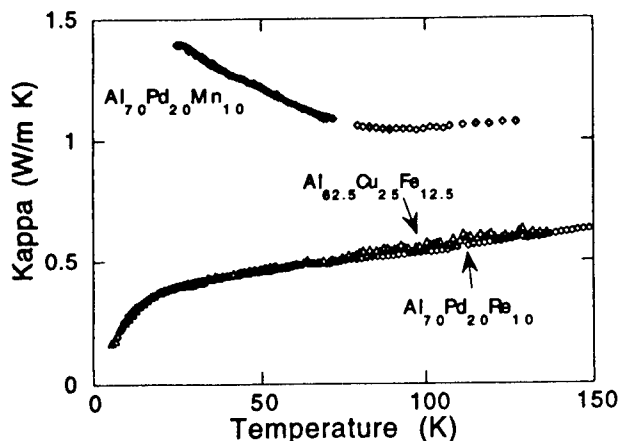


Figure 1, Thermal conductivity for AlPdRe, AlPdMn, and AlCuFe quasicrystals.

The electrical properties of these materials also display interesting behavior. Nearly all stable single-domain quasicrystals display semimetallic resistive behavior with $\rho(300\text{K})$ between 0.1 and $10\text{ m}\Omega\text{-cm}$. At low temperatures the resistivity increases by a factor of anywhere from 1 to 20. These data imply that quasicrystals have a small gap of less than 0.2 eV .² Quasicrystals are actually argued to have a pseudogap, with the gap caused by strong electron localization at the Fermi level. Due to localization, conduction at low temperatures is best described using models of weak localization and strong electron-electron scattering. One of the primary results of localization in these materials is that it is enhanced by the crystallinity of the sample. Hence, better atomic order (evidenced by sharper x-ray or electron diffraction lines) leads to higher resistivity.^{5,6} This is the opposite behavior to that typically observed for a metallic material. Hence, the resistivities measured on high-quality single-domain samples provide a maximum limit to the resistivity in a tuned material. Another key to the resistivity is that it tends to increase as the average atomic number of the alloy increases. This was first described in studies of single domain $\text{Al}_{70}\text{Cu}_{20}\text{Fe}_{10}$, $\text{Al}_{70}\text{Cu}_{20}\text{Ru}_{10}$ and $\text{Al}_{70}\text{Cu}_{20}\text{Os}_{10}$ quasicrystals.⁷ All these features provide one with handles with which to tune the electrical behavior of quasicrystalline materials.

The three materials studied here, $\text{Al}_{70}\text{Pd}_{20}\text{Re}_{10}$, $\text{Al}_{62.5}\text{Cu}_{25}\text{Fe}_{12.5}$, and $\text{Ti}_{54}\text{Zr}_{26}\text{Ni}_{20}$ show widely varying transport characteristics, indicative of the great variability inherent in the electrical properties of these materials. AlPdRe has a large resistivity which increases rapidly as T is lowered. AlCuFe , however, has a room temperature resistivity roughly half that of AlPdRe , and only increases by a factor of 2 down to 4 K . TiZrNi , then, displays the lowest resistivity and the smallest change in resistivity at low temperatures. This trend of lower resistivity correlating with smaller temperature dependence of the resistivity is a common feature to many quasicrystals studied and may be a universal property of these systems.⁵ While the resistivity of the AlPdRe and AlCuFe samples appear to be too large for good thermoelectric materials, the TiZrNi sample does have a large enough conductivity to be of interest. Most importantly, while the conductivity of the AlPdRe and AlCuFe samples differed by more than a factor of 2, their thermal conductivities were nearly indistinguishable. Thermal conductivity measurements on TiZrNi have yet to be performed.

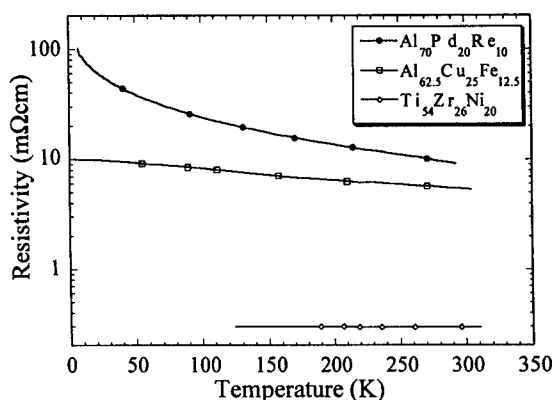


Figure 2, Resistivity vs. temperature for AlPdRe , AlCuFe , and TiZrNi quasicrystals.

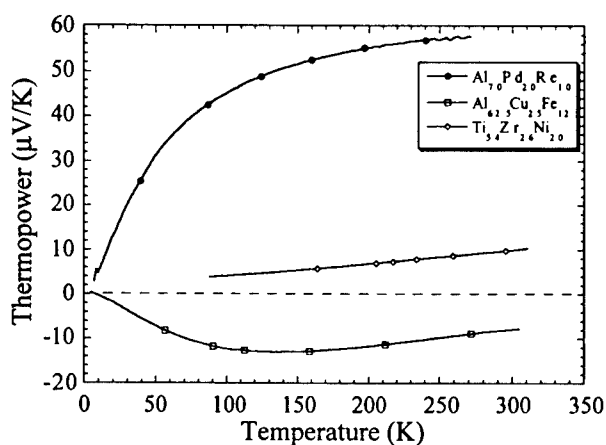


Figure 3, Thermoelectric power vs. temperature for AlPdRe, AlCuFe and TiZrNi Quasicrystals.

Finally, a good thermoelectric must have a large thermopower. Published data on the thermopower of quasicrystals is rather scarce. In the literature one finds thermopowers ranging from $-30 \mu\text{V/K}$ to $+50 \mu\text{V/K}$.⁸ While these are currently not yet large enough for thermoelectric application, the interest is that nearly this entire variability can be found in a single quasicrystalline compound, AlCuFe. At room temperature, the iron rich material ($\text{Al}_{62.5}\text{Cu}_{24.5}\text{Fe}_{13}$) has $\alpha = +45 \mu\text{V/K}$, while the iron poor composition ($\text{Al}_{62.5}\text{Cu}_{26.5}\text{Fe}_{11}$) has $\alpha = -30 \mu\text{V/K}$.⁸

For AlCuFe quasicrystals we find a thermopower in the range of the previously published data (Figure 3). AlPdRe on the other hand, is found to have a very large thermopower for a quasicrystal $+55 \mu\text{V/K}$ and to be fairly constant over the temperatures from 150 K to 300 K. This broad range of high thermopower is just what is needed for a widely useful low temperature TE cooling system. TiZrNi, while having the best conductive properties of the three systems studied also has the lowest thermopower. The variability and sensitivity of the thermopower to slight changes in the composition or structure are also borne out in band structure calculations^{9,10} and in photoemission measurements.¹¹ Both measurements predict large sharp features in the density of states surrounding the pseudogap at the Fermi energy.

SUMMARY

The quasicrystals are going to be interesting materials to study with regard to TE applications primarily because they closely match the concept of an ideal thermoelectric material being an electron crystal but a phonon glass. Quasicrystals have thermal conductivities approaching those of amorphous metals and insulators while they have conductive properties similar to those of bad metals and small gap semimetals. By changing the chemical composition, dopant concentrations, or crystallinity, the conductivity of quasicrystals should prove readily tunable. In addition, the great sensitivity of the magnitude and sign of the thermopower in the few quasicrystals so far studied provides hope that higher thermopowers can, and will, be found. Although the quasicrystals form a rather large class of compounds, for each quasicrystal, there also typically

exists at least one quasicrystalline approximant phase. These approximants should also be investigated for their potential as thermoelectric materials since they are known to have similar electrical properties to their related quasicrystals.¹

REFERENCES

- ¹ A.I. Goldman and R.I. Kelton, Rev. Mod. Phys. **65**, 2193 (1993).
- ² S.J. Poon, Adv. Phys. **41**, 303 (1992).
- ³ C. Janot, *Quasicrystals*, Clarendon Press, Oxford.
- ⁴ M.A. Chernikov, A. Bianchi, and H.R. Ott, Phys. Rev. B **51**, 153 (1995).
- ⁵ T. Klein, C. Berger, D. Mayou, and F. Cyrot-Lackmann, Phys. Rev. B **66**, 2907 (1991).
- ⁶ R. Tamura, A. Waseda, K. Kimura, and H. Ino, Phys. Rev. B **50**, 9640 (1994).
- ⁷ Y. Honda, K. Edagawa, S. Takeuchi, A.-P. Tsai and A. Inoue, Jpn. J. Appl. Phys. **34**, 2415 (1995).
- ⁸ F.S. Pierce, S.J. Poon, and B.D. Biggs, Phys. Rev. Lett. **70**, 3919 (1993).
- ⁹ G. Kasner, H. Schwabe and H. Böttger, Phys. Rev. B **51**, 10454 (1995).
- ¹⁰ S.E. Burkov, A.A. Varlamov and D.V. Livanov, Phys. Rev. B **53**, 11504 (1996).
- ¹¹ U. Mizutani, Y. Yamada, T. Takeuchi, K. Hashimoto, E. Belin, A. Sadoc, T. Yamauchi and T. Matsuda, J. Phys: Conds. Matter **6**, 7335 (1994).

ELECTRICAL PROPERTIES AND FIGURES OF MERIT FOR NEW CHALCOGENIDE-BASED THERMOELECTRIC MATERIALS

JON L. SCHINDLER[‡], TIM P. HOGAN[†], PAUL W. BRAZIS, AND CARL R. KANNEWURF
Department of Electrical and Computer Engineering,
Northwestern University, Evanston, IL 60208-3118

[‡] Present Address: CMRC-Display Technologies Group, Motorola, Inc., Schaumburg, IL 60196

[†] Present Address: Department of Physics, University of Houston, Houston, TX 77204-5506

DUCK-YOUNG CHUNG AND MERCOURI G. KANATZIDIS
Department of Chemistry and Center for Fundamental Materials Research,
Michigan State University, East Lansing, MI 48824-1322

ABSTRACT

New Bi-based chalcogenide compounds have been prepared using the polychalcogenide flux technique for crystal growth. These materials exhibit characteristics of good thermoelectric materials. Single crystals of the compound CsBi_4Te_6 have shown conductivity as high as 2440 S/cm with a p-type thermoelectric power of $\approx +110 \mu\text{V/K}$ at room temperature. A second compound, $\beta\text{-K}_2\text{Bi}_8\text{Se}_{13}$ shows lower conductivity $\approx 240 \text{ S/cm}$, but a larger n-type thermopower $\approx -200 \mu\text{V/K}$. Thermal transport measurements have been performed on hot-pressed pellets of these materials and the results show comparable or lower thermal conductivities than Bi_2Te_3 . This improvement may reflect the reduced lattice symmetry of the new chalcogenide thermoelectrics. The thermoelectric figure of merit for CsBi_4Te_6 reaches $ZT \approx 0.32$ at 260 K and for $\beta\text{-K}_2\text{Bi}_8\text{Se}_{13}$ $ZT \approx 0.32$ at room temperature, indicating that these compounds are viable candidates for thermoelectric refrigeration applications.

INTRODUCTION

The last several years have witnessed a renewed interest in thermoelectric materials, prompted by factors such as environmental concerns over existing refrigerants and also by new ideas of how to achieve improved thermoelectric performance [1,2]. In addition, advances in materials synthesis techniques that have occurred over the past few decades provide new approaches to materials preparation. Recent examinations of the significant, existing body of knowledge on thermoelectric materials, especially Bi_2Te_3 , have suggested several avenues of research. These routes primarily focus on achieving materials with lower thermal conductivity without sacrificing the relevant electrical properties of thermoelectric power (S) and conductivity (σ) [2,3].

One new solid-state synthesis technique, the polychalcogenide flux technique, employs alkali metal/chalcogenide fluxes to aid the formation of chalcogenide materials at temperatures below those used for traditional solid-state synthesis methods. This low temperature synthesis method was recently reviewed by Kanatzidis and Sutorik [4] and has proven itself as an effective route to new compounds derived chemically and/or structurally from Bi_2Te_3 . These new compounds represent kinetically favored, rather than thermodynamically favored reaction products, and this distinction has enabled the identification of new Bi-chalcogenide materials. The properties of these new materials are encouraging. They often exhibit electrical properties similar to Bi_2Te_3 [5-7], but thermal transport results suggest that the structural differences, which could be generally described as lower crystalline symmetry, act to reduce the thermal conductivity (κ). This result moves in the desired direction for improving the thermoelectric figure of merit, Z , defined as:

$$Z = \frac{S^2 \sigma}{\kappa} \quad (1)$$

and this provides impetus to develop these materials further. This report describes the electrical and thermal transport properties and the thermoelectric figure of merit for several new chalcogenide thermoelectric materials.

EXPERIMENTAL

Single crystal samples of the compounds CsBi_4Te_6 and $\beta\text{-K}_2\text{Bi}_8\text{Se}_{13}$ were prepared using a molten, polychalcogenide flux technique [4,8,9]. The resulting crystals showed a thin needle morphology of approximately rectangular cross-section, with typical cross-sectional dimensions $\sim 20 - 200 \mu\text{m}$. Samples having larger cross-section often consisted of a fused bundle of smaller crystals and such samples were not chosen for electrical measurements. The crystals exhibited lengths $\sim 2 - 20 \text{ mm}$ along the needle axis, providing a very good geometry for the electrical measurements. In order to obtain more accurate determinations of the thermoelectric figure of merit, Z , each single crystal was used for both conductivity and thermopower characterizations. Also, several samples of each material type were measured to screen for variations in the electrical properties among the crystals. Some crystals of the $\beta\text{-K}_2\text{Bi}_8\text{Se}_{13}$ compound were annealed under vacuum at 500°C for 36 h to increase the conductivity.

The electrical properties of the prepared single crystals were measured using a four-probe conductivity and a slow-ac thermopower measurement technique [10,11]. The measurement apparatus featured $\text{Au}(0.07\% \text{ Fe})/\text{Chromel}$ differential thermocouples for monitoring the applied thermal gradients. The sample and thermocouple voltages were measured with Keithley model 181 or model 182 nanovoltmeters. Electrical contacts to the crystals consisted of fine Au wire ($10 - 60 \mu\text{m}$ diameter) leads attached to the crystals with Au or Ag paste. The Au paste contacts were generally superior to those made with Ag paste. The excitation currents for conductivity measurement were kept as low as possible, typically 1.0 mA or less, to minimize the influence of non-ohmic voltage response. In addition, the conductivity measurements took place in a reduced pressure ($\sim 10 \text{ mTorr}$) of dry helium gas to improve the thermal equilibrium throughout the measurements. The thermopower measurements employed thermal gradients $\sim 0.1 - 0.3 \text{ K}$. These measurements took place under turbopumped vacuum of $< 2 \times 10^{-5} \text{ Torr}$ and the sample chamber was evacuated for several hours prior to the cooldown procedure to remove any residual water vapor.

The thermal conductivity measurements were taken on polycrystalline, pressed pellet samples. The automated measurement technique [12] was based on a pulsed heat method described by Maldonado [13]. This measurement yields both thermal conductivity and thermoelectric power data simultaneously. The sample mounting method incorporated a four probe measurement configuration, having the Cu/Constantan differential thermocouple junctions placed along the length of the sample, away from the ends of the pellet. Vacuum levels were below 10^{-5} Torr throughout the experiment. The thermocouple junctions were fixed to the sample with GE 7031 varnish. For thermoelectric power measurements, 10 micron diameter Au wires were Au pasted to the sample at the same locations as the differential thermocouple junctions. Reference measurements on a commercially prepared Bi_2Te_3 sample differed by less than 10% from the manufacturer's data [14].

RESULTS

The crystal structures of these Bi-chalcogenide compounds CsBi_4Te_6 and $\beta\text{-K}_2\text{Bi}_8\text{Se}_{13}$ have been examined by X-ray diffraction methods and the structures were solved and refined by standard analysis methods. The procedures employed for these solutions are detailed elsewhere [4,15]. These materials display layered crystal structures that derive from Bi_2Te_3 . Like other alkali-metal Bi-Te compounds, CsBi_4Te_6 exhibits a structure with the alkali metal atoms between adjacent Bi-Te layers. In contrast, the $\beta\text{-K}_2\text{Bi}_8\text{Se}_{13}$ structure contains fragments of the Bi_2Te_3 layer structure, along with other building blocks of NaCl and CdI_2 forms. These distinct blocks connect together into a complex three-dimensional network [15]. Thus, both materials possess lower symmetry than Bi_2Te_3 , and this represents one strategy for reducing thermal transport.

The electrical measurements identified temperature dependent properties reminiscent of Bi_2Te_3 . The conductivity versus temperature displayed a weak metallic dependence, with the conductivity decreasing as the temperature increased from 4 K to 295 K, as shown in Fig. 1. The CsBi_4Te_6 crystals exhibited some variation in conductivity, with room temperature values ranging from $\approx 350 \text{ S/cm}$ to a maximum of 2440 S/cm . The $\beta\text{-K}_2\text{Bi}_8\text{Se}_{13}$ crystals showed lower conductivities in comparison, with typical values of $200 - 240 \text{ S/cm}$ at room temperature. Annealing these crystals increased the room temperature conductivity to as high as 670 S/cm .

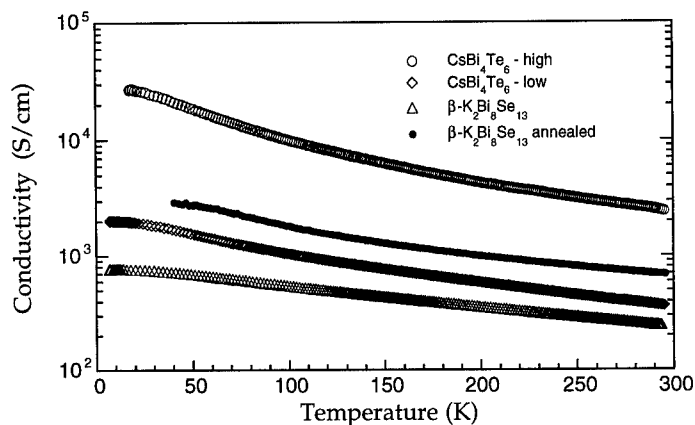


Fig. 1- Conductivity versus temperature for Bi-chalcogenide single crystals.

The thermopower results for these new Bi-chalcogenides also followed the behavior seen in Bi_2Te_3 compounds (see Fig. 2). The p-type thermoelectric response of CsBi_4Te_6 was large at room temperature $\sim +110 \mu\text{V/K}$, typical for a semiconductor, but the temperature dependence did not show the activated behavior of semiconductors. Instead, the thermopower tended toward zero at low temperatures as one would expect from a metal. The CsBi_4Te_6 crystals showed little sample to sample variation in thermopower, in contrast to the conductivity. As shown in Fig. 2a, the $S(T)$ data for both low and high conductivity samples were nearly identical over the entire range of temperature. The samples reached a peak in $S(T)$ just below room temperature. Figure 2b presents thermopower results for the as-prepared and annealed $\beta\text{-K}_2\text{Bi}_8\text{Se}_{13}$ crystals. This compound exhibits n-type conduction, unlike the p-type CsBi_4Te_6 , as indicated by the negative thermopower. The as-prepared crystals displayed $S(295 \text{ K}) \approx -200 \mu\text{V/K}$, with the magnitude still increasing.

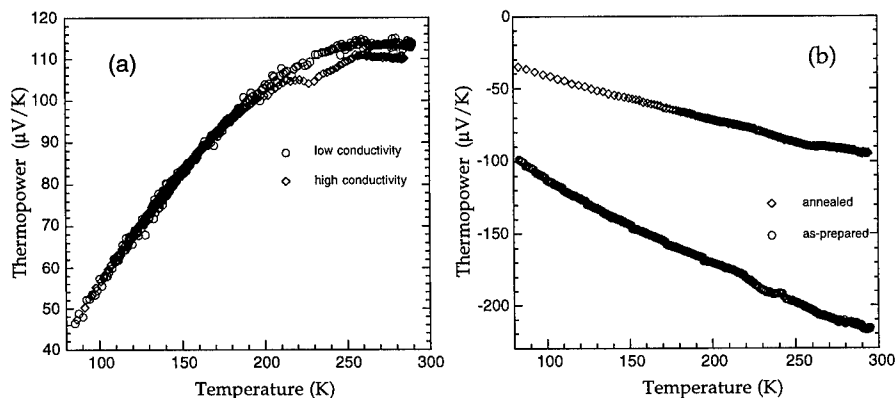


Fig. 2 - Thermopower versus temperature for a single crystals of: a) CsBi_4Te_6 ; b) $\beta\text{-K}_2\text{Bi}_8\text{Se}_{13}$.

Thermal transport measurements are more difficult to perform on thin, needle crystals. As a result, thermal conductivity measurements were performed on pressed pellets of these materials. Figure 3 presents thermal conductivity versus temperature data for a pellet of CsBi_4Te_6 , measured by the pulsed method described above. The thermal conductivity varied from 9 - 12 $\text{mW/cm}\cdot\text{K}$,

with a shallow minimum between 170 and 210 K. Thermal conductivity for the β -K₂Bi₈Se₁₃ compound was measured at room temperature only, yielding a value of 8.3 mW/cm•K.

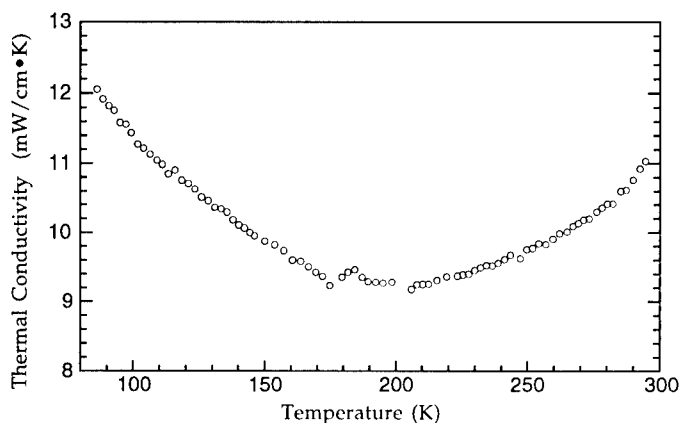


Fig. 3 - Thermal conductivity versus temperature for a pressed pellet of CsBi₄Te₆.

DISCUSSION

The conductivity results for CsBi₄Te₆ appear very promising. A number of the crystals we studied had $\sigma(295\text{ K})$ greater than 1000 S/cm, with the best sample reaching 2440 S/cm. As shown in Fig. 2, the thermopower results for two specimens, one having the highest and the other much lower conductivity, showed nearly identical response. The similar thermopower value among many samples suggests that these crystals have similar carrier densities and therefore the differences in conductivities may indicate mobility variations among the crystals. The sample geometry is another factor that would influence the measured conductivity but not the thermopower. The needle-like crystals possess small and sometimes irregular cross-sectional area, contributing to dimensional measurement inaccuracy. However, the cross-section geometries were always calculated conservatively to err on the side of lower conductivities. In the β -K₂Bi₈Se₁₃ crystals, the electrical measurements indicate that annealing under vacuum increases the number of carriers, as evidenced by an increase in conductivity along with a decrease in thermopower magnitude. Hall effect measurements should be valuable as a probe of the carrier densities and mobilities in the various crystals, and these measurements are in progress. The results will provide both a better understanding of these materials and some direction for optimizing the electrical properties to maximize the power factor.

The thermal conductivity results also appear promising. The electronic contribution to the thermal conductivity can be estimated from the Weidemann-Franz law for metals:

$$\kappa_{el} \approx (2.44 \times 10^{-8}) \sigma T \quad (\text{W/cm}\cdot\text{K}) \quad (2)$$

using the σ values for the pressed pellets. These calculations yield $\kappa_{el} \approx 1.3\text{ mW/cm}\cdot\text{K}$ or less, suggesting that the measured thermal conductivities are dominated by the lattice contribution. These preliminary results offer some evidence that the reduced symmetry in these materials may act to lower the lattice thermal transport compared to Bi₂Te₃.

The conductivity and thermopower results were combined to examine the power factors ($S^2\sigma$) in the different samples over temperature (see Fig. 4). The high conductivity sample of CsBi₄Te₆ stands out as the best, while the other samples are much closer to one another. The temperature dependence of the power factor in the CsBi₄Te₆ samples reaches a peak well below room temperature, while the β -K₂Bi₈Se₁₃ crystals are just reaching a peak at room temperature. For cooling applications, a peak in the power factor at lower temperatures would be desirable. In the β -K₂Bi₈Se₁₃ compound, the annealed sample shows a lower power factor than the as-prepared

material, as expected based on the significant drop in thermopower. As a result, the annealed sample would also demonstrate a lower figure of merit, Z . Therefore, the annealing treatment in this material is not effective for improving thermoelectric performance.

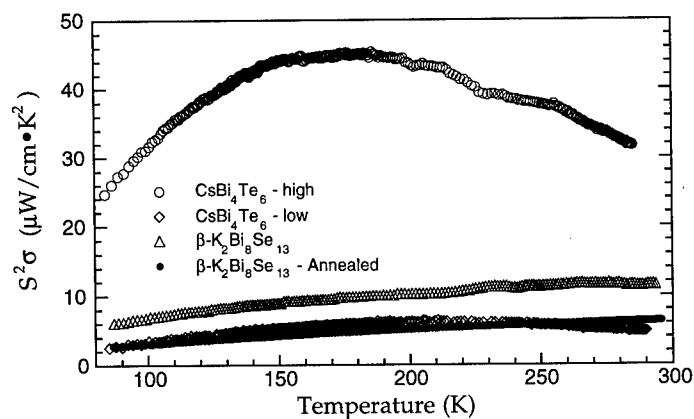


Fig. 4 - Power factor versus temperature for Bi-chalcogenide single crystals.

Finally, we can calculate the figure of merit, ZT , following Eq. 1. Ideally, the electrical and thermal properties would all be from the same sample. However, as these are exploratory studies of new materials, figures of merit based on the single crystal electrical properties provide valuable indications of the potential for these materials. In order to more accurately determine ZT for the single crystal samples, a revised κ is necessary. An additional contribution from κ_{el} was estimated using the Wiedemann-Franz law (Eq. 2) and the single crystal $\sigma(T)$ data. The resultant value was added to the measured κ . Based on this revised κ value, the as-prepared $\beta\text{-K}_2\text{Bi}_8\text{Se}_{13}$ shows a room temperature $ZT \approx 0.32$ at 295 K. Figure 5 presents the ZT versus temperature results for CsBi_4Te_6 , also obtained by combining the single crystal electrical data with the revised thermal conductivity data. The high conductivity crystal results peak at $ZT \approx 0.32$ near 260 K. By comparison, the ZT versus temperature for the low conductivity sample of CsBi_4Te_6 peaks at $ZT \approx 0.11$ near 250 K. The ZT data for both crystals show a relatively broad plateau below room temperature, which would predict good cooling performance over this wide temperature range.

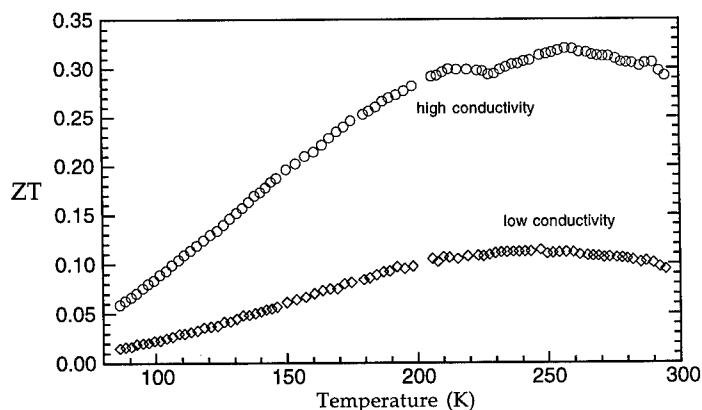


Fig. 5 - Figure of merit, ZT , versus temperature for CsBi_4Te_6 single crystals.

These figure of merit results provide definite encouragement to explore these new materials in more detail. It is important to note that because these materials derive from Bi_2Te_3 , they are probably closer to semiconductors than metals. As pointed out by Ioffe [16], Wiedemann-Franz calculations may overestimate κ_{el} in that case, especially for the lower conductivity crystals but so for the high conductivity CsBi_4Te_6 crystal at higher temperatures. This overestimation would reduce any calculated ZT values, so the numbers given above are conservative estimates. In addition, these results do not represent optimized materials, but rather the initial studies of some promising new thermoelectrics. Further studies of carrier concentration and carrier mobility and their influence on single crystal samples will indicate how to optimize these materials. It also remains to be seen whether preparation of these materials for working thermoelectric devices can achieve comparable properties to these single crystal results.

CONCLUSIONS

The polychalcogenide flux technique was used to prepare new, crystalline Bi-chalcogenide materials, derived from Bi_2Te_3 . Two new compounds, CsBi_4Te_6 and $\beta\text{-K}_2\text{Bi}_8\text{Se}_{13}$, have been identified as very promising materials for thermoelectric cooling applications, based on their electrical conductivity and Seebeck coefficients. Thermal conductivity results show reduced thermal transport relative to Bi_2Te_3 . The electrical and thermal properties yield figures of merit $ZT > 0.3$ near room temperature. These investigations continue in an effort to better understand the electrical properties and to prepare optimized samples with still higher figures of merit.

ACKNOWLEDGMENTS

This research was supported at NU and MSU by the Office of Naval Research (N00014-94-1-0935). Some work at NU made use of Central Facilities supported by the National Science Foundation through the NU Materials Research Center (DMR-9632472).

REFERENCES

- [1] T. Tritt, *Science*, vol. 272, no. 5266, pp. 1276 - 1277, 1996.
- [2] G. Mahan, B. Sales, and J. Sharp, *Physics Today*, March, 1997, pp. 42 - 47.
- [3] G. A. Slack, in *CRC Handbook of Thermoelectrics*, edited by D. M. Rowe, (CRC Press, Boca Raton, FL, 1995), pp. 407 - 440.
- [4] M. G. Kanatzidis and A. C. Sutorik, in *Progress in Inorganic Chemistry*, vol. 43, 1996, pp. 151 - 265.
- [5] H. Kaibe, Y. Tanaka, M. Sakata, and I. Nishida, *J. Phys. Chem. Solids*, vol. 50, no. 9, pp. 945 - 950, 1989.
- [6] H.-W. Jeon, H.-P. Ha, D.-B. Hyun, and J.-D. Shim, *J. Phys. Chem. Solids*, vol. 52, no. 4, pp. 579 - 585, 1991.
- [7] *CRC Handbook of Thermoelectrics*, edited by D. M. Rowe, (CRC Press, Boca Raton, FL, 1995).
- [8] D.-Y. Chung, T. Hogan, J. Schindler, L. Iordanidis, P. Brazis, C. R. Kannewurf, B. Chen, C. Uher, M. G. Kanatzidis, *Thermoelectric Materials - New Directions and Approaches*, edited by M. G. Kanatzidis, H. Lyon, G. Mahan, and T. Tritt, (Mater. Res. Soc. Proc. **478**, San Francisco, CA, 1997).
- [9] D.-Y. Chung, K.-S. Choi, L. Iordanidis, J. L. Schindler, P. W. Brazis, C. R. Kannewurf, B. Chen, C. Uher, and M. G. Kanatzidis, (in preparation).
- [10] J. W. Lyding, H. O. Marcy, T. J. Marks, and C. R. Kannewurf, *IEEE Trans. Instrum. Meas.*, vol. 37, no. 1, pp. 76 - 80, 1988.
- [11] H. O. Marcy, T. J. Marks, and C. R. Kannewurf, *IEEE Trans. Instrum. Meas.*, vol. 39, no. 5, pp. 756 - 760, 1990.
- [12] T. P. Hogan, Ph.D. thesis, Northwestern University, 1996.
- [13] O. Maldonado, *Cryogenics*, vol. 32, no. 10, pp. 908 - 912, 1992.
- [14] Marlow Industries, Inc., Reference data for Bi_2Te_3 samples, (1995).
- [15] M. G. Kanatzidis, T. J. McCarthy, T. A. Tanzer, L.-H. Chen, L. Iordanidis, T. Hogan, C. R. Kannewurf, C. Uher, and B. Chen, *Chem. Mater.*, vol. 8, no. 7, pp. 1465 - 1474, 1996.
- [16] A. F. Ioffe, *Semiconductor Thermoelements and Thermoelectric Cooling*, (Infosearch Limited, London, 1957), pp. 44 - 46.

SEARCHING FOR NEW THERMOELECTRICS IN CHEMICALLY AND STRUCTURALLY COMPLEX BISMUTH CHALCOGENIDES

Duck Young Chung^(a), Tim Hogan^(b), Jon Schindler^(b), Lykourgos Iordanidis^(a), Paul Brazis^(b), Carl R. Kannewurf^(b), Baoxing Chen^(c), Ctirad Uher^(c), Mercouri G. Kanatzidis^(a)

^(a)*Department of Chemistry and Center for Fundamental Materials Research, Michigan State University, East Lansing, MI 48824.* ^(b)*Department of Electrical Engineering and Computer Science, Northwestern University, Evanston, IL 60208* ^(c)*Department of Physics, University of Michigan, Ann Arbor, MI 48109*

ABSTRACT

A solid state chemistry synthetic approach towards identifying new materials with potentially superior thermoelectric properties is presented. Materials with complex compositions and structures also have complex electronic structures which may give rise to high thermoelectric powers and at the same time possess low thermal conductivities. The structures and thermoelectric properties of several new promising compounds with K-Bi-Se, K-Bi-S, Ba-Bi-Te, Cs-Bi-Te, and Rb-Bi-Te are reported.

INTRODUCTION

Interest in new thermoelectric (TE) materials with improved figures of merit is increasing rapidly [1,2]. The much increased sophistication of materials research coupled with many discoveries of new compounds, a wider variety of observed phenomena, and vastly improved capabilities for calculation of electronic structure and properties, provide a solid foundation for discovering new thermoelectrics once again. Efficient TE materials would revolutionize the small cooler industry by eliminating the use of freons and by eliminating the moving parts in coolers (except possibly for fans) and would allow cooling of distributed systems, and even faster electronics. To improve device performance one needs to maximize the thermoelectric figure of merit, $ZT = (S^2\sigma/\kappa)T$; where S is the thermopower, σ the electrical conductivity, κ the thermal conductivity and T is the temperature. All three of these properties are determined by the details of the electronic structure and scattering of charge carriers (electrons or holes) and thus are not independently controllable parameters. κ also has a contribution from lattice vibrations, κ_l , the phonon thermal conductivity. Thus $\kappa = \kappa_e + \kappa_l$, where κ_e is the carrier thermal conductivity. Therefore one must increase σ and S while minimizing κ . Since the electrical conductivity and thermopower of optimally n or p doped Bi_2Te_3 is in the range of 500-800 S/cm and $\pm 220 \mu\text{V/K}$ [3] respectively, significant improvements in thermoelectric figure of merit could occur if materials of comparable conductivities but thermopowers of 300 to 350 $\mu\text{V/K}$ can be found.

We have initiated an exploratory synthesis program to identify new multinary phases with Bi and Sb with narrow band-gaps which may be suitable as thermoelectric materials. This work is based on the proposition that materials with more complex compositions and structures should have complex electronic structures which may give rise to high thermoelectric powers according to the Mott formula below, and at the same time possess low thermal conductivities. The thermopower S is given by the Mott equation:

$$S = \frac{\pi^2}{3} \cdot \frac{k^2 T}{e} \cdot \left. \frac{d \ln \sigma(E)}{dE} \right|_{E=E_F}$$

where $\sigma(E)$ is the electrical conductivity determined as a function of band filling. The electronic conductivity $\sigma = \sigma(E) \big|_{E=E_F}$ where E_F is the Fermi energy. If the carrier scattering is independent of energy, then $\sigma(E)$ is just proportional to the density of states at E . In the general case, S is a measure of the difference in $\sigma(E)$ above and below the Fermi surface - specifically through the logarithmic derivative of it with respect to E , see the equation above. So by manipulating the energy dependence of $\sigma(E)$ one can control simultaneously σ and S . Since the thermopower of a material is a measure of the asymmetry in electronic structure and scattering rates near the Fermi level (E_F) [3], we aim to produce complexities in either or both in a small energy interval (a few kT) near E_F . While simple materials usually have simple band structures, cooperative electronic phenomena in a few materials lead to complex structures in the electronic excitations and thus also possibly to high thermopowers. Because metallic compounds typically have small thermopowers and large thermal conductivities we focus our efforts in materials which are narrow gap semiconductors or semimetals (band-gap $0 < E_g < 0.5$ eV).

Despite the empirical guidelines one has, it is still challenging to choose the particular system for exploration. The fact that Bi_2Te_3 is the best material known to date suggests that it combines many of the necessary features for high TE response. If there is something special about bismuth in giving rise to simultaneously high electrical conductivity and thermoelectric power, it should be manifested in other compounds of Bi as well. This suggests a research direction where one could explore other, more complex, chalcogenides of this element in the hope that some (or all) of the key properties would be superior to those of Bi_2Te_3 . Further, one can argue that structurally and compositionally more complex bismuth chalcogenides would, most likely, have a low lattice thermal conductivity. This is because a structure with a large unit cell is expected for complex materials, which would decrease the acoustic mode phonon velocities that are responsible for the transfer of heat in materials. The relatively weak Bi-Te bonding and the large atomic masses contribute as well to the low phonon velocities. Therefore, exploratory synthesis in this region of the periodic table becomes a reasonable activity and, as the preliminary results show, quite promising. In this article we present our efforts to synthesize bulk materials with enhanced TE figures of merit.

RESULTS AND DISCUSSION

Since the materials used in thermoelectric devices are chalcogenide compounds, we are searching for more complex compounds of this type. Since many chalcogenides - especially those that are complex - decompose at relatively low temperature (perhaps 500 to 1000 °C), a low temperature synthesis method is needed. We have been exploiting polychalcogenide fluxes [4] for exactly these purposes.

We have obtained many new phases of bismuth by reacting the metal with alkali metal chalcogenide salts in polychalcogenide melts. Table 1 summarizes some of the most interesting new materials we have discovered in the course of this work. The prototypical Bi_2Te_3 is also listed in this table for comparison. As can be gleaned from the table, Bi_2Te_3 still has the highest ZT, however, some of the new phases have sufficiently high starting ZTs to be promising for more extensive studies. We note that the new materials have not been optimized at all, while the best samples of Bi_2Te_3 have undergone four decades of continued development. We believe some of the new materials in Table 1 may indeed emerge as competitive thermoelectrics in the future if their development is seriously pursued. Only a few of the materials shown in Table 1 will be elaborated upon here.

One such phase is the orthorhombic BaBiTe_3 , which was prepared at 750 °C from a K_2Te_4 flux in which a mixture of Bi and Ba were dissolved. The structure of this material is two-dimensional with $[\text{BiTe}_3]^{2-}$ layers alternating with Ba cations, see Figure 1 [5]. Many interesting features exist in the structure, one of which is the presence of Te-Te bonds between Te atoms arranged in ribbons. The flat Te ribbons contain zig-zag Te chains and they are

Table 1. Thermoelectric and Other Properties of New Multinary Compounds Containing Bi and Chalcogens

Compound	Structure Type	Sample Type	σ_{RT} (S/cm)	S_{RT} (μ V/K)	κ_{RT} (W/m·K)	$E_{g,RT}$ (eV)	mp (°C)	ref.
$Bi_2Te_3^*$	Bi_2Te_3	crystal	~ 890	~ 210	1.4 - 1.6	0.15	585	[3]
$BaBiTe_3$	$BaSbSe_3$	crystal	42	205	0.63	0.28, 0.42	644	[5]
$KBi_{6.33}S_{10}$	New	ingot	~ 100	~ -25	~ 1.4	0.25	710	[8]
$K_2Bi_8S_{13}$	$Sr_4Bi_6Se_{13}$	ingot	~ 100	-100	~ 3.2	0.25	713	[8]
α - $K_2Bi_8Se_{13}$	New	crystal	2	~ -250	—	0.76	—	[11]
β - $K_2Bi_8Se_{13}$	$Sr_4Bi_6Se_{13}$	crystal	240	-200,-220	0.8 - 1.6	0.59	672	[10]
$K_{2.5}Bi_{8.5}Se_{14}$	New	ingot	150	-100	1.2 - 1.6	0.56	692	[10]
γ - $CsBiS_2$	($RbBiS_2$)	crystal	~ 0.01	-450	—	1.11	—	[11]
$CsBi_4Te_6$	New	crystal	350-2440	110	0.9 - 1.9	0.11	545	[12,13]
$Rb_{0.5}Bi_{1.83}Te_3$	New	crystal	532	-25	—	< 0.03	540	[14]
$RbBi_4Se_7$	New	crystal	0.1	-650	—	0.60	650	[15]
$Pb_5Bi_6Se_{14}$	New	crystal	770	-40	—	0.48	709	[16]
α - $CsPbBi_3Se_6$	New	crystal	—	-475	—	0.55	710	[17]

*values from Marlow Industries, Inc. RT=room temperature

Note : except for Bi_2Te_3 which is optimized for high ZT, the properties of all other compounds were measured on “as made” material.

alternating between Bi-Te blocks, which look like they have been excised out of a rock-salt structure [5].

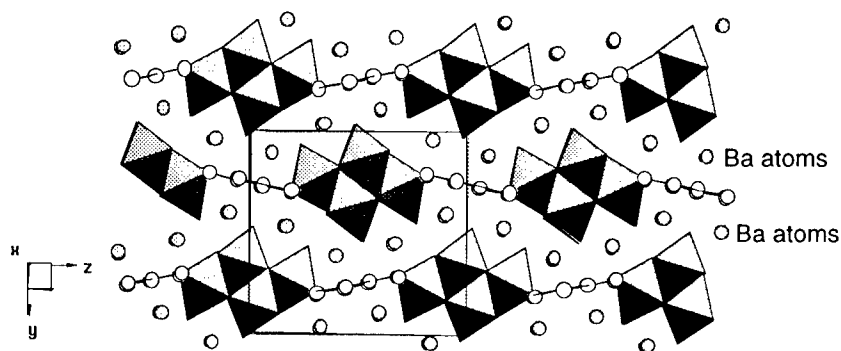


Figure 1. The anisotropic structure of BaBiTe_3 . The open white circles represent Te atoms.

BaBiTe_3 is a semiconductor with a narrow band-gap of 0.35 eV and has promising electrical properties. The electrical conductivity is reasonably high at ~ 50 S/cm and its thermoelectric power reaches 200-220 $\mu\text{V/K}$ at room temperature. The thermal conductivity, which is crucial in assessing the compound's potential, is only 65-70% that of the rhombohedral Bi_2Te_3 . The thermal conductivity is suppressed because of the low symmetry and because unit cell is much larger than that of Bi_2Te_3 . The compound also contains additional soft phonon modes from the Ba---Te interactions. The latter are absent in Bi_2Te_3 . This result supports the notion that ternary or quaternary compounds should possess lower thermal conductivity than the corresponding binary compounds. In order to fully assess the potential of this material for cooling devices, controlled n and p doping to moderately high levels is necessary. We have been successful in obtaining both n-type and p-type samples of this material based on preparation method. N-type material forms from Te-rich cesium polytelluride flux, and p-type forms from potassium polytelluride flux. In Cs_2Te_x flux Te substitution of Bi atoms could account for the n-type character of the material. Given the similar size of K^+ and Ba^{2+} , one may speculate that in K_2Te_x flux some substitution of Ba^{2+} by K^+ atoms renders the compound p-type by creating holes in the valence band.

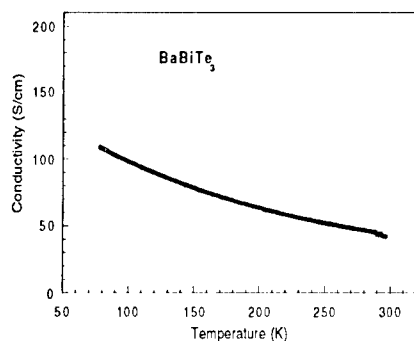


Figure 2. Variable temperature single crystal conductivity data for BaBiTe_3 .

Electronic band structure calculations on BaBiTe₃ show that it possesses substantial complexity near the Fermi level [5] and this suggests interesting thermoelectric properties according to the Mott equation. The conductivity of single crystals at room temperature was found between 20 and 50 S/cm with a weak negative temperature coefficient consistent with a metal-like or semimetallic material, see Figure 2. Qualitatively, the temperature dependence is similar to that of Bi₂Te₃. At room temperature the Seebeck coefficients of both n-type and p-type samples are large, ~ 200 μ V/K and $\sim +200$ μ V/K respectively, see Figure 3. The p-type samples exhibit a kink of unknown origin at ~ 215 K and an unusual sign reversal below 185 K. This behavior is not observed in the n-type samples where the Seebeck coefficient decreases but remains negative.

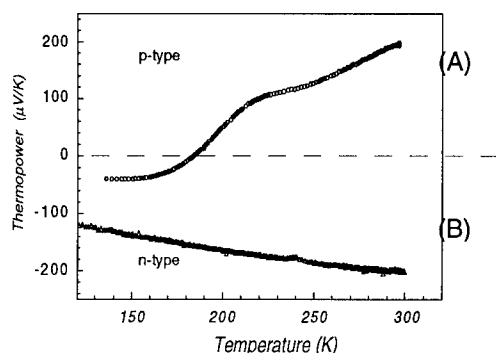


Figure 3. Variable temperature single crystal thermopower data for p-, and n-type BaBiTe₃.

The thermal conductivity of BaBiTe₃ at room temperature is remarkably low with respect to that of Bi₂Te₃ ($\kappa_L \sim 1.6$ W/m-K) [6]. Using the measured values of the electrical resistivity in conjunction with the Wiedemann-Franz law [7], we estimate the maximum possible value of the electronic thermal conductivity contribution to be below 1% of the total thermal conductivity of BaBiTe₃. Thus, essentially all heat in the compound is carried by lattice phonons. Hence, at least from the perspective of thermal transport, the BaBiTe₃ satisfies one of the key requirements for a useful thermoelectric material, and in fact, it possesses one of the lowest thermal conductivity values ever reported for a potential thermoelectric material. The very low thermal conductivity of BaBiTe₃ implies that the modification of the structure and composition of Bi₂Te₃ by the incorporation of BaTe_x or A₂Te_x (A=alkali metal) into it is a correct approach in lowering its lattice thermal conductivity. The calculated ZT at room temperature from a crystal having $\sigma=42$ S/cm, $S=205$ μ V/K and $\kappa=6.3$ mW/cm-K is 0.085 compared to ~ 0.9 for Bi₂Te₃. If ways could be found to enhance the electrical conductivity and, at the same time, preserve or even increase the already large thermopower a promising thermoelectric material might be obtained. To achieve this we need additional information regarding the transport properties including carrier concentrations and mobilities. Then optimization of these properties could be accomplished by controlling accurately the stoichiometry of these materials. This work is currently underway.

Two other interesting phases we discovered are the sulfides KBi_{6.33}S₁₀ and K₂Bi₈S₁₃. [8] They belong to the general family of compounds (A₂Q)_n(Bi₂Q₃)_m (A=alkali metal; Q=S, Se) with $n=1$ and $m=6.33, 4$, respectively. In an architectural context, both compounds can be thought of as an intimate composite of two different structure types interconnected to form a 3-

D network. They have three-dimensional orthorhombic structures made up of Bi_2Te_3 -type (NaCl-type) blocks and CdI_2 -type fragments that connect to form tunnels filled with eight-coordinate K^+ cations. This may be beneficial to the electronic properties of the compounds which may bear similarities to those of Bi_2Te_3 . The lower symmetry they possess may result in low thermal conductivity and could give rise to a superior thermoelectric material. The $[\text{Bi}_{6.33}\text{S}_{10}]$ framework is made of edge-sharing BiS_6 octahedra, as shown in Figure 4. The structure of $\text{K}_2\text{Bi}_8\text{S}_{13}$ is similar, but the Bi_2Te_3 -type (NaCl-type) blocks and CdI_2 -type fragments are arranged differently, Figure 5A. The features of both structure types found in both frameworks are highlighted in the figures. The isostructural selenium analog of $\text{K}_2\text{Bi}_8\text{S}_{13}$ has also been prepared. The structure of $\text{K}_2\text{Bi}_8\text{S}_{13}$ and $\beta\text{-K}_2\text{Bi}_8\text{Se}_{13}$ is closely related to that of $\text{Sr}_4\text{Bi}_6\text{Se}_{13}$ [9] by replacing two Sr^{2+} atoms with two K^+ atoms and the remaining two Sr^{2+} atoms with two Bi^{3+} atoms. These substitutions are isoelectronic on average and do not require compositional changes in the " $\text{Bi}_6\text{Se}_{13}$ " part of the compound.

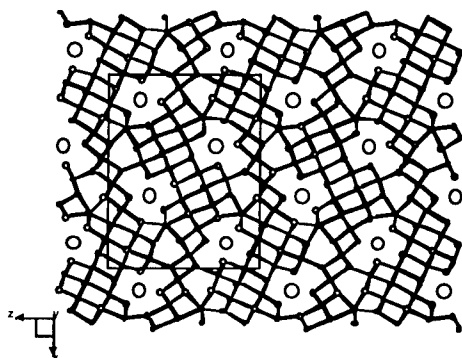


Figure 4. The structure of $\text{KBi}_{6.33}\text{S}_{10}$. Small white circles are sulfur atoms. Large circles are K atoms.

These ternary bismuth sulfides have promising electrical properties with maximum conductivity and thermopower of ~ 200 S/cm and $\sim 90 \mu\text{V/K}$, respectively. These are unoptimized values and we believe they can be greatly improved by further processing. Using the measured values of the electrical resistivity in conjunction with the Wiedemann-Franz law, we estimate the maximum possible value of the electronic thermal conductivity contribution to be below 1% of the total thermal conductivity. Thus, essentially all heat in these compounds is carried by lattice phonons. The pleasant surprise in these compounds comes from the rather low thermal conductivity they possess, as found especially in the sulfide $\text{KBi}_{6.33}\text{S}_{10}$. Taking as a bench mark the room temperature value of the total thermal conductivity of Bi_2Te_3 ($\kappa_1 = 1.6$ W/m-K), we note that the total thermal conductivity of $\text{KBi}_{6.33}\text{S}_{10}$ is actually lower (Figure 6). Hence, at least from the perspective of thermal transport, these compounds satisfy one of the key requirements for a useful thermoelectric materials, they possess low lattice thermal conductivity. This is an important finding because $\text{KBi}_{6.33}\text{S}_{10}$, being a sulfide, is expected to possess higher thermal conductivity compared to the heavier tellurides. If controlled doping can enhance the electrical conductivity and at the same time preserve or even increase the thermopower, in the case of $\text{KBi}_{6.33}\text{S}_{10}$ we indeed might have a promising thermoelectric material. To achieve this, we need additional information regarding the transport properties including carrier concentrations and mobilities. Both $\text{KBi}_{6.33}\text{S}_{10}$ and $\text{K}_2\text{Bi}_8\text{S}_{13}$ melt with no decomposition at 710°C and 713°C respectively, suggesting they will be amenable to thermoelectric element fabrication and processing, similar to that currently used in Bi_2Te_3 technology.

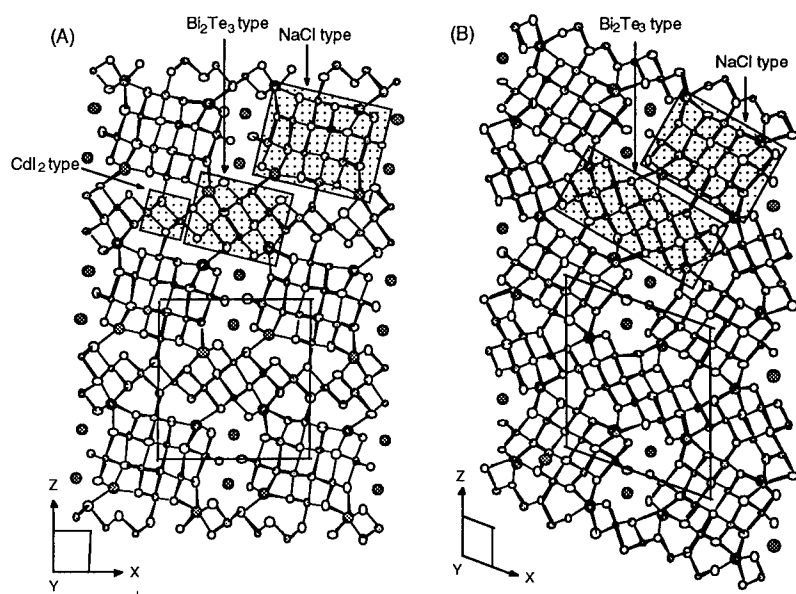


Figure 5. Left: The structure of $K_2Bi_8S_{13}$ and $\beta-K_2Bi_8Se_{13}$. Right: The structure of $K_{2.5}Bi_{8.5}Se_{14}$.

A related phase is that of $K_{2.5}Bi_{8.5}Se_{14}$ which differs from $\beta-K_2Bi_8Se_{13}$ in that it has in its formula an additional one half of an equivalent of $KBiSe_2$. In $K_{2.5}Bi_{8.5}Se_{14}$ only NaCl- and Bi_2Te_3 -type blocks exist. The addition of " $BiSe_2$ " in the CdI_2 -type blocks of $\beta-K_2Bi_8Se_{13}$ generates Bi_2Te_3 -type blocks which are five-bismuth atoms wide. This small structural modification preserves the same connectivity of the NaCl-type fragments and the same size and shape of the K atom sites as in $\beta-K_2Bi_8Se_{13}$, see Figure 5B.

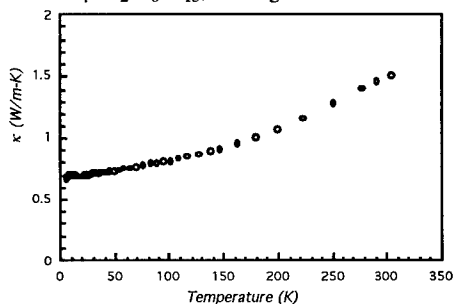


Figure 6. Variable temperature thermal conductivity data for a polycrystalline ingot of $KBi_{6.33}S_{10}$.

The electrical properties of $\beta-K_2Bi_8Se_{13}$ and $K_{2.5}Bi_{8.5}Se_{14}$ were measured on single crystal samples and polycrystalline ingot samples [10]. There is typically a variation of

conductivity among crystals of the same compound which may be due to a number of factors including errors associated with calculating the geometric factors of a given sample. The highest room temperature conductivity value obtained for single crystals of β - $\text{K}_2\text{Bi}_8\text{Se}_{13}$ was 240 S/cm with a weak negative temperature dependence consistent with a semi-metal or a narrow band-gap semiconducting material. There is a striking difference in conductivity when compared to α - $\text{K}_2\text{Bi}_8\text{Se}_{13}$ [11] which shows a room temperature value of 2 S/cm, and it is due to the substantial structural differences between the α - and β - forms. Polycrystalline compactions of these materials show similar trends where at room temperature the α - $\text{K}_2\text{Bi}_8\text{Se}_{13}$ has a conductivity of 0.01 S/cm while β - $\text{K}_2\text{Bi}_8\text{Se}_{13}$ and $\text{K}_{2.5}\text{Bi}_{8.5}\text{Se}_{14}$ show ~ 30 and ~ 150 S/cm (see Figure 7A), respectively. This enormous difference is attributed to the fact that β - $\text{K}_2\text{Bi}_8\text{Se}_{13}$ and $\text{K}_{2.5}\text{Bi}_{8.5}\text{Se}_{14}$ have more dense three-dimensional structures than α - $\text{K}_2\text{Bi}_8\text{Se}_{13}$, which gives rise to greater orbital overlap in the Bi-Se network and consequently lower band gap. Among β - $\text{K}_2\text{Bi}_8\text{Se}_{13}$ and $\text{K}_2\text{Bi}_8\text{S}_{13}$ the former has a higher electrical conductivity as would be expected.

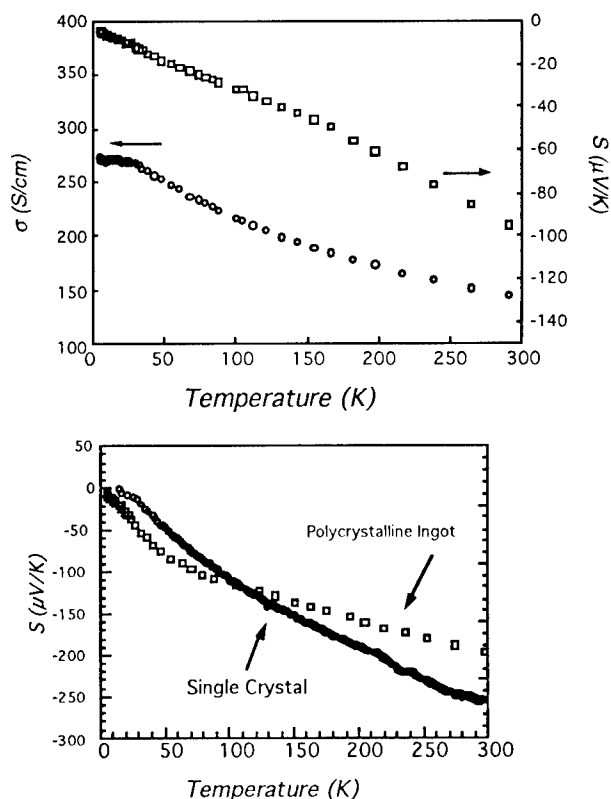


Figure 7. Top: Variable temperature electrical conductivity and thermoelectric power data for a polycrystalline ingot of $\text{K}_{2.5}\text{Bi}_{8.5}\text{Se}_{14}$. Bottom: Variable temperature thermoelectric power data for (a) a single crystal and (b) a polycrystalline ingot of β - $\text{K}_2\text{Bi}_8\text{Se}_{13}$.

The thermopower data for β -K₂Bi₈Se₁₃ and K_{2.5}Bi_{8.5}Se₁₄ show large negative Seebeck coefficients (-200 and -100 μ V/K at room temperature, respectively), which indicate the charge carriers are electrons (n-type), see Figures 7. It is remarkable that the thermopower behavior and magnitude of the β -K₂Bi₈Se₁₃ is similar to that of its α -analog [11] despite the large differences in conductivity. The thermopower values in these materials become less negative as the temperature is decreased from 300 K to 4 K, reminiscent of a metallic behavior, but the very large Seebeck coefficients suggest these materials are in fact semiconductors. The semiconducting character is also supported by the fact that optical gaps exist in the materials. Diffuse reflectance spectroscopy on β -K₂Bi₈Se₁₃ and K_{2.5}Bi_{8.5}Se₁₄ at room temperature revealed the presence of electronic transitions associated with the gap at 0.59 eV and 0.56 eV, respectively.

Annealing β -K₂Bi₈Se₁₃ in vacuum at 500 °C for 1.5 days more than doubles the room temperature electrical conductivity to values of 670 S/cm while maintaining the metal-like positive slope as a function of temperature, see Figure 8. At the same time the thermopower drops to -100 μ V/K from -200 μ V/K. The negative sign of the thermopower after annealing indicates that the carrier type has not changed, and suggests that this process generates more n-type carriers in the material perhaps through the creation of Se vacancies in the lattice. We plan to carry out extensive studies on this material to better understand the thermal effects operating during annealing and to improve its thermoelectric properties.

The room temperature thermal conductivities of β -K₂Bi₈Se₁₃ and K_{2.5}Bi_{8.5}Se₁₄ are comparable (1.28 and 1.21 W/m-K, respectively) and lower than that of optimized Bi₂Te₃. Some pressed pellets of β -K₂Bi₈Se₁₃, however, showed room temperature κ values of 0.83 W/m-K. This clearly suggests that it is possible to achieve lower thermal conductivity in ternary compounds with complex compositions and crystal structures compared to corresponding high symmetry binary compounds. Here again the maximum possible values of the κ_e contribution in both cases were estimated to be less than 1 % of κ_r , and so most of the heat in β -K₂Bi₈Se₁₃ and K_{2.5}Bi_{8.5}Se₁₄ is carried by lattice phonons. The thermal conductivity of β -K₂Bi₈Se₁₃ in the temperature range of 4-300 K is significantly lower than that of the isostructural compound K₂Bi₈S₁₃, which is consistent with the fact that the heavier Se atoms soften the lattice phonons thereby slowing down heat transport in the material.

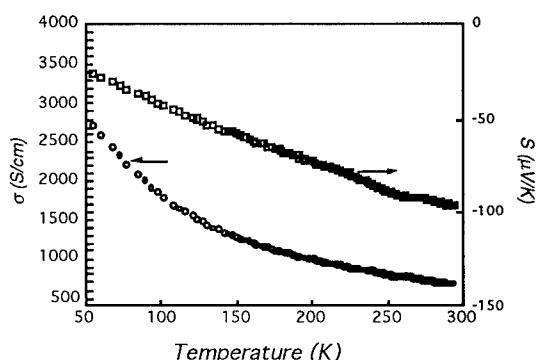


Figure 8. Electrical conductivity and thermopower data for annealed single crystal specimens of β -K₂Bi₈Se₁₃ as a function of temperature.

Based on these results β -K₂Bi₈Se₁₃ and K_{2.5}Bi_{8.5}Se₁₄ seem to be quite promising as thermoelectrics. The figure of merit (ZT) as a function of temperature for “as prepared” β -K₂Bi₈Se₁₃ is shown in Figure 9A. The room temperature zT value is 0.22 (0.39 if the lower κ

value of 0.83 W/m-K is considered. By comparison *optimized* Bi_2Te_3 has a ZT of 0.87 [2]. Given that the compounds reported here have not been optimized, it may be fairer to compare the ZT of $\beta\text{-K}_2\text{Bi}_8\text{Se}_{13}$ with that of unoptimized (i.e. as prepared) Bi_2Te_3 which is typically in the neighborhood of 0.55. The better performance of Bi_2Te_3 derives mainly from its higher electrical conductivity ($\sigma \sim 850 \text{ S/cm}$) since the thermopower of the materials reported here is comparable while their thermal conductivity is lower. Therefore, a reasonable approach to improve the thermoelectric figure of merit of the ternary compounds in this class could be sulfur doping or solid solutions of $\text{K}_x\text{Bi}_y(\text{SeS})_z$ based on the fact that sulfide compounds tend to adopt the same structure types as corresponding selenide compounds.

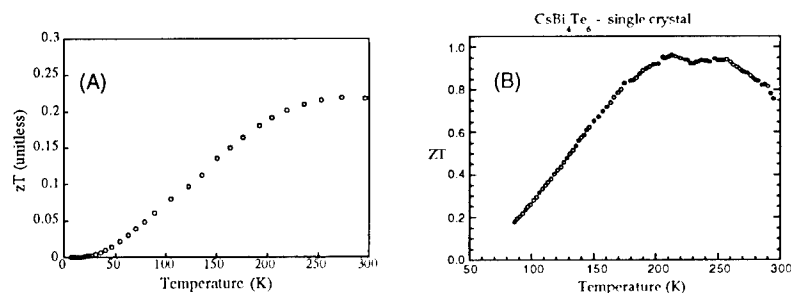


Figure 9. Temperature dependence of thermoelectric figure of merit (zT) for (A) crystals of $\beta\text{-K}_2\text{Bi}_8\text{Se}_{13}$. (B) for selected crystals of CsBi_4Te_6 .

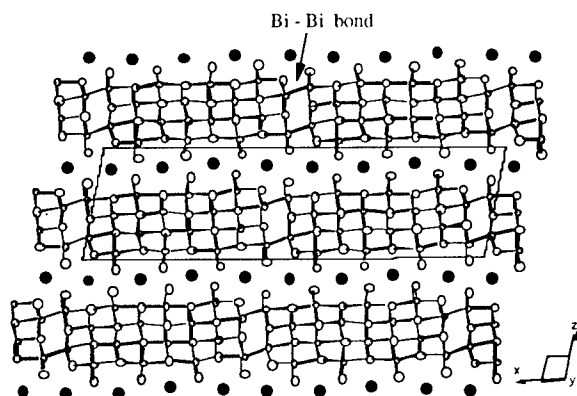


Figure 10. The structure of CsBi_4Te_6 . Large black circles are Cs atoms, open circles are Te atoms [12].

Finally, the new phase CsBi_4Te_6 also seems very promising [12, 13]. The compound is a layered anisotropic material which grows in a needle type morphology. It is composed of anionic $[\text{Bi}_4\text{Te}_6]$ layers alternating with layers of Cs ions, see Figure 10. The average oxidation state of Bi is less than three with some of the Bi atoms forming Bi-Bi bonds. The presence of such bonds is very unusual in bismuth chalcogenide chemistry and it is not clear at the moment whether they play a role in the enhanced thermoelectric properties of the material. The Bi coordination geometry is octahedral. Preliminary data show that crystals of CsBi_4Te_6

have room temperature electrical conductivities as high as 2440 S/cm which is much higher than that of optimized Bi_2Te_3 (~850 S/cm). The room temperature thermopower ranges from 90 to 120 $\mu\text{V/K}$, lower than the 220 $\mu\text{V/K}$ typically found for optimized Bi_2Te_3 . Thermal conductivity measurements on pressed pellets show values in the range 0.9-1.8 W/m·K which is comparable to that of Bi_2Te_3 . These values give rise to a relatively high room temperature ZT of 0.8 at a zT_{max} of 0.95. A plot of ZT versus temperature for selected crystals of CsBi_4Te_6 is shown in Figure 9B. To calculate the ZT we had to use thermal conductivity values obtained from a pressed pellet since we are unable to make such measurements on small single crystals. Therefore, the true ZT values may be off by 20-30%. Another important point is: does the Wiedeman-Franz law apply in such narrow gap semiconductors and if yes how much of the κ_{el} is accounted for by the measured value of the pressed pellet? To best address this question we need to obtain thermal conductivity data on large single crystals of CsBi_4Te_6 . Work to obtain such specimens is now under way. Nevertheless, these values are some of the highest ever reported (near room temperature) for a material other than Bi_2Te_3 , and we are optimistic that improvements in the sample preparation of CsBi_4Te_6 as well as appropriate doping will result in significant enhancements in these properties to approach or surpass those of Bi_2Te_3 . For further discussion of these results see reference 13.

CONCLUDING REMARKS

Exploratory synthetic investigations in complex bismuth chalcogenides are revealing new materials with promising thermoelectric properties. Several new compounds have been identified which show high enough zT values without any attempts at optimization. We believe further work of this type will uncover other equally interesting new phases. The most promising phases so far are BaBiTe_3 , $\beta\text{-K}_2\text{Bi}_8\text{Se}_{13}$, $\text{K}_{2.5}\text{Bi}_{8.5}\text{Se}_{14}$ and CsBi_4Te_6 , although $\text{KBi}_{6.33}\text{S}_{10}$ could also be viable if its doping could be controlled. One of the most valuable lessons we have learned in this study is that by creating complex multinary compounds with lower symmetry and larger cell asymmetric units, the thermal conductivity of thermoelectric materials can be decreased substantially below that of optimized Bi_2Te_3 . We believe the outlook for discovering new second generation thermoelectrics with enhanced performance is bright.

Acknowledgments Financial support from the Office of Naval Research (contract # N00014-94-1-0935, MGK and CRK and N00014-96-1-0181 for C.U.) is gratefully acknowledged. At NU this work made use of Central Facilities supported by NSF through the Materials Research Center (DMR-96-32472).

References

1. (a) *Naval Research Reviews*, 1996, vol. XLVIII, references therein. (b) Hicks, L. D.; Dresselhaus, M. S. *Phys. Rev. B*, 1996, 53, 1103.
2. (a) B. C. Sales, D. Mandrus, R. K. Williams, *Science*, **1996**, 272, 1325. (b) T. M. Tritt, *Science* 1996, 272, 1276.
3. *CRC Handbook of Thermoelectrics*; Rowe, D. M., Eds.; CRC Press, Inc.: Boca Raton, FL, 1995; references therein.
4. Sutorik, A. C.; Kanatzidis, M. G. *Prog. Inorg. Chem.* **1996**, 43, 151-265.
5. Chung, D.-Y.; Jovic, S.; Hogan, T.; Kannewurf, C. R.; Brec, R.; Rouxel, J.; Kanatzidis, M. G. *J. Am. Chem. Soc.*, **1997**, 119, 2505-2515.
6. Encyclopedia of Materials Science and Engineering, *Thermoelectric Semiconductors*; MIT Press: Cambridge, MA; Pergamon Press: Oxford, 1986, pp. 4968.

-
7. Kittel, C. *Introduction to Solid State Physics*, 6th Eds.: John Wiley & Sons, Inc.: 1986, p150.
 8. Kanatzidis, M. G.; McCarthy, T. J.; Tanzer, T. A.; Chen, L. -H.; Iordanidis, L.; Hogan, T.; Kannewurf, C. R.; Uher, C.; Chen, B. *Chem. Mater.*, **1996**, 8, 1465-1474
 9. Cordier, G.; Schäfer, H.; Schwidetzky, C. *Rev. Chim. Miner.* , **1985**, 22, 631-638
 10. Chung, D.-Y.; Choi, K.-S.; Iordanidis, L.; Schindler, J. L.; Brazis, P.; Kannewurf, C. R.; Chen, B.; Hu, S.; Uher, C.; Kanatzidis, M. G. submitted for publication.
 11. McCarthy, T. J.; Ngeyi, S.-P.; Liao, J.-H.; DeGroot, D.; Hogan, T.; Kannewurf, C. R.; Kanatzidis, M. G., *Chem. Mater.*, **1993**, 5, 331-340.
 12. Chung, D.-Y.; Hogan, T.; Chen, X.; Schindler, J.; Brazis, P.; Kannewurf, C. R.; Chen, B.; Hu, S.; Uher, C.; Kanatzidis, M. G. submitted for publication.
 13. Schindler, J.; Hogan, T.; Brazis, P.; Kannewurf, C. R.; Chung, D.-Y.; Kanatzidis, M. G. "Electrical Properties and Figures of Merit for New Chalcogenide-Based Thermoelectric Materials" presented at Materials Research Society Spring Meeting, Symposium Q, 1997. See elsewhere in this volume.
 14. Chung, D.-Y.; Hogan, T.; Sportouch, S.; Brazis, P.; Kannewurf, C. R.; Kanatzidis, M. G. to be submitted for publication.
 15. Iordanidis, L.; McCarthy, T.; Brazis, P.; Kannewurf, C. R.; Kanatzidis, M. G. to be submitted for publication.
 16. Chung, D.-Y.; Hogan, T.; Brazis, P.; Kannewurf, C. R.; C.; Kanatzidis, M. G. to be submitted for publication.
 17. Chung, D.-Y.; Brazis, P.; Kannewurf, C. R.; Kanatzidis, M. G. to be submitted for publication.

AUTHOR INDEX

- Aivazov, A.A., 279
 Ando, S., 273

 Behr, G., 255
 Boatner, Lynn A., 199, 217
 Borca-Tasciuc, T., 85
 Borshchevsky, A., 103, 175
 Brazis, Paul W., 327, 333
 Broido, D.A., 161
 Bucher, E., 109
 Budaguan, B.G., 279

 Caillat, T., 103, 175
 Chakoumakos, B.C., 199
 Chen, Baoxing, 315, 333
 Chen, G., 85
 Cho, Sunglae, 67
 Choi, Jae Shik, 121, 151
 Christen, Hans-Martin, 217
 Chung, Duck-Young, 327, 333
 Colpitts, T., 73, 145
 Cronin, S.B., 55

 Dai, P., 199
 Darling, T.W., 199, 231
 DiVenere, Antonio, 67
 Dresselhaus, G., 55
 Dresselhaus, M.S., 55, 169

 Ehrlich, A.C., 37

 Fakhruddin, M., 249
 Feger, C., 249
 Fess, K., 109
 Fleurial, J-P., 103, 175
 Freeman, E.J., 199
 Freibert, F., 231

 Gajewski, D.A., 199
 Gillespie, D.J., 37
 Gimán, Y., 133
 Griessmann, H., 255

 Hasegawa, M., 267
 Heinrich, A., 255
 Hoffman, Craig A., 67
 Hogan, Tim P., 327, 333
 Hohl, H., 109
 Hornbostel, Marc D., 211
 Hu, S., 315
 Hwu, S.J., 249
 Hyun, Dow-Bin, 121, 151

 Inoue, M., 133
 Iordanidis, Lykourgos, 333

 Johnson, A., 249
 Johnson, David C., 211

 Jung, Boo Yang, 121

 Kaefer, W., 109
 Kakemoto, H., 273
 Kanatzidis, Mercouri G., 327, 333
 Kannewurf, Carl R., 327, 333
 Katsumata, H., 267
 Keppens, V., 199
 Ketterson, John B., 67
 Kim, Hee-Jeong, 151
 Kim, J., 127
 Kim, S.G., 187
 Kloc, Ch., 109
 Kobayashi, N., 267
 Koga, T., 55
 Kolis, J., 249
 Kramer, C.D., 309
 Kulbachinskii, V.A., 133

 Lange, H., 255
 Lee, C., 127, 139
 LeGault, S., 321
 Levy, F., 249
 Littleton, Jr., R.L., 249
 Lyon, Jr., H.B., 285

 Mahan, G.D., 223
 Makhachev, K.B., 279
 Makita, Y., 267, 273
 Mandrus, David G., 199, 217
 Mangistu, E., 157
 Maple, M.B., 199
 Mateeva, N., 243
 Mazin, I.I., 187
 Meisner, G.P., 315
 Meyer, Jerry R., 67
 Migliori, A., 199, 231
 Morelli, Donald T., 297, 315
 Moshopoulou, E., 231

 Neagu, M., 85
 Negishi, H., 133
 Niculescu, H., 243
 Nolas, George S., 91
 Nordstrom, L., 187
 Norton, David P., 217

 Obara, A., 273
 Oh, Tae Sung, 121, 151
 Ohta, T., 115

 Park, K., 127, 139
 Pastor, M., 279
 Payne, J.E., 157

 Ramirez, A.P., 109
 Reinecke, T.L., 161

Sakuragi, S., 273
 Sales, Brian C., 199, 217
 Sarrao, J.L., 231
 Sasaki, M., 133
 Schindler, Jon L., 327, 333
 Schlenoff, J., 243
 Sellinschegg, Heike, 211
 Seo, J., 127, 139
 Sharp, Jeff W., 15, 91
 Shtern, Y.I., 279
 Singh, D.J., 187
 Slack, Glen A., 47
 Stroud, R.M., 321
 Sun, X., 55, 169

 Takada, T., 267
 Tanner, M.O., 169
 Teichert, S., 255
 Tessema, G.X., 157
 Testardi, L., 243
 Thompson, J.R., 199

 Thurner, Ch., 109
 Tritt, Terry M., 25, 249, 321
 Trugman, S.A., 231
 Tsai, Y., 273
 Tsukamoto, T., 273

 Uekusa, S., 267
 Uher, Ctirad, 315, 333

 Venkatasubramanian, R., 73, 145
 Verebelyi, D.T., 157, 249
 Vining, C.B., 3
 Volckmann, Edward H., 91

 Wang, K.L., 55, 169
 Watko, E., 145
 Williams, R.K., 199
 Wilson, M.L., 249, 321
 Wong, George K., 67

 Yamamoto, A., 115

SUBJECT INDEX

- β -FeSi₂, 273
- β -Zn₄Sb₃, 187
- δ -doping, 169
- advanced thermoelectric materials, 297
- antimonide, 91, 199
- automotive applications, 297

- Bi, 67
- biomedical engineering, 309
- Bi_{1-x}Sb_x, 67, 91
- Bi-Sb-Te, 115
- Bi_{0.5}Sb_{1.5}Te₃, 127, 139
- (Bi_{1-x}Sb_x)₂Te₃, 121
- bismuth, 63
- Bi_{2-x}Sn_xTe₃, 133
- Bi₂Te₃, 127
- Bi₂(Te_{1-x}Se_x)₃, 151
- Bi₂Te_{2.85}Se_{0.15}, 127
- Boltzmann transport, 85

- caged atoms, 47
- chalcogenides, 327, 333
- characterization and measurement, 25
- clathrate, 47
- climate control, 297
- conducting polymers, 243
- CoSb₃, 217
- cryogenic refrigeration, 231
- crypto-clathrate, 47

- ECPG, 199
- efficiency, 3
- electric resistivity, 133, 321
- electrical
 - conductivity, 37, 255
 - power output, 115
- electron(-)
 - beam-deposition, 267
 - crystal, phonon-glass, 199
- Ettingshausen effect, 231
- experimental proof-of-principle, 58

- fermiology, 37
- FeSi₂ with Mn, 267
- figure of merit, 3, 55, 103, 127, 139, 169, 223, 285, 315
- filled skutterudite, 91, 175, 199, 297
- fluorescence spectroscopy of ablation plume, 273

- graded structure, 115

- Hall
 - conductivity, 255
 - effect, 133

- heat
 - cycles, 3
 - pumps, 280
 - transfer, 85
 - transport, 161
- heating and cooling systems, 297
- HfNiSn, 109
- hot
 - extrusion, 139
 - pressing, 127

- impurity band, 133
- insulin, 279
- International Space Station, 309
- iron disilicide, 255

- KSnSb, 91

- La(Fe,Co)₄Sb₁₂, 187
- LaFe₃CoSb₁₂, 199
- laser ablation, 273
- low(-)
 - dimensional, 249
 - temperature, 211
- Lunar-Mars exploration, 309

- mechanical alloying, 121, 151
- metalorganic chemical vapor deposition, 145
- metastable, 211
- MgAgAs-type structure, 109
- Mir, 309
- mobility, 15
- modulated elemental reactants, 211
- multivalley, 15

- narrow bandgap semiconductors, 110
- NASA, 309
- ⁵⁵Nb⁺-implantation into β -FeSi₂ layers, 267
- new materials, 285
 - search, 231
- nonlinear Hall effect, 255
- n-type, 151

- I-V and C-V measurements, 267
- 1-1-1 intermetallic semiconductors, 297
- optical absorption, 273

- Peltier
 - coolers, 121
 - cooling modules, 151
 - effect, 25, 279
- pentatelluride, 249
- phonon-drag thermopower, 255
- PIES, 115
- p-n diode characteristics, 267

polyacetylene, 243
 polyaniline, 243
 polychalcogenide fluxes, 334
 polypyrrole, 243
 powder processing, 121
 p-type, 121
 β -FeSi₂, 267
 pulsed laser deposition, 217

 quantum
 confinement, 73, 169
 wells, 59
 quasicrystals, 321
 quasi-one-dimensional, 157

 Raman scattering, 273
 rare earth, 223
 refrigeration, 285
 resistivity, 249
 resonant ultrasound spectroscopy, 200

 scattering of carriers, 133
 Seebeck
 coefficient, 37, 139, 145
 effect, 15
 semiconductors, 91
 Si/Si_{1-x}Ge_x, 169
 skutterudite, 175, 187, 211, 217, 315
 solid solution, 103, 113
 superlattice(s), 67, 73, 85, 161
 synthesis, 334
 systems approach, 285

 Te dopant, 139
 ternary, 175
 theoretical modeling, 57

 thermal conductivity, 15, 37, 47, 73, 85,
 103, 145, 157, 175, 201, 315, 321, 337
 thermodynamic, 3
 thermoelectricity, 243
 thermoelectric(s), 15, 47, 55, 73, 91, 121,
 151, 157, 161, 169, 175, 187, 218, 223,
 249, 285, 309, 321
 cooling, 231
 container, 279
 devices, 279
 device, 73
 generator, 297
 materials, 25, 37, 85, 315, 327
 power, 67, 133, 321
 process, 3
 properties, 109, 127, 139
 thermomagnetic cooling, 231
 thermopower, 25, 249, 255, 315, 333
 thermostabilization, 280
 thin film, 67, 217
 Ti₂Mo₆Se₆, 157
 TiNiSn, 109
 transport, 161
 measurements, 327
 tunneling, 161
 2d
 quantum wells, 55
 systems, 55

 van der Pauw, 267

 x-ray diffraction, 273

 zinc antimonide, 103
 ZnSb films, 145
 ZrNiSn, 109
 Z(T), 169